Conference Proceedings of the Society for Experimental Mechanics Series

Tom Proulx *Editor*

Linking Models and Experiments, Volume 2

Proceedings of the 29th IMAC, A Conference on Structural Dynamics, 2011

SEM Springer

Conference Proceedings of the Society for Experimental Mechanics Series

For other titles published in this series, go to
www.springer.com/series/8922

Tom Proulx
Editor

Linking Models and Experiments, Volume 2

Proceedings of the 29th IMAC, A Conference on Structural Dynamics, 2011

Springer

Editor
Tom Proulx
Society for Experimental Mechanics, Inc.
7 School Street
Bethel, CT 06801-1405
USA
tom@sem1.com

ISSN 2191-5644 e-ISSN 2191-5652
ISBN 978-1-4419-9304-5 e-ISBN 978-1-4419-9305-2
DOI 10.1007/978-1-4419-9305-2
Springer New York Dordrecht Heidelberg London

Library of Congress Control Number: 2011922749

© The Society for Experimental Mechanics, Inc. 2011
All rights reserved. This work may not be translated or copied in whole or in part without the written permission of the publisher (Springer Science+Business Media, LLC, 233 Spring Street, New York, NY 10013, USA), except for brief excerpts in connection with reviews or scholarly analysis. Use in connection with any form of information storage and retrieval, electronic adaptation, computer software, or by similar or dissimilar methodology now known or hereafter developed is forbidden.
The use in this publication of trade names, trademarks, service marks, and similar terms, even if they are not identified as such, is not to be taken as an expression of opinion as to whether or not they are subject to proprietary rights.

Printed on acid-free paper

Springer is part of Springer Science+Business Media (www.springer.com)

Preface

Linking Models and Experiments represents one of six clusters of technical papers presented at the 29th IMAC, A Conference and Exposition on Structural Dynamics, 2011 organized by the Society for Experimental Mechanics, and held in Jacksonville, Florida, January 31 - February 3, 2011. The full proceedings also include volumes on: Advanced Aerospace Applications, Modal Analysis, Civil Engineering, Rotating Machinery, Structural Health Monitoring, Shock and Vibration; and Sensors, Instrumentation, and Special Topics.

Each collection presents early findings from experimental and computational investigations on an important area within structural dynamics. The current volume on *Linking Models and Experiments* includes studies on Finite Element Techniques, Model Updating, Experimental Dynamics Substructuring, Model Validation, and Uncertainty Quantification.

Modeling and simulation are major tools for today's engineers. It is, therefore, important that models and simulations be critically examined and modified to reflect real-world results. This grouping brings together researchers and engineers interested in this area. It provides a forum to facilitate technical interaction and exchange.

The organizers would like to thank the authors, presenters, session organizers and session chairs for their participation in this track.

Bethel, Connecticut

Dr. Thomas Proulx
Society for Experimental Mechanics, Inc

Contents

1 Modal Testing and FE-model Validation of Azimuthing Thruster 1
V. Nieminen, VTT Technical Research Centre of Finland; M. Tervonen, Seinäjoki University of Applied Sciences

2 POD Based Computation of Joint Interface Modes 19
W. Witteveen, University of Applied Sciences - Wels; K. Sherif, Linz Centre of Mechatronics GmbH

3 Area Wise Application of Contact Constraints in Reduced Mechanical Systems 29
W. Witteveen, University of Applied Sciences - Wels

4 On the Extension of Global Vibration Modes With Ritz-vectors Needed for Local Effects 37
K. Sherif, Linz Centre of Mechatronics GmbH; W. Witteveen, University of Applied Sciences; H. Irschik, H. Holl, Johannes Kepler University - Linz; K. Mayrhofer, Siemens VAI Metals Technologies GmbH

5 Direct Decoupling of Substructures Using Primal and Dual Formulation 47
W. D'Ambrogio, Universita dell'Aquila; A. Fregolent, Universita di Roma La Sapienza

6 Spectral Analysis of Vibrating Plates With General Shape 77
G. Catania, S. Sorrentino, University of Bologna

7 Smoothing Experimental Data in Dynamic Substructuring of Built up Systems 89
A. Culla, Università di Roma La Sapienza; W. D'Ambrogio, Università dell'Aquila; A. Fregolent, A. Schiavone, Università di Roma La Sapienza

8 Metrics for Diagnosing Negative Mass and Stiffness When Uncoupling Experimental and Analytical Substructures 111
M.S. Allen, D.C. Kammer, University of Wisconsin-Madison; R.L. Mayes, Sandia National Laboratory

9 Propagation of Free-interface Substructure Uncertainty into System Test-analysis Correlation 135
D.C. Kammer, S. Nimityongskul, D. Krattiger, University of Wisconsin

10 **Feature Extraction for Structural Dynamics Model Validation** 153
M. Nishio, University of Tokyo; F. Hemez, Los Alamos National Laboratory; K. Worden, University of Sheffield; G. Park, Los Alamos National Laboratory; N. Takeda, University of Tokyo; C. Farrar, Los Alamos National Laboratory

11 **Hybrid Sets of Merged Data for Modal Model Applications** 165
L. Thibault, B. LeBlanc, P. Avitabile, University of Massachusetts Lowell

12 **Dynamic Uncoupling of a System Model for Component Identification** 173
D. Cloutier, P. Avitabile, University of Massachusetts Lowell

13 **Full Field Dynamic Stress/Strain From Limited Sets of Measured Data** 187
P. Pingle, P. Avitabile, University of Massachusetts Lowell

14 **Limited Experimental Displacement Data Used for obtaining Full-field Dynamic Stress Strain Information** 201
P. Pingle, P. Avitabile, University of Massachusetts Lowell

15 **A Survey of Techniques to Estimate the Uncertainty in Material Parameters** 219
T. Simmermacher, Sandia National Laboratories

16 **Construction of DEM-base Traffic Model Using Optimal Velocity Model** 231
T. Koizumi, N. Tsujiuchi, R. Akatsuka, Doshisha University

17 **Confidence Intervals of Modal Parameters During Progressive Damage Test** 237
M. Döhler, INRIA; F. Hille, BAM Federal Institute for Material Research and Testing; X.-B. Lam, L. Mevel, INRIA; W. Rücker, BAM Federal Institute for Material Research and Testing

18 **Identification of Material Properties of Composite Plates Utilizing Model Updating and Response Surface Techniques** 251
K. Gurses, B. Kuran, C. Gencoglu, Roketsan A.S.

19 **Globally Enriched Substructuring Techniques for Vibro-acoustic Simulation** 263
U. Tabak, D.J. Rixen, Delft University of Technology

20 **A Modal-geometrical Selection Criterion for Master Nodes: Numerical and Experimental Testing** 281
E. Bonisoli, C. Delprete, C. Rosso, Politecnico di Torino

21 **Robust Optimization and Quality Control in Spot Welded Structures** 297
Q.I. Bhatti, M. Ouisse, S. Cogan, Université de Franche-Comté

22 **Interface Reduction in the Dual Craig-Bampton Method Based on Dual Interface Modes** 311
D.J. Rixen, Delft University of Technology

23 **A Truly Hybrid Approach to Substructuring Problems Using Mixed Assembly and Implicit Solving Strategies** 329
S.N. Voormeeren, P.L.C. van der Valk, D.J. Rixen, Delft University of Technology

24 **Model Updating Methodologies for Multibody Simulation Models: Application to a Full-scale Wind Turbine Model** 349
S. Manzato, B. Peeters, A. Toso, H. Van der Auweraer, LMS International; R. Osgood, National Renewable Energy Laboratory

25 **DOF Reduction Strategy for Large Order Finite Element Models** 359
R.N. Coppolino, Measurement Analysis Corporation

26 **Understanding Large Order Finite Element Model Dynamic Characteristics** 367
R.N. Coppolino, Measurement Analysis Corporation

27 **FEM Sensitivity Method for Uncertainty and Reconciliation Analyses** 375
R.N. Coppolino, Measurement Analysis Corporation

28 **Uncoupling Techniques for the Dynamic Characterization of Sub-structures** 383
F.C. Batista, Polytechnic Institute of Leiria; N.M.M. Maia, University of Lisbon

29 **Receptance Based Normalization of Operational Mode Shapes** 393
D. Bernal, Northeastern University

30 **Fault Simulation in a Gearbox Using Finite Element Model Reduction Techniques** 399
L. Deshpande, N. Sawalhi, R.B. Randall, University of New South Wales

31 **Response Measurements of DMS Cabinets and Supporting Truss Structures Under Environmental and Transient Wind Loads** 411
R.W. Bolton, University of Southern Denmark; B. Phares, T.J. Wipf, Iowa State University

32 **Variance Decomposition in the Presence of Epistemic and Aleatory Uncertainty** 417
J. McFarland, D. Riha, Southwest Research Institute

33 **A Forecasting Metric for Predictive Modeling** 431
S. Atamturktur, Clemson University; F. Hemez, C. Unal, Los Alamos National Laboratory

Modal Testing and FE-model Validation of Azimuthing Thruster

Vesa Nieminen, Research Scientist, VTT Technical Research Centre of Finland, Vuorimiehentie 5, Espoo, P.O.Box 1000, FI-02044 VTT, Finland

Matti Tervonen, Principal Lecturer, D. Sc. (Tech.), Seinäjoki University of Applied Sciences, Kampusranta 9A, FI-60320 Seinäjoki, Finland (previously in ABB Marine Oy)

ABSTRACT

Vibratory behavior of an azimuthing thruster was studied with FE-models and the results were verified by full-scale experiments. Studied thruster systems are used both for main propulsion and for steering of vessels. Modeling techniques were developed to take into account the most significant factors and phenomena affecting on the vibration behavior of the structure in real operation conditions. Modeling of structural properties such as bearings, hydraulic steering system, electro-mechanical interaction and rotor dynamics were investigated. The FE-model included also a part of the ship structure. Influence of the surrounding water on the vibration behavior was also studied. A combined FE-model for the structure and surrounding water were constructed and natural frequencies and modes were calculated. Vibration measurements were conducted in dry dock as well as during normal ship operations. Modal parameters in air and in water during operations were determined experimentally. In water the excitation came from ice block impacts and the modal parameters were estimated by Operational Modal Analysis. Operational Deflection Shape analysis was also utilized. Differences between the calculated and experimentally determined modal parameters in air were found to be small. The calculated global natural frequencies in water also corresponded reasonably well with the measured ones.

Introduction

Operating conditions and vessel installations have great effects on the dynamic behavior of marine structures. This is one of the main challenges met when reliable simulation and dimensioning models were developed for Azipod® [1)] azimuthing thrusters, Fig. 1. So, the developed large and complicated FE-models had to be tested and verified in several stages and conditions.

The main goals of this and the larger background study have been:

- to find out all the phenomena that have significant effects on the dynamic behavior of the structure in real operating conditions
- to develop modeling principles and techniques to take into account the phenomena affecting considerably on the vibration behavior of the structure in real operation conditions
- to develop reliable measuring system for use in real severe operating conditions
- to make the simulation models more accurate by developing them according to the measurement results
- to find out explicit numerical values for the effects and significance of the real operating conditions on the dynamic behavior of the system

Full-scale dynamic tests with different analyses, i.e. conventional modal analysis, operating deflections shape analysis (ODS) and operational modal analysis (OMA), were performed both in dry-dock (thruster installed to the vessel but not in the water) and in totally real operation conditions. Modeling techniques and significance of the following topics for the vibration behavior were studied, see also Fig. 1:

- main supporting bearing, i.e. slewing bearing
- hydraulic steering system
- surrounding ship structure
- fluid-structure interaction

1) Azipod® is a registered trademark of ABB

T. Proulx (ed.), *Linking Models and Experiments, Volume 2*, Conference Proceedings of the Society for Experimental Mechanics Series 5,
DOI 10.1007/978-1-4419-9305-2_1, © The Society for Experimental Mechanics, Inc. 2011

- rotor bearings
- rotor dynamics
- electro-mechanical interaction between rotor and stator

Studied azimuthing thruster was designed for an ice-breaking vessel. The vessel had two azimuthing thrusters symmetrically both side of the center line of the ship hull. The overall length of the vessel was 100 m. Propulsion power of one thruster was 6.5 MW and mass of the thruster was about 160 tons.

Finite Element Modeling

The whole azimuthing thruster was modeled as well as a part of the surrounding ship structure. Parabolic brick and tetrahedron elements were used for casting parts as well as for forged parts while parabolic shell elements were used for structures made of welded plates. A finite element model of the azimuthing thruster is shown in Fig. 1. The model was created using the commercial finite element software I-DEAS 12 NX. The model contained about 206 000 elements and 445 000 nodes (without model of surrounding water).

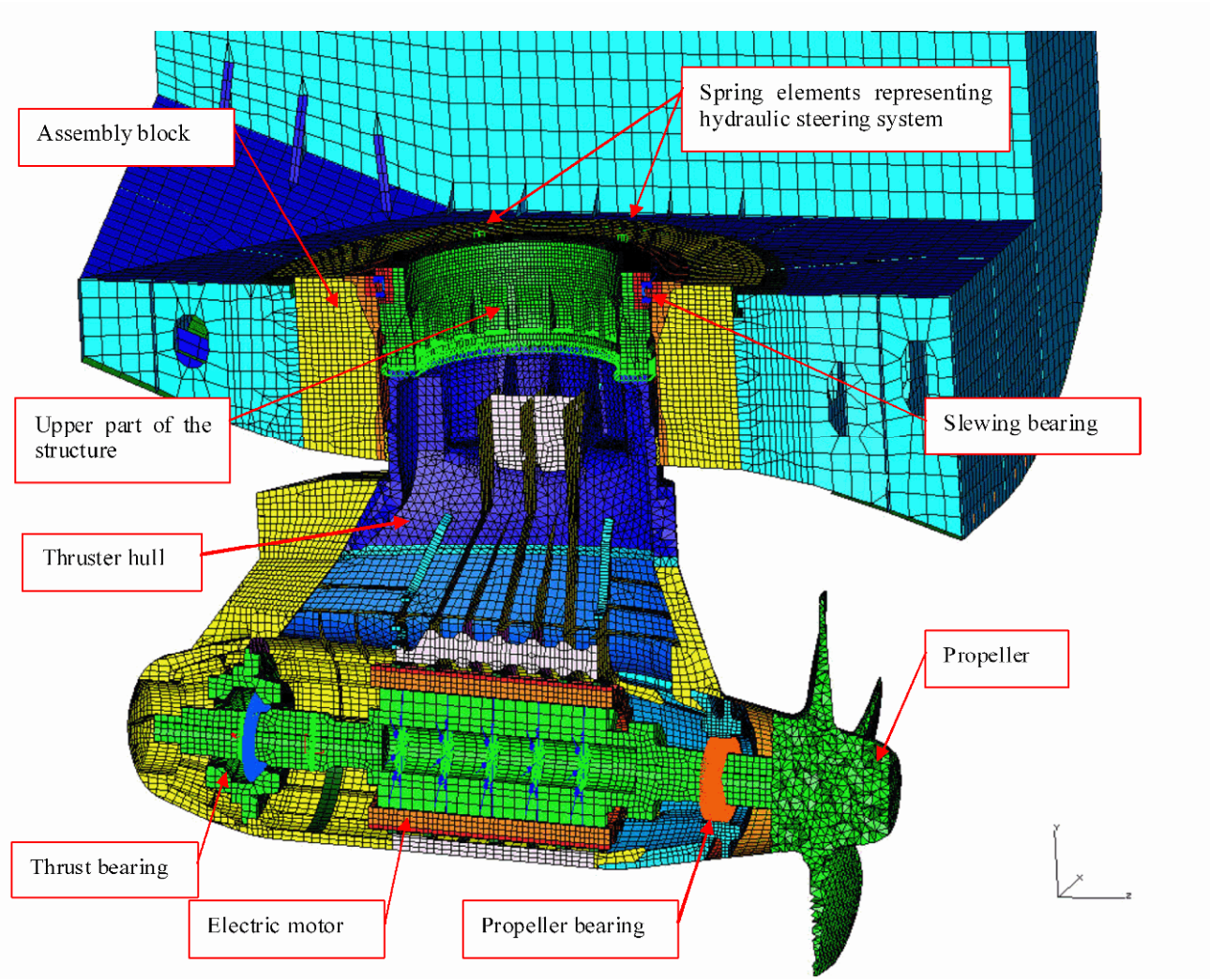

Fig. 1 Finite Element Model of azimuthing thruster and part of the surrounding ship structure (cross section)

Assembly Block and Surrounding Ship Structure

Lowest modes of the azimuthing thruster are strongly affected by stiffness properties of the surrounding structure, i.e. assembly block and the surrounding ship structure. The thruster is supported by the slewing bearing at the upper part of the thruster

structure so that all reaction forces during operation except steering moment goes through the slewing bearing from the thruster to the ship structure.

Modeling of whole ship structure is very laborious work. Therefore only part of the ship structure was modeled around the assembly block, which represents local stiffness properties of the ship structure. Boundary conditions of this section of the ship structure were varied and corresponding results were also compared to the experiments.

Lowest torsional and bending modes of the ship hull could be studied and included to the model for example by using an equivalent beam model. However, global dynamics of the ship hull was excluded from this study.

Slewing Bearing

Slewing bearing consist of three cylindrical rolling bearings, two axial and one radial as shown in Fig. 2. Individual rolling elements were modeled with two spring elements as shown in the figure. Load-deflection relationship of the individual rolling element and for the complete bearing was calculated according to the Herzian contact theory. Contact model between a cylinder and a plane was applied for axial rolling elements [1]. For radial cylindrical rolling elements equations derived in reference [2] was applied. These equations are also based on the Herzian contact theory.

The load-deflection relationships between rolling elements and bearing races are non-linear. The stiffness of individual rolling element contact was linearized around an operation point as follows:

$$k_a(F_a) = \frac{\partial F_a}{\partial \delta_a(F_a)} \tag{1}$$

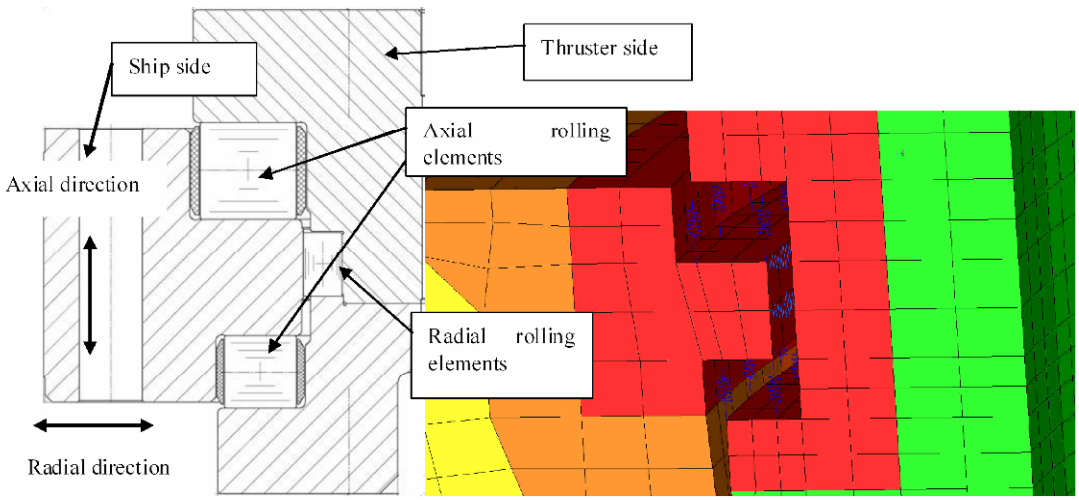

Fig. 2 Slewing bearing

Hydraulic Steering System

Steering moment of the azimuthing thruster is produced by four hydraulic motors. The hydraulic motors are driven by two adjustable-displacement hydraulic pumps, forming a closed hydraulic circuit.

The lowest rotational mode around steering axis is dominated by stiffness of this hydraulic steering system. Most of the flexibility originates from compressibility of the hydraulic fluid, flexibility of the pipelines and hoses. Flexibility of the steering gear mechanism (gear ring and pinions) was assumed to be significantly smaller than flexibility of the hydraulic system and these were neglected in the calculation. The hydraulic fluid "spring" was characterized by the value for the bulk modulus B. Mechanical compliance of the pipelines and hoses were taken into account by calculating radial displacement of the inner surface of the pipe due to internal pressure increase. By using this displacement "bulk modulus" for pipeline B_p and hoses B_h were calculated. The effective bulk modulus for the hydraulic system was then obtained by combining these bulk moduli analogously to the total resistance of parallel resistors as follows [3]:

$$B_e = \frac{1}{\frac{1}{B} + \frac{V_p}{V_{tot}}\frac{1}{B_p} + \frac{V_h}{V_{tot}}\frac{1}{B_h}} \quad (2)$$

where V_p is volume of the pipeline, V_h is volume of the hoses and V_{tot} total volume. By means of specific displacement (displacement/revolution) and specific torque (torque/pressure difference) of the hydraulic motor, stiffness of the hydraulic system was obtained.

Shaft Line

The thrust bearing consist of two spherical roller bearings having contact angle about 45 degrees. Thus, the thrust bearing was capable to carry both axial and radial loads. The propeller bearing was a toroidal roller bearing, so called CARB-type bearing. This type of bearing carries only radial load and allows both axial and angular deflections of the rotor shaft.

Stiffness of the thrust and propeller bearings at operational loads were also determined by the linearization method. The operational loads used for linearization were static reaction forces during normal operation. Cross coupling terms were neglected. Bearings were modeled as spring elements having stiffness coefficients equivalent to the bearing stiffness, radial and axial for thrust bearing and only radial for propeller bearing. One end of this spring element was connected to the shaft and other end by means of constraint equations to the outer race of the bearing housing.

It was found that radial stiffness of the bearings were much higher than bending stiffness of the rotor shaft. Therefore calculation results were not very sensitive to the bearing stiffness values.

Electromechanical Interaction

Magnetic field around the rotor of electrical machine induces electromagnetic forces between rotor and stator. When the rotor is not concentric with the stator bore, the magnetic forces are unbalanced around the rotor. The total force tends to deflect the rotor in the direction of minimum air gap. This force is called unbalanced magnetic pull (UMP). Because the force is directly proportional to the radial displacement of the rotor, it can be modeled by a spring having negative spring constant. Effect of this force is to reduce the effective spring constant of the shaft and thus reduce the rotor natural frequency. The spring constant can be roughly estimated by following equation [5]:

$$k_e = \frac{\pi d_r l_r B_r^{\,2}}{4\mu_0 \delta_0} \quad (3)$$

where d_r is inner diameter of the stator, l_r is stator core length, B_r is amplitude of magnetic flux density, μ_0 is permeability of air and δ_0 is air gap length.

In FE-model the unbalanced magnetic pull was modeled by spring elements between stator and rotor. The elements were distributed in five cross sections and there were 8 spring elements in each cross section equally directed around the cross section so that total negative spring constant in the radial direction equals the estimated value.

In reality the electromagnetically induced force consists of several harmonic components and has components also in axial and tangential directions. However, in this study these components were not taken into account.

Rotordynamics

Influence of gyroscopic forces caused by rotation for vibratory behavior of the shaft line was studied by a separate rotor model. As a consequence of the gyroscopic forces the natural frequencies of the rotor are functions of rotation speed and the natural modes split into forward and backward whirling modes. Considering angular momentum balance of spinning disk, it can be shown that linearized equations of motion for spinning disk become [6]:

$$\begin{Bmatrix} M_x \\ M_y \end{Bmatrix} = \begin{bmatrix} I_d & 0 \\ 0 & I_d \end{bmatrix} \begin{Bmatrix} \ddot{\alpha} \\ \ddot{\beta} \end{Bmatrix} + \Omega \begin{bmatrix} 0 & I_a \\ -I_a & 0 \end{bmatrix} \begin{Bmatrix} \dot{\alpha} \\ \dot{\beta} \end{Bmatrix} \qquad (4)$$

$$M_z = I_a \dot{\Omega}$$

where M_x and M_y are moments around two orthogonal axes perpendicular to the spin axis, α and β are angular deviations around corresponding x and y axes, M_z is moment around spin axis, I_d is diametral moment of inertia, I_a is moment of inertia around spin axis and Ω is angular velocity around spin axis. The second term in the equation (4) representing gyroscopic torques is called gyroscopic matrix. Considering a continuum model, gyroscopic matrix can also be derived for beam element. Equation of motion including the gyroscopic matrix cannot be diagonalized. However, the equation of motion can be written in state space form by defining new state vector $\boldsymbol{q}$ as follows [6]:

$$\begin{bmatrix} \boldsymbol{0} & \boldsymbol{M} \\ \boldsymbol{M} & \boldsymbol{C} \end{bmatrix} \begin{Bmatrix} \ddot{\boldsymbol{u}} \\ \dot{\boldsymbol{u}} \end{Bmatrix} + \begin{bmatrix} -\boldsymbol{M} & \boldsymbol{0} \\ \boldsymbol{0} & \boldsymbol{K} \end{bmatrix} \begin{Bmatrix} \dot{\boldsymbol{u}} \\ \boldsymbol{u} \end{Bmatrix} = \hat{\boldsymbol{A}}\dot{\boldsymbol{q}} + \hat{\boldsymbol{B}}\boldsymbol{q} = 0 \qquad (5)$$

where $\boldsymbol{M}$ and $\boldsymbol{K}$ are mass and stiffness matrices of the system and damping matrix $\boldsymbol{C}$ includes also terms caused by gyroscopic torques according to equation (4). This first order eigenvalue problem can be solved leading to complex eigenvalues and eigenvectors.

The rotor shaft was modeled by beam elements including also gyroscopic matrices. Propeller as well as rotor core was modeled as disk elements. Bearings were modeled as spring elements. Cross coupling terms were neglected. The model did not contain model of thruster body structure nor the ship structure. The model was constructed and solved by using a code created on Matlab environment.

Fluid-Structure Interaction

As the structure which is in contact with fluid vibrates, the fluid surrounding the structure must vibrate as well. This causes increasing of the kinetic energy and degreasing of natural frequencies of the total system. The coupled problem of fluid-structure interaction of thruster and surrounding water was solved by modeling also water domain with finite elements. The fluid was assumed to be compressible and inviscid medium. In addition small displacements were assumed. At an accelerating fluid-structure interface momentum and continuity considerations require that [8]:

$$\frac{\partial p}{\partial n} = -\rho \ddot{u}_n \qquad (6)$$

where p is the dynamic fluid pressure, n is direction of outward normal to the boundary, ρ is fluid density and $\ddot{u}_n$ is the normal component of fluid particle acceleration. At rigid wall right side of equation (6) equals zero. At free surface the surface waves were in this case neglected and the boundary condition used was $p = 0$. Boundary conditions are illustrated in Fig. 3. Generalization of equation (6) to three dimension is given as:

$$\nabla p = -\rho \frac{\partial^2 \{d\}}{\partial t^2} \qquad (7)$$

Definition of bulk modulus in three dimension is $p = -B \nabla \cdot d$. Three-dimensional wave equation can be constructed by taking divergence of equation (7) and differentiating definition of bulk modulus twice with respect to time, leading to:

$$\nabla^2 p = \frac{\rho}{B} \ddot{p} = \frac{1}{c^2} \ddot{p} \qquad (8)$$

where ∇^2 is Laplacian operator and $c = (B/\rho)^{0.5}$ is the wave speed in the fluid. Approximation of the dynamic pressure using the finite element method is then given by [9, 10, 11, 12]:

$$\tilde{p} = [N_f]\{p\} \tag{9}$$

where matrix $[N_f] = [N_1\, N_2 \ldots N_m]$ includes fluid element shape functions. Substituting approximation (9) into equations (8) and (7), using Galerkin's method of weighted residuals and applying Green's theorem, following equation can be derived:

$$\int_V (\{\nabla\}[N_f])^T \{\nabla\}[N_f]\{p\}dV - \rho\int_A [N_f]^T \{n\}^T [N_s]\{\ddot{u}_s\}dA + \frac{1}{c^2}\int_V [N_f]^T [N_f]\{\ddot{p}\}dV = \{0\} \tag{10}$$

where matrix $[N_s]$ includes structure element shape functions and $\{n\}$ denotes a unit normal vector pointing into the structure. Equation (10) can also be written shortly by:

$$\overline{Q}\,\ddot{p} + \overline{H}\,p - \rho\overline{L}\,\ddot{u}_s = \{0\} \tag{11}$$

In the structure point of view, a nodal force vector equivalent to the fluid pressure can be expressed using the pressure approximation (9) as:

$$\{r_t\} = \int_A [N_s]^T \{n\}pdA = \int_A [N_s]^T \{n\}[N_f]dA\{p\} = \overline{L}^T\{p\} \tag{12}$$

If external force of the structure and damping will be neglected, so called pressure formulation for the coupled fluid-structure problem can be expressed as [9]:

$$\begin{bmatrix} M & 0 \\ -\rho\overline{L} & \overline{Q} \end{bmatrix}\begin{Bmatrix} \ddot{u} \\ \ddot{p} \end{Bmatrix} + \begin{bmatrix} K & \overline{L}^T \\ 0 & \overline{H} \end{bmatrix}\begin{Bmatrix} u \\ p \end{Bmatrix} = \{0\} \tag{13}$$

where M and K are structural mass and stiffness matrices. Equation (13) is unsymmetric and therefore it is difficult to solve. However, the fluid-structure matrix system can be symmetrized for instance by defining new fluid unknown as presented in reference [13].

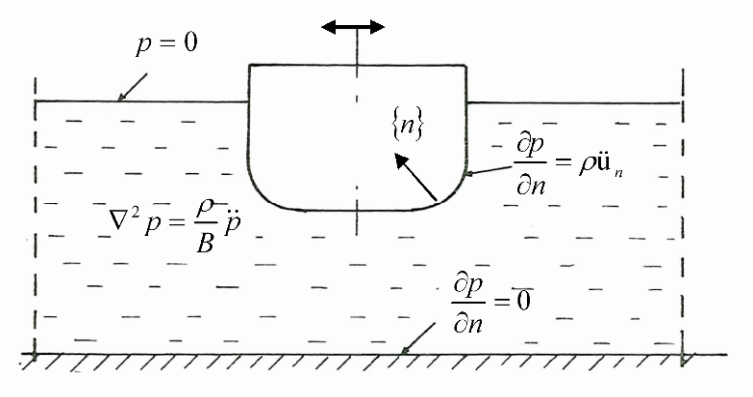

Fig. 3 Boundary conditions of the fluid

ABAQUS software was used to create and solve FE-model of combined structure and fluid [14]. Fluid was modeled with acoustic tetrahedron elements. Modeling of the water was first studied by a simple structure such as sphere and circular disk. Meshing properties such as element size, size of the water model and element order as well as boundary conditions at exterior surfaces of the water model were varied. Results of these simple finite element studies were compared with analytical solutions and with some experimental results found in the literature [7, 15, 16, 17, 18]. It was found that if the model of the fluid is large enough, boundary conditions at outer surfaces of the fluid has not significant effect on the natural frequencies of the structure. On the basis of these studies, water model for the azimuthing thruster was constructed. The water model contained about 267 000 elements and 55 000 nodes.

Experimental Studies

Experimental Modal Analysis in Dry Dock

Modal testing of the azimuthing thruster was carried out in dry dock. The thruster was excited by a pendulum made by mass of 50 kg, see Fig. 4. The steering mechanism was locked during testing. Excitation force was measured by an accelerometer installed on the end of the mass and response of the azimuthing thruster was measured by 10 triaxial accelerometers. Sampling frequency used was 512 Hz. Signal processing and FRF calculation was carried out by using LMS Scadas III front-end and LMS Cada-X software. Modal parameters (frequencies, modal damping ratios and mode shapes) were estimated using LMS TestLab and LMS Cada-X softwares [19, 20]. The parameters were estimated by using PolyMAX algorithm [21].

Frequency range of interest was from zero to the most significant excitation frequencies during normal operation. One of the most significant excitation was blade frequency.

Identified modes are presented in Table 1. For reasons of confidentiality all frequencies and modal damping factors in this paper are presented as scaled values. The reference frequency f_{ref} used in scaling is the natural frequency of first longitudinal mode of the azimuthing thruster measured in dry dock. Also the reference modal damping factor ζ_{ref} is the damping factor of first longitudinal mode of the azimuthing thruster measured in dry dock. Lowest transversal mode shape is shown in Fig. 6.

In order to quantify orthogonality or independency of measured modes, AutoMAC criterion [22, 23] was applied, see Fig. 5. MAC takes values between 0 and 1; the closer to 1 means high correlation, while the closer to 0 means that those modes are orthogonal or independent. As can be seen, between modes 1 and 2 there is quite high MAC value. These modes are global mode of the ship hull and lowest transversal mode of the thruster. Also there is quite high off-diagonal term in AutoMAC matrix between modes 6 and 7. These modes relates to vertical bending modes of the rotor. High off-diagonal values originate from the fact that the number of measuring points is too small to identify these modes (spatial aliasing). In order to identify global modes of the ship there should be more measuring points on the ship hull. Also there should be more measuring points on the rotor and propeller blades in order to identify more accurately rotor bending modes. However, used measuring points was noticed to be sufficient for identifying satisfactory the lowest modes.

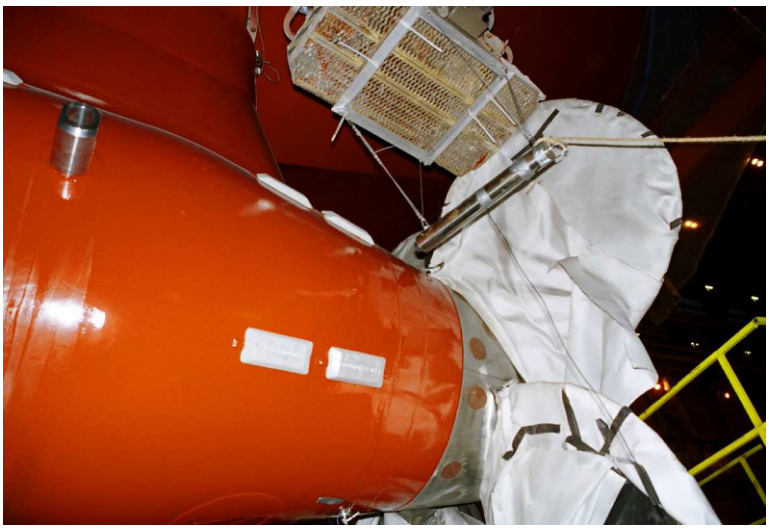

Fig. 4 Impact testing of thruster by using pendulum

Table 1 Measured modes of azimuthing thruster in air

Mode no	Frequency (f_i/f_{ref})	Modal damping (ζ_i/ζ_{ref})	Description
1	0,636	0,1	Global mode of astern ship hull
2	0,826	0,3	1st transversal mode
3	0,906	1,7	Rotation around steering axis
4	1,000	1,0	1st longitudinal mode
5	1,182	1,1	Global mode of the ship hull
6	2,217	1,5	Vertical bending of the rotor, vertical translation of the thruster in phase
7	2,501	0,8	Vertical bending of the rotor, vertical translation of the thruster out of phase
8	3,061	1,4	Transversal bending of the rotor, rotation of the thruster around steering axis out of phase
9	4,643	1,1	First elastic mode of the thruster hull, torsion around vertical axis

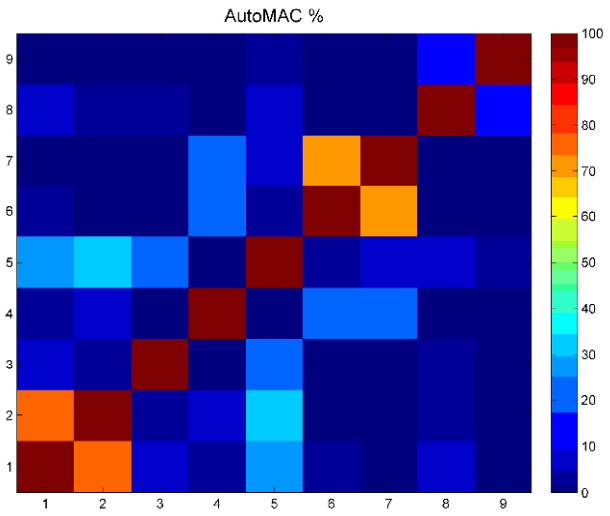

Fig. 5 AutoMAC for measured mode shapes

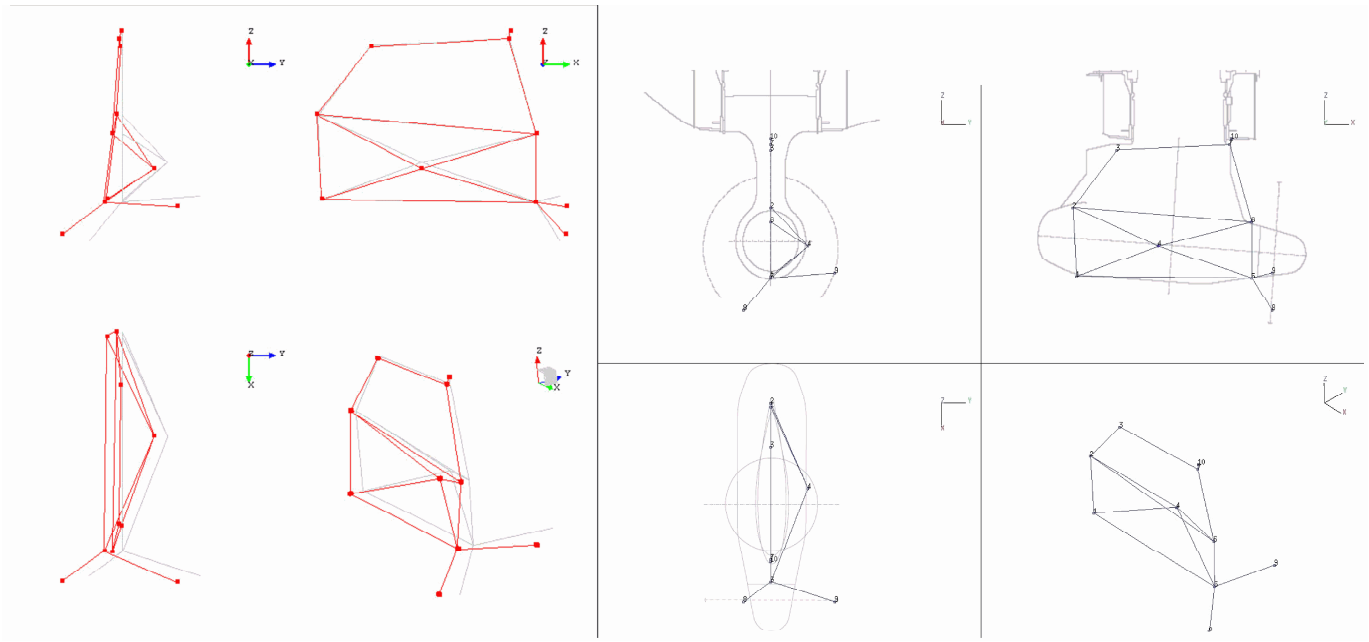

Fig. 6 Lowest transversal mode in air (left). Measuring points 8 and 9 are on two propeller blades. Point 10 is on the bottom of the ship hull

Calibration measurements by static forces

The azimuthing thruster was instrumented by several strain gages and other measuring devices for long-term ice load monitoring. The ice load measuring system was calibrated by applying external static forces on the propulsion unit in dry dock. The applied forces were measured by load cells. Radial relative displacement between the thruster body and the ship hull was also measured during calibrations with two inductive displacement sensors, see figure Fig. 7. These measurements provided information about flexibility of slewing bearing as well as thruster body for verification of the used FE-model.

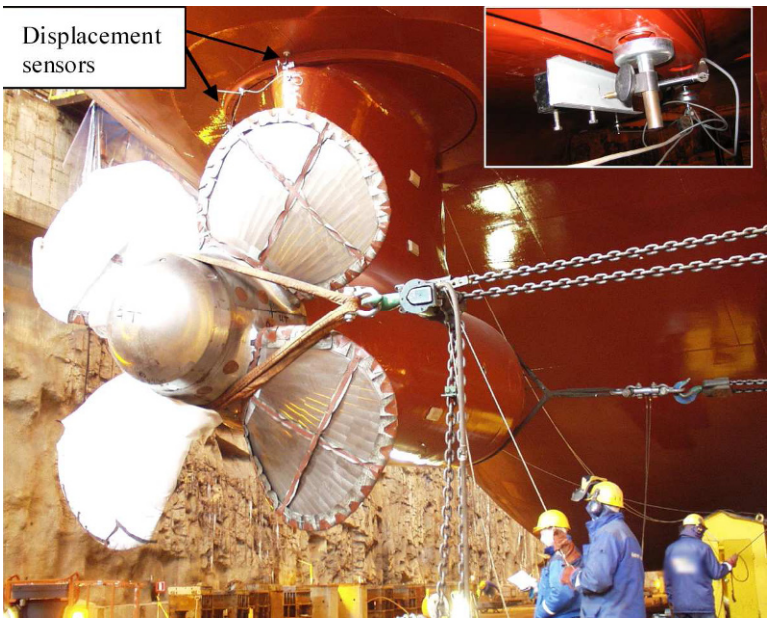

Fig. 7 Calibration of ice load measuring system in transversal direction

Measurements During Ship Operation

Vibrations of azimuthing thruster were measured during normal operation by accelerometers. Accelerations of propeller bearing housing as well as thrust bearing housing were measured by triaxial accelerometers. Vibrations of slewing bearing near the outer race were measured at four locations by uniaxial accelerometers. Shaft displacements relative to the bearing housings were measured by eddy current displacement sensors. Radial displacements at propeller bearing and thrust bearing were measured in two perpendicular directions. In addition axial displacement was measured at propeller bearing. Hydraulic pressure of the steering system was also measured. Several most important operational parameters of azimuthing thrusters and ship were also recorded, for example rotation speeds of the propellers and azimuthing angles.

During normal operation in ice conditions the most significant excitation came from the ice block impacts. When the propeller penetrated in the ice, the rotation speed of the propeller varied widely due to ice loads. Therefore the blade frequency and other harmonic excitation frequencies also changed, exciting the natural modes of the thruster. In this driving condition the excitation resembled periodic chirp excitation signal [23].

A typical 28 min long period where the vessel proceeded in ice was selected for the vibration analysis. Spectral map (vibration spectra as a function of time) for transversal acceleration of the propeller bearing is presented in Fig. 8. Fluctuation of the blade frequency component can be detected in the figure. The rotation speed varied between about 0.5…1 times the nominal speed. The first transversal mode of the azimuthing thruster at about 0.7 f_i/f_{ref} can be can be seen in the map.

Averaged autospectra are presented in Fig. 9. The number of averages was about 1700. On the averaging process the rotational speed related vibration components were averaged out due to relative high fluctuation of rotation speed. Most of the significant peaks in the averaged autospectra are natural frequencies of the thruster.

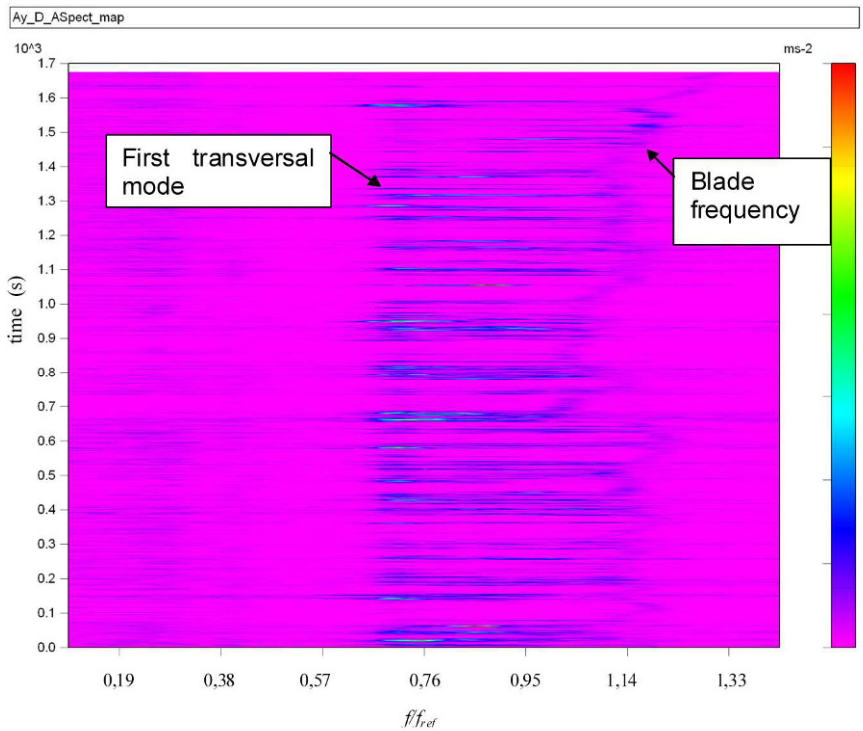

Fig. 8 Spectral map of transversal acceleration of propeller bearing.

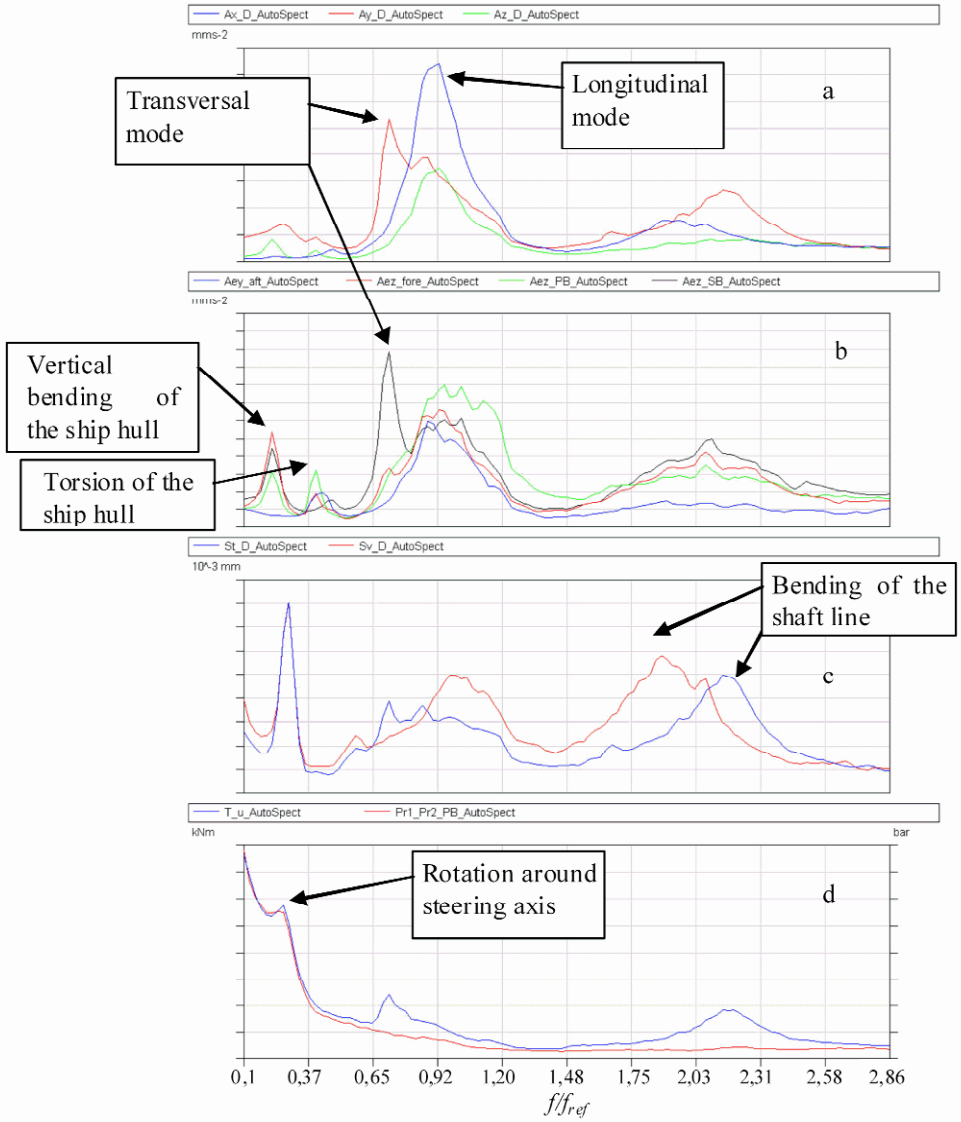

Fig. 9 Averaged autospectra. a: propeller accelerations (Ax = axial, Ay = transversal, Az = vertical), b: slewing bearing accelerations, c: relative shaft displacements at propeller bearing (St = transversal, Sv = vertical), d: torque of the thruster body around steering axis (T_u) and hydraulic pressure of the steering system (Pr1_Pr2)

Operating Deflection Shapes (ODS) at frequencies of most significant peaks in the averaged spectra were determined. It was found that these modes resembled natural mode shapes of the thruster.

Operational Modal Analysis (OMA) was also carried out in order to identify natural modes of the thruster during operation. Measured accelerations of 6 points were used and PolyMAX algorithm was applied for modal parameter identification [24]. Identified modal parameters are given in Table 2. Natural modes in air obtained from modal testing in dry dock are also presented in the table for comparison.

Lowest rotor bending modes were estimated by separate analysis. Before this analysis all measured accelerations were integrated twice and relative shaft displacement signals were summed to absolute bearing displacements in order to get absolute shaft displacements. Modal parameters of rotor bending modes were then estimated by PolyMAX algorithm by using these signals. It should be noted that the used OMA method does not include assumptions of nonlinearities and whirling modes. Therefore, obtained modal parameters of rotor bending modes contain uncertainties. However, it is possible that the natural frequencies obtained may be reasonably reliable.

Due to practical limitations the number of measuring points during operation was rather small. In order to get more accurate mode shape and damping estimates especially for higher modes it is recommended that more measuring points should be included in the analysis. However, in this case the used configuration was able to identify parameters for lowest modes of the thruster reasonably well, especially natural frequencies.

Table 2 Experimental modal analysis results

In dry dock		During operation in water (OMA)		
frequency (f_i/f_{ref})	damping (ζ_i/ζ_{ref})	frequency (f_i/f_{ref})	damping (ζ_i/ζ_{ref})	description
-	-	0,218	0,97	Global mode of the ship hull (apparently vertical bending)
0,906	1,69	0,279	4,31	Rotation around steering axis
-	-	0,402	0,34	Global mode of the ship hull (apparently torsion)
0,826	0,34	0,707	0,71	1st transversal mode
1,000	1,00	0,911	1,63	1st longitudinal mode
2,217	1,51	1,944	1,49	Vertical bending of the rotor, vertical translation of the thruster in phase
2,501	0,83	-	-	Vertical bending of the rotor, vertical translation of the thruster out of phase
3,061	1,40	2,178	1,40	Transversal bending of the rotor, rotation of the thruster around steering axis out of phase

Numerical Results and Correlation with Experiments

Azimuthing Thruster in Air

Before analyses the mass of the model of the mechanical structure was calculated. It was noted that the mass of the model was about 2 % smaller than weighted mass of the real structure. Considering the simplifications in the model the difference is quite small.

The ship had two azimuthing thrusters symmetrically both side of the centre line of the ship hull. Symmetrical boundary condition was applied at the centre line of the ship structure model in most of the analyses. Symmetric boundary condition implies that the thrusters vibrate transversally out of phase. At the other edges of the ship model displacements were fixed. Natural modes were also calculated with anti-symmetric boundary condition at the centre line, which implies that the thrusters vibrate in phase. The calculated transversal mode of the thruster with anti-symmetric boundary condition was about 2% higher than with symmetric boundary condition. Differences for the other global modes were negligible. Thus, it was concluded that coupling between the thrusters modes was rather small.

Influence of stiffness of the slewing bearing on the thruster modes was studied. Because the stiffness of the bearing depends on the loading, the stiffness was calculated with different loading scenarios. At first, gravity of the thruster was applied as evenly distributed load for the upper axial bearing. The lower axial bearing was assumed to have a clearance between rolling elements and bearing races, thus having no contact force and no stiffness. The goal was to simulate the corresponding modal testing condition in dry dock. It was found that frequency of the lowest transversal mode was about 6 % higher than the measured one and frequency of the longitudinal mode was about 3 % smaller than the measured one. Calibration measurements with static external force were also simulated in order to study static stiffness of the thruster. Results showed that the static stiffness in the transversal direction was about 9 % higher than measured one and stiffness in the longitudinal direction was about 4 % smaller than measured one.

Sensitivity analysis showed that stiffness of the axial slewing bearing had significant effect on the natural frequencies, while stiffness of the radial slewing bearing had only minor effect. It was noted that displacements between the upper rolling elements and the bearing race due to gravity of the thruster were very small, significantly smaller than for instance flatness tolerance of the raceway. Also due to challenging construction and installation of the assembly block and the slewing bearing, it is very difficult to determine the real stiffness distribution of the slewing bearing. However, it is possible to study possible variation range of the stiffness. Assuming that gravity of the thruster is evenly distributed for rolling elements of the upper axial bearing and lower axial rolling elements to be just in contact with very low contact force, the stiffness of the whole slewing bearing was found to increase about 52 % compared to the previous case. Assuming that rolling elements of upper axial bearing are just in contact with very low contact force and lower axial bearing having a clearance between rolling elements and raceway, the stiffness was found to degrease about 45 %. By changing the stiffness of individual rolling elements of axial slewing bearing in the model within limits described above, close results with experiments were achieved, see Table 3. Difference between calculated and simulated static stiffness of the thruster was also smaller, about 4.7 % in the transversal direction and 0.5 % in the longitudinal direction.

MAC-criterion was used to evaluate the correlation between experimentally determined and calculated mode shapes, see Fig. 10. As can be seen, diagonal values are over 70 % indicating good correlation for all modes except mode no 6 (transversal bending of the rotor). The rotation angle of the propeller was slightly different during testing compared to the model, which can be one possible reason for the low MAC value. Experimentally determined mode shapes were complex whereas numerically obtained were real modes. This can also contribute the MAC values.

Table 3 Numerical and experimental natural frequencies in air

No	Description	Numerical Frequency (f_i/f_{ref})	Experimental Frequency (f_i/f_{ref})	Difference (%)
1	1st transversal mode	0,840	0,826	1,7
2	Rotation around steering axis	0,929	0,906	2,6
3	1st longitudinal mode	0,990	1,000	-1,0
4	Vertical bending of the rotor, vertical translation of the thruster in phase	2,158	2,217	-2,7
5	Vertical bending of the rotor, vertical translation of the thruster out of phase	2,571	2,501	2,8
6	Transversal bending of the rotor, rotation of the thruster around steering axis out of phase	2,935	3,061	-4,1

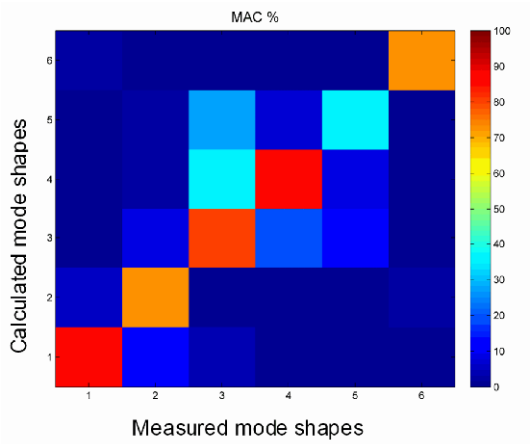

Fig. 10 MAC values between experimental and numerical mode shapes in air

Both experimental and numerical results showed that rotor modes are strongly coupled with the thruster. Therefore there is significant difference between frequencies of rotor transversal and vertical bending modes. In addition, the first vertical

bending mode was split into two modes, in the other mode the thruster body translates in phase and in the other mode the thruster body translates out of phase. Significant errors will be encountered if natural modes of the shaft line will be calculated without taking into account the whole azimuthing thruster and ship structure. Effect of the thruster body and surrounding structure on rotor bending modes are presented in Table 4.

Table 4 Effect of the thruster body and surrounding structure on rotor bending modes

Rotor model only, supported by bearings (spring elements)		Whole model of the azimuthing thruster (rotor + thruster body + part of the ship structure)		Measured, in air
freq. (f_i/f_{ref})	description	freq. (f_i/f_{ref})	description	freq. (f_i/f_{ref})
2,296	1st vertical bending	2,158	1st vertical bending, vertical translational mode of the thruster body in phase	2,217
		2,571	1st vertical bending, vertical translational mode of the thruster body out of phase	2,501
2,305	1st transversal bending	2,935	1st transversal bending, rotation of the thruster around steering axis out of phase	3,061
4,695	2nd vertical bending	4,856	2nd vertical bending	
4,776	2nd transversal bending	5,224	2nd transversal bending	

Results of separate rotordynamic studies are presented in Fig. 11. The Campbell diagram presents lowest natural frequencies of the rotor as a function of the rotation speed. Excitation frequencies of rotation speed as well as blade frequency are also shown in the diagram. Intersection of these lines and curves of natural frequencies indicates critical speeds. As can be seen, the natural modes were split into forward and backward whirling modes. Difference between forward and backward whirling frequencies of first mode at typical rotation speed was about 7 %. These results were not verified by experiments, but influence of the gyroscopic forces on natural frequencies can be evaluated by presented studies.

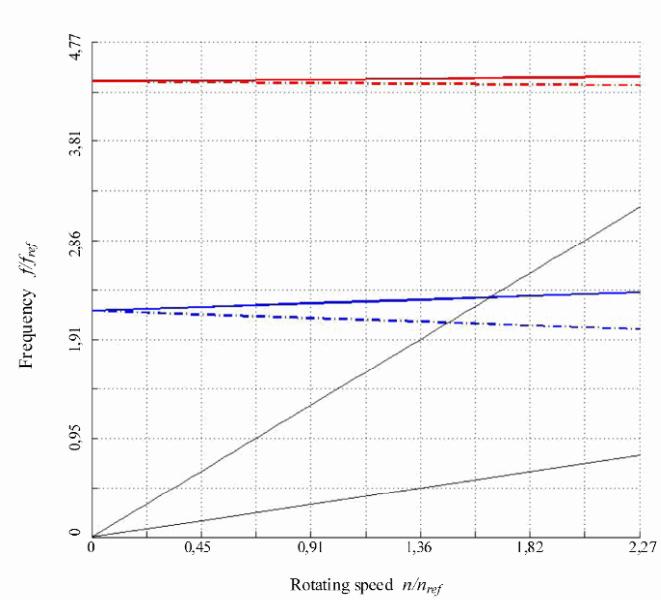

Fig. 11 Campbell diagram. Reference rotation speed n_{ref} is maximum rotation speed

Natural frequencies of the shaft line were calculated with and without UMP. Due to UMP the natural frequencies of shaft line was degreased only about 0.4 %. The banding stiffness of the rotor in this case was very high compared to the forces of UMP. Therefore, electromechanical interaction has only minor effect on the natural frequencies for this type of azimuthing thrusters.

A response analysis was carried out by using modal superposition method. Modal damping factors determined through experimental modal analysis were used. Excitation and response points were the same which were used modal testing in dry dock. Fig. 12 shows the Frequency Response Function (FRF) comparison at point near the propeller bearing. Excitation force has been directed in the transversal direction and acceleration response has also measured and calculated in the transversal direction. The lowest peaks in the measured FRF indicate global natural modes of the ship hull. These peaks can not be seen in the calculated FRF, because the model contained only small part of the ship structure.

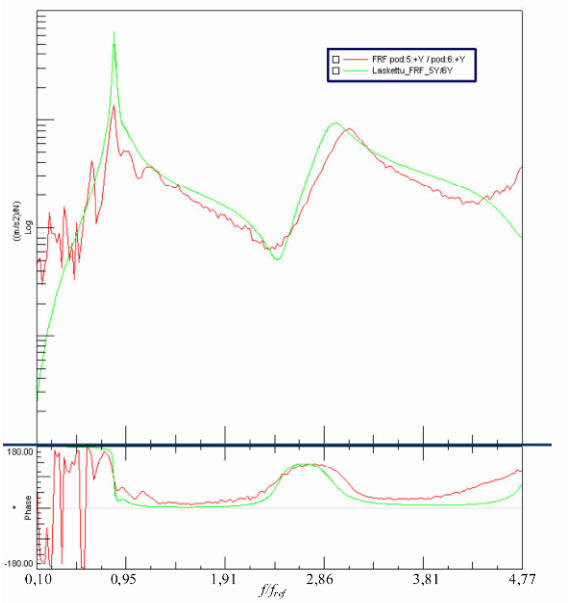

Fig. 12 FRF comparison of measured (red line) and FE-analysis (green line)

Azimuthing Thruster in Operation in Water

Comparison of calculated and experimentally determined natural modes during operation in water is presented in Table 5. The 6th column presents differences between natural frequencies in air and in water calculated by FE-model. The corresponding differences for experimentally determined natural frequencies are shown in the last column. As can be seen, the calculated natural frequencies of lowest global modes in water corresponded reasonably well with the measured ones. Due to added mass of the surrounding water, natural frequencies of the lowest longitudinal and transversal modes were degreased in this case about 5 % and 14 %, respectively. The lowest rotational mode around steering axis is dominated during operation by stiffness of the hydraulic steering system. During modal testing in dry dock the steering mechanism was locked. Therefore the natural frequency of this mode in water is significantly smaller than in air.

Calculated frequency of the lowest vertical bending of the rotor was about 6 % lower than experimentally determined one. Difference for transversal bending mode was even higher. Influence of the gyroscopic forces was not taken into account in this calculation. This can be one possible reason for the differences. It is possible that influence of the gyroscopic forces for the coupled shaft line bending and thruster translational modes is different than the previously presented studies with the shaft line model indicated.

Because vertical bending modes of the shaft line are coupled with vertical translation of the thruster, there are also significant deformations of the ship bottom. Therefore it is important that the structural-acoustic coupling is used between ship bottom and water model. Natural modes were also calculated without the coupling between ship bottom and water. It was found that the frequency of the vertical bending mode of the shaft line was increased as much as 14 % compared to the analysis where the coupling between the ship hull bottom and water was taken into account.

Table 5 Natural modes during operation in water

No	Description	FE-model, **in water** frequency (f_i/f_{ref})	Experi-mental **in water** frequency (f_i/f_{ref})	Difference FE-model - Experimen-tal **in water** (FE – Exp) (%)	**FE-model** Diff. in air – in water (in water – in air) (%)	**Experimental** Diff. in air – in water (in water – in air) (%)
1	Rotation around steering axis	0,277	0,279	-0,9	-69,7	-69,2
2	1st Transversal mode	0,724	0,707	2,4	-13,5	-14,3
3	1st Longitudinal mode	0,940	0,953	-1,4	-4,6	-4,7
4	Vertical bending of the rotor, vertical translation of the thruster in phase	1,806	1,920	-5,9	-17,1	-13,4
5	Vertical bending of the rotor, vertical translation of the thruster out of phase	2,098	-	-	-16,9	-
6	Transversal bending of the rotor, rotation of the thruster around steering axis out of phase	2,498	2,186	14,3	-15,3	-28,6

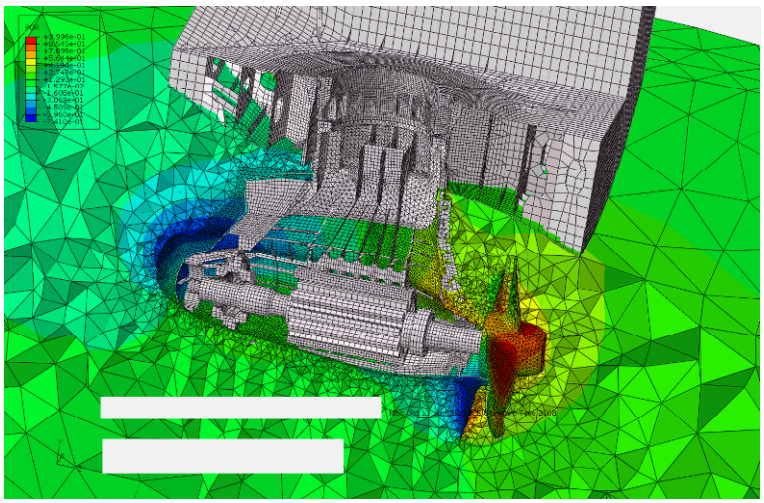

Fig. 13 First longitudinal mode shape in water. Pressure in the acoustic medium is presented as colors

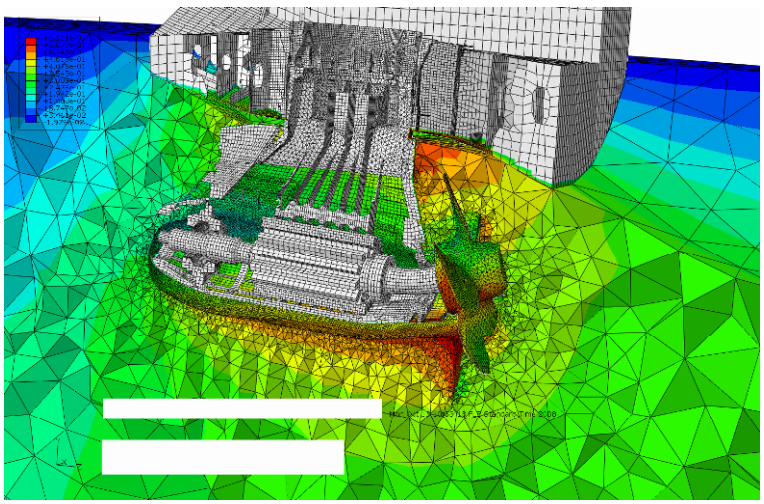

Fig. 14 Vertical bending mode of the rotor coupled with vertical translation of the thruster in phase

Conclusions

Close results were obtained from finite element analyses and experimental investigations. Maximum difference between calculated and experimentally determined natural frequencies in air was about 4 %. The calculated global natural frequencies in water also corresponded reasonably well with the measured ones. Due to the surrounding water natural frequencies of the lowest longitudinal and transversal modes were degreased in this case about 5 % and 14 %, respectively. Based on the modeling method presented in this paper, sufficiently accurate calculation results can be achieved.

From the modeling point of view the following conclusions can be made:

- Slewing bearing stiffness and local stiffness of ship affect significantly natural frequencies and modes
- Shaft line bending modes are strongly coupled with the global modes of the thruster body
- Fluid-structure interaction can be modeled with sufficient accuracy with the used modeling method
- Stiffness of the hydraulic steering system dominates the thruster rotation modes around steering axis
- Electromechanical interaction has only minor effect on the natural frequencies for this type of azimuthing thrusters

The presented case study proved applicability of OMA and ODS analyses in challenging operating conditions where conventional modal testing is practically impossible. These analyses provided necessary information for model verification. Due to practical limitations, the number of measuring points during operation was rather small. In order to get more accurate mode shape and damping estimates especially for higher modes, it is recommended that more measuring points should be included in the analysis. However, in this case used configuration was able to identify parameters for lowest modes of the thruster reasonably well.

In the future studies it is recommended that the gyroscopic effect will be taken into account with the whole model of the azimuthing thruster. This can be done for example by combining rotor model and the thruster body model using substructuring technique.

Acknowledgements

This paper is based on Master's Thesis "Modelling of Vibratory Behaviour of Azimuthing Thruster", in finnish. The thesis has been done for Helsinki University of Technology for department of Applied Mechanics in 2009. Financial support for this study was provided by ABB Marine.

References

1. Pilkey, Walter D. Formulas for stress, strain and structural matrices. John Wiley & Sons Inc, New York, ISBN 0-471-52746-7 1458 p. 1994.

2. Harris, Tedric A. Rolling Bearing Analysis. 4th Edition. John Wiley & Sons Inc, ISBN 0-471-35457-0, 1086 p. 2001.

3. Merritt, Herbert E. Hydraulic Control Systems. John Wiley & Sons, ISBN 0471596175. 357 p. 1967.

4. Jelali, Mohieddine & Kroll, Andreas. Hydraulic Servo-systems: Modelling, Identification, and Control. Springer, ISBN 1852336927, 9781852336929. 355 p. 2003.

5. Merrill, E.F. Dynamics of AC electrical machines. Industry Applications, IEEE Transactions on, Vol. 30:2. pp. 277-285. 1994.

6. Ehrich, Fredric F. Handbook of Rotordynamics. McGraw-Hill, ISBN 0070193304. 496 p. 1992.

7. Blevins, R.D. Formulas for natural frequency and mode shape, New York: Van Nostrand Reinhold, ISBN 0-442-20710-7. 492 p. 1979.

8. Junger, M. C. & Feit, D. Sound, Structures, and Their Interaction. 2nd Edition. The MIT Press, Cambridge, Massachusetts, London. MA ISBN 0-262-10034-7. 448 p. 1986.

9. Everstine, G.C. Finite element formulations of structural acoustics problems. Computers & Structures, Vol. 65 (3). pp. 307-321. 1997.

10. Pani, P.K. & Bhattacharyya, S.K. Fluid-structure interaction effects on dynamic pressure of a rectangular lock-gate. Finite Elements in Analysis and Design Vol. 43. pp. 739-748. 2007.

11. Hakala, Matti. Numerical modelling of fluid-structure and structure-structure interaction. Espoo, VTT Publications / Technical Research Centre of Finland; 22. ISBN 951-38-2305-9. 62 p. 1985

12. Klinge, P., Äärettömät elementit. (in finnish) Master's Thesis. Helsinki University of Technology. Espoo. 124 p. 1985.

13. Everstine, G.C. A symmetric potential formulation for fluid-structure interaction. Journal of Sound and Vibration, Vol. 79:1. pp. 157-160. 1981.

14. Abaqus Theory Manual, version 6.8.2 Dassault Systèmes Simulia Corp., Providence, RI, USA. 2008.

15. Amabili, M., Dalpiaz, G. & Santolini, C. Free vibration of free-edge circular plates immersed in water. Proceedings of the 12th International Modal Analysis Conference, Honolulu, HI, pp. 349-355. 1994.

16. Kwak, M.K. Vibration of Circular Plates in Contact with Water, Journal of Applied Mechanics, Vol. 58. pp. 480-483. 1991.

17. Amabili, M. & Kwak, M.K. Free Vibrations of Circular Plates Coupled with Liquids: Revising the Lamb Problem. Journal of Fluids and Structures Vol. 10. pp. 743-761. 1996.

18. Patton, K. T. Tables of Hydrodynamic Mass Factors for Translational Motion. ASME Paper No. 65-WA/Unt-2, 1965.

19. LMS Cada-X Manuals Rev 3.5.F. Leuven, Belgium: LMS International. n.d.

20. LMS TestLab Manuals Rev 8B. Leuven, Belgium: LMS International. 2007.

21. Peeters, B et al. The PolyMAX frequency-domain method: a new standard for modal parameter estimation?. Shock and Vibration, Vol. 11 pp. 395-409. 2004.

22. Ewins, D. J. Modal Testing: Theory, Practice and Application. Second edition. England: Reseach Studies Press Ltd. ISBN 0-86380-218-4. 562 p. 2000.

23. Heylen, W. & Lammens, Stefan, & Sas. Paul. Modal Analysis Theory and Testing. Belgium: Katholieke Universiteit Leuven. ISBN 90-73802-61-X. 1997.

24. Peeters, B. & Auweraer, HV. Polymax: A Revolution in Operational Modal Analysis. 1st International Operational Modal Analysis Conference. 2005.

POD based computation of Joint Interface Modes

Wolfgang Witteveen, University of applied sciences - Wels, Stelzhammerstr. 69, 4600 Wels, Austria, Phone: +43 (0) 7242 72811 3260, wolfgang.witteveen@fh-wels.at

Karim Sherif, Linz Centre of Mechatronics GmbH, Altenbergerstr. 69, 4040 Linz, Austria, Phone: +43 (0)70 2468 6117, karim.sherif@lcm.at

Nomenclature

n	number of DOF of FE model
$\mathbf{x}$	nodel DOF vector of FE model
$\mathbf{f}^B$	external forces acting on FE model
$\mathbf{f}^{IJ}$	contact forces inside the joint
$\tilde{\mathbf{M}}$	mass matrix of FE model
$\tilde{\mathbf{K}}$	stiffness matrix of FE model
n_B	number of boundary DOF
$\mathbf{x}_B$	vector of boundary DOF
n_{IJ}	number of joint DOF
$\mathbf{x}_{IJ}$	vector of joint DOF
r	number of Ritz vectors for static reduction
$\tilde{\mathbf{X}}$	reduction matrix
$\tilde{\mathbf{K}}^{red}$	reduced stiffness matrix
$\tilde{\mathbf{M}}^{red}$	reduced mass matrix
$\tilde{\mathbf{\Phi}}^{*,red}$	full matrix of eigenvectors
k	considered numbers of eigenvectors
$\tilde{\mathbf{\Phi}}^{red}$	matrix of considered eigenvectors
$\tilde{\mathbf{\Phi}}^{JIM}$	matrix of joint interface modes
m	vector dimension
$\mathbf{y}$	arbitrary vector
$\tilde{\mathbf{Y}}$	matrix with column vectors $\mathbf{y}$
m	number of POM
$\mathbf{u}$	proper orthogonal mode (POM)
i, j	index variables
J	cost function
$\mathbf{v}$	eigenvector
w	ratio of considered energy
$\tilde{\mathbf{A}}$	matrix
$\tilde{\mathbf{\Phi}}^{POD,JIM}$	matrix of POD based JIM

1. Abstract

Recently proposed joint interface modes (JIM), which have been presented at the IMAC 25th, do consider Newton's 3rd law across a joint already at the stage of mode generation which leads to significant improvements in the subsequent mode based computation where nonlinear contact forces are applied.
In the latter publication the computation of the JIM is based on a general eigenvalue problem of a statically reduced mass and stiffness matrix. This approach has certain drawbacks in terms of interpretability and in terms of an 'a priory' - estimation of the required number of JIM.
In this contribution a prober orthogonal decomposition (POD) based method for the computation of the JIM is introduced. In this context the JIM can be interpreted as kind of 'energy modes' so that this procedure holds a meaningful physical interpretation as well as an 'a priory' – estimation of the required number of JIM.

2. Introduction and Motivation

It is a well known fact that the global stiffness and damping properties of a metallic structure, which consists of jointed substructures, are strongly influenced by the local and nonlinear characteristics of the involved joints such as bolted joints or spot welded seams, see exemplarily [1] and [2].
In the industrial practice this kind of problems are typically investigated either by the direct Finite Element Method (FEM) or a Ritz vector based (commonly called 'modal') approach.

T. Proulx (ed.), *Linking Models and Experiments, Volume 2*, Conference Proceedings of the Society for Experimental Mechanics Series 5,
DOI 10.1007/978-1-4419-9305-2_2, © The Society for Experimental Mechanics, Inc. 2011

- The strength of the FEM is the high resolution of the domain of interest which leads in general to a satisfying accuracy. The drawback of this method is the huge number of degrees of freedom (DOF) which makes it unfeasible for time integration.
- The strength of a Ritz vector (commonly called 'mode') based approach is the dynamics (time integration) of linear structures. Various Ritz vector based reduction methods have been presented during the last decades. Reviews have been done, among others, by Craig [3], Noor [4] and Zu [5]. Typically, the nonlinearity due to the contact inside a joint has been either neglected or somehow linearized. While this approach preserves the computational efficiency, it may lead to remarkable errors, see exemplarily [6] and [7].

Another approach was introduced by the author and Prof. Irschik at the IMAC 25th [8], 26th [9] and 27th [10]. An extended version of [8] and [9] can be found in [11]. The main idea of the latter approach is the enrichment of existing, well proven mode bases (e.g. Craig – Bampton [12]), by certain problem oriented 'contact modes', which we called joint interface modes (JIM). The JIM represent a generalization of the nodal FE DOF of the involved joint surfaces. It has been demonstrated in [8] and [13] that the convergence is superior to the one of the so called interface modes, where the involved contact surfaces are not related to each other at the time of mode generation via Newton's 3rd law. However, this approach has several drawbacks, namely:

- The JIM are obtained by a generalized eigenvalue problem of statically reduced mass and stiffness matrices. So, in principle, the JIM are computed like vibration modes, which is difficult to interpret in a physical sense.
- Consequently, the eigenvalues of the mentioned eigenvalue problem are more a mathematical quantity than a meaningful physical frequency for the estimation of the required number of JIM. So to say, the method does not provide an 'a – priory' estimation of the required number of JIM.
- For the latter mentioned static reduction Guyans method was suggested in [8]. As an improvement in terms of computational efficiency it has been suggested in [10] to discretize the joint area in a certain number of subareas. An open question up to now was, if the chosen discretization is fine enough to represent the joints mechanical characteristics.

In this paper a modified computation of JIM is suggested. Instead of a generalized eigenvalue problem of the statically reduced mass and stiffness matrix a orthogonal decomposition (POD) of the statically stiffness matrix is suggested. In a first section the former introduced JIM computation approach is briefly reviewed. Then a rough review on POD is given followed by it's application for the computation of JIM. Finally two numerical examples are discussed. It will be demonstrated that the JIM gained by a POD based approach converge as quick as the former method and the Hankel singular values can be used for an a priory estimation of the number of required JIM as well as for the evaluation of the joint area discretization.

3. Short review on the former introduced approach for the computation of JIM

A jointed flexible body modeled by the FEM can be represented by the equation of motion in the form of

$$\tilde{\mathbf{M}}\ddot{\mathbf{x}} + \tilde{\mathbf{K}}\mathbf{x} = \mathbf{f}^{B} + \mathbf{f}^{IJ}, \tag{1}$$

where $\mathbf{x}$ is the (n x 1) vector of nodal DOF and the (n x n) time invariant matrices $\tilde{\mathbf{M}}$ and $\tilde{\mathbf{K}}$ denote the bodies mass and stiffness. The load is a combination of the (n x 1) vectors of external loads $\mathbf{f}^{B}$ and contact forces $\mathbf{f}^{IJ}$.

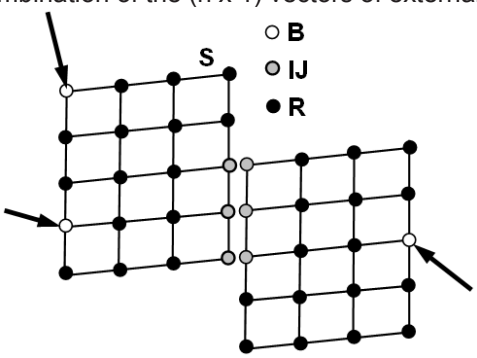

Figure 1: Arbitrary Finite Element structure with a joint

The considered FE structure with n nodal DOF consists of two jointed substructures as outlined in figure 1. Note that for the reasons depicted in [11] the jointed structure is considered as a single structure with 6 rigid body DOF. The external forces $\mathbf{f}^{B}$ are acting on the structure exclusively via the interface B and the according DOF are collected in the (n_B x 1) vector $\mathbf{x}_B$. The nodal DOF of $\mathbf{x}_B$ are outlined in figure 1 by white dots. The non-linear contact forces, which are represented by $\mathbf{f}^{IJ}$, act on the nodal DOF of the joint which are collected in the (n_{IJ} x 1) vector $\mathbf{x}_{IJ}$ and outlined in figure 1 by grey dots. The remaining (n - n_B - n_{IJ}) DOF are denoted as $\mathbf{x}_R$. According to that scheme, the vector of DOF can be written as

$$\mathbf{x} = \left[\mathbf{x}_B^{\,T} \quad \mathbf{x}_{IJ}^{\,T} \quad \mathbf{x}_R^{\,T} \right]^T . \tag{2}$$

In a first step, the number of DOF n is reduced via a linear superposition of Ritz vectors in the form of

$$\mathbf{x} = \tilde{\mathbf{X}}\mathbf{q} , \tag{3}$$

where the (n x r) matrix $\tilde{\mathbf{X}}$ contains r Ritz vectors in its columns. Please refer to [10] for a more detailed description of the reduction procedure. As mentioned, the reduction is based on a discretization of the entire joint area in r subareas.

Based on these reduction the reduced (r x r) mass and stiffness matrixes can be given as

$$\tilde{\mathbf{M}}^{red} = \tilde{\mathbf{X}}^T \tilde{\mathbf{M}} \tilde{\mathbf{X}} \text{ and} \tag{4}$$

$$\tilde{\mathbf{K}}^{red} = \tilde{\mathbf{X}}^T \tilde{\mathbf{K}} \tilde{\mathbf{X}} . \tag{5}$$

The computation of the JIM in the space of $\tilde{\mathbf{X}}$ is based on the eigenvalue problem

$$\left[\tilde{\mathbf{K}}^{red} - \left[\tilde{\boldsymbol{\Omega}}^{*,red} \right]^2 \tilde{\mathbf{M}}^{red} \right] \tilde{\boldsymbol{\Phi}}^{*,red} = \tilde{\mathbf{0}} \tag{6}$$

where r eigenvalues are stored in the (r x r) diagonal matrix $\tilde{\boldsymbol{\Omega}}^{*,red}$ and r eigenvectors in the (r x r) matrix $\tilde{\boldsymbol{\Phi}}^{*,red}$. The significant reduction of DOF is obtained by considering just the first k eigenvectors for the further considerations where k << r. The considered eigenvectors a collected in the (r x k) matrix $\tilde{\boldsymbol{\Phi}}^{red}$. The JIM for the entire structure can be computed by applying the reduction rule (3) in the form of

$$\tilde{\boldsymbol{\Phi}}^{JIM} = \tilde{\mathbf{X}} \tilde{\boldsymbol{\Phi}}^{red} , \tag{7}$$

where the (n x k) matrix $\tilde{\boldsymbol{\Phi}}^{JIM}$ contains the JIM for the joint contact.

In the final Ritz vector based computation the matrix of JIM is suggested as enrichment of established mode bases like the one of Craig-Bampton [12]. An exemplarily final transformation rule can be given as

$$\mathbf{x} = \left[\tilde{\boldsymbol{\Phi}}^{\text{Craig-Bampton}} \quad \tilde{\boldsymbol{\Phi}}^{JIM} \right] \mathbf{q} . \tag{8}$$

As already mentioned in the introduction three drawbacks of this method can be given, namely:

- In equation (6) the JIM are obtained by a generalized eigenvalue problem. In principle the JIM are the vibration modes of an artificial structure which is difficult to interpret.
- Consequently, the eigenvalues of (6) are more a mathematical quantity than a physical meaningful frequency. These eigenvalues can not be used as an ‘a – priory’ estimation of the required number of JIM.
- The reduction (3) determines the quality of the latter JIM. With an increasing number of subareas k the quality of the JIM as well as the computational effort is increasing. The question, whether a particular selection of k is high enough is an open issue.

4. Short Review: POD

In this section, a short introduction in the proper orthogonal decomposition is given based on [14].

Let us assume p independent (m x 1) vectors $\mathbf{y}_1$ to $\mathbf{y}_p$ which are collected in the (m x p) matrix $\tilde{\mathbf{Y}}$. Proper orthogonal decomposition (POD) of rank g delivers g orthonormal (m x 1) vectors $\mathbf{u}_1$ to $\mathbf{u}_g$ which approximate the space spanned by $\tilde{\mathbf{Y}}$ optimal in a Euclidean sense. Note, that the vectors $\mathbf{u}_1$ to $\mathbf{u}_g$ are named proper orthogonal modes (POM).

Proper orthogonal modes of rank g minimize a cost function J in the form of

$$J(\mathbf{u}_1,\cdots,\mathbf{u}_g)=\sum_{j=1}^{m}\left\|\mathbf{y}_j-\sum_{i=1}^{g}\left(\mathbf{y}_j^{\mathsf{T}}\mathbf{u}_i\right)\mathbf{u}_i\right\|^2\longrightarrow\min, \tag{9}$$

so that

$$\mathbf{u}_i^{\mathsf{T}}\mathbf{u}_j=\begin{cases}1 & i=j\\ 0 & i\neq j\end{cases}, \tag{10}$$

where the Euclidian norm is defined as

$$\|\mathbf{y}\|=\sqrt{\mathbf{y}^{\mathsf{T}}\mathbf{y}}\,. \tag{11}$$

The POM $\mathbf{u}_1$ to $\mathbf{u}_g$ can be found by the solution of an eigenvalue problem in the form of

$$\tilde{\mathbf{Y}}^{\mathsf{T}}\tilde{\mathbf{Y}}\mathbf{v}_i=\lambda_i\mathbf{v}_i \qquad \text{for i = 1, … ,g} \tag{12}$$

and a subsequent transformation

$$\mathbf{u}_i=\frac{1}{\sqrt{\lambda_i}}\tilde{\mathbf{Y}}\mathbf{v}_i \qquad \text{for i = 1, … ,g.} \tag{13}$$

The maximum error in a Euclidean sense can be given as error of the function J in the form of

$$J(\mathbf{u}_1,\cdots,\mathbf{u}_g)=\sum_{j=1}^{m}\left\|\mathbf{y}_j-\sum_{i=1}^{g}\left(\mathbf{y}_j^{\mathsf{T}}\mathbf{u}_i\right)\mathbf{u}_i\right\|^2=\sum_{i=g+1}^{m}\lambda_i\,. \tag{14}$$

The slightly different POD method with a weighted inner product minimizes a cost function in the form of

$$J(\mathbf{u}_1,\cdots,\mathbf{u}_g)=\sum_{j=1}^{m}\alpha_j\left\|\mathbf{y}_j-\sum_{i=1}^{g}\left(\mathbf{y}_j^{\mathsf{T}}\tilde{\mathbf{A}}\mathbf{u}_i\right)\mathbf{u}_i\right\|_A^2\longrightarrow\min, \tag{15}$$

where the matrix $\tilde{\mathbf{A}}$ hast to be symmetric, of the dimension (m x m) and positive semi definite, α_j are nonnegative weights and the induced norm is of the form

$$\|\mathbf{y}\|_W=\sqrt{\mathbf{y}^{\mathsf{T}}W\mathbf{y}}\,. \tag{16}$$

Now the eigenvalue problem takes on the form

$$\tilde{\mathbf{Y}}^{\mathsf{T}}\tilde{\mathbf{A}}\tilde{\mathbf{Y}}\mathbf{v}_i=\lambda_i\mathbf{v}_i \qquad \text{for i = 1, … ,g} \tag{17}$$

and the final POM can be computed along equation (13).

From a mechanical point of view, the characteristics of the matrix $\tilde{\mathbf{A}}$ are the same as the ones of the stiffness matrix of a linear FE model. In that context, the POM can be interpreted as kind of ‘energy’ modes. For more information on the physical interpretation of POD refer to [15].

The singular values λ_i can be used as an estimation of how many number of POM are required because they hold a ratio of the modeled to the total energy contained in the system $\tilde{\mathbf{Y}}$, which is expressed by

$$w(g)=\frac{\sum_{i=1}^{p}\lambda_i}{\sum_{i=1}^{g}\lambda_i} \tag{18}$$

5. POD based Joint Interface Modes

The application of the POD method to the problem under consideration is quite straight forward. The space spanned by $\tilde{\mathbf{Y}}$ is replaced by $\tilde{\mathbf{X}}$ from equation (3) and, in case of POD weighted inner product, the matrix $\tilde{\mathbf{A}}$ of equation (17) is replaced by the stiffness matrix $\tilde{\mathbf{K}}$ from the equation of motion (1).

Four different sets of JIM will be numerical investigated, namely:

- POD based on linear discretization of the joint area
- POD with weighted inner product based on linear discretization of the joint area
- POD based on nonlinear discretization of the joint
- POD with weighted inner product based on nonlinear discretization of the joint

5.1. POD based on linear discretization of the joint area

As explained in detail in [10] the joint area is subdivided into r subareas. Each subarea is loaded with a unit pressure distribution on both sides of the joint. This leads to r linear static response computations and the deformations due to this loads are collected in the (n x r) matrix $\tilde{\mathbf{X}}^{\mathrm{Lin}}$.
The POM are computed via the eigenvalue problem

$$\left[\tilde{\mathbf{X}}^{\mathrm{Lin}}\right]^{\mathrm{T}}\tilde{\mathbf{X}}^{\mathrm{Lin}}\mathbf{v}_{\mathrm{i}}^{\mathrm{Lin}}=\lambda_{\mathrm{i}}^{\mathrm{Lin}}\mathbf{v}_{\mathrm{i}}^{\mathrm{Lin}} \qquad \text{for i = 1, … , r.} \tag{19}$$

Using $\tilde{\mathbf{V}}^{\mathrm{Lin}}$ as the (r x k) matrix of considered POM, the according JIM can be given as the (n x k) matrix

$$\tilde{\boldsymbol{\Phi}}^{\mathrm{Lin}}=\tilde{\mathbf{X}}^{\mathrm{Lin}}\tilde{\mathbf{V}}^{\mathrm{Lin}}. \tag{20}$$

5.2. POD with weighted inner product based on linear discretization of the joint area

In difference to the latter approach the stiffness matrix $\tilde{\mathbf{K}}$ is considered for the POM computation in the form of

$$\left[\tilde{\mathbf{X}}^{\mathrm{Lin}}\right]^{\mathrm{T}}\tilde{\mathbf{K}}\tilde{\mathbf{X}}^{\mathrm{Lin}}\mathbf{v}_{\mathrm{i}}^{\mathrm{Lin,K}}=\lambda_{\mathrm{i}}^{\mathrm{Lin,K}}\mathbf{v}_{\mathrm{i}}^{\mathrm{Lin,K}} \qquad \text{for i = 1, … , r.} \tag{21}$$

Using $\tilde{\mathbf{V}}^{\mathrm{Lin,K}}$ as the (r x k) matrix of considered POM, the according JIM can be given as the (n x k) matrix

$$\tilde{\boldsymbol{\Phi}}^{\mathrm{Lin,K}}=\tilde{\mathbf{X}}^{\mathrm{Lin}}\tilde{\mathbf{V}}^{\mathrm{Lin,K}}. \tag{22}$$

5.3. POD based on nonlinear discretization of the joint area

In contrast to the approaches before, the nonlinear contact is considered during the r static response computations and the resulting deformations are collected in the (n x r) matrix $\tilde{\mathbf{X}}^{\mathrm{NoLin}}$.
The POM are computed via the eigenvalue problem

$$\left[\tilde{\mathbf{X}}^{\mathrm{NoLin}}\right]^{\mathrm{T}}\tilde{\mathbf{X}}^{\mathrm{NoLin}}\mathbf{v}_{\mathrm{i}}^{\mathrm{NoLin}}=\lambda_{\mathrm{i}}^{\mathrm{NoLin}}\mathbf{v}_{\mathrm{i}}^{\mathrm{NoLin}} \qquad \text{for i = 1, … , r.} \tag{23}$$

Using $\tilde{\mathbf{V}}^{\mathrm{NoLin}}$ as the (r x k) matrix of considered POM, the according JIM can be given as the (n x k) matrix

$$\tilde{\boldsymbol{\Phi}}^{\mathrm{NoLin}}=\tilde{\mathbf{X}}^{\mathrm{NoLin}}\tilde{\mathbf{V}}^{\mathrm{NoLin}}. \tag{24}$$

5.4. POD with weighted inner product based on linear discretization of the joint area

The POM are computed along

$$\left[\tilde{\mathbf{X}}^{\mathrm{NoLin}}\right]^{\mathrm{T}}\tilde{\mathbf{K}}\tilde{\mathbf{X}}^{\mathrm{NoLin}}\mathbf{v}_{\mathrm{i}}^{\mathrm{NoLin,K}}=\lambda_{\mathrm{i}}^{\mathrm{NoLin,K}}\mathbf{v}_{\mathrm{i}}^{\mathrm{NoLin,K}} \quad \text{for i = 1, … , r.} \tag{25}$$

Using $\tilde{\mathbf{V}}^{\mathrm{NoLin,K}}$ as the (r x k) matrix of considered POM, the according JIM can be given as the (n x k) matrix

$$\tilde{\boldsymbol{\Phi}}^{\mathrm{NoLin,K}}=\tilde{\mathbf{X}}^{\mathrm{NoLin}}\tilde{\mathbf{V}}^{\mathrm{NoLin,K}}. \tag{26}$$

In the following, these four methods are applied at different structures and compared with respect to each other and with the former approach which based on a generalized eigenvalue problem.

6. Examples

6.1. Generic beam example

6.1.1. FE model

A generic cantilever beam has been modelled according to Figure 2. The entire structure consists of two beam-like substructures, which are denoted with orange and blue colour in Figure 2. The two sub-structures are connected by two beams (Ø 8mm) which could represent two rivets or weld spots. Around the latter connectors

where the two substructures do overlap the lap joint is located. Each sub-beam has a dimension of 100mm x 20 mm x 1mm and the overlapping area is of the dimension 40mm x 20 mm. The used material is iron and linear four node shell elements with a dimension of 2mm x 2mm have been used.

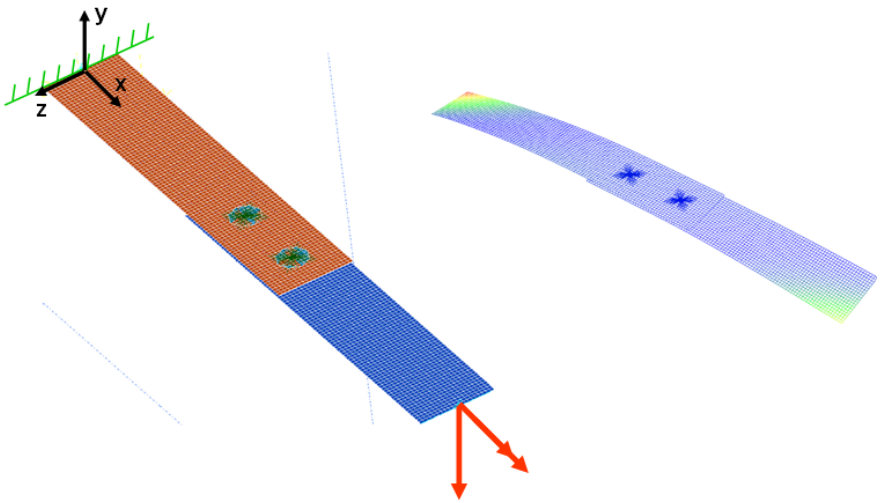

Figure 2: FE model of generic beam example and deformation shape of static force response computation

In a first step five different joint interface mode bases have been computed. One according to the general eigenvalue problem based approach outlined in section 3 and four more according to the POD based approaches of section 5.1 to 5.4 .

Note that the joint interface modes are computed for normal contact (y direction) only. Consequently, no tangential or friction forces are considered in the subsequent mode based analyses.

$\tilde{\Phi}^{JIM}$	$\tilde{\Phi}^{Lin,K}$	$\tilde{\Phi}^{NoLin,K}$	$\tilde{\Phi}^{Lin}$	$\tilde{\Phi}^{NoLin}$
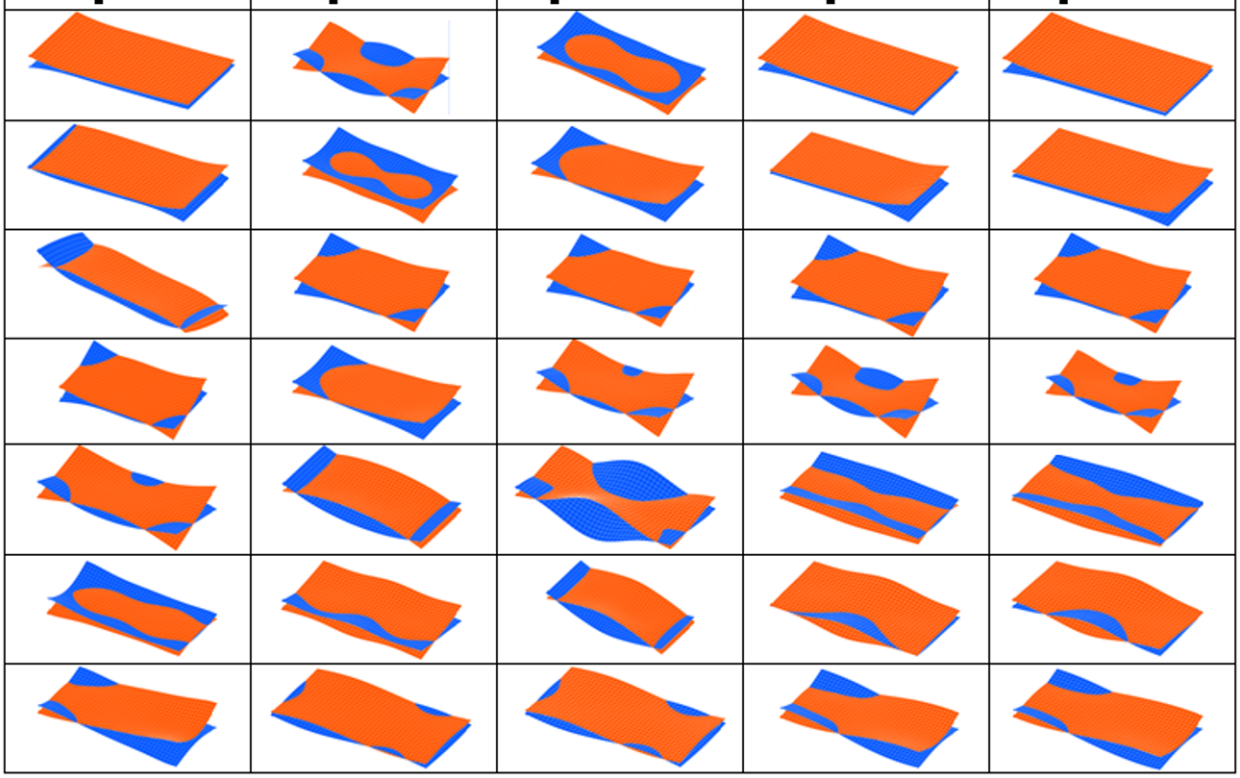				

Table 1: First seven JIM according to different approaches

For a convergence analysis of the Euclidean norm of the gap between the contact partners with respect to the considered JIM a series of nonlinear analysis has been performed. The structure is mounted at the location of the reference frame, which is outlined green in Figure 2. The orange arrows in Figure 2 denote a force acting along the y axis and a torque acting around the x axis. The resulting deformation is outlined on the right hand side of Figure 2. Note, that a nonlinear penalty contact model has been implemented for the contact pressure.

6.1.2. Results

Table 1 contains a visualization of the first seven JIM due to the different approaches. Note, that the JIM of the generalized eigenvalue bases approach (first column of Table 1) is sorted by increasing eigenvalues while the others (column 2 to 5) are sorted by decreasing eigenvalues (or Hankel singular values).

Figure 3 contains on the right hand side a convergence analysis of the modelled energy with respect to the number of considered JIM according to equation (18). Using all available JIMs leads to a modelled energy of 100%. It can be seen, that already much less than the available 400 JIM covers almost all energy which can be modelled. On the left hand side the convergence of the Euclidian norm of the gap is depicted.

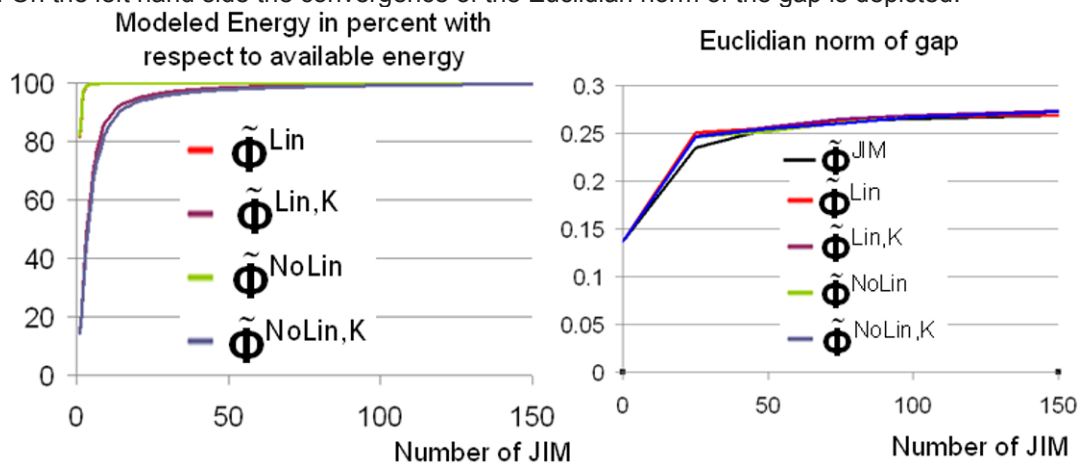

Figure 3: Convergence of modeled energy and of Euclidian gap in the contact with respect to the number of JIM

The latter 400 available JIM indicates, that the joint area is subdivided into 400 subareas in order to determine the mechanical joint characteristics, refer to [11]. In a final computation the JIM according to the POD based method of section 5.2 has been computed with 800, 400, 200, 100, 50, 25 and 13 subareas and the energy distribution has been evaluated in Figure 4. The according convergence analysis of the Euclidian norm of the gap and the joint pressure can be seen in Figure 5.

6.1.3. Conclusions

The conclusions drawn from the Table 1, Figure 3, Figure 4 and Figure 5 are:

- A visual evaluation of the different JIM in Table 1 reveals no significant qualitative difference. This 'intuitive' impression is underlined by the convergence analysis of the gap due to a certain static load. The five approaches lead to almost the same convergence rate.
- Figure 3 shows, that in case of a POD based approach which uses the stiffness matrix $\tilde{\mathbf{K}}$ according to sections 5.2 and 5.4, the convergence of the energy is somehow similar to the convergence of the Euclidian norm of the gap. Consequently, the Hankel singular values can be used as kind of 'a – priory' estimation of the required number of JIM. Note that the POD based approaches without using the stiffness matrix $\tilde{\mathbf{K}}$ (sections 5.1 and 5.3) yields Hankel singular values which do not represent the gap convergence. This is because just the deformations itself are approximated, while in the other case the strain energy is approximated.
- Figure 3 reveals that a nonlinear discretization of the joint area according to [11] is not necessary. There is no gain of accuracy while the nonlinear computation of $\tilde{\mathbf{X}}$ will take much more computational effort as the linear does.
- The question whether a joint is discretized fine enough can be answered by the results depicted in Figure 4 and Figure 5. A necessary criterion for a satisfying discretization seems to be a distinct convergence to the 100% limit. For this particular example, 50 to 100 subareas lead to an energy convergence with distinct convergence characteristics to the 100% limit.

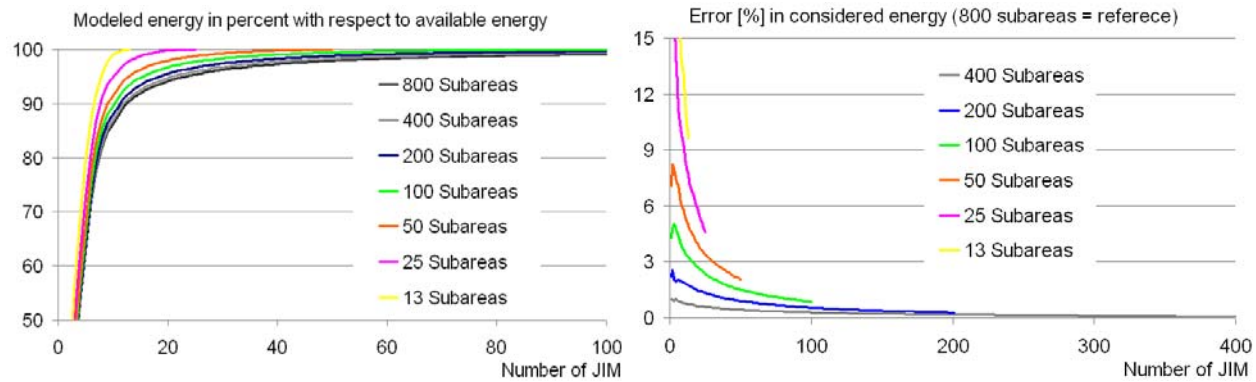

Figure 4: Convergence of modeled energy with respect to the number of JIM and to the number of subareas

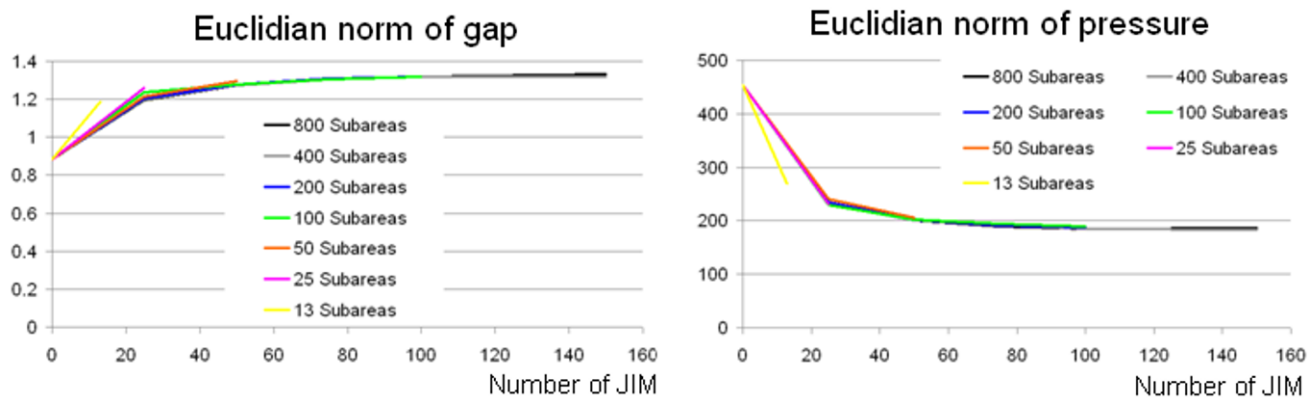

Figure 5: Convergence analysis of Euclidian norm of the gap and the joint pressure with respect to the number of JIM and to the number of subareas

6.2. Hertzian stress example

A Hertz type contact problem, as outlined in Figure 6, has been investigated. The plane strain problem consists of a plane part and a curved part which are moved towards each other so that contact occurs. The joint area for which joint interface modes are computed is outlined with red dots in Figure 6. The JIM have been computed along the approach outlined in section 4 and 5.2. A reference computation has be done using the commercial software ABAQUS using all nodal degrees of freedom.

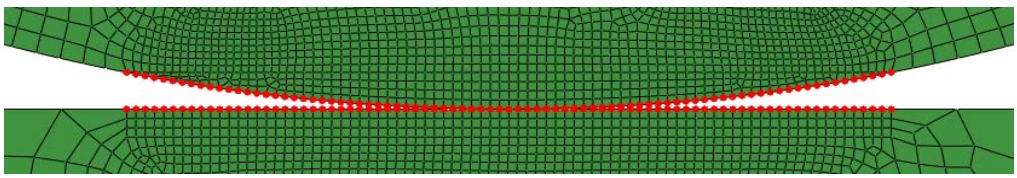

Figure 6: Hertzian contact problem

See Figure 7 for a qualitative convergence study of the von Mises stress in the contact area. It can be seen, that both approaches leads to a similar convergence characteristics and the use of 30 JIM delivers very good results.

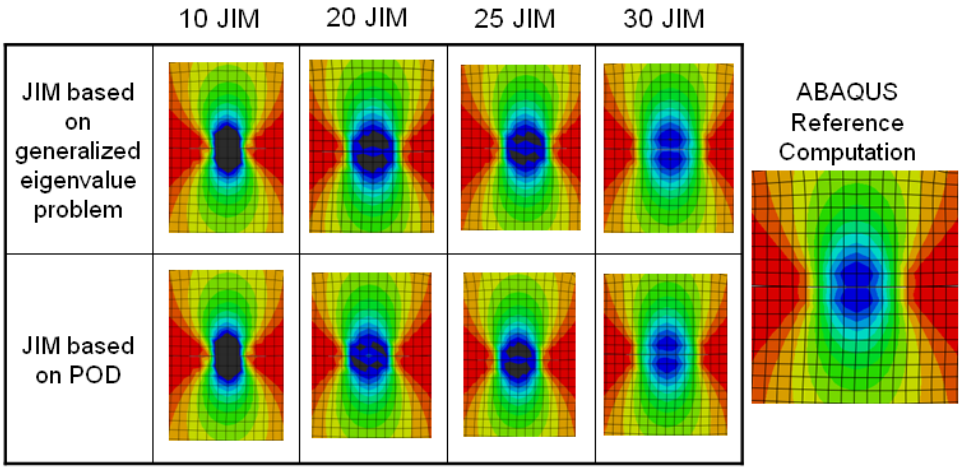

Figure 7: Von Mises Stress distribution in the contact area

7. Conclusion

It has been shown, that the POD based approach can be used for the computation of joint interface modes. Even the convergence characteristic is similar to the already existing method the POD based method has four important practical advantages:

- The POD based JIM have a clear physical meaning. POD with weighted inner product approximates a given subspace in terms of energy.
- Using a POD based method instead of an approach which is based on a generalized eigenvalue problem delivers a useful a-priory estimation of the number of necessary JIM.
- The proposed method gives an indication whether the number of subareas for the computation of the mechanical joint characteristics is high enough.
- Finally it is worth to mention that the POD based approach does not need any system matrixes at all. This is a very important fact when it comes to the commercial realisation of the proposed method which has been done by MAGNA Powertrain. The developed software code is called MAMBA [16].

8. Acknowledgement

Most of the content of this publication is a result of research activities during the first author's employment at the Linz Center of Mechatronics GmbH (LCM). The investigations have been completed by the author's follower DI Markus Breitfuss. Support of the authors by the LCM, the Engineering Center Steyr (MAGNA Powertrain) and the K2 Austria Center of Competence in Mechatronics (ACCM) is gratefully acknowledged.

9. Bibliography

[1] Gaul L., Nitsche R., *The role of friction in mechanical joints*, Appl. Mech. Rev.; Vol. 54; No. 2; pp. 93 – 105, March 2001

[2] Ungar E.E., *The status of engineering knowledge concerning the damping of built-up structures*, Journal of Sound and Vibration, Vol 26(1), pp 141-154, 1973

[3] Craig R. J., *A Review of Time-Domain and Frequency-Domain Component Mode Synthesis Methods*, Int. J. Anal. and Exp. Modal Analysis, Vol. 2, No. 2, 1987, pp. 59-72

[4] Noor A. K., *Recent advances and applications of reduction methods*, Appl. Mech. Rev., Vol. 47, No. 5, 1994, pp. 125 – 146.

[5] Zu Q. Q., *Model order reduction techniques*, Springer Verlag London, 2004

[6] W. Witteveen, Irschik H., Riener H., Engelbrechtsmüller M., Plank A., *An efficient mode based approach for the dynamic analysis of jointed and local damped structures: Joint Interface Modes*, Proceedings of ISMA 2008, Leuven, Belgium, pp. 1815-1824

[7] Bograd S., Schmidt A., Gaul L., *Joint damping prediction by thin layer elements*, Proceedings of IMAC 26th, Society of Experimental Mechanics Inc, Bethel, Connecticut, US, 2008, Paper Nr. 288
[8] Witteveen W., Irschik H., *Efficient modal formulation for vibration analysis of solid structures with bolted joints*, Proceedings of IMAC 25th, Society of Experimental Mechanics Inc, Bethel, Connecticut, US, 2007, Paper Nr. 385
[9] Witteveen W., Irschik H., *Joint Interface Modes: Numerical 3D-Benchmark Studies*, Proceedings of IMAC 26th, Society of Experimental Mechanics Inc, Bethel, Connecticut, US, 2008, Paper Nr. 318
[10] Witteveen W., Irschik H., *Efficient Computation of Joint Interface Modes*, Proceedings of IMAC 27th, Society of Experimental Mechanics Inc, Bethel, Connecticut, US, 2009, Paper Nr. 16
[11] Witteveen W., Irschik H., *Efficient Mode-Based Computational Approach for Jointed Structures: Joint Interface Modes*, AIAA Journal, Vol. 47, No. 1, pp. 252-263, 2009
[12] Craig R.R., Bampton M.C.C., *Coupling of Substructures for Dynamic Analysis*, AIAA Journal, Vol. 6, No. 7, pp. 1313 – 1319, 1968
[13] Becker J., Gaul L., *CMS Methods for Efficient Damping Prediction for Structures with Friction*, Proceedings of IMAC 26th, Society of Experimental Mechanics Inc, Bethel, Connecticut, US, 2008, Paper Nr. 74
[14] Volkwein S., *Model reduction using proper orthogonal decomposition*, http://www.uni-graz.at/imawww/volkwein/POD.pdf, cited July 2010
[15] Feeny B. F., Kappagantu R., *On the physical interpretation of proper orthogonal modes in vibrations*, Journal of Sound and Vibration, Vol. 211, Nr. 4, pp 607-616, 1998
[16] www.mamba.ecs.steyr.com

Area wise application of contact constraints in reduced mechanical systems

Wolfgang Witteveen, University of applied sciences - Wels, Stelzhammerstr. 69, 4600 Wels, Austria, Phone: +43 (0) 7242 72811 3260, wolfgang.witteveen@fh-wels.at

Nomenclature

n	number of DOF of FE model
$\mathbf{x}$	nodel DOF vector of FE model
$\mathbf{f}^B$	external forces acting on FE model
$\tilde{\mathbf{K}}$	stiffness matrix of FE model
n_B	number of boundary DOF
$\mathbf{x}_B$	vector of boundary DOF
n_{IJ}	number of joint DOF
$\mathbf{x}_{IJ}$	vector of joint DOF
m	number of master surface DOF
$\mathbf{x}_{IJ,M}$	vector of master surface DOF
s	number of slave surface DOF
$\mathbf{x}_{IJ,S}$	vector of slave surface DOF
g	number of master surface FE nodes
$\mathbf{g}$	vector of relative joint normal displacement
$\mathbf{a}$	vector of master surface FE node related areas
r	number of Ritz vectors
$\tilde{\mathbf{\Phi}}$	reduction matrix
$\tilde{\mathbf{K}}^{red}$	reduced stiffness matrix
$\mathbf{f}^{red}$	reduced force vector
$\mathbf{q}$	generalized coordinate
g_i	i-th constraint equation based on $\mathbf{x}$
g_i^{red}	i-th constraint equation based on $\mathbf{q}$
$\tilde{\mathbf{Q}}$	transformation matrix
m_i	number of master surface DOF in subarea number i
$\mathbf{x}_{IJ,M,i}$	vector of master surface DOF of subarea number i
g_i	number of master surface FE nodes in subarea number i
$\mathbf{g}_i$	vector of relative joint normal displacements of subarea number i
$\mathbf{a}_i$	vector of master surface FE node related areas in subarea number i
g_i^*	averaged penetration of subarea i
e	relative Error

1. Abstract

Solid joint contact is characterized by nonlinear contact forces inside the joint. In case of gaping no contact forces are acting on the involved surfaces while penetration is avoided by the application of proper contact forces. In the common Finite Element (FE) method such forces are typically applied at nodal degree of freedom (DOF) inside the joint. This can be done using unilateral constraint equations or nonlinear penalty stiffness's.
In the frame work of modally reduced jointed structures just the penalty stiffness approach can be directly applied. In that case, the contact forces are computed based on the joint state and projected into the modal space. The problem is reduced to the question whether the mode base is capable to describe the relative displacements of the involved joint surfaces.
This paper is a contribution to the more challenging problem when the contact is implemented using unilateral constraint equations. In that case the FE approach will not work in general because the number of nodal constraint equation will be higher than the number considered modes (DOF) which leads to on over constraint system. In order to overcome that problem an area wise application of the unilateral constraint equations is suggested instead of the common node wise one. After an introduction the presented idea will be outlined followed by a static example. The contribution ends with a discussion of the result and some conclusions.

T. Proulx (ed.), *Linking Models and Experiments, Volume 2*, Conference Proceedings of the Society for Experimental Mechanics Series 5,
DOI 10.1007/978-1-4419-9305-2_3, © The Society for Experimental Mechanics, Inc. 2011

2. Introduction and Motivation

The presence of joints, like bolted joints, spot welded seems and others, is a computational challenge in assembled structures. From a mechanical point of view, a joint leads to a contact and friction problem with a possibly time invariant contact area. It is well documented that these local nonlinearities can significantly influence the structures local and global response, see exemplarily [1], [2] and [3].
For the accurate consideration of contact phenomenon's inside complex jointed structures typically the Finite Element Method (FEM, [4] and [5]) has been used. The FEM is characterized by accurate results in case of a satisfying discretization of the domain of interest. This, on the other hand, leads to a high number of degrees of freedom (DOF) which disqualifies the method for the time integration of jointed structures.
Recently developed Joint Interface Modes (JIM) overcome that problem. Joint Interface Modes (see [6]) are a problem oriented Ritz vector type extension to existing, well proven mode bases like the one of Craig and Bampton [7]. The basic idea of JIM is the generalization and reduction of the joint DOF. Based on a proper mode base which is enriched with JIM, an efficient and accurate time integration of jointed structure is possible even the nonlinear contact problem is considered, see [6] and [8].
The publications [6] and [8] have in common that the contact forces are realized via a penalty approach. The penalty approach works like a nonlinear spring which connects both contact surfaces. This 'virtual' spring has zero stiffness in case of gaping and a nonzero stiffness in case of penetration. The penalty approach is quiet straight forward to implement. The contact forces are computed as a function of the gap state and finally projected into the subspace for the time integration. This approach does not influence the number of degrees of freedom of the equation of motion.
Another approach for computational contact mechanics is the use of non penetration constraints which modify the structure of the equation of motion because a set of active constraint equations has to be considered as well. Normally the number of nodal joint DOF of the FE model is higher as the number of considered Ritz vectors. The straight forward approach to impose a non penetration constraint onto all nodal joint DOF will lead to an over constraint system and is therefore not applicable.
One possibility to overcome that problem will be introduced in this contribution. Instead of a FE node oriented application of the non penetration constraints, an area wise application of the latter constraint is suggested and investigated. The joint area will be subdivided into several subareas and the non penetration constraint is applied in an averaged form.
After the idea is formally introduced in the next section a static example will be given. The contribution ends with a discussion of the results and some conclusions.

3. Theory

A FE structure with n nodal DOF which contains a joint is outlined in figure 1. Note that for the reasons of simplicity the FE structure as no rigid body DOF. The external forces $\mathbf{f}^B$ are acting on the structure exclusively via the interface B and the according DOF are collected in the (n_B x 1) vector $\mathbf{x}_B$. The nodal DOF of $\mathbf{x}_B$ are outlined in figure 1 by white dots. The nodal DOF which are involved in the non-linear joint contact are collected in the (n_{IJ} x 1) vector $\mathbf{x}_{IJ}$ and are outlined in figure 1 by grey dots. Note, that the problem under consideration can be characterized as self contact. The remaining (n - n_B - n_{IJ}) DOF are denoted as $\mathbf{x}_R$. The nodal DOF of $\mathbf{x}_R$ are outlined in figure 1 by black dots. According to that scheme, the vector of DOF can be written as

$$\mathbf{x} = \left[\mathbf{x}_B{}^T \quad \mathbf{x}_{IJ}{}^T \quad \mathbf{x}_R{}^T \right]^T \text{ and} \tag{1}$$

the vector of external forces $\mathbf{f}^B$ takes on the form

$$\mathbf{f}^B = \left[\mathbf{f}_B{}^T \quad \mathbf{0}^T \quad \mathbf{0}^T \right]^T. \tag{2}$$

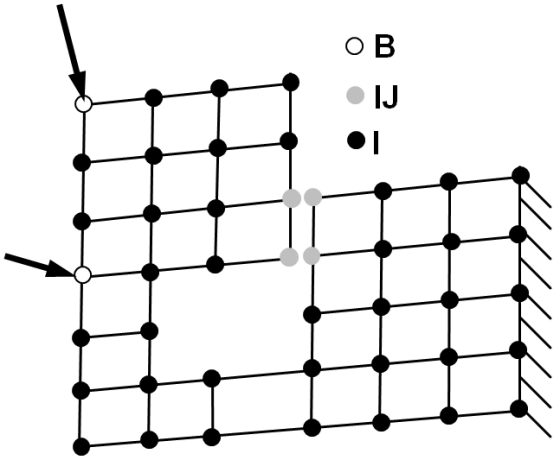

Figure 1: Arbitrary Finite Element structure with a joint

For the characterization of the contact inside the joint, the involved surfaces and corresponding DOF are subdivided into a master and a slave surface.

$$\mathbf{x}_{IJ} = \left[\mathbf{x}_{IJ,M}{}^{T} \quad \mathbf{x}_{IJ,S}{}^{T} \right]^{T} \tag{3}$$

where the vector of master DOF $\mathbf{x}_{IJ,M}$ is of the dimension (m x 1) and the one of the slave DOF $\mathbf{x}_{IJ,S}$ is of the dimension (s x 1). An additional (g x 1) vector $\mathbf{g}$ is introduced holding the relative normal displacement between the master and the slave surface at the master DOF. The quantity g is equal to the number of master surface FE nodes. A negative value at the i-th entry of $\mathbf{g}$ means, that the i-th node of the master surface penetrates the slave surface while a positive entry indicates gaping. For the sake of simplicity it is assumed that s=m and that the master and slave nodes do coincide at the unstressed reference position. The latter assumptions lead to a simple computation of $\mathbf{g}$ in the form of

$$\mathbf{g} = \tilde{\mathbf{Q}} \left[\mathbf{x}_{IJ,M} - \mathbf{x}_{IJ,S} \right] \tag{4}$$

where the invariant (g x m) matrix $\tilde{\mathbf{Q}}$ projects the physical displacements into a displacement along the corresponding normal vector of each master node.

Finally a (g x 1) vector $\mathbf{a}$ is introduced. The component a_i (i = 1..g) of the latter vector holds the joint area which is associated with master FE node number i. The sum of all entries of $\mathbf{a}$ gives the entire joint area.

The literature offers several approaches for doing computational contact mechanics. For this contribution the self contact problem under consideration is treated as a quadratic programming problem. In the latter context the static problem is completely described by a minimization problem in the form of

$$\min_{\mathbf{x}} \left(\frac{1}{2} \mathbf{x}^{T} \tilde{\mathbf{K}} \mathbf{x} - \left[\mathbf{f}^{B} \right]^{T} \mathbf{x} \right) \tag{5}$$

so that

$$g_i \geq 0 \qquad \text{for i = 1..g,} \tag{6}$$

see [9] and [10]. The (n x n) matrix $\tilde{\mathbf{K}}$ denotes the stiffness matrix of full rank. In case of FE structures the condition i > n is always fulfilled because the vector of joint DOF is a subset of the entire DOF vector $\mathbf{x}$. When the minimization problem (5) is not written in $\mathbf{x}$ but the conditions (6) are, the problem over constraining can occur. This is the case when a transformation in the form of

$$\mathbf{x} = \tilde{\mathbf{\Phi}} \mathbf{q} \tag{7}$$

is applied where the (n x r) matrix $\tilde{\mathbf{\Phi}}$ holds in its columns r Ritz type trial vectors. The (r x 1) vector $\mathbf{q}$ is a generalized coordinate. The minimization problem takes on the form

$$\min_{\mathbf{x}} \left(\frac{1}{2} \mathbf{q}^{T} \tilde{\mathbf{K}}^{red} \mathbf{q} - \left[\mathbf{f}^{red} \right]^{T} \mathbf{q} \right) \tag{8}$$

so that

$$g_i^{red} \geq 0 \qquad \text{for i = 1..g,} \tag{9}$$

where the (r x r) matrix $\tilde{\mathbf{K}}^{red}$ can be written as

$$\tilde{\mathbf{K}}^{red} = \tilde{\mathbf{\Phi}}^T \tilde{\mathbf{K}} \tilde{\mathbf{\Phi}}, \tag{10}$$

the (r x 1) vector $\mathbf{f}^{red}$ as

$$\mathbf{f}^{red} = \tilde{\mathbf{\Phi}}^T \mathbf{f} \tag{11}$$

and g_i^{red} as

$$g_i^{red} = \tilde{\mathbf{Q}}_i \left[\tilde{\mathbf{\Phi}}_{IJ,M,i} - \tilde{\mathbf{\Phi}}_{IJ,S,i} \right] \mathbf{q}. \tag{12}$$

The (3 x r) matrixes $\tilde{\mathbf{\Phi}}_{IJ,M,i}$ and $\tilde{\mathbf{\Phi}}_{IJ,S,i}$ denote the rows which belong to the master and slave surface node number i and the (1 x 3) transformation matrix $\tilde{\mathbf{Q}}_i$ is the corresponding sub-matrix of $\tilde{\mathbf{Q}}$. The right subscript 'red' indicates, that a quantity is computed based on generalized coordinates according to equation (12).
For the common case, that g > r the system (8) and (9) has more constraints as DOF and can be therefore over constrained.
For the further considerations, the joint surfaces will be subdivided into b mutual exclusive subareas about the same size. The vector of master surface DOF can then be written as

$$\mathbf{x}_{IJ,M} = \left[\mathbf{x}_{IJ,M,1}^T \quad \cdots \quad \mathbf{x}_{IJ,M,i} \quad \cdots \quad \mathbf{x}_{IJ,M,b}^T \right]^T \tag{13}$$

where the (m_i x 1) vector $\mathbf{x}_{IJ,M,i}$ contains the DOF of the i-th subsurface. The corresponding vector of relative normal joint displacements of the master FE nodes takes on the form

$$\mathbf{g}^{red} = \left[\left[\mathbf{g}_1^{red} \right]^T \quad \cdots \quad \mathbf{g}_i^{red} \quad \cdots \quad \left[\mathbf{g}_b^{red} \right]^T \right]^T \tag{14}$$

where the (g_i x 1) vector $\mathbf{g}_i^{red}$ holds the relative normal joint displacements of the master FE nodes in subsurface number i. Finally the vector of FE node related areas is subdivided similarly into

$$\mathbf{a} = \left[\mathbf{a}_1^T \quad \cdots \quad \mathbf{a}_i \quad \cdots \quad \mathbf{a}_b^T \right]^T \tag{15}$$

where the (g_i x 1) vector $\mathbf{a}_i$ holds the master FE node related areas in subsurface number i.

A possibility to overcome the over constraining issue of equations (8) and (9) is an averaged formulation of the non penetration constraints. Applying this idea to equations (8) and (9) the minimization problem takes on the form

$$\min_{\mathbf{x}} \left(\frac{1}{2} \mathbf{q}^T \tilde{\mathbf{K}}^{red} \mathbf{q} - \left[\mathbf{f}^{red} \right]^T \mathbf{q} \right) \tag{16}$$

so that

$$g_i^* \geq 0 \qquad \text{for i = 1..b,} \tag{17}$$

where

$$g_i^* = \frac{1}{\sum_{j=1}^{g_i} a_{i,j}} \sum_{j=1}^{g_i} g_{i,j}^{red} a_{i,j} \tag{18}$$

and $a_{i,j}$ represents the j-th entry of $\mathbf{a}_i$ and $g_{i,j}^{red}$ holds the j-th entry of $\mathbf{g}_i^{red}$.

Note, when b is equal to the number of FE nodes in the master surface, that latter formulation converges to the FEM type formulation of equation (6).

4. Numerical example

The latter idea has been applied to the FE structure printed on the right side of figure 2. The structure consists of two 0.5mm iron sheets which are connected with four spot welds. The sheets are outlined in blue and orange color and the positions of the spot welds are indicated by green 'spiders'. The joint is defined by the overlapping area of the two sheets. The dimension of the joint can be given as 155mm x 75mm. Both ends of the structure are considered as rigid, which is indicated by a black color in figure 2. One end is constrained and the other end is loaded by a single force which is indicated by the arrow in orange color.

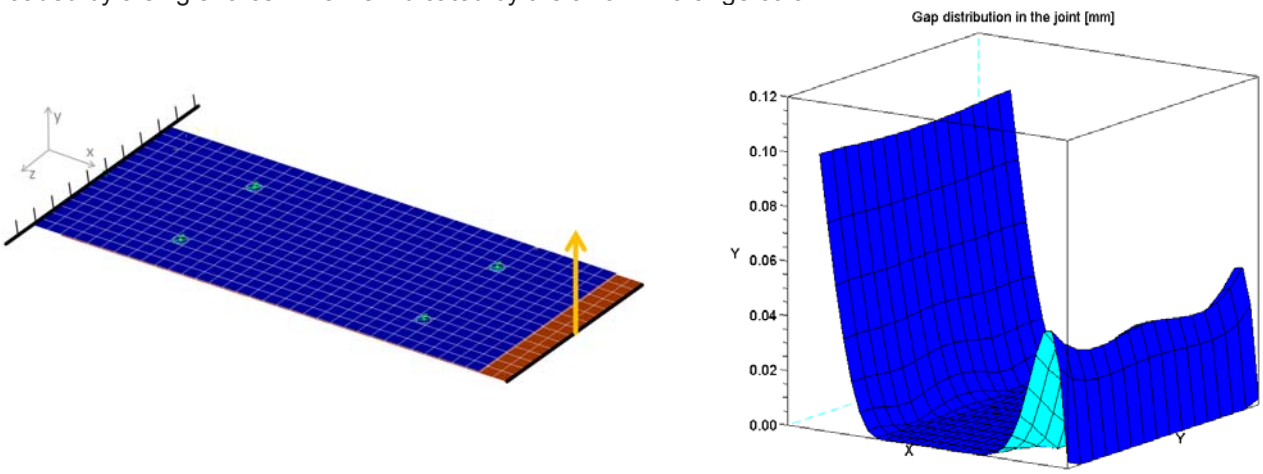

Figure 2: FE structure and reference gap

The reference computation has been done with all nodal FE DOF and with the non penetrations condition (6) for all 512 master surface FE nodes in the joint. The selection of the master surface is unimportant because the FE nodes in the joint coincide in unstressed reference position. All computations have been performed using the 'qpsolve' routine of the software Scilab 5.2.2 [11]. The gap distribution of this reference computation can be seen on the left hand side of figure 2. The tip deflection of this computation is 5.3 mm.
A series of mode based computations according to the equations (16) to (18) have been performed. Each computation varies either in the number of considered JIM or/and in the number of constraints (=subareas). The considered JIM are used as extension to 10 modes which have been computed based on an eigenvalue problem of the stiffness matrix $\tilde{\mathbf{K}}$. Four different relative errors in percent have been evaluated. The first one is the relative error in the tip deflection which is computed according to

$$e_T = \left(\frac{x_T^{red} - x_T}{x_T} \right) 100 \tag{19}$$

where x_T^{red} is the tip deflection of the load application point in y direction computed with the modal approach. The quantity x_T is the according reference value based on the reference computation done with all DOF and all available joint constraints. Three other errors are based on the different norms of the vector $\mathbf{g}$. Formally these errors can be written as

$$e_i = \left(\frac{\left\| \mathbf{g}^{red} \right\|_i - \left\| \mathbf{g} \right\|_i}{\left\| \mathbf{g} \right\|_i} \right) 100 \quad \text{and } i=1,2,\infty . \tag{20}$$

If i = 1 the error of the Manhattan norm, if i = 2 the error of the Euclidian norm and if i = ∞ the error of the maximum norm is computed.

The computations have been performed for 0, 10, 20, 30, 40 and 50 considered JIM and the number of constraints (=subareas) have been 1, 2, 4, 8, 16, 32, 64, 128, 256 and 512.

The results are plotted as contour plots and can be seen in figure 3. The four plots indicate that there is an optimum number of considered constraints (=subareas) with respect to the used number of JIM. Both, too less

and too much constraints deliver bad results. An a-priory estimation of the optimal distribution and number of subareas cannot be given yet.

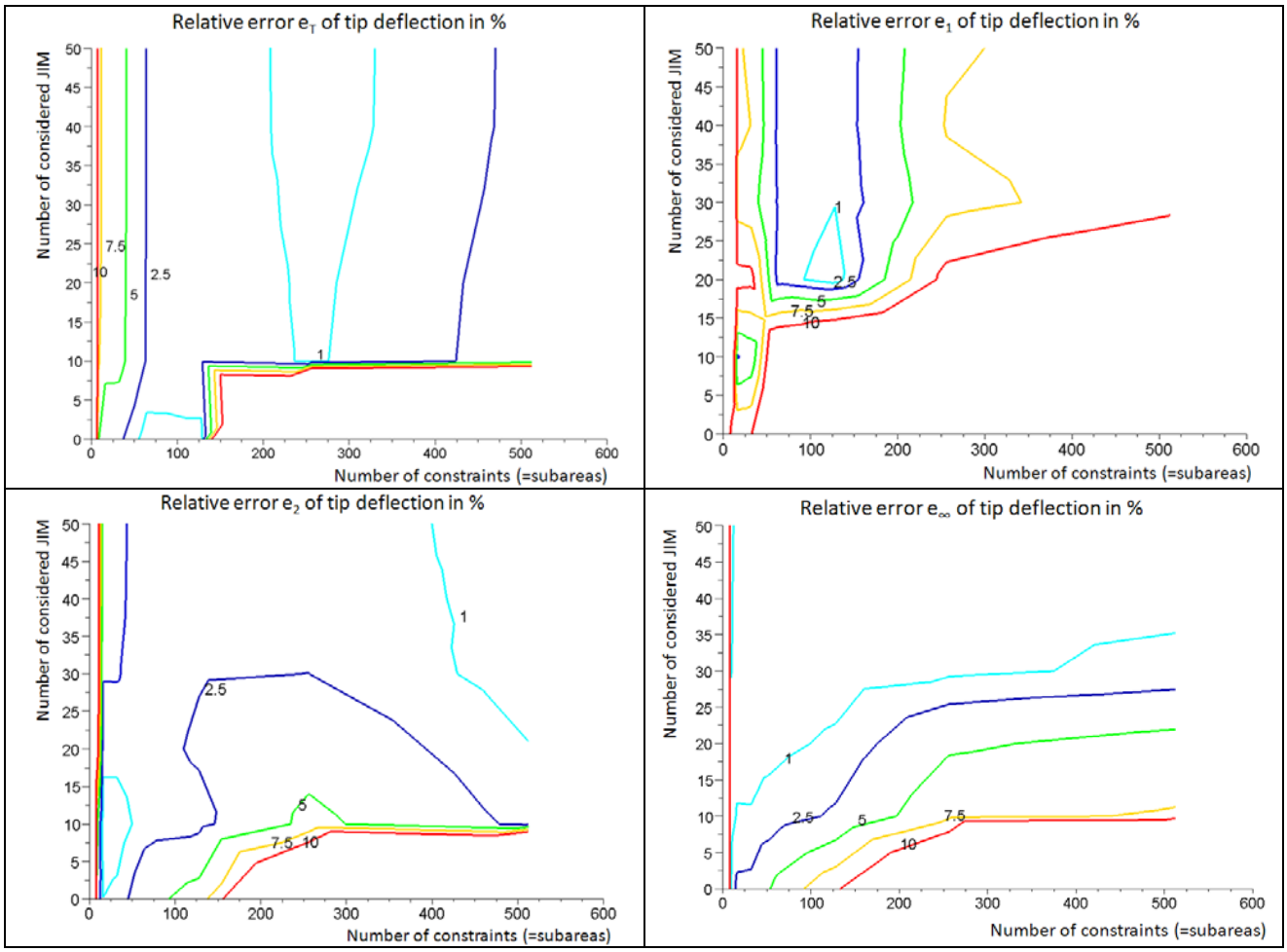

Figure 3: Contour plot of relative errors of mode based computation with respect to reference computation

Figure 4 contains on the left hand side an exemplarily gap distribution with 20 considered JIM and 64 subareas (=constraints). On the right hand side the distribution of the absolute error with respect to the reference computation, depicted in figure 2, is given.
Note, that even the difference in the gap distribution is small, a lot of DOF could have been saved. The reference computation needed 1025 nodal DOF and 512 non penetration constraints which are, in fact, a kind of internal DOF for the quadratic programming problem. The modal based computation, on the other hand, needed 35 modal DOF and 64 constraint equations which is much less. The difference in the CPU time for the 'qpsolve' routine of Scilab was about a factor of 113 which was measured with the 'timer' routine of Scilab.

5. Conclusion

It has been shown that computational contact mechanics based on non penetration constraints in the framework of modal analysis is not straight forward as it would be when a penalty approach is used. In this contribution non penetration constraints based on subareas instead of FE nodes, is discussed. It has been shown that accurate displacement results can be obtained even if the considered number of DOF and constraint equations is significantly smaller as by the node based FEM. An obvious drawback of the presented method is the absence of an a-priory estimation of an optimal distribution of subareas with respect to selected mode base.
Even the approach was very intuitive, it indicates a potential for future work to save a lot of computational effort for joint contact computations with non penetration constraints in the framework of modally reduced systems.

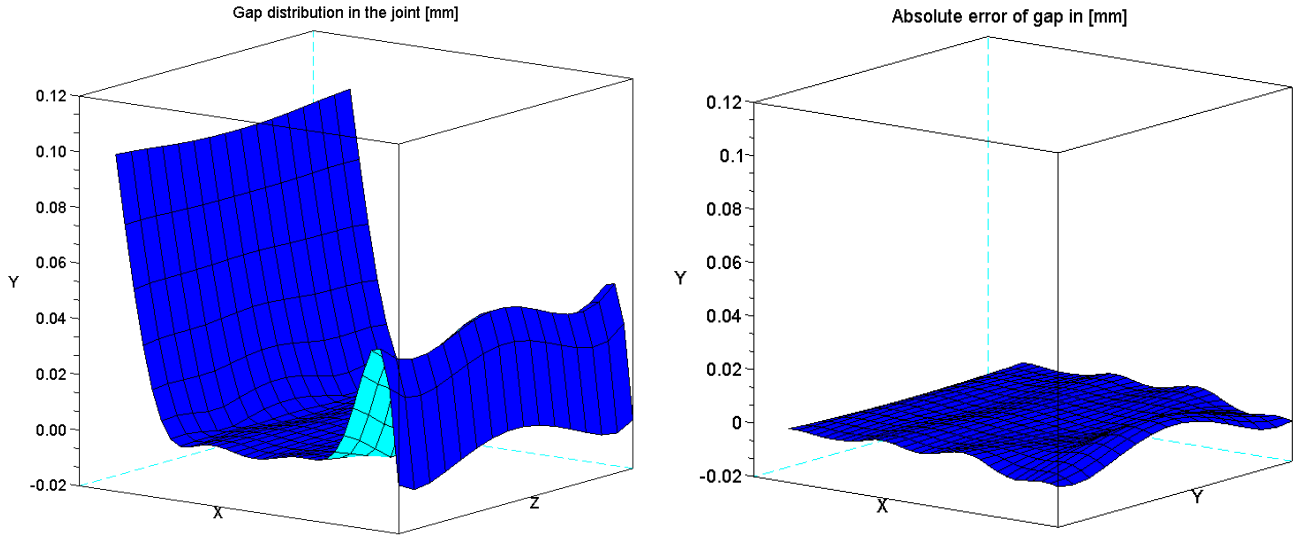

Figure 4: Exemplarily result of mode based computation (20 JIM and 64 subareas)

6. Acknowledgement

Most of the content of this publication is a result of research activities during the author's employment at the Linz Center of Mechatronics GmbH (LCM). Support of the authors by the LCM, the Engineering Center Steyr (MAGNA Powertrain) and the K2 Austria Center of Competence in Mechatronics (ACCM) is gratefully acknowledged.

7. Bibliography

[1] Gaul L., Nitsche R., *The role of friction in mechanical joints*, Appl. Mech. Rev.; Vol. 54; No. 2; pp. 93 – 105, March 2001

[2] W. Witteveen, Irschik H., Riener H., Engelbrechtsmüller M., Plank A., *An efficient mode based approach for the dynamic analysis of jointed and local damped structures: Joint Interface Modes*, Proceedings of ISMA 2008, Leuven, Belgium, pp. 1815-1824

[3] Ungar E.E., *The status of engineering knowledge concerning the damping of built-up structures*, Journal of Sound and Vibration, Vol 26(1), pp 141-154, 1973

[4] Zienkieviecz O.C., Taylor R.L., *The Finite Element Method – Vol.1 – Basic Formulations and Linear Problems*, 4th Edition, McGraw-Hill Book Company, 1993

[5] Zienkieviecz O.C., Taylor R.L., *The Finite Element Method – Vol.2 – Solid and Fluid Mechanics, Dynamics and Non-Linearity*, 4th Edition, McGraw-Hill Book Company, 1993

[6] Witteveen W., Irschik H., *Efficient Mode-Based Computational Approach for Jointed Structures: Joint Interface Modes*, AIAA Journal, Vol. 47, No. 1, pp. 252-263, 2009

[7] Craig R. J., *A Review of Time-Domain and Frequency-Domain Component Mode Synthesis Methods*, Int. J. Anal. and Exp. Modal Analysis, Vol. 2, No. 2, 1987, pp. 59-72

[8] Witteveen W., Irschik H., *Joint Interface Modes: Numerical 3D-Benchmark Studies*, Proceedings of IMAC 26th, Society of Experimental Mechanics Inc, Bethel, Connecticut, US, 2008, Paper Nr. 318

[9] Kloosterman G., Contact Methods in Finite Element Simulations, PhD Thesis, University Twente, Netherlands, 2002

[10] Baniotopoulos C. C., Abdalla K. M., Panagiotopoulos P. D., *A variational inequality and quadratic programming approach to the separation problem of steel bolted brackets*, Computers & Structures, Vol. 53, Nr. 4, pp. 983-991, 1994

[11] www.scilab.org

On the extension of global vibration modes with Ritz-vectors needed for local effects

Karim Sherif, Linz Center of Mechatronics GmbH, Altenbergerstr. 69, 4040 Linz, Austria, karim.sherif@lcm.at

Wolfgang Witteveen, University of Applied Science - Wels, Stelzhammerstr. 23, 4600 Wels, Austria, Wolfgang.Witteveen@fh-wels

Hans Irschik, Johannes Kepler University - Linz, Altenbergerstr. 69, 4040 Linz, Austria, irschik@mechatronik.uni-linz.ac.at

Helmut Holl, Johannes Kepler University - Linz, Altenbergerstr. 69, 4040 Linz, Austria, helmut.holl@jku.at

Karl Mayrhofer, Siemens VAI Metals Technologies GmbH, Turmstr. 44, 4031 Linz, Austria, mayrhofer.karl@siemens.com

Nomenclature

M^{FE}	mass matrix of FE model	f_b	forces acting on u_b
K^{FE}	stiffness matrix of FE model	f_{ext}	external force vector
C^{FE}	damping matrix of FE model	f_k	force vector due to local effects
u	nodal DOF vector of FE model	Φ_n	full matrix of eigenvectors
$\dot{u}$	second time-derivative of u	Φ_k	matrix of retained eigenvectors
$\ddot{u}$	first time-derivative of u	Ψ_c	matrix of constrained modes
f	force vector of FE model	Φ_{cb}	Craig-Bampton transformation matrix
u_b	boundary DOF of FE model	Ψ_j	matrix of Joint Interface modes
u_i	interior DOF of the FE model	$\hat{\Psi}_j$	mass-orthogonal local Ritz-vectors
n_b	number of boundary DOF	ω_u	upper frequency limit
n_i	number of interior DOF	q	generalized coordinates of reduced model

1 Abstract

In Ritz-vector based model reduction techniques, the problem-oriented combination of different kind of Ritz-vectors may significantly influence the quality of the reduction base. It is common to combine global vibration modes with Ritz-vectors, which are necessary to characterize local effects. Even if the global vibration modes and the local Ritz-vectors may be separately orthogonal with respect to the mass and stiffness matrix, the combined reduced system is usually not decoupled. By using common decoupling strategies the separation of the two mode groups is lost. In this contribution, we will present a transformation procedure in order to obtain a combined and decoupled mode base, which is still separable into global vibration modes and Ritz-vectors due to local effects. Due to the clear separation of the two kinds of modes it is possible to give a frequency limit for the relevance of the inertia effects of the second mode group. In case the inertia effects of the second mode group may be neglected, the dimension of the differential equation of motion can be reduced once more again. At our theoretical considerations, an example is presented for the sake of illustration.

T. Proulx (ed.), *Linking Models and Experiments, Volume 2*, Conference Proceedings of the Society for Experimental Mechanics Series 5,
DOI 10.1007/978-1-4419-9305-2_4, © The Society for Experimental Mechanics, Inc. 2011

2 Introduction

Accurate Finite Element (FE) models typically require a large number of degrees of freedom (DOF). Due to this huge number of DOF, the time integration of such systems is very expensive. Component Mode Synthesis (CMS) methods significantly reduce the dimension of structural dynamic models, which leads to reduced simulation time and reduced memory requirements. The term 'component modes' characterizes Ritz type trial vectors which are used as base vectors in order to approximate the displacement field of a single component.

There are two general types of CMS methods; they are known as the fixed-interface and the free-interface approaches. The fixed-interface CMS technique presented by Hurty [1, 2] and modified by Craig and Bampton [3] is widely used, since the reduction procedure is straightforward and typically produces highly accurate models with relatively few component modes [4]. The free-interface CMS approaches are more attractive than the fixed-interface methods when the component modes are obtained from modal testing. Highly accurate free-interface CMS methods have been developed e.g. by Craig und Chang [5, 6]. The Craig-Chang method is a modified version of the widely used Rubin method [7] and the MacNeal method [8]. A detailed discussion and a comprehensive review on the different CMS methods are given in [9], [10] and [11]. However, in this contribution only the fixed-interface Craig-Bampton method is considered.

The Craig-Bampton CMS method can be effectively and consistently used for the reduction of large linear elastic structures, but it is not applicable for structures with nonlinear local effects in terms of contact problems in its original form. This is due to the fact that the latter reduction method does preserve the nodal DOF at interfaces and each interface DOF thus leads to an additional Ritz-vector in the mode base. For an accurate and local application of contact and friction laws in the contact region (nonlinear local effects), the nodal DOF of a contact surface need to be considered as interface DOF, and this leads to an inefficient number of modes.

A reduction method for structures with nonlinear local effects has been published in [12], by Apiwattanalunggarn. In the latter approach the fixed-interface Craig-Bampton method has been extended by nonlinear normal modes. Witteveen and Irschik [13] presented an extension of the Craig-Bampton method that permits solving contact problems of jointed structures. This is possible by extending the component modes of the Craig-Bampton method with local Ritz-vectors or so called Joint Interface Modes (JIM). The latter modes form together with the component modes of the Craig-Bampton method a suitable Rayleigh-Ritz coordinate transformation for nonlinear contact problems when the potential contact area is time invariant. Due to the fact that for the computation of the JIM, Newton's third law (principle of equivalence of forces) across the contact region is explicitly accounted at the time of mode generation, only a small number of JIM has to be considered in order to approximate the solution of the contact problem in a reduced subspace.

It is the scope of the present contribution to present a decoupling procedure for a mode base consisting of global vibration modes and Ritz-vectors needed for local effects, where the resulting decoupled mode base is still separable into global vibration modes and Ritz-vectors. The paper is organized as follows. Firstly, the fixed-interface Craig-Bampton CMS method and its extension by the JIM are reviewed. Then modified JIM are introduced in order to achieve a reduced system with a block-diagonal decoupled mass matrix. Finally, a generic 501-mass nonlinear structural system is used as an example to demonstrate the method, and some conclusions are drawn.

3 Component mode synthesis

The next two subsections give a short review of the fixed-interface Craig-Bampton CMS method and of the computation of its component modes.

3.1 Fixed-interface normal modes and interface constraint modes

The equation of motion of a FE model can be formally written as

$$\mathrm{M}^{\mathrm{FE}}\ddot{\mathrm{u}} + \mathrm{K}^{\mathrm{FE}}\mathrm{u} = \mathrm{f}\,, \tag{1}$$

where M^{FE} and K^{FE} are the symmetric mass and stiffness matrices, f represents the time-varying force vector, and the vector u contains the nodal DOF (usually displacements) of the FE model. The vector $\ddot{\mathrm{u}}$ is the second derivative of u with respect to time. The following partitioned form of Eq.(1) will

be useful in the derivation of the fixed-interface normal modes and the interface constraint modes, where the n_b boundary coordinates are assembled in the set u_b and the n_i free (interior) coordinates are gathered in the set u_i:

$$\begin{bmatrix} M_{bb} & M_{bi} \\ M_{ib} & M_{ii} \end{bmatrix} \begin{bmatrix} \ddot{u}_b \\ \ddot{u}_i \end{bmatrix} + \begin{bmatrix} K_{bb} & K_{bi} \\ K_{ib} & K_{ii} \end{bmatrix} \begin{bmatrix} u_b \\ u_i \end{bmatrix} = \begin{bmatrix} f_b \\ 0 \end{bmatrix}. \tag{2}$$

Restraining all boundary DOF and solving the eigenvalue problem

$$\left(K_{ii} - \omega_p^2 M_{ii} \right) \Phi_p = 0 , \tag{3}$$

one obtains the fixed-interface normal modes, which can be stacked in the modal base Φ_{in}. Upon normalization of the fixed-interface normal modes with respect to the mass matrix, the generalized orthogonality of the modes can be expressed in the following compact form:

$$\Phi_{in}^T M_{ii} \Phi_{in} = I_{ii} \quad , \quad \Phi_{in}^T K_{ii} \Phi_{in} = \Lambda_{nn} = \mathrm{diag}\left(\omega_p^2 \right), \tag{4}$$

where I_{ii} is $(n_i \times n_i)$ the identity matrix and Λ_{nn} is the diagonal matrix of squared linear natural frequencies of the fixed-interface normal modes. According to the partitioning of Eq.(2), the fixed interface modal matrix Φ_n for all coordinates of the FE model takes on the form

$$\Phi_n = \begin{bmatrix} 0_{bn} \\ \Phi_{in} \end{bmatrix}. \tag{5}$$

The interface constraint modes are the static deformations of the interior coordinates by imposing a unit displacement at one physical coordinate of the set u_b, while the remaining DOF of the same set are restrained. This procedure is applied consecutively to all coordinates of the set u_b. That is,

$$\begin{bmatrix} K_{bb} & K_{bi} \\ K_{ib} & K_{ii} \end{bmatrix} \begin{bmatrix} I_{bb} \\ \Psi_{ib} \end{bmatrix} = \begin{bmatrix} R_{bb} \\ 0_{ib} \end{bmatrix}, \tag{6}$$

where R_{bb} is the corresponding external force matrix and I_{bb} is the $(n_b \times n_b)$ identity matrix. Consequently, the constraint-mode matrix Ψ_c is given by

$$\Psi_c = \begin{bmatrix} I_{bb} \\ \Psi_{ib} \end{bmatrix} = \begin{bmatrix} I_{bb} \\ -\left[K_{ii}^{-1} K_{ib} \right] \end{bmatrix}. \tag{7}$$

3.2 Craig-Bampton method

The displacement-based CMS methods are based on a Rayleigh-Ritz transformation of the form

$$u = \Phi q , \tag{8}$$

where the solution is approximated in a reduced subspace by representing the physical coordinates, u, in terms of component generalized coordinates q. The matrix Φ is called the reduction base, Ritz-vector base, dynamic component mode superset, or simply the transformation matrix. The columns of the transformation matrix consist of preselected component modes of the following type: rigid body modes, normal modes of the undamped system (global vibration modes), attachment modes,

constrained modes, inertia-relief modes and local Ritz-vectors. Other types of assumed modes e.g. Krylov vectors [14] or nonlinear normal modes [12] may also be employed as component modes.
The transformation matrix of the fixed-interface Craig-Bampton method, which approximates the solution in a reduced subspace, consists of two parts: the interface constrained modes, which have been defined by Eq.(7), and the first m_k fixed-interface normal modes of Eq.(5), which are assembled to the matrix Φ_k. Typically, only those m_k normal modes are retained and assembled to the matrix Φ_k, which are associated with an eigenfrequency below the maximum frequency of interest. That is,

$$\Phi_{cb} = \left[\Psi_c \quad \Phi_k\right]. \tag{9}$$

It is worth noting that the Craig-Bampton transformation preserves all physical coordinates of set u_b in the reduced subsystem.
Eq.(8) and Eq.(9) together with the equation of motion form the reduced equation of motion or the so called component modal model. The reduced equation of motion in generalized coordinates is

$$M_{cb}\ddot{q}_{cb} + K_{cb}q_{cb} = \left(\Phi_{cb}\right)^T f\,, \tag{10}$$

where the reduced mass and stiffness matrices, M_{cb} and K_{cb}, are defined as:

$$M_{cb} = \left(\Phi_{cb}\right)^T M^{FE}\Phi_{cb}, \quad K_{cb} = \left(\Phi_{cb}\right)^T K^{FE}\Phi_{cb} \tag{11}$$

4 On a proper extension of the Craig-Bampton reduction base by local Ritz-vectors

In this section we shortly review and modify the fixed-interface CMS method developed by Witteveen and Irschik [15], where the Craig-Bampton method is extended by Ritz-vectors needed for nonlinear local effects. This type of Ritz-vectors will be further denoted as 'local Ritz-vectors'. In the subsection 4.1 the local Ritz-vectors will be modified in order to get an efficient formulation of the reduced equation of motion.
The typical Craig-Bampton CMS [3] does preserve the nodal DOF at interfaces. The interface is defined as those DOF on which external forces may act. According to the partitioning of Eq.(2), the interface DOF have to be interpreted as boundary DOF. Furthermore, each interface DOF leads to an additional constraint mode in the final mode base. For an accurate and local application of contact and friction laws in the contact region, the nodal DOF of the involved contact surfaces need to be considered as interface DOF. This leads to an inefficient number of modes. In [13], [14] and [16] local Ritz-vectors, so called Joint Interface Modes (JIM), have been introduced. The latter modes together with the component modes of the Craig-Bampton method form a suitable Rayleigh-Ritz coordinate transformation for problems including local contact and friction effects. For the computation of the JIM, Newton's third law (principle of equivalence of forces) across the contact region is explicitly accounted for. This leads to a remarkable small number of JIM, which have to be considered in order to approximate the solution of the contact problem. The considered m_j JIM are assembled in the matrix Ψ_j. The extension of the classical Craig-Bampton transformation [3] with the matrix Ψ_j leads to a Rayleigh-Ritz coordinate transformation in the form of

$$u = \left[\Phi_{cb} \quad \Psi_j\right] q\,. \tag{12}$$

Substituting Eq.(12) into Eq.(1) and premultiplying the resulting equation by $\left[\Phi_{cb} \quad \Psi_j\right]^T$ gives

$$\begin{bmatrix} M_{cb} & M_{cbj} \\ \left(M_{cbj}\right)^T & M_{jj} \end{bmatrix}\begin{bmatrix} \ddot{q}_{cb} \\ \ddot{q}_j \end{bmatrix} + \begin{bmatrix} K_{cb} & K_{cbj} \\ \left(K_{cbj}\right)^T & K_{jj} \end{bmatrix}\begin{bmatrix} q_{cb} \\ q_j \end{bmatrix} = \begin{bmatrix} \left(\Phi_{cb}\right)^T \\ \left(\Psi_j\right)^T \end{bmatrix} f\,, \tag{13}$$

where

$$M_{cbj} = (\Phi_{cb})^T M^{FE} \Psi_j, \quad K_{cbj} = (\Phi_{cb})^T K^{FE} \Psi_j, \quad M_{jj} = (\Psi_j)^T M^{FE} \Psi_j, \quad K_{jj} = (\Psi_j)^T K^{FE} \Psi_j . \tag{14}$$

The combined reduced system, Eq.(13), is usually not decoupled.
For problems with nonlinear local effects, it is useful to separate the force vector f of Eq.(1) in an external non-state dependent force vector f_{ext} and a state dependent force vector f_k:

$$f = f_{ext} + f_k \tag{15}$$

The external force vector f_{ext} is the vector of nodal forces due to applied external forces and does not include forces, which result form local effects of the system (e.g. contact forces). The latter forces are assembled in the force vector f_k. Regarding local contact effects, the forces of the vector f_k are formulated as a nonlinear function of the state variable vector, namely,

$$f_k = f_k(u) . \tag{16}$$

Thus, in terms of a component modal model the vector f_k depends on the generalized coordinates q_{cb} and q_j.

4.1 Mass-orthogonal local Ritz-vectors

Due to the fact that the extension of the Craig-Bampton component modes with JIM leads to a reduced system which is not decoupled, see Eq.(13), it is not possible to neglect the inertia effects of the joint interface mode group. To achieve a mass decoupled reduced system, the JIM have to be modified so that they are mass-orthogonal to the component modes of the Craig-Bampton mode base. To get mass-orthogonal local Ritz-vectors, $\hat{\Psi}_j$, it is necessary to remove the content of the component modes, which are assembled to the transformation matrix Φ_{cb}, from the local Ritz-vectors Ψ_j. This can be formally written as

$$\hat{\Psi}_j = \Psi_j - \Phi_{cb}\kappa, \quad \text{subject to} \quad (\Phi_{cb})^T M^{FE} \hat{\Psi}_j = M_{cbj} = 0 , \tag{17}$$

where κ is a scaling matrix. Premultiplying the first part of Eq.(17) with $(\Phi_{cb})^T M^{FE}$ yields

$$\kappa = \left((\Phi_{cb})^T M^{FE} \Phi_{cb} \right)^{-1} (\Phi_{cb})^T M^{FE} \Psi_j . \tag{18}$$

Finally, Eqs.(17) and (18) may be combined to give:

$$\hat{\Psi}_j = \Psi_j - \Phi_{cb} \left((\Phi_{cb})^T M^{FE} \Phi_{cb} \right)^{-1} (\Phi_{cb})^T M^{FE} \Psi_j , \tag{19}$$

where the modified matrix $\hat{\Psi}_j$ contains mass-orthogonal local Ritz-vectors. The transformation matrix thus obtained can be written as

$$u = \left[\Phi_{cb} \quad \hat{\Psi}_j \right] \hat{q} . \tag{20}$$

Using the latter reduction rule, a reduced system in the form

$$\begin{bmatrix} M_{cb} & 0 \\ 0 & \hat{M}_{jj} \end{bmatrix} \begin{bmatrix} \ddot{q}_{cb} \\ \ddot{\hat{q}}_j \end{bmatrix} + \begin{bmatrix} K_{cb} & \hat{K}_{cbj} \\ \left(\hat{K}_{cbj}\right)^T & \hat{K}_{jj} \end{bmatrix} \begin{bmatrix} q_{cb} \\ \hat{q}_j \end{bmatrix} = \begin{bmatrix} \left(\Phi_{cb}\right)^T \\ \left(\hat{\Psi}_j\right)^T \end{bmatrix} f_{ext} + \begin{bmatrix} \left(\Phi_{cb}\right)^T \\ \left(\hat{\Psi}_j\right)^T \end{bmatrix} f_k\left(q_{cb}, \hat{q}_j\right) \tag{21}$$

is obtained, where the reduced mass and stiffness matrices are

$$\hat{K}_{cbj} = \left(\Phi_{cb}\right)^T K^{FE} \hat{\Psi}_j, \quad \hat{K}_{jj} = \left(\hat{\Psi}_j\right)^T K^{FE} \hat{\Psi}_j, \quad \hat{M}_{jj} = \left(\hat{\Psi}_j\right)^T M^{FE} \hat{\Psi}_j . \tag{22}$$

Moreover, the mass-orthogonal local Ritz-vectors are normalized, in order to satisfy $\hat{M}_{jj} = I$ and $\hat{K}_{jj} = \hat{\Lambda}_{jj} = \mathrm{diag}\left(\hat{\omega}_j^2\right)$. It should be pointed out that the matrices M_{cb} and K_{cb}, as well as the generalized coordinates q_{cb} of Eq.(21), are the same as those of Eq.(13).
The original Craig-Bampton mode base is more or less accurate for a predefined frequency range. The latter frequency range is determined by the considered fixed-interface normal modes, and an upper frequency limit, ω_u, may be declared. Due to the fact that for the computation of the mass-orthogonal local Ritz-vectors the content of the Craig-Bampton component modes is totally removed, the eigenfrequencies of the local mass-orthogonal Ritz-vectors are above ω_u. Consequently, the dynamics of the mass-orthogonalized local Ritz-vectors can be neglected, while the quasistatic influence on the local displacement field can not. It should be mentioned that the frequencies of the mass-orthogonal local Ritz-vectors are - from a physical point of view - just numerical quantities, but regarding numerical time integration, they specify whether the inertia effects have to be taken into account or not.
In case of weak stiffness coupling between the DOF of the global vibration modes and the local Ritz-vectors, it can be moreover assumed that

$$\left\| \hat{M}_{jj} \ddot{\hat{q}}_j \right\| \ll \left\| \left(\hat{K}_{cbj}\right)^T q_{cb} + \hat{K}_{jj} \hat{q}_j \right\|, \tag{23}$$

where a ‘weak stiffness coupling’ means that

$$\left\| \left(\hat{K}_{cbj}\right)^T q_{cb} \right\| \ll \left\| \hat{K}_{jj} \hat{q}_j \right\| . \tag{24}$$

A mathematical proof of the range of Eq.(24) is left to a future contribution.
Applying the assumption of Eq.(23) to Eq.(21) leads to a reduced equation of motion in the form of

$$\begin{aligned} M_{cb} \ddot{q}_{cb} + \left[K_{cb} - \hat{K}_{cbj} \left(\hat{K}_{jj}\right)^{-1} \left(\hat{K}_{cbj}\right)^T \right] q_{cb} &= \left[\left(\Phi_{cb}\right)^T - \hat{K}_{cbj} \left(\hat{K}_{jj}\right)^{-1} \left(\hat{\Psi}_j\right)^T \right] \left[f_{ext} + f_k\left(q_{cb}, \hat{q}_j\right) \right] \\ 0 &= \hat{q}_j - \left(\hat{K}_{jj}\right)^{-1} \left[\left(\hat{\Psi}_j\right)^T \left[f_{ext} + f_k\left(q_{cb}, \hat{q}_j\right) \right] - \left(\hat{K}_{cbj}\right)^T q_{cb} \right] \end{aligned} , \tag{25}$$

where the differential equations due to the local Ritz-vector DOF are replaced by a set of (nonlinear) algebraic constrain equations.
A comparison of the equation of motion, Eq.(21), and its modified form, Eq.(25), shows that the dimension of the system of differential equations, which needs to be time integrated, is much smaller for the latter formulation. The penalty which needs to be paid is an additional set of algebraic equations.

5 Numerical Example

In this section a generic dynamical example will be presented in order to illustrate the proposed algorithm and to demonstrate its advantages.

5.1 A 501-DOF system with nonlinear springs

A generic system is considered which consists of 501 masses connected by linear springs and dampers, see Figure 1.

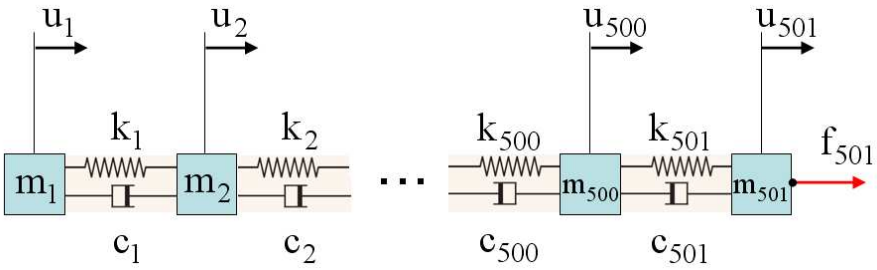

Figure 1: 501-DOF system

The system is supported at the left hand side ($u_1 = 0$), and is loaded by a step load f_{501} on the right hand side. Thus, the set of boundary coordinates u_b includes the coordinates u_1 and u_{501}. All other coordinates are interior coordinates and assembled in the set u_i. Additionally to the linear springs, nonlinear springs are added to the system in the area between mass 400 up to mass 450, see Figure 2. The load deflection relation of the additional nonlinear springs has the form

$$f_{nl} = k_{nl,1}\Delta u + k_{nl,2}\left(\Delta u\right)^3, \tag{26}$$

where Δu is the relative displacement between two involved masses. However, the nonlinear springs are considered on the right hand side of the equation of motion by the state-dependent force vector f_k.

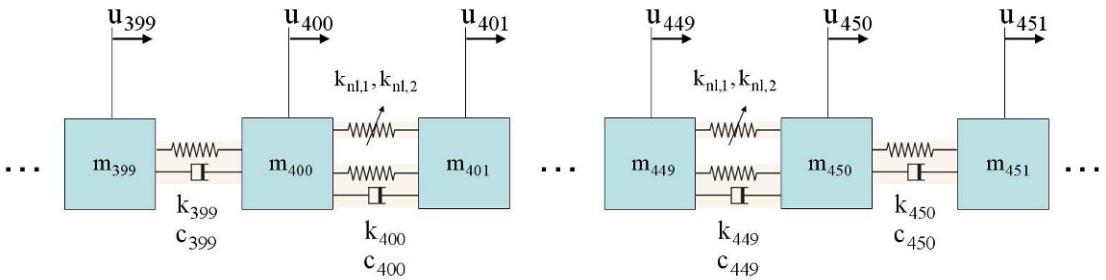

Figure 2: 501-DOF system

Beside the two interface constraint modes, the first three fixed-interface normal modes are assembled to the Craig-Bampton transformation matrix Φ_{cb}. From the 50 existing mass-orthogonal local Ritz-vectors only the first 12 are assembled to the matrix $\hat{\Psi}_j$.
Figure 3 shows the eigenfrequencies of both, the retained normal modes and the first three mass-orthogonal local Ritz-vectors (m.-o. JIM 1, m.-o. JIM 2, m.-o. JIM 3). Figure 3 indicates that the eigenfrequencies of the mass-orthogonal local Ritz-vectors are significantly higher as those of the retained fixed-interface normal modes.

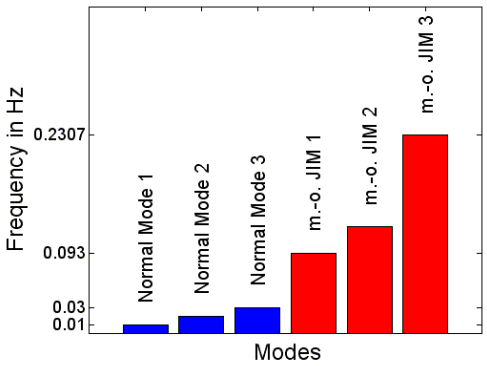

Figure 3: Natural frequencies of both, the retained normal modes and the first three modified local Ritz-vectors

The parameters used for this example are given by

$$\begin{aligned} &k_1 = k_2 = \ldots = k_{500} = 100\ \frac{N}{m}, \quad m_1 = m_2 = \ldots = m_{500} = 1\ kg, \quad k_{nl,1} = 1000\ \frac{N}{m}, \quad k_{nl,2} = 1000\ \frac{N}{m^3} \\ &c_1 = c_2 = \ldots = c_{500} = 1500\ \frac{kg}{s}, \quad t = 0\ldots1000\ s, \quad m_k = 3, \quad m_j = 25, \quad f_{501} = \begin{cases} 0\ N: & t \le 0\ s \\ 1\ N: & t > 0\ s \end{cases} \end{aligned} \tag{27}$$

Due to fact that this system includes dampers, the damping has to be considered in the reduced model as well. The reduced damping matrix C_{red} may be written as:

$$C_{red} = \left[\Phi_{cb} \quad \hat{\Psi}_j\right]^T C^{FE} \left[\Phi_{cb} \quad \hat{\Psi}_j\right], \tag{28}$$

where C^{FE} is the damping matrix of the non-reduced system.
The reference solution (I) has been computed using the entire non-reduced system. This is a nonlinear system of differential equations with 501 DOF of the form

$$M^{FE}\ddot{u} + C^{FE}\dot{u} + K^{FE}u = f_{ext} + f_k(u)\,. \tag{29}$$

An approximation of the solution (II) is achieved by solving Eq.(21). Thus, the transformation matrix comprises 17 modes and consequently a nonlinear system of differential equations with 17 DOF has to be solved. Finally, another approximation of the solution (III) is obtained by solving the nonlinear differential-algebraic system of Eq.(25). There, the system of differential equations has 5 DOF and the algebraic side-condition has 12 DOF. For all systems the time integration has been performed with the MATLAB solver ODE15s. It is worth noting that MATLAB ODE solver accept only first-order differential equations. Therefore, all three systems have been rewritten to equivalent systems of first-order nonlinear differential equations.
Figure 4 shows the displacement-time graph of mass 425 (left figure of Figure 4) and the relative displacement Δu between mass 424 and mass 425 with respect to time (right figure of Figure 4). The displacement field of all 501 masses at t = 1000 s can be seen in Figure 5.

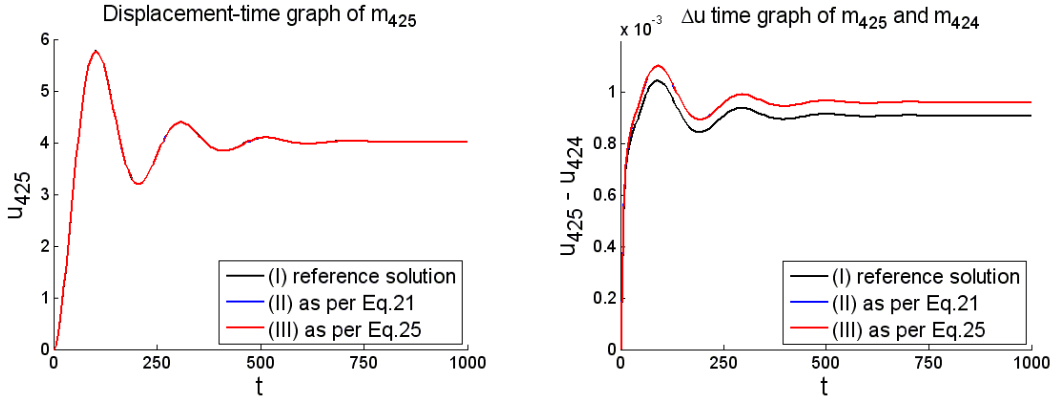

Figure 4: Displacement-time graph of mass 425 and relative displacement between mass 425 and mass 424

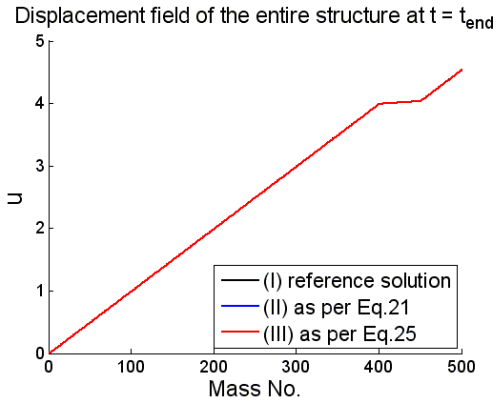

Figure 5: Displacement field of the entire structure at t_{end}

Figure 4 and Figure 5 indicate that the results of methods (II) and (III) are almost equivalent and thus, the assumption that Eq.(23) is valid for this example is verified. Moreover, (II) and (III) are coinciding with the reference solution. The minor deviation in the right figure of Figure 4 results form both, considering only the first three fixed-interface normal modes and retaining only 12 local Ritz-vectors. It has to be pointed out that the left and right figures of Figure 4 are scaled differently. Figure 5 shows, that the additionally nonlinear springs between mass 400 up to mass 450 act almost like a rigid connection. This is caused by the 10-times higher spring stiffness of the additionally nonlinear springs with respect to the linear springs of the system. In this example, the required computational time for solving Eq.(25) is approximately 25 % lower than for solving Eq.(21).
Contact problems of two elastic bodies could be computed analogously to this example. Therefore each elastic body has to be represented by both global vibration modes and mass-orthogonal local Ritz-vectors, and for such problems the contact force depends of course on the generalized coordinates of both elastic bodies.

6 Conclusion

This contribution is devoted to a more efficient handling of a system, which is reduced by global vibration modes together with Ritz-vectors needed for local effects. By a mass decoupling procedure together with the reasonable assumption of weak stiffness coupling, the differential equations of the local Ritz-vector DOF are replaced by nonlinear algebraic constraints. The presented generic example demonstrates the successful reduction of the system of differential equations, while the numerical results show acceptable accurate.

7 Acknowledgments

Support of this work in the framework of the K2-Austrian Center of Competence in Mechatronics (ACCM) and the Siemens VAI Metals Technologies GmbH is gratefully acknowledged.

8 References

[1] Hurty, W.C.: Vibration of structural systems by component mode synthesis, Journal of Engineering Mechanics (ASCE), 86 (4), pp. 51-69, 1960.

[2] Hurty, W.C. : Dynamic Analysis of structural systems using Component Modes, *AIAA Journal* 3 (4), pp. 678-685, 1965.

[3] Craig, R.R., Bampton, M.C.C.: Coupling of substructures for dynamic analyses, *AIAA Journal* 6(7), pp. 1313-1319, 1968.

[4] Craig, R.R.: Substructure methods in vibration, *Journal of Mechanical Design*, 117, pp. 207-213, 1995.

[5] Craig. R.R., Chang C.J.: Free Interface Methodes of substructure coupling for dynamic analysis, *AIAA Journal*, 14 (11), pp. 1633-1635, 1976.

[6] Craig. R.R., Chang C.J.: On the use of attachment modes in substructure coupling for dynamic analysis. In *AIAA/ASME 18th Structures, Structural Dynamic and Mechanic Conference*, San Diego, CA, No. 77-405, pp. 89-99, 1977.

[7] Rubin S.: Improved component-mode representation for structural dynamic analysis, *AIAA Journal* 13(8), pp. 995-1006, 1975.

[8] MacNeal, R.H.: A hybrid method of component mode synthesis, *Computers and Structures* 1(4), pp 581-601, 1971.

[9] Craig, R.R.: A review of time-domain and frequency-domain Component mode synthesis methods, *Int. J. Analytical and Experimental Modal Analysis*, 2 (2), pp. 59-72, 1987.

[10] Craig, R.R.: Coupling of substructures for dynamic analysis: An Overview, *In AIAA Paper, No 2000-1573, AIAA Dynamics Specialists Conference*, Atlanta, GA, April 5, 2000.

[11] Craig, R.R., Kurdila, A.J.: *Fundamentals of Structural Dynamics.* John Wiley & Sons Inc., New Jersey, 2006.

[12] Apiwattanalunggarn P., Shaw S.W., Pierre C.: Component Mode Synthesis Using Nonlinear Modes, *Nonlinear Dynamics*, 41 (1-3), pp.17-46, 2005.

[13] Witteveen, W., Irschik, H.: Efficient Mode-Based Computational Approach for Jointed Structures: Joint Interface Modes, *AIAA Journal,* 47 (1), pp. 252-263, 2009.

[14] Craig, R.R., Hale, A.L.: Block-Krylov Component Synthesis Method for Structural Model Reduction, *AIAA Journal of Guidance, Control, and Dynamics,* 11 (6), pp.562-570, 1988.

[15] Witteveen, W.: *Modal based computation of jointed structures.* Dissertation, Johannes Kepler University, Linz, 2007.

[16] Witteveen, W., Irschik, H.: Efficient Computation of Joint Interface Modes, in: CD-Rom *Proceedings 27th Int. Modal Analysis Conference*, Orlando, Florida, USA, 2009. Bethel, Conn.: Society of Experimental Mechanics.

Direct decoupling of substructures using primal and dual formulation

Walter D'Ambrogio and Annalisa Fregolent

Abstract The paper considers the decoupling problem, i.e. the identification of the dynamic behaviour of a structural subsystem, starting from the known dynamic behaviour of the coupled system, and from information about the remaining part of the structural system (residual subsystem). Substructure decoupling techniques can be classified as inverse coupling techniques or direct decoupling techniques. In inverse coupling, the equations written for the coupling problem are rearranged to isolate (as unknown) one of the substructures instead of the coupled structure. Examples of inverse coupling are impedance and mobility approaches. Direct decoupling consists in adding to the coupled system a fictitious subsystem which is the negative of the residual subsystem. Starting from the 3-field formulation (dynamic balance, compatibility and equilibrium at the interface), the problem can be solved in a primal or in a dual manner. Compatibility and equilibrium can be required either at coupling DoFs only, or at additional internal DoFs of the residual subsystem. Furthermore DoFs used to enforce equilibrium might be not the same as DoFs used for compatibility: this generates the so called non collocated approach. In this paper, direct decoupling techniques are considered: primal and dual formulation are compared in combination with collocated and non collocated interface.

1 Introduction

Dynamic substructuring consists in building the structural dynamic model of a complex system by assembling the dynamic models of simpler components (substruc-

Walter D'Ambrogio
Dipartimento di Ingegneria Meccanica, Energetica e Gestionale, Università dell'Aquila, Via G. Gronchi, 18 - I-67100, L'Aquila (AQ), Italy, e-mail: walter.dambrogio@univaq.it

Annalisa Fregolent
Dipartimento di Ingegneria Meccanica e Aerospaziale, Università di Roma La Sapienza, Via Eudossiana 18, I 00184 Rome, Italy e-mail: annalisa.fregolent@uniroma1.it

T. Proulx (ed.), *Linking Models and Experiments, Volume 2*, Conference Proceedings of the Society for Experimental Mechanics Series 5,
DOI 10.1007/978-1-4419-9305-2_5, © The Society for Experimental Mechanics, Inc. 2011

tures or subsystems). This kind of problem is also known in the literature as coupling problem or subsystem addition. Many well established techniques exist, when all substructures are modeled theoretically. However, a very important issue is the possibility of combining different kind of models, some obtained from a theoretical or numerical analysis such as a Finite Element Model (FEM) and some others derived from experimental tests (Frequency Response Functions: FRFs). When the model of at least one subsystem derives from experimental tests, the process is called experimental dynamic substructuring. The subject is particularly relevant in virtual prototyping of complex systems and responds to actual industrial needs. Due to modal truncation problems, in experimental dynamic substructuring, the use of FRFs (Frequency Based Substructuring) is preferred with respect to the use of modal parameters. The main algorithm for frequency based substructuring is the improved impedance coupling [4] that involves just one matrix inversion with respect to the classical impedance coupling technique that requires three inversions. A general framework for dynamic substructuring is provided in [6, 5], where primal and dual formulation are introduced.

Sometimes the opposite need arises, namely how to extract a substructure model from the assembled system. In this case one speaks of decoupling problem or subsystem subtraction. A trivial application of decoupling is mass cancellation, to get rid of the effect of the accelerometer mass on FRF measurements. Another application is joint identification. More generally, decoupling is a relevant issue for subsystems that cannot be measured separately, but only when coupled to their neighboring substructure(s) (e.g. a fixture needed for testing or subsystems that are very delicate or in operational conditions). To be more precise, the decoupling problem is defined as the identification of the dynamic behaviour of a structural subsystem, starting from the known dynamic behaviour of the assembled system, and from information about the remaining part of the structural system (residual subsystem).

Substructure decoupling techniques can be classified as inverse coupling techniques or direct decoupling techniques. In inverse coupling, the equations written for the coupling problem are rearranged to isolate (as unknown) one of the substructures instead of the assembled structure. Examples of inverse coupling are impedance and mobility approaches [1, 7].

Direct decoupling consists in adding to the assembled system a fictitious subsystem, which is the negative of the residual subsystem. The technique starts from the 3-field formulation: one set of equations expressing the dynamic balance of the assembled system and, separately, of the fictitious subsystem; one set of equations enforcing compatibility at interface DoFs, one set of equations enforcing equilibrium of constraint forces at interface DoFs. To solve the problem, a primal approach or a dual approach can be used. Compatibility and equilibrium can be required either at coupling DoFs only (standard interface), or at additional internal DoFs of the residual subsystem (extended interface): as shown in [3] for the dual approach, the choice of interface DoFs determines a set of frequencies at which the decoupling problem is ill conditioned. Apparently, when using an extended interface, the problem is singular at all frequencies, although this singularity is easily removed by using standard smart inversion techniques. To circumvent this problem, in [8, 9]

it is pointed out that DoFs used to enforce equilibrium need not to be the same as DoFs used to enforce compatibility: this gives rise to the so called non collocated approach, as opposite to the traditional approach in which such DoFs are the same, which is called collocated.

In this paper, direct decoupling techniques are considered. Specifically, primal formulation for decoupling is developed and compared with dual formulation: it is shown that both formulation provide the same result when the number of DoFs used to enforce compatibility is equal to the number of DoFs used to enforce equilibrium, i.e. in the collocated approach and in some special case of non collocated approach. On the contrary, when the number of DoFs used to enforce compatibility is different from the number of DoFs used to enforce equilibrium, the two approaches provide different results. The techniques are applied using simulated data from a torsional system describing a two-speed transmission.

2 Direct decoupling techniques

The coupled structural system AB (N_{AB} DoFs) is assumed to be made by an unknown subsystem A (N_A DoFs) and a residual subsystem B (N_B DoFs) joined through a number of couplings (see fig. 1). The residual subsystem (B) can be made by one or more substructures. The degrees of freedom (DoFs) of the coupled system can be partitioned into internal DoFs (not belonging to the couplings) of subsystem A (a), internal DoFs of subsystem B (b), and coupling DoFs (c).

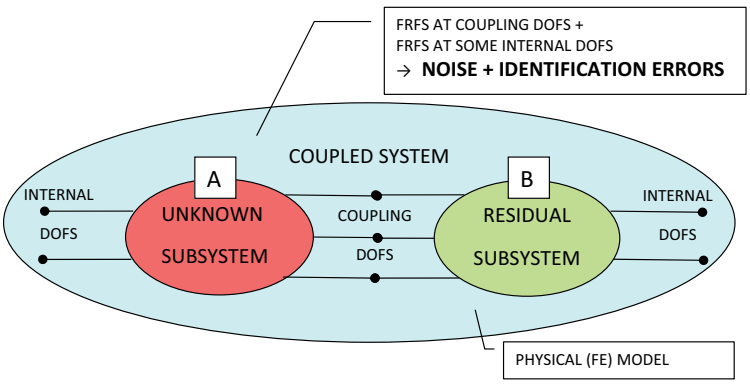

Fig. 1 Scheme of the decoupling problem

It is required to find the FRF of the unknown substructure A starting from the FRF of the coupled system AB. The subsystem A can be extracted from the coupled system AB by cancelling the dynamic effect of the residual subsystem B. This

can be accomplished by adding to the coupled system AB a fictitious subsystem with a dynamic stiffness opposite to that of the residual subsystem B and satisfying compatibility and equilibrium conditions. The dynamic equilibrium of the coupled system AB and of the fictitious subsystem can be expressed in block diagonal format as:

$$\begin{bmatrix} [Z^{AB}] & [0] \\ [0] & -[Z^{B}] \end{bmatrix} \begin{Bmatrix} \{u^{AB}\} \\ \{u^{B}\} \end{Bmatrix} = \begin{Bmatrix} \{f^{AB}\} \\ \{f^{B}\} \end{Bmatrix} + \begin{Bmatrix} \{g^{AB}\} \\ \{g^{B}\} \end{Bmatrix} \tag{1}$$

where:

- $[Z^{AB}]$, $[Z^{B}]$ are the dynamic stiffness matrices of the coupled system AB and of the residual subsystem B, respectively;
- $\{u^{AB)}\}$, $\{u^{B)}\}$ are the vectors of degrees of freedom of the coupled system AB and of the residual subsystem B, respectively;
- $\{f^{AB}\}$, $\{f^{B}\}$ are the external force vectors on the coupled system AB and on the fictitious subsystem, respectively;
- $\{g^{AB}\}$, $\{g^{B}\}$ are the vectors of connecting forces between the coupled system and the fictitious subsystem, and viceversa (constraint forces associated with compatibility conditions).

According to this point of view, the interface between the coupled system AB and the fictitious subsystem should not only include all the coupling DoFs between subsystems A and B, but should as well include all the internal DoFs of subsystem B. However, by taking into account that the problem can be solved by considering just coupling DoFs, the number of interface DoFs should be greater than or equal to the number of coupling DoFs n_c. Therefore, three options for interface DoFs can be considered:

- standard interface, including only the coupling DoFs (c) between subsystems A and B;
- extended interface, including also a subset of internal DoFs ($i \subseteq b$) of the residual substructure;
- mixed interface, including a subset of coupling DoFs ($d \subseteq c$) and a subset of internal DoFs ($i \subseteq b$) of the residual substructure.

The compatibility condition at the (standard, extended, mixed) interface DoFs implies that any pair of matching DoFs u_l^{AB} and u_m^B, i.e. DoF l on the coupled system AB and DoF m on subsystem B must have the same displacement, that is $u_l^{AB} - u_m^B = 0$. Let the number of interface DoFs on which compatibility is enforced be denoted as N_C.

The compatibility condition can be generally expressed as:

$$\begin{bmatrix} [B_C^{AB}] & [B_C^{B}] \end{bmatrix} \begin{Bmatrix} \{u^{AB}\} \\ \{u^{B}\} \end{Bmatrix} = \{0\} \tag{2}$$

where each row of $[B_C] = \left[[B_C^{AB}]\,[B_C^{B}]\right]$ corresponds to a pair of matching DoFs. Note that $[B_C]$ has size $N_C \times (N_{AB} + N_B)$ and is, in most cases, a signed Boolean matrix.

Before deriving the equilibrium condition, it should be noted that the interface DoFs involved in the equilibrium condition are not necessarily the same used to enforce the compatibility condition, as long as controllability between equilibrium and compatibility DoFs is ensured. If the compatibility and the equilibrium DoFs are not the same, the approach is called non-collocated [8]. Note that a non-collocated approach requires an extended or mixed interface and therefore it is only possible in the decoupling problems (in coupling problems only standard interface can be defined). Obviously, the traditional approach, in which compatibility and equilibrium DoFs are the same, is called collocated.

Let N_E denote the number of interface DoFs on which equilibrium is enforced. The equilibrium condition for constraint forces implies that, when the connecting forces are added for a pair of matching DoFs, their sum must be zero, i.e. $g_r^{AB} + g_s^B = 0$: this holds for any pair of matching DoFs. Furthermore, if DoF k on the coupled system AB (or to the residual subsystem B) does not belong to the equilibrium interface, it must be $g_k^{AB} = 0$ ($g_k^B = 0$): this holds for any DoF not involved in the equilibrium condition.

Overall, the above conditions can be expressed as:

$$\begin{bmatrix} [L_E^{AB}] \\ [L_E^B] \end{bmatrix}^T \begin{Bmatrix} \{g^{AB}\} \\ \{g^B\} \end{Bmatrix} = \{0\} \tag{3}$$

where the matrix $[L_E] = \left[[L_E^{AB}]\,[L_E^B]\right]$ is a Boolean localisation matrix. Note that the number of columns of $[L_E]$ is equal to the number N_E of equilibrium interface DoFs plus the number N_{NE} of DoFs not belonging to the equilibrium interface. Note that $N_{NE} = N_{AB} + N_B - 2N_E$: in fact, the number of DoFs belonging to the equilibrium interface must be subtracted once from N_{AB} and once from N_B. Therefore, the size of $[L_E]$ is $(N_{AB} + N_B) \times (N_{AB} + N_B - N_E)$.

Eqs. (1-3) can be put together to obtain the so-called 3-field formulation:

$$\begin{cases} \begin{bmatrix} [Z^{AB}] & [0] \\ [0] & -[Z^B] \end{bmatrix} \begin{Bmatrix} \{u^{AB}\} \\ \{u^B\} \end{Bmatrix} = \begin{Bmatrix} \{f^{AB}\} \\ \{f^B\} \end{Bmatrix} + \begin{Bmatrix} \{g^{AB}\} \\ \{g^B\} \end{Bmatrix} & (4) \\ \\ \left[[B_C^{AB}]\ \ [B_C^B]\right] \begin{Bmatrix} \{u^{AB}\} \\ \{u^B\} \end{Bmatrix} = \{0\} & (5) \\ \\ \begin{bmatrix} [L_E^{AB}] \\ [L_E^B] \end{bmatrix}^T \begin{Bmatrix} \{g^{AB}\} \\ \{g^B\} \end{Bmatrix} = \{0\} & (6) \end{cases}$$

2.1 Primal formulation

In the primal formulation, a unique set of DoFs is defined:

$$\begin{Bmatrix} \{u^{AB}\} \\ \{u^{B}\} \end{Bmatrix} = \begin{bmatrix} [L_C^{AB}] \\ [L_C^{B}] \end{bmatrix} \{q\} \tag{7}$$

where $\{q\}$ is the unique set of DoFs, and $[L_C]$ is a localisation matrix similar to $[L_E]$ introduced previously. Note that $[L_C]$ is a $(N_{AB}+N_B)\times(N_{AB}+N_B-N_C)$ matrix. Since there is a unique set of DoFs, $\{q\}$, the compatibility condition is satisfied automatically for any set $\{q\}$, i.e.

$$\begin{bmatrix} [B_C^{AB}] & [B_C^{B}] \end{bmatrix} \begin{Bmatrix} \{u^{AB}\} \\ \{u^{B}\} \end{Bmatrix} = \begin{bmatrix} [B_C^{AB}] & [B_C^{B}] \end{bmatrix} \begin{bmatrix} [L_C^{AB}] \\ [L_C^{B}] \end{bmatrix} \{q\} = \{0\} \qquad \forall \{q\} \tag{8}$$

Hence, $[L_C]$ is the nullspace of $[B_C]$ and, viceversa, $[B_C]^T$ is the nullspace of $[L_C]^T$:

$$\begin{cases} \begin{bmatrix} [B_C^{AB}] & [B_C^{B}] \end{bmatrix} \begin{bmatrix} [L_C^{AB}] \\ [L_C^{B}] \end{bmatrix} = \{0\} \\ \begin{bmatrix} [L_C^{AB}] \\ [L_C^{B}] \end{bmatrix}^T \begin{bmatrix} [B_C^{AB}] & [B_C^{B}] \end{bmatrix}^T = \{0\} \end{cases} \tag{9}$$

Since the compatibility condition, Eq. (5), is satisfied (see Eq. (8)) by the choice of the unique set $\{q\}$, the 3-field formulation reduces to:

$$\begin{cases} \begin{bmatrix} [Z^{AB}] & [0] \\ [0] & -[Z^{B}] \end{bmatrix} \begin{bmatrix} [L_C^{AB}] \\ [L_C^{B}] \end{bmatrix} \{q\} = \begin{Bmatrix} \{f^{AB}\} \\ \{f^{B}\} \end{Bmatrix} + \begin{Bmatrix} \{g^{AB}\} \\ \{g^{B}\} \end{Bmatrix} & (4^*) \\ \begin{bmatrix} [L_E^{AB}] \\ [L_E^{B}] \end{bmatrix}^T \begin{Bmatrix} \{g^{AB}\} \\ \{g^{B}\} \end{Bmatrix} = \{0\} & (6) \end{cases}$$

Pre-multiplying the equation (4*) by $[L_E]^T$ and noting that $[L_E]^T\{g\} = \{0\}$, the formulation reduces to:

$$\begin{bmatrix} [L_E^{AB}] \\ [L_E^{B}] \end{bmatrix}^T \begin{bmatrix} [Z^{AB}] & [0] \\ [0] & -[Z^{B}] \end{bmatrix} \begin{bmatrix} [L_C^{AB}] \\ [L_C^{B}] \end{bmatrix} \{q\} = \begin{bmatrix} [L_E^{AB}] \\ [L_E^{B}] \end{bmatrix}^T \begin{Bmatrix} \{f^{AB}\} \\ \{f^{B}\} \end{Bmatrix} \tag{10}$$

from which:

$$\{q\} = \left(\begin{bmatrix} [L_E^{AB}] \\ [L_E^{B}] \end{bmatrix}^T \begin{bmatrix} [Z^{AB}] & [0] \\ [0] & -[Z^{B}] \end{bmatrix} \begin{bmatrix} [L_C^{AB}] \\ [L_C^{B}] \end{bmatrix} \right)^+ \begin{bmatrix} [L_E^{AB}] \\ [L_E^{B}] \end{bmatrix}^T \begin{Bmatrix} \{f^{AB}\} \\ \{f^{B}\} \end{Bmatrix} \tag{11}$$

where the superscript $+$ denotes the generalized inverse.

To obtain a determined or overdetermined matrix for the generalized inversion operation, the following condition must be satisfied:

$$\text{number of columns of } [L_E] \geq \text{number of columns of } [L_C]$$

i.e.

$$(N_{AB}+N_B-N_E) \geq (N_{AB}+N_B-N_C) \quad \Rightarrow \quad N_C \geq N_E \geq n_c \tag{12}$$

where it is worth to recall that n_c ia the number of coupling DoFs.

Note that, if $N_C > N_E$, Eq. (10) is not satisfied exactly by vector $\{q\}$ given by Eq. (11), but only in the minimum square sense. This implies that also Eq. (6) is not satisfied exactly, i.e. equilibrium conditions at interface are approximately satisfied. On the contrary, compatibility is satisfied exactly due to the unique choice of $\{q\}$.

From Eq. (11), the FRF of the unknown subsystem A can be written as:

$$\left[H^A\right] = \left(\begin{bmatrix} \left[L_E^{AB}\right] \\ \left[L_E^{B}\right] \end{bmatrix}^T \begin{bmatrix} \left[Z^{AB}\right] & [0] \\ [0] & -\left[Z^{B}\right] \end{bmatrix} \begin{bmatrix} \left[L_C^{AB}\right] \\ \left[L_C^{B}\right] \end{bmatrix} \right)^+ \begin{bmatrix} \left[L_E^{AB}\right] \\ \left[L_E^{B}\right] \end{bmatrix}^T \tag{13}$$

$$\left[H^A\right] = \left(\left[L_E^{AB}\right]^T \left[Z^{AB}\right] \left[L_C^{AB}\right] - \left[L_E^{B}\right]^T \left[Z^{B}\right] \left[L_C^{B}\right] \right)^+ \left[\left[L_E^{AB}\right]^T \left[L_E^{B}\right]^T \right] \tag{14}$$

With the primal formulation, the columns of $[H^A]$ corresponding to the equilibrium interface DoFs appear twice. Furthermore, when using an extended interface, $[H^A]$ contains some meaningless rows and columns: those corresponding to the internal DoFs of the residual substructure B. Obviously, only meaningful and independent entries are retained.

2.2 Dual formulation

In the dual formulation, the total set of DoFs is retained, i.e. each interface DoF is present as many times as there are substructures connected through that DoF. The equilibrium condition $g_l^{(r)} + g_m^{(s)} = 0$ at a pair of equilibrium interface DoFs is ensured by choosing, for instance, $g_l^{(r)} = -\lambda$ and $g_m^{(s)} = \lambda$. Due to the construction of $[B_E]$, the overall interface equilibrium can be ensured by writing the connecting forces in the form:

$$\begin{Bmatrix} \{g^{AB}\} \\ \{g^{B}\} \end{Bmatrix} = - \begin{bmatrix} \left[B_E^{AB}\right]^T \\ \left[B_E^{B}\right]^T \end{bmatrix} \{\lambda\} \tag{15}$$

where $\{\lambda\}$ are Lagrange multipliers corresponding to connecting force intensities.

The interface equilibrium condition (6) is thus written:

$$\begin{bmatrix} [L_E^{AB}] \\ [L_E^B] \end{bmatrix}^T \begin{Bmatrix} \{g^{AB}\} \\ \{g^B\} \end{Bmatrix} = - \begin{bmatrix} [L_E^{AB}] \\ [L_E^B] \end{bmatrix}^T \begin{bmatrix} [B_E^{AB}]^T \\ [B_E^B]^T \end{bmatrix} \{\lambda\} = \{0\} \tag{16}$$

Then $[B_E]^T$ is the nullspace of $[L_E]^T$, and viceversa $[L_E]$ is the nullspace of $[B_E]$:

$$\begin{cases} \begin{bmatrix} [B_E^{AB}] & [B_E^B] \end{bmatrix} \begin{bmatrix} [L_E^{AB}] \\ [L_E^B] \end{bmatrix} = \{0\} \\ \begin{bmatrix} [L_E^{AB}] \\ [L_E^B] \end{bmatrix}^T \begin{bmatrix} [B_E^{AB}] & [B_E^B] \end{bmatrix}^T = \{0\} \end{cases} \tag{17}$$

Since Eq. (16) is always satisfied, the 3-field formulation reduces to:

$$\begin{cases} \begin{bmatrix} [Z^{AB}] & [0] \\ [0] & -[Z^B] \end{bmatrix} \begin{Bmatrix} \{u^{AB}\} \\ \{u^B\} \end{Bmatrix} + \begin{bmatrix} [B_E^{AB}]^T \\ [B_E^B]^T \end{bmatrix} \{\lambda\} = \begin{Bmatrix} \{f^{AB}\} \\ \{f^B\} \end{Bmatrix} & (4^{**}) \\ \begin{bmatrix} [B_C^{AB}] & [B_C^B] \end{bmatrix} \begin{Bmatrix} \{u^{AB}\} \\ \{u^B\} \end{Bmatrix} = \{0\} & (5) \end{cases}$$

To eliminate $\{\lambda\}$, Eq. (4^{**}) can be written:

$$\begin{Bmatrix} \{u^{AB}\} \\ \{u^B\} \end{Bmatrix} = - \begin{bmatrix} [Z^{AB}] & [0] \\ [0] & -[Z^B] \end{bmatrix}^{-1} \begin{bmatrix} [B_E^{AB}]^T \\ [B_E^B]^T \end{bmatrix} \{\lambda\} + \begin{bmatrix} [Z^{AB}] & [0] \\ [0] & -[Z^B] \end{bmatrix}^{-1} \begin{Bmatrix} \{f^{AB}\} \\ \{f^B\} \end{Bmatrix} \tag{18}$$

which substituted in Eq. (5) gives:

$$\begin{aligned} \begin{bmatrix} [B_C^{AB}] & [B_C^B] \end{bmatrix} \begin{bmatrix} [Z^{AB}] & [0] \\ [0] & -[Z^B] \end{bmatrix}^{-1} \begin{bmatrix} [B_E^{AB}]^T \\ [B_E^B]^T \end{bmatrix} \{\lambda\} = \\ = \begin{bmatrix} [B_C^{AB}] & [B_C^B] \end{bmatrix} \begin{bmatrix} [Z^{AB}] & [0] \\ [0] & -[Z^B] \end{bmatrix}^{-1} \begin{Bmatrix} \{f^{AB}\} \\ \{f^B\} \end{Bmatrix} \end{aligned} \tag{19}$$

from which $\{\lambda\}$ is obtained:

$$\begin{aligned} \{\lambda\} = \left(\begin{bmatrix} [B_C^{AB}] & [B_C^B] \end{bmatrix} \begin{bmatrix} [Z^{AB}] & [0] \\ [0] & -[Z^B] \end{bmatrix}^{-1} \begin{bmatrix} [B_E^{AB}]^T \\ [B_E^B]^T \end{bmatrix} \right)^+ \times \\ \times \begin{bmatrix} [B_C^{AB}] & [B_C^B] \end{bmatrix} \begin{bmatrix} [Z^{AB}] & [0] \\ [0] & -[Z^B] \end{bmatrix}^{-1} \begin{Bmatrix} \{f^{AB}\} \\ \{f^B\} \end{Bmatrix} \end{aligned} \tag{20}$$

To obtain a determined or overdetermined matrix for the generalized inversion operation, the following condition must be satisfied:

$$\text{number of rows of } [B_C] \geq \text{number of rows of } [B_E]$$

i.e.

$$N_C \geq N_E \geq n_c \tag{21}$$

which is the same as (12).

Note that, if $N_C > N_E$, Eq. (19) is not satisfied exactly by vector $\{\lambda\}$ given by Eq. (20), but only in the minimum square sense. This implies that also Eq. (5) is not satisfied exactly, i.e. compatibility conditions at interface are approximately satisfied. On the contrary, equilibrium is satisfied exactly due to the introduction of the connecting force intensities $\{\lambda\}$ as in Eq. (15).

Substituting $\{\lambda\}$ in Eq. (4^{**}), it is obtained:

$$\begin{aligned}
&\begin{bmatrix} [Z^{AB}] & [0] \\ [0] & -[Z^B] \end{bmatrix} \begin{Bmatrix} \{u^{AB}\} \\ \{u^B\} \end{Bmatrix} + \begin{bmatrix} [B_E^{AB}]^T \\ [B_E^B]^T \end{bmatrix} \times \\
&\times \left(\begin{bmatrix} [B_C^{AB}] & [B_C^B] \end{bmatrix} \begin{bmatrix} [Z^{AB}] & [0] \\ [0] & -[Z^B] \end{bmatrix}^{-1} \begin{bmatrix} [B_E^{AB}]^T \\ [B_E^B]^T \end{bmatrix} \right)^+ \times \\
&\times \begin{bmatrix} [B_C^{AB}] & [B_C^B] \end{bmatrix} \begin{bmatrix} [Z^{AB}] & [0] \\ [0] & -[Z^B] \end{bmatrix}^{-1} \begin{Bmatrix} \{f^{AB}\} \\ \{f^B\} \end{Bmatrix} = \begin{Bmatrix} \{f^{AB}\} \\ \{f^B\} \end{Bmatrix}
\end{aligned} \tag{22}$$

Finally, $\{u\}$ can be written in the form $\{u\} = [H]\{f\}$, which provides the FRF of the unknown subsystem A:

$$\begin{aligned}
\begin{Bmatrix} \{u^{AB}\} \\ \{u^B\} \end{Bmatrix} = &\begin{bmatrix} [Z^{AB}] & [0] \\ [0] & -[Z^B] \end{bmatrix}^{-1} - \begin{bmatrix} [Z^{AB}] & [0] \\ [0] & -[Z^B] \end{bmatrix}^{-1} \begin{bmatrix} [B_E^{AB}]^T \\ [B_E^B]^T \end{bmatrix} \times \\
&\times \left(\begin{bmatrix} [B_C^{AB}] & [B_C^B] \end{bmatrix} \begin{bmatrix} [Z^{AB}] & [0] \\ [0] & -[Z^B] \end{bmatrix}^{-1} \begin{bmatrix} [B_E^{AB}]^T \\ [B_E^B]^T \end{bmatrix} \right)^+ \times \\
&\times \begin{bmatrix} [B_C^{AB}] & [B_C^B] \end{bmatrix} \begin{bmatrix} [Z^{AB}] & [0] \\ [0] & -[Z^B] \end{bmatrix}^{-1} \begin{Bmatrix} \{f^{AB}\} \\ \{f^B\} \end{Bmatrix}
\end{aligned} \tag{23}$$

i.e., by noting that the inverted dynamic stiffness matrices $[Z^{AB}]^{-1}$ and $[Z^B]^{-1}$ are equal to the FRF matrices $[H^{AB}]$ and $[H^B]$ at the full set of DoFs:

$$\begin{aligned}\left[H^A\right] = &\begin{bmatrix}\left[H^{AB}\right] & [0]\\ [0] & -\left[H^B\right]\end{bmatrix} - \begin{bmatrix}\left[H^{AB}\right] & [0]\\ [0] & -\left[H^B\right]\end{bmatrix}\begin{bmatrix}\left[B_E^{AB}\right]^T\\ \left[B_E^B\right]^T\end{bmatrix} \times \\ &\times \left(\begin{bmatrix}\left[B_C^{AB}\right] & \left[B_C^B\right]\end{bmatrix}\begin{bmatrix}\left[H^{AB}\right] & [0]\\ [0] & -\left[H^B\right]\end{bmatrix}\begin{bmatrix}\left[B_E^{AB}\right]^T\\ \left[B_E^B\right]^T\end{bmatrix}\right)^+ \times \\ &\times \begin{bmatrix}\left[B_C^{AB}\right] & \left[B_C^B\right]\end{bmatrix}\begin{bmatrix}\left[H^{AB}\right] & [0]\\ [0] & -\left[H^B\right]\end{bmatrix}\end{aligned} \tag{24}$$

With the dual formulation, the rows and the columns of $[H^A]$ corresponding to all the interface DoFs appear twice. Furthermore, when using an extended interface, $[H^A]$ contains some meaningless rows and columns: those corresponding to the internal DoFs of the residual substructure B. Obviously, only meaningful and independent entries are retained.

In Eq. (24), the product of the three matrices to be inverted can be defined as *interface flexibility matrix*. The interface flexibility matrix can be rewritten as:

$$\begin{aligned}&\begin{bmatrix}\left[B_C^{AB}\right] & \left[B_C^B\right]\end{bmatrix}\begin{bmatrix}\left[H^{AB}\right] & [0]\\ [0] & -\left[H^B\right]\end{bmatrix}\begin{bmatrix}\left[B_E^{AB}\right]^T\\ \left[B_E^B\right]^T\end{bmatrix} = \\ &\qquad = \left[B_C^{AB}\right]\left[H^{AB}\right]\left[B_E^{AB}\right]^T - \left[B_C^B\right]\left[H^B\right]\left[B_E^B\right]^T\end{aligned} \tag{25}$$

It can be noticed that

$$\left[B_C^{AB}\right]\left[H^{AB}\right]\left[B_E^{AB}\right]^T = \left[\hat{H}^{AB}\right]$$

where $[\hat{H}^{AB}]$ is a subset of the FRF matrix of the coupled structure: pre-multiplication by $[B_C^{AB}]$ extracts rows at compatibility DoFs, and post-multiplication by $[B_E^{AB}]$ extracts columns at the equilibrium DoFs. Similarly,

$$\left[B_C^B\right]\left[H^B\right]\left[B_E^B\right]^T = \left[\hat{H}^B\right]$$

where $[\hat{H}^B]$ is the FRF of the residual structure at the same DoFs as above.

Therefore, the interface flexibility matrix becomes:

$$\left[B_C^{AB}\right]\left[H^{AB}\right]\left[B_E^{AB}\right]^T - \left[B_C^B\right]\left[H^B\right]\left[B_E^B\right]^T = \left[\hat{H}^{AB}\right] - \left[\hat{H}^B\right] \tag{26}$$

Note that, whenever compatibility and equilibrium DoFs are the same, $[\hat{H}^{AB}]$ and $[\hat{H}^B]$ can be seen as the inverse of the condensed dynamic stiffness matrices of the coupled structure $[\hat{Z}^{AB}]$ and the residual structure $[\hat{Z}^B]$, respectively. In this case, the interface flexibility matrix can be rewritten as:

$$\begin{aligned}\left[\hat{H}^{AB}\right]-\left[\hat{H}^{B}\right]&=\left[\hat{Z}^{AB}\right]^{-1}\left[\hat{Z}^{AB}\right]\left(\left[\hat{H}^{AB}\right]-\left[\hat{H}^{B}\right]\right)\left[\hat{Z}^{B}\right]\left[\hat{Z}^{B}\right]^{-1}=\\&=\left[\hat{Z}^{AB}\right]^{-1}\left(\left[\hat{Z}^{B}\right]-\left[\hat{Z}^{AB}\right]\right)\left[\hat{Z}^{B}\right]^{-1}=\left[\hat{H}^{AB}\right]\left(\left[\hat{Z}^{B}\right]-\left[\hat{Z}^{AB}\right]\right)\left[\hat{H}^{B}\right]\end{aligned}\tag{27}$$

In the following, the influence of the choice of compatibility and equilibrium DoFs on singularity and ill-conditioning of $([\hat{H}^{AB}]-[\hat{H}^{B}])$ will be analysed.

2.3 Singularity of the interface flexibility matrix (dual formulation)

As shown in [3], and recalled in the Appendix, $\left[\hat{Z}^{B}\right]$ and $\left[\hat{Z}^{AB}\right]$ differ only in the upper left *cc* block, i.e. that relative to the coupling DoFs, and they can be conveniently written in block matrix form as:

$$\left[\hat{Z}^{AB}\right]=\begin{bmatrix}\left[\hat{Z}^{AB}\right]_{cc}&\left[\hat{Z}^{B}\right]_{ci}\\\left[\hat{Z}^{B}\right]_{ic}&\left[\hat{Z}^{B}\right]_{ii}\end{bmatrix}\qquad\left[\hat{Z}^{B}\right]=\begin{bmatrix}\left[\hat{Z}^{B}\right]_{cc}&\left[\hat{Z}^{B}\right]_{ci}\\\left[\hat{Z}^{B}\right]_{ic}&\left[\hat{Z}^{B}\right]_{ii}\end{bmatrix}\tag{28}$$

where subscripts *c* and *i* represent coupling DoFs and internal DoFs, respectively. Therefore:

$$\left[\hat{Z}^{B}\right]-\left[\hat{Z}^{AB}\right]=\begin{bmatrix}\left[\hat{Z}^{B}\right]_{cc}-\left[\hat{Z}^{AB}\right]_{cc}&[0]_{ci}\\[0]_{ic}&[0]_{ii}\end{bmatrix}\tag{29}$$

Therefore, the interface flexibility matrix in Eq. (27) can be expanded as:

$$\begin{aligned}&\begin{bmatrix}\left[\hat{H}^{AB}\right]_{cc}&\left[\hat{H}^{AB}\right]_{ci}\\\left[\hat{H}^{AB}\right]_{ic}&\left[\hat{H}^{AB}\right]_{ii}\end{bmatrix}-\begin{bmatrix}\left[\hat{H}^{B}\right]_{cc}&\left[\hat{H}^{B}\right]_{ci}\\\left[\hat{H}^{B}\right]_{ic}&\left[\hat{H}^{B}\right]_{ii}\end{bmatrix}=\\&=\begin{bmatrix}\left[\hat{H}^{AB}\right]_{cc}&\left[\hat{H}^{AB}\right]_{ci}\\\left[\hat{H}^{AB}\right]_{ic}&\left[\hat{H}^{AB}\right]_{ii}\end{bmatrix}\begin{bmatrix}\left[\hat{Z}^{B}\right]_{cc}-\left[\hat{Z}^{AB}\right]_{cc}&[0]_{ci}\\[0]_{ic}&[0]_{ii}\end{bmatrix}\begin{bmatrix}\left[\hat{H}^{B}\right]_{cc}&\left[\hat{H}^{B}\right]_{ci}\\\left[\hat{H}^{B}\right]_{ic}&\left[\hat{H}^{B}\right]_{ii}\end{bmatrix}\end{aligned}\tag{30}$$

Note that the interface flexibility matrix is expressed as a product of three matrices, and it is singular if just one of these matrices is singular. In fact, the determinant of a matrix product equals the product of the determinants.

2.3.1 Singularity using collocated extended interface

When using collocated approach with extended interface, the interface flexibility matrix can be singular for several reasons.

1. Because $([\hat{Z}^{B}]-[\hat{Z}^{AB}])$ is singular at all frequencies: this is true if *i* is not an empty set as assumed for the extended interface. Note that the matrix is truly

singular only when all data are known without errors or noise. In any case, the use of smart inversion techniques, e.g. the truncated SVD, allows to deal with the problem.

2. Because, as shown in [3] and recalled in appendix, $[\hat{H}^{AB}]$ is singular at the resonant frequencies of the coupled structure AB with interface DoFs grounded.
3. Because $[\hat{H}^{B}]$ is singular at the resonant frequencies of the residual substructure B with interface DoFs grounded.
   Note that the resonant frequencies of the residual substructure B, with interface DoFs grounded are a subset of the resonant frequencies of the coupled structure AB with interface DoFs grounded. (This is also apparent from Fig. 2, showing that the unknown subsystem A and the residual subsystem B are independent one of another when interface DoFs are grounded.) Therefore, the interface flexibility matrix is twice singular at the resonant frequencies of the residual subsystem B with coupling DoFs grounded.
   It should be noted that, differently from what could be expected from previous statements, the interface flexibility matrix is not singular at the resonant frequencies of the unknown subsystem A with interface DoFs grounded. In fact these are cancelled by the frequencies at which the determinant of $[\hat{Z}^{B}] - [\hat{Z}^{AB}] = -[\hat{Z}^{A}]$ tends to infinity, that (see Appendix) are the resonant frequencies of the unknown subsystem A with interface DoFs grounded.
   In cases 2 and 3, if noise is present as usual, the problem becomes ill conditioned but smart inversion techniques are not able to remove ill conditioning.

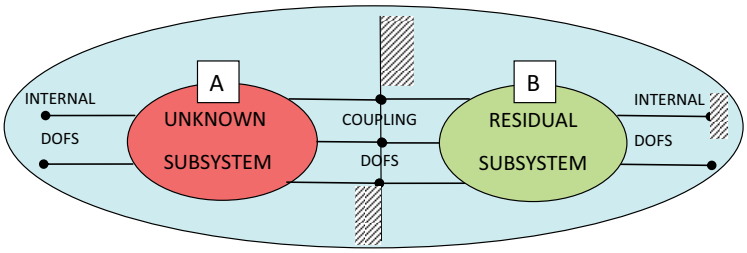

Fig. 2 Structure with (extended) interface DoFs grounded

A particular case is that of standard interface where Eq. (30) reduces to:

$$\left[\hat{H}^{AB}\right]_{cc} - \left[\hat{H}^{B}\right]_{cc} = \left[\hat{H}^{AB}\right]_{cc} \left(\left[\hat{Z}^{B}\right]_{cc} - \left[\hat{Z}^{AB}\right]_{cc}\right) \left[\hat{H}^{B}\right]_{cc} \tag{31}$$

and singularity occurs only, but twice, at the resonant frequencies of the residual substructure B with coupling DoFs grounded.

2.3.2 Singularity using non collocated extended interface

For the sake of simplicity, a special case of non collocated approach is considered where compatibility is enforced at DoFs c and i and equilibrium only at DoFs c. In this case, Eq. (30) becomes:

$$\begin{bmatrix} \left[\hat{H}^{AB}\right]_{cc} \\ \left[\hat{H}^{AB}\right]_{ic} \end{bmatrix} - \begin{bmatrix} \left[\hat{H}^{B}\right]_{cc} \\ \left[\hat{H}^{B}\right]_{ic} \end{bmatrix} = \begin{bmatrix} \left[\hat{H}^{AB}\right]_{cc} \\ \left[\hat{H}^{AB}\right]_{ic} \end{bmatrix} \left(\left[\hat{Z}^{B}\right]_{cc} - \left[\hat{Z}^{AB}\right]_{cc} \right) \left[\hat{H}^{B}\right]_{cc}$$

It can be noticed that $[\hat{H}^B]_{cc}$ is singular at resonances of the residual substructure B with coupling DoFs grounded. Therefore, the use of non collocated approach does not prevent from this kind of singularity.

3 Primal vs dual formulation

In this section, the expressions of the FRF of the unknown subsystem A provided by primal formulation and dual formulation are compared to establish whether they are the same or not, and under which conditions. The FRF of subsystem A provided by the primal formulation, Eq. (13), can be rewritten in compact form as:

$$[H^A]_P = \left([L_E]^T [Z] [L_C] \right)^+ [L_E]^T \tag{13}$$

where the subscript P stands for primal. If $N_C = N_E$, Eq. (13) becomes:

$$[H^A]_P = \left([L_E]^T [Z] [L_C] \right)^{-1} [L_E]^T \tag{32}$$

Premultiplying by $[L_E]^T [Z] [L_C]$, one obtains:

$$[L_E]^T [Z] [L_C] [H^A]_P = [L_E]^T \tag{33}$$

The FRF of the unknown subsystem A provided by dual formulation, Eq. (24), can be rewritten in compact form for $N_C = N_E$:

$$[H^A]_D = [H] - [H] [B_E]^T \left([B_C] [H] [B_E]^T \right)^{-1} [B_C] [H] \tag{34}$$

where the subscript D stands for dual. Premultiplying by $[Z]$, one obtains:

$$[Z] [H^A]_D = [I] - [B_E]^T \left([B_C] [H] [B_E]^T \right)^{-1} [B_C] [H] \tag{35}$$

Premultiplying by L_E^T, one obtains:

$$[L_E]^T [Z] [H^A]_D = [L_E]^T - [L_E]^T [B_E]^T \left([B_C] [H] [B_E]^T \right)^{-1} [B_C] [H] \tag{36}$$

from which, being $[L_E]^T [B_E]^T = 0$ since B_E^T is the nullspace of L_E^T (see Eq. 17):

$$[L_E]^T [Z] [H^A]_D = [L_E]^T \tag{37}$$

By comparing Eq. (37) and Eq. (33), it is found that:

$$[H^A]_D = [L_C] [H^A]_P \tag{38}$$

The former equation shows that, if $N_C = N_E$, primal and dual formulations provide the same result. In fact, by considering the primal formulation, the relation between the unique set of DoFs $\{q\}$ and the redundant set of DoFs $\{u\}$ is given by $\{u\} = [L_C] \{q\}$.

On the contrary, if $N_C > N_E$, Eq. (33) can not be obtained from Eq. (13) since:

$$\left([L_E]^T [Z] [L_C] \right) \left([L_E]^T [Z] [L_C] \right)^+ \neq [I]$$

due to the definition of pseudoinverse.

In fact in case of overdetermined system, the pseudoinverse of a matrix $[A]$ (number of rows $>$ number of columns) is:

$$[A]^+ = \left([A]^T [A] \right)^{-1} [A]^T$$

from which:

$$[A]^+ [A] = \left([A]^T [A] \right)^{-1} [A]^T [A] = [I]$$
$$[A] [A]^+ = [A] \left([A]^T [A] \right)^{-1} [A]^T \neq [I]$$

Therefore, if $N_C > N_E$, the primal and the dual formulation provide different results.

4 Application

A relatively simple application is considered on a torsional system that represents a model of a two-speed transmission. The complete system consists in three shafts: an input shaft, a layshaft and an output shaft (see Fig. 3). The layshaft is coupled both to the input shaft and to the output shaft by helical gears. Power flows through the gear that is locked to the output shaft by the shift collar (e.g. through gears 5 and 7 in Fig. 3). Input and output shafts are assumed to be fixed at the outer ends. Such a boundary condition is a good approximation whenever the mass moments of inertia upstream and downstream the transmission are very large compared to those within the transmission.

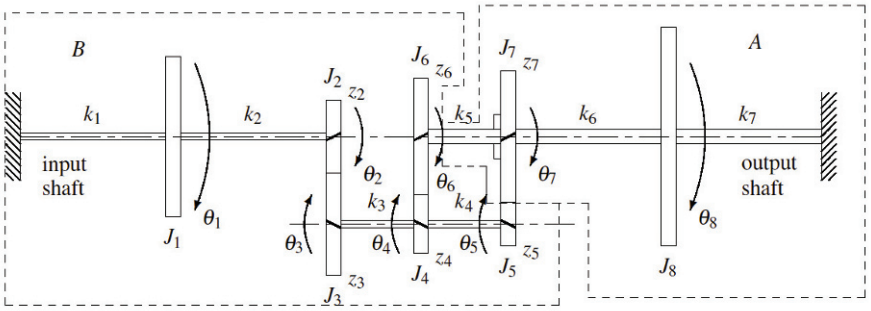

Fig. 3 Sketch of the test system: a two speed transmission in first gear

Rotational inertias and torsional stiffnesses, as well as torsional dampings, are shown in Table 1 together with the number of teeth z of each gear.

Table 1 Physical parameter values and number of teeth

Item	J [kg m^2]	c [Nm s/rad]	k [Nm/rad]	z
1	$3 \cdot 10^{-3}$	$8.25 \cdot 10^{-4}$	82.5	–
2	$1.98 \cdot 10^{-4}$	$8.25 \cdot 10^{-4}$	82.5	30
3	$7.62 \cdot 10^{-4}$	$1.65 \cdot 10^{-3}$	165	42
4	$8.13 \cdot 10^{-5}$	$1.65 \cdot 10^{-3}$	165	24
5	$2.57 \cdot 10^{-5}$	$6.875 \cdot 10^{-3}$	687.5	18
6	$1.3 \cdot 10^{-3}$	$3.435 \cdot 10^{-3}$	343.5	48
7	$2.08 \cdot 10^{-3}$	$3.435 \cdot 10^{-3}$	343.5	54
8	$1 \cdot 10^{-2}$	–	–	–

The rotations of meshing gear pairs are related by their gear ratio, e.g. the rotations θ_2, θ_6 and θ_7 are related to rotations θ_3, θ_4 and θ_5, respectively. The whole set of rotations $\theta_1 \cdots \theta_8$ can be expressed through a reduced set of five independent rotations, as shown by Eq. (39):

$$\begin{Bmatrix} \theta_1 \\ \theta_2 \\ \theta_3 \\ \theta_4 \\ \theta_5 \\ \theta_6 \\ \theta_7 \\ \theta_8 \end{Bmatrix} = \begin{bmatrix} 1 & 0 & 0 & 0 & 0 \\ 0 & z_3/z_2 & 0 & 0 & 0 \\ 0 & 1 & 0 & 0 & 0 \\ 0 & 0 & 1 & 0 & 0 \\ 0 & 0 & 0 & 1 & 0 \\ 0 & 0 & z_4/z_6 & 0 & 0 \\ 0 & 0 & 0 & z_5/z_7 & 0 \\ 0 & 0 & 0 & 0 & 1 \end{bmatrix} \begin{Bmatrix} \theta_1 \\ \theta_3 \\ \theta_4 \\ \theta_5 \\ \theta_8 \end{Bmatrix} \tag{39}$$

Therefore, the coupled system can be modelled as a 5 DoFs lumped parameter system.

As outlined in Fig. 3, the unknown subsystem A is a 2-DoFs system made by the output shaft to which gear 7 and flywheel 8 are locked. Note that gear 6 is not locked to the output shaft so that it can be considered as belonging to the residual subsystem B.

For the residual subsystem B, rotations $\theta_1^B \cdots \theta_6^B$ can be expressed through a reduced set of four independent rotations, as shown by Eq. (40):

$$\begin{Bmatrix} \theta_1^B \\ \theta_2^B \\ \theta_3^B \\ \theta_4^B \\ \theta_5^B \\ \theta_6^B \end{Bmatrix} = \begin{bmatrix} 1 & 0 & 0 & 0 \\ 0 & z_3/z_2 & 0 & 0 \\ 0 & 1 & 0 & 0 \\ 0 & 0 & 1 & 0 \\ 0 & 0 & 0 & 1 \\ 0 & 0 & z_4/z_6 & 0 \end{bmatrix} \begin{Bmatrix} \theta_1^B \\ \theta_3^B \\ \theta_4^B \\ \theta_5^B \end{Bmatrix} \tag{40}$$

Therefore, subsystem B can be modelled as a 4 DoFs lumped parameter system.

To have an idea of the dynamic behaviour of the torsional system, the natural frequencies of the subsystems A and B, and of the coupled system AB are shown in Table 2.

Table 2 Natural frequencies of the systems [Hz]

	Mode				
System	1	2	3	4	5
A	26.3881	72.2981	–	–	–
B	22.7742	56.3484	120.4927	416.6248	–
AB	23.3477	37.5007	59.7304	106.7501	184.4634

4.1 Decoupling

It is assumed that the rotational FRFs (mobilities) describing the angular velocity/torque relationship of the coupled system AB, and the mechanical impedance of the residual subsystem B are known. It is desired to determine the rotational mobility of subsystem A. The exact FRFs $\hat{H}_{ij}$ of the coupled system AB and the impedances of subsystem B are computed starting from the physical parameters shown in Table 1. To simulate the effect of noise on the FRFs of the coupled system, a complex random perturbation is added to the true FRFs:

$$H_{ij}(\omega_k) = \hat{H}_{ij}(\omega_k) + m_{ij,k} + i n_{ij,k} \tag{41}$$

where $m_{ij,k}$ and $n_{ij,k}$ are independent random variables with gaussian distribution, zero mean and a standard deviation of 0.1 rad/sNm. The effect of such perturbation

on the drive point rotational mobility at the coupling DoF is shown in Fig. 4 together with the FRF obtained after curve-fitting.

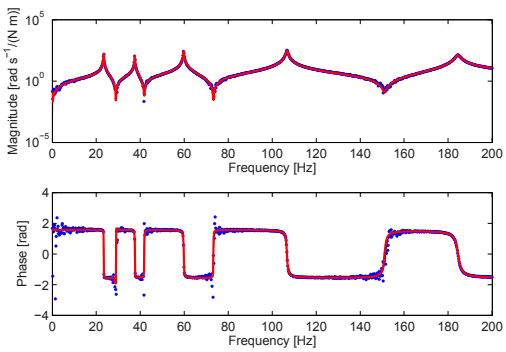

Fig. 4 Drive point rotational mobility of the complete system at the coupling DoF: true (—), perturbed by noise (***) and fitted (—)

In the sequel, only FRFs perturbed by simulated noise will be considered. In fact, if noise-free FRFs of the coupled system are used, the FRF of the unknown subsystem is always predicted without errors (although the problem may be singular for several reasons, as stated in section 2.3, the use of smart inversion techniques completely removes the singularity). Furthermore, perturbed FRFs are not used in raw form but are smoothed through a curve fitting procedure.

The rotational mobility of subsystem A can be determined by using the procedure described in section 2. The compatibility condition is written generally as:

$$[B_C]\{u\} = \left[B_C^{AB}\right]\left\{u^{AB}\right\} + \left[B_C^{B}\right]\left\{u^{B}\right\} = \{0\}$$

where

$$\left\{u^{AB}\right\}^T = \left[\theta_1\ \theta_3\ \theta_4\ \theta_5\ \theta_8\right] \qquad \left\{u^{B}\right\}^T = \left[\theta_1^B\ \theta_3^B\ \theta_4^B\ \theta_5^B\right]$$

and $\left[B_C^{AB}\right]$ and $\left[B_C^{B}\right]$ built as detailed afterwards. In non collocated approach, the compatibility and the equilibrium DoFs are not the same. Therefore, a localization matrix $[L_E] \neq [L_C]$, where $[L_C]$ is the nullspace of $[B_C]$, is defined to enforce equilibrium of constraint forces. A matrix $[B_E]$ can be defined accordingly, such that $[L_E]^T[B_E]^T = 0$.

4.1.1 Compatibility

Compatibility is alternatively enforced:

- only at the coupling DoFs (standard interface). In this case, it is:

$$[B_C] = \underset{\left[B_C^{AB}\right]}{\begin{matrix}\theta_1 & \theta_3 & \theta_4 & \theta_5 & \theta_8\end{matrix}} \underset{\left[B_C^{B}\right]}{\begin{matrix}\theta_1^B & \theta_3^B & \theta_4^B & \theta_5^B\end{matrix}}$$
$$\left[\begin{matrix}0 & 0 & 0 & 1 & 0\end{matrix}\ \middle|\ \begin{matrix}0 & 0 & 0 & -1\end{matrix}\right]$$

- also at some internal DoFs of the residual subsystem B (extended interface). By adding all internal DoF, it is:

$$[B_C] = \begin{array}{c} \begin{matrix} \theta_1 & \theta_3 & \theta_4 & \theta_5 & \theta_8 \end{matrix} \quad \begin{matrix} \theta_1^B & \theta_3^B & \theta_4^B & \theta_5^B \end{matrix} \\ \left[\begin{array}{ccccc|cccc} 0 & 0 & 0 & 1 & 0 & 0 & 0 & 0 & -1 \\ 1 & 0 & 0 & 0 & 0 & -1 & 0 & 0 & 0 \\ 0 & 1 & 0 & 0 & 0 & 0 & -1 & 0 & 0 \\ 0 & 0 & 1 & 0 & 0 & 0 & 0 & -1 & 0 \end{array}\right] \\ \left[B_C^{AB}\right] \qquad\qquad \left[B_C^B\right] \end{array}$$

  By adding only one internal DoF, it is:

  – using θ_1 as additional internal DoF:

$$[B_C] = \begin{array}{c} \begin{matrix} \theta_1 & \theta_3 & \theta_4 & \theta_5 & \theta_8 \end{matrix} \quad \begin{matrix} \theta_1^B & \theta_3^B & \theta_4^B & \theta_5^B \end{matrix} \\ \left[\begin{array}{ccccc|cccc} 0 & 0 & 0 & 1 & 0 & 0 & 0 & 0 & -1 \\ 1 & 0 & 0 & 0 & 0 & -1 & 0 & 0 & 0 \end{array}\right] \\ \left[B_C^{AB}\right] \qquad\qquad \left[B_C^B\right] \end{array}$$

  – using θ_3 as additional internal DoF:

$$[B_C] = \begin{array}{c} \begin{matrix} \theta_1 & \theta_3 & \theta_4 & \theta_5 & \theta_8 \end{matrix} \quad \begin{matrix} \theta_1^B & \theta_3^B & \theta_4^B & \theta_5^B \end{matrix} \\ \left[\begin{array}{ccccc|cccc} 0 & 0 & 0 & 1 & 0 & 0 & 0 & 0 & -1 \\ 0 & 1 & 0 & 0 & 0 & 0 & -1 & 0 & 0 \end{array}\right] \\ \left[B_C^{AB}\right] \qquad\qquad \left[B_C^B\right] \end{array}$$

  – using θ_4 as additional internal DoF:

$$[B_C] = \begin{array}{c} \begin{matrix} \theta_1 & \theta_3 & \theta_4 & \theta_5 & \theta_8 \end{matrix} \quad \begin{matrix} \theta_1^B & \theta_3^B & \theta_4^B & \theta_5^B \end{matrix} \\ \left[\begin{array}{ccccc|cccc} 0 & 0 & 0 & 1 & 0 & 0 & 0 & 0 & -1 \\ 0 & 0 & 1 & 0 & 0 & 0 & 0 & -1 & 0 \end{array}\right] \\ \left[B_C^{AB}\right] \qquad\qquad \left[B_C^B\right] \end{array}$$

4.1.2 Equilibrium

In collocated approach, $[B_C] = [B_E]$ in all the above cases.

Except for three cases whose results will be shown afterwards, in non collocated approach equilibrium is enforced only at the coupling Dofs. Therefore:

$$[B_E] = \begin{array}{c} \begin{matrix} \theta_1 & \theta_3 & \theta_4 & \theta_5 & \theta_8 \end{matrix} \quad \begin{matrix} \theta_1^B & \theta_3^B & \theta_4^B & \theta_5^B \end{matrix} \\ \left[\begin{array}{ccccc|cccc} 0 & 0 & 0 & 1 & 0 & 0 & 0 & 0 & -1 \end{array}\right] \\ \left[B_E^{AB}\right] \qquad\qquad \left[B_E^B\right] \end{array}$$

4.2 Results

First of all, the case of standard interface (rotational mobility only at the coupling DoF θ_5) is considered. In Fig. 5, the true drive point rotational mobility at the coupling DoF of subsystem A is compared with the corresponding FRF computed using the dual formulation, Eq. (24), starting from the fitted perturbed FRF of the coupled system. The same result is obtained using the primal formulation, Eq. (14).

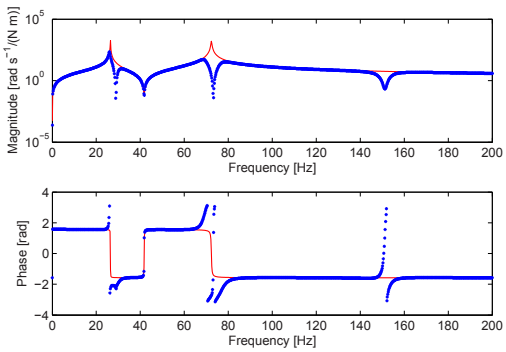

Fig. 5 Rotational mobility at the coupling DoF of subsystem A: true (—), computed from fitted perturbed FRF (***) without additional internal DoFs

As discussed in previous papers [2, 3], the predicted rotational mobility of subsystem A is badly identified at frequencies around 30, 70 and 150 Hz. This depends on ill conditioning due to unmeasured internal DoFs, as explained in section 2.3. In fact, the coupled system AB and the residual subsystem B, with the "measured" coupling DoF θ_5 grounded, share three resonance frequencies, namely $f_{n1} = 28.94$ Hz, $f_{n2} = 72.23$ Hz and $f_{n3} = 151.5$ Hz. Around these frequencies, $[\hat{H}^{AB}] - [\hat{H}^{B}]$ is ill-conditioned and noise is greatly amplified.

A way to circumvent this problem is to use an extended interface, i.e. to assume that the FRF matrix of the coupled system is known not only at the coupling DoF but also at a subset of the three internal DoFs (θ_1, θ_3, θ_4) of the residual subsystem B. The predicted rotational mobility of the unknown subsystem A, obtained using collocated approach with all the internal DoFs, is shown in Fig. 6: in this case, the residual subsystem is fully grounded and no ill-conditioned frequencies appear. The predicted rotational mobility of the unknown subsystem A, obtained using non collocated approach with compatibility at all DoFs and equilibrium at the coupling DoF θ_5, is shown in Fig. 7 for primal formulation and in Fig. 8 for dual formulation. As discussed in section 2.3.2, ill conditioned frequencies are the same as for standard interface but they affect the predicted FRFs to a lower extent if compared with the standard interface.

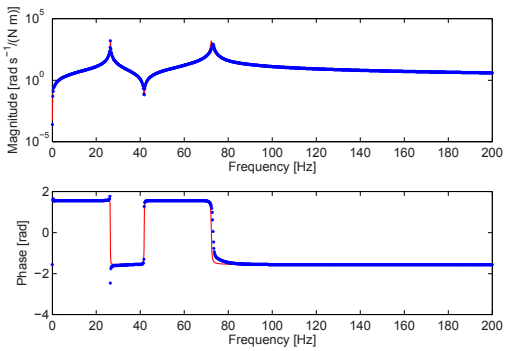

Fig. 6 Rotational mobility at the coupling DoF of subsystem A: true (—), computed from fitted perturbed FRF (***) using collocated approach with all the internal DoFs

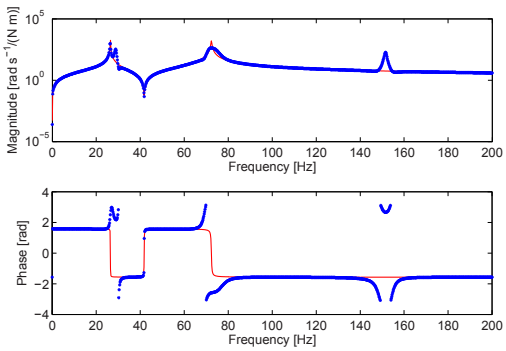

Fig. 7 Rotational mobility at the coupling DoF of subsystem A: true (—), computed from fitted perturbed FRF (***) using primal formulation with compatibility at all DoFs and equilibrium at the coupling DoF θ_5

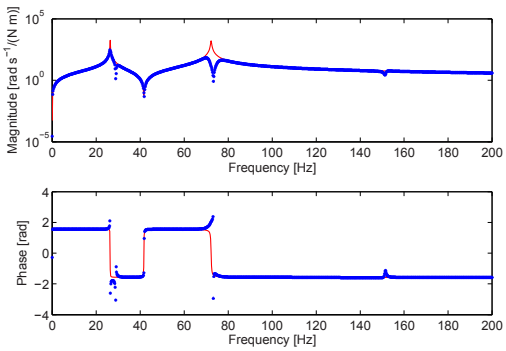

Fig. 8 Rotational mobility at the coupling DoF of subsystem A: true (—), computed from fitted perturbed FRF (***) using dual formulation with compatibility at all DoFs and equilibrium at the coupling DoF θ_5

Since the full set of internal DoFs can be difficult to measure in practice, results obtained by adding only one internal DoF are considered. The resonant frequencies of the residual subsystem B, with the measured DoFs grounded (the coupling DoF and one additional internal DoF), are shown in Table 3 versus the added internal DoF.

Table 3 Resonant frequencies of the residual subsystem B with extended interface DoFs grounded (the coupling DoF θ_5 and one additional internal DoF)

Added DoF	$f_{n1}[Hz]$	$f_{n2}[Hz]$
θ_1	69.4	151.5
θ_3	37.3	143.4
θ_4	31.5	87.15

The predicted rotational mobility of the unknown subsystem A obtained using collocated approach with the additional internal DoF θ_1 is shown in Fig. 9: in this case, troubles arise at frequencies close to 70 and 150 Hz, as shown in Table 3, around which the inversion of an ill conditioned matrix is performed. The predicted rotational mobility of the unknown subsystem A obtained using non collocated approach with compatibility at DoFs θ_1 and θ_5 and equilibrium at the coupling DoF θ_5 is shown in Fig. 10 for primal formulation and in Fig. 11 for dual formulation. Ill conditioned frequencies are the same as for standard interface.

Fig. 12 shows the predicted FRF of subsystem A using collocated approach with the additional internal DoF θ_3: in this case, troubles could arise at frequencies close to 37 and 143 Hz as shown in Table 3, but they do not appear. Using non collocated approach with compatibility at DoFs θ_3 and θ_5 and equilibrium at the coupling DoF θ_5, results are shown in Fig. 13 for primal formulation and in Fig. 14 for dual formulation. Again, ill conditioned frequencies are the same as for standard interface.

Fig. 15 shows the predicted FRF of subsystem A using collocated approach with the additional internal DoF θ_4: in this case, troubles could arise at frequencies close to 31 and 87 Hz as shown in Table 3, but only very slight effects can be noticed. Using non collocated approach with compatibility at DoFs θ_4 and θ_5 and equilibrium at the coupling DoF θ_5, results are shown in Fig. 16 for primal formulation and in Fig. 17 for dual formulation. Again, ill conditioned frequencies are the same as for standard interface.

Generally, collocated approach seems to provide the best results, because in non collocated approach, with equilibrium enforced only at coupling DoFs, ill conditioning occurs at the same frequencies that are troublesome with standard interface.

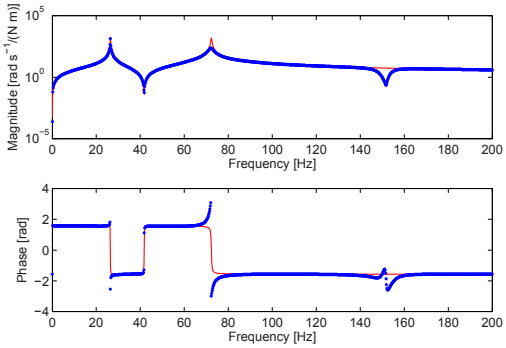

Fig. 9 Rotational mobility at the coupling DoF of subsystem A: true (—), computed from fitted perturbed FRF (***) using collocated approach with internal DoF θ_1

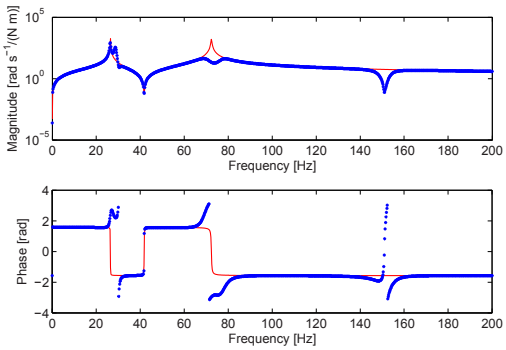

Fig. 10 Rotational mobility at the coupling DoF of subsystem A: true (—), computed from fitted perturbed FRF (***) using primal formulation with compatibility at DoFs θ_1 and θ_5 and equilibrium at the coupling DoF θ_5

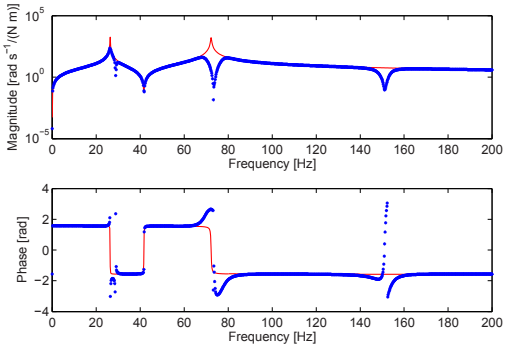

Fig. 11 Rotational mobility at the coupling DoF of subsystem A: true (—), computed from fitted perturbed FRF (***) using dual formulation with compatibility at DoFs θ_1 and θ_5 and equilibrium at the coupling DoF θ_5

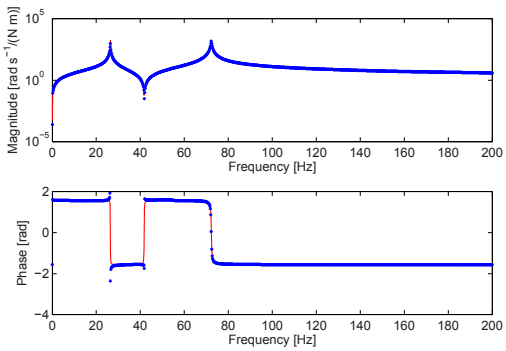

Fig. 12 Rotational mobility at the coupling DoF of subsystem A: true (—), computed from fitted perturbed FRF (***) using collocated approach with internal DoF θ_3

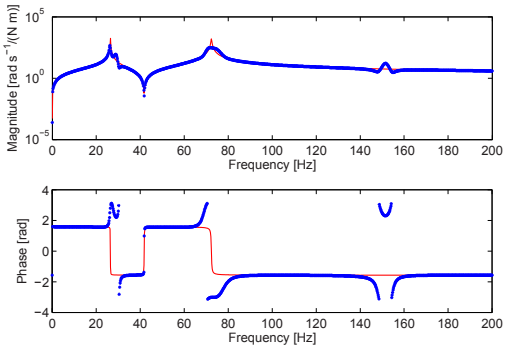

Fig. 13 Rotational mobility at the coupling DoF of subsystem A: true (—), computed from fitted perturbed FRF (***) using primal formulation with compatibility at DoFs θ_3 and θ_5 and equilibrium at the coupling DoF θ_5

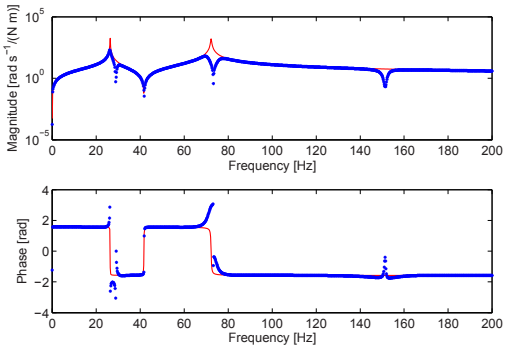

Fig. 14 Rotational mobility at the coupling DoF of subsystem A: true (—), computed from fitted perturbed FRF (***) using dual formulation with compatibility at DoFs θ_3 and θ_5 and equilibrium at the coupling DoF θ_5

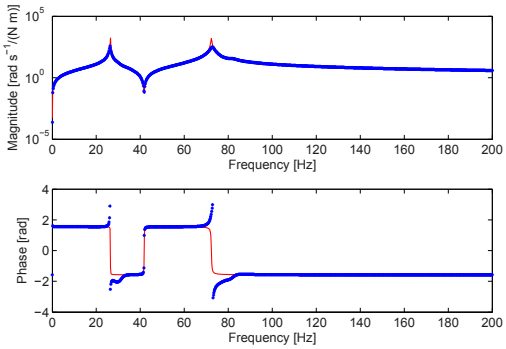

Fig. 15 Rotational mobility at the coupling DoF of subsystem A: true (—), computed from fitted perturbed FRF (***) using collocated approach with internal DoF θ_4

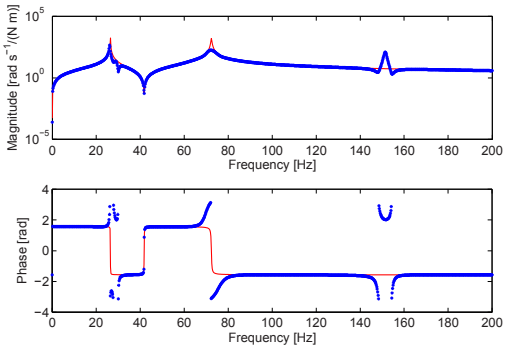

Fig. 16 Rotational mobility at the coupling DoF of subsystem A: true (—), computed from fitted perturbed FRF (***) using primal formulation with compatibility at DoFs θ_4 and θ_5 and equilibrium at the coupling DoF θ_5

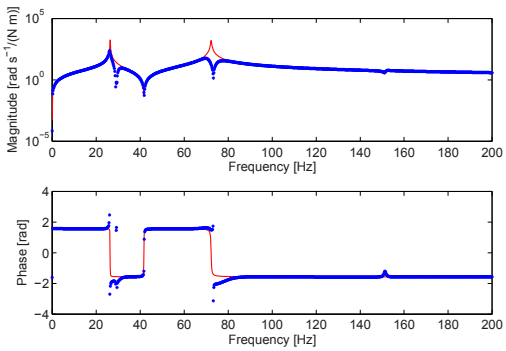

Fig. 17 Rotational mobility at the coupling DoF of subsystem A: true (—), computed from fitted perturbed FRF (***) using dual formulation with compatibility at DoFs θ_4 and θ_5 and equilibrium at the coupling DoF θ_5

In the sequel, non collocated approach is used with $N_C = N_E$. The coupling DoF θ_5 is always included among both compatibility and equilibrium DoFs. As demonstrated in section 3, primal and dual formulation give the same results when the number of equilibrium DoFs is the same as the number of compatibility DoFs.

Fig. 18 shows the predicted rotational mobility of unknown subsystem A obtained using non collocated approach with compatibility at DoFs θ_1 and θ_5 and equilibrium at DoFs θ_3 and θ_5. Figure 19 is obtained by exchanging compatibility and equilibrium DoFs. The second option seems to give better results.

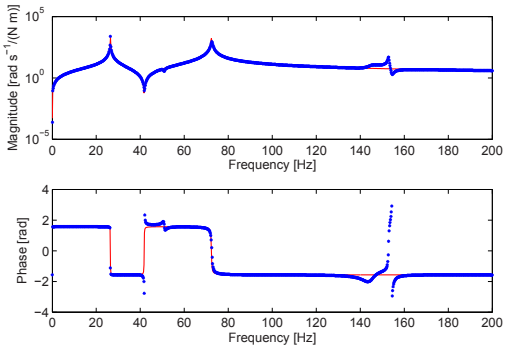

Fig. 18 Rotational mobility at the coupling DoF of subsystem A: true (—), computed from fitted perturbed FRF (⁎⁎⁎) with compatibility at DoFs θ_1 and θ_5 and equilibrium at DoFs θ_3 and θ_5

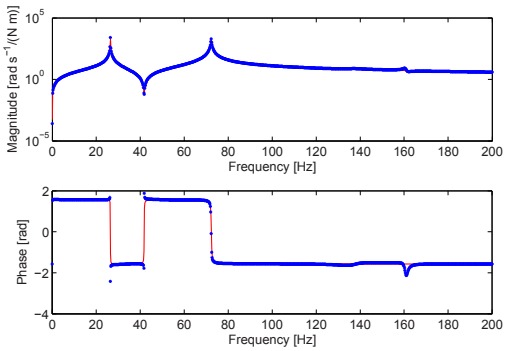

Fig. 19 Rotational mobility at the coupling DoF of subsystem A: true (—), computed from fitted perturbed FRF (⁎⁎⁎) with compatibility at DoFs θ_3 and θ_5 and equilibrium at DoFs θ_1 and θ_5

Fig. 20 shows the predicted rotational mobility of unknown subsystem A obtained using non collocated approach with compatibility at DoFs θ_1 and θ_5 and equilibrium at DoFs θ_4 and θ_5. Figure 21 is obtained by exchanging compatibility and equilibrium DoFs. The second option seems to give slightly better results.

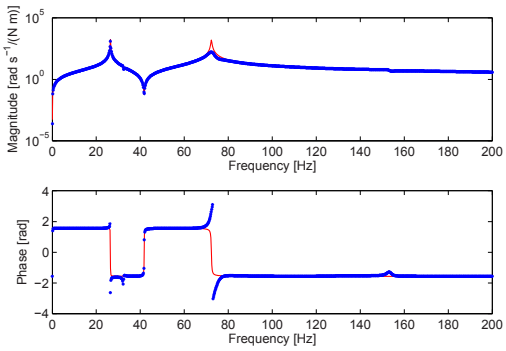

Fig. 20 Rotational mobility at the coupling DoF of subsystem A: true (—), computed from fitted perturbed FRF (***) with compatibility at DoFs θ_1 and θ_5 and equilibrium at DoFs θ_4 and θ_5

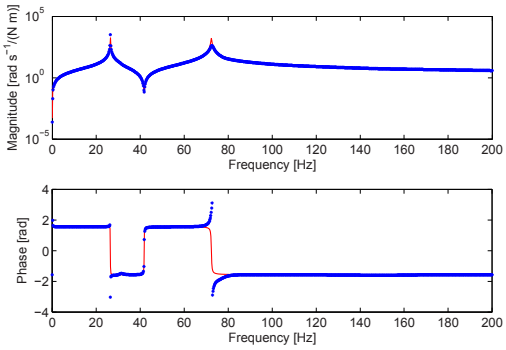

Fig. 21 Rotational mobility at the coupling DoF of subsystem A: true (—), computed from fitted perturbed FRF (***) with compatibility at DoFs θ_4 and θ_5 and equilibrium at DoFs θ_1 and θ_5

Fig. 22 shows the predicted rotational mobility of unknown subsystem A obtained using non collocated approach with compatibility at DoFs θ_3 and θ_5 and equilibrium at DoFs θ_4 and θ_5. Figure 23 is obtained by exchanging compatibility and equilibrium DoFs. The second option seems to give the best results.

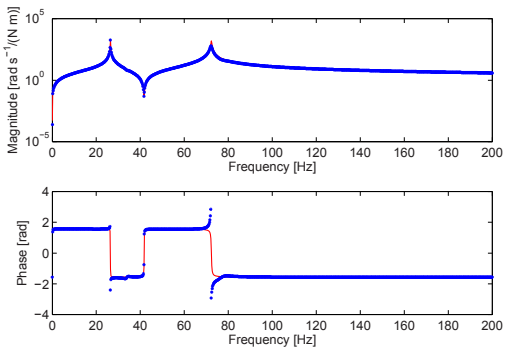

Fig. 22 Rotational mobility at the coupling DoF of subsystem A: true (—), computed from fitted perturbed FRF (***) with compatibility at DoFs θ_3 and θ_5 and equilibrium at DoFs θ_4 and θ_5

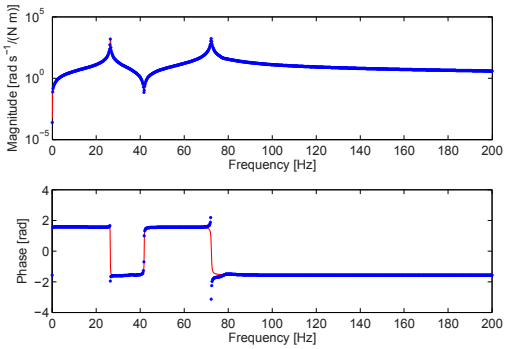

Fig. 23 Rotational mobility at the coupling DoF of subsystem A: true (—), computed from fitted perturbed FRF (***) with compatibility at DoFs θ_4 and θ_5 and equilibrium at DoFs θ_3 and θ_5

5 Summary and discussion

The paper considers the decoupling problem, i.e. the identification of the dynamic behaviour of a structural subsystem, starting from the known dynamic behaviour of the assembled system, and from information about the residual subsystem, i.e. the remaining part of the structural system. Direct decoupling techniques are considered, that consist in adding to the assembled system a fictitious subsystem, which is the negative of the residual subsystem. Starting from the 3-field formulation (dynamic balance, compatibility and equilibrium), a primal approach for decoupling is developed and compared with a dual approach.

Compatibility and equilibrium can be required either at coupling DoFs only (standard interface), or at additional internal DoFs of the residual subsystem (extended interface): for the dual approach, the choice of interface DoFs determines a set of frequencies at which the decoupling problem is ill conditioned. Apparently, when using an extended interface, the problem is singular at all frequencies, although this singularity is easily removed by smart inversion techniques. To avoid this problem, the non collocated approach, in which DoFs used to enforce equilibrium are not the same as DoFs used to enforce compatibility, can be considered: in this case the number of DoFs used to enforce compatibility must be less than the

number of DoFs used to enforce equilibrium. However, it is shown that, when equilibrium is enforced at coupling DoFs only, the use of non collocated approach gives rise to an interface flexibility matrix that is ill conditioned at the same frequencies as for standard interface.

Furthermore, it is shown that primal formulation and dual formulation provide the same result when the number of DoFs used to enforce compatibility is equal to the number of DoFs used to enforce equilibrium, i.e. in the collocated approach and in some special case of non collocated approach. On the contrary, when the number of DoFs used to enforce compatibility is greater than the number of DoFs used to enforce equilibrium, the two approaches provide different results: in fact, using the primal approach, compatibility is enforced exactly whilst equilibrium of constraint forces is only approximate; the opposite occurs using the dual approach, i.e. compatibility is only approximate whilst equilibrium of constraint forces is enforced exactly.

The techniques are applied using simulated data from a torsional system describing a two-speed transmission. Results agree with theory.

Acknowledgements This research is supported by grants from University of Rome La Sapienza.

Appendix: Format and properties of dynamic stiffness matrices

To obtain the condensed dynamic stiffness matrices of the coupled structure AB and of the residual substructure B, master DoFs M (interface DoFs to be measured and to be reatined after condensation) and slave DoFs S (unmeasured and to be eliminated after condensation) must be defined. According to which option is selected for interface DoFs, master DoFs and slave DoFs are:

a) When standard interface is considered:

- $M \equiv c$, that is interface DoFs are just the coupling DoFs;
- for the residual subsystem B, $S \equiv b$, that is the slave DoFs are all its internal DoFs;
- for the coupled system AB, $S \equiv a \cup b$, that is the slave DoFs are all its internal DoFs.

b) When extended interface is considered, also some internal DoFs i of the residual substructure are included among master DoFs:

- $M \equiv c \cup i$, as stated previously;
- for the residual subsystem B, $S \equiv b \backslash i \equiv u$, that is the slave DoFs are given by the set difference between its internal DoFs and the internal DoFs included in the interface;
- for the coupled system AB, $S \equiv a \cup u$.

b1) A special case occurs when $i \equiv b$. In this case, u is an empty set.

The dynamic stiffness matrices of the residual subsystem B and of the coupled system AB can be partitioned as follows:

$$\left[Z^B\right] = \begin{bmatrix} \left[Z^B\right]_{MM} & \left[Z^B\right]_{MS} \\ \left[Z^B\right]_{SM} & \left[Z^B\right]_{SS} \end{bmatrix} = \begin{bmatrix} \left[Z^B\right]_{cc} & \left[Z^B\right]_{ci} & \left[Z^B\right]_{cu} \\ \left[Z^B\right]_{ic} & \left[Z^B\right]_{ii} & \left[Z^B\right]_{iu} \\ \left[Z^B\right]_{uc} & \left[Z^B\right]_{ui} & \left[Z^B\right]_{uu} \end{bmatrix} \tag{42}$$

$$\left[Z^{AB}\right] = \begin{bmatrix} \left[Z^{AB}\right]_{MM} & \left[Z^{AB}\right]_{MS} \\ \left[Z^{AB}\right]_{SM} & \left[Z^{AB}\right]_{SS} \end{bmatrix} = \begin{bmatrix} \left[Z^A\right]_{cc} + \left[Z^B\right]_{cc} & \left[Z^B\right]_{ci} & \left[Z^B\right]_{cu} & \left[Z^A\right]_{ca} \\ \left[Z^B\right]_{ic} & \left[Z^B\right]_{ii} & \left[Z^B\right]_{iu} & [0]_{ia} \\ \left[Z^B\right]_{uc} & \left[Z^B\right]_{ui} & \left[Z^B\right]_{uu} & [0]_{ua} \\ \left[Z^A\right]_{ac} & [0]_{ai} & [0]_{au} & \left[Z^A\right]_{aa} \end{bmatrix} \tag{43}$$

where the zero blocks arise from the fact that the unknown subsystem A is joined to the residual subsystem B only through the coupling DoFs c. Note that, when standard interface is considered, i is an empty set, and $u \equiv b$.

Using dynamic condensation, the condensed dynamic stiffness matrix of the residual subsystem B is:

$$\begin{aligned} \left[\hat{Z}^B\right] &= \begin{bmatrix} \left[Z^B\right]_{cc} & \left[Z^B\right]_{ci} \\ \left[Z^B\right]_{ic} & \left[Z^B\right]_{ii} \end{bmatrix} - \begin{bmatrix} \left[Z^B\right]_{cu} \\ \left[Z^B\right]_{iu} \end{bmatrix} \left[Z^B\right]_{uu}^{-1} \begin{bmatrix} \left[Z^B\right]_{uc} & \left[Z^B\right]_{ui} \end{bmatrix} = \\ &= \begin{bmatrix} \left[Z^B\right]_{cc} & \left[Z^B\right]_{ci} \\ \left[Z^B\right]_{ic} & \left[Z^B\right]_{ii} \end{bmatrix} - \begin{bmatrix} \left[Z^B\right]_{cu}\left[Z^B\right]_{uu}^{-1}\left[Z^B\right]_{uc} & \left[Z^B\right]_{cu}\left[Z^B\right]_{uu}^{-1}\left[Z^B\right]_{ui} \\ \left[Z^B\right]_{iu}\left[Z^B\right]_{uu}^{-1}\left[Z^B\right]_{uc} & \left[Z^B\right]_{iu}\left[Z^B\right]_{uu}^{-1}\left[Z^B\right]_{ui} \end{bmatrix} \end{aligned} \tag{44}$$

and the condensed dynamic stiffness matrix of the coupled subsystem AB is:

$$\begin{aligned} \left[\hat{Z}^{AB}\right] &= \begin{bmatrix} \left[Z^A\right]_{cc} + \left[Z^B\right]_{cc} & \left[Z^B\right]_{ci} \\ \left[Z^B\right]_{ic} & \left[Z^B\right]_{ii} \end{bmatrix} - \\ &- \begin{bmatrix} \left[Z^B\right]_{cu} & \left[Z^A\right]_{ca} \\ \left[Z^B\right]_{iu} & [0]_{ia} \end{bmatrix} \begin{bmatrix} \left[Z^B\right]_{uu} & [0]_{ua} \\ [0]_{au} & \left[Z^A\right]_{aa} \end{bmatrix}^{-1} \begin{bmatrix} \left[Z^B\right]_{uc} & \left[Z^B\right]_{ui} \\ \left[Z^A\right]_{ac} & [0]_{ai} \end{bmatrix} = \\ &= \begin{bmatrix} \left[Z^A\right]_{cc} + \left[Z^B\right]_{cc} & \left[Z^B\right]_{ci} \\ \left[Z^B\right]_{ic} & \left[Z^B\right]_{ii} \end{bmatrix} - \\ &- \begin{bmatrix} \left[Z^B\right]_{cu}\left[Z^B\right]_{uu}^{-1}\left[Z^B\right]_{uc} + \left[Z^A\right]_{ca}\left[Z^A\right]_{aa}^{-1}\left[Z^A\right]_{ac} & \left[Z^B\right]_{cu}\left[Z^B\right]_{uu}^{-1}\left[Z^B\right]_{ui} \\ \left[Z^B\right]_{iu}\left[Z^B\right]_{uu}^{-1}\left[Z^B\right]_{uc} & \left[Z^B\right]_{iu}\left[Z^B\right]_{uu}^{-1}\left[Z^B\right]_{ui} \end{bmatrix} \end{aligned} \tag{45}$$

It can be observed that $\left[\hat{Z}^B\right]$ and $\left[\hat{Z}^{AB}\right]$ differ in only the upper left *cc* block, i.e. that relative to the coupling DoFs, and they are conveniently written as:

$$\left[\hat{Z}^{AB}\right] = \begin{bmatrix} \left[\hat{Z}^{AB}\right]_{cc} & \left[\hat{Z}^{B}\right]_{ci} \\ \left[\hat{Z}^{B}\right]_{ic} & \left[\hat{Z}^{B}\right]_{ii} \end{bmatrix} \qquad \left[\hat{Z}^{B}\right] = \begin{bmatrix} \left[\hat{Z}^{B}\right]_{cc} & \left[\hat{Z}^{B}\right]_{ci} \\ \left[\hat{Z}^{B}\right]_{ic} & \left[\hat{Z}^{B}\right]_{ii} \end{bmatrix} \tag{28}$$

Note that, when standard interface is considered, only the upper left *cc* block exists because i is an empty set.

By looking at Eq. (44), it can be noticed that $[Z^B]_{uu}$ must be inverted. $[Z^B]_{uu}$ is the dynamic stiffness matrix of the residual subsystem B with master (interface) DoFs grounded, and it is singular at its own resonant frequencies. Therefore, $\det([\hat{Z}^B])$ tends to infinity at the resonant frequencies of $[Z^B]_{uu}$: at those frequencies, $\det([\hat{H}^B])$ tends to zero and $[\hat{H}^B]$ is singular. Similarly, $\det([\hat{Z}^{AB}])$ tends to infinity at the resonant frequencies of the coupled structure AB with master (interface) DoFs grounded: at those frequencies, $[\hat{H}^{AB}]$ is singular. By looking at Eq. (45), where the matrix to be inverted is a block diagonal matrix including $[Z^B]_{uu}$ and $[Z^A]_{aa}$, it can be noticed that the resonant frequencies of the residual substructure B, with interface DoFs grounded $[Z^B]_{uu}$, are a subset of the resonant frequencies of the coupled structure AB with interface DoFs grounded.

References

1. D'Ambrogio, W., Fregolent, A.: Promises and pitfalls of decoupling procedures. In: Proceeding of 26th IMAC. Orlando (U.S.A.) (2008)
2. D'Ambrogio, W., Fregolent, A.: Decoupling procedures in the general framework of frequency based substructuring. In: Proceedings of 27th IMAC. Orlando (U.S.A.) (2009)
3. D'Ambrogio, W., Fregolent, A.: The role of interface dofs in decoupling of substructures based on the dual domain decomposition. Mechanical Systems and Signal Processing **24**(7), 2035–2048 (2010). Doi:10.1016/j.ymssp.2010.05.007, also in Proceedings of ISMA 2010, pp. 1863-1880, Leuven (Belgium)
4. Jetmundsen, B., Bielawa, R., Flannelly, W.: Generalised frequency domain substructure synthesis. Journal of the American Helicopter Society **33**(1), 55–64 (1988)
5. de Klerk, D.: Dynamic response characterization of complex systems through operational identification and dynamic substructuring. Ph.D. thesis, TU Delft (2009)
6. de Klerk, D., Rixen, D.J., Voormeeren, S.: General framework for dynamic substructuring: History, review, and classification of techniques. AIAA Journal **46**(5), 1169–1181 (2008)
7. Sjõvall, P., Abrahamsson, T.: Substructure system identification from coupled system test data. Mechanical Systems and Signal Processing **22**(1), 15–33 (2008)
8. Vormeeren, S.N., Rixen, D.J.: A dual approach to substructure decoupling techniques. In: Proceeding of 28th IMAC. Jacksonville (U.S.A.) (2010)
9. Vormeeren, S.N., Rixen, D.J.: A family of substructure decoupling techniques based on a dual assembly approach. In: P. Sas, B. Bergen (eds.) Proceedings of ISMA 2010 - International Conference on Noise and Vibration Engineering, pp. 1955–1968. Leuven (Belgium) (2010)

Spectral analysis of vibrating plates with general shape

Giuseppe Catania, Silvio Sorrentino
DIEM, Department of Mechanical Engineering,
University of Bologna, Viale del Risorgimento 2, 40136 Bologna, Italy

ABSTRACT

Lightweight plate structures are widely used in many engineering and practical applications. The analysis and design of such structures call for efficient computational tools, since exact analytical solutions for vibrating plates are currently known only for some standard shapes in conjunction with a few basic boundary conditions. The present paper deals with the adoption of a set of eigenfunctions evaluated from a simple structure as a basis for the analysis of plates with both general shape and general boundary conditions in the Rayleigh-Ritz condensation method. General boundary conditions are introduced in the functional of the potential energy by additional terms, and both trigonometric and polynomial interpolation functions are implemented for mapping the shape of the plate in Cartesian coordinates into natural coordinates. Flexural free vibration analysis of different shaped plates is then performed: skew, trapezoid and triangular plates, plates with parabolic edges, elliptic sector and annular plates. The proposed method can also be directly applied to variable thickness plates and non-homogeneous plates, with variable density and stiffness. Purely elastic plates are considered; however the method may also be applied to the analysis of viscoelastic plates. The results are compared to those available in the literature and using standard finite element analysis.

Keywords

Vibrating Plates, Rayleigh-Ritz method, Coordinate mapping.

Nomenclature

a	reference-length parameter	w	displacement
D	flexural stiffness of the plate	x	Cartesian coordinate
E	Young's modulus	y	Cartesian coordinate
h	thickness of the plate	ϕ	beam eigenfunction
$\mathbf{J}$	Jacobian matrix	η	natural coordinate
$\mathbf{K}$	stiffness matrix	κ	distributed stiffness
$\mathbf{M}$	mass matrix	λ	dimensionless frequency
n	modal index	ν	Poisson's ratio
P	interpolation function	Π	total potential energy
q	modal coordinate	ρ_h	mass per unit area
U	potential of the strain energy	ω_n	modal natural frequency
V	potential of applied loads	ξ	natural coordinate

1 Introduction

In recent decades, lightweight plate structures have been widely used in many engineering and practical applications. The analysis and design of such structures call for efficient computational tools, since exact analytical solutions for vibrating plates are currently known only for some standard shapes in conjunction with a few basic boundary conditions [1]. For the analysis of plates of arbitrary shape, or with general boundary conditions, numerical methods such as the finite difference method, the finite element method or the finite strip method are usually applied to the problem.
Vibration analyses of plates of different shapes have been carried out extensively by several researches. Durvasula [2] computed the natural frequencies of clamped skew plates, Babu and Reddy [3] studied skew orthotropic plates by means of

T. Proulx (ed.), *Linking Models and Experiments, Volume 2*, Conference Proceedings of the Society for Experimental Mechanics Series 5,
DOI 10.1007/978-1-4419-9305-2_6, © The Society for Experimental Mechanics, Inc. 2011

the finite strip method, Ramakrishnan and Kunukkasseril [4] studied the free vibration of annular sector plates, Cheung *et al.* [5] analyzed arbitrarily shaped plates by mapping the Cartesian coordinate system into the natural coordinate plane by means of serendipity shape functions using polynomial splines as displacement functions, Mizusawa [6] studied skew plates with different boundary constraints, Geannakakes [7] applied the semi-analytical finite strip method for the analysis of arbitrarily shaped plates using Hermitian polynomials as shape functions.

In the present study, the problem of arbitrary-shaped vibrating Kirchhoff plates with general boundary conditions is analyzed using the Rayleigh-Ritz method [8]. The solution is expressed in terms of a linear combination of functions, which in the present study are selected as products of eigenfunctions of homogeneous uniform prismatic beams in flexural vibration [9]. General boundary conditions are introduced in the functional of the potential energy by additional terms, and both trigonometric and polynomial interpolations are implemented for mapping the shape of the plate in Cartesian coordinates into natural coordinates [5-7]. Flexural free vibration analysis of different shaped plates is then performed: skew, trapezoid and triangular plates, plates with parabolic edges, elliptic sector and annular plates. The proposed method can be directly applied also to variable thickness plates and nonhomogeneous plates, with variable density and stiffness. Purely elastic plates are considered; however the method may also be applied to the analysis of viscoelastic plates, as proposed by Catania *et al.* [10-11].

2 Mapping technique

An arbitrary-shaped plate in Cartesian coordinates x and y can be expressed by the mapping of a square plate defined in its natural coordinates ξ and η [5], as shown in Fig. 1. The (generally non-conformal) mapping of the Cartesian system can be expressed as:

$$x(\xi,\eta)=\sum_{i=1}^{p}x_i P_i(\xi,\eta),\quad y(\xi,\eta)=\sum_{i=1}^{p}y_i P_i(\xi,\eta) \tag{1}$$

where x_i and y_i (i = 1, 2, … p) are the coordinates of p points on the boundary of the plate, and P_i are interpolation functions.

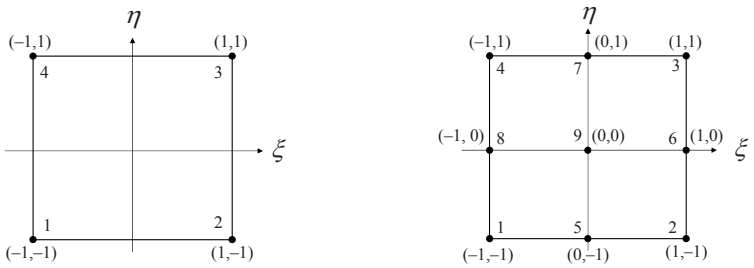

Fig. 1 Linear (left) and quadratic Lagrange (right) regions

In order to evaluate the differential operators needed in plate analysis, the following relations can be written in the form:

$$\begin{Bmatrix}\dfrac{\partial}{\partial\xi}\\[2mm]\dfrac{\partial}{\partial\eta}\end{Bmatrix}=\mathbf{J}\begin{Bmatrix}\dfrac{\partial}{\partial x}\\[2mm]\dfrac{\partial}{\partial y}\end{Bmatrix},\quad \mathbf{J}(\xi,\eta)=\begin{bmatrix}\displaystyle\sum_{i=1}^{p}x_i\frac{\partial P_i}{\partial\xi} & \displaystyle\sum_{i=1}^{p}y_i\frac{\partial P_i}{\partial\xi}\\[2mm]\displaystyle\sum_{i=1}^{p}x_i\frac{\partial P_i}{\partial\eta} & \displaystyle\sum_{i=1}^{p}y_i\frac{\partial P_i}{\partial\eta}\end{bmatrix} \tag{2}$$

and consequently:

$$\begin{Bmatrix}\dfrac{\partial^2}{\partial x^2}\\[2mm]\dfrac{\partial^2}{\partial y^2}\\[2mm]\dfrac{\partial^2}{\partial x\partial y}\end{Bmatrix}=\mathbf{A}\left[\begin{Bmatrix}\dfrac{\partial^2}{\partial\xi^2}\\[2mm]\dfrac{\partial^2}{\partial\eta^2}\\[2mm]\dfrac{\partial^2}{\partial\xi\partial\eta}\end{Bmatrix}-\mathbf{B}\begin{Bmatrix}\dfrac{\partial}{\partial\xi}\\[2mm]\dfrac{\partial}{\partial\eta}\end{Bmatrix}\right]=\mathbf{C}\begin{Bmatrix}\dfrac{\partial^2}{\partial\xi^2} & \dfrac{\partial^2}{\partial\eta^2} & \dfrac{\partial^2}{\partial\xi\partial\eta} & \dfrac{\partial}{\partial\xi} & \dfrac{\partial}{\partial\eta}\end{Bmatrix}^{\mathrm{T}},\quad \mathbf{C}=\left[\mathbf{A}\,\middle|\,-\mathbf{AB}\right] \tag{3}$$

with:

$$\mathbf{A}(\xi,\eta)=\frac{1}{\det^2[\mathbf{J}]}\begin{bmatrix} \mathrm{J}_{22}^2 & \mathrm{J}_{12}^2 & -2\mathrm{J}_{12}\mathrm{J}_{22} \\ \mathrm{J}_{21}^2 & \mathrm{J}_{11}^2 & -2\mathrm{J}_{11}\mathrm{J}_{21} \\ -\mathrm{J}_{21}\mathrm{J}_{22} & -\mathrm{J}_{11}\mathrm{J}_{12} & \mathrm{J}_{11}\mathrm{J}_{22}+\mathrm{J}_{12}\mathrm{J}_{21} \end{bmatrix} \quad , \quad \mathbf{B}(\xi,\eta)=\frac{1}{\det[\mathbf{J}]}\begin{bmatrix} \mathrm{J}_{22}\mathrm{J}_{11,\xi}-\mathrm{J}_{21}\mathrm{J}_{12,\xi} & \mathrm{J}_{11}\mathrm{J}_{12,\xi}-\mathrm{J}_{12}\mathrm{J}_{11,\xi} \\ \mathrm{J}_{22}\mathrm{J}_{21,\eta}-\mathrm{J}_{21}\mathrm{J}_{22,\eta} & \mathrm{J}_{11}\mathrm{J}_{22,\eta}-\mathrm{J}_{12}\mathrm{J}_{21,\eta} \\ \mathrm{J}_{22}\mathrm{J}_{11,\eta}-\mathrm{J}_{21}\mathrm{J}_{22,\xi} & \mathrm{J}_{11}\mathrm{J}_{22,\xi}-\mathrm{J}_{12}\mathrm{J}_{11,\eta} \end{bmatrix} \tag{4}$$

where the subscripts ξ and η denote differentiation with respect to the natural variables. The elements in the Jacobian matrix **J** as well as those in matrices **A** and **B** depend on the mapping of the Cartesian coordinate system.

3 Analysis technique

An isotropic homogeneous Kirchhoff rectangular plate in free flexural vibration is considered [12]. The functional of the total potential energy can be written as the sum of a term U due to the strain energy of the system plus a term V representing the potential of all applied loads (including the inertial forces), and a term ΔV taking into account lumped and distributed elastic constraints:

$$\Pi = U + V + \Delta V \tag{5}$$

The potential of the strain energy can be written in terms of second order derivatives of the out-of-plane displacement w:

$$U=\frac{1}{2}\int_S D\left[w_{xx}^2+w_{yy}^2+2\nu\, w_{xx}w_{yy}+2(1-\nu)w_{xy}^2\right]dS \;, \quad dS(\xi,\eta)=\det[\mathbf{J}]\,d\xi d\eta \tag{6}$$

In Eq. 6 the subscripts denote differentiation with respect to the spatial variables, S is the spatial domain and D is the flexural stiffness of the plate, which can be expressed as a function of Young's modulus E, Poisson's ratio ν and the thickness of the plate h [12]:

$$D=\frac{Eh^3}{12(1-\nu^2)} \tag{7}$$

In the present formulation the inertial forces are included in the potential of applied loads:

$$V=\int_S \rho_h w\ddot{w}dS \tag{8}$$

where ρ_h denotes the mass per unit area of the plate. The additional term ΔV in Eq. 5 is considered to take into account lumped and distributed elastic constraints. In the case of translational constraints it can be expressed in the form:

$$\Delta V=\frac{1}{2}\int_\gamma \kappa w^2 d\gamma, \quad \begin{cases} \gamma \text{ constraint domain} \\ \kappa(x,y) \text{ distributed stiffness} \end{cases} \tag{9}$$

In Eq. 9 γ can refer to surfaces, lines and separate points. Terms ΔV with rotational stiffness may be included as well, for modelling rotational elastic constraints.

The out-of-plane displacement w is expressed by means of a linear combination of shape functions [8-9]. If external constraints do not explicitly appear in the functional of Eq. 5, i.e. $\Delta V = 0$, then each of these functions must respect the essential conditions at the boundary of the plate (also known as principal or kinematic conditions).

In the present study, the shape functions are selected as products of homogeneous uniform prismatic beam eigenfunctions ϕ. In natural coordinates they can be expressed as:

$$w=\sum_{i=1}^{N_\xi}\sum_{j=1}^{N_\eta} q_{ij}(t)\,\phi_i(\xi)\,\phi_j(\eta) \tag{10}$$

where N_ξ and N_η are the number of beam eigenfunctions in the ξ and η parametric directions, respectively. If an integer n is assigned at any combination i, j, then the flexural displacement Eq. 10 can be rewritten as:

$$w = \sum_{n=1}^{N} q_n \, \phi_n(\xi,\eta) \quad \Rightarrow \quad w = \boldsymbol{\phi}^{\mathrm{T}} \mathbf{q} \tag{11}$$

where $N = N_\xi \times N_\eta$ and $\mathbf{q}$ is the generalized coordinate vector. Introducing the displacement expansion Eq. 11 in the quadratic functional Eq. 5, and imposing the stationarity of the potential energy [13]:

$$\frac{\partial \Pi}{\partial \mathbf{q}} = \mathbf{0} \tag{12}$$

yields the approximate natural eigenfrequencies of the plate by solving the algebraic eigenproblem:

$$\mathbf{M}\,\ddot{\mathbf{q}} + [\mathbf{K} + \Delta\mathbf{K}]\,\mathbf{q} = \mathbf{0} \tag{13}$$

where:

$$\begin{aligned}
\mathbf{M} &= \int_s \rho_h (\boldsymbol{\phi}\boldsymbol{\phi}^{\mathrm{T}})\, dS \\
\mathbf{K} &= \int_s D[\boldsymbol{\phi}_{,xx}\boldsymbol{\phi}_{,xx}^{\mathrm{T}} + \boldsymbol{\phi}_{,yy}\boldsymbol{\phi}_{,yy}^{\mathrm{T}} + \nu(\boldsymbol{\phi}_{,xx}\boldsymbol{\phi}_{,yy}^{\mathrm{T}} + \boldsymbol{\phi}_{,yy}\boldsymbol{\phi}_{,xx}^{\mathrm{T}}) + 2(1-\nu)(\boldsymbol{\phi}_{,xy}\boldsymbol{\phi}_{,xy}^{\mathrm{T}})]\, dS \\
\Delta\mathbf{K} &= \int_s \kappa (\boldsymbol{\phi}\boldsymbol{\phi}^{\mathrm{T}})\, dS
\end{aligned} \tag{14}$$

are the mass matrix and stiffness matrix, computed according to Eqs. 8, 6 and 9 respectively. The integrals in Eq. 14 can be computed in the natural coordinates ξ and η through Eqs. 3 and 4. In particular, the stiffness matrix $\mathbf{K}$ can be computed by means of the following expression:

$$\hat{\boldsymbol{\phi}} = [\boldsymbol{\phi}_{\xi\xi} \quad \boldsymbol{\phi}_{\eta\eta} \quad \boldsymbol{\phi}_{\xi\eta} \quad \boldsymbol{\phi}_{\xi} \quad \boldsymbol{\phi}_{\eta}] \quad \Rightarrow \quad \mathbf{K} = \int_s D\,\hat{\boldsymbol{\phi}}[\mathbf{L}]\hat{\boldsymbol{\phi}}^{\mathrm{T}} \det[\mathbf{J}]\, d\xi\, d\eta \tag{15}$$

where the elements in the symmetric 5×5 matrix $\mathbf{L}$ are given by:

$$\begin{aligned}
\mathrm{L}_{11} &= \mathrm{C}_{11}^2 + \mathrm{C}_{21}^2 + 2\nu\,\mathrm{C}_{11}\mathrm{C}_{21} + 2(1-\nu)\mathrm{C}_{31}^2 \\
\mathrm{L}_{22} &= \mathrm{C}_{12}^2 + \mathrm{C}_{22}^2 + 2\nu\,\mathrm{C}_{12}\mathrm{C}_{22} + 2(1-\nu)\mathrm{C}_{32}^2 \\
\mathrm{L}_{33} &= \mathrm{C}_{13}^2 + \mathrm{C}_{23}^2 + 2\nu\,\mathrm{C}_{13}\mathrm{C}_{23} + 2(1-\nu)\mathrm{C}_{33}^2 \\
\mathrm{L}_{44} &= \mathrm{C}_{14}^2 + \mathrm{C}_{24}^2 + 2\nu\,\mathrm{C}_{14}\mathrm{C}_{24} + 2(1-\nu)\mathrm{C}_{34}^2 \\
\mathrm{L}_{55} &= \mathrm{C}_{15}^2 + \mathrm{C}_{25}^2 + 2\nu\,\mathrm{C}_{15}\mathrm{C}_{25} + 2(1-\nu)\mathrm{C}_{35}^2 \\
\mathrm{L}_{12} &= \mathrm{L}_{21} = \mathrm{C}_{11}\mathrm{C}_{12} + \mathrm{C}_{21}\mathrm{C}_{22} + \nu(\mathrm{C}_{11}\mathrm{C}_{22} + \mathrm{C}_{12}\mathrm{C}_{21}) + 2(1-\nu)\mathrm{C}_{31}\mathrm{C}_{32} \\
\mathrm{L}_{13} &= \mathrm{L}_{31} = \mathrm{C}_{11}\mathrm{C}_{13} + \mathrm{C}_{21}\mathrm{C}_{23} + \nu(\mathrm{C}_{11}\mathrm{C}_{23} + \mathrm{C}_{13}\mathrm{C}_{21}) + 2(1-\nu)\mathrm{C}_{31}\mathrm{C}_{33} \\
\mathrm{L}_{14} &= \mathrm{L}_{41} = \mathrm{C}_{11}\mathrm{C}_{14} + \mathrm{C}_{21}\mathrm{C}_{24} + \nu(\mathrm{C}_{11}\mathrm{C}_{24} + \mathrm{C}_{14}\mathrm{C}_{21}) + 2(1-\nu)\mathrm{C}_{31}\mathrm{C}_{34} \\
\mathrm{L}_{15} &= \mathrm{L}_{51} = \mathrm{C}_{11}\mathrm{C}_{15} + \mathrm{C}_{21}\mathrm{C}_{25} + \nu(\mathrm{C}_{11}\mathrm{C}_{25} + \mathrm{C}_{15}\mathrm{C}_{21}) + 2(1-\nu)\mathrm{C}_{31}\mathrm{C}_{35} \\
\mathrm{L}_{23} &= \mathrm{L}_{32} = \mathrm{C}_{12}\mathrm{C}_{13} + \mathrm{C}_{22}\mathrm{C}_{23} + \nu(\mathrm{C}_{12}\mathrm{C}_{23} + \mathrm{C}_{13}\mathrm{C}_{22}) + 2(1-\nu)\mathrm{C}_{32}\mathrm{C}_{33} \\
\mathrm{L}_{24} &= \mathrm{L}_{42} = \mathrm{C}_{12}\mathrm{C}_{14} + \mathrm{C}_{22}\mathrm{C}_{24} + \nu(\mathrm{C}_{12}\mathrm{C}_{24} + \mathrm{C}_{14}\mathrm{C}_{22}) + 2(1-\nu)\mathrm{C}_{32}\mathrm{C}_{34} \\
\mathrm{L}_{25} &= \mathrm{L}_{52} = \mathrm{C}_{12}\mathrm{C}_{15} + \mathrm{C}_{22}\mathrm{C}_{25} + \nu(\mathrm{C}_{12}\mathrm{C}_{25} + \mathrm{C}_{15}\mathrm{C}_{22}) + 2(1-\nu)\mathrm{C}_{32}\mathrm{C}_{35} \\
\mathrm{L}_{34} &= \mathrm{L}_{43} = \mathrm{C}_{13}\mathrm{C}_{14} + \mathrm{C}_{23}\mathrm{C}_{24} + \nu(\mathrm{C}_{13}\mathrm{C}_{24} + \mathrm{C}_{14}\mathrm{C}_{23}) + 2(1-\nu)\mathrm{C}_{33}\mathrm{C}_{34} \\
\mathrm{L}_{35} &= \mathrm{L}_{53} = \mathrm{C}_{13}\mathrm{C}_{15} + \mathrm{C}_{23}\mathrm{C}_{25} + \nu(\mathrm{C}_{13}\mathrm{C}_{25} + \mathrm{C}_{15}\mathrm{C}_{23}) + 2(1-\nu)\mathrm{C}_{33}\mathrm{C}_{35} \\
\mathrm{L}_{45} &= \mathrm{L}_{54} = \mathrm{C}_{14}\mathrm{C}_{15} + \mathrm{C}_{24}\mathrm{C}_{25} + \nu(\mathrm{C}_{14}\mathrm{C}_{25} + \mathrm{C}_{15}\mathrm{C}_{24}) + 2(1-\nu)\mathrm{C}_{34}\mathrm{C}_{35}
\end{aligned} \tag{16}$$

Each element of matrix $\mathbf{L}$ is a functions of Poisson's coefficient and of the elements in matrix $\mathbf{C}$, Eq. 3.

4 Numerical examples

Five example cases are considered, the first one regarding skew plates with non-standard boundary conditions, the second and third ones regarding trapezoid and triangular plates, the fourth one regarding plates with curved parabolic edges, the last one regarding elliptic annular plates. In all cases the dimensionless frequency parameters λ^2 are computed according to the above described technique. The natural frequencies are then given by:

$$\omega = \frac{\lambda^2}{a^2}\sqrt{\frac{D}{\rho_h}} \tag{17}$$

where a is a reference-length parameter.
The shape functions are selected in the form of products of beam eigenfunctions: free-free, clamped-clamped and clamped-free [12].

Skew plates

A skew plate as represented in Fig. 2 is considered, with $b = a$ and angle α. For a plate with straight edges, the interpolation functions can be defined in the form:

$$P_i(\xi,\eta) = (1+\xi_i\xi)(1+\eta_i\eta)/4 \quad i = 1,2,3,4 \tag{18}$$

in which ξ_i and η_i are the natural coordinates of the i-th corner, as shown in Fig. 1. Introducing the coordinates of points 1 to 4 in Eq. 18 yields the coordinate mapping:

$$\begin{cases} x = \left[(1+\xi) + \sin\alpha\,(1+\eta)\right]/2 \\ y = \cos\alpha\,(1+\eta)/2 \end{cases} \tag{19}$$

In this case the determinant of the Jacobian matrix **J** is constant.

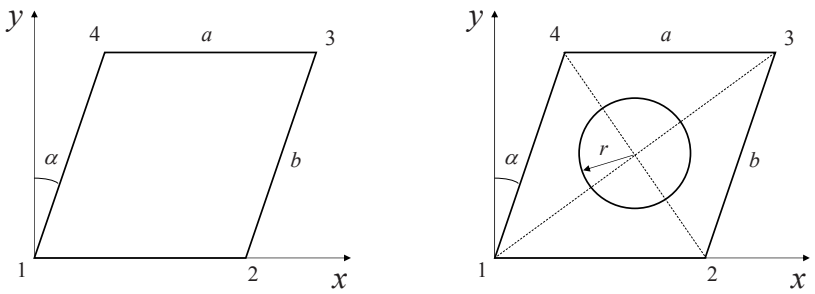

Fig. 2 Skew plate (left) and skew plate with annular support (right)

Example 1. A free skew plate simply supported on an annular constraint as represented in Fig. 2 is considered, with $\alpha = \pi/6$, $a = b = 1$ and $r = 0.3$. The equation describing the shape of the support γ, expressed in polar form, can be given in natural coordinates using Eq. 19:

$$\begin{cases} \xi = 2r(\cos\vartheta - \tan\alpha\sin\vartheta) \\ \eta = 2r\sin\vartheta/\cos\alpha \end{cases} \tag{20}$$

The frequencies computed using 6×6 to 12×12 free-free beam eigenfunctions (assuming $\nu = 0.3$ and $\kappa = 10^9 \times D/a^3$) are reported in Tab. 1, where they are compared with those computed with the finite element method (15912 dofs, using quadratic serendipity plane elements with 8 nodes each). Shapes of modes 1 and 3 are plotted in Fig. 3.

Table 1 Example 1, dimensionless frequency parameter λ^2 ($\nu = 0.3$, $\alpha = \pi/6$, $a = b = 1$, $r = 0.3$)

Mode	Present approach				FEM*
	6×6 dofs	8×8 dofs	10×10 dofs	12×12 dofs	
1	15.013	14.873	14.814	14.773	14.652
2	16.671	16.397	16.295	16.234	16.012
3	53.532	51.883	51.157	50.841	49.563
4	60.943	57.217	56.872	56.741	55.967
5	62.272	60.392	59.644	59.317	57.900
* 1715 elements, 5304 nodes, 15912 dofs.					

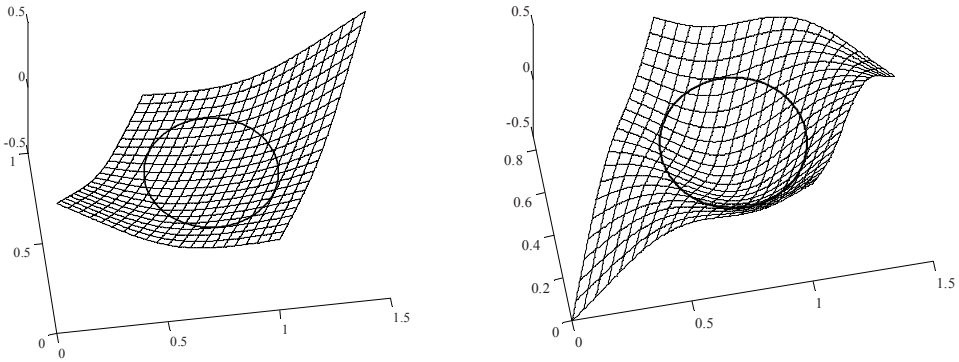

Fig. 3 Skew plate on annular support ($\nu = 0.3$, $\alpha = \pi/6$, $a = b = 1$, $r = 0.3$): modes 1 (left) and 3 (right)

Trapezoid and triangular plates

A trapezoid plate as represented in Fig. 4 is considered. The interpolation functions are linear, as in Eq. 18. Introducing the coordinates of points 1 to 4 yields the coordinate mapping:

$$\begin{cases} x = \left\{(a_1 - a_2) + (a_1 + a_2 + 2\varepsilon)\xi + \left[(a_1 - a_2) + (a_1 + a_2 - 2\varepsilon)\xi\right]\eta\right\}/4 \\ y = \left[(b_1 + b_2) + (b_1 - b_2)\xi\right](1+\eta)/4 \end{cases} \tag{21}$$

Letting $\varepsilon \to 0$ yields the coordinate mapping for a triangle (Fig. 4):

$$\begin{cases} x = \left[(a_1 - a_2) + (a_1 + a_2)\xi\right](1+\eta)/4 \\ y = \left[(b_1 + b_2) + (b_1 - b_2)\xi\right](1+\eta)/4 \end{cases} \tag{22}$$

Note that the determinant of the Jacobian matrix becomes singular for $\eta \to -1$, however not affecting the results in the case of zero displacement in point 1.

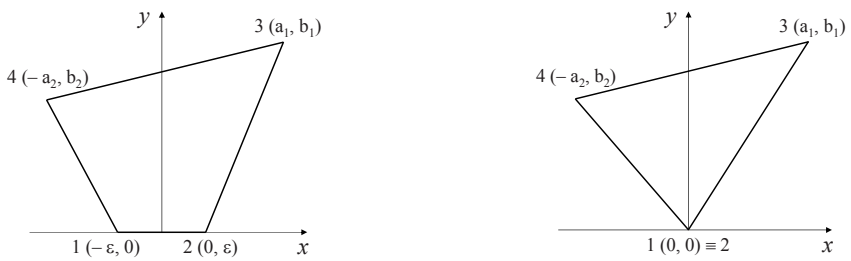

Fig. 4 Trapezoid (left) and triangular (right) plate

Example 2. A trapezoid plate is considered, clamped on three edges and free on the longest one, with parameters $\varepsilon = 1$, $a_1 = a_2 = 0.5$, $b_1 = b_2 = \sqrt{3}/2$, and $\nu = 0.3$. In Tab. 2, the dimensionless frequencies λ^2 computed using 6 (clamped-clamped) × 6 (clamped-free) eigenfunctions (36 global dofs) are compared with those obtained using the finite element method (14883 dofs). Shapes of modes 3 and 4 are plotted in Fig. 5.

Table 2 Example 2, dimensionless frequency parameter λ^2 ($\nu = 0.3$, $\varepsilon = 1$, $a_1 = a_2 = 0.5$, $b_1 = b_2 = \sqrt{3}/2$).

Mode	Present approach [6×6 dofs]	FEM*
1	10.715	10.632
2	24.288	24.061
3	35.517	35.283
4	45.028	44.452
5	53.611	53.181
6	70.977	69.981
7	78.671	77.493
8	91.418	90.758
9	101.094	100.001
10	105.546	101.320
* 1600 elements, 14883 dofs.		

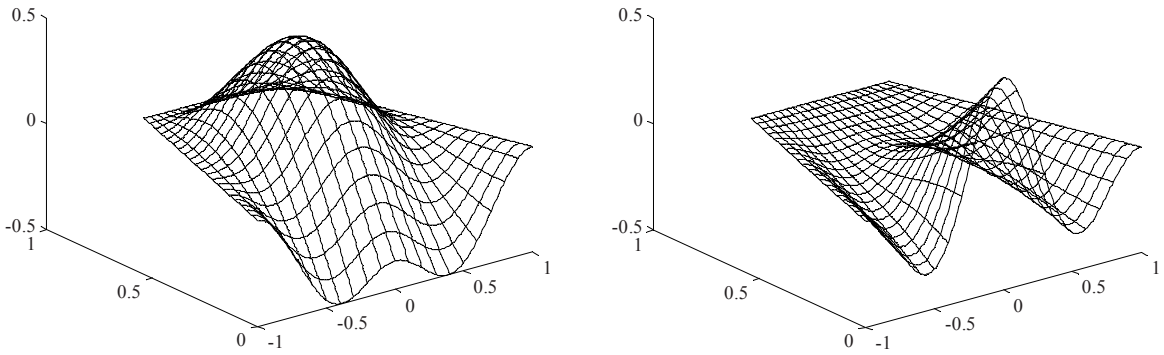

Mode 3 Mode 4

Fig. 5 Trapezoid clamped-free plate: modes 3 and 4

Example 3. A triangular plate is considered, clamped on all three edges, with $a_1 = 1/\sqrt{2}$, $a_2 = 1/\sqrt{6}$, $b_1 = 1/\sqrt{2}$, $b_2 = 1/\sqrt{6}$, and $\nu = 0.3$ (angles $\alpha_{12} = 90°$, $\alpha_3 = 30°$, $\alpha_4 = 60°$). In Tab. 3, the dimensionless frequencies λ^2 computed using 6×6 (clamped-clamped) eigenfunctions (36 global dofs) are compared with those reported in Ref. [15], computed using boundary characteristic orthogonal polynomials in two dimensions as shape functions. Note that the singularity in $\eta = -1$ does not affect the results. Shapes of modes 1, 2, 3 and 4 are plotted in Fig. 6.

Table 3 Example 3, dimensionless frequency parameter λ^2 ($\nu = 0.3$, $a_1 = 1/\sqrt{2}$, $a_2 = 1/\sqrt{6}$, $b_1 = 1/\sqrt{2}$, $b_2 = 1/\sqrt{6}$).

Mode	Ref. [15]	Present approach [6×6 dofs]
1	176.58	176.618
2	280.95	280.046
3	380.92	380.058
4	416.53	412.145
5	558.48	532.878

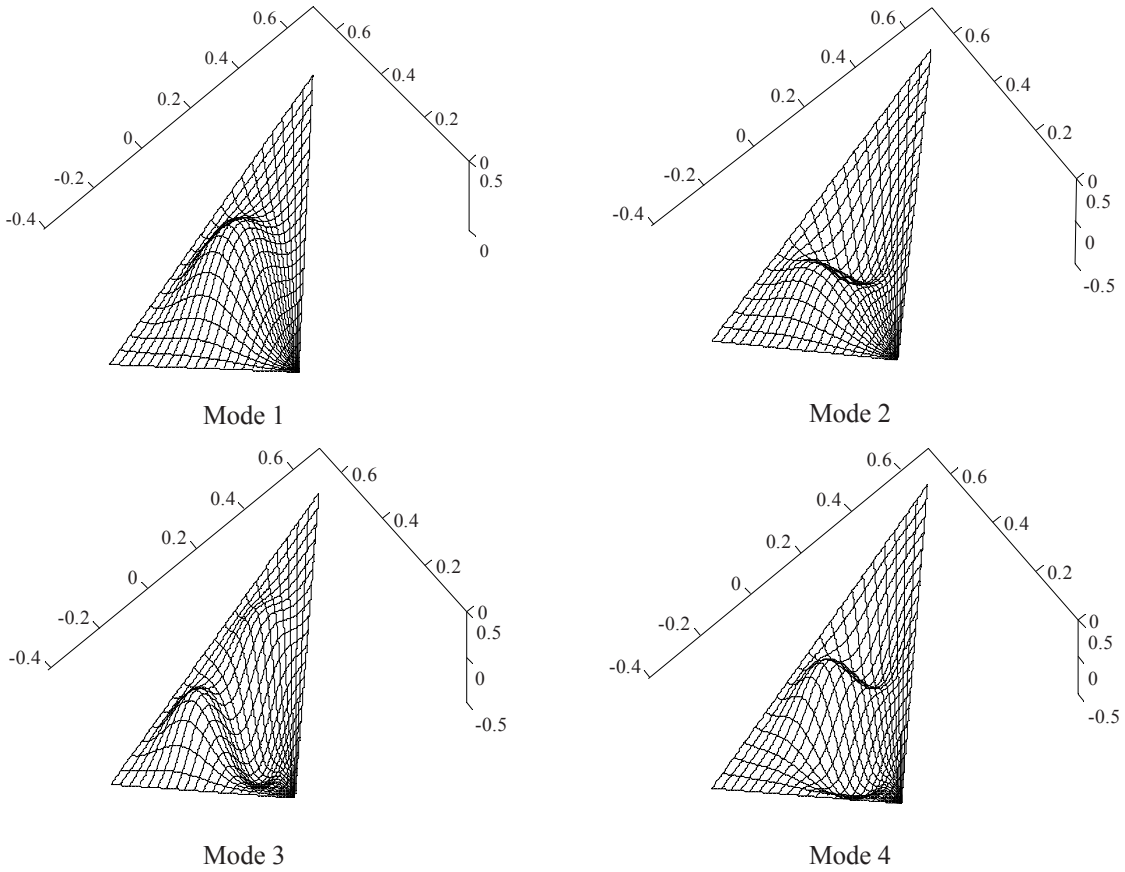

Fig. 6 Triangular clamped plate: modes 1, 2, 3 and 4

Plates with curved edges

A plate with curved parabolic edges as represented in Fig. 7 is considered. Since in Eq. 1 the number of boundary points with predefined coordinates should be increased according to the polynomial order of the edges, in this example the quadratic Lagrange function is adopted:

$$\begin{aligned} P_i(\xi,\eta) &= \xi\eta(\xi+\xi_i)(\eta+\eta_i)/4 \qquad i=1,2,3,4 \\ P_i(\xi,\eta) &= \eta(\eta+\eta_i)(1-\xi^2)/2 \qquad i=5,7 \\ P_i(\xi,\eta) &= \xi(\xi+\xi_i)(1-\eta^2)/2 \qquad i=6,8 \\ P_i(\xi,\eta) &= (1-\xi^2)(1-\eta^2) \qquad i=9 \end{aligned} \tag{23}$$

where the numbering convention is shown in Fig. 1. Introducing the coordinates of points 1 to 9 in Eq. 23 yields the coordinate mapping:

$$\begin{cases} x = \xi(\eta^2+1) \\ y = \eta(3-\xi^2) \end{cases} \tag{24}$$

Example 4. A free plate on all edges is considered, assuming $\nu = 0.3$. In Tab. 4, the dimensionless frequencies computed using 6×6 and 12×12 free-free beam eigenfunctions (with $N \times N = 144$ global dofs) are compared with those obtained using the finite element method (8463 dofs). Shapes of modes 4, 5, 6 and 9 are plotted in Fig. 8. The first three modes are rigid body motions.

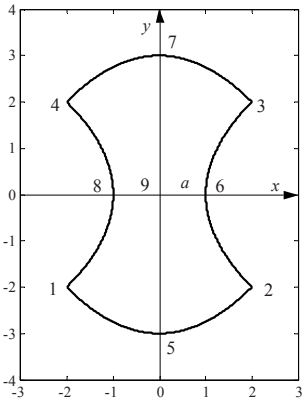

Fig. 7 Plate with curved edges

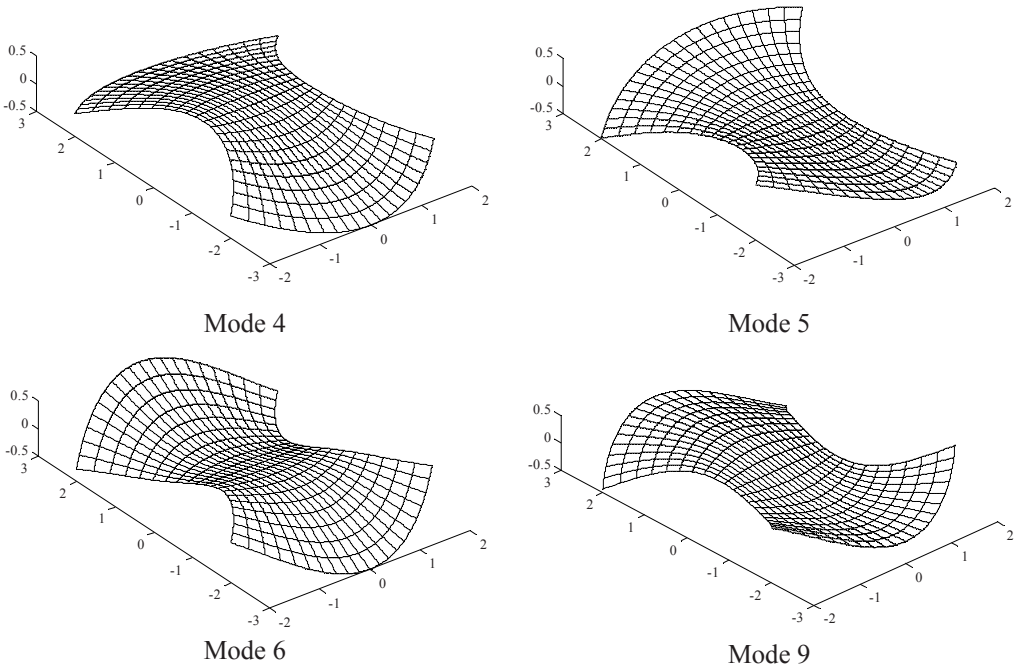

Fig. 8 Free plate with curved edges ($\nu = 0.3$, $a = 1$): modes 4, 5, 6 and 9 (1 to 3 are rigid body modes)

Table 5 Example 5, dimensionless frequency parameter λ^2 ($\nu = 0.3$)

Mode	Present approach		FEM*
	6×6 dofs	12×12 dofs	
1	0	0	0
2	0	0	0
3	0	0	0
4	0.655	0.634	0.620
5	0.733	0.717	0.650
6	1.875	1.813	1.689
7	2.101	2.085	2.062
8	2.268	2.161	2.094
9	2.461	2.439	2.424
10	3.795	3.614	3.369
* 900 elements, 2821 nodes, 8463 dofs.			

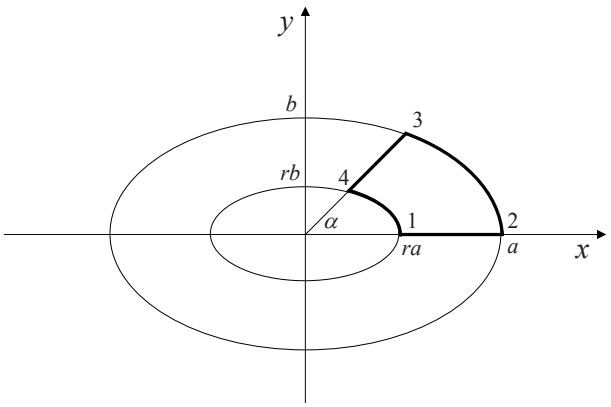

Fig. 9 Sector or annular plate

Sector and annular elliptic plates

Circular plates are special cases of elliptic plates and are quite simple to analyze using polar coordinates, since the solution can be expressed in the form of Bessel functions for all nine cases for inner and outer boundary conditions [14]. When compared with the amount of information available for circular plates, studies on the vibration of elliptic plates are limited, especially on elliptic annular plates [15]. The main difficulty in studying elliptic plates is the choice of coordinates: elliptic coordinates can be used with the exact mode shape in the form of Mathieu functions, but they are quite cumbersome to handle [15-16].

In the present study, a general case is considered, consisting of a sector elliptic plate as represented in Fig. 9. Annular elliptic plates, sector circular plates and annular circular plates can be considered as special cases, and they can be solved following the same approach within the proposed technique. In this case the domain mapping can be given in polar coordinates:

$$\begin{cases} x = \dfrac{a\,[(1-r)\xi + r]}{\sqrt{1+\left(k^2-1\right)\sin^2(\alpha\eta)}}\cos(\alpha\eta) & \xi \in [0,1] \\ y = \dfrac{a\,[(1-r)\xi + r]}{\sqrt{1+\left(k^2-1\right)\sin^2(\alpha\eta)}}\sin(\alpha\eta) & \eta \in [0,1] \end{cases} \tag{25}$$

where $\alpha \in (0,2\pi]$ is the sector angle, a and b are the lengths of the major and minor semiaxes of the external ellipse, $k = a/b$ is their ratio, $a\times r$ and $b\times r$ with $r \in [0,1)$ are the lengths of the major and minor semiaxes of the internal ellipse. Clearly, $\alpha = 2\pi$ yields a circular or elliptic annular plate, $\alpha = 2\pi$ and $r = 0$ yields a circular or elliptic plate and $k = 1$ yields a circular annular plate. In the latter case Eq. 25 reduces to the simpler form:

$$\begin{cases} x = a\,[(1-r)\xi + r]\cos(\alpha\eta) & \xi \in [0,1] \\ y = a\,[(1-r)\xi + r]\sin(\alpha\eta) & \eta \in [0,1] \end{cases} \tag{26}$$

If $\alpha = 2\pi$ (annular plate) the shape functions along the η coordinate can be selected as terms of the Fourier series:

$$\phi(\eta) = \begin{cases} \cos(2\pi i\eta) & i = 0,1,2... \\ \sin(2\pi j\eta) & j = 1,2,3... \end{cases} \tag{27}$$

Example 5. An elliptic annular plate ($\alpha = 2\pi$) is considered, clamped on the external edge and free on the internal one, with $k = 2$, $a = 1$, $r = 0.4$ and $\nu = 1/3$. In Tab. 8, the dimensionless frequencies λ^2 computed using 4×11, 7×11 and 4×22 (44, 77 and 88 global dofs) eigenfunctions are compared with those reported in Ref. [15]. Note how the different composition of eigenfunction sets in the cases 7×11 and 4×22 affects the results: the 7×11 set yields better results on modes 2 and 3, while the 4×22 set gives better results on modes 1, 4, 5 and 6. Shapes of modes 1 to 6 are plotted in Fig. 10.

Table 5 Example 5, Dimensionless frequency parameter λ^2 ($\nu = 1/3$, $k = 2$, $r = 0.4$)

Mode	Ref. [15]	Present approach		
		4×11 dofs	7×11 dofs	4×22 dofs
1	36.347	36.398	36.382	36.298
2	41.041	41.516	41.283	41.428
3	54.029	55.828	55.114	55.349
4	62.686	65.382	64.625	63.759
5	77.093	77.605	77.287	76.327
6	82.638	86.545	86.362	82.690

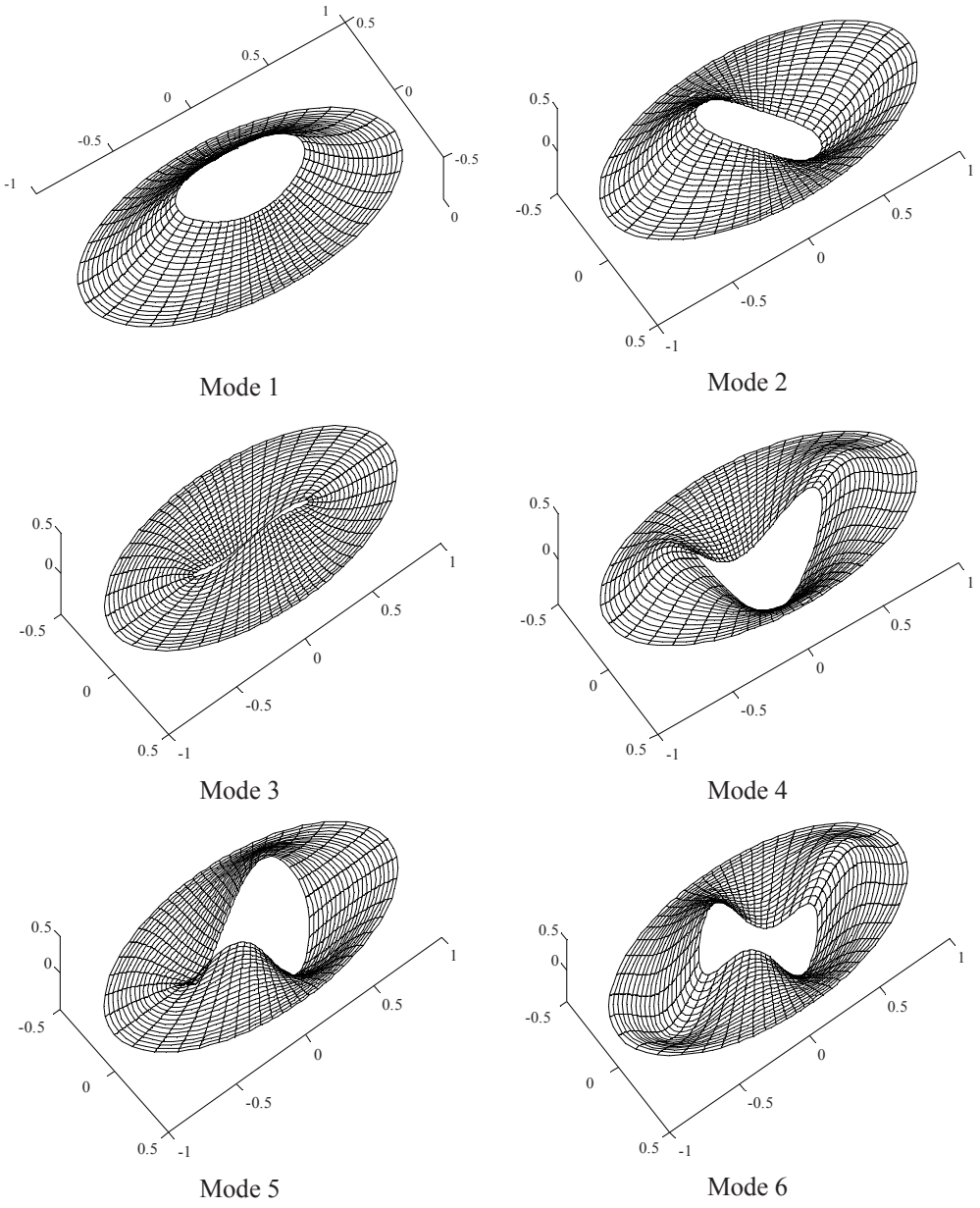

Fig. 10 Clamped-free elliptic annular plate ($\nu = 1/3$, $k = 2$, $a = 1$, $r = 0.4$): modes 1 to 6

5 Conclusions and future work

In the present study, the problem of arbitrary-shaped vibrating Kirchhoff plates was analyzed using the Rayleigh-Ritz method. General boundary conditions were introduced in the functional of potential energy, and natural coordinates were employed to express the geometry of plates of arbitrary shape in a simple form. Flexural free vibration analysis of different shaped plates was performed, showing the effectiveness of the method. The flexural frequencies obtained were compared with those found in the literature and with those of standard finite element analysis, and the results were in very good agreement.
Future studies will be devoted to analyzing the effectiveness of varying the composition of a given set of such functions.

Acknowledgments

This study was developed within the INTERMECH laboratory with the contribution of the Regione Emilia Romagna - Assessorato Attività Produttive, Sviluppo Economico, Piano telematico, PRRIITT misura 3.4 azione A Obiettivo 2.

References

[1] Leissa A.W., "Recent research in plate vibrations: classical theory", *The Shock and Vibration Digest* 9 (10), pp. 13-24, 1977.

[2] Durvasula S., "Natural frequencies and modes of clamped skew plates", *American Institute of Aeronautics and Astronautics Journal* 7, pp. 1164-1167, 1969.

[3] Babu P.V.T., Reddy D.V., "Frequency analysis of skew orthotropic plates by the finite strip method", *Journal of Sound and Vibration* 18 (4-5), pp. 465-474, 1971.

[4] Ramakrishnan R., Kunukkasseril V., "Free vibration of annular sector plates", *Journal of Sound and Vibration* 30, pp. 127-129, 1973.

[5] Li W.Y., Cheung Y.K., Tham L.G., "Spline finite strip analysis of general plates", *Journal of Engineering Mechanics* 112, pp. 43-54, 1986.

[6] Mizusawa. T., Kajita. T., Naruoka. M., "Analysis of skew plate problems with various constraints", *Journal of Sound and Vibration* 73 (4), pp. 575-584, 1980.

[7] Geannakakes G., "Vibration analysis of arbitrarily shaped plates using beam characteristic orthogonal polynomials in the semi-analytical finite strip method", *Journal of Sound and Vibration* 137 (2), pp. 283-303, 1990.

[8] Ritz W., "Theorie der transversalschwingungen einer quadratischen Platte mit freien Rändern", *Ann. Physik* 28, pp. 737-786, 1909.

[9] Catania G., Sorrentino S., "Rayleigh-Ritz analysis of vibrating plates based on a class of eigenfunctions". In proceedings of ASME IDETC/CIE, San Diego, USA, August 30 - September 2, 2009.

[10] Catania G., Sorrentino S., "Discrete spectral modelling of continuous structures with fractional derivative viscoelastic behaviour". In proceedings of ASME IDETC/CIE, Las Vegas, USA, September 4-7, 2007.

[11] Catania G., Fasana A., Sorrentino S., "A condensation technique for the FE dynamic analysis with fractional derivative viscoelastic models", *Journal of Vibration and Control* 14 (9-10), pp. 1573-1586, 2008.

[12] Timoshenko S., Young D.H., Weaver W., *Vibration problems in engineering*, *4th edition*, Wiley, New York, USA, 1974.

[13] Cook R.D., Malkus D.S., Plesha M.E., Witt R.J., *Concepts and applications of finite element analysis*, *4th edition*, Wiley, New York, USA, 2002.

[14] Blevins R.D., *Formulas for natural frequency and mode shape*, Krieger, Malabar, USA, 1979-2001.

[15] Chakraverty S., *Vibration of plates*, CRC Press, New York, USA, 2009.

[16] Leissa A.W., *Vibration of Plates*, Nasa SP 160, U.S. Government Printing Office, Washington D.C., USA, 1969.

Smoothing experimental data in dynamic substructuring of built up systems

A. Culla, W. D'Ambrogio, A. Fregolent and A. Schiavone

Abstract In experimental dynamic substructuring two main problems can be defined: addition of substructures (coupling) and subtraction of substructures (decoupling). Decoupling can be important in built-up structures where some components (critical subsystems or joints) cannot be removed or accessed easily. Whilst addition of substructures often leads to satisfactory results even in relatively complex cases, subtraction of substructures is a source of problems even in apparently trivial applications. In the literature, critical issues of decoupling (such as ill-conditioning around a discrete number of frequencies) have been highlighted and verified by using simulated data corrupted by random noise. In this paper, experimental data acquired on a benchmark system are used to check previously obtained results both in coupling and decoupling, and to look for additional issues (systematic errors, inconsistencies, etc.) that can not be observed from simulated data.

Antonio Culla
Dipartimento di Ingegneria Meccanica e Aerospaziale, Università di Roma La Sapienza, Via Eudossiana 18, I 00184 Rome, Italy e-mail: antonio.culla@uniroma1.it

Walter D'Ambrogio
Dipartimento di Ingegneria Meccanica, Energetica e Gestionale, Università dell'Aquila, Via G. Gronchi, 18 - I-67100, L'Aquila (AQ), Italy, e-mail: walter.dambrogio@univaq.it

Annalisa Fregolent
Dipartimento di Ingegneria Meccanica e Aerospaziale, Università di Roma La Sapienza, Via Eudossiana 18, I 00184 Rome, Italy e-mail: annalisa.fregolent@uniroma1.it

Alessandro Schiavone
Dipartimento di Ingegneria Meccanica e Aerospaziale, Università di Roma La Sapienza, Via Eudossiana 18, I 00184 Rome, Italy e-mail: schiavone.a@gmail.com

T. Proulx (ed.), *Linking Models and Experiments, Volume 2*, Conference Proceedings of the Society for Experimental Mechanics Series 5,
DOI 10.1007/978-1-4419-9305-2_7, © The Society for Experimental Mechanics, Inc. 2011

1 Introduction

In experimental dynamic substructuring two main problems can be defined: addition of substructures (coupling) and subtraction of substructures (decoupling). Coupling is important to find out the dynamic behaviour of complex structures from a dynamic description of their components. Decoupling can be important in built-up structures where some components (critical subsystems or joints) cannot be removed or accessed easily. Decoupling involves the identification of the dynamic behaviour of a structural subsystem, starting from information about the remaining part of the structural system (residual subsystem) and from the known dynamic behaviour of the complete system.

Addition of substructures (coupling) can be seen as a structural modification problem [6]. Similarly, the decoupling problem can be seen as a structural modification problem with negative modification.

Due to modal truncation problems, in experimental dynamic substructuring, the use of FRFs (Frequency Based Substructuring) is preferred with respect to the use of modal parameters. The main algorithm for frequency based substructuring is the improved impedance coupling [8] that involves just one matrix inversion with respect to the classical impedance coupling technique that requires three inversions. A general framework for dynamic substructuring is provided in [12, 10]: an interesting formulation is the so called dual domain decomposition that allows to retain the full set of global DoFs by ensuring equilibrium at the interface between substructures.

Whatever be the used approach, the dynamic behaviour at all the coupling DoFs must be determined. Therefore, if coupling involves transmission of moments, rotational measurements are required. Lack of or bad information about rotational DoFs is always a problem. Several techniques have been devised to circumvent this problem, such as equivalent multi point connection [1, 10] or transmission simulator method [13]. Furthermore, when using experimental data, several issues can be considered [14].

Whilst addition of substructures often leads to satisfactory results even in relatively complex cases, subtraction of substructures is a source of problems, mainly due to ill-conditioning, even in apparently trivial applications. There are several different reasons leading to ill-conditioning: inertia ratios at interface [9], different stiffnesses at interface [7], internal resonances of the residual subsystem with fixed interface [2, 15]. Some critical issues of decoupling (such as ill-conditioning around a discrete number of frequencies) have been highlighted and verified by using simulated data corrupted by random noise.

In this paper, experimental data acquired on a lumped parameter benchmark system with translating masses are used to check previously highlighted problems both in coupling and decoupling, and to look for additional issues (systematic errors, inconsistencies, etc.) that can not be observed from simulated data. The use of a lumped parameter benchmark allows to avoid two series of problems: problems due to rotational DoFs and modal truncation problems which may appear even using an FRF based approach because of curve fitting.

Substructuring is performed using the dual domain decomposition: the coupling problem can be directly formulated from [12], while a similar formulation for the decoupling problem is developed and discussed in [3, 4] for collocated approach and in [16, 5] for non collocated approach.

In the coupling problem, the FRF matrix of the component subsystems is assumed to be known at the coupling DoFs. With regard to the decoupling problem, the FRF matrix of the coupled system is assumed to be known at the coupling DoFs (standard interface). Information about the residual subsystem can consist either of measured FRFs or of a physical model. Here, the first assumption is considered. To circumvent ill-conditioning due to internal resonances of the residual subsystems with fixed interface, FRFs at some internal DoFs of the residual subsystem are used (extended interface) [2, 15, 4]. Since FRFs are curve-fitted from experimental tests, errors due to measurement inaccuracies and to identification can be expected.

2 Addition and subtraction of subsystems

The coupled structural system AB is assumed to be made by two subsystems (A and B) joined through a number of couplings (see Fig. 1). The degrees of freedom (DoFs) of the coupled system can be partitioned into internal DoFs (not belonging to the couplings) of subsystem A (a), internal DoFs of subsystem B (b), and coupling DoFs (c).

If addition of subsystems (coupling problem) is considered, subsystems A and B are assumed to be known whilst the FRF of the coupled system AB is unknown.

If subtraction of subsystems (decoupling problem) is considered, the coupled structural system AB and a residual subsystem B are assumed to be known whilst the FRF of subsystem A is unknown.

2.1 Addition of subsystems

In the frequency domain, the equation of motion of a linear time-invariant subsystem r may be written as:

$$\left[Z^{(r)}(\omega)\right]\left\{u^{(r)}(\omega)\right\} = \left\{f^{(r)}(\omega)\right\} + \left\{g^{(r)}(\omega)\right\} \tag{1}$$

where:

$[Z^{(r)}]$ is the dynamic stiffness matrix of subsystem r;
$\{u^{(r)}\}$ is the vector of degrees of freedom of subsystem r;
$\{f^{(r)}\}$ is the external force vector;
$\{g^{(r)}\}$ is the vector of connecting forces with other subsystems (constraint forces associated with compatibility conditions).

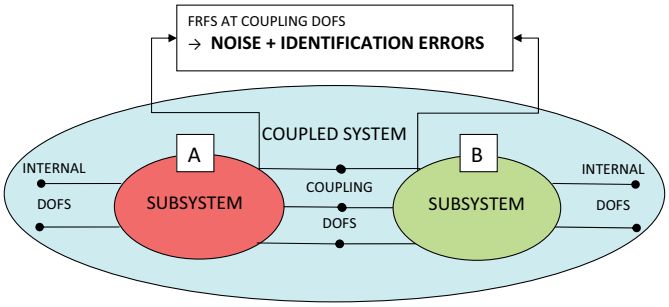

Fig. 1 Scheme of substructuring problem

For the sake of simplicity, the explicit frequency dependence will be omitted.

The equation of motion of the subsystems to be coupled can be written in a block diagonal format as:

$$[Z]\{u\} = \{f\} + \{g\} \qquad \text{i.e.} \qquad \begin{bmatrix} [Z^A] & [0] \\ [0] & [Z^B] \end{bmatrix} \begin{Bmatrix} \{u^A\} \\ \{u^B\} \end{Bmatrix} = \begin{Bmatrix} \{f^A\} \\ \{f^B\} \end{Bmatrix} + \begin{Bmatrix} \{g^A\} \\ \{g^B\} \end{Bmatrix} \quad (2)$$

The compatibility condition at the interface DoFs implies that any pair of matching DoFs u_l^A and u_m^B, i.e. DoF l on subsystem A and DoF m on subsystem B must have the same displacement, that is $u_l^A - u_m^B = 0$.

This condition can be generally expressed as:

$$[B]\{u\} = \{0\} \qquad \text{i.e.} \qquad \begin{bmatrix} [B^A] & [B^B] \end{bmatrix} \begin{Bmatrix} \{u^A\} \\ \{u^B\} \end{Bmatrix} = 0 \quad (3)$$

where each row of $[B]$ corresponds to a pair of matching DoFs. Note that $[B]$ is, in most cases, a signed Boolean matrix and it can be written by distinguishing the contribution of the different subsystems.

The equilibrium condition for constraint forces associated with the compatibility conditions implies that, when the connecting forces are added for a pair of matching DoFs, their sum must be zero, i.e. $g_l^A + g_m^B = 0$: this holds for any pair of matching DoFs. Furthermore, if DoF k on subsystem A (or B) is not a connecting DoF, it must be $g_k^A = 0$: this holds for any non-interface DoF.

Overall, the above conditions can be expressed as:

$$[L]^T \{g\} = \{0\} \quad (4)$$

where the matrix $[L]$ is a Boolean localisation matrix. Note that the number of rows of $[L]^T$ is equal to the number of non-interface DoFs plus the number of pairs of interface DoFs.

Eqs. (2-4) can be put together to obtain the so called 3-field formulation [12]:

$$\begin{cases} [Z]\{u\} = \{f\} + \{g\} \\ [B]\{u\} = \{0\} \\ [L]^T\{g\} = \{0\} \end{cases} \tag{5}$$

2.1.1 Dual formulation in the frequency domain [12, 11]

In the dual formulation, the total set of DoFs is retained, i.e. each interface DoF is present as many times as there are substructures connected through that DoF. The equilibrium condition $g_l^A + g_m^B = 0$ at a pair of interface DoFs is ensured by choosing, for instance, $g_l^A = -\lambda$ and $g_m^B = \lambda$. Due to the construction of $[B]$, the overall interface equilibrium can be ensured by writing the connecting forces in the form:

$$\{g\} = -[B]^T\{\lambda\} \tag{6}$$

where $\{\lambda\}$ are Lagrange multipliers corresponding to connecting force intensities.

The interface equilibrium condition (4) is thus written:

$$[L]^T\{g\} = -[L]^T[B]^T\{\lambda\} = \{0\} \tag{7}$$

Because $[B]^T$ is the nullspace of $[L]^T$ (see for instance [4]), Eq. (7) is always satisfied and the system of equations (5) becomes:

$$\begin{cases} [Z]\{u\} + [B]^T\{\lambda\} = \{f\} \\ [B]\{u\} = \{0\} \end{cases} \tag{8}$$

In matrix notation:

$$\begin{bmatrix} [Z] & [B]^T \\ [B] & [0] \end{bmatrix} \begin{Bmatrix} \{u\} \\ \{\lambda\} \end{Bmatrix} = \begin{Bmatrix} \{f\} \\ \{0\} \end{Bmatrix} \tag{9}$$

that is:

$$\begin{bmatrix} [Z^A] & [0] & [B^A]^T \\ [0] & [Z^B] & [B^B]^T \\ [B^A] & [B^B] & [0] \end{bmatrix} \begin{Bmatrix} \{u^A\} \\ \{u^B\} \\ \{\lambda\} \end{Bmatrix} = \begin{Bmatrix} \{f^A\} \\ \{f^B\} \\ \{0\} \end{Bmatrix} \tag{10}$$

Note that $[B^A]$ and $[B^B]$ extract the coupling DoFs among the full set of DoFs.

By eliminating $\{\lambda\}$, it is possible to obtain a relation in the form $\{u\} = [H]\{f\}$, which provides the FRF of the coupled system AB [4]:

$$\{u\} = \left([Z]^{-1} - [Z]^{-1}[B]^T \left([B][Z]^{-1}[B]^T \right)^{-1} [B][Z]^{-1} \right) \{f\} \tag{11}$$

In expanded notation:

$$\begin{Bmatrix} \{u^A\} \\ \{u^B\} \end{Bmatrix} = \left(\begin{bmatrix} [Z^A] & [0] \\ [0] & [Z^B] \end{bmatrix}^{-1} - \begin{bmatrix} [Z^A] & [0] \\ [0] & [Z^B] \end{bmatrix}^{-1} \begin{bmatrix} [B^A]^T \\ [B^B]^T \end{bmatrix} \times \right.$$
$$\times \left(\begin{bmatrix} [B^A] & [B^B] \end{bmatrix} \begin{bmatrix} [Z^A] & [0] \\ [0] & [Z^B] \end{bmatrix}^{-1} \begin{bmatrix} [B^A]^T \\ [B^B]^T \end{bmatrix} \right)^{-1} \times \tag{12}$$
$$\left. \times \begin{bmatrix} [B^A] & [B^B] \end{bmatrix} \begin{bmatrix} [Z^A] & [0] \\ [0] & [Z^B] \end{bmatrix}^{-1} \right) \begin{Bmatrix} \{f^A\} \\ \{f^B\} \end{Bmatrix}$$

i.e., by introducing the FRFs $[H^A]$ and $[H^B]$ at the full set of DoFs instead of $[Z^A]^{-1}$ and $[Z^B]^{-1}$:

$$[H^{AB}] = \begin{bmatrix} [H^A] & [0] \\ [0] & [H^B] \end{bmatrix} - \begin{bmatrix} [H^A] & [0] \\ [0] & [H^B] \end{bmatrix} \begin{bmatrix} [B^A]^T \\ [B^B]^T \end{bmatrix} \times$$
$$\times \left(\begin{bmatrix} [B^A] & [B^B] \end{bmatrix} \begin{bmatrix} [H^A] & [0] \\ [0] & [H^B] \end{bmatrix} \begin{bmatrix} [B^A]^T \\ [B^B]^T \end{bmatrix} \right)^{-1} \times \tag{13}$$
$$\times \begin{bmatrix} [B^A] & [B^B] \end{bmatrix} \begin{bmatrix} [H^A] & [0] \\ [0] & [H^B] \end{bmatrix}$$

With the dual formulation, the rows and columns corresponding to the coupling DoFs appear twice in $[H^{AB}]$. Obviously, only independent entries are retained.

2.2 *Subtraction of subsystems using the dual domain decomposition [5]*

The coupled structural system is assumed to be made by an unknown subsystem (A) and a residual subsystem (B) joined through a number of couplings (see Fig. 2).

It is required to find the FRF of the unknown substructure A starting from the FRF of the coupled system AB. The subsystem A can be extracted from the coupled system AB by cancelling the dynamic effect of the residual subsystem B. This can be accomplished by adding to the coupled system AB a fictitious subsystem with a dynamic stiffness opposite to that of the residual subsystem B and satisfying compatibility and equilibrium conditions. According to this point of view, the interface between the coupled system AB and the fictitious subsystem should not only include

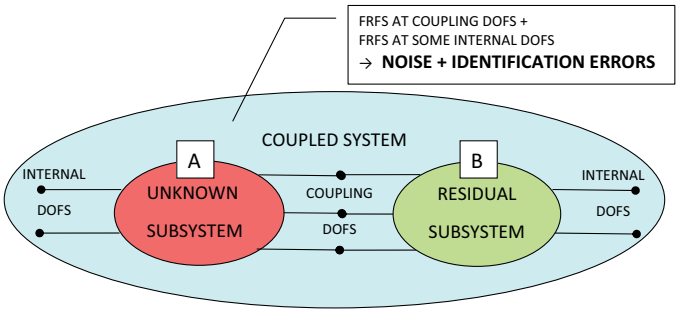

Fig. 2 Scheme of the decoupling problem

the coupling DoFs between subsystems A and B, but should as well include the internal DoFs of subsystem B. However, by taking into account that the problem can be solved by considering only coupling DoFs, the number of interface DoFs should be greater than or equal to the number of coupling DoFs n_c. Therefore, three options for interface DoFs can be considered:

- standard interface, including only the coupling DoFs (c) between subsystems A and B;
- extended interface, including also some internal DoFs ($i \subseteq b$) of the residual substructure;
- mixed interface, including some coupling DoFs ($d \subseteq c$) and some internal DoFs ($i \subseteq b$) of the residual substructure.

The compatibility condition at the (standard, extended, mixed) interface DoFs implies that any pair of matching DoFs u_l^{AB} and u_m^B, i.e. DoF l on the coupled system AB and DoF m on subsystem B must have the same displacement, that is $u_l^{AB} - u_m^B = 0$. Let N_C be the number of interface DoFs on which compatibility is enforced.

The compatibility condition can be generally expressed as:

$$\left[\left[B_C^{AB}\right] \left[B_C^B\right] \right] \left\{ \begin{matrix} \{u^{AB}\} \\ \{u^B\} \end{matrix} \right\} = \{0\} \tag{14}$$

where each row of $[B_C] = \left[\left[B_C^{AB}\right] \left[B_C^B\right]\right]$ corresponds to a pair of matching DoFs. Note that $[B_C]$ is, in most cases, a signed Boolean matrix.

Before deriving the equilibrium condition, it should be noted that the interface DoFs involved in the equilibrium condition are not necessarily the same used to enforce the compatibility condition, as long as controllability between equilibrium and compatibility DoFs is ensured. If the compatibility and the equilibrium DoFs are not the same, the approach is called non-collocated [16], as opposite to the collocated approach, i.e. same compatibility and equilibrium DoFs.

The equilibrium condition for constraint forces implies that, when the connecting forces are added for a pair of matching DoFs, their sum must be zero, i.e.

$g_r^{AB} + g_s^B = 0$: this holds for any pair of matching DoFs. Furthermore, if DoF k on the coupled system AB (the residual subsystem B) does not belong to the equilibrium interface, it must be $g_k^{AB} = 0$ ($g_k^B = 0$): this holds for any DoF not involved in the equilibrium condition. Let N_E be the number of interface DoFs on which equilibrium is enforced.

Overall, the above conditions can be expressed as:

$$\begin{bmatrix} [L_E^{AB}] \\ [L_E^B] \end{bmatrix}^T \begin{Bmatrix} \{g^{AB}\} \\ \{g^B\} \end{Bmatrix} = \{0\} \tag{15}$$

where the matrix $[L_E] = \left[[L_E^{AB}] \, [L_E^B] \right]$ is a Boolean localisation matrix.

In the framework of the dual formulation in the frequency domain (see Section 2.1.1), the union between the coupled system AB and the fictitious subsystem can be written (see Eq. 10) as:

$$\begin{bmatrix} [Z^{AB}] & [0] & [B_E^{AB}]^T \\ [0] & -[Z^B] & [B_E^B]^T \\ [B_C^{AB}] & [B_C^B] & [0] \end{bmatrix} \begin{Bmatrix} \{u^{AB}\} \\ \{u^B\} \\ \{\lambda\} \end{Bmatrix} = \begin{Bmatrix} \{f^{AB}\} \\ \{f^B\} \\ \{0\} \end{Bmatrix} \tag{16}$$

Following the same procedure used in Section 2.1.1, it is possible to obtain the FRF of the unknown subsystem A.

$$\begin{aligned} [H^A] = & \begin{bmatrix} [H^{AB}] & [0] \\ [0] & -[H^B] \end{bmatrix} - \begin{bmatrix} [H^{AB}] & [0] \\ [0] & -[H^B] \end{bmatrix} \begin{bmatrix} [B_E^{AB}]^T \\ [B_E^B]^T \end{bmatrix} \times \\ & \times \left(\begin{bmatrix} [B_C^{AB}] & [B_C^B] \end{bmatrix} \begin{bmatrix} [H^{AB}] & [0] \\ [0] & -[H^B] \end{bmatrix} \begin{bmatrix} [B_E^{AB}]^T \\ [B_E^B]^T \end{bmatrix} \right)^{-1} \times \\ & \times \begin{bmatrix} [B_C^{AB}] & [B_C^B] \end{bmatrix} \begin{bmatrix} [H^{AB}] & [0] \\ [0] & -[H^B] \end{bmatrix} \end{aligned} \tag{17}$$

Note that $[H^{AB}]$ and $[H^B]$ are the FRFs at the full set of DoFs of the coupled system and the residual subsystem.

3 Application

The decoupling technique is tested on an experimental benchmark, chosen in order to be quite simple, at least theoretically, easy to modify, and free from problems due to rotational degrees of freedom. Therefore, a benchmark that can be modelled as a lumped parameter system is selected. The model is shown in Fig. 3: the coupled system are a 4 DoFs system and the two subsystems, denoted by letters A and B, have 3 DoFs.

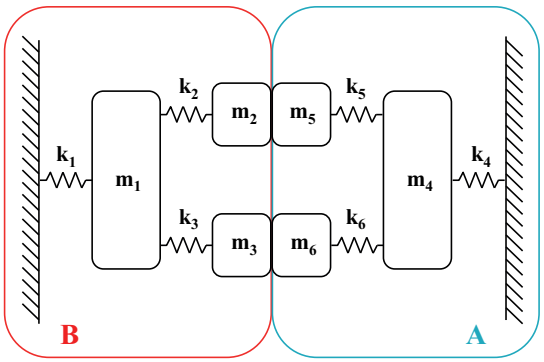

Fig. 3 Lumped model benchmark

3.1 Experimental benchmark

A first version of the benchmark is shown in Fig. 4. It consists of 2 rail guides bolted on an horizontal table and eight guide carriages. Mass m_1 consists of two rigidly connected guide carriages lying on different rails, as mass m_4. Each lumped stiffness consists of two springs in parallel.

However, sliding of the carriages within the guides proves to be quite difficult due to several problems, as for instance the fact that the rail guides are not perfectly parallel.

Therefore a second version of the benchmark is built without using the guides. In this case the motion occurs along a vertical direction, as shown in Fig. 5. However, without the guides, small displacements orthogonal to the vertical direction may occur, as well as small rotations.

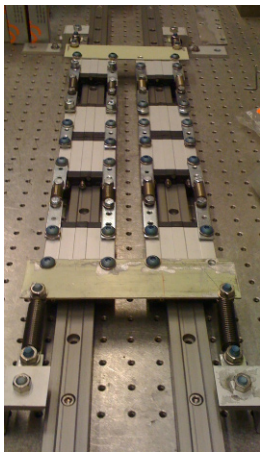

Fig. 4 Benchmark: version 1

Fig. 5 Benchmark: version 2

Fig. 6 Subsystem B

The nominal system parameters are shown in Table 1.

Table 1 Mass values and spring constants of the benchmark

i	1	2	3	4	5	6
m [kg]	0.822	0.414	0.407	0.867	0.443	0.452
k [N/m]	1046	2000	460	1411	709	1059

3.2 Tests

The FRFs of both the coupled system and the subsystems need to be measured either to apply coupling procedure (FRF of the components) and to check the results (FRF of the coupled system), or to apply the decoupling procedure (FRF of the coupled system and FRF of the residual subsystem) and to check the results (FRFs of the 'unknown' subsystem).

The measured FRFs are curve fitted using a polyreference least square frequency domain identification technique in order to regenerate FRFs from a consistent modal model. The complete FRF matrix of the coupled system is measured. Figs. 7 and 8 show the measured raw and fitted point FRFs at the connections between the two subsystems.

With regard to the subsystems, the used tension springs can not work in compression, so additional springs are needed to have a traction preload (Fig. 6). Therefore, the measured FRFs will be affected by the additional springs. The complete FRF matrix of both modified subsystems is measured. Figs. 9, 10, 11 and 12 show the measured raw and fitted point FRFs at the coupling DoFs.

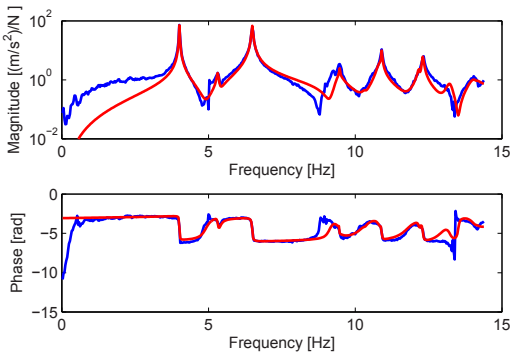

Fig. 7 Inertance H_{22} of the coupled system AB: measured raw (blue) and fitted (red)

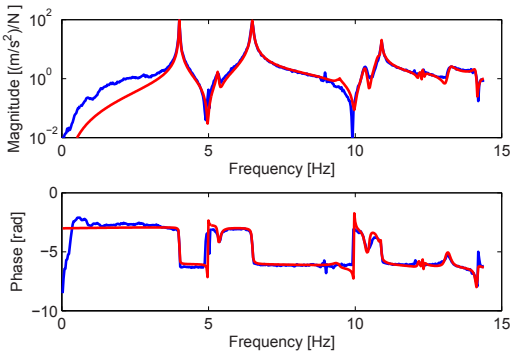

Fig. 8 Inertance H_{33} of the coupled system AB: measured raw (blue) and fitted (red)

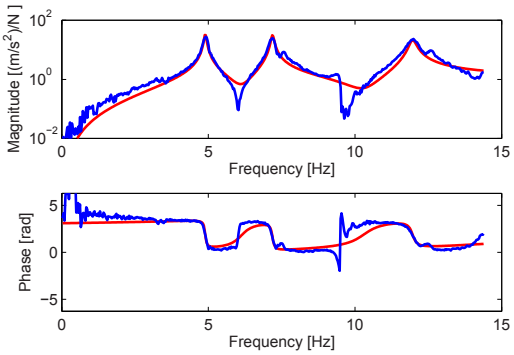

Fig. 9 Inertance H_{22} of subsystem B: measured raw (blue) and fitted (red)

The stiffness values of the additional springs are shown in Table 2.

Table 2 Additional springs used to preload subsystems A and B

$k's$	k_5^A	k_6^A	k_2^B	k_3^B
[N/m]	361	268	218	274

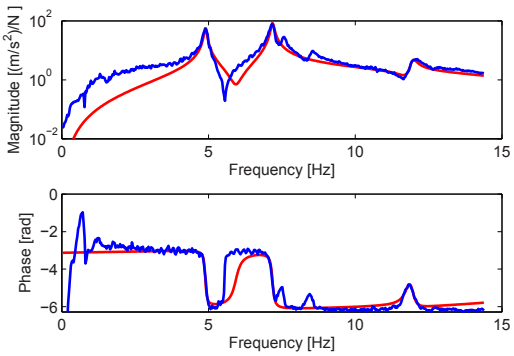

Fig. 10 Inertance H_{33} of subsystem B: measured raw (blue) and fitted (red)

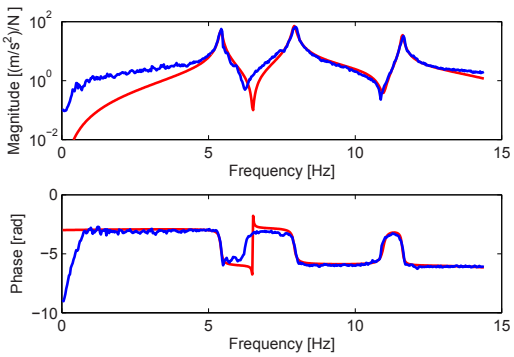

Fig. 11 Inertance H_{55} of subsystem A: measured raw (blue) and fitted (red)

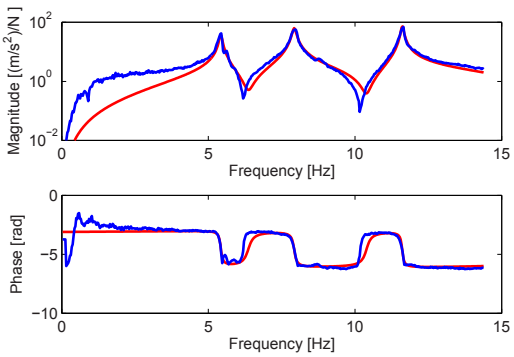

Fig. 12 Inertance H_{66} of subsystem A: measured raw (blue) and fitted (red)

To cancel the effect of the additional springs from the FRFs of the subsystems, a local structural modification procedure is used. Results are shown in Figs. 13 and 14.

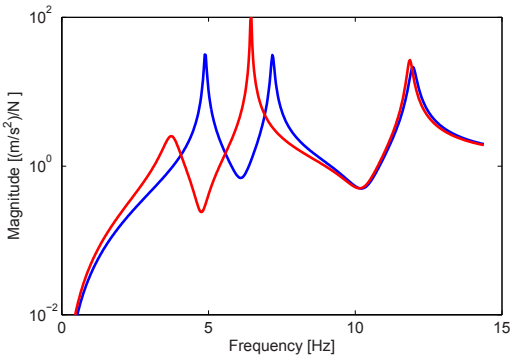

Fig. 13 Inertance H_{22} of subsystem B before and after cancelling the effect of additional springs: before (blue) and after (red) spring cancellation.

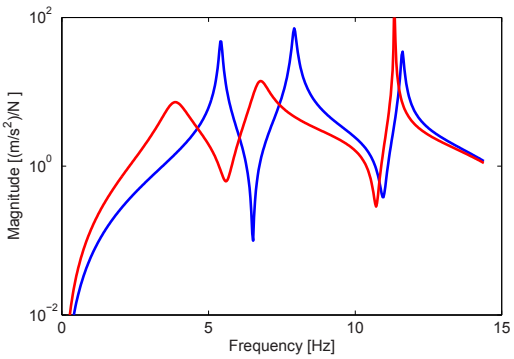

Fig. 14 Inertance H_{55} of subsystem A before and after cancelling the effect of additional springs: before (blue) and after (red) spring cancellation.

To have an idea about the theoretical natural frequencies of the different (sub)systems, the physical parameters shown in Table 1 are used. In Table 3, these values are compared with those obtained by curve fitting the experimental measurements and (in case of subsystems A and B) removing the effects of additional springs. It can be noticed that the largest relative error occurs for the third frequency of the subsystem B, partly due to additional spring removal and for the third frequency of the coupled system AB.

Moreover, additional frequencies can be recognised in the experimental coupled system, but not in the 4 DoFs lumped model. This is due to lateral motion not controlled by the benchmark version 2 (without rail guides).

Table 3 Theoretical and experimental natural frequencies

Systems		f_{model} [Hz]	f_{exp} [Hz]	Δf [%]
A	f_1	4.016	3.861	3.86
	f_2	6.912	6.787	1.81
	f_3	11.360	11.330	0.26
B	f_1	3.612	3.705	-2.57
	f_2	6.538	6.445	1.42
	f_3	14.260	11.860	16.83
AB	f_1	3.892	3.985	-2.39
	f_2	6.663	6.476	2.81
	f_3	10.240	10.900	-6.45
	f_4	12.700	12.330	2.91

3.3 Results for subsystem addition

Starting from the FRFs of subsystems *A* and *B* after spring cancellation, the FRFs of the coupled system is computed using the procedure outlined in Section 2.1. Results at the coupling DoFs are shown in Figs. 15 and 16. The first two natural frequencies are satisfactorily located. The errors in the third and fourth natural frequencies are probably due to inaccuracies in the identification of the subsystem *B* (see Table 3).

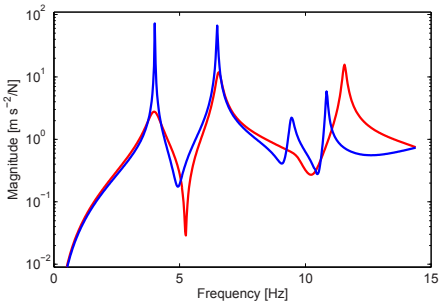

Fig. 15 Inertance H_{22} of the coupled system: fitted (blue); from coupling (red)

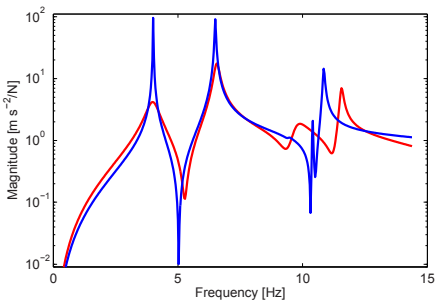

Fig. 16 Inertance H_{33} of the coupled system: fitted (blue); from coupling (red)

3.4 Results for subsystem subtraction

Starting from the FRFs of coupled systems *AB* and residual subsystem *B* (after spring cancellation), the FRFs of the unknown subsystem *A* is computed using the procedure outlined in Section 2.2. Results at the coupling DoFs are shown in Figs. 17 and 18.

As expected, the result is worse than the one obtained for structure addition. A spurious frequency seems to appear around 5 Hz. Having used an extended interface, it can not be explained as an internal resonance of the residual subsystem with interface DoFs grounded [4]. It might be ascribed to inconsistencies between the FRFs of the coupled system and the FRFs of the residual subsystem.

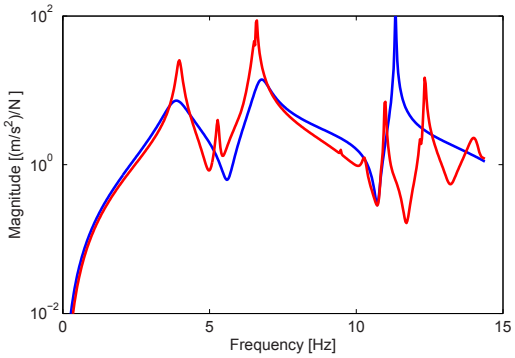

Fig. 17 Inertance H_{55} of the unknown subsystem *A*: fitted (blue); after decoupling (red)

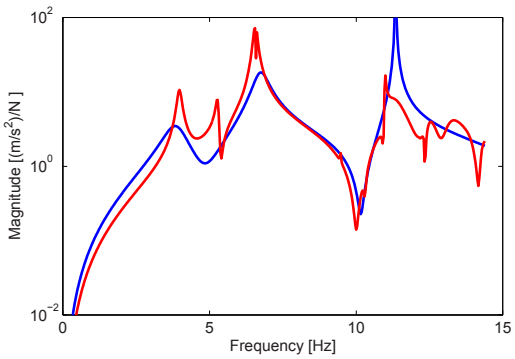

Fig. 18 Inertance H_{66} of the unknown subsystem *A*: fitted (blue); after decoupling (red)

The obtained results could be improved by selecting a lower number of poles in curve fitting the FRFs of the coupled system *AB*. Specifically (compare Figs. 19 and 20 with Figs. 7 and 8) the natural frequency around 5 Hz, probably due to lateral motion of the coupled system, can be neglected. No such lateral motion occurs during tests on the residual subsystem *B*, thus avoiding a source of inconsistency. Results of the decoupling procedure at the coupling DoFs shown in Figs. 21 and 22

can be compared with the previous results (Figs. 17 and 18): it is clear that the natural frequency around 5 Hz is not consistent with the model.

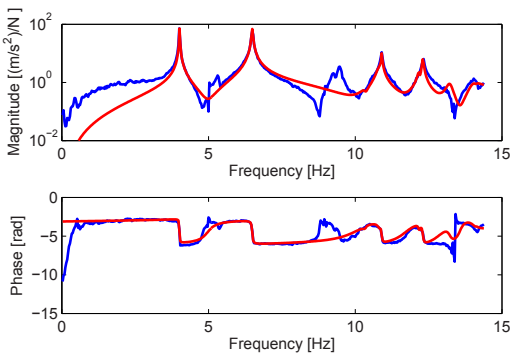

Fig. 19 Inertance H_{22} of the coupled system changing the fitting poles: measured raw (blue) and fitted (red)

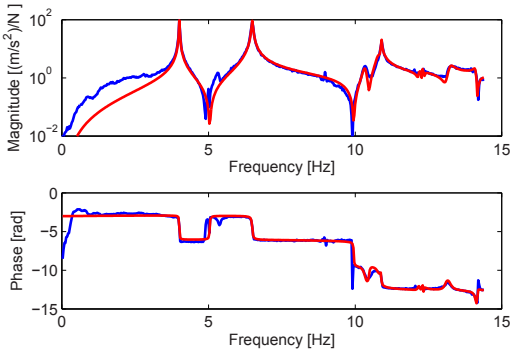

Fig. 20 Inertance H_{33} of the coupled system changing the fitting poles: measured raw (blue) and fitted (red)

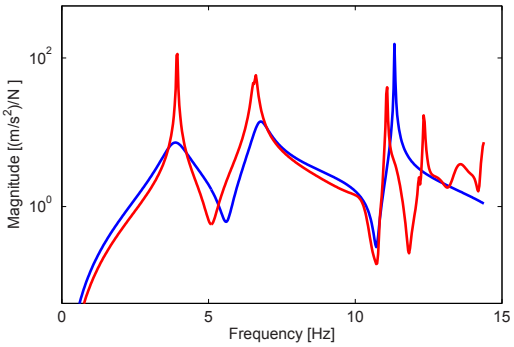

Fig. 21 Inertance H_{55} of the unknown subsystem A changing the fitting poles: fitted (blue); after decoupling (red)

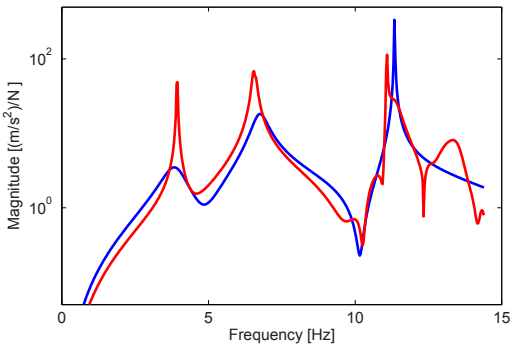

Fig. 22 Inertance H_{66} of the unknown subsystem A changing the fitting poles: fitted (blue); after decoupling (red)

The following figures shows different results obtained using the proposed approach with different choices of interface DoFs, as summarised in Table 4.

Table 4 Dual Decoupling Methods

Interface	Compatibility DoFs	Equilibrium DoFs	Figure
Standard	2,3	2,3	Fig. 23, 24
Non collocated ($N_C > N_E$)	1,2,3	2,3	Fig. 25, 26
	1,2,3	1,2	Fig. 27
	1,2,3	1,3	Fig. 28
Non collocated ($N_C = N_E$)	2,3	1,2	Fig. 29
	2,3	1,3	Fig. 30

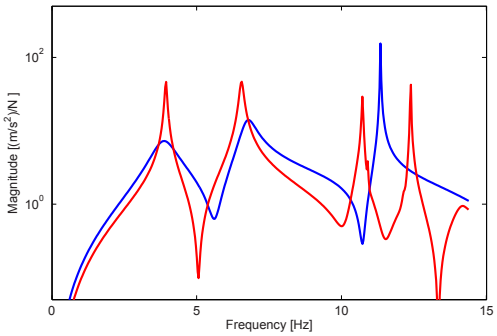

Fig. 23 Inertance H_{55} of the unknown subsystem A using standard interface: fitted (blue); after decoupling (red)

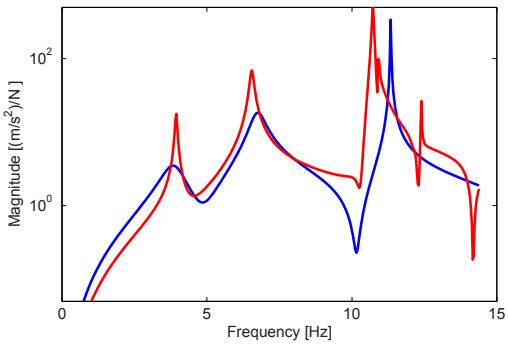

Fig. 24 Inertance H_{66} of the unknown subsystem A using standard interface: fitted (blue); after decoupling (red)

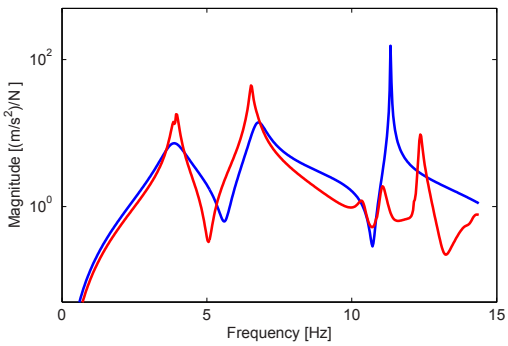

Fig. 25 Inertance H_{55} of the unknown subsystem A using compatibility at all DoFs and equilibrium at the coupling DoFs: fitted (blue); after decoupling (red)

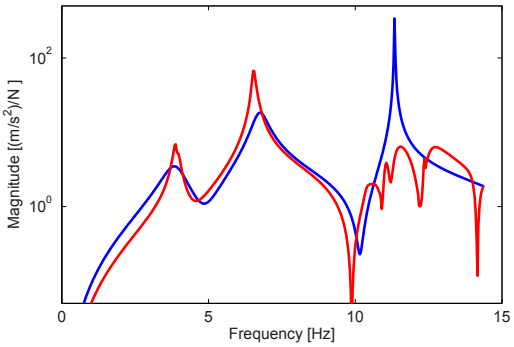

Fig. 26 Inertance H_{66} of the unknown subsystem A using compatibility at all DoFs and equilibrium at the coupling DoFs: fitted (blue); after decoupling (red)

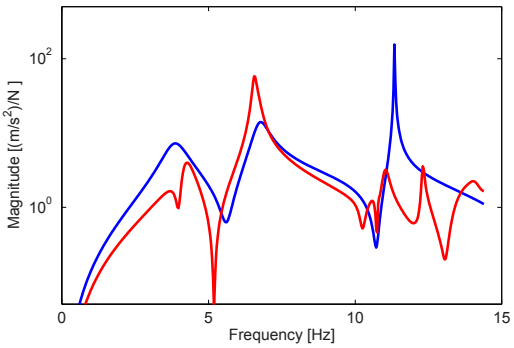

Fig. 27 Inertance H_{55} of the unknown subsystem A using compatibility at all DoFs and equilibrium at the coupling DoF 2 and at the internal Dof 1: fitted (blue); after decoupling (red)

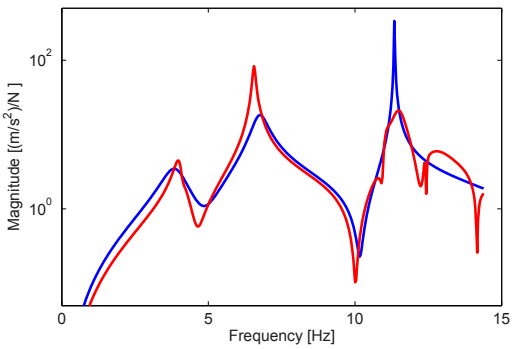

Fig. 28 Inertance H_{66} of the unknown subsystem A using compatibility at all DoFs and equilibrium at the coupling DoF 3 and at the internal Dof 1: fitted (blue); after decoupling (red)

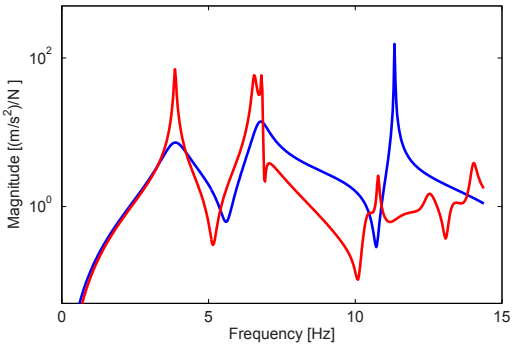

Fig. 29 Inertance H_{55} of the unknown subsystem A using compatibility at the coupling DoFs and equilibrium at the coupling DoF 2 and at the internal Dof 1: fitted (blue); after decoupling (red)

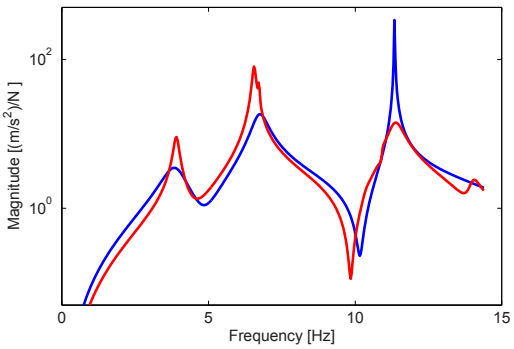

Fig. 30 Inertance H_{66} of the unknown subsystem A using compatibility at the coupling DoFs and equilibrium at the coupling DoF 3 and at the internal Dof 1: fitted (blue); after decoupling (red)

The best results (see Figs. 28 and 30) are obtained when the coupling DoF 2 is not considered as equilibrium DoF, thus implying that the drive point inertance H_{22} of the coupled system is not necessary. Probably this FRFs is affected by some systematic errors due to unmeasured rotational DoFs or to non linearities not accounted in the model.

4 Discussion

In this paper, FRFs acquired on a lumped parameter benchmark system with translational DoFs are used to check coupling and decoupling procedures and to look for additional issues (systematic errors, inconsistencies, etc.) that are not observed when using simulated data.

The use of a lumped parameter benchmark should avoid problems due to unmeasured coupling DoFs and problems due to modal truncation. In practice, the used benchmark (version 2) allows small transverse motion: therefore, some coupling DoFs are not measured; furthermore, due to the transverse sensitivity of the accelerometers, additional modes are observed in the measured FRFs which can pro-

duce inconsistencies. In fact, by removing such modes during curve fitting, better results are observed.

Results can be badly affected by inaccurate measurements. Non collocated approach allows to discard the least accurate measurements thus improving the result.

Acknowledgements This research is supported by grants from University of Rome La Sapienza.

References

1. D'Ambrogio, W., Fregolent, A.: Prediction of substructure properties using decoupling procedures. Structural Dynamics - Eurodyn 2005, Proceedings of the 6th International Conference on Structural Dynamics, pp. 1893–1898. Paris (France) (2005)
2. D'Ambrogio, W., Fregolent, A.: Promises and pitfalls of decoupling procedures. In: Proceeding of 26th IMAC. Orlando (U.S.A.) (2008)
3. D'Ambrogio, W., Fregolent, A.: Decoupling procedures in the general framework of frequency based substructuring. In: Proceedings of 27th IMAC. Orlando (U.S.A.) (2009)
4. D'Ambrogio, W., Fregolent, A.: The role of interface dofs in decoupling of substructures based on the dual domain decomposition. Mechanical Systems and Signal Processing **24**(7), 2035–2048 (2010). Doi:10.1016/j.ymssp.2010.05.007, also in Proceedings of ISMA 2010, pp. 1863-1880, Leuven (Belgium)
5. D'Ambrogio, W., Fregolent, A.: Direct decoupling of substructures using primal and dual formulation. In: Proceedings of 29th IMAC. Jacksonville (U.S.A.) (2011)
6. D'Ambrogio, W., Sestieri, A.: A unified approach to substructuring and structural modification problems. Shock and Vibration **11**(3-4), 295–310 (2004)
7. Ind, P., Ewins, D.: Impedance based decoupling and its application to indirect modal testing and component measurement: a numerical investigation. In: Proceedings of 21st IMAC, p. 9. Kissimmee (USA) (2003)
8. Jetmundsen, B., Bielawa, R., Flannelly, W.: Generalised frequency domain substructure synthesis. Journal of the American Helicopter Society **33**(1), 55–64 (1988)
9. Kalling, P., Abrahamsson, T., McKelvey, T.: Subsystem state-space model identification and its sensitivity to test variability. In: P. Sas, M. De Munck (eds.) Proceedings of ISMA 2004 - International Conference on Noise and Vibration Engineering, pp. 2729–2744. Leuven (Belgium) (2004)
10. de Klerk, D.: Dynamic response characterization of complex systems through operational identification and dynamic substructuring. Ph.D. thesis, TU Delft (2009)
11. de Klerk, D., Rixen, D.J., de Jong, J.: The frequency based substructuring (FBS) method reformulated according to the dual domain decomposition method. In: Proceeding of 24th IMAC. St. Louis, Missouri (U.S.A.) (2006)
12. de Klerk, D., Rixen, D.J., Voormeeren, S.: General framework for dynamic substructuring: History, review, and classification of techniques. AIAA Journal **46**(5), 1169–1181 (2008)
13. Mayes, R.L., Arviso, M.: Design studies for the transmission simulator method of experimental dynamic substructuring. In: P. Sas, B. Bergen (eds.) Proceedings of ISMA 2010 - International Conference on Noise and Vibration Engineering, pp. 1929–1938. Leuven (Belgium) (2010)
14. Nicgorski, D., Avitabile, P.: Experimental issues related to frequency response function measurements for frequency-based substructuring. Mechanical Systems and Signal Processing **24**(5), 1324–1337 (2010). Doi:10.1016/j.ymssp.2009.09.006
15. Sjõvall, P., Abrahamsson, T.: Substructure system identification from coupled system test data. Mechanical Systems and Signal Processing **22**(1), 15–33 (2008)
16. Vormeeren, S.N., Rixen, D.J.: A dual approach to substructure decoupling techniques. In: Proceeding of 28th IMAC. Jacksonville (U.S.A.) (2010)

Metrics for Diagnosing Negative Mass and Stiffness when Uncoupling Experimental and Analytical Substructures

Mathew S. Allen
Daniel C. Kammer
Department of Engineering Physics
University of Wisconsin
Madison, WI 53706
msallen@engr.wisc.edu, kammer@engr.wisc.edu

Randy L. Mayes
Structural Dynamics
Sandia National Laboratory
Albuquerque, NM
rlmayes@sandia.gov

ABSTRACT

Recently, a new substructure coupling/uncoupling approach has been introduced, called Modal Constraints for Fixture and Subsystem (MCFS) [Allen, Mayes, & Bergman, *Journal of Sound and Vibration,* vol. 329, 2010]. This method reduces ill-conditioning by imposing constraints on substructure modal coordinates instead of the physical interface coordinates. The experimental substructure is tested in a free-free configuration, and the interface is exercised by attaching a flexible fixture. An analytical representation of the fixture is then used to subtract its effects in order to create an experimental model for the subcomponent of interest. However, it has been observed that indefinite mass and stiffness matrices can be obtained for the experimental substructure in some situations. This paper presents two simple metrics that can be used by the analyst to determine the cause of indefinite mass or stiffness matrices after substructure uncoupling. The metrics rank the experimental and fixture modes based upon their contribution to offending negative eigenvalues. Once the troublesome modes have been identified, they can be inspected and often reveal why the mass has become negative. Two examples are presented to demonstrate the metrics and to illustrate the physical phenomena that they reveal.

T. Proulx (ed.), *Linking Models and Experiments, Volume 2*, Conference Proceedings of the Society for Experimental Mechanics Series 5,
DOI 10.1007/978-1-4419-9305-2_8, © The Society for Experimental Mechanics, Inc. 2011

1. INTRODUCTION

Component mode synthesis (CMS) has been a fundamental tool for the structural analysis of large complex systems for years. Instead of the system being modeled as a whole, it is broken up into substructures that are then modeled and reduced. This approach is often a necessity due to shear model size, and individual system components are often constructed by different companies. This is especially true in the aerospace community. The Craig-Bampton substructure representation [1] has become the most popular and efficient approach within the aerospace industry. In recent years, there has been a renewed interest in combining analytical based and experimental based substructures using CMS and the imposition of constraints. The direct approach would be to enforce compatibility in the physical connection degrees of freedom between two substructures, but this proves difficult in many problems for several reasons.

Recently, a new approach has been introduced, called Modal Constraints for Fixture and Subsystem (MCFS) [2]. This method reduces ill-conditioning by imposing constraints on substructure modal coordinates instead of the physical interface coordinates. The experimental substructure is tested in a free-free configuration, and the interface is exercised by attaching a flexible fixture, which was dubbed a "transmission simulator" in subsequent works [3]. An analytical representation of the transmission simulator is then used to subtract its effects to produce the desired experimental model of the substructure. This process produces a substructure model that is typically much more accurate than a simple free-free model would be, because of the mass-loading effect of the transmission simulator. However, it has been observed that indefinite mass and stiffness matrices can be obtained for the experimental substructure if the analyst is not careful (e.g. the system has negative mass or stiffness). Similar problems were encountered by other researchers when removing rigid masses from a structure [4]. This paper derives simple metrics that can be used by the analyst to determine which of the systems' modes contribute most to offending negative eigenvalues of either the mass or stiffness matrices. The metrics reveal problems with the subcomponent models that can sometimes be addressed by removing problematic modes or by refining the subcomponent models. Two examples are presented illustrating the metrics and the physics that they reveal.

2. THEORY

2.1. Application of Modal Constraint

The MCFS component mode synthesis approach uses free-free substructure representations, since free-free modal tests are typically more convenient and accurate than the alternatives. In order to properly exercise a substructure during a free-free vibration test, the interface is connected to the transmission simulator [3]. Ultimately this transmission simulator must be subtracted in order to have an experimental representation of the desired substructure. A simple beam example, shown in Fig. 1, will be used to illustrate the process. Component *C* is the system tested to obtain an experimental model, component *A* is a finite element model (FEM) representation of the transmission simulator, and component *B* is the substructure for which an experimental representation is desired. Component *C* is the Combination (hence the letter *C*) of the Base system *B* and the Added transmission simulator *A*, so $C = A+B$. We wish to infer the properties of *B* from the measurements that were acquired on the assembly *C*. The transmission simulator mass-loads the left end of beam *C*, so the model that is obtained for *B* will form a good basis for *B* when it is subsequently assembled to some other structure at the same point (its left end).

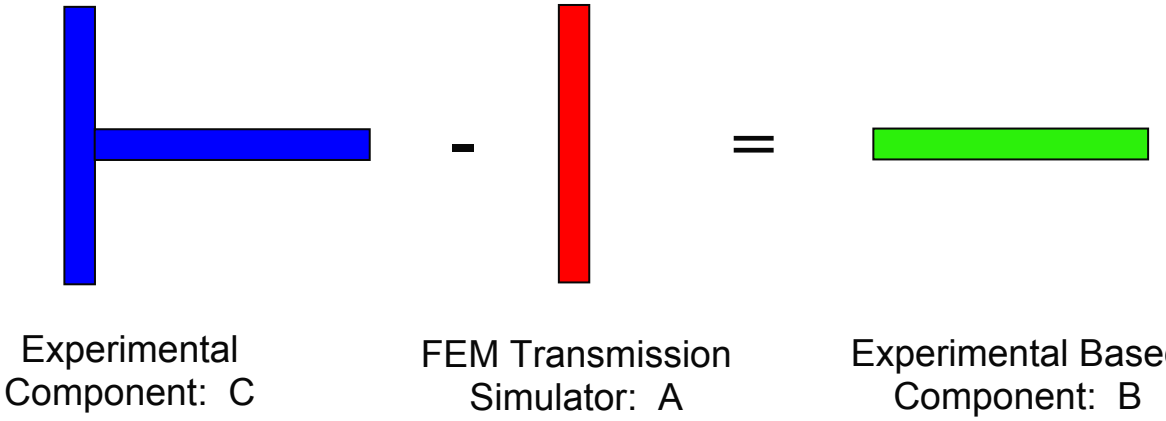

Figure 1: Subtraction of a fixture (or transmission simulator) from an experimental substructure.

The experimental representation of *B* is obtained by coupling *C* and a negative modal representation of *A* (written as B = C-A), which was shown in [2] to cancel the forces exerted by *A* onto *C* under certain basic conditions. The uncoupled equation of motion in modal coordinates is given by

$$\begin{bmatrix} \omega_C^2 & 0 \\ 0 & -\omega_A^2 \end{bmatrix} \begin{Bmatrix} q_C \\ q_A \end{Bmatrix} - \omega^2 \begin{bmatrix} I_C & 0 \\ 0 & -I_A \end{bmatrix} \begin{Bmatrix} q_C \\ q_A \end{Bmatrix} = \begin{Bmatrix} \phi_C{}^{\mathrm{T}} f_C \\ \phi_A{}^{\mathrm{T}} f_A \end{Bmatrix} \tag{1}$$

where ω_C is a diagonal matrix of n_C experimentally derived modal frequencies for component *C,* and ω_A is a diagonal matrix of n_A transmission simulator frequencies computed from its FEM model. For either system, ϕ denotes a matrix of mass normalized mode shapes and *f* the forces applied at the physical coordinates x.

It is assumed that the response of component *C* is measured at n_m locations during the vibration test. In order to couple component *C* and negative component *A*, the usual approach is to enforce compatible displacements at the interface degrees of freedom. However, in general, it is difficult to place sensors and measure all of the degrees of freedom at the interface, especially the rotations. The next best approach would be to enforce displacement compatibility between the two components at the measured locations,

$$x_{Cm} - x_{Am} = 0 \tag{2}$$

but this leads to several difficulties due to measurement errors at the measurement points. An alternative emerges after transforming to modal coordinates,

$$\phi_{Cm} q_C - \phi_{Am} q_A = 0 \tag{3}$$

where ϕ_{Cm} and ϕ_{Am} are the measured partitions of the experimental and transmission simulator components, respectively. Equation (3) can be solved for the transmission simulator modal response

$$q_A = \left[\phi_{Am}^T \phi_{Am}\right]^{-1} \phi_{Am}^T \phi_{Cm} q_C = \phi_{Am}^\dagger \phi_{Cm} q_C \tag{4}$$

in which $\phi_{Am}^\dagger$ is the left generalized inverse of the transmission simulator modes at the measurement locations. This solution requires that the transmission simulator modal partition at the measurement degrees of freedom be full column rank, which implies that $n_m \geq n_A$. The modal coordinates cannot be directly measured, so these constraints must be written in terms of the physical coordinates before they can be implemented. Premultiplying (4) by ϕ_{Am} and then transforming back into physical coordinates produces

$$x_{Am} = \phi_{Am} \phi_{Am}^\dagger x_{Cm} = P_{Am} x_{Cm} = \hat{x}_{Cm} \tag{5}$$

where P_{Am} is an orthogonal projector onto the column space of ϕ_{Am}, and $\hat{x}_{Cm}$ is then the orthogonal projection of the response of substructure *C* at the measurement locations onto this space. Therefore, the modal constraints used in the MCFS approach do not strictly enforce the constraint in Eq. (3), but instead enforce the least-squares fit given in Eq. (5). The best synthesis result will be obtained if $\hat{x}_{Cm} \approx x_{Cm}$, in which case the columns in ϕ_{Cm} can be written as a linear combination of columns in ϕ_{Am}, or $R(\phi_{Cm}) \subset R(\phi_{Am})$.

The modal constraints can be enforced and the constrained generalized coordinates eliminated from eq. (1) with the transformation

$$\left\{ \begin{array}{c} q_C \\ q_A \end{array} \right\} = \left[\begin{array}{c} I_C \\ \tau \end{array} \right] q_C = T q_C \tag{6}$$

in which $\tau = \phi_{Am}^\dagger \phi_{Cm}$. The unforced equation of motion for the reduced or coupled system then has the form

$$m_r \ddot{q}_C + k_r q_C = 0 \tag{7}$$

where

$$m_r = T^T \left[\begin{array}{cc} I_C & 0 \\ 0 & -I_A \end{array} \right] T = I_C - \tau^T \tau \tag{8}$$

and

$$k_r = T^T \begin{bmatrix} \omega_C^2 & 0 \\ 0 & -\omega_A^2 \end{bmatrix} T = \omega_C^2 - \tau^T \omega_A^2 \tau \tag{9}$$

since the matrices in Eqs. (8) and (9) actually represent approximations for the experimental based substructure *B* mass and stiffness matrices using the modal coordinates of *C* as a basis (see eq. (6) above). The synthesized equation of motion for experimental based substructure *B* is then

$$\hat{m}_B \ddot{q}_C + \hat{k}_B q_C = 0 \tag{10}$$

with

$$\hat{m}_B = I_C - \tau^T \tau \tag{11}$$

and

$$\hat{k}_B = \omega_C^2 - \tau^T \omega_A^2 \tau \tag{12}$$

In order for the experimental substructure *B* to be physically realistic, the mass matrix and the stiffness matrix must be positive definite, and positive semi-definite, respectively.

The following section presents an alternative derivation, which shows that the MCFS substructure modal uncoupling technique is equivalent to approximating the transmission simulator mass and stiffness matrices using a SEREP TAM representation [5] for the measured degrees of freedom and then removing the approximated transmission simulator mass and stiffness from a finite element model for *C*. The approach will only be accurate if the modes of the *C* system at all points on the transmission simulator can be accurately represented using the modes of the transmission simulator as a basis. The metrics for ranking the contributions of the subcomponent modes to negative mass and stiffness are presented in Sections 2.3 and 2.4 respectively.

2.2. Alternate Derivation of MCFS Uncoupling by Decomposition

An alternative approach for deriving the relationships for the experimentally based substructure *B* mass and stiffness matrices is based on the more physically intuitive decomposition of substructure *C*. In practice, one does not have a finite element model for C, which is the reason that one is trying to perform experimental substructure uncoupling. However, if the finite element model for *C* were known, its equation of motion in physical coordinates could be written as,

$$M_C \ddot{x}_C + K_C x_C = F_C \tag{13}$$

where the displacement vector can be partitioned into degrees of freedom associated with substructure *A* and substructure *B* as $x_C = \begin{bmatrix} x_{CA}^T & x_{CB}^T \end{bmatrix}^T$. The physical mass matrix M_C can be transformed to modal coordinates using

$$m_C = \begin{bmatrix} \phi_{CA}^T & \phi_{CB}^T \end{bmatrix} \begin{bmatrix} M_{AA} & M_{AB} \\ M_{BA} & M_{BB} \end{bmatrix} \begin{bmatrix} \phi_{CA} \\ \phi_{CB} \end{bmatrix} \tag{14}$$
$$= \phi_{CA}^T M_{AA} \phi_{CA} + \phi_{CB}^T M_{BA} \phi_{CA} + \phi_{CA}^T M_{AB} \phi_{CB} + \phi_{CB}^T M_{BB} \phi_{CB}$$

The mass coupling tends to be small in structural finite element models, so the cross terms are often negligible. (This assumption is not necessary, see the derivation below for stiffness for an alternative.) Neglecting those mass coupling terms, one obtains $m_C = \phi_{CA}^T M_{AA} \phi_{CA} + \phi_{CB}^T M_{BB} \phi_{CB}$ and if the modes are mass normalized the mass matrix of the C system can be written as

$$m_C = I = m_A + m_B \tag{15}$$

in which

$$\begin{aligned} m_A &= \phi_{CA}^T M_{AA} \phi_{CA} \\ m_B &= \phi_{CB}^T M_{BB} \phi_{CB} \end{aligned} \tag{16}$$

are the modal mass representations of substructures *A* and *B* in substructure *C* modal space. Equation (15) can then be written as

$$m_B = I - m_A \tag{17}$$

If one had a finite element model for *C*, the mass matrix for *B* could be computed using these relationships. Of course, if one had a FEM for *C* one could simply delete *A*, but this derivation shows how the models for the subcomponents are related. At this point, one can note a similarity between Eq. (17) and Eq. (11). This reveals that the modal substructuring result produces an estimate of the mass matrix for system A, denoted $\hat{m}_A$, which is given by

$$\hat{m}_A = \tau^T \tau \tag{18}$$

Performing the same analysis for stiffness gives

$$k_C = \omega_C^2 = k_A + k_{AB} + k_{BA} + k_B \tag{19}$$

where

$$\begin{aligned} k_A &= \phi_{CA}^T K_{AA} \phi_{CA} \\ k_{AB} &= k_{BA}^T = \phi_{CA}^T K_{AB} \phi_{CB} \\ k_B &= \phi_{CB}^T K_{BB} \phi_{CB} \end{aligned} \tag{20}$$

In contrast with mass, the stiffness coupling terms k_{AB} and k_{BA} are not zero. Rearranging Eq. (19) produces

$$\hat{k}_B = k_B + k_{AB} + k_{BA} = \omega_C^2 - k_A \tag{21}$$

in which $\hat{k}_B$ is the modal stiffness approximation for substructure *B*. Comparing Eq. (21) with Eq. (12) gives the approximation of the transmission simulator modal stiffness as

$$\hat{k}_A = \tau^T \omega_A^2 \tau \tag{22}$$

To develop the comparison further, consider a finite element model for the transmission simulator, substructure *A*, alone. In physical coordinates, the equation of motion can be written as

$$M_{AA}\ddot{x}_A + K_{AA}x_A = F_A \tag{23}$$

The displacement vector x_A can be partitioned into the measured degrees of freedom and their compliment

$$x_A = \begin{Bmatrix} x_{Am} \\ x_{Ao} \end{Bmatrix} \tag{24}$$

The transmission simulator modes can be partitioned in the same manner

$$\phi_A = \begin{bmatrix} \phi_{Am} \\ \phi_{Ao} \end{bmatrix} \tag{25}$$

Note that that the modal partition ϕ_{Am} was assumed to be full column rank in the previous derivation in Section 2.1. If this is the case, then the physical mass and stiffness matrices in Eq. (23) can be reduced to the measurement degrees of freedom using any of a number of different reduction techniques. This is usually done to generate a reduced mass representation, or test-analysis model (TAM), that is used in test-analysis correlation and analytical model validation [6]. A popular technique for TAM development is called the System Equivalent Reduction Expansion Process (SEREP) [5]. Using this approach, the complete mode shapes of *A* are written in terms of the measured modal partition ϕ_{Am} as

$$\phi_A = T_A\phi_{Am} = \begin{bmatrix} \phi_{Am}\phi_{Am}^{\dagger} \\ \phi_{Ao}\phi_{Am}^{\dagger} \end{bmatrix}\phi_{Am} = \phi_A\phi_{Am}^{\dagger}\phi_{Am} \tag{26}$$

The reduced mass and stiffness matrices for component A at the measurement degrees of freedom are then computed using

$$M_{Ar} = T_A^T M_{AA} T_A \tag{27}$$

$$K_{Ar} = T_A^T K_{AA} T_A \tag{28}$$

It was previously assumed that ϕ_{Cm} can be written as a linear combination of columns in ϕ_{Am}. If this is the case, then ϕ_{Cm} can be written as follows,

$$\phi_{Cm} = \phi_{Am}\gamma \tag{29}$$

where γ is an $n_A \times n_C$ coefficient matrix. Post-multiplying Eq. (26) by γ gives the approximation of the mode shapes of C at all of the points on the transmission simulator, $\hat{\phi}_{CA}$, using the mode shapes of A as a basis.

$$\hat{\phi}_{CA} = \phi_A\gamma = T_A\phi_{Am}\gamma = T_A\phi_{Cm} \tag{30}$$

Substituting Eq. (30) into the first of Eqs. (16) gives the approximation for the transmission simulator modal mass

$$\hat{m}_A = \hat{\phi}_{CA}^T M_{AA}\hat{\phi}_{CA} = \phi_{Cm}^T T_A^T M_{AA} T_A \phi_{Cm} \tag{31}$$

Substituting for transformation T_A from Eq. (26) produces

$$\hat{m}_A = \phi_{Cm}^T \phi_{Am}^{\dagger T} \phi_A^T M_{AA} \phi_A \phi_{Am}^{\dagger} \phi_{Cm} \tag{32}$$

or, assuming modes ϕ_A are mass normalized

$$\hat{m}_A = \phi_{Cm}^T \phi_{Am}^{\dagger T} \phi_{Am}^{\dagger} \phi_{Cm} = \tau^T\tau \tag{33}$$

which agrees with Eq. (18). The corresponding modal stiffness approximation is then

$$\hat{k}_A = \hat{\phi}_{CA}^T K_{AA}\hat{\phi}_{CA} = \phi_{Cm}^T \phi_{Am}^{\dagger T} \phi_A^T K_{AA} \phi_A \phi_{Am}^{\dagger} \phi_{Cm} \tag{34}$$

or

$$\hat{k}_A = \phi_{Cm}^T \phi_{Am}^{\dagger T} \omega_A^2 \phi_{Am}^{\dagger} \phi_{Cm} = \tau^T \omega_A^2 \tau \tag{35}$$

which agrees with Eq. (22). Hence, this analysis has shown that the MCFS substructure modal coupling technique is equivalent to approximating the transmission simulator mass and stiffness matrices using a SEREP TAM representation for the measured degrees of freedom and then removing them from a FEM model for *C*. The accuracy of the approach is dependent upon the accuracy of the approximation $\phi_{CA} \approx \hat{\phi}_{CA}$.

2.3. Ranking Modes based on Mass Approximation

Given a set of experimental modes for substructure *C* and a set of analytical modes for transmission simulator *A*, it is desirable to determine how each mode contributes to negative mass and stiffness in the estimate for *B*. Once the modes that contribute most have been identified the problem can be remedied as discussed in Section 3, sometimes by simply removing them from the model for *C*. From the previous analysis, the approximation for the mass matrix of substructure *B* is given by $\hat{m}_B = I - \hat{m}_A$, where the transmission simulator mass is approximated by $\hat{m}_A = \tau^T \tau$. Matrix τ has dimension $n_A \times n_C$ and was previously shown to have the form

$$\tau = \phi_{Am}^{\dagger} \phi_{Cm} = \left[\phi_{Am}^T \phi_{Am} \right]^{-1} \phi_{Am}^T \phi_{Cm} \tag{36}$$

Prior to ranking modes, it is interesting to develop a better understanding of what matrix τ represents. It was previously illustrated that for the MCFS synthesis method to be accurate, the experimental modes at the measurement locations for substructure *C*, ϕ_{Cm}, must lie in the range space of the transmission simulator modes at the same measurement locations, ϕ_{Am}. As mentioned previously, if this is the case then one can write the modes of *C* as linear combinations of the modes of *A* using $\phi_{Cm} = \phi_{Am} \gamma$, where γ is the corresponding coefficient matrix. Premultiplying this expression by the generalized inverse of ϕ_{Am} gives

$$\phi_{Am}^{\dagger} \phi_{Cm} = \phi_{Am}^{\dagger} \phi_{Am} \gamma = \gamma \tag{37}$$

and since $\tau = \phi_{Am}^{\dagger} \phi_{Cm}$, τ and γ can be interchanged and one can write,

$$\phi_{Cm} = \phi_{Am} \tau \tag{38}$$

A least squares solution for τ gives back the expression in Eq. (36). If this solution is then substituted into Eq. (38), the result is

$$\hat{\phi}_{Cm} = \phi_{Am} \left[\phi_{Am}^T \phi_{Am} \right]^{-1} \phi_{Am}^T \phi_{Cm} = P_{Am} \phi_{Cm} \tag{39}$$

which is consistent with Eq. (5). Therefore, the use of τ in the MCFS synthesis approach produces an approximation of the substructure *C* experimental modes at the measurement locations, $\hat{\phi}_{Cm}$, which minimizes the norm of the error, $e = \phi_{Cm} - \hat{\phi}_{Cm}$. Matrix τ then just represents the linear combination of transmission simulator modes that produces the best fit to the experimental modes.

As mentioned previously, in order for $\hat{m}_B$ to be a physically meaningful representation of the mass of substructure *B*, it must be positive definite, meaning its eigenvalues must be positive. This then implies that the eigenvalues of $\hat{m}_A = \tau^T \tau$ must be less than 1.0, which implies that the singular values of τ must be less than 1.0. This condition may or may not be satisfied, depending on several factors. In the event that this is not satisfied, one would like to determine which modes of the subcomponents are causing the mass matrix to become negative. The following subsections present methods for ranking the contribution of each subcomponent mode to the negative mass or stiffness. These methods are loosely based on the Effective Independence method for ranking sensor locations in vibration testing [7].

2.3.1. Rank Substructure C Experimental Modes

In this subsection, it is assumed that there is a given set of transmission simulator modes to be used in the construction of τ. The objective is to determine the contribution of the experimental modes of substructure *C* to the singular values of τ, such that experimental modes can be included or excluded, depending on their contributions to singular values greater than 1.0.

Define the $n_A \times n_A$ matrix $Q_{CM} = \tau\tau^T$. Let L_{CM} represent a diagonal matrix of the eigenvalues of Q_{CM} sorted in descending order, and let Ψ_{CM} be the corresponding eigenvectors. Note that the eigenvalues of Q_{CM} are the squares of the singular values of τ. Therefore, determining the contributions of the experimental modes to the eigenvalues of Q_{CM} is equivalent to determining their contributions to the singular vales of τ. Define the expression

$$e_{CM} = \left[\tau^T \Psi_{CM} \right]^{\wedge 2} \tag{40}$$

where $[\ ]^{\wedge 2}$ represents a term-by-term square. Each row represents one of the substructure *C* experimental modes, and each column represents one of the eigenvalues of Q_{CM}. It was shown in [7] that each column of e_{CM} adds to the corresponding eigenvalue of Q_{CM}. Therefore, term e_{CMij} gives the contribution of the *i*th experimental mode of substructure *C* to the *j*th eigenvalue of Q_{CM}. If e_{CM} is normalized with respect to the eigenvalues of Q_{CM}

$$e_{CMn} = \left[\tau^T \Psi_{CM} \right]^{\wedge 2} L_{CM}^{-1} \tag{41}$$

then term e_{CMnij} gives the fractional contribution of the *i*th experimental mode of substructure *C* to the *j*th eigenvalue. Using Eqs. (40) and (41), experimental modes that contribute significantly to offending eigenvalues of Q_{CM} can be identified for possible omission from the *C* mode set. However, it is important to note that while e_{CMij} gives the contribution if the *i*th *C* mode to the *j*th eigenvalue of Q_{CM} for the current mode set, deleting this mode does not mean that the corresponding eigenvalue will be reduced by this amount. As a mode is deleted, the matrix Q_{CM} must be recomputed for the new mode set, which in general may have different eigenvalues with a different distribution over the remaining modes. Therefore, once identified modes are deleted from the *C* mode set, the eigenvalues of the new matrix Q_{CM} must be calculated to make sure they are less than 1.0.

2.3.2. Rank Substructure A Finite Element Model Modes

In this subsection, it is assumed that there is a given set of experimental modes for substructure *C* to be used in the construction of τ. The objective is to determine the contribution of the transmission simulator modes, substructure *A*, to the singular values of τ, such that transmission simulator modes can be included or excluded, depending on their contributions.

Analogous to the previous subsection, define the $n_C \times n_C$ matrix $Q_{AM} = \tau^T \tau = \hat{m}_A$. Let L_{AM} represent a matrix of the eigenvalues of Q_{AM} sorted in descending order, and let Ψ_{AM} be the corresponding eigenvectors. Note that the eigenvalues of Q_{AM} are also the squares of the singular values of τ. Therefore, determining the contributions of the transmission simulator modes to the eigenvalues of Q_{AM} is also equivalent to determining their contributions to the singular values of τ. As before, define the expression

$$e_{AM} = \left[\tau \Psi_{AM}\right]^{\wedge 2} \tag{42}$$

Now each row represents one of the substructure *A* transmission simulator modes, and each column represents one of the eigenvalues of Q_{AM}. Each column of e_{AM} adds to the corresponding eigenvalue of Q_{AM}, so term e_{AMij} gives the contribution of the *i*th transmission simulator mode to the *j*th eigenvalue of Q_{AM}. Normalizing with respect to the eigenvalues of Q_{AM} yields

$$e_{AMn} = \left[\tau \Psi_{AM}\right]^{\wedge 2} L_{AM}^{-1} \tag{43}$$

where e_{AMnij} gives the fractional contribution of the *i*th transmission simulator mode to the *j*th eigenvalue. Using Eqs. (42) and (43), transmission simulator modes that contribute significantly to offending eigenvalues of Q_{AM} can be omitted, or the transmission simulator mode set can be truncated such that the resulting eigenvalues of Q_{AM} are less than 1.0.

2.4. Ranking Modes based on Stiffness Approximation

In all of the cases analyzed to date, it has been the mass approximation of substructure *B* that has been most restrictive with respect to the proper sign definiteness of the resulting matrix after subtraction of transmission simulator *A*. However, the stiffness approximation for substructure *B*, $\hat{k}_B = \omega_C^2 - \tau^T \omega_A^2 \tau$, should also be examined to verify positive semi-definiteness. Note that both ω_C and ω_A will in general contain 6 zeros on the diagonal corresponding to rigid body modes. The generalized inverse of the diagonal matrix ω_C then has the simple form

$$\omega_C^{\dagger} = \begin{bmatrix} 0 & 0 \\ 0 & \omega_{Ce}^{-1} \end{bmatrix} \tag{44}$$

in which ω_{Ce} is a diagonal matrix of the elastic experimental frequencies for substructure *C*. The stiffness approximation can then be written as

$$\hat{k}_B = \omega_C \left[I - \omega_C^{\dagger} \tau^T \omega_A \omega_A \tau \omega_C^{\dagger} \right] \omega_C \tag{45}$$

Defining $\tau_K = \omega_A \tau \omega_C^{\dagger}$, Eq. (45) becomes

$$\hat{k}_B = \omega_C \left[I - \tau_K^T \tau_K \right] \omega_C \tag{46}$$

For $\hat{k}_B$ to be positive semi-definite, the matrix $I - \tau_K^T \tau_K$ must be positive definite. This condition has the same form as that used in the mass approximation. The singular values of τ_K must therefore be less than 1.0. As in the case of mass, modes can now be ranked with respect to the substructure *B* stiffness approximation.

2.4.1. Rank Substructure C Experimental Modes

As in the previous case of mass, it is assumed that there is a given set of transmission simulator modes to be used in the construction of τ_K. The objective is to determine the contribution of the experimental modes of substructure *C* to the singular values of τ_K. Define the $n_A \times n_A$ matrix $Q_{CK} = \tau_K \tau_K^T$. Let L_{CK} represent a matrix of the eigenvalues of Q_{CK} sorted in descending order, and let Ψ_{CK} be the corresponding eigenvectors. Analogous to the mass problem, define the expression

$$e_{CK} = \left[\tau_K^T \Psi_{CK} \right]^{\wedge 2} \tag{47}$$

Each row represents one of the substructure *C* experimental modes, and each column represents one of the eigenvalues of Q_{CK}. Each column of e_{CK} adds to the corresponding eigenvalue of Q_{CK}. Therefore, term e_{CKij} gives the contribution of the *i*th experimental mode of substructure *C* to the *j*th eigenvalue of Q_{CK}. The metric can also be normalized as was done for e_{AM} and e_{CM} and used to determine which modes contribute most to the offending eigenvalues of the stiffness matrix.

2.4.2. Rank Substructure A Finite Element Model Modes

One can also rank the modes of the transmission simulator *A* to the offending eigenvalues of the stiffness matrix. The derivation follows the same form as those presented previously with $Q_{AK} = \tau_K^T \tau_K = \hat{k}_A$, resulting in the following metric.

$$e_{AK} = \left[\tau_K \Psi_{AK} \right]^{\wedge 2} \tag{48}$$

3. Numerical Examples

This section applies the proposed metrics to two different systems. The first is an assembly of beams which was studied in a prior publication [8]. Many of the results presented there are repeated here because they are important to illustrate the issues that can arise. The

second system is part of the three-dimensional assembly studied in [2], and it illustrates the complexities that can arise in a more complicated problem.

3.1. Two Dimensional T-beam System

Consider the substructure uncoupling problem pictured in Fig. 1, which was described in Section 2. For the following example all of the subcomponents were modeled with finite elements in order to eliminate any measurement uncertainties. Beam *A* was 152 mm long, 25 mm wide and 19 mm thick, while Beam *B* was 305 mm long with the same cross section. The finite element model was set up so that only in-plane motion, both axial and bending, was possible. The mesh for beams *A* and *B* consisted of 21 and 30 nodes respectively.

The first fifteen modes of *C* will be used in the uncoupling, corresponding to a modal test in which all modes out to 20kHz have been extracted. Each system has three rigid body modes with zero natural frequencies and the natural frequencies of the elastic modes are shown in Table 1. The corresponding mode shapes are not shown, but the lower modes were all observed to involve bending of the horizontal beam, *B*, while the vertical one (transmission simulator *A*) undergoes rigid body rotation. Some of the higher frequency modes show the horizontal beam vibrating axially as the transmission simulator bends. The first six free-modes of *A* are used in the transmission simulator model, three of which are rigid body modes, the 4th and 5th involve bending of beam *A* and mode 6 involves axial motion of beam *A*. Six modal constraints are used to join the negative transmission simulator *A* to *C*. Displacement in both the axial and bending directions at all 21 nodes of the finite element model of *A* are used in forming the modal constraints, although in an experiment one would likely not have such a detailed set of measurements. The rotations at those nodes are not used, since one cannot usually measure rotations in practice.

Table 1 shows the natural frequencies of the *B* system estimated by the modal substructure uncoupling procedure. The actual FEA natural frequencies of the *B* system are also shown as well as the percent difference. All of the natural frequencies below 17kHz are very accurately predicted, having less than 3% error. However, the modal substructuring procedure returns three natural frequencies which are purely imaginary and do not correspond to any of the analytical natural frequencies. Recall that the negative transmission simulator model is still part of the B system even after substructure uncoupling. Its effect is to cancel the force exerted on B by the actual transmission simulator *A* (see [2]), but each of the nodes on the transmission simulator are still valid points on the *B* system and one can determine how the negative transmission simulator moves in each of *B*'s modes. The deformation shape of each of the modes corresponding to the three imaginary natural frequencies was observed and they were found to involve motion primarily on the negative transmission simulator model subsystem *A*; the motion was three orders of magnitude smaller on component *B* in each of these modes. A few FRFs of the *B* system were reconstructed (not shown here) in the axial and bending directions, and they were seen to overlay the analytical FRFs out to 17kHz, confirming that the spurious modes did not have a large effect on the FRFs. In some applications there would be no need to eliminate these spurious modes since they do not seem to affect the model for B. However, one may not always be so fortunate and in any event these spurious modes are problematic since they cannot be imported into most finite element packages.

	Subcomponents		System B		
Mode	**$f_{n,A}$**	**$f_{n,C}$**	**MS est. $f_{n,B}$**	**Actual $f_{n,B}$**	**% Error**
4	4326.5	652.3	1083.3	1081.6	0.2%
5	11926.4	1453.6	0+i*1334.2	-	-
6	16853.0	2924.7	2996.4	2981.6	0.5%
7	-	3090.5	5903.3	5845.1	1.0%
8	-	5751.6	8421.5	8422.1	0.0%
9	-	7285.6	0+i*9157.5	-	-
10	-	9251.0	9824.0	9662.5	1.7%
11	-	12615.3	14832.6	14434.8	2.8%
12	-	13919.7	16965.1	16868.9	0.6%
13	-	14950.0	18066.0	20162.6	-10.4%
14	-	16853.0	0+i*20213	25365.3	-
15	-	19507.0	33706.2	26847.1	25.5%

Table 1: Elastic Natural Frequencies (Hz) of Subsystems C and A, and those that result from using MCFS to compute B=C-A. The actual natural frequencies of the FEA model for B are also shown.

The eigenvalues of the mass matrix of *B* that was estimated with the modal substructuring procedure were found and the lowest five were: -0.012, -0.00038, 3.9e-016, 0.0077, 0.074. Two of these are negative and one is practically zero, indicating that the model for *B* is not physically realizable. A model such as this is incompatible with certain solvers in FEA packages (which require positive definite mass), so one would prefer to find a physically realizable approximation to this model.

In order to investigate this further, the source of these negative eigenvalues was investigated using the metrics developed in this paper. The matrix τ was formed and Q_{CM} was found to have two eigenvalues that were slightly greater than one and a third that was almost exactly equal to one. The EFI procedure was used to compute the contribution of each of the modes of *C* to the eigenvalues of the mass matrix. The elements of e_{CM} corresponding to the modes that contributed most to those eigenvalues are shown in the table below. Each column heading gives the corresponding eigenvalue of Q_{CM} (recall that the eigenvalues of $\hat{m}_B$ are one minus the eigenvalues of Q_{CM}), and the e_{CM} values give the contribution of each mode to that eigenvalue. Contributions below 0.01 have been shown with zeros to improve readability.

Mode of C	**Contribution to Eigenvalues of Q_{CM}**		
	e_{CM} for **$\lambda = 1.012$**	e_{CM} for **$\lambda = 1.00038$**	e_{CM} for **$\lambda = 1$**
14	0	0	1
6	0.77	0	0
5	0	0.38	0
4	0	0.37	0
3	0.08	0.01	0
7	0	0.08	0
9	0.07	0	0
11	0	0.06	0
2	0.02	0.03	0
12	0.04	0	0

Table 2: Contribution, e_{CM}, of each mode of C to the eigenvalues of Q_{CM}.

Several interesting observations can be made. First, mode 14 is entirely responsible for the zero eigenvalue in $\hat{m}_B$. Visual inspection reveals that mode 14 involves purely axial motion

of beam A. A corresponding mode exists in subsystem A, with the exact same natural frequency. That mode was completely unaltered when A was joined to C since it has a node at the connection point, so essentially the same mode exists in both A and C. The zero eigenvalue in $\hat{m}_B$ apparently comes about because this mode's mass is entirely removed from C by the substructure uncoupling process. Recall from eqs (7-12), that the B system has exactly the same number of modes as the C system, so if a mode is removed completely from C by the uncoupling process then a spurious mode must remain in the model for B.

The other two offending eigenvalues are more difficult to interpret. The table shows that the sixth mode of C is the dominant contributor to the first negative eigenvalue, contributing 0.77 of the total value of 1.012. Mode 6, shown with a blue line and open circles in Figure 2, involves axial motion of beam B and bending motion of beam A. As mentioned previously, the lower modes of C all exhibit bending motion of B with beam A undergoing approximately rigid body rotation, so this is the first mode to show significant bending in A. The fact that this mode contributes 0.77 of the 1.012 eigenvalue signifies that this mode carries a significant proportion of the mass associated with bending motion of the transmission simulator, mass which must be removed to accurately predict the natural frequencies of B. Hence, the uncoupling algorithm is working with regard to this mode so long as the amount of mass subtracted is correct. To diagnose the situation further, the orthogonal projection of C's motion onto the space of A's modes, $\hat{x}_{Cm}$, was found using the orthogonal projector P_{Am} in eq. (5) and it is also shown in Figure 2 with a red line and with dots at each of the node points. The zoom view shows that the reconstructed motion matches the true motion very well; the maximum difference between the two is 1.4%. Hence, it seems that this mode's contribution to Q_{CM} is physical and represents mass that should be removed.

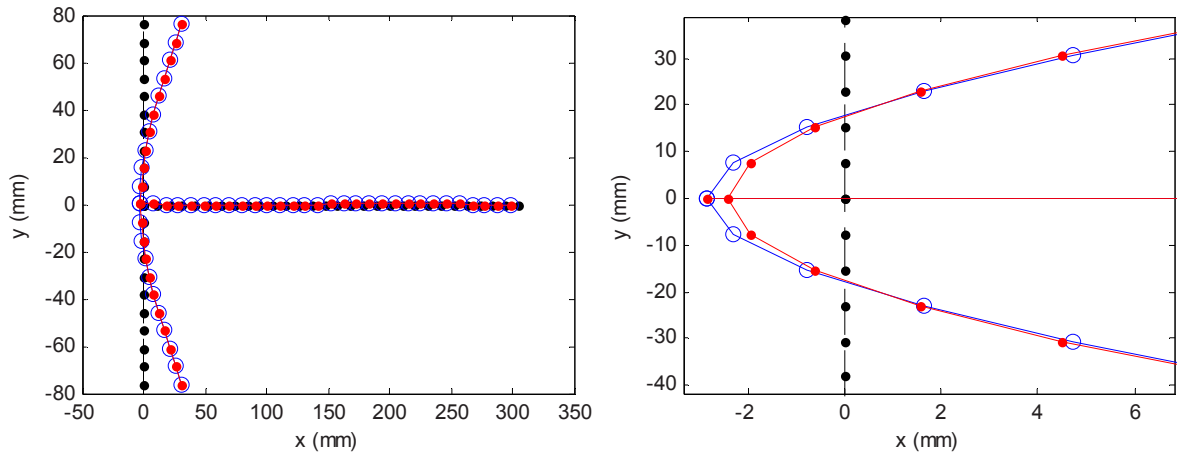

Figure 2: Shape of Mode 6 of system C: (black/dots) undeformed structure, (blue/circles) mode of C, (red/dots) projection, $\hat{x}_{Cm}$, of C onto the free modes of A.

The other mode shapes that contribute to this eigenvalue were also viewed, revealing that there were significant errors when projecting modes 9 and 12 onto the transmission simulator's motion; the maximum difference between the actual motion and the projection was 9.4% and 44.6% respectively. Mode 12's shape is shown in Figure 3 with a blue line. The plot reveals that the 3rd bending mode of the beam would be needed to describe the observed motion, but the model that was used for A only included the first two bending modes (and one axial mode). This reveals that the modal basis of the transmission simulator is inadequate to describe mode 12's motion. Because the transmission simulator model does not contain the third bending mode, the uncoupling process might erroneously attribute the third-mode motion to other modes, and hence

remove more mass from the first and second bending modes than it should. This might explain why too much mass is removed from the system when the transmission simulator model is subtracted, resulting in negative eigenvalues in the estimated mass matrix. The first eigenvalue of Q_{CM} is 1.012, and the table shows that mode 12 contributes 0.04 to it, so if mode 12 were not present then this eigenvalue might reduce below 1.0 resulting in a positive definite model for *B*.

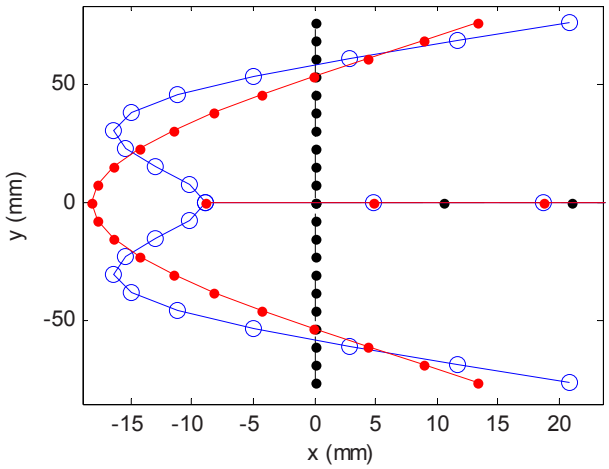

Figure 3: Shape of Mode 12 of system C: (black/dots) undeformed structure, (blue/circles) mode of C, (red/dots) projection, $\hat{x}_{Cm}$, of C onto the free modes of A.

Various modifications to the substructuring process were explored, revealing that the discrepancy in Figure 3 could be reduced greatly by increasing the number of modes in system *A* to seven. When that was done, the maximum discrepancy between $\hat{x}_{Cm}$ and x_{Cm} was found to reduce from 44.6% to 6.2%. The substructuring calculations were repeated and the corresponding negative eigenvalue of $\hat{m}_B$ had disappeared (although the other remained).

Another alternative would be to reduce the number of modes used in *C* so that the six-mode model for *A* would adequately span the observed motion of *C*. Using six modes for system *A* and eleven modes for system *C*, a positive definite mass matrix was obtained with the smallest eigenvalue being 0.00034. However, since fewer modes were used for *C*, the model obtained for *B* was only accurate up to 14kHz, whereas the FRFs were accurately reconstructed out to 17kHz when 15 modes were used for *C*.

3.2. Three Dimensional Cylinder/Fixture System

The next example considered is one of the system's discussed in [2] where the concept of modal constraints was introduced. Substructure *C*, illustrated in Fig. 1, consists of a hollow cylinder and an attached ring-shaped fixture with tabs. The objective is to obtain an experimental representation of the cylinder alone, substructure *B*, by subtracting off a finite element representation of the fixture (or transmission simulator) using the MCFS approach. For this illustrative example, it is assumed that the response of the cylinder and transmission simulator is measured in three degrees of freedom at 12 points on the transmission simulator, as described in [2]. One hundred modes for substructure *C* were simulated with a finite element model, including six rigid body modes and elastic modes ranging between 433.8 and 6165 Hz. Fifty modes were calculated for the transmission simulator using finite element model, including six rigid body modes and elastic modes ranging between 200.4 and 9,382.0 Hz.

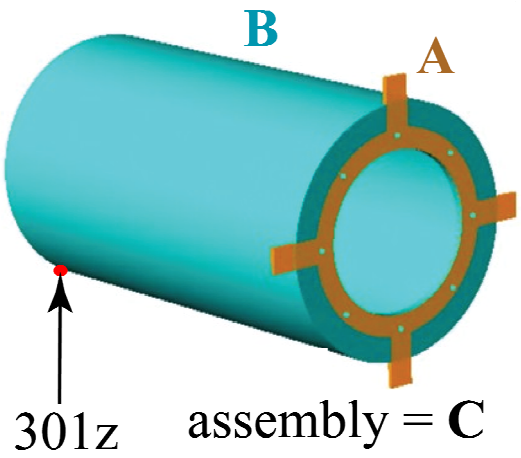

Figure 4: Experimental substructure C consisting of cylinder (B) and transmission simulator (A). Substructure uncoupling will be used to remove the gold colored transmission simulator A from the assembly.

3.2.1. Ranking modes of C

The first application studied is the case where the first 18 modes will be retained for the transmission simulator with frequencies up to 1853.8 Hz and all 100 modes will be included for the composite substructure *C*. When this is done, the mass matrix obtained is not positive definite. The lowest six eigenvalues of the mass matrix are: -0.197, -0.0764, -0.134, -0.118, 0.398 and 0.679. Four of the eigenvalues are below zero, caused by four corresponding eigenvalues of Q_{CM} that are greater than 1.0. The metrics proposed in this paper will be used to rank the *C* modes to determine how they contribute to the mass approximation for substructure *B*. Equation (40) was again used to compute the contributions of the experimental *C* modes to each of the eigenvalues of Q_{CM}. Figure 5 illustrates the cumulative sum over the rows of e_{CM} for the first six columns corresponding to the six largest eigenvalues of Q_{CM}. The four largest eigenvalues slowly increase in value until the 19th-22nd modes are added, at which point they jump above 1.0 and settle at values between 1.5 and 2.2. In contrast, the fifth and sixth eigenvalues increase slowly over all of the modes always remaining below 0.5.

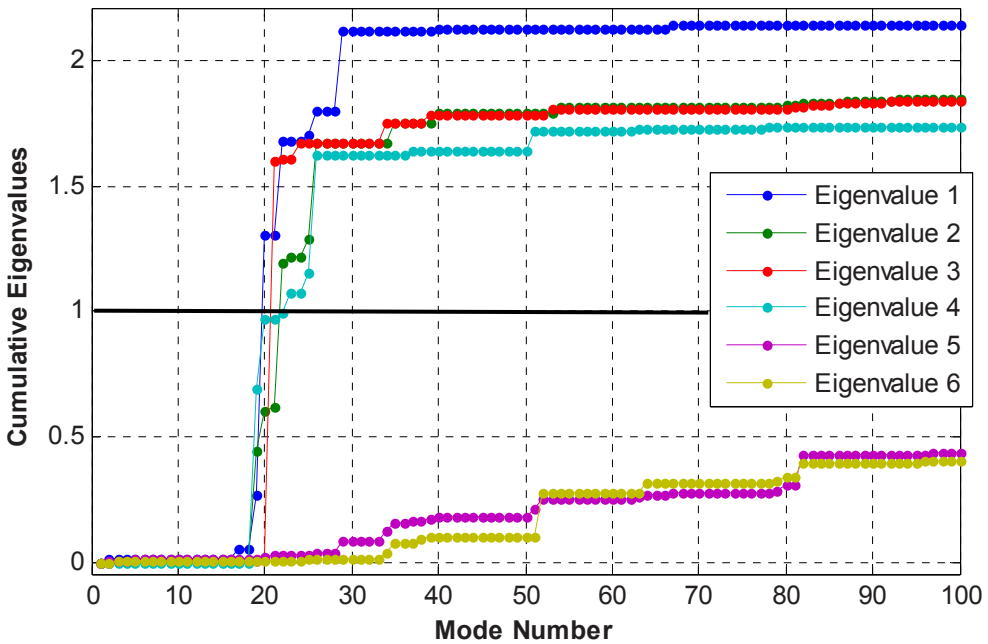

Figure 5: Cumulative sum of eigenvalues of Q_{CM} versus number of modes included in the sum.

The numerical values of e_{CM} are shown in Table 3, in the same format that was used in the previous section. An additional column is also shown that gives the total contribution of each mode to all of the eigenvalues of Q_{CM} that are greater than one (all four that are shown in this case). One observes that mode 21 contributes the most to the large eigenvalues of Q_{CM}, contributing over 86% to the 3rd eigenvalue. The total contributions of modes 19, 20 and 22 make up a similar fraction of the other eigenvalues.

Mode of C	**Eigenvalues of Q_{CM}**				
	Sum	e_{CM} for $\lambda_1 = 2.140$	e_{CM} for $\lambda_2 = 1.845$	e_{CM} for $\lambda_3 = 1.838$	e_{CM} for $\lambda_4 = 1.734$
21	1.60	0	0.01	1.59	0
20	1.48	1.04	0.17	0	0.27
19	1.34	0.21	0.43	0	0.69
22	0.98	0.37	0.58	0	0.03
26	0.95	0.10	0.38	0	0.47
29	0.32	0.32	0	0	0
25	0.17	0.02	0.07	0	0.08
23	0.11	0	0.02	0	0.08
34	0.08	0	0	0.08	0
35	0.08	0	0.08	0	0

Table 3: Contribution, e_{CM}, of each mode of C to the eigenvalues of Q_{CM}.

These results suggest that if modes 19-22 are eliminated from system *C*, then Q_{CM} should be less than 1.0. However, when this is done, one of the eigenvalues remains above 1.0. The 26th mode must also be eliminated from the database to produce a positive definite mass matrix. However, one should not discard modes without cause since they may be important to the model for *B* and to the substructuring predictions obtained with it. To check whether these modes might be important to the model of the cylinder, each mode was plotted. For example, the 20th mode of the *C* substructure is shown in Fig. 6. This and the other mode shape plots reveal that all of the modes in question are dominated by motion of the transmission simulator. The ratio between the maximum displacement of the cylinder part of the structure to the maximum displacement of the transmission simulator was between 4.1% and 10% for these modes. Once the transmission simulator is subtracted, one would expect that this mode might contribute very little to the modal mass of *B*, so small errors and approximation due to the truncated modal basis could cause this mode to have negative mass after substructure uncoupling.

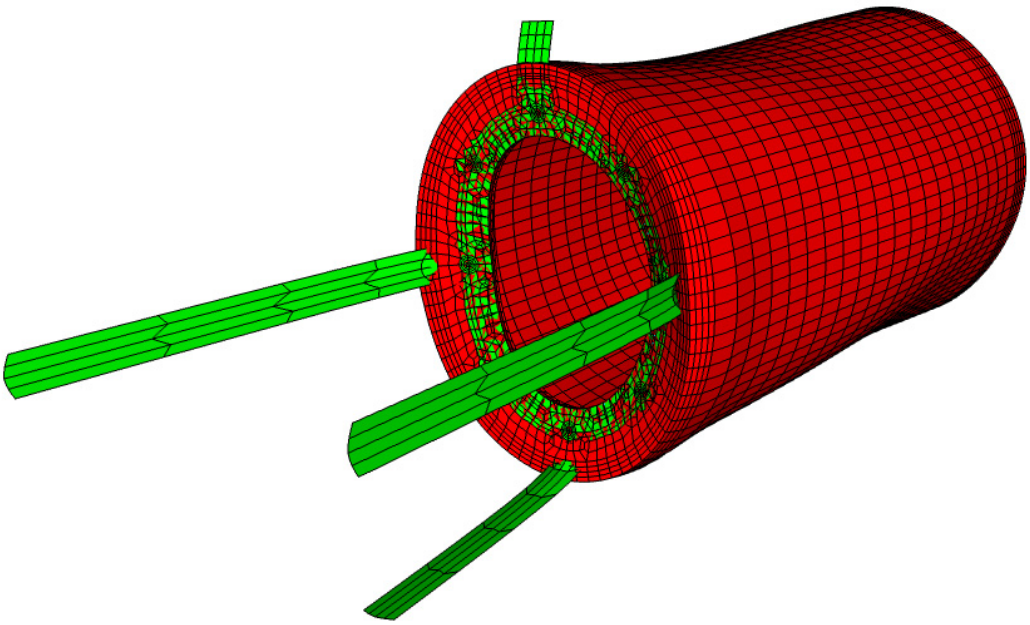

Figure 6: 20th Mode of the Cylinder + transmission simulator.

To see whether these modes were truly insignificant for the substructure model, the full system described in [2] was assembled and its frequency response functions were calculated. Figures 7 and 8 show the drive point FRF of the coupled system at point 301z, which is shown in Fig. 4. Three cases are shown. The solid blue line labeled "analytical" is the FRF of a finite element truth model. The green dashed line is the FRF predicted by substructuring using all of the modes of the cylinder (the C system), and is the same result that was reported in [2]. One can see that the substructuring prediction agrees very well with the truth model. The red dash-dot line is the substructuring prediction obtained after deleting modes 19-22 and mode 26 of the cylinder, as just described. The truncated substructuring prediction also agrees very well with the truth model, except near a few peaks at 1300 and 2300 Hz. The region where the discrepancies occur is magnified in Fig. 8. The FRFs of the system in the axial direction were also shown in [2], but they are not repeated here since there was no discernible difference between the predictions when modes 19-22 and 26 were deleted. These results seem to confirm that these modes are not very important to the subcomponent model. Even then, one would prefer to avoid decreasing the accuracy of the subcomponent model, but for this system none of these problematic modes can be discarded without degrading the substructuring predictions to some extent at least.

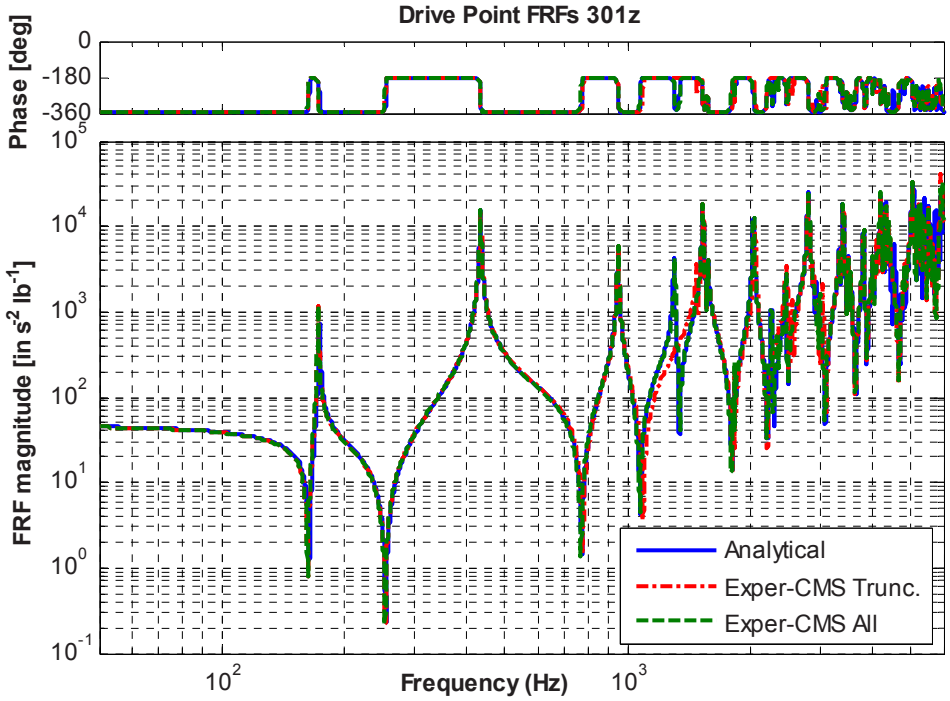

Figure 7: FRF of Cylinder-Plate system described in [2] including all modes of the Cylinder+Transmission simulator ("All") and after eliminating modes 19-22 and 26 ("Trunc.").

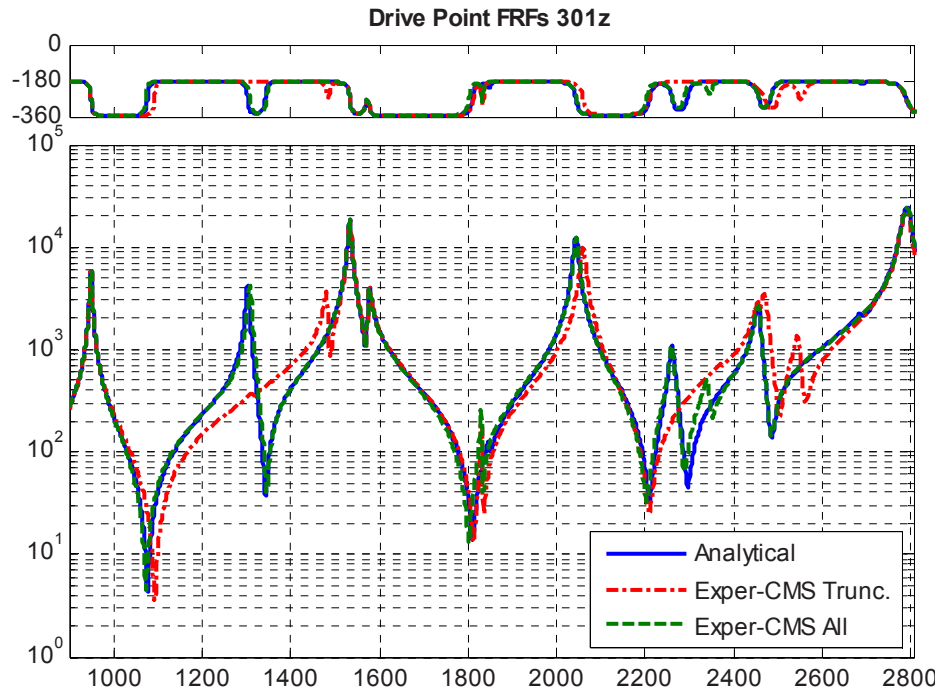

Figure 8: Zoom view of Fig. 7 showing the high frequency region where the substructuring predictions are seen to degrade when modes 19-22 and 26 are excluded from the cylinder model.

3.2.2. Ranking modes of A

For this case the same subcomponents C and A will be used once again with 100 and 18 modes respectively, only now we shall see how the modes of A contribute to the negative eigenvalues. The eigenvalues of $Q_{AM} = \tau^T \tau = \hat{m}_A$ are the same as those of Q_{CM}. Following the

procedure previously outlined, the contributions, e_{AM}, of each of the modes of A to those eigenvalues are shown in Table 4. Modes 9 and 7 contribute significantly to the first and fourth of the eigenvalues of Q_{AM}, but there are a total of seven modes that contribute at least moderately to the negative eigenvalues. There is no justification for removing any of these modes from the model for A, but it is possible that the transmission simulator model is more massive than it should be due to an inaccurate value for its density. To explore this, the modal mass of the seven dominant modes in Table 4 was reduced to attempt to eliminate the negative eigenvalues. Trial and error revealed that the modal mass of these modes had to be reduced to 40% of the original value to obtain a positive definite mass matrix. There does not seem to be a physical justification for such a large reduction; this is a topic of ongoing research. However, it is interesting to note that the substructuring predictions for this system were still very accurate (identical to those shown above and in [2]) even after reducing the modal mass of the transmission simulator so dramatically.

Mode of A	**Eigenvalues of Q_{AM}**				
	Sum	e_{AM} for λ_1=2.140	e_{AM} for λ_2=1.845	e_{AM} for λ_3=1.838	e_{AM} for λ_4=1.734
9	1.42	1.41	0	0	0
7	1.35	0	0.01	0	1.34
6	0.90	0.15	0.47	0.29	0
1	0.88	0.16	0.48	0.23	0
10	0.80	0	0.48	0.32	0
11	0.79	0	0.30	0.49	0
2	0.79	0.37	0	0.42	0
12	0.37	0	0.01	0	0.35
13	0.11	0	0.05	0.03	0.02
14	0.09	0	0.03	0.06	0

Table 4: Contribution, e_{AM}, of each mode of A to the eigenvalues of Q_{AM}.

3.2.3. Ranking modes of C with respect to stiffness

The final application considered is the ranking of the C structure modes based on the stiffness approximation. The case of 18 transmission simulator modes and 100 C modes is again examined. Applying the previously presented procedure, the eigenvalues of $Q_{CK} = \tau_K \tau_K^T$ are computed. In contrast with the mass analysis, all of the eigenvalues of are less than 1.0, therefore the stiffness approximation for substructure B will be positive semi-definite. This is consistent with the authors' experience that the mass approximation of B is usually the most restrictive.

4. CONCLUSION

The Modal Constraints for Fixture and Subsystem method of component mode synthesis has recently been introduced as a means of deriving experimental models of substructures. The experimental substructure is tested in a free-free configuration while the interface is exercised by attaching a flexible fixture or transmission simulator. An analytical representation of the transmission simulator is then used to subtract its effects to produce the desired experimental model of the base structure. It has been observed that indefinite mass and (possibly) stiffness matrices can be obtained in this process. This paper presented simple metrics that can be used by the analyst to determine which modes of each of the subcomponents causes the mass matrix to

become indefinite, by ranking the experimental and transmission simulator modes based upon their contribution to the offending negative eigenvalues.

The metrics were applied to two systems and were found to produce significant insight into the cause of the negative mass. The mass was found to become negative for two reasons: 1.) the system contains modes that are completely removed by the substructuring process leaving mass near zero or 2.) the modal model of the transmission simulator is inadequate to describe the motion of the transmission simulator in the *C* system, leading to inaccuracies that cause too much mass to be removed. The first problem can sometimes be addressed by removing certain modes from the *C* system, although this was found to degrade the substructuring predictions somewhat for the cylindrical system. To address the second problem, one must either increase the number of modes used to describe the transmission simulator A, or reduce the number of modes in *C*.

The metrics presented here can also be used to determine which of the transmission simulator's modes (*A*) contribute most to the negative eigenvalues. Once those modes have been identified, their modal mass can be reduced so that *C* minus *A* does not produce negative mass. One example was presented where the negative mass was eliminated by identifying which transmission simulator modes contributed most to the negative mass and increasing their modal scale factors by 58% (i.e. decreasing their modal mass to 40% of its original value). This was found to produce a physically realizable model, but such a large reduction in modal mass does not seem reasonable. This is just an initial effort into the idea of mass adjustment and further research is needed to understand when this is or is not a viable solution.

The issue of the transmission simulator modes not spanning the space of the modes of *C* was also explored, and the proposed metrics were found to sometimes point to modes for which the span was inadequate. For the beam system, this problem was remedied by increasing the number of modes in the transmission simulator model or by decreasing the number of modes in *C*, although with a consequent reduction in the bandwidth of the model that was obtained for *B*.

The authors suspect that there may be other ways of remedying the problem of negative mass that have not yet been explored. For example, one may find that the transmission simulator model is inaccurate and must be improved before adequate results can be obtained. In any event, the metrics presented in this work should help to guide the analyst to the source of problem so an appropriate solution can be found.

5. ACKNOWLEDGEMENT

This material is based on work supported by Sandia National Laboratories. Sandia is a multi-program laboratory operated by Sandia Corporation, a Lockheed Martin Company, for the United States Department of Energy's National Nuclear Security Administration under Contract DE-AC04-94AL85000.

6. REFERENCES

[1] R. R. Craig and M. C. C. Bampton, "Coupling of Substructures for Dynamic Analysis," *AIAA Journal,* vol. 6, pp. 1313-1319, 1968.

[2] M. S. Allen, R. L. Mayes, and E. J. Bergman, "Experimental Modal Substructuring to Couple and Uncouple Substructures with Flexible Fixtures and Multi-point Connections," *Journal of Sound and Vibration,* vol. 329, pp. 4891–4906, 2010.

[3] R. L. Mayes and M. Arviso, "Design Studies for the Transmission Simulator Method of Experimental Dynamic Substructuring," in *International Seminar on Modal Analysis (ISMA2010)* Lueven, Belgium, 2010.

[4] C. Yasuda, P. J. Riehle, D. L. Brown, and R. J. Allemang, "Estimation Method for Rotational Degrees of Freedom Using a Mass Additive Technique," in *2nd International Modal Analysis Conference (IMAC II)* Orlando, Florida, 1984.

[5] J. O'Callahan, P. Avitable, and R. Riemer, "System Equivalent Reduction Expansion Process," in *7th International Modal Analysis Conference*, Las Vegas, NV, 1989, pp. 29-37.

[6] D. C. Kammer, "Test-Analysis Model Development Using an Exact Modal Reduction," *International Journal of Analytical and Experimental Modal Analysis,* vol. 2, pp. 174-179, 1987.

[7] D. C. Kammer, "Sensor Placement for On-Orbit Modal Identification and Correlation of Large Space Structures," vol. 14, pp. 251-259, 1991.

[8] M. S. Allen, D. C. Kammer, and R. L. Mayes, "Uncertainty in Experimental/Analytical Substructuring Predictions: A Review with Illustrative Examples," in *ISMA2010 - International Conference on Noise and Vibration Engineering* Leuven, Belgium, 2010.

Propagation of Free-Interface Substructure Uncertainty into System Test-Analysis Correlation

Daniel C. Kammer
Sonny Nimityongskul
Dimitri Krattiger

Department of Engineering Physics
University of Wisconsin
1500 Engineering Dr.
Madison, WI 53706, USA

ABSTRACT
As space structures become larger and more complex, ground based vibration tests of the entire spacecraft become either problematic or impossible. Instead, the spacecraft is tested and validated only at the substructure level. The substructure tests are usually performed in a simulated free-free configuration for simplicity and accuracy. A methodology is presented for studying the effects of uncertainty on metrics used for test-analysis correlation of complex spacecraft that are validated on a substructure-by-substructure basis. The objective is to quantify the level of accuracy required at the substructure level to produce acceptable accuracy at the system level. This is done by propagating uncertainty in test-analysis correlation metrics from free-free substructure vibration tests into uncertainty in synthesized system correlation metrics. The correlation uncertainty in each substructure can either be prescribed, for the purpose of numerical experimentation, or it may be available from existing substructure test data. Linear covariance propagation is used to propagate the substructure modal matrix uncertainty into the uncertainty in the corresponding Craig-Bampton substructure representations. Linear covariance propagation is then used again to propagate the substructure uncertainties into the full system modal matrices. The uncertainties in the system correlation metrics are then extracted from the modal matrix uncertainties to determine the impact of uncertainty at the substructure level. Organizations, such as NASA and the Air Force make critical decisions on spacecraft performance and survivability based on the results of test-analysis correlation metrics. In order to ensure the success of finite element model validation where there is no system level test, uncertainty in the substructures must be propagated into the system level correlation metrics. It is believed that the method presented in this paper offers a unique and efficient approach for the required uncertainty propagation.

T. Proulx (ed.), *Linking Models and Experiments, Volume 2*, Conference Proceedings of the Society for Experimental Mechanics Series 5,
DOI 10.1007/978-1-4419-9305-2_9, © The Society for Experimental Mechanics, Inc. 2011

1. INTRODUCTION

Prior to the flight of a spacecraft, a test-validated finite element model (FEM) must be developed to provide accurate loads analysis and controls simulation. The FEM validation process is comprised of several activities, such as determining the model's fidelity with respect to test data, quantification of uncertainty, and determining predictive accuracy [1-3]. Determining the fidelity-to-data is an exercise of fundamental importance. This process consists of comparing test and analysis predictions, also called test-analysis correlation, and then determining optimum changes in parameters that will update, calibrate, or tune the model [4]. Model correlation is usually performed in modal space, where the accuracy of the FEM is determined by comparing modal parameters derived from vibration tests with those predicted by the analytical model. Frequencies are compared directly, while corresponding mode shapes are compared using metrics based on orthogonality and cross-orthogonality of the modes with respect to a reduced analytical mass matrix [5]. The use of these metrics, and the required values for acceptable test-analysis correlation, are dictated by agencies such as NASA [6] and the United States Air Force. The requirements differ, depending on the agency. The Air Force, for example, requires test-analysis frequency errors less than or equal to 3.0%, cross-generalized mass values greater than 0.95, and coupling terms between modes of less than 0.10 in both cross-orthogonality and orthogonality [7].

Recently, work in the structural dynamics community on analytical model validation has focused on the quantification of model uncertainty within large numerical simulations, and its propagation into predicted results [8-10]. The concept of model uncertainty is the reality of design and construction. An engineer may design a single structure based on drawings, analysis, and experiments, but the item produced is one of a statistical population due to variations and uncertainties in geometry, material parameters, construction, etc. This leads to random populations of frequencies and mode shapes. There is a corresponding uncertainty and error in the measured test data. In the low frequency regime of modal-based test-analysis correlation and model updating, it is common practice to ignore the effects of both model and test uncertainty. However, if one does not examine the agreement between measurements and predictions relative to uncertainty, very erroneous and dangerous decisions can be made regarding the models ability to make accurate predictions within untested regimes [11]. Hasselman and his coauthors have produced a large body of work in the area of structural dynamics uncertainty quantification [12-14]. They have used and compared several techniques for propagating uncertainty through structural dynamic simulations, such as linear covariance propagation, the Vertex Method for fuzzy variables, Monte Carlo analysis, etc.

As space structures become larger and more complex, ground based vibration tests of the entire spacecraft become either problematic or impossible due to lack of structural integrity, cost, complexity of the test, or simply lack of time. Instead, the spacecraft is validated on a substructure-by-substructure basis. Unavoidable uncertainty in substructure models and testing will have large, and possibly negative, impact on this new paradigm for model validation. To insure the success of this new model validation approach, several key questions must be addressed. For example, what level of accuracy or correlation do the substructures need to exhibit to have a required level of correlation at the system level? More specifically, how does uncertainty and error within each substructure propagate into, and affect model validation at the system level? Even if the spacecraft will be tested as a system prior to flight, an understanding of the required level of substructure correlation, and how the related uncertainties propagate into the system, will save a great deal of time, effort, and cost during the system level test and analysis.

Researchers have recently started to investigate the effects of substructure uncertainty on synthesized system response using component mode synthesis techniques (CMS). The CMS approach has been used for years to solve large structural dynamics problems, and is built into many standard finite element analysis codes. Hinke et al. [15] consider uncertainty in the form of experimental measured variability, or noise, in substructure free-free modes. They use linear perturbation theory to determine the sensitivities of both fixed interface substructure, and global system modal parameters in terms of unconstrained substructure eigenvalues, based on the Craig-Bampton (CB) substructure representation [16]. Free substructure eigenvalue variance is propagated into fixed CB eigenvalue statistics using inverse linear covariance propagation, which can be subject to numerical ill-conditioning. In addition, they only consider uncertainty due to substructure eigenvalues. Mace and Shorter [17] also consider the effects of substructure model uncertainty on the system modal parameters and resulting frequency response. They use the CB formulation and linear perturbation theory to determine system modal parameters in terms of the random substructure eigenvalues. Uncertainty in the substructure eigenvalues is propagated into system modal parameters using a decoupled Monte Carlo approach. Uncertainty in the system level frequency response can then be recovered. De Klerk and Voormeeren [18] also consider substructure uncertainty in the form of experimental noise, but instead, it is in the frequency response measured during the substructure vibration test. They use a frequency domain CMS approach [19]. Linear perturbation theory is used to propagate the substructure uncertainty into the global response. Voormeeren and Rixen [20] use the same approach, but study the effects of uncertainty on the decoupling of a system into its component

substructures. None of the work performed in this area addresses the test-analysis correlation component of model validation, at either the substructure or system level.

The goal of this investigation is to develop a methodology for studying the effects of uncertainty on accepted metrics for test-analysis correlation of complex spacecraft that are validated on a substructure-by-substructure basis. The objective is to be able to quantify the level of accuracy required at the substructure level to produce acceptable correlation at the system level. Linear perturbation analysis is used to relate uncertainty in test-analysis correlation metrics to uncertainty in substructure modal mass and stiffness. A previously developed statistical model for modal based test-analysis correlation metrics [21] is discussed, which results in a corresponding covariance matrix. Linear covariance propagation is then used to propagate free-interface modal correlation metric uncertainty in the substructures into the expected free-free correlation metric uncertainty for the system using CB based component mode synthesis and reduced order modeling. This work is of special interest because substructures are most often tested in a free-free configuration. Understanding substructure correlation requirements will positively impact the speed of the loads analysis process. A simple example is investigated, and the results are substantiated using Monte Carlo analysis.

Organizations, such as NASA and the Air Force make critical decisions on spacecraft performance and survivability based on the results of test-analysis correlation metrics. Currently there is no uncertainty quantification performed or required by these agencies for test-analysis correlation in the low-frequency regime. The approach presented in this paper offers several advantages over other methods. A user can choose to propagate either an assumed level of test-analysis correlation uncertainty, or uncertainty derived from vibration test results, etc. It is not reliant on the knowledge of any specific model design parameters. It includes all forms of model uncertainty. It is fast, compared with Monte Carlo techniques, and it propagates uncertainty in the correlation metrics directly.

2. THEORY

2.1 Quantification of Substructure Uncertainty

In this work, uncertainty in the substructures is quantified in terms of uncertainty in the substructure test-analysis correlation metrics, modal frequency and cross-orthogonality. In this case, the substructures are assumed to have been tested in a free-free configuration. Uncertainty in substructure modal mass and stiffness must then be related to the uncertainty in modal frequency and cross-orthogonality. A detailed analysis can be found in Kammer et al. [21], but the results are summarized again here.

The uncertainty is defined with respect to the nominal substructure FEM. The nominal substructure modes are assumed to be normalized with respect to mass, such that the nominal substructure modal mass and stiffness are $m = I$ and $k = \Omega$, where Ω is the matrix of nominal eigenvalues. The "truth" model of the substructure can also be represented in nominal modal coordinates as m_T and k_T. The uncertainty in the modal mass and stiffness can then be defined as

$$\Delta m = m_T - m = m_T - I \qquad \Delta k = k_T - k = k_T - \Omega \tag{1}$$

Uncertainty in substructure modes and eigenvalues can likewise be expressed as

$$\Delta\phi = \phi_T - \phi \qquad \Delta\Omega = \Omega_T - \Omega \tag{2}$$

It is assumed that the truth modes can be well approximated as a linear combination of the nominal modes, such that $\phi_T \approx \phi\gamma$. The cross-orthogonality between the nominal and truth modes can then be written as $\phi^T M \phi_T = \phi^T M \phi\gamma = \gamma$. It is also assumed that the truth modes, ϕ_T, are normalized with respect to the nominal mass matrix, instead of the unknown truth mass matrix. This is done to be consistent with the definitions of cross-orthogonality used by both the United States Air Force [7] and NASA [6]. Therefore, for the *j*th mode

$$\phi_{Tj}^T M \phi_{Tj} = \gamma_j^T \gamma_j = 1 \tag{3}$$

in which the subscript *j* indicates the corresponding matrix column of γ. In an actual application of test-analysis correlation, the cross-orthogonality between test and FEM modes is calculated with respect to a reduced FEM mass matrix called a test-analysis model (TAM), instead of the full mass matrix M. However, if the truth modes are spanned by the nominal modes and an exact model reduction is used, such as the Modal TAM [22], then the cross-orthogonality results are the same.

Uncertainty in the cross-orthogonality matrix, $\Delta\gamma$, can be defined using the expression $\gamma = I + \Delta\gamma$. The constraint on the *j*th column of γ in Eq. (3) can then be expressed as

$$\sum_{\substack{i=1 \\ i\neq j}}^{n_q} \Delta\gamma_{ij}^2 = 1 - \gamma_{jj}^2 = -\Delta\gamma_{jj}^2 - 2\Delta\gamma_{jj} \tag{4}$$

or

$$\sum_{i=1}^{n_q} \Delta\gamma_{ij}^2 = -2\Delta\gamma_{jj} \tag{5}$$

where n_q is the number of nominal FEM and truth modes being correlated. Equation (4) indicates that within each column of the cross-orthogonality matrix γ, there is a constraint between the diagonal term and the off-diagonal terms, and Eq. (5) indicates that the uncertainty $\Delta\gamma_{jj}$ is always negative.

Following the approach presented in Ref. [21], using linear perturbation theory, uncertainty in the correlation metrics $\Delta\gamma$ and $\Delta\Omega$ can be related to uncertainty in the substructure modal mass and stiffness Δm and Δk. The first order representation of the substructure modal mass uncertainty is given by

$$\Delta m_{jj} = \Delta_{Mjj} \tag{6}$$

$$\Delta m_{ij} = -\Delta\gamma_{ij} - \Delta\gamma_{ji} \qquad i \neq j \tag{7}$$

where Δ_{Mjj}, defined by $\Delta_{Mjj} = \phi_{Tj}^T M_T \phi_{Tj} - 1$, represents the uncertainty in the *j*th generalized mass with respect to the truth modal space. The corresponding first order representation of the modal stiffness uncertainty has the form

$$\Delta k_{jj} = 2\omega_j \Delta\omega_j + \Delta_{Mjj}\Omega_j \tag{8}$$

$$\Delta k_{ij} = -\Delta\gamma_{ij}\Omega_i - \Delta\gamma_{ji}\Omega_j \qquad i \neq j \tag{9}$$

Note that the terms Δ_{Mjj} can be determined through careful modal testing as discussed in Ref. [23].

One of the main contributions of Ref. [21] was the derivation of the form of the substructure modal mass and stiffness covariance matrices in terms of test- or truth-analysis correlation uncertainty using analytical and numerical experimentation results. It was assumed that the expected values of the uncertainty in the substructure physical mass and stiffness matrices, $E(\Delta M)$ and $E(\Delta K)$, are both zero. The same is then true for the modal matrices, $E(\Delta m) = 0$ and $E(\Delta k) = 0$. This then implies that the expected value of the uncertainty in the generalized masses, $E(\Delta_{Mjj}) = 0$, and the expected value of uncertainties in natural frequencies, $E(\Delta\omega_j) = 0$. Assuming that uncertainty in mass and stiffness are independent, it was shown that the variance of the off-diagonal substructure modal mass uncertainty terms is given by

$$E(\Delta m_{ij}^2) = \frac{\Omega_j - \Omega_i}{\Omega_j + \Omega_i}\left[E(\Delta\gamma_{ij}^2) - E(\Delta\gamma_{ji}^2)\right] \tag{10}$$

The variance of the diagonal modal stiffness uncertainty can be computed using

$$E(\Delta k_{jj}^2) = 4\Omega_j E(\Delta\omega_j^2) - \Omega_j^2 E(\Delta_{Mjj}^2) \tag{11}$$

while the variance of off-diagonal terms Δk_{ij} is given by

$$E(\Delta k_{ij}^2) = \frac{\Omega_j - \Omega_i}{\Omega_j + \Omega_i}\left[\Omega_j^2 E(\Delta\gamma_{ji}^2) - \Omega_i^2 E(\Delta\gamma_{ij}^2)\right] \tag{12}$$

2.2 Propagation of Uncertainty into Craig-Bampton Substructure

The CB substructure representation is well suited as a building block for model validation of substructured systems. The *i*th substructure representation is generated using the coordinate transformation

$$u^i = \left\{ \begin{array}{c} u_o^i \\ u_a^i \end{array} \right\} = \left[\begin{array}{cc} \phi_o^i & \psi^i \\ 0 & I \end{array} \right] \left\{ \begin{array}{c} q^i \\ u_a^i \end{array} \right\} = T_{CB}^i u_{CB}^i \tag{13}$$

in which u_a^i represents the displacement of the substructure interface, and u_o^i is the displacement of the interior of the substructure. This representation is characterized by a combination of fixed interface substructure mode shapes, ϕ_o^i, and a set of static shapes, $\Psi^i = \left[\begin{array}{cc} \psi^{iT} & I \end{array} \right]^T$, called constraint modes, in which $\psi^i = -\left(K_{oo}\right)^{-1} K_{ao}$. The $n_{CB}^i \times n_{CB}^i$ substructure mass and stiffness matrices in the CB space are then given by

$$M_{CB}^i = T_{CB}^{iT} M^i T_{CB}^i = \left[\begin{array}{cc} I & M_{qa}^i \\ M_{aq}^i & M_S^i \end{array} \right] \qquad K_{CB}^i = T_{CB}^{iT} K^i T_{CB}^i = \left[\begin{array}{cc} \Omega_o^i & 0 \\ 0 & K_S^i \end{array} \right] \tag{14}$$

where Ω_o^i is the matrix of fixed-interface eigenvalues for the *i*th substrcture, M_{qa}^i is the mass coupling between fixed modal degrees of freedom and the physical interface degrees of freedom, and M_S^i and K_S^i represent the substructure mass and stiffness matrices statically reduced to the interface, respectively. If all of the fixed-interface modes are retained, then the transformation into the CB substructure representation is exact. However, a significant reduction in model size can be achieved by truncating the number of fixed-interface modes based on frequency.

The uncertainty in *i*th substructure modal mass can be related to the uncertainty in the CB mass matrix using

$$\Delta m^i = \phi_{CB}^{iT} \Delta M_{CB}^i \phi_{CB}^i \tag{15}$$

where ϕ_{CB}^i are the n_s^i mass normalized nominal free substructure modes of interest in CB coordinates. Remember that the uncertainty in the substructure modal mass is obtained from a substructure test-analysis correlation process. The corresponding mode sets are sometimes called target modes. Pre- and post-multiplying each side of Eq, (15) by $M_{CB}^i \phi_{CB}^i$ and its transpose, respectively, gives

$$M_{CB}^i \phi_{CB}^i \Delta m^i \phi_{CB}^{iT} M_{CB}^i = P_T^{iT} \Delta M_{CB}^i P_T^i = \Delta M_{CBT}^i \tag{16}$$

in which the matrix $P_T^i = \phi_{CB}^i \phi_{CB}^{iT} M_{CB}^i$ is an oblique projector [24] onto the column space spanned by the nominal substructure target modes being considered in the correlation analysis. Therefore, ΔM_{CBT}^i is the uncertainty in the CB mass matrix due to the substructure target modes. Note that $P_T^i \phi_{CB}^i = \phi_{CB}^i \phi_{CB}^{iT} M_{CB}^i \phi_{CB}^i = \phi_{CB}^i$, therefore Eq. (15) can be rewritten as

$$\Delta m^i = \phi_{CB}^{iT} P_T^{iT} \Delta M_{CB}^i P_T^i \phi_{CB}^i = \phi_{CB}^{iT} \Delta M_{CBT}^i \phi_{CB}^i \tag{17}$$

This indicates that Δm^i only contains information concerning the uncertainty from the target modes. The same can be said for the substructure modal stiffness uncertainty Δk^i. Therefore, the process of recovering both the CB mass and stiffness uncertainty matrices using Eq. (16) does not result in any additional loss of information.

In order to proceed, the uncertainty matrices in Eq. (16) must be transformed to vectors using the $vec(X)$ operator, in which the columns in matrix *X* are stacked column-wise. It can be shown that for compatible matrices *A*, *X*, and *B*

$$vec(AXB) = \left(B^T \otimes A\right) vec(X) \tag{18}$$

in which the symbol $\otimes$ represents the Kronecker product between two matrices [25], given by

$$A \otimes B = \begin{bmatrix} A_{11}B & A_{11}B & \cdots & A_{1m}B \\ A_{21}B & A_{22}B & \cdots & \vdots \\ \vdots & \vdots & \ddots & \vdots \\ A_{n1}B & \cdots & \cdots & A_{nm}B \end{bmatrix} \tag{19}$$

where A is an $n \times m$ matrix. Using these results, the expression for mass uncertainty in Eq. (16) can be rewritten as

$$vec\left(\Delta M^i_{CBT}\right) = \left[R^i_{CBT} \otimes R^i_{CBT}\right] vec\left(\Delta m^i\right) \tag{20}$$

in which $R^i_{CBT} = M^i_{CB}\phi^i_{CB}$, $vec\left(\Delta M^i_{CBT}\right)$ is a $\left(n^i_{CB}\right)^2 \times 1$ vector, Δp^i_m is $\left(n^i_s\right)^2 \times 1$. The uncertainty matrices Δm^i and ΔM^i_{CBT} are both symmetric, so only the lower triangular terms must be included in the propagation analysis. The $vech(X)$ operator [25] can be used to extract the lower triangular terms of a symmetric $n \times n$ matrix and stack them column-wise in a $n(n+1)/2$ dimensional column vector. The elimination matrix, S_n [26], can be used to relate the $vec(X)$ and $vech(X)$ operators as

$$vech(X) = S_n vec(X) \tag{21}$$

where S_n is a $\left[n(n+1)/2\right] \times n^2$ full row rank matrix with a single 1.0 in each row. The inverse elimination matrix, or duplication matrix, can be formed such that

$$vec(X) = S_n^{-1} vech(X) \tag{22}$$

in which S_n^{-1} is an $n^2 \times \left[n(n+1)/2\right]$ full column rank matrix, also with a single 1.0 in each row, and $S_n S_n^{-1} = I_{n(n+1)/2}$.

Applying these definitions to Eq. (20) produces

$$vech\left(\Delta M^i_{CBT}\right) = S^i_{n_{CB}}\left[R^i_{CBT} \otimes R^i_{CBT}\right]\left(S^i_{n_{CB}}\right)^{-1} vech\left(\Delta m^i\right) \tag{23}$$

or using the simplifying notation, $\Delta p^i_{M_{CBT}} = vech\left(\Delta M^i_{CBT}\right)$, $\Delta p^i_m = vech\left(\Delta m^i\right)$, and $\tilde{R}^i = S^i_{n_{CB}}\left[R^i_{CBT} \otimes R^i_{CBT}\right]\left(S^i_{n_{CB}}\right)^{-1}$, Eq. (23) becomes

$$\Delta p^i_{M_{CBT}} = \tilde{R}^i \Delta p^i_m \tag{24}$$

where matrix $\tilde{R}^i$ has dimension $\left[n^i_{CB}\left(n^i_{CB}+1\right)/2\right] \times \left[n^i_s\left(n^i_s+1\right)/2\right]$. The corresponding equation relating substructure modal stiffness and CB stiffness uncertainties is given by

$$\Delta p^i_{K_{CBT}} = \tilde{R}^i \Delta p^i_k \tag{25}$$

Variance in free substructure modal mass can be related to variance in the CB substructure mass using linear covariance propagation [12]. Taking the expectation of the outer product of Eq. (25) with itself gives

$$E\left(\Delta p^i_{M_{CBT}} \Delta p^{iT}_{M_{CBT}}\right) = C^i_{\Delta M_{CBT}} = \tilde{R}^i E\left(\Delta p^i_m \Delta p^{iT}_m\right)\tilde{R}^{iT} = \tilde{R}^i C^i_{\Delta m}\tilde{R}^{iT} \tag{26}$$

in which $C^i_{\Delta M_{CBT}}$ and $C^i_{\Delta m}$ are the covariance matrices for uncertainty in CB substructure mass and free interface substructure modal mass, respectively. The analogous stiffness equation is given by

$$C^i_{\Delta K_{CBT}} = \tilde{R}^i C^i_{\Delta k} \tilde{R}^{iT} \tag{27}$$

The diagonal terms in the covariance matrices correspond to the mean square values, or variances, of the mass and stiffness uncertainties in the corresponding vector Δp_X. Through extensive numerical experimentation, it was found that the covariance matrices for both the modal mass and stiffness are diagonal, meaning that the terms within each of the vectors Δp^i_m and Δp^i_k are uncorrelated. By either specifying, or being given, the variances of the correlation metrics $E\left[\left(\Delta\omega^i_j\right)^2\right]$, $E\left[\left(\Delta^i_{Mjj}\right)^2\right] = E\left[\left(m^i_{jj}\right)^2\right]$, and $E\left[\left(\gamma^i_{ij}\right)^2\right]$, the substructure modal uncertainty covariance matrices for each substructure can be easily constructed using Eqs. (10) through (12).

2.3 Propagation of Substructure Uncertainty into System

The system matrices can be synthesized from the CB substructure representations by applying the appropriate constraints at the substructure interfaces. The uncoupled system displacement vector u_G can be related to the coupled system displacement vector u_{SYS} using the transformation

$$u_G = \begin{Bmatrix} u^1_{CB} \\ u^2_{CB} \\ \vdots \\ u^{n_{sub}}_{CB} \end{Bmatrix} = \begin{bmatrix} T^1 \\ T^2 \\ \vdots \\ T^{n_{sub}} \end{bmatrix} \begin{Bmatrix} u_Q \\ u_A \end{Bmatrix} = T u_{SYS} \tag{28}$$

where

$$u_Q = \begin{Bmatrix} q^{1T} & q^{2T} & \cdots & q^{n_{sub}T} \end{Bmatrix}^T$$

is a partition of the coupled system displacement containing all of the component modal degrees of freedom from the substructures, and u_A is the partition containing all the non-redundant substructure interface degrees of freedom. For example, in the case of two CB substructures

$$u_G = \begin{Bmatrix} q^1 \\ u^1_a \\ q^2 \\ u^2_a \end{Bmatrix} = \begin{bmatrix} I & 0 & 0 \\ 0 & 0 & I \\ 0 & I & 0 \\ 0 & 0 & I \end{bmatrix} \begin{Bmatrix} q^1 \\ q^2 \\ u^1_a \end{Bmatrix} = \begin{bmatrix} T^1 \\ T^2 \end{bmatrix} u_{SYS} \tag{29}$$

in which

$$T^1 = \begin{bmatrix} I & 0 & 0 \\ 0 & 0 & I \end{bmatrix} \qquad T^2 = \begin{bmatrix} 0 & I & 0 \\ 0 & 0 & I \end{bmatrix}$$

Uncertainty in the uncoupled CB substructure mass matrices can then be related to the uncertainty in the system coupled mass matrix using the expression

$$\Delta M_{SYS} = T^T \Delta M_G T = \begin{bmatrix} T^{1T} & T^{2T} & \cdots & T^{n_{sub}T} \end{bmatrix} \begin{bmatrix} \Delta M^1_{CBT} & 0 & \cdots & 0 \\ 0 & \Delta M^2_{CBT} & 0 & \vdots \\ \vdots & 0 & \ddots & 0 \\ 0 & \cdots & 0 & \Delta M^{n_{sub}}_{CBT} \end{bmatrix} \begin{bmatrix} T^1 \\ T^2 \\ \vdots \\ T^{n_{sub}} \end{bmatrix} \tag{30}$$

Transforming to system modal coordinates then gives the uncertainty in the system modal mass

$$\Delta \mathscr{M}_{SYS} = \phi_{SYS}^T T^T \Delta M_G T \phi_{SYS} = \sum_{i=1}^{n_{sub}} \phi_{SYS}^T T^{iT} \Delta M_{CBT}^i T^i \phi_{SYS} \tag{31}$$

where ϕ_{SYS} are the system modes of interest. Vectorizing the uncertainty matrices in Eq. (31) and employing elimination matrices gives

$$vech\left(\Delta \mathscr{M}_{SYS}\right) = \sum_{i=1}^{n_{sub}} \left[\phi_{SYS}^T T^{iT} \otimes \phi_{SYS}^T T^{iT}\right] vech\left(\Delta M_{CBT}^i\right) \tag{32}$$

or

$$\Delta p_{\mathscr{M}_{SYS}} = \begin{bmatrix} W^1 & W^2 & \cdots & W^{n_{sub}} \end{bmatrix} \begin{Bmatrix} \Delta p_{M_{CBT}}^1 \\ \Delta p_{M_{CBT}}^2 \\ \vdots \\ \Delta p_{M_{CBT}}^{n_{sub}} \end{Bmatrix} = W \Delta p_{M_{CBT}} \tag{33}$$

in which matrices $W^i = \phi_{SYS}^T T^{iT} \otimes \phi_{SYS}^T T^{iT}$ are of dimension $\left(n_{SYS}\right)^2 \times n_{CB}^i$ for n_{SYS} system modes. Using the procedure outlined in the previous section, the system modal mass covariance matrix is then given by

$$C_{\Delta \mathscr{M}_{SYS}} = W \begin{bmatrix} C_{\Delta M_{CBT}}^1 & 0 & \cdots & 0 \\ 0 & C_{\Delta M_{CBT}}^2 & 0 & \vdots \\ \vdots & 0 & \ddots & 0 \\ 0 & \cdots & 0 & C_{\Delta M_{CBT}}^{n_{sub}} \end{bmatrix} W^T = W C_{M_{CBT}} W^T \tag{34}$$

where it is assumed that the individual substructure uncertainties are uncorrelated with one another. A parallel analysis produces the same form for the system modal stiffness uncertainty

$$C_{\Delta \mathscr{K}_{SYS}} = W C_{K_{CBT}} W^T \tag{35}$$

The mean square values of the uncertainties in the system modal mass and stiffness matrices can then be recovered from the diagonal of the matrices $C_{\Delta \mathscr{M}_{SYS}}$ and $C_{\Delta \mathscr{K}_{SYS}}$, respectively.

Once the uncertainty in the system modal mass and stiffness is recovered, the uncertainty in the system modal correlation metrics can be determined using the methods presented in Ref. [21]. It was shown that the variance of the off-diagonal system cross-orthogonality terms can be expressed as

$$E\left(\Delta \gamma_{SYSij}^2\right) = \frac{1}{\left(\Omega_{SYSi} - \Omega_{SYSj}\right)^2} \left[E\left(\Delta \mathscr{K}_{SYSij}^2\right) + \Omega_{SYSj}^2 E\left(\Delta \mathscr{M}_{SYSij}^2\right)\right] \tag{36}$$

where Ω_{SYSi} is the *i*th system eigenvalue. The variance of the system natural frequencies is given by

$$E\left(\Delta \omega_{SYSj}^2\right) = \frac{1}{4\Omega_{SYSj}} \left[E\left(\Delta \mathscr{K}_{SYSjj}^2\right) + \Omega_{SYSj}^2 E\left(\Delta \mathscr{M}_{SYSjj}^2\right)\right] \tag{37}$$

Using numerical experiments, it was shown that the off-diagonal uncertainty terms $\Delta \gamma_{SYSij}$ are not only zero mean, but normally distributed, and within each column, independent. Equation (4) then indicates that the term $c_j = 1 - \gamma_{SYSjj}^2$ is the sum of the squares of $n_{SYS} - 1$ zero mean, normally distributed variables $\Delta \gamma_{SYSij}$. If the terms $\Delta \gamma_{SYSij}$ all had unit variance, c_j would be represented by a chi-square distribution with $n_{SYS} - 1$ degrees of freedom [3]. In the current case, the off-

diagonal terms $\Delta\gamma_{SYSij}$ will have different non-unit variances. Therefore, c_j follows a generalized chi-square distribution. In general, the number of degrees of freedom is not $n_{SYS}-1$ because many of the terms $\Delta\gamma_{SYSij}$ are small due to weak coupling between the nominal FEM modes and the *j*th truth mode.

In terms of standard normal variables z_i, c_j can be expressed in the form

$$c_j = 1-\gamma_{SYSjj}^2 = \sum_{\substack{i=1\\ i\neq j}}^{n_{SYS}} \sigma_i^2 z_i^2 \tag{38}$$

in which $\sigma_i^2 = E\left(\Delta\gamma_{SYSij}^2\right)$ are the off-diagonal cross-orthogonality variances recovered for the *j*th column using Eq. (36). A distribution for c_j can then be constructed by taking a linear combination of single degree of freedom chi-square distributions $\chi^2(1)$ using

$$c_j = \sum_{\substack{i=1\\ i\neq j}}^{n_{SYS}} \sigma_i^2 \chi^2(1) \tag{39}$$

The $(1-\alpha)$ th percentile for c_j can easily be computed and then the corresponding value for the *j*th cross-generalized mass, given by $\gamma_{SYSjj\alpha} = \sqrt{1-c_{j\alpha}}$, can be compared to designated correlation metric criteria.

3.0 NUMERICAL EXAMPLE

A simple example is considered to illustrate the application of the proposed uncertainty propagation technique. The system consists of two steel beams attached in the shape of a T. The cross member, substructure 1, is 12.0 in. long with a 0.5 by 0.5 in. cross section, while substructure 2 is 48 in. long with a 0.5 by 0.35 in. cross section. Both substructures are constrained to plane motion. The rotational degrees of freedom perpendicular to the plane of motion were statically reduced out, except at the substructure interface nodes, the midpoint of substructure 1 and the endpoint of substructure 2. Substructure 1 has nine nodes with 27 degrees of freedom, while substructure 2 has 49 nodes and 99 degrees of freedom. All degrees of freedom are retained in the CMS analysis, therefore substructure 1 has 24 fixed interface modes and 3 constraint modes, while substructure 2 has 96 fixed interface modes and 3 constraint modes in their respective CB representations.

For illustration, only substructure 2 is assumed to have uncertainty. The uncertainty is quantified in terms of test-analysis correlation metrics, as discussed in Section 2.1. The uncertainty can either be specified by the analyst, as a part of a numerical experiment, or it can be based on available test-analysis correlation results. In this example, it is assumed that correlation uncertainty is available for substructure 2 from a free-free test for the first 20 elastic modes with frequencies between 45.4 Hz. and 6355.9 Hz, as listed in Table 1. The test results were simulated using Monte Carlo (MC) analysis. At each iteration, the nominal CB mass and stiffness matrices for substructure 2 were randomized using the Maximum Entropy approach developed by Soize [27]. A dispersion level is selected that can be thought of as being analogous to the global fractional uncertainty believed to exist in the matrix, and then the matrix is randomized subject to the constraints of maintaining symmetry and positive definiteness for the mass matrix, and positive semi-definiteness for the stiffness matrix. In this example, a dispersion level of 15% was selected for both mass and stiffness, and 10,000 iterations were performed. Details of the process can be found in Soize's paper [27]. The advantage of this nonparametric approach, over the usual parameter sensitivity or perturbation methods, is that this randomization process automatically accounts for uncertainties that are not easily described by model parameters, such as model form, geometry, joints, etc.

The resulting test-analysis correlation statistics for substructure 2 are listed in Table 1. All 20 elastic modes have one-sigma frequency uncertainties, σ_ω, less than 1.50%, therefore they would pass the Air Force's (AF) 3.0% allowable frequency error criterion 95% of the time. One-sigma percent uncertainty in generalized mass σ_{Δ_M} is approximately 2.0% for all the modes. The RMS cross-orthogonality matrix is illustrated in Fig. 1. The 95th percentile for cross-generalized mass, $\gamma_{jj.05}$, indicates that modes 10, 11, 15, 16, 19, and 20 do not pass the AF criterion for cross-orthogonality, $\gamma_{jj} \geq 0.95$, with 95% confidence. Maximum one-sigma off-diagonal cross-orthogonality terms listed in Table 1 indicate that only modes 1 through 8 pass the

AF criterion $\gamma_{ij} \le 0.10$ with 95% confidence. Taking the intersections of the results, only the first 8 elastic modes for random substructure 2 strictly pass all of the AF correlation criteria at the 95% confidence level.

Uncertainties in the modal mass and stiffness for the first 20 elastic modes of substructure 2 are recovered from the test-analysis correlation uncertainty using Eqs. (10-12). Figure 2 shows the recovered RMS modal mass uncertainty, while Fig. 3 illustrates the corresponding RMS modal stiffness uncertainty. The technique described in Section 2.2 was then used to propagate the uncertainties in the substructure 2 modal matrices into the uncertainties in the corresponding CB representation mass and stiffness matrices. The covariance propagation approach outlined in Section 2.3 was then used to propagate the substructure uncertainty into the modal mass and stiffness uncertainties for the first 20 elastic system modes. Figure 4 shows the RMS system modal mass uncertainty, while Fig. 5 presents the corresponding RMS modal stiffness uncertainty. Equations (36-37) and (39) were then used to recover the uncertainties in the system correlation metrics for the first 20 free elastic modes from the propagated system modal matrix uncertainties. Figure 6 shows the recovered RMS system cross-orthogonality matrix.

In order to demonstrate the accuracy of the proposed covariance propagation procedure and the corresponding linear perturbation equations relating uncertainties in correlation metrics and modal matrices, a corresponding 10,000 iteration MC analysis was performed. The substructure 2 CB mass and stiffness matrices were randomized with 15% dispersion using the maximum entropy approach discussed previously [27]. As mentioned in Section 2.2, the substructure modal mass and stiffness matrices only contain information regarding the uncertainties due to the modes used in substructure test-analysis correlation. Only this uncertainty can be propagated from the free substructure test-analysis correlation results into the system level correlation uncertainty. In order to simulate this in the MC analysis, the randomized CB matrices must be filtered to the contribution from the 20 free substructure modes prior to the synthesis of the random system. This is accomplished by using the projector defined in Eq. (16), giving

$$\Delta M^2_{CBT} = P_T^{2T} \Delta M^2_{CB} P_T^2 \qquad \Delta K^2_{CBT} = P_T^{2T} \Delta K^2_{CB} P_T^2$$

where ΔM^2_{CB} and ΔK^2_{CB} are the fully randomized substructure 2 CB mass and stiffness matrices, respectively.

Table 2 compares the system correlation metric uncertainties computed using covariance propagation with those computed using the MC analysis results. One-sigma percent frequency uncertainties recovered using covariance propagation, σ_ω^{COV}, are all less than 1.5%, indicating that all 20 system modes pass the 3.0% allowable frequency error criterion 95% of the time. The frequency uncertainty values range between 0.02% and 1.43%, and are overall somewhat less than the values found at the substructure level. One-sigma percent frequency uncertainties recovered from MC analysis, σ_ω^{MC}, listed in Table 2, agree very well with the covariance values. The largest error is 7% for mode 6, which has the smallest uncertainty value. The average error magnitude is 2.48%. Table 2 also lists the 95th percentile for cross-generalized mass recovered using covariance propagation, $\gamma_{jj.05}^{COV}$. The results indicate that all system modes except two pairs, 11-12 and 19-20, which are closely spaced in frequency, pass the AF criterion for cross-orthogonality, $\gamma_{jj} \ge 0.95$, with 95% confidence. The actual values recovered using Eq. (39) for modes 19 and 20 are not reported because they are not physically realizable, due to very poor correlation. Corresponding results recovered from MC analysis, $\gamma_{jj.05}^{MC}$, agree very closely with values produced using covariance propagation. The largest discrepancy is 8.7% for closely spaced mode pair 11-12, while the average error over the first 18 modes is 1.0%. The 95th percentile values predicted using MC for closely spaced mode pair 19-20 are so low that they indicate essentially no correlation at all between truth and FEM modes. This is consistent with the unrealizable values predicted using covariance propagation and the corresponding linear perturbation formulas.

Maximum one-sigma off-diagonal cross-orthogonality terms computed using covariance propagation, $\sigma_{\gamma_{ij}}^{COV}$, and the coupled mode number are listed in Table 3. Only modes 1 through 10 pass the AF criterion $\gamma_{ij} \le 0.10$ with 95% confidence. The MC statistics for off-diagonal cross-orthogonality are also listed in Table 3, as well as the identity of the corresponding coupled mode. Once again, the MC results agree very well with the covariance predicted results, except for the closely spaced modes, however the trend is the same. The coupling between modes is exactly the same in both analyses. Both methods also predict that only the first 10 system modes strictly pass all of the AF correlation at the 95% confidence level. Therefore, at least for this application, the MC analysis validates the accuracy of the covariance propagation approach and the corresponding linear perturbation equations relating the correlation metrics and the modal mass and stiffness matrices. While

no specific timing values are listed here, the covariance propagation method offers a significant advantage in required computation time over the MC analysis, especially as the system becomes large.

4.0 CONCLUSION

As space structures become larger and more complex, ground based vibration tests of the entire spacecraft become either problematic or impossible. Instead, the spacecraft is tested and validated only at the substructure level. The substructure tests are usually performed in a simulated free-free configuration for simplicity and accuracy. A methodology has been presented here for studying the effects of uncertainty on metrics used for test-analysis correlation of complex spacecraft that are validated on a substructure-by-substructure basis. The objective is to quantify the level of accuracy required at the substructure level to produce acceptable accuracy at the system level. This is done by propagating uncertainty in test-analysis correlation metrics from free-free substructure vibration tests into uncertainty in the synthesized system correlation metrics. Previously derived results are used to relate uncertainty in accepted correlation metrics to substructure modal mass and stiffness uncertainties. The correlation uncertainty in each substructure can either be prescribed, for the purpose of numerical experimentation, or it may be available from existing substructure test data. Linear covariance propagation is used to propagate the substructure modal matrix uncertainty into the uncertainty in the corresponding Craig-Bampton substructure representations. Linear covariance propagation is then used again to propagate the substructure uncertainties into the full system modal matrices. The uncertainties in the system correlation metrics are then extracted from the modal matrix uncertainties to determine the impact of uncertainty at the substructure level.

For illustration, the proposed method was applied to a simple two-substructure system shaped as a T-beam. A Monte Carlo analysis was performed in which only one of the substructures was randomized using the Maximum Entropy approach. This resulted in corresponding substructure correlation uncertainty statistics in which only the first 8 elastic free-free substructure modes passed all of the Air Force mandated correlation criteria at the 95% confidence level. The covariance propagation approach presented in this paper was then used to propagate the substructure uncertainty into the full system. The results showed that the first 10 elastic system modes passed all of the Air Force correlation criteria with 95% confidence. A full system Monte Carlo analysis was also performed to validate the accuracy of the covariance propagation method. The results of the two methods agreed very well, except in the case of closely spaced modes, but even then the error was less than 10%. The overall system correlation results with respect to which modes passed the required correlation criteria were identical.

Organizations, such as NASA and the Air Force make critical decisions on spacecraft performance and survivability based on the results of test-analysis correlation metrics. In order to ensure the success of finite element model validation where there is no system level test, uncertainty in the substructures must be propagated into the system level correlation metrics. It is believed that the method presented in this paper offers a unique and efficient approach for the required uncertainty propagation. A user can choose to propagate either an assumed level of substructure test-analysis correlation uncertainty, or correlation uncertainty derived from vibration test results. The method is not reliant on the specification of uncertainty in individual model design parameters. It includes all forms of model uncertainty. It is fast, compared with Monte Carlo techniques, and it propagates uncertainty in the correlation metrics directly. Even if the spacecraft will be tested as a system prior to flight, an understanding of the required level of substructure correlation, and how the related uncertainties propagate into the system, will save a great deal of time, effort, and cost during the system level test and analysis.

Future work will focus on studying and mitigating observed sensitivities in the method for closely spaced modes, as well as the application of the method to representative spacecraft models.

Acknowledgment

This material is based on work supported by the Air Force Office of Scientific Research under grant FA9550-09-1-0180. This funding is gratefully acknowledged.

References

[1] F. M. Hemez, S. W. Doebling, and M. C. Anderson, "A Brief Tutorial on Verification and Validation," presented at 22nd International Modal Analysis Conference, Dearborn, MI, 2004.

[2] ASME, "Guide for Verification and Validation in Copmputational Solid Mechanics," ASME V&V 10-2006, P. T. C. C. 60, Ed.: ASME, 2006.

[3] T. L. Paez, "Introduction to Model Validation," presented at 27th International Modal Analysis Conference, Orlando, FL, 2009.

[4] R. L. Mayes, "Model Correlation and Calibration," presented at 27th International Modal Analysis Conference, Orlando, FL, 2009.

[5] T. K. Hasselman, R. N. Coppolino, and D. C. Zimmerman, "Criteria for Modeling Accuracy: A State-of-the-Practice Survey," presented at 18th International Modal Analysis Conference, San Antonio, TX, 2000.
[6] NASA, "NASA-STD-5002, Loads Analyses of Spacecraft and Payloads," NASA June, 1996.
[7] DoD, "DoD Handbook-340A (USAF), Test Requirements for Launch, Upper Stage, and Space Vehicles, Volume II: Applications and Guidelines," April, 1999.
[8] R. Rebba, S. Huang, Y. Liu, and S. Mahadevan, "Statistical Validation of Simulation Models," *Int. J. Materials and Product Technology*, vol. 25, pp. 164-181, 2006.
[9] F. M. Hemez, A. C. Rutherford, and R. D. Maupin, "Uncertainty Analysis of Test Data Shock Responses," presented at 24th International Modal Analysis Conference, Saint Louis, MO, 2006.
[10] M. Basseville and A. Benveniste, "Handling Uncertainties in Identification and Model Validation: A Statistical Approach," presented at 24th International Modal Analysis Conference, Saint Louis, MO, 2006.
[11] E. J. Bergman, M. S. Allen, D. C. Kammer, and R. L. Mayes, "Probalistic Investigation of Sensitivities of Advanced Test-Analysis Model Correlation Methods," presented at 26th International Modal Analysis Conference, Orlando, FL, 2008.
[12] T. K. Hasselman and J. D. Chrowstowski, "Propagation of Modeling Uncertainty Through Structural Dynamic Models," presented at 35th Structures, Structural Dynamics, and Materials Conference, Hilton Head, SC, 1994.
[13] T. Hasselman and G. Wathugala, "Top-Down vs. Bottom-Up Uncertainty Quantification for Validation of a Mechanical Joint Model," presented at 23rd International Modal Analysis Conference, Orlando, FL, 2005.
[14] T. Hasselman, "Uncertainty Quantification in Verification and Validation of Computational Solid Mechanics Models - Modeling," presented at 50th AIAA/ASME/ASCE/AHS/ASC Structures, Structural Dynamics, and Materials Conference, Palm Springs, CA, 2009.
[15] L. Hinke, B. R. Mace, and N. S. Ferguson, "Uncertainty Quantification and CMS: Free and Fixed-Interface Methodologies," presented at 25th International Modal Analysis Conference, Orlando, FL, 2007.
[16] R. R. Craig and M. C. C. Bampton, "Coupling of Substructures for Dynamic Analysis," *AIAA Journal*, vol. 6, pp. 1313-1319, 1968.
[17] B. R. Mace and P. J. Shorter, "A local Modal/Perturbational Method for Estimating Frequency Response Statistics of Built-Up Structures with Uncertain Properties," *Journal of Sound and Vibration*, vol. 242, pp. 793-811, 2001.
[18] D. de Klerk and Voormeeren, "Uncertainty Propagation in Experimental Dynamic Substructuring," presented at 26th International Modal Analysis Conference, Orlando, FL, 2008.
[19] D. de Klerk, D. J. Rixen, and J. de Jong, "The Frequency Based Substructuring (FBS) Method reformulated according to the Dual Domain Decomposition Method," presented at 24th International Modal Analysis Conference, St. Louis, MO, 2006.
[20] S. N. Voormeeren and D. J. Rixen, "Substructure Decoupling Techniques - a Review and Uncertainty Propagation Analysis," presented at 27th International Modal Analysis Conference, Orlando, FL, 2009.
[21] D. C. Kammer and S. Nimityongskul, "Propagation of Uncertainty in Test-Analysis Correlation of Substructured Spacecraft," presented at 28th International Modal Analysis Conference, Jacksonville, FL, 2010.
[22] D. C. Kammer, "Test-Analysis Model Development Using an Exact Modal Reduction," *International Journal of Analytical and Experimental Modal Analysis*, vol. 2, pp. 174-179, 1987.
[23] M. S. Allen and M. W. Sracic, "Mass Normalized Mode Shapes Using Impact Excitation and Continuous-Scan Laser Doppler Vibrometry," presented at 8th International Conference on Vibration Measurements by Laser Techniques, Ancona, Italy, 2008.
[24] T. N. E. Greville and A. Ben-Israel, *Generalized Inverses: Theory and Applications*. New York: Wiley, 1974.
[25] W. H. Steeb, *Matrix Calculus and Kronecker Product with Applications and C++ Programs*. Singapore: World Scientific, 1997.
[26] J. R. Magnus and H. Neudecker, *Matrix Differential Calculus with Applications in Statistics and Econometrics*: John Wiley & Sons, 1988.
[27] C. Soize, "Maximum Entropy Approach for Modeling Random Uncertainties in Transient Elastodynamics," *Journal of the Acoustic Society of America*, vol. 109, pp. 1979-1996, 2001.

Table 1. Correlation statistics for random substructure 2.

Mode	Freq.(Hz)	σ_{ω}	σ_{Δ_M}	$\gamma_{jj.05}$	$\sigma_{\gamma_{ij}}$
1	45.40	1.45	2.01	0.9991	0.0149
2	125.14	1.47	2.06	0.9987	0.0178
3	245.32	1.47	2.00	0.9981	0.0224
4	405.53	1.49	2.08	0.9972	0.0266
5	605.80	1.47	2.07	0.9962	0.0320
6	846.13	1.44	2.04	0.9949	0.0381
7	1126.52	1.45	2.08	0.9934	0.0435
8	1447.00	1.49	2.07	0.9914	0.0482
9	1807.58	1.48	2.12	0.9853	0.0625
10	2118.66	1.42	2.08	0.8147	0.2829
11	2208.29	1.43	2.08	0.8026	0.2906
12	2649.18	1.45	2.11	0.9827	0.0656
13	3130.30	1.47	2.07	0.9809	0.0693
14	3651.74	1.47	2.09	0.9749	0.0759
15	4213.60	1.20	2.03	0.1117	0.6435
16	4237.31	1.28	2.13	0.1112	0.6448
17	4816.03	1.45	2.09	0.9636	0.0904
18	5459.21	1.47	2.10	0.9641	0.0934
19	6143.39	1.37	2.15	0.6607	0.3458
20	6355.95	1.39	2.14	0.6428	0.3529

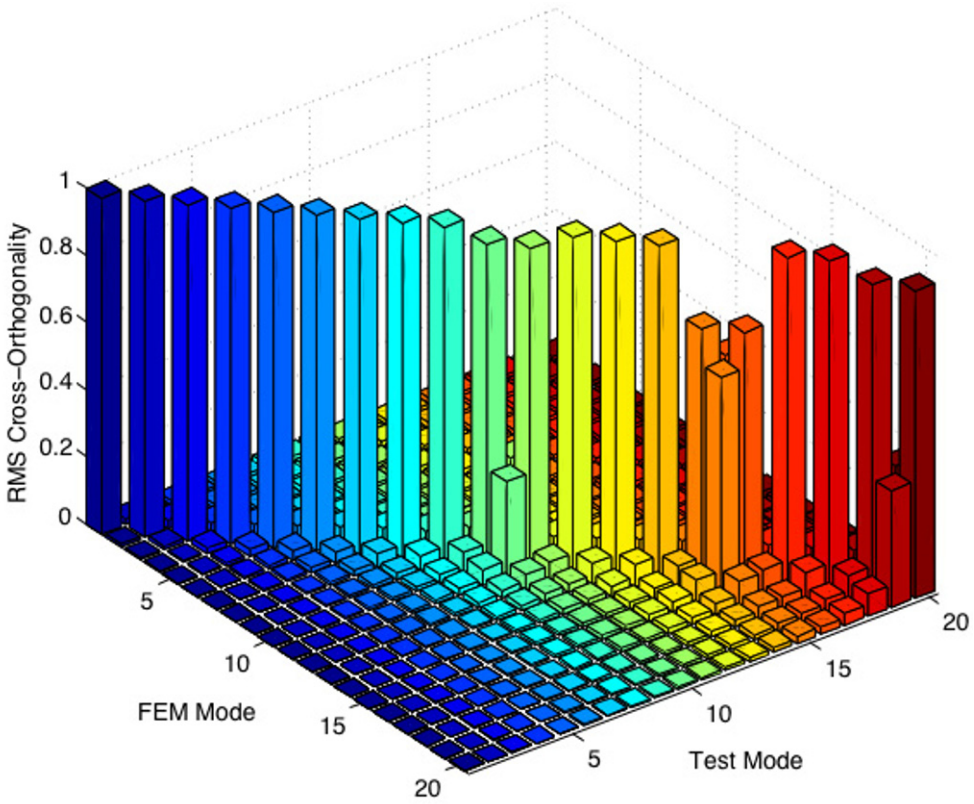

Fig. 1. Substructure 2 RMS cross-orthogonality.

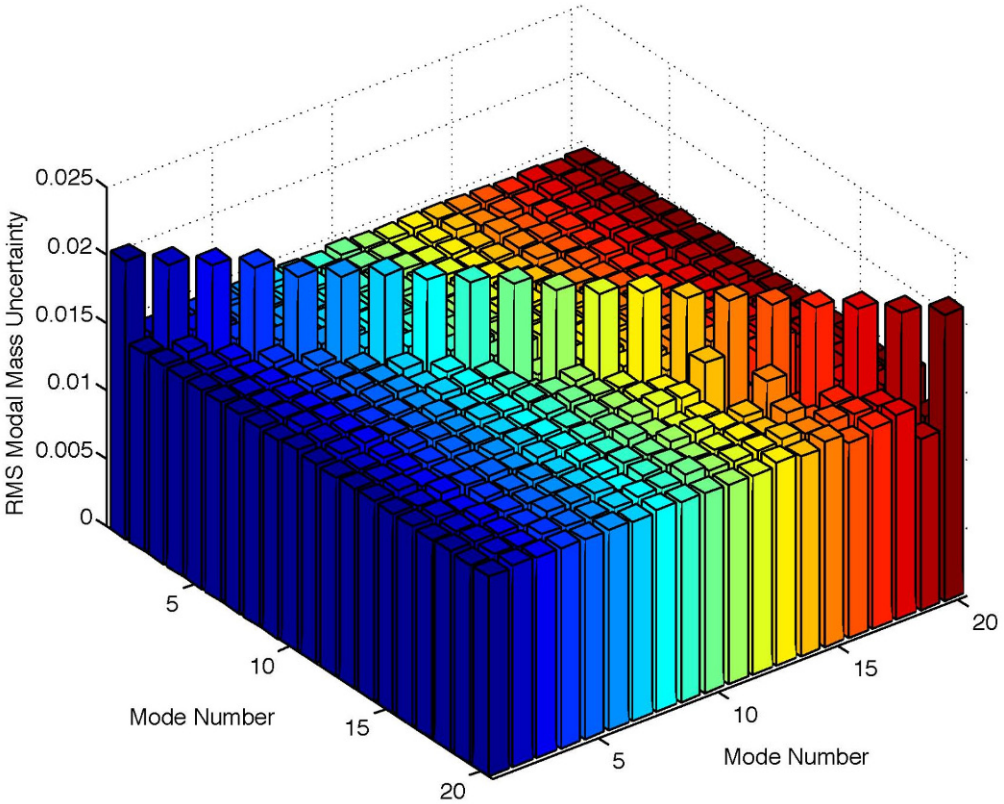

Fig. 2. Substructure 2 rms modal mass uncertainty.

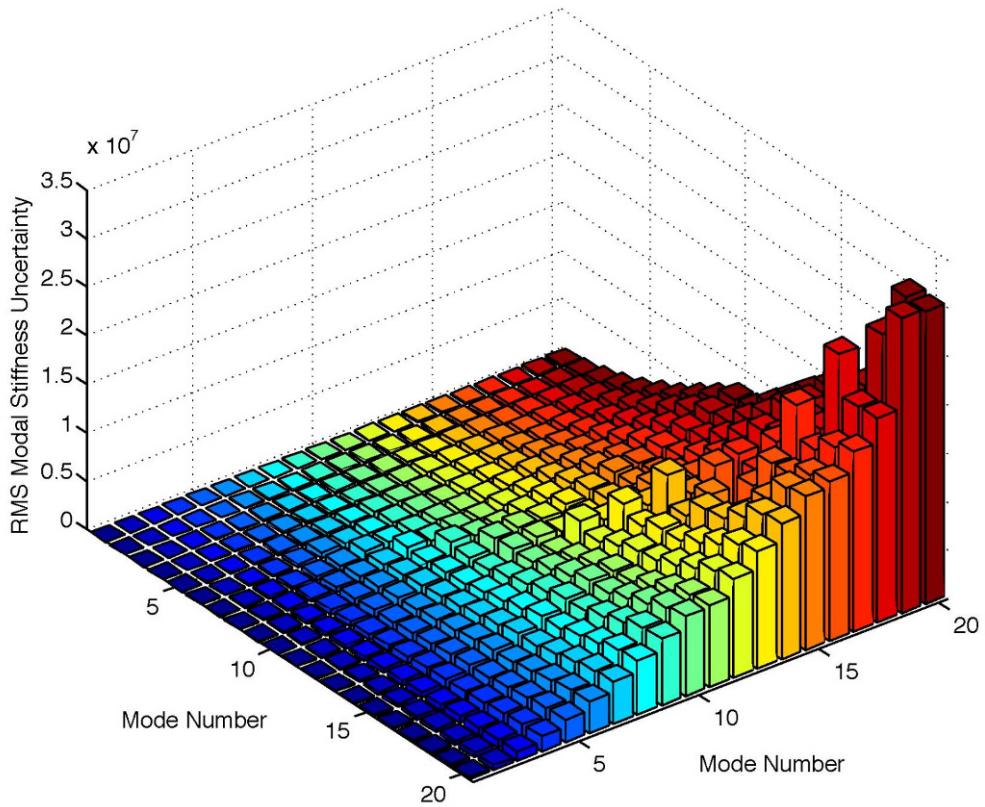

Fig. 3. Substructure 2 RMS modal stiffness uncertainty.

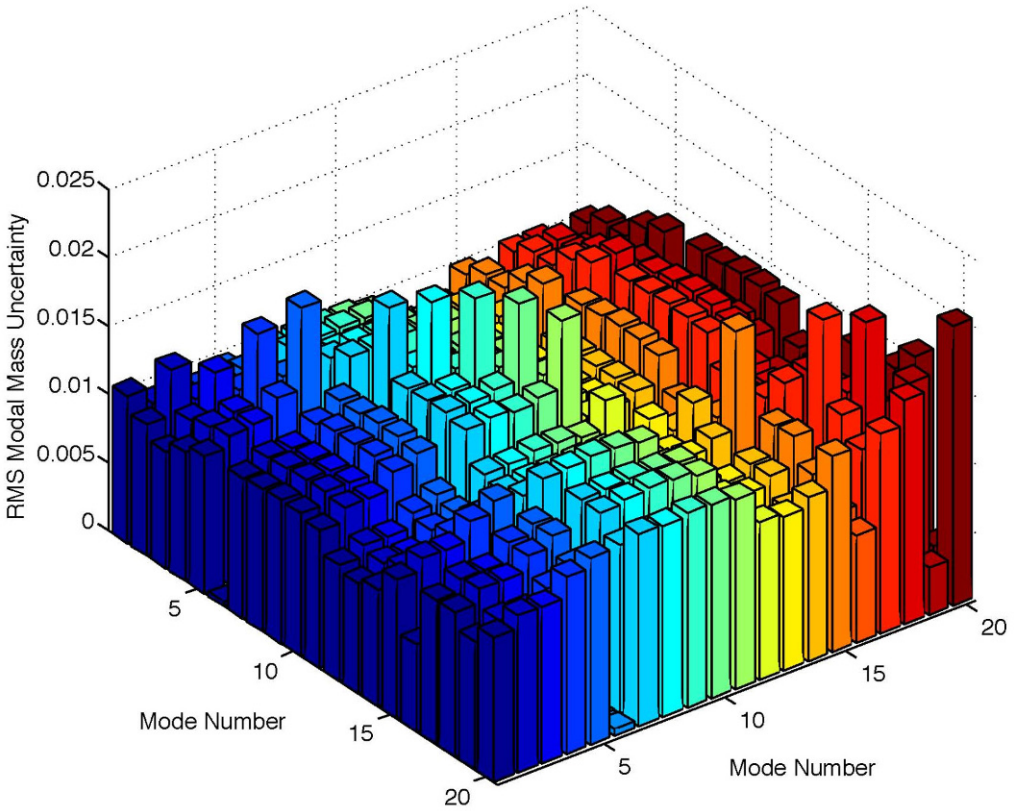

Fig. 4. Propagated system RMS modal mass uncertainty.

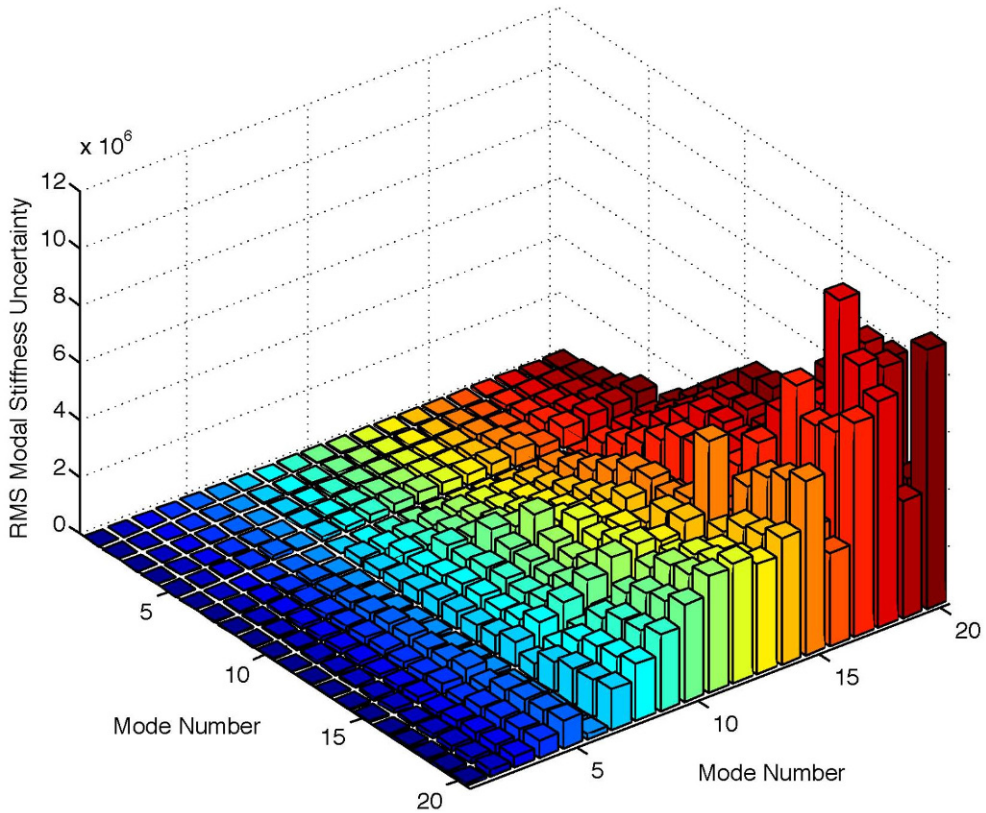

Fig. 5. Propagated system RMS modal stiffness uncertainty.

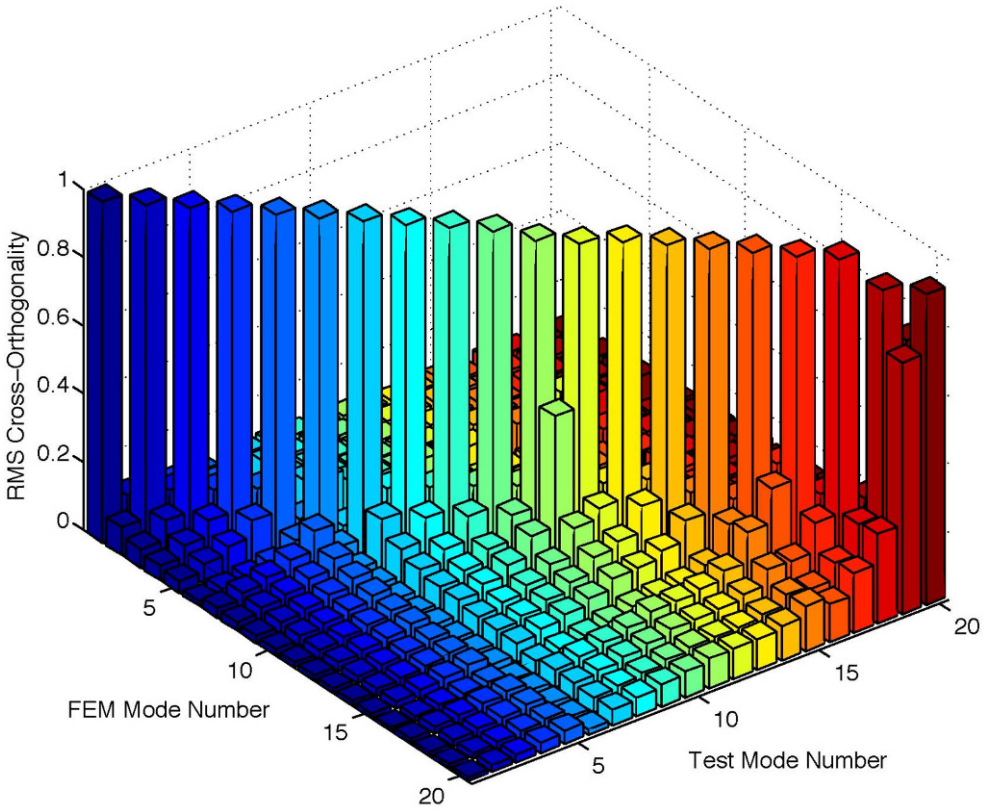

Fig. 6. System RMS cross-orthogonality for first 20 elastic modes.

Table 2. Correlation statistics for first 20 system elastic modes.

Mode	Freq.(Hz)	σ_{ω}^{COV}	σ_{ω}^{MC}	$\gamma_{jj.05}^{COV}$	$\gamma_{jj.05}^{MC}$
1	33.94	1.19	1.20	0.9999	0.9999
2	91.64	1.22	1.24	0.9995	0.9995
3	163.59	1.13	1.14	0.9990	0.9990
4	266.71	1.21	1.25	0.9986	0.9985
5	416.68	1.31	1.32	0.9980	0.9978
6	491.64	0.02	0.03	0.9999	0.9999
7	609.98	1.34	1.38	0.9970	0.9969
8	843.93	1.39	1.42	0.9958	0.9955
9	1116.97	1.39	1.43	0.9943	0.9940
10	1426.77	1.41	1.41	0.9919	0.9918
11	1764.61	1.32	1.27	0.8641	0.7948
12	1825.82	1.05	1.08	0.8548	0.7867
13	2071.27	0.85	0.88	0.9832	0.9831
14	2296.75	0.93	0.96	0.9841	0.9833
15	2669.45	1.34	1.34	0.9844	0.9828
16	2977.97	0.47	0.51	0.9706	0.9633
17	3130.36	1.40	1.40	0.9626	0.9539
18	3639.52	1.43	1.44	0.9782	0.9757
19	4163.99	1.01	1.07	***	0.1136
20	4190.33	1.21	1.19	***	0.1121

Table 3. RMS off-diagonal cross-orthogonality for first 20 system elastic modes.

Mode	Freq.(Hz)	$\sigma_{\gamma_{ij}}^{COV}$	Mode	$\sigma_{\gamma_{ij}}^{MC}$	Mode
1	33.94	0.0066	2	0.0066	2
2	91.64	0.0129	1	0.0133	1
3	163.59	0.0186	2	0.0192	2
4	266.71	0.0219	3	0.0222	3
5	416.68	0.0254	4	0.0263	4
6	491.64	0.0068	5	0.0069	5
7	609.98	0.0305	5	0.0309	5
8	843.93	0.0359	7	0.0361	7
9	1116.97	0.0407	8	0.0416	8
10	1426.77	0.0466	9	0.0471	9
11	1764.61	0.2531	12	0.2903	12
12	1825.82	0.2601	11	0.2958	11
13	2071.27	0.0670	14	0.0698	14
14	2296.75	0.0746	13	0.0774	13
15	2669.45	0.0595	14	0.0605	14
16	2977.97	0.1156	17	0.1272	17
17	3130.36	0.1219	16	0.1341	16
18	3639.52	0.0725	17	0.0748	17
19	4163.99	0.5455	20	0.6260	20
20	4190.33	0.5472	19	0.6283	19

Feature Extraction for Structural Dynamics Model Validation

Mayuko Nishio[1], Francois Hemez[2], Keith Worden[3], Gyuhae Park[4], Nobuo Takeda[5], Charles Farrar[6]

[1] University of Tokyo, Dept. Civil Engineering, 7-3-1 Hongo, Bunkyo-ku, Tokyo 113-8656, Japan, nishio@bridge.t.u-tokyo.ac.jp
[2] Los Alamos National Laboratory, XCP-1, Los Alamos, NM 87545, hemez@lanl.gov
[3] University of Sheffield, Dept. Mechanical Engineering, Mappin St., Sheffield S1 3JD, UK, k.worden@sheffield.ac.uk
[4] Los Alamos National Laboratory, INST-OFF, Los Alamos, NM 87545, gpark@lanl.gov
[5] University of Tokyo, Dept. Advanced Energy, 7-3-1 Hongo, Bunkyo-ku, Tokyo 113-8656, Japan, takeda@smart.k.u-tokyo.ac.jp
[6] Los Alamos National Laboratory, INST-OFF, Los Alamos, NM 87545, farrar@lanl.gov

ABSTRACT This study focuses on defining and comparing response features that can be used for structural dynamics model validation studies. Features extracted from dynamic responses obtained analytically or experimentally, such as basic signal statistics, frequency spectra, and estimated time-series models, can be used to compare characteristics of structural system dynamics. By comparing those response features extracted from experimental data and numerical outputs, validation and uncertainty quantification of numerical model containing uncertain parameters can be realized. In this study, the applicability of some response features to model validation is first discussed using measured data from a simple test-bed structure and the associated numerical simulations of these experiments. Issues that must be considered were sensitivity, dimensionality, type of response, and presence or absence of measurement noise in the response. Furthermore, we illustrate a comparison method of multivariate feature vectors for statistical model validation. Results show that the outlier detection technique using the Mahalanobis distance metric can be used as an effective and quantifiable technique for selecting appropriate model parameters. However, in this process, one must not only consider the sensitivity of the features being used, but also correlation of the parameters being compared.

1. Introduction

The purpose of structural model validation is to assess whether a numerical model, such as a finite element model, has adequate predictive capability for the model's intended purpose by comparing analytical predicted and experimentally observed structural responses quantities. In constructing numerical models of structures, many quantities are assigned based on incomplete and/or unavailable knowledge of their true value. Uncertainties can result from measurement error, environmental variability, allowable manufacturing tolerances and variability associated with assembly procedures; while others are due to lack-of-knowledge about the actual structural condition; i.e., materials, loads, friction, energy dissipation (damping), and boundary condition. Therefore, it is important to assess whether the assumptions used in the modeling process provide accurate simulations on the intended purpose of the model.

T. Proulx (ed.), *Linking Models and Experiments, Volume 2*, Conference Proceedings of the Society for Experimental Mechanics Series 5,
DOI 10.1007/978-1-4419-9305-2_10, © The Society for Experimental Mechanics, Inc. 2011

In this study, the model validation is more generally defined that it should be validating statistically accurate models. Some previous studies were carried out on the basis of this definition according to the uncertainty quantification of the numerical model, e.g., [1]. In those works, it was indicated that it was so important to use appropriate response features to compare the numerical output and the measurement data. A response feature is the quantity extracted from the dynamic response that is used to compare the structural system's experimentally observed response characteristic to those predicted by its numerical model. Fundamentally, the feature extraction process is based on processing the data waveforms or spectra of waveforms, or fitting some model to the data. Many feature extraction techniques have been developed for structural health monitoring. Those include finding indications of nonlinear response and identifying system changes due to damages on structures, e.g., [2] and [3]. Many of these features can potentially be used for the model validation applications.

This paper focuses on defining and illustrating some response features that can be used for structural dynamics model validation studies. After a brief general discussion regarding response features, the application of these features for dynamic model validation are studied using experimental and numerical response data from a test-bed structure. Then, a comparison procedure for multivariate feature vectors based on Mahalanobis distance analysis is presented for the statistical model validation. This paper concludes with an additional discussion regarding the importance of appropriate feature selections.

2. Test-bed structure and numerical model description

The LANL three-story share building structure shown in Fig.1 (a) was used as a test-bed structure in this study [2]. The structure consists of aluminum plates and columns assembled using bolted joints. The structure slides on rails that allow movement only in the x-direction. The input force was applied in the x-direction by an electromagnetic shaker connected to the base floor. A force transducer was attached at the end of a stinger to measure the input force, and four accelerometers were attached at the centerline of each floor on the opposite side from the excitation to measure the system response at each floor.

This structure was modeled as a 4-DOF lumped-mass system as shown in Fig.1 (b). Mass, stiffness and damping of i-th story was defined as m_i, k_i and c_i (i= 1~4), respectively. The values of m_i and k_i (except k_1), were determined from the measured sizes of structural members and nominal values for Young's Modulus, and the mass density of aluminum. The stiffness k_i (i= 2~4) was the summation of the bending stiffness of four columns treated as beams that are constrained against rotation at their ends. For stiffness k_1, a relatively low numerical value was assigned because the friction between the rails and the structure was negligible. Notice that the model includes the base mass that slides on the rails. The equation of motion of the structure was described in a matrix notation using mass, stiffness, and damping matrixes; [M], [K], and [C], as follows

$$[M]\{\ddot{x}\}+[C]\{\dot{x}\}+[K]\{x\}=\{F(t)\}, \tag{1}$$

where vector $\{F(t)\}$ is the input force vector, and $\{x\}$ is the displacement vector of x_1~x_4 in Fig.1 (b). In the application of time-response analysis, the displacement vector $\{x(t)\}$ was calculated by a Runge-kutta numerical integration scheme. A proportional damping was adopted to assign a damping matrix [C] that could be discribed as

$$[C]=\alpha[M]+\beta[K]. \tag{2}$$

Theoretically, coefficients α and β can be related to k-th mode resonant frequency ω_k and modal damping ratio ζ_k as in

$$\zeta_k=\frac{1}{2}\left(\frac{\alpha}{\omega_k}+\beta\omega_k\right). \tag{3}$$

Therefore, α and β can be assigned when two modal parameter sets (ω_k, ζ_k) are given.

Additionally, this structure included a center column suspended from the 3rd floor, and a bumper mechanism attached on the 2nd floor as shown in Fig.2 (a). This system produces nonlinearity in the system response when the column impacts the bumper mechanism. The clearance (gap) between the bumper and the column can be adjusted to vary the extent of impacting that occurs during a particular excitation. This nonlinearity is intended to produce a small perturbation to an essentially stationary process, causing a nonlinear phenomenon. In the modeling, this nonlinearity can be described by adopting a kind of bilinear model in stiffness k_4 as shown in Fig.2 (b), where k_c is the summation of the bending stiffness of four assembled columns, and the k_b is the bending stiffness of the suspended column, corresponding to a cantilever beam. In the modeling here, distance Δ was defined to make a smooth transition between two stiffness states by a quadric function to satisfy C_1-continuity. This transition area indicates that the actual structural condition should not show a complete discontinuous point at X=*Gap* because, in reality, some kinds of compliance should exist in the actual assembling system.

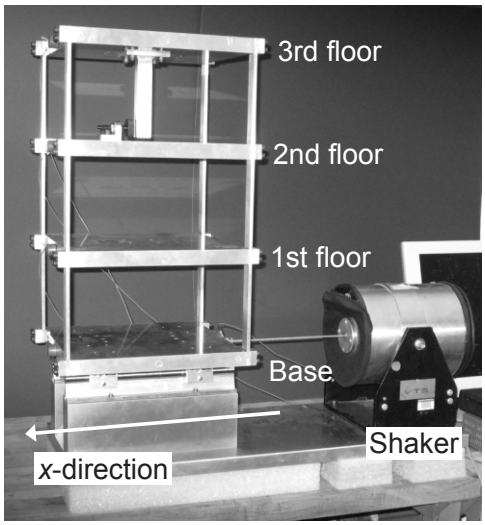

(a) Three-story share building set-up

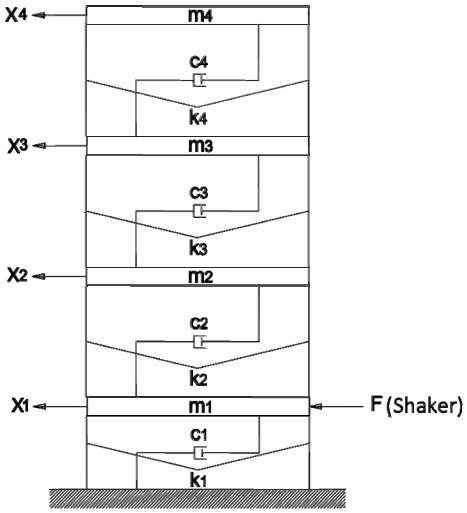

(b) 4DOF lumped-mass model

Fig.1. Test-bed structure setup and its numerical model

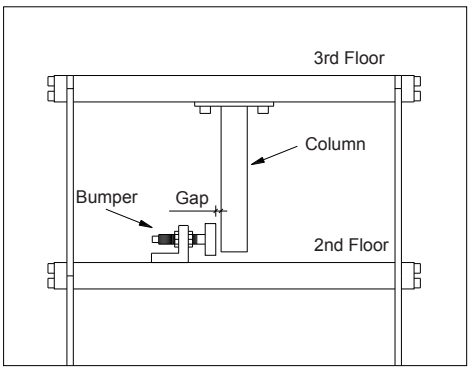

(a) Bumper and suspended column mechanism

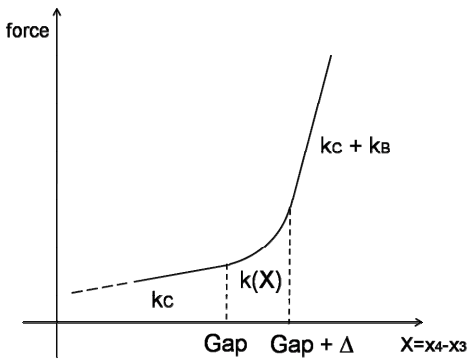

(b) Bi-linear model for stiffness k_4

Fig.2. Nonlinear behaviour mechanism between 2nd and 3rd floor

Some uncertain parameters were then recognized in the modeling of this lumped-mass model. Notice that the application of this model was defined to be the accurate prediction of the system's time-history response. From this viewpoint, not only m_i and k_i, but also damping parameters related to c_i will influence this prediction. The damping parameters were thus considered to be uncertain parameters in the calculation. Furthermore, the parameters, *Gap* and Δ, were also considered to have uncertain values in the nonlinear system calculation.

3. Response feature for structural model validation

3.1. General about feature selection

Response features are quantities that can be used to compare the measured and calculated system response. When used for model validation, the extracted response features should be sensitive to the target uncertain parameters of the numerical model. It should be noted that the intended purpose of the numerical simulation should also be considered when performing feature selection because the parameters that most influence the response may be different depending on in the intended purpose of the analysis. Dimensionality is another important consideration in the feature selection process. The feature dimension is the number of independent scalar quantities that are necessary to describe the feature. Low-dimensional features are preferable to high-dimensional features because this makes it easier to compare values and to statistically analyze their trends. Furthermore, the feature selection should reflect the type of response that is being considered, such as linearity or nonlinearity. Some response features that have been suggested for dynamic response calculations are [4]:

- Linear, stationary, Gaussian vibrations: Direct and inverse Fourier transforms, Power spectral density, Input-output transfer functions, Frequency responses, Modal parameter.
- Transient dynamics and mechanical shock response: Peak values, Energy content, Decrement and exponential damping, Shock response spectrum, temporal moments.
- General-purpose time-series analysis: AR, ARMA, ARX, AR-ARX models, Time-frequency transforms, Wavelet transform, Principal component decomposition.
- Unstable, chaotic, multiple-scale dynamics: Holder exponent, State-space maps, Time-frequency and higher-order transforms, Symmetric dot pattern, Fractal analysis.

It should be emphasized that there is no one feature that will be applicable to all structural dynamics predictive modeling scenarios. If multiple aspects of the system response are of interest, the model validation process may require different features to be extracted from the data in an effort to validate different aspects of the modeling process.

3.2. Discussion: feature extraction for the structural dynamics model validation

In this study, the damping parameters were defined to be the most influential uncertain parameters in the application of dynamic response analysis of the test-bed structure. Table 1 presents some extracted response features expected to be used in the damping parameters validation. Blue results are all from experimental data, and red and green results are from numerical outputs. Notice that the numerical output used in deriving green results was more accurate than red one because assigned damping ratios in the green output were values obtained form an experimental modal analysis. Considering the physical meaning of damping, the parameters should influence on the amplitude behaviour of the response, which is directly related to the energy dissipating behaviour. In the use of a random and stationary response from the linear system; i.e., w/o the bumper-column mechanism, the standard deviation, which was one of basic statistics, showed sensitivity to the accuracies of damping parameters. The feature that had the same physical meaning for a transient response was the energy value of temporal moments, and it also showed almost similar sensitivity as the standard deviation.

On the other hand, the features that were not extracted directly from the waveform, such as features derived by a subsequent model fitting process, were not as sensitive as previous two features. The parameters set of a decaying function fit to the data is an example of such features (see Table 1). It was considered that this low-sensitivity was caused by the difference of error components between experimental and numerical responses. The experimental data generally includes the measurement noise and environmental variability. However, numerical responses are free from such noise components. The result of fitting process was greatly influenced by variability in the experimental data; therefore, it was not considered to be appropriate to use such features for comparing experimental and numerical outputs. High dimensional features such as frequency response function were not considered because of difficulties in making quantified comparisons of such high-dimensional quantities.

For validating nonlinearity modelling parameters; *Gap* and Δ, we found that some time-series model parameters; e.g., AR model parameters as shown in Table 2, had sensitivity to the accuracy of response. This point was also indicated in the previous work that summarized response features for analysing nonlinearity in dynamic responses for the application of structural monitoring [2].

Table 1. Examples of response features for validating damping parameters
(Blue: experiment, Red: numerical with all 1% damping ratios,
Green (accurate); numerical with damping ratios from experimental modal analysis)

	Feature description and definition: output x_i	Response feature plot
Standard deviation (Basic statistics)	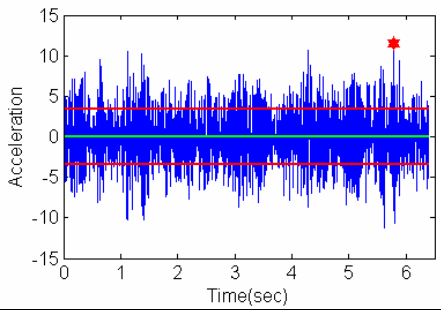	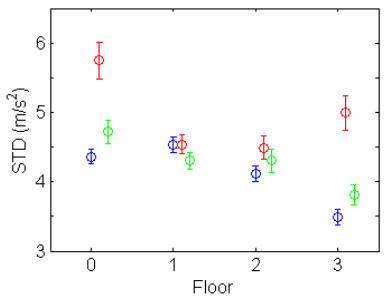
Energy (Temporal moments)	$M_k = \sum_{i=1}^{N} t_i^k x_i^2$ in k=0	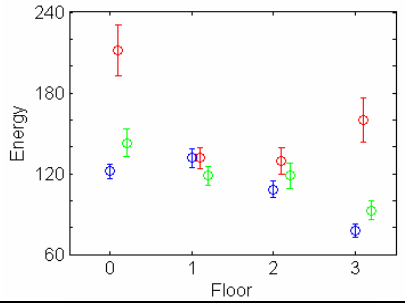
Decaying function fitting	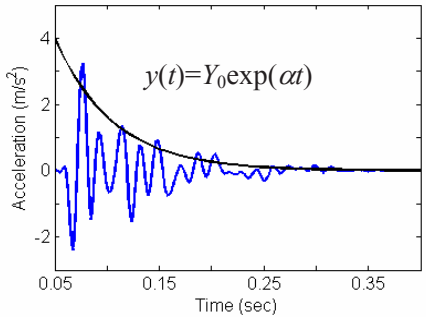	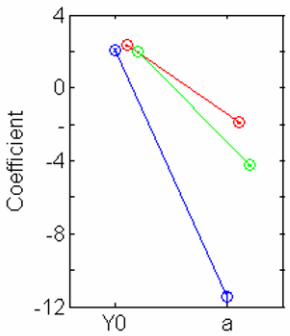

The time-resolution was also recognized as an important factor for investigating the nonlinear phenomena. The parameters; *Gap* and Δ, greatly influenced the frequency and the amplitude of impact events. Therefore, the feature that is sensitive to the number of impact events (i.e., the skewness for random response), had great sensitivity to the accuracy of numerical output as shown in the table. However, this feature alone could not be used in the detail validation of *Gap* and Δ because the dynamic amplitude behaviour during the impact events was not well captured by this feature. The response feature that provided a time-resolution measure was the Holder exponent [5]; however, there was trade-off between the feature dimension and the time-resolution.

Table 2. Examples of response features for validating nonlinearity modeling
(Blue: experiment, Red (accurate): numerical with Δ=0.5mm,
Green; numerical with Δ=0.1mm)

	Feature description and definition: output x_i	Response feature plot
AR model parameter	$\hat{x}_i = \sum_{j=1}^{p} \alpha_j x_{i-j} + \varepsilon_i$	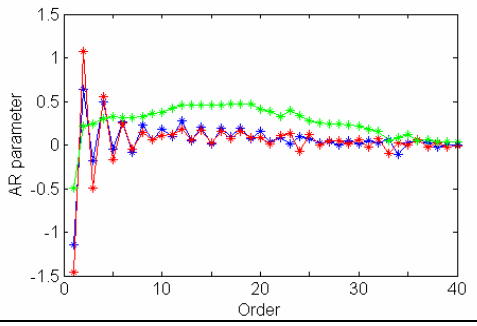
Skewness (Basic statistics)	$S_x = \frac{1}{\sigma_x^3} \cdot \frac{1}{N} \sum_{i=1}^{N} (x_i - \mu_x)^3$	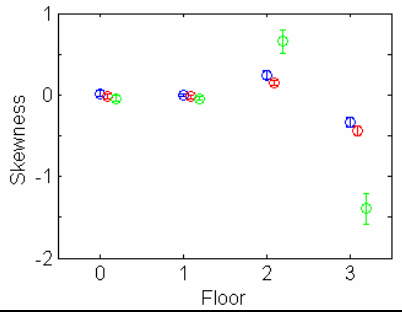
Holder exponent	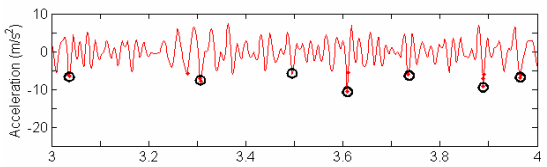	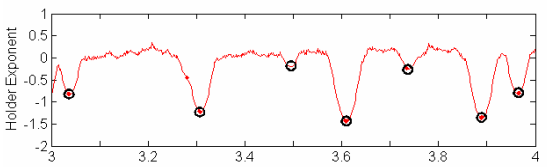

4. Statistical model validation using Mahalanobis distance comparison method

As mentioned in previous section, if multiple aspects of the system response are of interest, the model validation process may require comparing several features that have sensitivity to each uncertain parameter. A multivariate analysis technique was then expected to be useful in this process. Worden et al. had proposed a Mahalanobis distance outlier detection method for comparing multivariate feature vectors for the application of statistical structural damage detection in their previous study [6]. Applicability of the same approach for the statistical model validation was investigated in this study.

4.1. Mahalanobis distance outlier detection method

Mahalanobis distance is a distance measure used for multivariate statistics defined as

$$D_k = (\mathbf{y}_k - \bar{\mathbf{y}})^{\mathrm{T}} \mathbf{S}^{-1} (\mathbf{y}_k - \bar{\mathbf{y}}), \tag{4}$$

where $\mathbf{y}_k$ is a multi-dimensional feature vector for which the normalized distance from the mean is being calculated, $\bar{\mathbf{y}}$ and $\mathbf{S}$ are a mean vector and a covariance matrix based on all acquired vectors defining the nominal condition, respectively. The low distance value D_k can be obtained if $\mathbf{y}_k$ is similar to the set of feature vectors that defines the nominal condition. The outlier detection procedure is then summarized as follows.

(1) Acquire experimental responses (experimental data set) from the target structure.

(2) Calculate a feature vector from each measured set.

(3) Derive a Mahalanobis distance each experimental data set k, given as

$$D_k^{\mathrm{E}} = (\mathbf{y}_k^{\mathrm{E}} - \bar{\mathbf{y}}^{\mathrm{E}})^{\mathrm{T}} \mathbf{S}_{\mathrm{E}}^{-1} (\mathbf{y}_k^{\mathrm{E}} - \bar{\mathbf{y}}^{\mathrm{E}}). \tag{5}$$

Notice that mean feature vector $\bar{\mathbf{y}}^{\mathrm{E}}$ and covariance matrix $\mathbf{S}_{\mathrm{E}}$ are calculated from all acquired experimental data. A set of D_k^{E} is then the experimental baseline distribution of Mahalanobis distance.

(4) Create a feature vector from a numerical output, and calculate a Mahalanobis distance D^{N} using the mean vector and the covariance matrix from the experimental data set; $\bar{\mathbf{y}}^{\mathrm{E}}$ and $\mathbf{S}_{\mathrm{E}}$,

$$D^{\mathrm{N}} = (\mathbf{y}^{\mathrm{N}} - \bar{\mathbf{y}}^{\mathrm{E}})^{\mathrm{T}} \mathbf{S}_{\mathrm{E}}^{-1} (\mathbf{y}^{\mathrm{N}} - \bar{\mathbf{y}}^{\mathrm{E}}). \tag{6}$$

(5) Compare D^{N} with the experimental baseline distribution D^{E}.

If the feature vector form numerical output were similar to those from the experimental data set, D^{N} would show a lower value. The validity of a numerical model was then expected to be investigated statistically by comparing D^{N} with the experimental baseline distribution.

4.2. Damping parameters validation using linear system responses

4.2.1. Experimental baseline distribution and numerical run set

An experimental baseline distribution was created by acquiring twenty acceleration data sets (Exp. data #1~#20) under the same linear condition (w/o the bumper-column mechanism) of the test-bed structure. The input force was the band-limited random excitation with frequency range of 20-200Hz. Accelerations from each floor was acquired; the length of data was 16384 points with sampling frequency of 640Hz.

A numerical run set consisted of 200 calculation outputs was created using variable damping parameter sets; variable 2nd and 4th modal damping ratios. 200 parameter sets were sampled from the ranges of the two damping ratios indicated in Table 3 using Latin hypercube sampling method. 200 time-response accelerations (Run #1~#200) were then calculated by using each parameter set. Notice that the input force in all calculations was the same time-history that was measured in one of the experimental data set acquisitions; Exp. data #10.

Table 3. Parameter ranges for Latin hypercube sampling

	Minimum	Maximum
2nd mode damping ratio ζ_2	0.01	0.08
4th mode damping ratio ζ_4	0.001	0.02

The accuracy of all 200 numerical outputs against the experimental data #10 was plotted in Fig.3. The RMS error values were calculated using the 3rd floor acceleration outputs. The highest accuracy was shown in Run #114, and the lowest one was in Run #174 corresponding to damping values of (ζ_2, ζ_4) = (0.046, 0.070) and (ζ_2, ζ_4) = (0.0122, 0.0013), respectively. By examining these two responses when overlaid on the experimental data they were attempting to predict as shown in Fig.4, it can be seen that the different damping parameters mainly influence the amplitude of response as mentioned in the previous chapter.

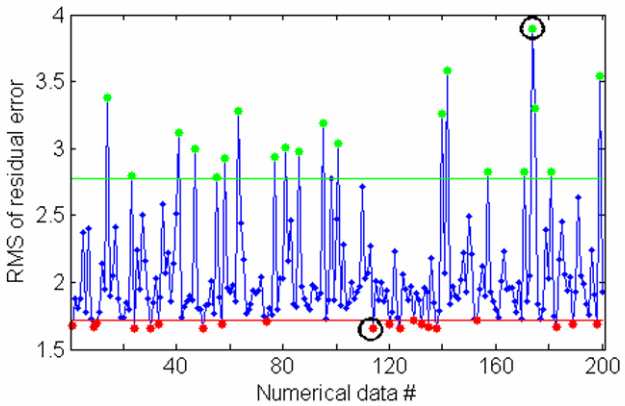

Fig.3. RMSE plots of all 200 numerical data

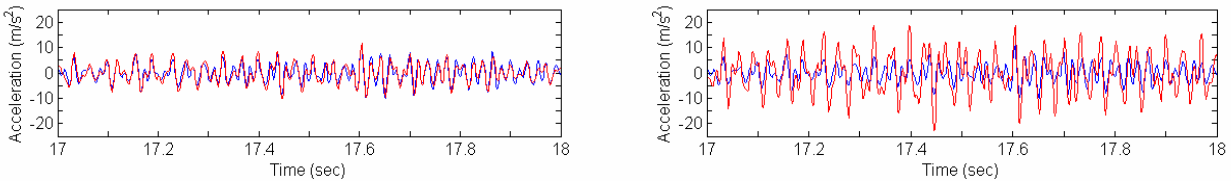

(a) The highest RMSE numerical run #114 (b) The lowest RMSE numerical run #174

Fig.4. Overlays of numerical (Red) and experimental (Blue) time-histories from linear system

4.2.2. Response feature extraction and Mahalanobis distance comparison

Response features selected for validating the damping parameters from random and linear responses here were then the peak amplitude and the standard deviation. The two values were extracted from outputs in the 2nd and 3rd floors producing a four-dimensional feature vector. Figure 5 is the corresponding Mahalanobis distance plot. Notice that the blue dots are the experimental baseline distribution, and the black dots are distances of the 200 numerical runs. Accurate and inaccurate numerical runs, which showed 10% lowest and highest RMSE values in Fig.3, are indicated by red and green circles, respectively. Seeing this figure, the accurate numerical runs have Mahalanobis distance values that predominantly fall within the experimental baseline distribution. In addition, the numerical runs that show the minimum/maximum Mahalanobis distance agree with Run #114 and #174, respectively as identified by an arrow. It can be said that the Mahalanobis distance derived by using the peak amplitude and standard deviation response features, has appropriate sensitivity to the time-histories; to be appropriated features for validation of the damping parameters.

The consistency check was then also carried out to confirm the effectiveness of this method for the statistical model validation. Consistency here meant that the parameter set that showed the low Mahalanobis distance provided accurate responses to any input forces. Additional twenty numerical runs were created by using each of twenty input force data in Exp. data #1~#20. Notice that the damping

parameter set that showed the lowest Mahalanobis distance in Fig.5 was used in all calculations. Figure 6 (a) is the RMSE plot of additional twenty numerical runs, indicated in green points, presented with that of previous 200 runs. It was clearly observed that comparably high accuracies were obtained in all runs. Calculated Mahalanobis distances from the twenty runs are also presented in Fig.6 (b). All of them are thus distributed in the same Mahalanobis distance order as that of the experimental distribution. These results indicate that the parameter set that shows a low Mahalanobis distance can constantly provide accurate numerical outputs and vice versa. It can then be concluded that the statistical validity of uncertain parameters can be evaluated by this Mahalanobis distance comparison method.

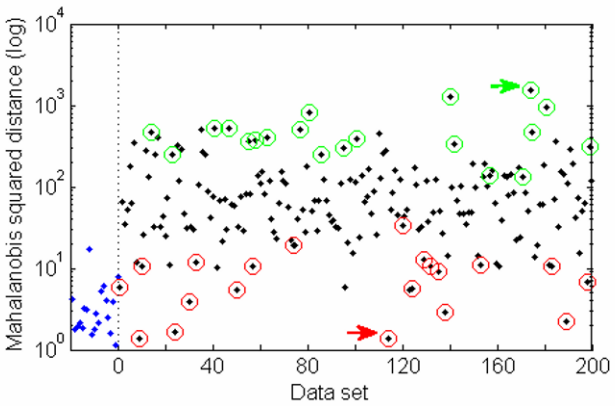

Fig.5. Mahalanobis distance plot for validating damping parameters

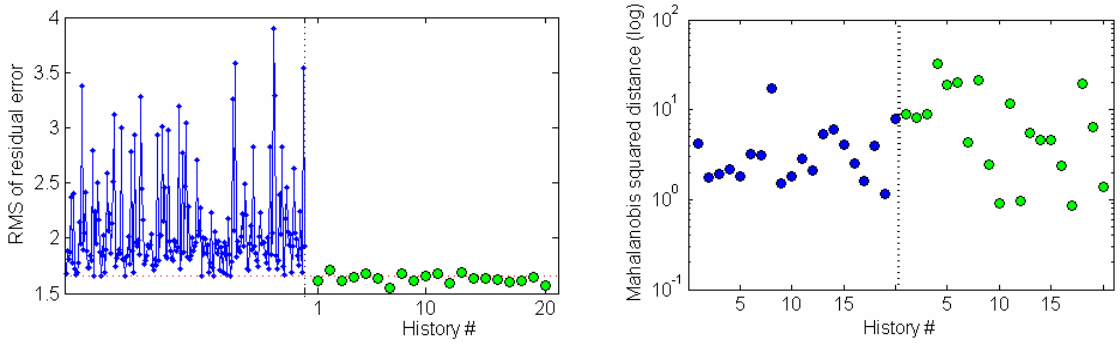

(a) RMSE plots using the accurate parameter set (b) Mahalanobis distance distributions

Fig.6. Consistency check of the Mahalanobis distance comparison method

4.2.3. Discussion: difficulty in validating correlated uncertain parameters

The success in the damping parameters validation presented in the previous section was realized by appropriate response feature selection. This need for appropriate response feature selection was further confirmed in the nonlinearity modeling parameters validation study. The uncertain parameters were *Gap* and Δ; however, it was difficult to find appropriate features that could assess the validity of each parameter independently.

In the validation, the experimental baseline distribution was created from twenty experimental data acquired under the same random excitation as that in the linear system data acquisition. Notice that the clearance between the bumper and the suspended column (= *Gap*) was set to 0.1mm in all measurements. However, the clearance adjustment was carried out in each data acquisition using a feeler gauge. This measurement method led to variability in actual conditions related to *Gap* and Δ. Four-hundred numerical runs were then created using sampled parameter sets (*Gap*, Δ). The same

Mahalanobis distance comparison procedure was carried out as that used in the damping parameters validation study. Even though some response features that were expected to be sensitive to the impact event; such as skewness, kurtosis, and time-series model parameters, the Mahalanobis distances from the most accurate numerical runs (as assess by RMSE) never distributed in the same order of the experimental baseline distribution. One main reason for these results was that the two parameters; *Gap* and Δ, were strongly correlated and response features that could have sensitivity to each of two parameters independently had to be used. Figure 8 is the parameter set plot, which indicates all parameter sets sampled in the creation of numerical runs. In this figure, the red dots are accurate numerical runs, which show low RMSE values, and the green dots indicate inaccurate numerical runs. Although the gap was set to 0.1mm in the experiment, the runs calculated using smaller *Gap* but with large Δ are also recognized as accurate outputs; i.e., two parameters are correlated. This observation indicates that the correlation of uncertain parameters in the numerical model also is a significant issue for the feature selection process. If such correlation cannot be prevented in the numerical model construction, it will require using response features that are independently sensitive to the validity of each uncertain parameter. Moreover, results here then confirmed that the Mahalanobis distance comparison method could be effectively applied to the statistical model validation only by using appropriate response features.

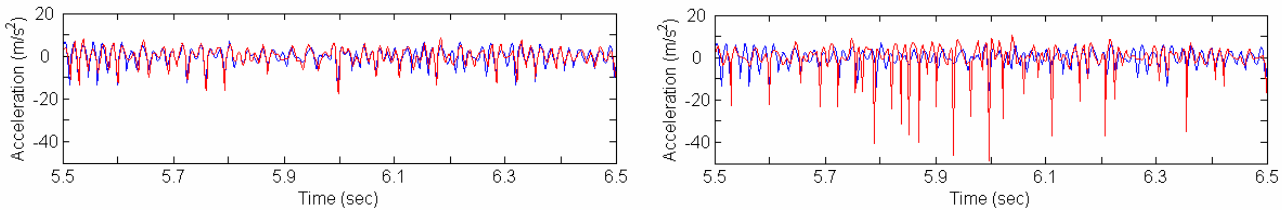

(a) Accurate numerical run (b) Inaccurate numerical run

Fig.7. Overlays of numerical (Red) and experimental (Blue) time-histories from nonlinear system

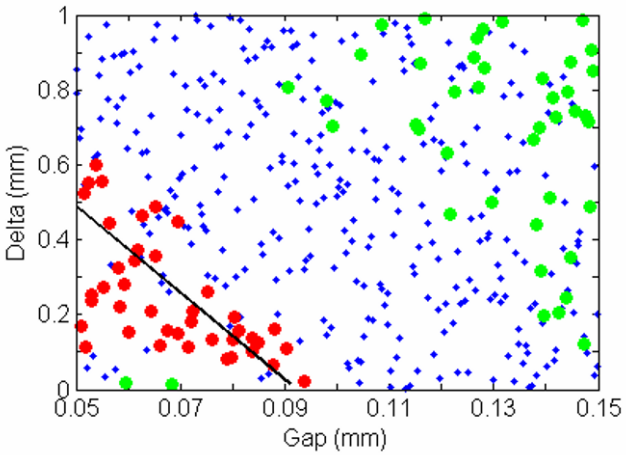

Fig.8. Map of sampled parameter sets with indicating correlation between *Gap* and Δ

5. Conclusions

- When selecting features for the model validation, issues that must be considered are not only dimension of the feature vector and type of response, but also the difference in sources of variability between experimental and numerical outputs. When using some features that require a fitting procedure, this variability can influence the feature's sensitivity to the parameters of interest.

- It was shown that the Mahalanobis distance comparison method was useful for the statistical m validation based on multivariate feature vectors.
- Correlation of uncertain parameters in the numerical model greatly influences the success of Mahalanobis distance comparison. This issue should be considered both in the construction of a numerical model and in the response feature selection.

The first and third issues should be advanced in the future works. They will become important considerations to realize more generalized structural dynamics model validation strategy and accurate uncertainty quantifications.

References

[1] Atamturktur, S., Hemez, F., Unal, C., Calibration under Uncertainty for Finite Element Models Masonry, LA-14414, Los Alamos, NM, Los Alamos National Laboratory, 2010.

[2] Figueiredo, E., Park, G., Figueiras. J., Farrar, C., Worden, K., Structural Health Monitoring Algorithm Comparisons Using Standard Data Sets, LA-14393, Los Alamos, NM: Los Alamos National Laboratory, 2009.

[3] Farrar, C., Worden, K., Todd, M., Park, G., Nichols, J., Adams, D., Bement, M., Farinholt, K., Nonlinear System Identification for Damage Detection, LA-14353, Los Alamos, NM: Los Alamos National Laboratory, 2007.

[4] Hemez, F., Farrar, C., Lecture notes: Finite Element Model Validation, Updating, and Uncertainty Quantification, Los Alamos National Laboratory, 2009.

[5] Robertson, A., Farrar, C., Sohn, H., Singularity Detection for Structural Health Monitoring using Holder exponent, Mechanical Systems and Signal Processing, Vol. 17, Issue 6, 1163-1184, 2003.

[6] Worden, K., Manson, G., Fieller N.R.J., Damage Detection using Outlier Analysis, J. Sound and Vibration, 229 (3), 647-667, 2000.

Hybrid Sets of Merged Data for Modal Model Applications

Louis Thibault, Bruce LeBlanc, Peter Avitabile
Structural Dynamics and Acoustic Systems Laboratory
University of Massachusetts Lowell
One University Avenue
Lowell, Massachusetts 01854

ABSTRACT

Often times, data is collected from a variety of different measurement systems that address different frequency ranges where the particular measurement system is well suited. These data sets may come from traditional accelerometer measurements and laser measurements and need to be merged into one complete data set. This can pose some difficulties when the measurement points are not collocated and reside at different points on the structure. With the advent of the use of optical measuring systems such as digital photogrammetry and digital image correlation techniques, the sets of points become even more complicated and a strategy is needed to merge all the data into one complete, scaled data set.

This paper presents an approach to take multiple sets of data collected over different frequency ranges and different sets of points to form one complete set of modal vectors to be used for the description of the modal data set. The use of model expansion approaches and a finite element model are used for this work. A set of data is collected to illustrate the approach. Discussion of the results obtained is presented.

INTRODUCTION

Experimental modal models are typically developed from a test where a specified set of transducers are used to measure dynamic response. However, in many applications where the frequency range needed to address the dynamic characteristics is very broad, then generally it is very difficult to use one set of transducers for the complete test or frequency range to be covered. This is most often the case where rigid body modes of a structure require a completely different set of transducers with appropriate sensitivities and frequency ranges suitable to the extraction of rigid body mode information [1]. This set of transducers used to measure these critical modes is not appropriate for mid range frequency and definitely not suitable for higher frequency ranges.

Therefore, the modal test must be conducted several times with different transducers that are specifically suited for the appropriate frequency range. This implies that there may be one test with transducers used to measure rigid body mode information, a set of transducers used to measure lower frequency flexible modes, and yet another set of transducers that are well suited for higher frequency type response. Figure 1 is a schematic showing the problem described with the different transducers that are best suited to measure the various broad frequency ranges that may be required.

On top of this logistical nightmare with several tests being required to address the entire frequency range desired, there may be an assortment of different transducers which are advantageous for these different frequency ranges. Displacement type transducers may be most appropriate for the very low frequency response or specifically designed low frequency accelerometers for the low frequency response to be measured. Normal ICP accelerometers may be adequate for the low frequency flexible modes of the structure but may be inappropriate for higher frequency ranges due to lack of adequate frequency response characteristics, insufficient sensitivity, as well as causing mass loading effects on the structural modes to be acquired. In these cases, non-contacting type measurements such as laser doppler vibrometery may be required to make these high fidelity measurements that are not prone to mass loading the structure [2, 3]. To further add to the array of different transducers available, recently, optical methods have become another viable technique that are well suited for low frequency measurements and are extremely useful for the extraction of rigid body mode information [1].

T. Proulx (ed.), *Linking Models and Experiments, Volume 2*, Conference Proceedings of the Society for Experimental Mechanics Series 5,
DOI 10.1007/978-1-4419-9305-2_11, © The Society for Experimental Mechanics, Inc. 2011

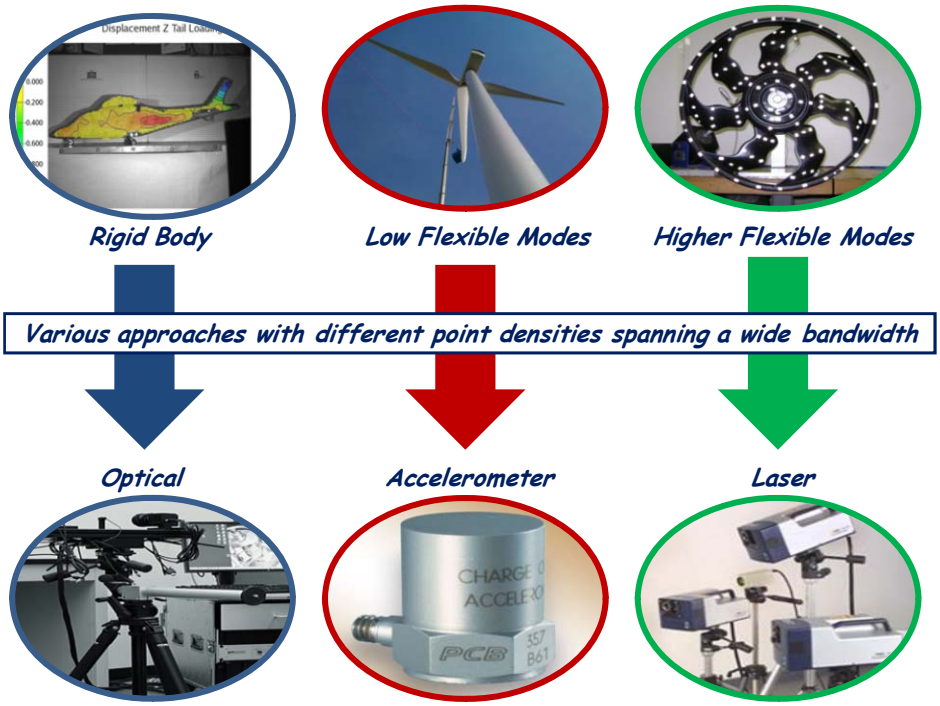

Figure 1 – Schematic of Different Transducers for Different Applications

In many cases, collection of data points that have common geometric locations is very important especially when the modal test is being conducted for validation of a finite element model of the structure. But many times the collocation of all the measurement points may not be possible. This may result from inadequate communication between all the various test parties conducting the different tests required. But this may also result from the inability to make measurements at all the same locations. This can result from geometric access (or lack thereof) to certain locations on the structure; it may not be possible to locate a larger accelerometer case in the same location where a teardrop accelerometer can be easily placed. This can also result from "line of sight" issues related with lasers where measurement points may not be easily visible from the laser orientation for the test performed.

In addition to these geometric problems that may occur, there can often be a mismatch from the total number of measurements that can be obtained from a practical standpoint. For instance, accelerometer measurements will be limited by the number of transducers available and the number of channels available on the data acquisition system. Of course roving patches of accelerometers can be performed (and the total number of measurement points may be several hundred) but the mass loading, time to conduct the test, consideration of time variance, etc. may render this impractical for many cases. In comparison, a laser may be set up to take a large number of measurements (on the order of a thousand or two thousand points) and that test can be performed but the measurements can only be made available on the surface where "line of sight" is not an issue; in addition the time to conduct the test, consideration of time variance, etc. also affect the practicality of the test. Once optical measuring approaches are also considered, the total number of measurement points may reach ten thousand or more.

All in all, the range of total measurements possible creates a serious mismatch in the definition of points that describe the structural characteristics over such a wide frequency range with no guarantee that there will be points in common unless extreme care is exercised. But even with such care there may be sets of points that do not have corresponding locations that span the entire frequency ranges that are identified by the different tests that are possible.

This paper presents an approach to merge all these different data sets into one complete, cohesive set of mode shapes that have a consistent set of scaled modal vectors that are extracted from multiple, different sets of data extracted from various types of data collection systems.

THEORY

The approach used in the merging of the different sets of data finds its roots in model reduction and model expansion with some extension of those approaches to address the problem identified. The specific theory of the approach can be found in the reference papers identified; only summarizing equations will be presented herein and details can be found in the references.

Model Reduction

Model reduction is necessary in order to develop expansion approaches for modal data for the various sets of data to be expanded. For this work, the reduction transformation matrices are used for the expansion process. The key is that the reduced set of ADOF will be different for all the various sets of data to be extracted. The expansion can be performed to the full space of the finite element model or to an intermediate space which is reduced from the full size of the finite element model but larger than the largest of the different measurement systems/scenarios utilized.

The reduction techniques are the basis of the expansion discussed in this work. These techniques have been presented in earlier work cited in the references; only summarizing equations are presented below. Several model reduction methods have commonly been used for expansion of measured data. Four common methods are Guyan [4], Dynamic Condensation [5], SEREP [6], and a Hybrid method [7]. In these methods, the relationship between the full set of degrees of freedom and a reduced set of degrees of freedom can be written as

$$\{X_n\}=[T]\{X_a\} \tag{1}$$

All of these methods require the formation of a transformation matrix that can project the full mass and stiffness matrices to a smaller size. The reduced matrices can be formulated as

$$[M_a]=[T]^T[M_n][T] \tag{2}$$

$$[K_a]=[T]^T[K_n][T] \tag{3}$$

For the specific work in this paper, only the SEREP method has been used for the expansion of mode shapes.
The System Equivalent Reduction Expansion Process (SEREP) produces reduced matrices for mass and stiffness that yield the exact frequencies and mode shapes as those obtained from the eigensolution of the full size matrix. The SEREP transformation is formed as

$$[T_U]=[U_n][U_a]^g \tag{4}$$

Implementation of Reduction/Expansion

For the work presented in this paper, each of the different types of data acquired from each of the different types of measuring systems needs to be merged together to form one hybrid/combined set of data. The schematic of Figure 2 shows this process schematically. The bottom of the schematic shows the full space finite element model representation of the structure; this may possibly be reduced to a relatively large model with fewer DOFs than the full finite element model but more than any of the test ADOF sets considered. The data set for the rigid body modes will have a set of measurement points at ADOF(RB) that are used in conjunction with the U(RB) modes to form a Tu(RB) expansion matrix. Next the data set for the low frequency flexible modes will have a set of measurement points at ADOF(LF) that are used in conjunction with the U(LF) modes to form a Tu(LF) expansion matrix. And finally, the data set for the high frequency modes will have a set of measurement points at ADOF(HF) that are used in conjunction with the U(HF) modes to form a Tu(HF) expansion matrix. It is very important to note that all of the individual ADOF sets can be totally different from each other and do not need to contain any similar or corresponding points. The “jelling mechanism” comes from the transformation matrix for each of the techniques which expands all the different data sets to a common set of points; this can be the full set of finite element DOFs or the larger reduced order ADOF model which is an umbrella for all the individual ADOF sets from the different test scenarios.

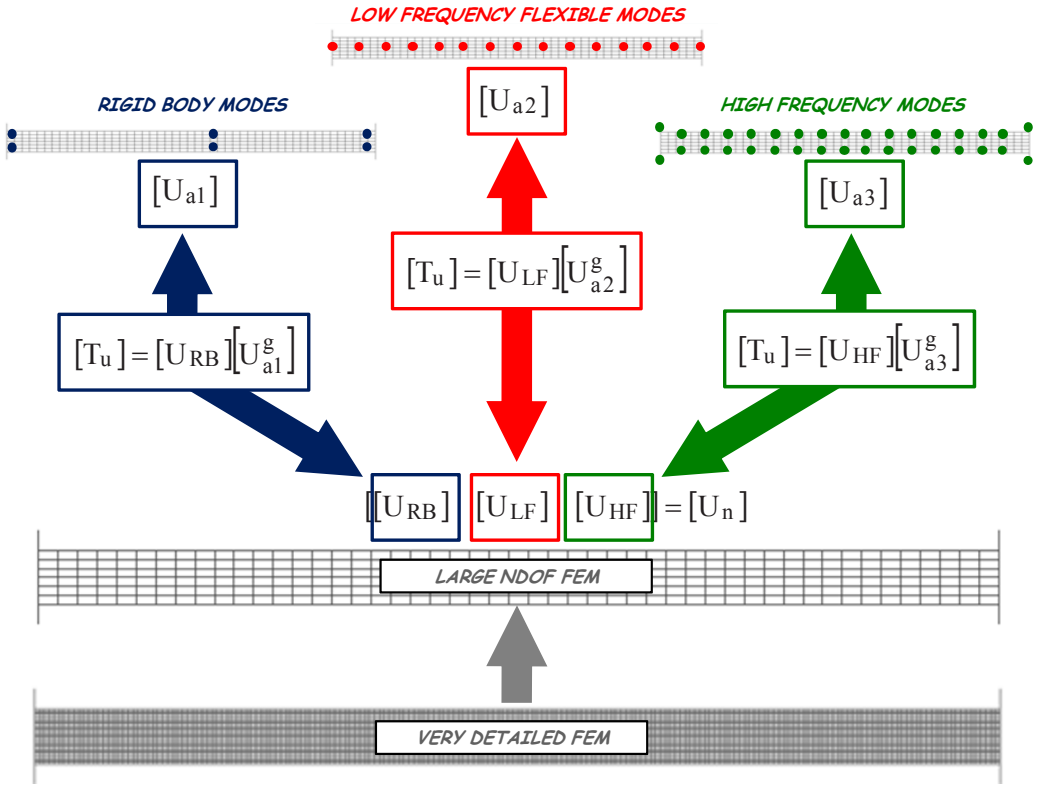

Figure 2 – Schematic of Overall Reduction/Expansion/Merging of Hybrid Sets of Data

MODEL DESCRIPTION AND CASES STUDIED

The beam consisted of a 50" long rectangular tubular cross section beam 3/16" thick with two 3 1/2" x 5" x 3/8" thick flanges. A finite element model was developed using FEMAP [8] to generate the mesh and then processed using FEMTools [9] software package for the eigensolution as well as correlation to all the different data sets. The model consisted of 1000 elements and 1337 nodes to describe the system; the system was analyzed in a free free condition and only planar motion about the weaker beam axis was considered for the studies performed for this demonstration. The mode shapes are typical as would be expected for this simple structure.

The experimental planar modes of the beam were obtained in three separate tests - one for the rigid body modes, one for the low frequency flexible modes, and one for the higher frequency flexible modes.

Rigid Body Modes

The beam response was measured using an optical measurement system using digital image correlation and dynamic photogrammetry with the Aramis/Pontos system [10, 11]. Impact excitation was performed to measure the response at many locations. However, for the studies in this paper only 6 measurement locations were chosen to describe the rigid body motion. Frequency response functions were obtained from processing the time data captured from the optically measured data; additional information on the collection and processing of this type of data can be found in previous studies [12]. Two low frequency rigid body modes were extracted from the data – a bounce mode and a rocking mode as expected.

Low Frequency Flexible Modes

The beam response was measured using traditional accelerometers for the low frequency flexible modes of the system. These measurements can be obtained from either shaker tests or from impact tests; shaker excitation using burst random was used to extract the response. The frequency response functions were collected at 15 measurement locations over a span of 1000 Hz and modal data was extracted using conventional approaches available in LMS Test.LAB [13]. The first three flexible modes of the structure were extracted and were typical of the expected mode shapes for these modes.

High Frequency Flexible Modes

The beam response was measured using a laser vibrometer with shaker excitation methods as well as with accelerometers more suitable for higher frequency ranges with low mass loading effects using impact excitation techniques. For the data in this paper either data set could have been used for the identification of the modes. The frequency response functions were collected at 34 measurement locations over a span of 3000 Hz and modal data was extracted using convention approaches available in LMS Test.LAB [13]. The next four flexible modes of the structure were extracted and were typical of the expected mode shapes for these modes.

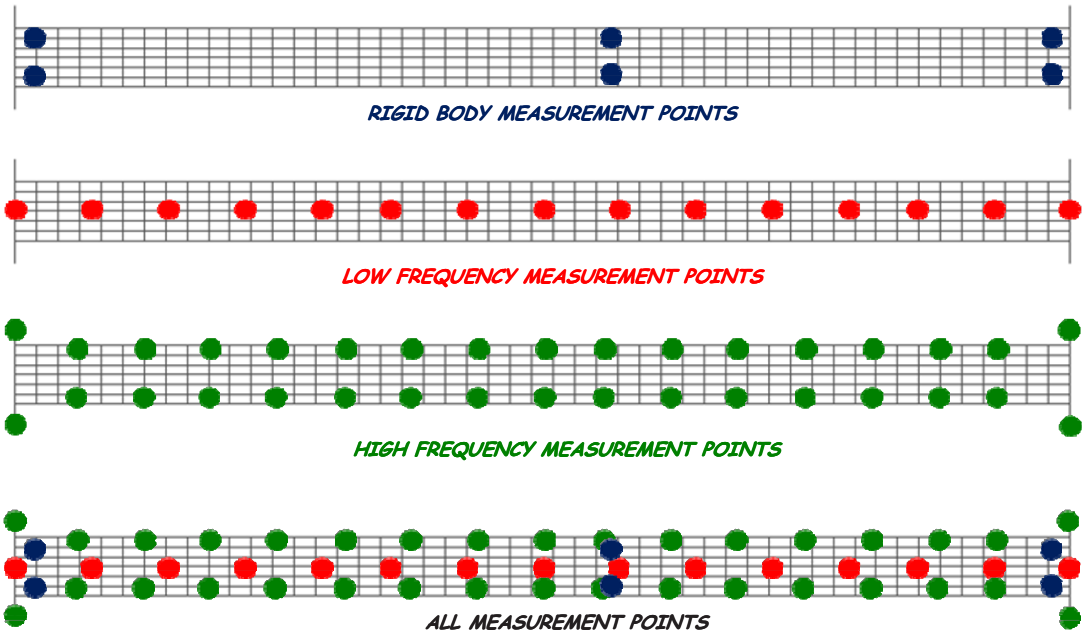

Figure 3 – Overlay of All Measurement Points on the Test Structure

One important item to note is that none of the DOF from the three separate tests contained any coincident measurement points; each contained a completely unique set of points. The collection of data points for each of the tests is shown in Figure 3 for the three separate tests along with an overlay of all the measurement points superimposed on the test structure.

Each of the separate test data sets were correlated to the finite element model and very good overall correlation was observed for each of the sets. Then each data set was used in an expansion process as described in the theory section. The mode shapes were expanded and again correlated to the finite element model with essentially similar correlation results. The Modal Assurance Criteria was used for the correlation of the different data sets. The correlation of each of the different vector data sets is shown in Figure 4 along with the MAC; note that due to the large amount of data points obtained from the expansion process only the original collected data from each of the separate tests is shown superimposed on the finite element model.

All of the data sets showed very good correlation with the model and, after expansion, each of the separate test data sets now has a common set of points to describe the model. In addition, the process of expansion has blended together data from different sources – optical, accelerometer, laser and ultimately any other types of modal data that could possibly be collected.

	#	FEA	Hz	EMA	Hz	Diff.	MAC
Rigid Body Modes	1	1	0	1	0.4	___	98.5
	2	2	0	2	0.5	___	99.4

	#	FEA	Hz	EMA	Hz	Diff.	MAC
Low Frequency Flexible Modes	1	1	127	1	128	-0.62	99.7
	2	2	354	2	357	-0.67	99.5
	3	3	685	3	689	-0.64	99.3

	#	FEA	Hz	EMA	Hz	Diff.	MAC
High Frequency Flexible Modes .	1	1	1091	1	1108	-1.52	99.9
	2	2	1540	2	1569	-1.83	99.6
	3	3	1996	3	2045	-2.37	99.5
	4	4	2427	4	2497	-2.81	98.7

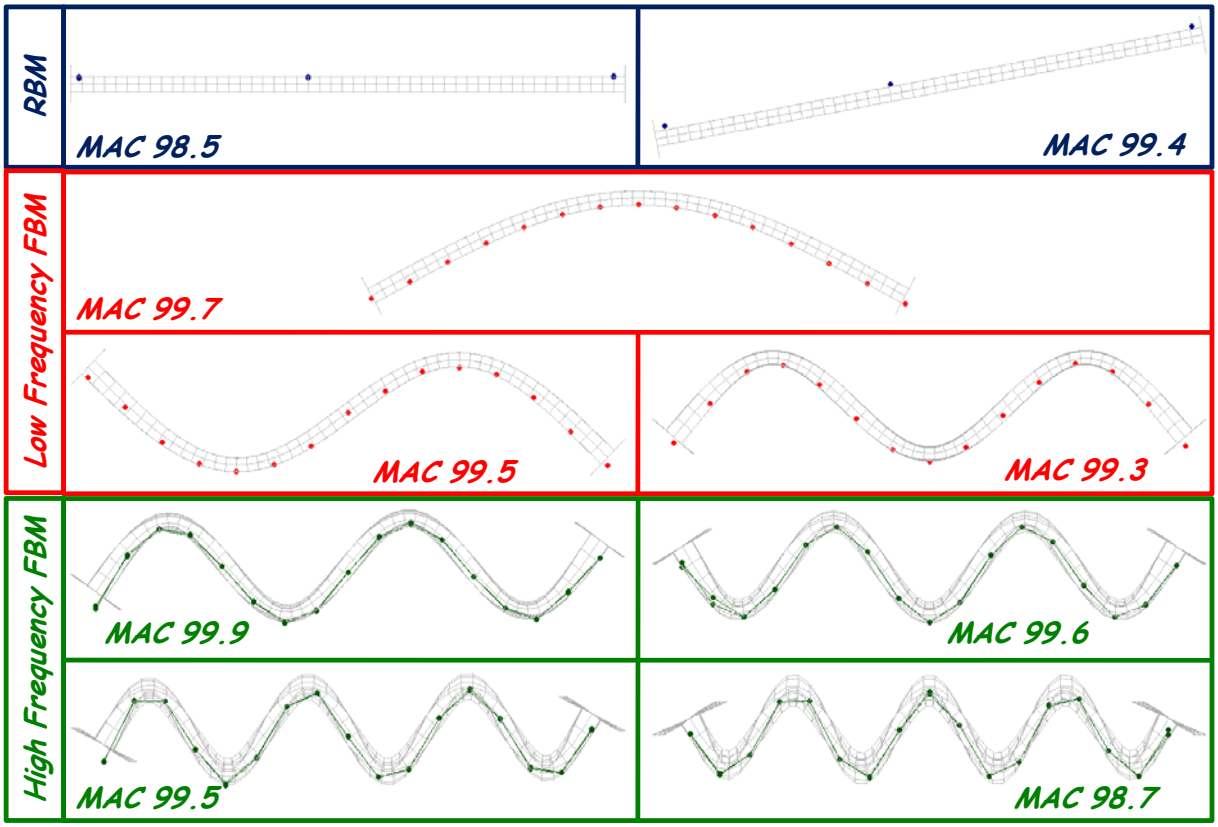

Figure 4 – Frequencies, MAC and Overlay of Correlated Modes from Different Measurement Sets

OBSERVATIONS

Often times, data sets are collected by different groups with different overall objectives as well as different measuring methodologies and systems. The integration of these vastly different databases can pose problems. With the expansion processes discussed in this paper, the subsets of different measurement points over different frequency ranges can be achieved very effectively. For the measurements made in this study, a wide assortment of measuring devices and systems were employed. Obviously, accelerometer measurements are very common in the development of any structural dynamic models; traditional impact and shaker excitation approaches are typically used for the measurement of frequency response functions and the data is reduced using conventional modal parameter estimation approaches. For the very low frequency measurements, several approaches are possible including low frequency accelerometer transducers. However, for the tests identified in this study, optical measurements were employed; digital image correlation and/or dynamic photogrammetry approaches were used. These very low frequency measurements employed dynamic photogrammetry to obtain time response at very limited sets of test locations. FFT processing of the data was performed to obtain frequency response functions. At the very high frequency range, either low mass accelerometers or laser vibrometer measurements could be employed using impact or shaker excitation approaches. Again, these measurements were processed to obtain modal parameters.

For the studies performed herein, there was no care exercised to select measurement locations that had any common data points to illustrate the approach suggested in this paper. Obviously, if these measurements can be obtained at a common set of measurement locations then advantages can be obtained. But even if many points are selected in common, there is really no reason to collect the same number of points for all the frequency ranges to be addressed. For instance, in order to properly characterize high frequency modes, many points are required to define the shape sufficiently. However, this large number of points is totally unnecessary in the definition of the rigid body modes. So the expansion process is still necessary in order to meld all the data together for a unified data set to describe the structure. But due to the way the expansion process has been defined, there is no required common set of measurement points.

CONCLUSION

The development of a hybrid set of mode shapes that come from an assortment of different measurement systems, with drastically different transducer configurations and with a non-coincident set of measurement points, was described. The modal expansion process was used to develop a common data set from each of the individual data sets. A unique set of measurement points was used to expand each of the different measured arrays of points from each of the different tests to obtain one complete, unified set of data that can be used for further processing.

Using either Dynamic Expansion or the System Equivalent Reduction Expansion Process (SEREP), test data sets that come from completely different sources (optical, accelerometer, laser, etc), with completely different sets of measured points, can be effectively combined to form one unified set of modal data to describe a structure. This was demonstrated for an example structure and shown to produce useful results.

NOMENCLATURE

Symbols:

$\{X_n\}$	full set displacement vector	$[U_a]^g$	generalized inverse of reduced shape matrix
$\{X_a\}$	reduced set displacement vector	$[U_n]$	expanded shape matrix
$[M_a]$	reduced mass matrix	$[T]$	transformation matrix.
$[M_n]$	expanded mass matrix	$[T_U]$	SEREP transformation matrix.
$[K_a]$	reduced stiffness matrix	$[REF_n]$	reference data at all degrees of freedom (dofs)
$[K_n]$	expanded stiffness matrix	$[RTO_a]$	real time operating data at measured dofs
$[U_a]$	reduced shape matrix	$[ERTO_n]$	expanded real time operating data at all dofs

REFERENCES

1 A.Williams, P.Avitabile, “Comparison of Some Rigid Body Mode Estimation Techniques for System Model Development”, Proceedings of the Twenty-Sixth International Modal Analysis Conference, Orlando, FL, Feb 2008

2 P.Pingle, J.Sailhamer, P.Avitabile, Proceedings “Comparison of 3D Laser Vibrometer and Accelerometer Frequency Measurements”, of the Twenty- Seventh International Modal Analysis Conference, Orlando, FL, Feb 2009

3 C.Warren,P.Pingle,C.Niezrecki, P.Avitabile, “Comparison of Image Based, Laser, and Accelerometer Measurements”, Proceedings of the Twenty-Eighth International Modal Analysis Conference, Jacksonville, FL, Feb 2010

4 Guyan, R.J., "Reduction of Stiffness and Mass Matrices", AIAA Journal, Vol. 3, No 2, 1965

5 Paz, M, "Dynamic Condensation", AIAA Journal, Vol22, No 5, May 1984

6 O'Callahan,J.C., Avitabile,P., Riemer,R., "System Equivalent Reduction Expansion Process", Seventh International Modal Analysis Conference, Las Vegas, Nevada, February 1989

7 Kammer, DC, "A Hybrid Approach to Test Analysis Model Development for Large Space Structures", Journal of Vibration and Acoustics, Vol 113, July 1991

8 Femap – Finite Element Modeling And Postprocessing, Version 9.3.1, Copyright © 2007 UGS Corp.

9 FEMtools 3.0 – Dynamic Design Solutions, Leuven, Belgium.

10 ARAMIS, v. 6.0 User’s Manual, GOM mbH, Braunschweig, Germany, 2007

11 PONTOS, User’s Manual, Revision A, GOM mbH, Braunschweig, Germany 2004

12 C.Warren, “Modal Analysis and Vibrations Applications of Sterophotogrammetry Techniques“, MS Thesis, University of Massachusetts Lowell, 2010.

13 LMS Test.Lab – Leuven Measurement Systems, Leuven, Belgium

14 Polytec Scanning Laser Doppler Vibrometer, Polytec Optical Measurement Systems

Dynamic Uncoupling of a System Model for Component Identification

David Cloutier, Dr. Peter Avitabile
Structural Dynamics and Acoustic Systems Laboratory
University of Massachusetts Lowell
One University Avenue
Lowell, Massachusetts 01854

ABSTRACT

System model description from component modes is a common approach for model development. Dynamic uncoupling of a system model to obtain component information is very useful and currently under significant research. Uncoupling can be performed different ways and several approaches are considered for the evaluation of component uncoupling from the system. These approaches are compared with several models to better understand the strengths and weaknesses of each of the techniques often employed. Several cases using both analytical models and experimental data sets are studied and shown in the paper.

INTRODUCTION

While system assembly modeling has been a valuable tool for many years [1-6], current efforts have also shifted to include decoupling of system models for component identification [7-17]. System assembly is typically performed using frequency response functions of two components, such as Frequency Based Substructuring, or by using modal information of the two components to obtain the fully assembled system characteristics. Dynamic uncoupling of a system presents the inverse problem, where an individual component's characteristics are desired while measurements are only available on the fully assembled system.

Very similar problems found in system assembly are also present in uncoupling. These problems include measurement inaccuracies inherent in test data, inability to measure all coupling degrees of freedom (ie. rotational degrees of freedom) and modal truncation. This paper presents several decoupling techniques performed on analytical and experimental models to determine their sensitivities to measurement inaccuracies.

THEORY

In general, two components A and B can be used to form a system representation AB. The two components are coupled at a connection point(s), and external forces may be applied at coupling degrees of freedom (DOF) ($\{f\}_c$), or internal DOF ($\{f\}_i$). For the work presented in this paper, the general system coupling equations are presented first, followed by the three separate decoupling approaches investigated.

General System Modeling Equations

Frequency response functions (FRF) of a structure can be portioned into coupling DOF (c) and internal DOF (i). The response of the system AB can then be written as,

T. Proulx (ed.), *Linking Models and Experiments, Volume 2*, Conference Proceedings of the Society for Experimental Mechanics Series 5,
DOI 10.1007/978-1-4419-9305-2_12, © The Society for Experimental Mechanics, Inc. 2011

$$\begin{Bmatrix} \{u\}_c^{AB} \\ \{u\}_i^{AB} \end{Bmatrix} = \begin{bmatrix} [H]_{cc}^{AB} & [H]_{ci}^{AB} \\ [H]_{ic}^{AB} & [H]_{ii}^{AB} \end{bmatrix} \begin{Bmatrix} \{f\}_c^{AB} \\ \{f\}_i^{AB} \end{Bmatrix} \tag{1}$$

and for the known component A,

$$\begin{Bmatrix} \{u\}_c^{A} \\ \{u\}_i^{A} \end{Bmatrix} = \begin{bmatrix} [H]_{cc}^{A} & [H]_{ci}^{A} \\ [H]_{ic}^{A} & [H]_{ii}^{A} \end{bmatrix} \begin{Bmatrix} \{f\}_c^{A} \\ \{f\}_i^{A} \end{Bmatrix} \tag{2}$$

The coupling conditions at connection DOF are:

$$\{u\}_c^{AB} = \{u\}_c^{A} = \{u\}_c^{B} \tag{3}$$

$$\{f\}_c^{AB} = \{f\}_c^{A} + \{f\}_c^{B} \tag{4}$$

and at internal DOFs on component B:

$$\{u\}_i^{AB} = \{u\}_i^{B} \tag{5}$$

$$\{f\}_i^{AB} = \{f\}_i^{B} \tag{6}$$

Impedance Approach

For the Impedance based approach, subtracting the inverse of (2) by the inverse of (1) and introducing the conditions (3), (4), (5) and (6), with some algebraic manipulation one can obtain,

$$[H]_{cc}^{B} = \begin{bmatrix} [N]_{cc} \\ [N]_{cc} \end{bmatrix}^{+} \begin{bmatrix} [H]_{cc}^{AB} \\ [H]_{ic}^{AB} \end{bmatrix} \tag{7}$$

with,

$$[N]_{cc} = [I]_{cc} - [H]_{cc}^{AB} [H]_{cc}^{A^{-1}} - [H]_{ci}^{AB} [H]_{ic}^{A^{-1}} \tag{8}$$

$$[N]_{ic} = -[H]_{ic}^{AB} [H]_{cc}^{A^{-1}} - [H]_{ii}^{AB} [H]_{ic}^{A^{-1}} \tag{9}$$

If only connection DOF are measured, then (7) simplifies to

$$[H]_{cc}^{B} = \left([I]_{cc} - [H]_{cc}^{AB} [H]_{cc}^{A^{-1}} \right)^{-1} [H]_{cc}^{AB} \tag{9}$$

Mobility Approach

For the Mobility based approach, subtracting (2) from (1) and introducing the coupling conditions (3), (4), (5) and (6), with some algebraic manipulation one can obtain

$$[H]_{cc}^{B} = \begin{bmatrix} [H]_{cc}^{AB} & [H]_{ci}^{AB} \end{bmatrix} \left(\begin{bmatrix} [I]_{cc} & [0]_{ci} \end{bmatrix} - \begin{bmatrix} [H]_{cc}^{A} \\ [H]_{ic}^{A} \end{bmatrix}^{+} \begin{bmatrix} [H]_{cc}^{AB} & [H]_{ci}^{AB} - [H]_{ci}^{A} \\ [H]_{ic}^{AB} & [H]_{ii}^{AB} - [H]_{ii}^{A} \end{bmatrix} \right)^{+} \tag{10}$$

If only connection DOF are measured, then (10) simplifies to

$$[H]_{cc}^{B} = [H]_{cc}^{AB}\left([I]_{cc} - [H]_{cc}^{A-1}[H]_{cc}^{AB}\right)^{-1} \tag{11}$$

Both approaches obtain the same solution when only connection DOF are used, as seen by comparing (9) to (11).

Inverse Frequency Based Substructuring Approach

The Inverse Frequency Based Substructuring Approach (Inverse FBS) reformulates the Frequency Based Substructuring (FBS) equations to solve for a single component [15]. For this technique, measurements are required at either side of the connection. The subscript c(a) represents a connection DOF on component A of the system, and the subscript c(b) represents a connection DOF on component B of the system. With this nomenclature, the drive point FRF on the unknown component can be written in terms of purely system FRFs as,

$$\begin{aligned}[H]_{c(b)c(b)}^{B} = &\left([H]_{c(a)c(a)}^{AB}[H]_{c(b)c(a)}^{AB^{-1}}[H]_{c(b)c(b)}^{AB} - [H]_{c(a)c(b)}^{AB}\right) \\ &\bullet\left([H]_{c(a)c(a)}^{AB} - [H]_{c(a)c(b)}^{AB}\right)^{-1}[H]_{c(a)c(b)}^{AB}\end{aligned} \tag{12}$$

APPLICATION

System Description – Analytical Models

A basic six DOF mass-spring has been previously studied [17] to investigate the effects of noise and modal parameter estimation on the Mobility and Impedance decoupling approaches. Both techniques produced promising results, especially with the use of internal DOF. An additional technique, the Constraint Force Approach [17] was also developed to uncouple a system, and compared to the Mobility and Impedance approaches using the six DOF model. While this technique could successfully uncouple the model, only a single connection could be uncoupled at a time. This feature made the technique impractical on complex models and experimental structures where it may be impossible to couple a single DOF at a time.

While the basic six DOF model was useful to study the effects of noise on each technique, a more complex model was needed to study issues inherent with experimental data. Issues such as truncation and lack of rotational DOF [6] have been shown to be detrimental to frequency based system modeling approaches. To address these issues, a finite element model (FEM) of a laboratory test structure was created in MATLAB [18]. The structure consists of two identical aluminum hollow rectangular beams, Beam A and Beam B, bolted together at two locations. Figure 1 displays the cross section of the beams, and Table 1 lists the physical properties used in the model.

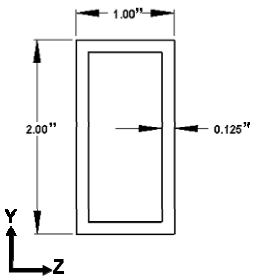

Figure 1. Beam Cross Section.

Table 1. Physical Properties of Beam Models.

Physical Property	Value	
Length	1.524	m
Hieght	50.8	mm
Width	25.4	mm
Thickness	3.175	mm
Density	2805	kg/m^3
Modulus of Elasticity	68.9	GPa
Free Free Springs	1.0	N/m
Transverse Connection	79.7	MN/m
Rotary Connection	563.6	Nm/rad

The beams were considered planar and modeled using thirty elements each having two DOF per node (translational and rotational). Soft springs were connected to each end node to simulate a free-free boundary condition. Figure 2 displays a physical representation of each beam model. Table 2 lists the natural frequencies of each beam. As the models contained only mass and stiffness matrices, a one percent damping was assigned to each mode to limit the dynamic range.

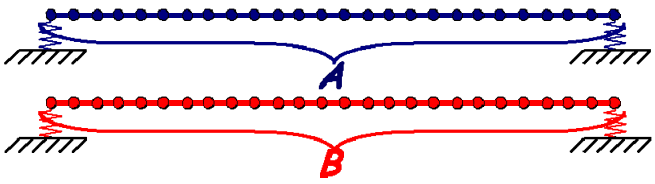

Figure 2. Physical Representation of Beams.

Table 2. Modal Properties of Beams.

Mode	Beam A		Beam B	
	Freq. (Hz)	Damp. (%)	Freq. (Hz)	Damp. (%)
1	0.16	1.00	0.16	1.00
2	0.28	1.00	0.28	1.00
3	75.43	1.00	75.43	1.00
4	207.94	1.00	207.94	1.00
5	406.59	1.00	406.59	1.00
6	671.02	1.00	671.02	1.00

System Description – AB-TR

Two systems were considered for the analytical studies. The first system, AB-**TR**, contains two sets of **T**ranslational and **R**otational stiffness connections. To correlate with the experimental structure, a translational stiffness of 8E7 N/m and a rotational stiffness of 6E2 rad/Nm were used at nodes 6 and 26. Figure 3 displays a physical representation of the two beam system, AB-TR. Both a physical FEM system model, as well as an FBS system model was created. The FBS system model will be used for all of the cases studied, in order to avoid error associated with lack of damping in the physical system model. Table 3 lists the natural frequencies of both sets of system models. A maximum frequency difference of 0.59% exists in the first flexible mode. The natural frequencies of the FBS models were determined using modal parameter estimation in LMS Test.Lab [19]. Note that the two rigid body modes were not extracted due to low frequency limitations of the modal parameter estimation software.

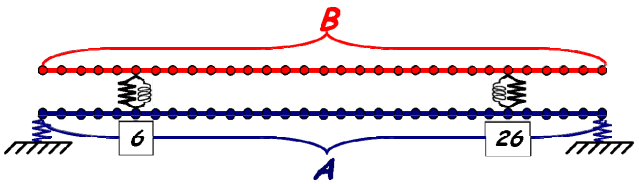

Figure 3. Physical Representation of System AB-TR.

Table 3. Modal Properties of System AB-TR.

Mode	FEM Model Frequency (Hz)	FBS Model Frequency (Hz)	Difference (%)
1	0.16	N/A	N/A
2	0.28	N/A	N/A
3	73.08	72.65	0.59
4	75.43	75.43	0.00
5	197.38	196.97	0.21
6	207.94	207.94	0.00
7	286.80	286.66	0.05
8	406.59	406.59	0.00
9	451.29	451.30	0.00
10	671.02	671.05	-0.01

System Description – AB-TT

The second system, AB-**TT**, contains **T**wo closely-spaced **T**ranslational springs at each connection location. An appropriate distance was determined to have the equivalent translational and rotational connection stiffness as system AB-TR, a similar approach as the Equivalent Multiple Point Constraint technique. The EMPC method has been previously used to address rotational DOF for FBS modeling [5], in which multiple translational DOF are used to approximate rotational DOF. A physical FEM system model as well as an FBS system model was again created. A physical representation of system AB-TT is shown in Figure 4. Table 4 lists the natural frequencies and percent differences of the two models. Both system models of AB-TT produce nearly identical results.

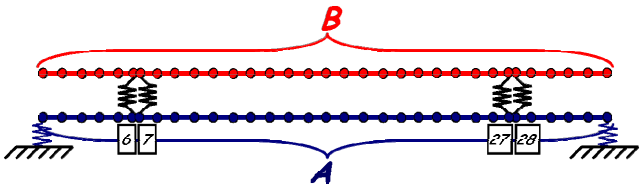

Figure 4. Physical Representation of System AB-TT.

Table 4. Modal Properties of System AB-TT.

Mode	FEM Model Frequency (Hz)	FBS Model Frequency (Hz)	Difference (%)
1	0.16	N/A	N/A
2	0.28	N/A	N/A
3	72.51	72.51	0.00
4	75.48	75.48	0.00
5	196.84	196.81	0.01
6	208.05	208.08	-0.01
7	286.65	286.66	0.00
8	407.87	407.87	0.00
9	451.38	451.32	0.01
10	674.25	674.27	0.00

Table 5 lists the comparisons of the two FEM system models, AB-TR and AB-TT. Minimal differences exist in the natural frequencies, confirming the accuracy of the rotational stiffness approximation in model AB-TT. Table 6 lists the natural frequencies and damping of both FBS system models obtained using modal parameter estimation. A similar degree of difference exists in natural frequencies of the FBS models as the FEM models, further validating the rotational stiffness approximation. Minimal differences also exist in the percent critical damping between the two FBS models.

Table 5. FEM System Model Comparison.

Mode	System AB-TR Frequency (Hz)	System AB-TT Frequency (Hz)	Difference (% Diff.)
1	0.16	0.16	-0.29
2	0.28	0.28	-0.38
3	73.08	72.51	0.79
4	75.43	75.48	-0.07
5	197.38	196.84	0.27
6	207.94	208.05	-0.06
7	286.80	286.65	0.05
8	406.59	407.87	-0.32
9	451.29	451.38	-0.02
10	671.02	674.25	-0.48

Table 6. FBS System Model Comparison.

Mode	System AB-TR		System AB-TT		Difference	
	Freq. (Hz)	Damp. (%)	Freq. (Hz)	Damp. (%)	Freq. (% Diff.)	Damp. (% Diff.)
1	N/A	N/A	N/A	N/A	N/A	N/A
2	N/A	N/A	N/A	N/A	N/A	N/A
3	73.08	0.82	72.51	0.84	0.79	-1.92
4	75.43	1.00	75.48	1.00	-0.07	0.20
5	197.38	0.89	196.85	0.90	0.27	-1.11
6	207.94	1.00	208.05	1.00	-0.05	0.30
7	286.80	0.69	286.65	0.68	0.06	0.77
8	406.59	1.00	407.89	1.00	-0.32	-0.40
9	451.30	0.68	451.37	0.67	-0.02	0.59
10	671.05	1.00	674.27	1.00	-0.48	0.10

Perturbation of Frequency Response Functions

Perturbation of FRF was performed in FEMtools [20] by applying a one percent random noise to the FRF. FEMtools applies this percentage of noise by first performing an inverse Fourier transform on all FRFs and finding the maximum value within all the time histories produced. The software then produces uniform random time histories for each function using the specified percentage of this maximum value. A uniform random time history is added to each function and a Fourier transform is then performed to put all functions back in the frequency domain. Note that this technique does produce a significantly higher level of noise at less active DOF, which in test one would typically use more sensitive accelerometers or reduce the acquisition range to minimize noise at these locations. However, modal parameter estimation was performed to remove the noise prior to performing decoupling.

Decoupling of System – Analytical Models

The first case considers system AB-TR in which there is translational and rotational springs connecting the two beams at two locations, as previously shown in Figure 3. Using system FRF from the FBS models and FRF of beam A, the drive point connection FRF of beam B were computed. Using true FRF without noise or truncation, all techniques produce accurate results. While four DOF were coupled in the system model (two translational and two rotational), decoupling produced accurate results without the use of rotational FRF in the computation due to the low coupling stiffness relative to the transverse coupling stiffness. However, excluding rotational DOF in decoupling a system with significant rotational coupling stiffness can produce error.

To determine each technique's sensitivity to noise, a one percent uniform random noise was applied to the FRF as previously mentioned. Performing the decoupling directly with the noisy FRFs produced resulting FRFs with a significant level of

noise. To reduce this noise, new FRF were synthesized from modal parameters obtained using modal parameter estimation in LMS Test.Lab. While modal parameter estimation and FRF synthesis removes all of the noise, very slight shifts in antiresonances are produced in the synthesized FRF. These shifts are detrimental to the resulting FRF produce by the decoupling techniques, as shown in Figure 5. The Inverse FBS approach is most sensitive to this perturbation, whereas only minimal error is produced in the Impedance and Mobility results.

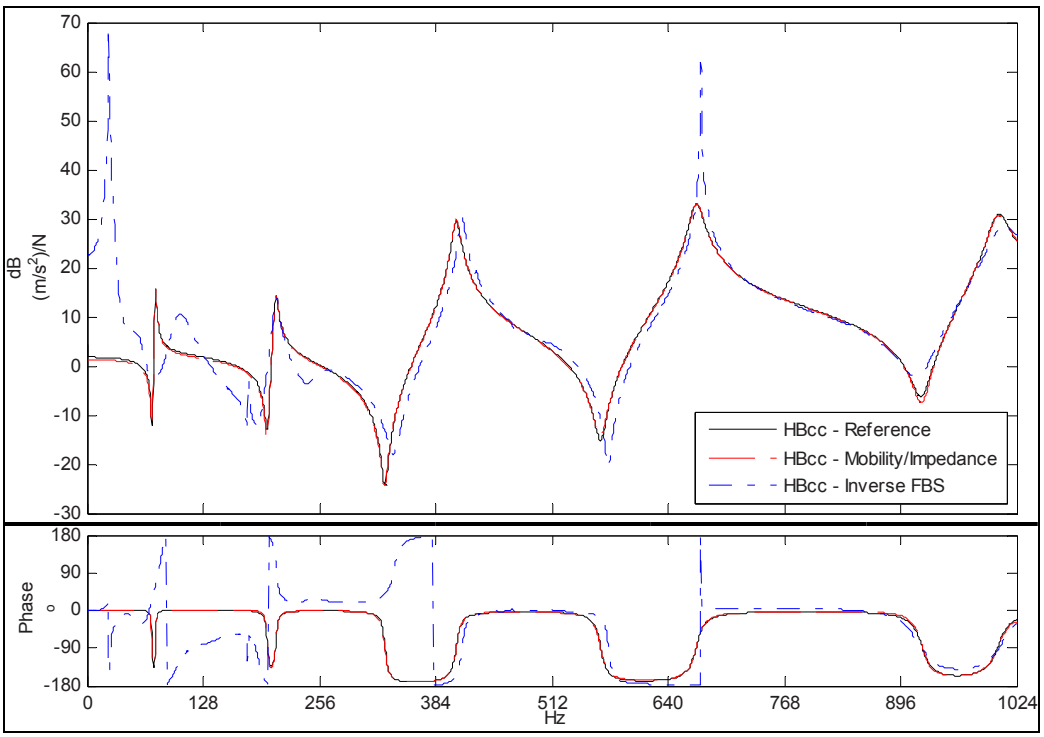

Figure 5. System AB-TR Estimation of Beam B Translation FRF at Node 6 using Synthesized Perturbed FRFs.

Decoupling was performed on model AB-TT in a similar manner. As with AB-TR, all techniques produced accurate resulting FRF when true system and component FRF are used. However, using the perturbed synthesized FRF for model AB-TT produces greater error than with model AB-TR, as shown in Figure 6. In this case, Mobility and Impedance contain spurious peaks which occur near antiresonances in the component and system FRF. The Inverse FBS approach produces overall poor results for this case, with minimal correlation.

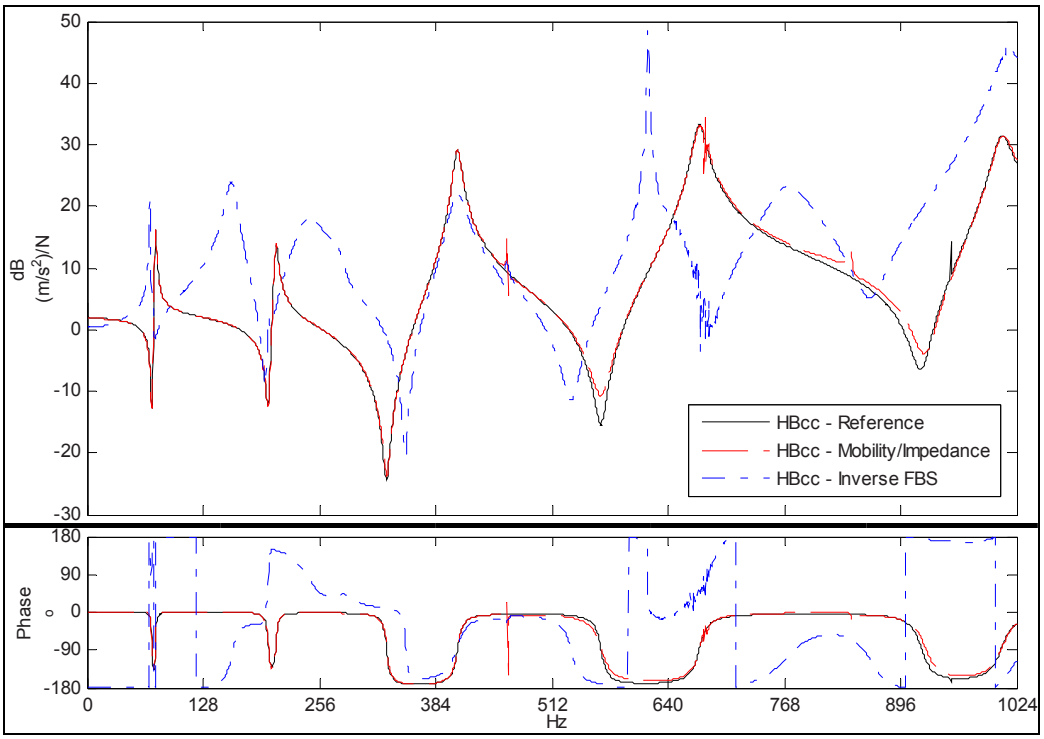

Figure 6. System AB-TT Estimation of Beam B Translational FRF at Node 6 using Synthesized Perturbed FRF.

To improve the results, additional internal DOF can be included in both the Mobility and Impedance approaches. Many cases were studied to determine an optimal procedure for choosing internal DOF. Techniques typically employed in pretest analysis (kinetic energy, modal displacements) were investigated; however, no technique produced a clear determination of best internal DOF to choose. While each DOF was used to improve the results of decoupling, only two DOF will be presented for brevity. Figure 7 displays the location of the two DOF used, translational DOF at node 1 and translational DOF at node 16.

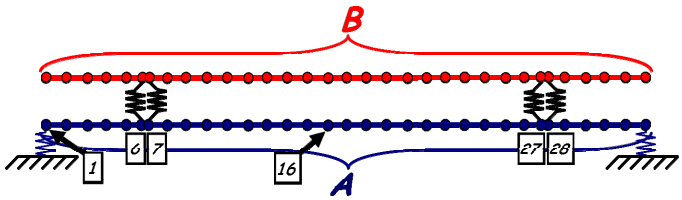

Figure 7. Internal DOF on AB-TT Presented in Mobility and Impedance Approaches.

Figure 8 and Figure 9 presents the resulting translational FRF at Node 6 of Beam B using internal translational DOF located at node 1 and node 16, respectively. Translation DOF at node 1 removes the spurious peaks produced in the resulting FRF when only connection DOF are considered. Mobility approach produces the most accurate results with node 1, as a spurious peak is still present when using the translational DOF at node 16. The Impedance approach suffers at lower frequencies with either internal DOF, and is less accurate than results using only connection DOF.

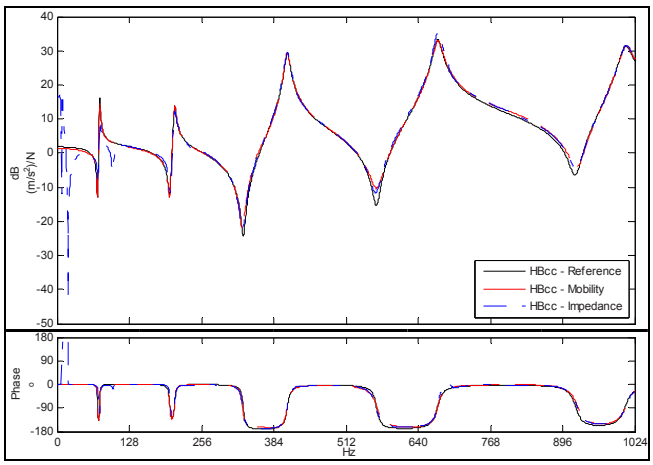

Figure 8. System AB-TT Estimation of Beam B Translational FRF at Node 6 using Synthesized Perturbed FRF with Internal Translational DOF at Node 1.

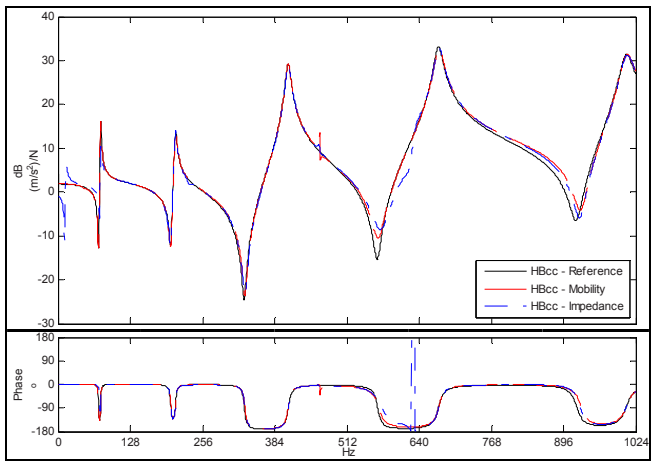

Figure 9. System AB-TT Estimation of Beam B Translational FRF at Node 6 using Synthesized Perturbed FRF with Internal Translational DOF at Node 16.

While multiple internal DOF can be used in a single computation, averaging of results using a single internal DOF was also considered. Figure 10 displays the results when both internal DOF at node 1 and node 16 are used in a single computation with the Mobility approach, as well as results when each of the FRF are averaged together from the previous case. Figure 11 presents the same results using the Impedance approach.

For this case, averaging degrades the results when using Mobility approach. As previously shown, a spurious peak is produced in the resulting FRF when the translational DOF at node 16 is included. While this peak is reduced when averaged, using both internal DOF with the Mobility approach produces more accurate results. However, for the Impedance approach, averaging the results significantly improves the results and minimizes the error produced at lower frequencies.

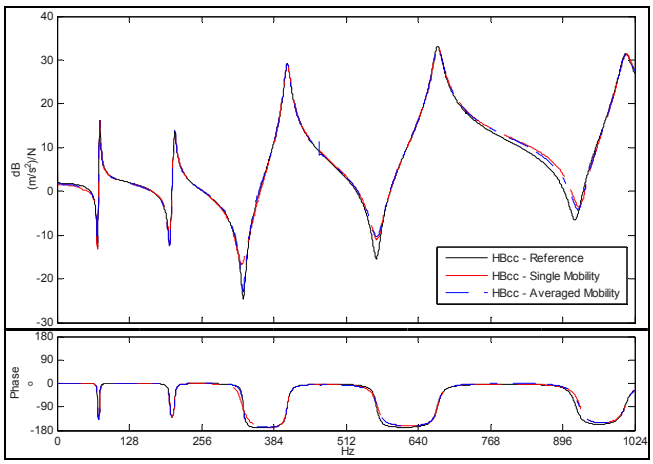

Figure 10. System AB-TT Estimation of Beam B Translational FRF at Node 6 using Mobility Approach with Internal Translational DOF at Nodes 1 and 16.

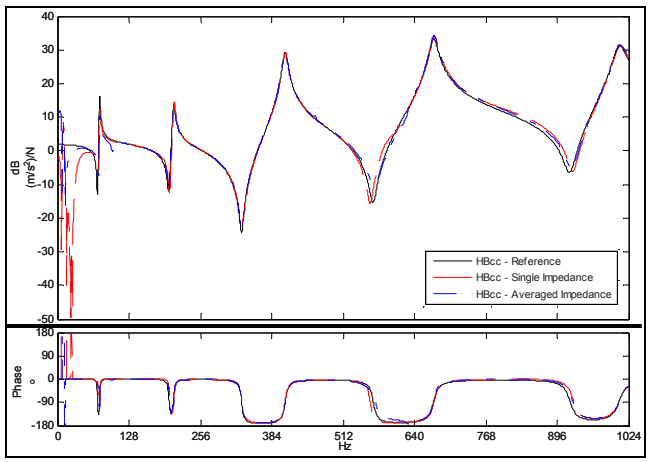

Figure 11. System AB-TT Estimation of Beam B Translational FRF at Node 6 using Impedance Approach with Internal Translational DOF at Nodes 1 and 16.

System Description – Experimental Models

The experimental structure of the two-beam system is shown in Figure 12. The structure consists of two hollow aluminum beams with approximate cross section and physical properties as presented in Figure 1 and Table 1, respectively. The beams were bolted together using threaded rod and nuts were used to secure each beam in place. Enough space between the beams

allowed for installation of accelerometers on the inside face of the beam. Figure 13 displays a close up view of the connection. For these studies, beam A was tested with the hardware installed, and beam B was the beam alone.

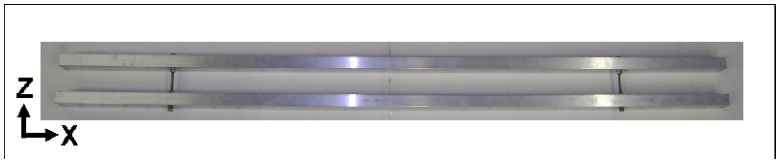

Figure 12. Experimental Two-Beam System.

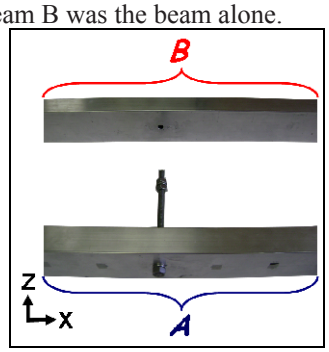

Figure 13. Individual Beam Components at Connection.

As with the analytical studies, two configurations will be considered, system AB-TR and system AB-TT. The analytical studies showed that exclusion of the rotational connection DOF in the decoupling approaches did not produce error in the estimated FRF of system AB-TR. For this reason, only two connection DOF will be considered on system AB-TR. To obtain drive point connection measurements as well as two internal DOF, four shakers were mounted to Beam A using impedance heads to measure force and acceleration, as shown in Figure 14. The impedance heads were adhered to the middle of the beam at the internal DOF locations and directly to the threaded rod at coupling DOF using a cyanoacrylate adhesive.

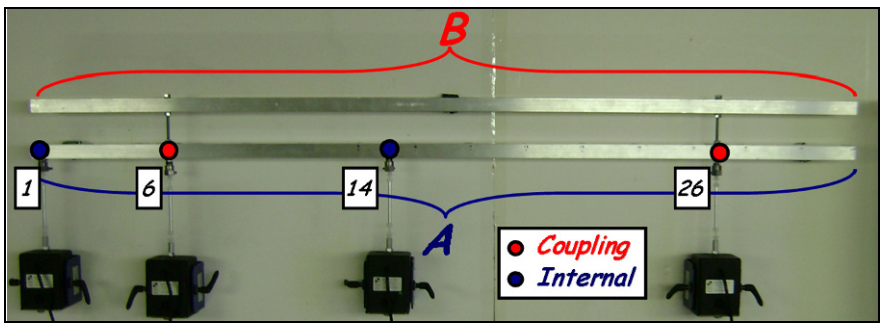

Figure 14. Shaker Test Setup for Two-Beam System AB-TR.

For system AB-TT, an impact hammer and accelerometers were used to obtain drive point measurements at all connection and internal DOF. Figure 15 displays the locations of the accelerometers at each connection. The accelerometers were mounted to the inside face of the beam using a cyanoacrylate adhesive. Drive point measurements were made using an impact hammer on the outer face of the beams, directly across from the accelerometers. Figure 16 displays the six drive point measurement locations made on system AB-TT.

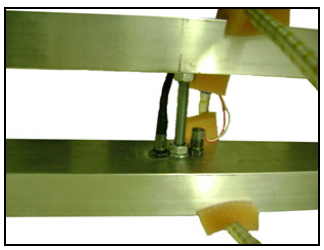

Figure 15. Connection DOF Accelerometer Configuration.

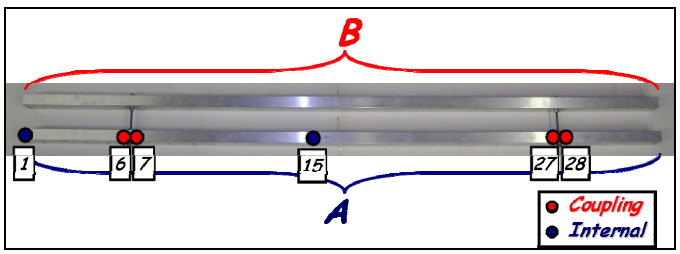

Figure 16. DOF Locations on System AB-TT.

Modal parameter estimation was performed on the measured FRF in LMS Test.Lab. The modal parameters of the first five flexible modes of the individual beams are listed in Table 7. Table 8 lists the modal parameters of the assembled system.

Table 7. Individual Beam Modal Properties from Test.

Mode	Beam A		Beam B	
	Frequency (Hz)	**Damping (% Critical)**	**Frequency (Hz)**	**Damping (% Critical)**
1	73.34	0.29	75.35	0.12
2	199.14	0.16	206.54	0.02
3	380.03	0.23	399.82	0.13
4	609.76	0.31	649.87	0.22
5	900.62	0.48	950.90	0.81

Table 8. Two-Beam System Modal Properties from Test.

Mode	System AB	
	Frequency (Hz)	**Damping (% Critical)**
1	69.20	0.32
2	80.41	0.16
3	187.10	0.21
4	210.36	0.14
5	265.99	0.14
6	391.50	0.28
7	409.60	0.20
8	630.57	0.25
9	926.96	0.74
10	1108.11	0.59

The drive point measurements on system AB-TR and AB-TT at connection node 6 are shown in Figure 17 and Figure 18, respectively.

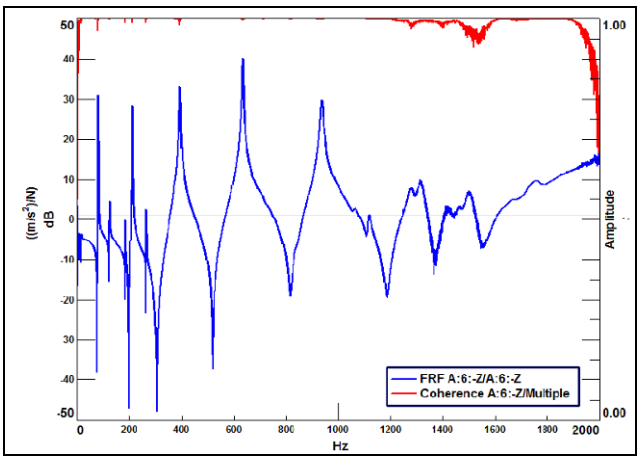

Figure 17. Typical Drive Point Measurement on AB-TR at Connection DOF.

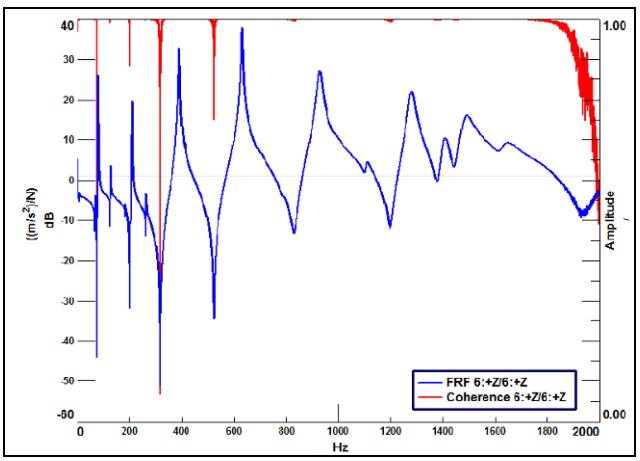

Figure 18. Typical Drive Point Measurement on AB-TT at Connection DOF.

Decoupling of System – Experimental Models

As with the analytical models, many cases were studied to better understand the characteristics of each decoupling technique. For brevity, only the most promising results for each model will be presented. In all experimental cases, the Inverse FBS technique was excluded, as this technique was shown to produce extremely poor results with the perturbed synthesized FRF.

While the measured FRF were of high quality, when used directly in the decoupling techniques the minimal noise contained in the FRF is magnified due to the matrix inversion performed in the computation. To remove this noise, modal parameter estimation was performed on all FRF in LMS Test.Lab, and new FRF were synthesized from the modal parameters using lower and upper residual compensation terms.

The resulting FRF using the Mobility and Impedance approach with only connection DOF for system AB-TR and AB-TT are shown in Figure 19 and Figure 20, respectively. Three dominant peaks can be seen in the resulting FRF for both models; however, shifts in frequencies are present. For system AB-TT, an increase in damping is also present, and the antiresonance between the second and third peak is completely distorted.

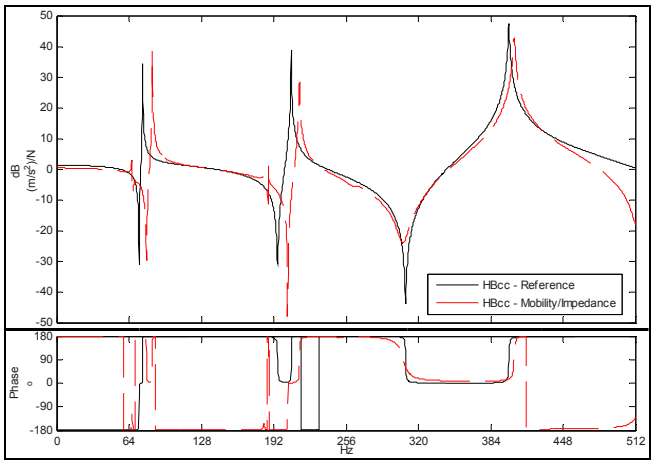

Figure 19. System AB-TR Estimation of Beam B Drive Point FRF at DOF 6 using Synthesized Test FRF.

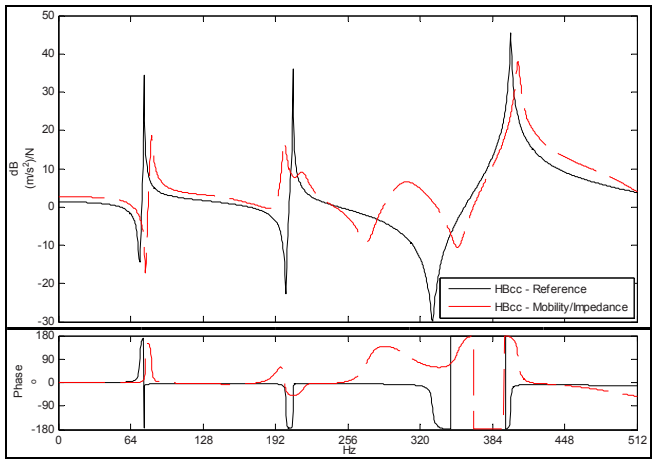

Figure 20. System AB-TT Estimation of Beam B Drive Point FRF at DOF 6 using Synthesized Test FRF.

Including either a single or both internal DOF on system AB-TR did not improve the results. However, including both internal DOF on system AB-TT significantly improves the results using the Mobility approach. Figure 21 and Figure 22 display the resulting FRF at DOF 6 and DOF 28, respectively. Discrepancies are still present in damping and antiresonance regions; however, the peaks are fairly accurate in amplitude and frequency.

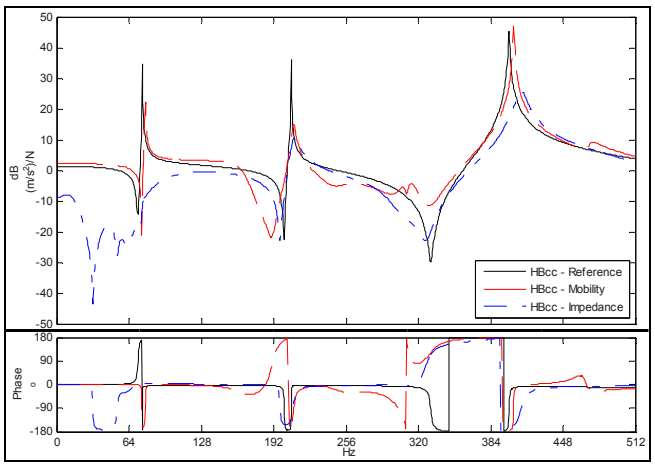

Figure 21. System AB-TT Estimation of Beam B Drive Point FRF at DOF 6 using Synthesized FRF with Internal DOF 1 and 15.

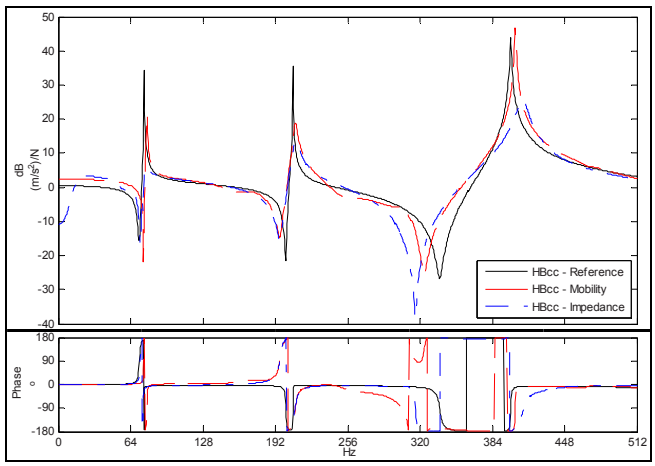

Figure 22. System AB-TT Estimation of Beam B Drive Point FRF at DOF 28 using Synthesized FRF with Internal DOF 1 and 15.

CONCLUSIONS

Frequency based decoupling techniques allow for component identification without ever taking measurements on the individual component. The Impedance, Mobility and Inverse FBS decoupling techniques were studied in this paper. Analytical and experimental models were used to determine the robustness of each technique, and attempt to address issues common with experimentally obtained FRF. All techniques produce accurate results when using pure analytical FRF, however, the Inverse FBS technique requires measurements to be on both components of the system, on opposing sides of each connection. Obtaining this measurement is very difficult if not impossible in many practical applications.

When noise is introduced to the FRF, all techniques amplify the noise due to the matrix inversions. This amplification is significantly higher with the Inverse FBS technique as multiple inversions are performed. Impedance and Mobility are especially advantageous when internal DOF are available, as this was shown to greatly improve the accuracy analytically and experimentally.

For the beam models studied in this paper, rotational DOF were address by using two translational DOF to approximate rotational DOF. While this method was shown to be a valid approximation, the rotational coupling stiffness in this model was very low and decoupling was shown to be accurate without including these DOF. Without including internal DOF, experimental model AB-TR produced more accurate results than AB-TT. However, including two internal DOF with experimental model AB-TT significantly improved the results and provided the most accurate experimental results.

RECOMMENDATIONS

Promising results have been produced using the Mobility technique with experimentally obtained FRF. However, this structure was measured in a way to represent a planar structure with only two DOF per node (translational and rotational). The connection stiffness was relatively small for the rotary stiffness when compared to the translational stiffness. Future work should address higher coupling stiffness. Also, cases should be run to address relative subcomponent size. The structure in this work was symmetrical in which modes of each of the components are approximately at the same frequencies. Future work should address the sensitivity of the Mobility approach to relative component mass and/or stiffness.

REFERENCES

1 Otte, D., “Development and Evaluation of Singular Value Analysis Methodologies for Studying Multivariate Noise and Vibration Problems”, Doctorate Dissertation, Catholic University Leuven, Leuven, Belgium, May 1994.

2 Ren, Y., Beards, C., “On Substructure Synthesis with FRF Data”, Journal of Sound and Vibration, Vol. 185, No. 5, pp. 845-866, Sept 1995.

3 Piergentili, F., “Rotational Degree of Freedom Estimation of Frequency Response Functions for Substructured Experimental Components”, Master’s Thesis, University of Massachusetts Lowell, Aug 1999.

4 Cuppas, K., Sas, P., Hermans, L., “Evaluation of the FRF Based Substructuring and Modal Synthesis Technique Applied to Vehicle FE Data”, Proceedings of the Twenty-Fifth International Seminar on Modal Analysis, Leuven, Belgium, Sept 2000.

5 De Klerk, D., Rixen, D., Voormeeren, S., Pasteuning, F., “Solving the RDoF Problem in Experimental Dynamic Substructuring”, Proceedings of the Twenty-Sixth International Modal Analysis Conference, Orlando, Florida, Feb. 2008.

6 Nicgorski, D., Avitabile, P., “Conditioning of FRF Measurements for use with Frequency Based Substructuring”, Proceedings of the Twenty-Seventh International Modal Analysis Conference, Orlando, Florida, Feb. 2009.

7 D’Ambrogio, W., Fregolent, A., “Decoupling of a Substructure from Modal Data of the Complete Structure”, Proceedings of ISMA 2008 - International Conference on Noise and Vibration Engineering, Leuven, Belgium, Sept 2004..

8 D’Ambrogio, W., Fregolent, A., “Prediction of Substructure Properties using Decoupling Procedures”, Proceedings of EURODYN 2005 – Sixth European Conference on Structural Dynamics, Paris, France, Sept 2005..

9 D’Ambrogio, W., Fregolent, A., “Promises and Pitfalls of Decoupling Procedures”, Proceedings of the Twenty-Sixth International Modal Analysis Conference, Orlando, Florida, Feb 2008.

10 D’Ambrogio, W., Fregolent, A., “Sensitivity of Decoupling Techniques to Uncertainties in the Properties”, Proceedings of ISMA 2008 - International Conference on Noise and Vibration Engineering, Leuven, Belgium, Sept 2008.

11 D’Ambrogio, W., Fregolent, A., “Decoupling Procedures in the General Framework of Frequency Based Substructuring”, Proceedings of the Twenty-Seventh International Modal Analysis Conference, Orlando, Florida, Feb 2009.

12 Gray, S., Starkey, J., “Dynamic Substructure Separation Using Physical and Modal Models”, Proceedings of the Sixth International Modal Analysis Conference, Kissimmee, Florida, Feb 1988.

13 Sjövall, P., Abrahamsson, T., “Substructure System Identification from Coupled System Test Data”, Mechanical Systems and Signal Processing, Vol. 22, No. 1, pp. 15-33, Jan 2008.

14 Voormeeren, S., Rixen, D., “Substructure Decoupling Techniques – a Review and Uncertainty Propagation Analysis”, Proceedings of the Twenty-Seventh International Modal Analysis Conference, Orlando, Florida, Feb 2009.

15 Zhen, J., Lim, T., Lu, G., “Determination of System Vibratory Response Characteristics Applying a Spectral-Based Inverse Sub-Structuring Approach. Part I: Analytical Formulation”, International Journal of Vehicle Noise and Vibration, Vol. 1, No. 1/2, pp. 1-30, 2004.

16 Zhen, J., Lim, T., Lu, G., “Determination of System Vibratory Response Characteristics Applying a Spectral-Based Inverse Sub-Structuring Approach. Part II: Motor Vehicle Structures”, International Journal of Vehicle Noise and Vibration, Vol. 1, No. 1/2, pp. 31-67, 2004.

17 Cloutier, D., “Investigation of Various System Model Decoupling Techniques”, Master’s Thesis, University of Massachusetts Lowell, May 2010

18 MATLAB R2009b, The MathWorks, Natick, Massachusetts.

19 LMS Test.Lab 9b, Leuven Measurement Systems, Leuven, Belgium.

20 FEMtools 3.1, Dynamic Design Solutions, Leuven, Belgium

Full Field Dynamic Stress/Strain from Limited Sets of Measured Data

Pawan Pingle, Peter Avitabile
Structural Dynamics and Acoustic Systems Laboratory
University of Massachusetts Lowell
One University Avenue
Lowell, Massachusetts 01854

ABSTRACT

Often times occasional events may cause significant displacement and corresponding stress strain damage to a structure. Using limited sets of measured data, expansion of real time data has been shown to provide accurate full field displacement results. This displacement data can be used in conjunction with the finite element model to identify full field dynamic stress-strain results. This approach is demonstrated for an analytical model to show the methodology proposed. Examples illustrating different configurations of measured data sets along with simulated noise are presented to illustrate the technique.

NOMENCLATURE

Symbols:

$\{X_n\}$	full set displacement vector	$[U_a]^g$	generalized inverse of reduced shape matrix
$\{X_a\}$	reduced set displacement vector	$[U_n]$	expanded shape matrix
$[M_a]$	reduced mass matrix	$[T]$	transformation matrix.
$[M_n]$	expanded mass matrix	$[T_U]$	SEREP transformation matrix.
$[K_a]$	reduced stiffness matrix	$[REF_n]$	reference data at all degrees of freedom (dofs)
$[K_n]$	expanded stiffness matrix	$[RTO_a]$	real time operating data at measured dofs
$[U_a]$	reduced shape matrix	$[ERTO_n]$	expanded real time operating data at all dofs

INTRODUCTION

Failure of a structure due to dynamic loading invariably involves occurrence of dynamic stresses and strains in the structure. The induced dynamic stresses and strains may be higher than the maximum permissible limit. Periodic estimation of such induced dynamic stresses and strains is extremely crucial for averting any dangerous accidents. Different loading conditions will impact the structure's health differently. General design processes use a factor of safety to counter the problem of keeping the induced stresses and strains within the permissible limits. However, there is no accurate way to estimate the remaining fatigue life of the structure especially when occasional, unexpected locating conditions occur. To accurately predict the remaining useful life of a structure, correct estimation of dynamic stresses and strains induced in the structure is of prime importance.

There are primarily two approaches traditionally used to evaluate such transient stresses in structures. The first approach would be to collect the transient response information at limited locations. Such a process, although predicts the real-time response of the structure under severe dynamic loadings, but does so at only limited locations. Massive structures such as

T. Proulx (ed.), *Linking Models and Experiments, Volume 2*, Conference Proceedings of the Society for Experimental Mechanics Series 5,
DOI 10.1007/978-1-4419-9305-2_13, © The Society for Experimental Mechanics, Inc. 2011

bridges, ships, wind-turbines would need thousands of sensors to get the required data, which is highly improbable and unfeasible. The second approach would be to predict the transient forces that the structure experiences and then using the analytical model find the dynamic stresses the structure experiences. The problem herein lies with the force estimation process which is highly sensitive to the number of chosen degrees of freedom and their distribution on the structure. Apart from this, the other issues such as approximations while developing a finite element model invariably induce errors in estimation of dynamic stresses on the structure.

The approach used in this paper has been introduced in [1] where full-field real-time displacements were obtained successfully from limited sets of displacement data using a real time operating data expansion technique recently studied by Chipman [2]. The limited set of sensors would provide displacement data and the expansion algorithm would expand the limited data set to a full-field displacement solution thereby completely eliminating the force estimation step required in the previous approach. In this paper, the full-field displacements are used to obtain full-field dynamic stress strain information. The estimated dynamic stress-strains using this approach are then compared with reference stress-strain solutions to validate the proposed approach.

THEORY

The approach presented in this work is conceptually explained in the schematic shown in Figure 1. Traditional finite element design process involves discretization of the component into elements, assembling the system matrices and applying appropriate approximations of boundary conditions and loading to estimate the dynamic stress-strain that the component sees throughout the designed life of the component/structure. The approach presented in this work involves collecting experimental displacement data at limited measurable locations, then a real-time operating data expansion technique is used to expand the limited displacement data set to full-field displacements. The expansion technique uses mode shape information which is obtained from the analytical model of the structure.

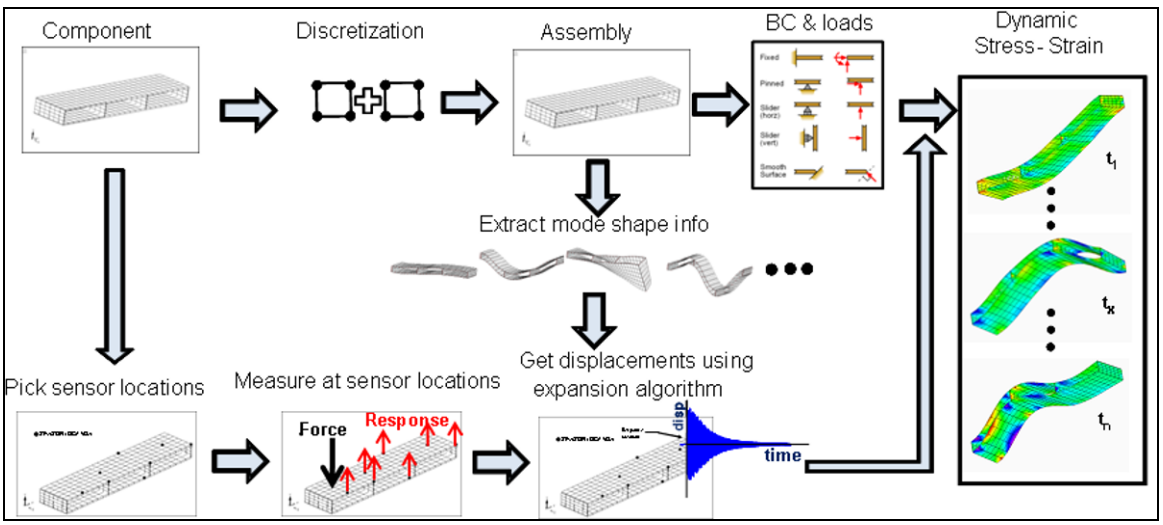

Figure 1: Schematic showing various design approaches to estimate dynamic stress-strain

Finally the full-field displacement data set is used to recover the dynamic stress-strain information by using back-substitution process shown in Figure 2. The finite element process is interrupted to incorporate the expanded full-field displacement solution in order to obtain the full-field dynamic stress-strain solution. In Figure 2, the full-field strain solution is shown at one time step; however, the full-field strain solution is obtained for all the required time steps through the recovery process.

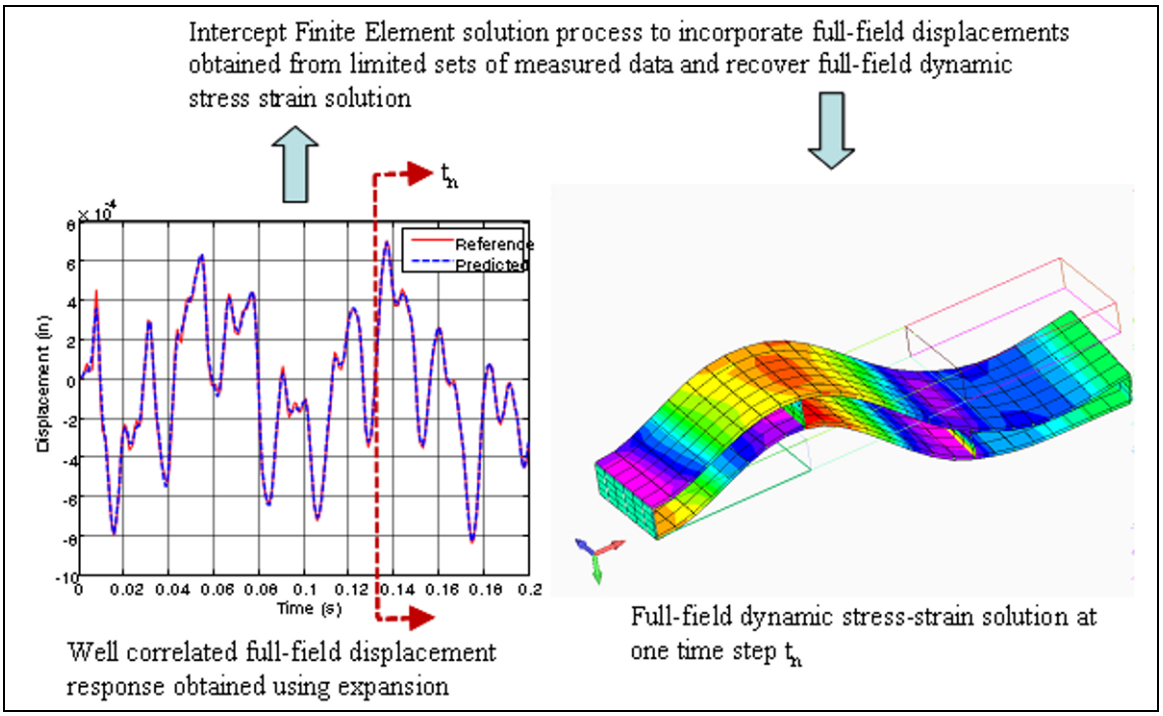

Figure 2: Recovery of dynamic stress-strain from full-field displacement data

MODEL REDUCTION

Model reduction is necessary in order to develop expansion approaches for modal data for the unmeasured translational DOF as well as for rotational DOF. For this work, the expansion is needed for augmenting the limited set real-time operating data to provide a full field displacement solution. The reduction techniques are the basis of the expansion discussed in this work. These techniques have been presented in earlier work cited in the references; only summarizing equations are presented below. Several model reduction methods have commonly been used for expansion of measured data. Four common methods are Guyan [5], Dynamic Condensation [6], SEREP [7], and a Hybrid method [8]. In these methods, the relationship between the full set of degrees of freedom and a reduced set of degrees of freedom can be written as

$$\{X_n\}=[T]\{X_a\} \tag{1}$$

All of these methods require the formation of a transformation matrix that can project the full mass and stiffness matrices to a smaller size. The reduced matrices can be formulated as

$$[M_a]=[T]^T[M_n][T] \tag{2}$$

$$[K_a]=[T]^T[K_n][T] \tag{3}$$

For the specific work in this paper, only the SEREP method has been used for the expansion of mode shapes.
The System Equivalent Reduction Expansion Process (SEREP) produces reduced matrices for mass and stiffness that yield the exact frequencies and mode shapes as those obtained from the eigensolution of the full size matrix. The SEREP transformation is formed as

$$[T_U]=[U_n][U_a]^g \tag{4}$$

The SEREP transformation is developed with analytical mode shapes for the structure (but can also be evaluated using measured modal vectors as well as done in Chipman's work [2]).

Equation 1 is used for expansion of real-time operating data and is written as

$$[\mathrm{ERTO}_n] = [\mathrm{T}][\mathrm{RTO}_a] \tag{5}$$

CORRELATION TOOLS

The correlation tools utilized to compare the results of the expanded RTO [ERTO_n] and "reference time solution" [REF_n] are briefly discussed here in order to help clarify the differences between the techniques. Correlation tools such as, the Modal Assurance Criterion (MAC) [9] and the Time Response Assurance Criterion (TRAC) [10] will be used to verify the accuracy of the expanded RTO in each case. These functions are summarized here with details found in [2]. The MAC as used for this work will identify the correlation of the expanded real time operating displacement solution obtained with the reference solution. The MAC can be computed at each time step t to compare the transient displacement solution with time. The MAC is written as

$$\mathrm{MAC\_RTO} = \frac{\left[\{\mathrm{REF}_n\}^{\mathrm{T}}\{\mathrm{ERTO}_n\}\right]^2}{\left[\{\mathrm{REF}_n\}^{\mathrm{T}}\{\mathrm{REF}_n\}\right]\left[\{\mathrm{ERTO}_n\}^{\mathrm{T}}\{\mathrm{ERTO}_n\}\right]} \tag{6}$$

Similar to the MAC, the TRAC is a tool used to determine the degree of correlation between two time traces. For the cases presented here, the TRAC is the correlation for one DOF over all time for the expanded time data [ERTO_n] compared to the actual measured data [REF_n]. The TRAC is written as

$$\mathrm{TRAC\_RTO} = \frac{\left[\{\mathrm{REF}_n(t)\}^{\mathrm{T}}\{\mathrm{ERTO}_n(t)\}\right]^2}{\left[\{\mathrm{REF}_n(t)\}^{\mathrm{T}}\{\mathrm{REF}_n(t)\}\right]\left[\{\mathrm{ERTO}_n(t)\}^{\mathrm{T}}\{\mathrm{ERTO}_n(t)\}\right]} \tag{7}$$

The values produced by both the MAC and TRAC will range from 0 to 1; values approaching 1 indicate good correlation. A schematic is shown in Figure 3 showing the MAC and the TRAC correlations. Typically, the TRAC is comparison of the displacement - time response solutions (predicted and reference solutions) while the MAC is comparison between the deformed shape of the structure at each time instant as shown in Figure 3.

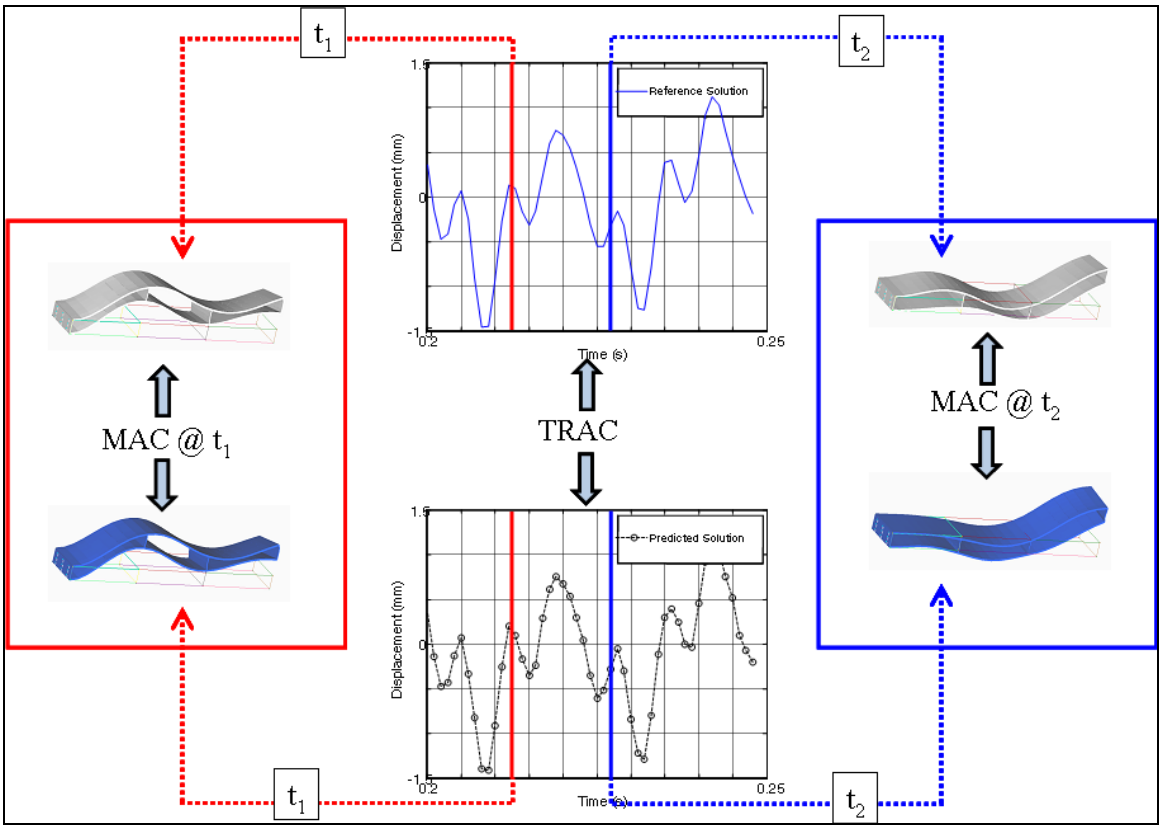

Figure 3: Schematic showing MAC and TRAC

MODEL DESCRIPTION

To demonstrate the expansion technique to be used for determining displacement for dynamic stress and strain from limited sensor locations, an analytical study was performed on a model that resembles typical blade construction of a wind turbine. The box-beam model used for analysis is shown in Figure 4a. The dimensions of the model are:

1. Length (l) = 60 inches
2. Breadth (b) = 12 inches
3. Width (w) = 6 inches
4. Thickness of top and bottom plates (t_1) = 0.5 inches
5. Thickness of internal ribs (t_2) = 0.25 inches
6. Material – Aluminum

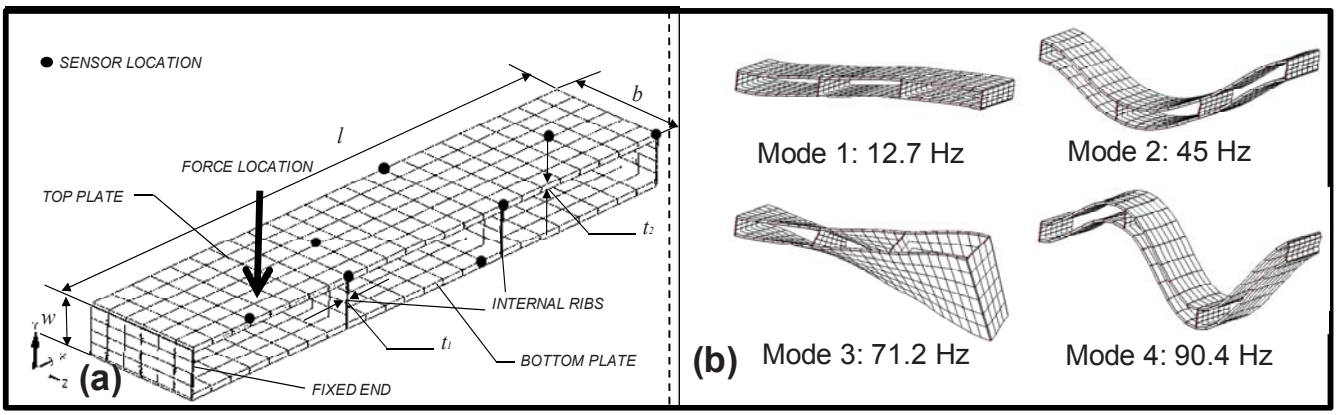

Figure 4: (a) Box-beam model used for analytical study of the expansion algorithm along with typical set of sensor locations; (b) First four mode shapes of the structure.

The finite element model of the box-shaped structure contains a total of 434 nodes. The natural frequencies and mode shapes of the beam are shown in Figure 4b. The frequencies typically are well separated. The model has an assortment of modes containing transverse and lateral bending and torsion modes which will be excited using a time pulse where, primarily, the first four frequencies are excited.

Modal damping typically seen in these types of structures was added to the model. The excitation used was a time pulse applied vertically downwards, 10 inches from the bottom right corner of the box-beam. The input time pulse is shown in Figure 5a. The time pulse is a combination of two triangular functions which when seen in frequency domain show a very uniform excitation over the frequency range of interest as shown in Figure 5b. The time pulse primarily excites the first four modes of the structure as seen in FFT of the output response as shown in Figure 5c, but there is also some additional response of smaller magnitude from several higher frequencies.

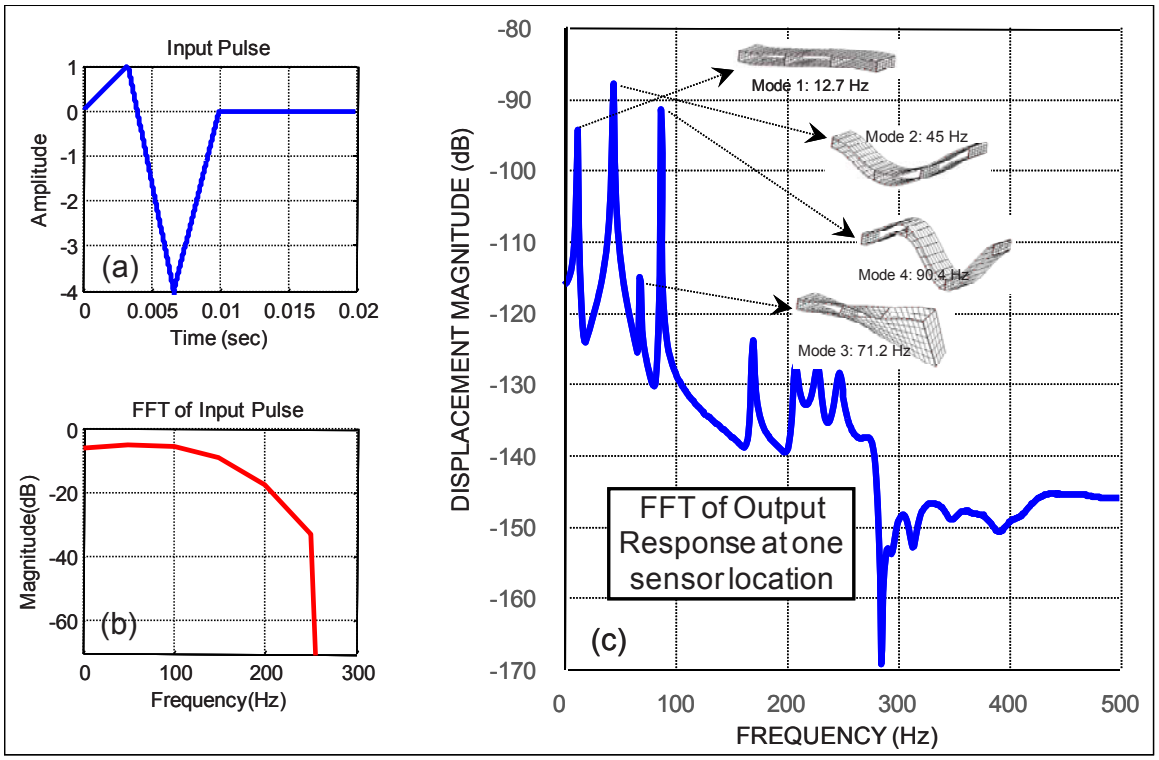

Figure 5: Details of the excitation force and response of the structure.

CASES STUDIED

The comparison between reference solution and expansion solution is made in this section. Several different analytical cases have been studied to evaluate the effectiveness of the proposed expansion algorithm. The cases studied are based on some important factors that affect the implementation of the technique. The cases studied in this section are based on three important factors that need to be considered for successful implementation of proposed approach:

1. Number of modes used in expansion process.
2. Effect of different noise levels on solution obtained through proposed technique.
3. Different sensor configurations used for obtaining full-field expanded data set.

Foremost among the prominent factors affecting the expansion solution is the number of modes used in the expansion algorithm. Theoretically, there is no upper limit for the number of modes to be used for expansion, but from a practical standpoint only a limited number of modes can be used for expansion. The Case 1 deals with the study of the number of modes used for expansion.

Different noise levels have been studied in Case 2 to gage the performance of the expansion algorithm in the presence of noise. Noise is another important issue that has been shown to have an affect on the successful implementation of the expansion algorithm.

Case 3 discusses the different sensor configurations and their effect on the solution obtained through expansion algorithm. The sensors used for obtaining the real-time data (adof measurements), invariably plays an important role in accuracy of the solution.

CASE 1

For obtaining full-field displacement response from limited sets of displacement data, using real-time operating data expansion technique, the formulation of the expansion transformation matrix is known to be an important factor. The transformation matrix for SEREP expansion technique is formulated using mode shape information. The expansion transformation matrix should contain at least those structure modes which are primarily excited. For reference, the displacement response solution obtained using limited sets of displacement data is shown for typical response locations (tip and interior of the box-beam) in Figure 6. Note that the full-field displacement solution obtained from limited sets of displacement data has been discussed in detail in [1]. The first six modes were used in formulation of expansion transformation matrix. As observed in Figure 6, the expansion solution matches well with the reference solution with TRAC values of 99.9+% showing that the prediction of full-field displacement response through the expansion process is very accurate.

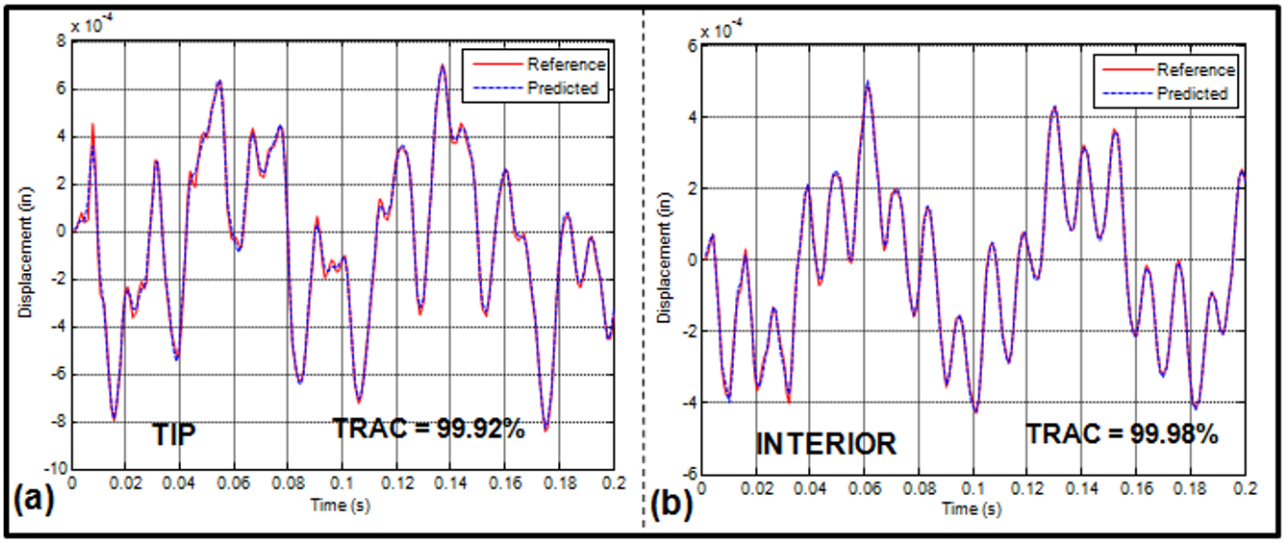

Figure 6: Overlay of the displacement response from reference and predicted solution using first six modes for expansion; (a) response location on the top plate, (d) response location inside the rib.

The full-field displacements obtained from using first six modes are used for obtaining dynamic strain solution. This predicted dynamic strain solution (Y normal strain) is shown in comparison with reference strain solution in Figures 7a & 7b with response location at the tip of the box-beam and in the rib of the box-beam respectively. Recall that the force pulse primarily excites the first four modes of the system. Only 14 y (vertical) direction points of a total of 434 finite element model nodes were used as sensor locations measuring vibration displacement response. The strain response is shown for a sample time period of 0.05 seconds. Although the full-field displacements obtained using first six modes provided excellent correlation with reference displacement solution, the full-field strain results obtained after incorporating the six-mode full-field displacement solution is not as good as expected (Figures 7a &b) because the strain solution is more sensitive than the displacement solution due to the contribution from higher modes. However when the full-field displacement solution obtained from using first ten modes is used to obtain the full-field dynamic stress-strain solution then excellent correlation is seen with reference strain solution as seen in Figures 8a & b. This trend is more prominent for higher strain regions (strain in the rib) as seen from Figures 7b & 8b.

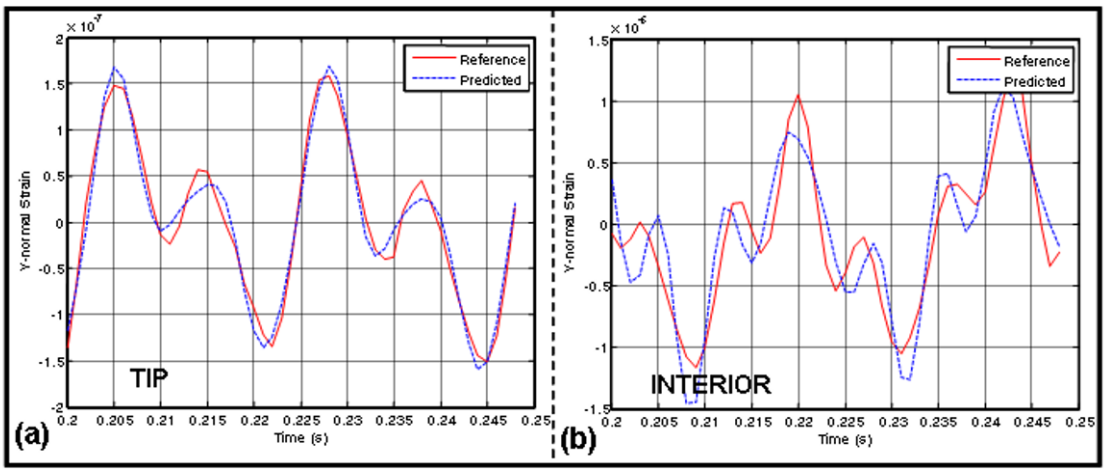

Figure 7: Overlay of strain response of box-beam at (a) tip and (b) interior location; predicted solution used first 6 modes in expansion process.

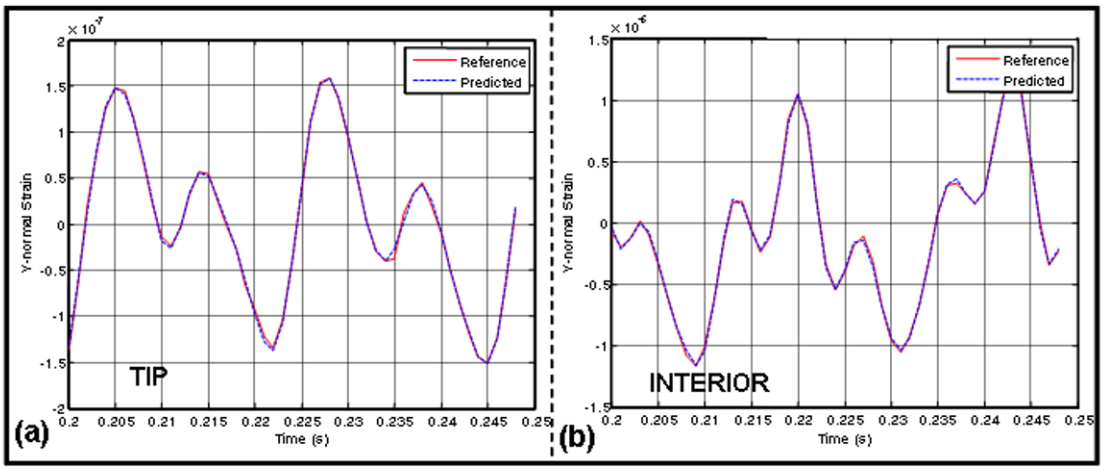

Figure 8: Overlay of strain response of box-beam at (a) tip and (b) interior location; predicted solution used first 10 modes in expansion process.

To study the sensitivity of strain solution in detail, the displacement solution correlation was performed. Figure 9a, b &c shows the MAC for displacement solution between the predicted and reference model responses for time period corresponding to the strain time period (0.2 – 0.25 seconds). The MAC plots are shown for three different mode configurations – using first six, eight and then ten modes in expansion solution. The MAC for all the three mode configurations is very good because they all over-specify the required number of modes for expansion (recall that the forcing pulse excites first four modes primarily). So to show the difference between six, eight and ten mode configuration, the MAC plots are shown from 0.9 -1 indicating that the MAC for that particular time period is better than 90% always. Notice that even though with six-mode configuration, the displacement responses show good correlation (better than 90%), the correlation however improves with eight and ten-mode configuration confirming that greater number of modes used in the solution process will always yield better expansion results. Therefore, as a general rule, more modes will be required especially when considering strain rather than displacement.

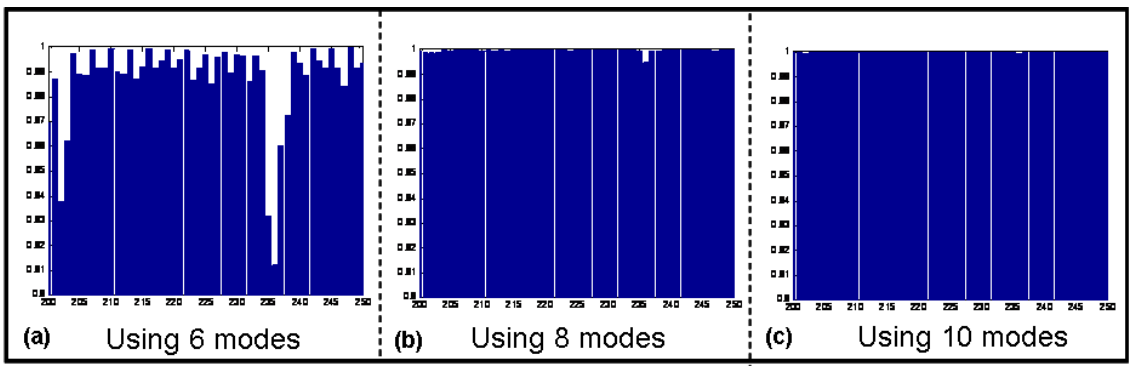

Figure 9: MAC between displacement response vectors of reference and expansion algorithm solutions with different number of modes used for expansion, (a) using first 6 modes (b) using first 8 modes, (c) using first 10 modes in expansion process; MAC performed for time steps 200-250 and shown for 0.9 – 1.

CASE 2

Experimental noise is a very common phenomenon which corrupts the data. While collecting experimental data, the noise component is always inevitable. To study the expansion technique realistically, some random noise is added to the base-line measurements using

$$\{Noise\ \ Induced\ \ Measurement\} = \{Original\ \ Measurement\} + r\{maximum\ \ amplitude\ \ of\ \ measurment\} \qquad (8)$$

where, r is random set of numbers ranging from -1% to +1% of the maximum amplitude of measurement. Figure 10 shows the noise induced in the model to simulate experimental conditions.

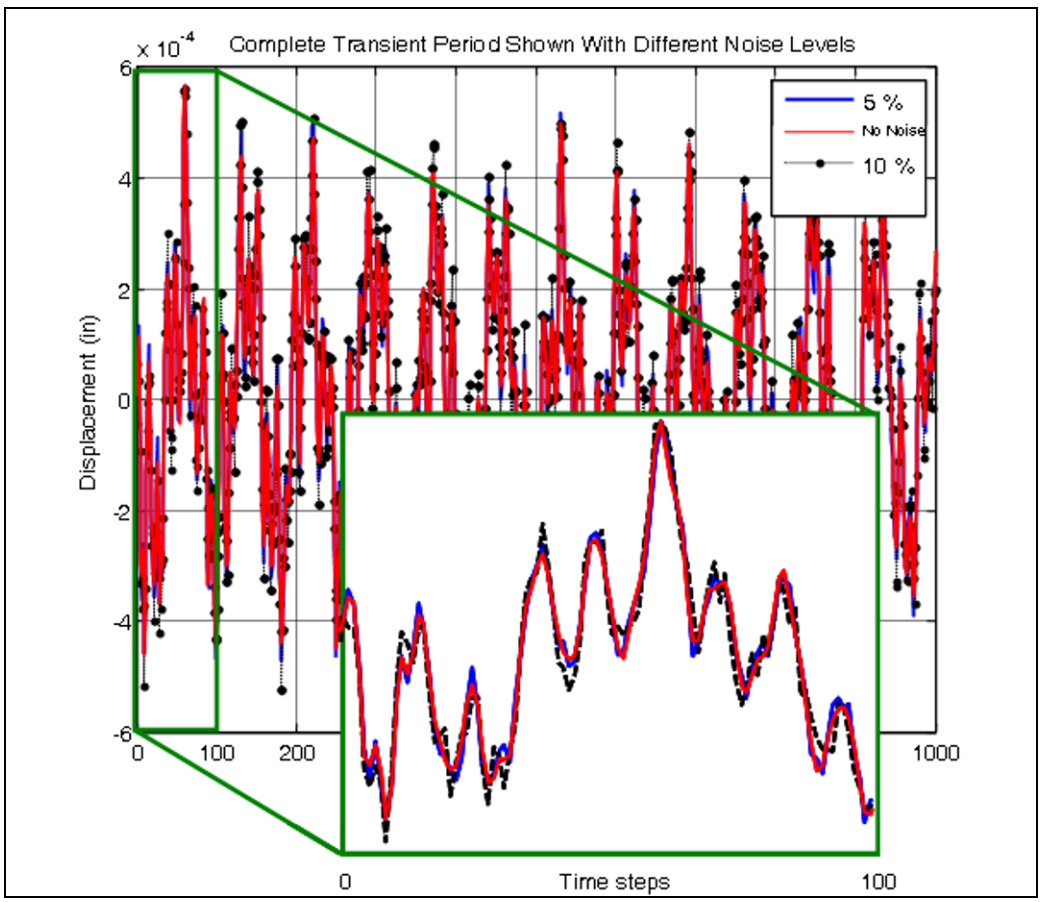

Figure 10: Effect of different noise levels (5% and 10%) on displacement-time response.

Case 1 showed the expansion algorithm to be an accurate tool when appropriate number of modes are used for expansion. However, the expansion algorithm could also be affected by noise as shown in Figure 10. A varying percentage of noise was added on the model used in Case 1 to simulate the experimental conditions of real-time data acquisition; noise levels ranging from typical levels of noise (5%) and higher levels of noise (10%) were studied. The full-field displacement solution was obtained from the noisy adof measurements through expansion. The full-field displacements thus obtained were then back-substituted into the finite element process to recover the stress-strain solution. The dynamic strain solution for 5% noise on adof measurements is shown in Figure 11 and the strain solution for 10% noise case is shown in Figure 12. Comparison is made between the predicted strain solution with reference solution at two typical response locations (at the tip and at an interior location in the rib of the box beam). As seen from Case 1, more than 6 modes are needed for accurate expansion results for predicting strain. Hence first ten modes of the structure were used in expansion process for obtaining the full-field displacement solution. As seen from Figure 11, addition of low levels of noise (up to 5%) did not significantly

impact the strain prediction using proposed technique. However, the solution starts to degrade with higher levels of noise, especially for high strain regions as seen from Figure 12b.

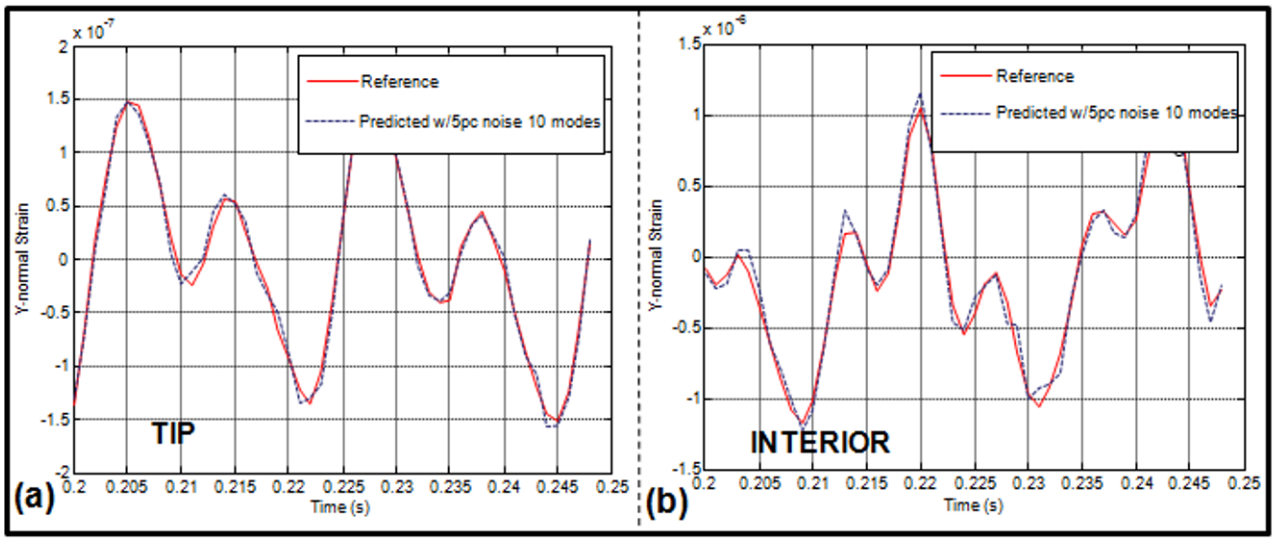

Figure 11: Overlay of strain response of box-beam at (a) tip and (b) interior point; comparison made between reference solution and predicted solution with 5% noise.

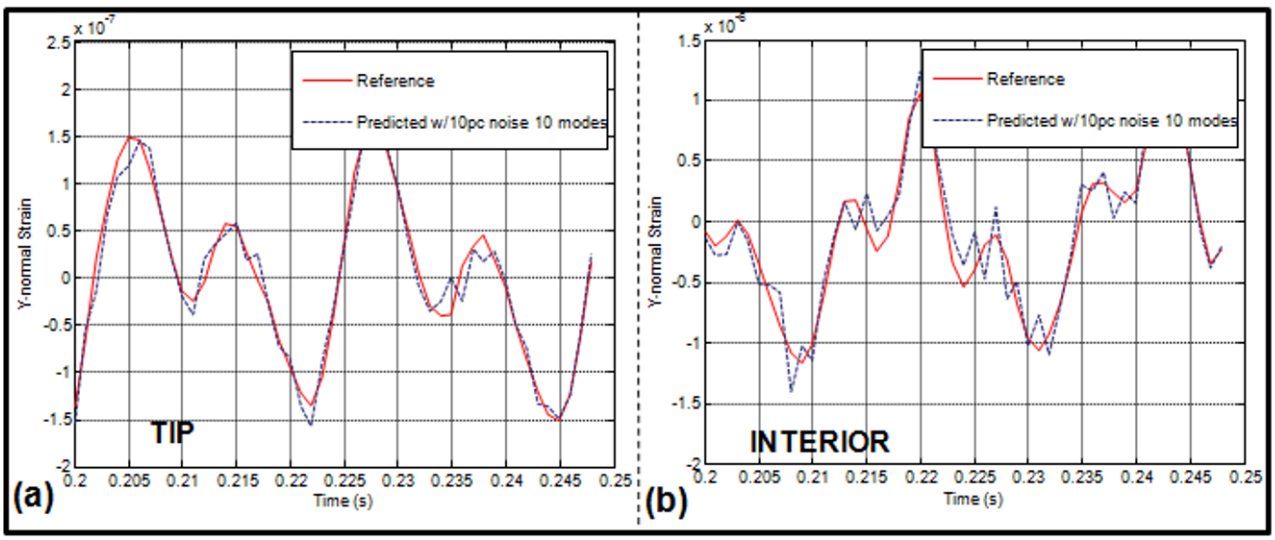

Figure 12: Overlay of strain response of box-beam at (a) tip and (b) interior point; comparison made between reference solution and predicted solution with 10% noise.

CASE 3

There were 14 adof simulated measurements used for expansion up to 434 nodes for all the cases discussed in this paper. In case 3, 10 redundant sensor measurements are simulated in addition to the 14 adof simulated measurements to study the effect of greater number of sensors on the strain prediction. A total of 24 sensors are used for generating simulated adof measurements. The 14 and 24 sensor set-ups are shown in Figure 13. Notice that the 24 sensor set-up has sensors located somewhat redundantly at locations that are considered to be critically important locations for expansion. Redundant

information at strategically important locations will ensure that important information is not lost during actual experimentation.

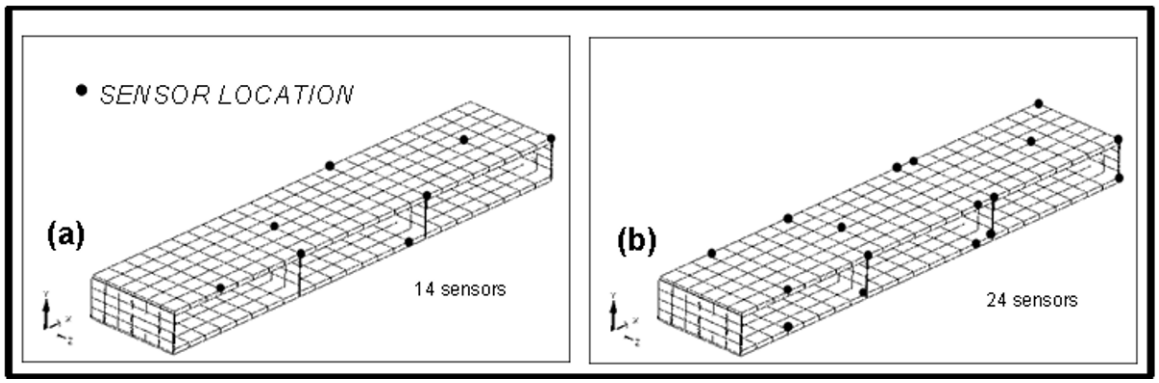

Figure 13: Different sensor locations used to determine the response of the structure using expansion algorithm at all 434 FEA node locations, (a) 14 sensors, (b) 24 sensors.

Figures 14 and 15 show comparison between predicted and reference Y normal strain solution for 14 sensor (a) and 24 sensor (b) set-ups at the tip and inside the box-beam, respectively. Observe that the 24 sensor set-up show slight improvement in the strain prediction as compared to the 14 sensor set-up. However, none of the sensor set-ups provide accurate strain prediction because only the first six modes are used in the expansion process. Recall that for accurate strain prediction, more than six modes were shown to be required in case 1. This indicates that use of more number of sensors does not necessarily satisfy the requirement of use of greater number of modes (more than six modes) in the expansion process. However, in general, use of redundant sensors at strategically important locations could be beneficial from a practical stand-point.

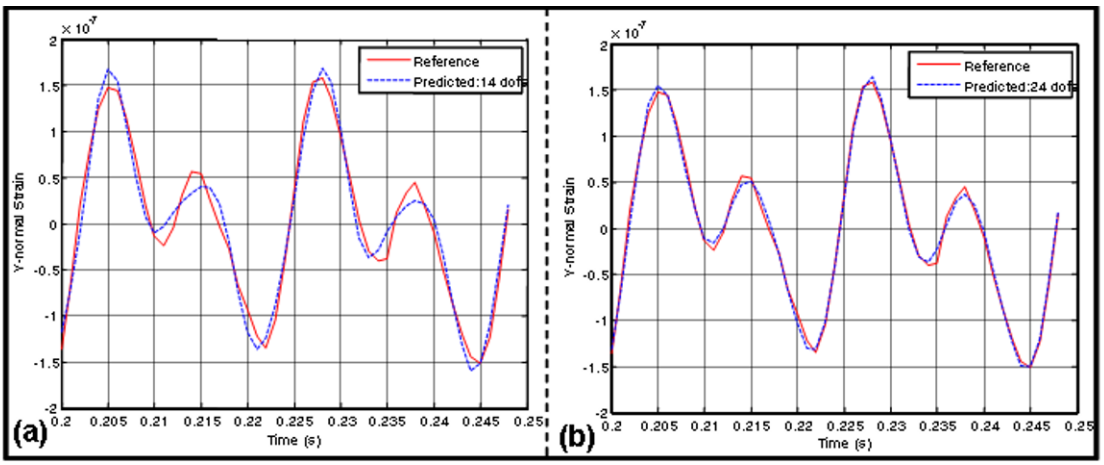

Figure 14: Strain response comparison at the tip of the box-beam by reference and predicted solutions using first six modes for expansion, (a) with 14 sensors, (b) with 24 sensors.

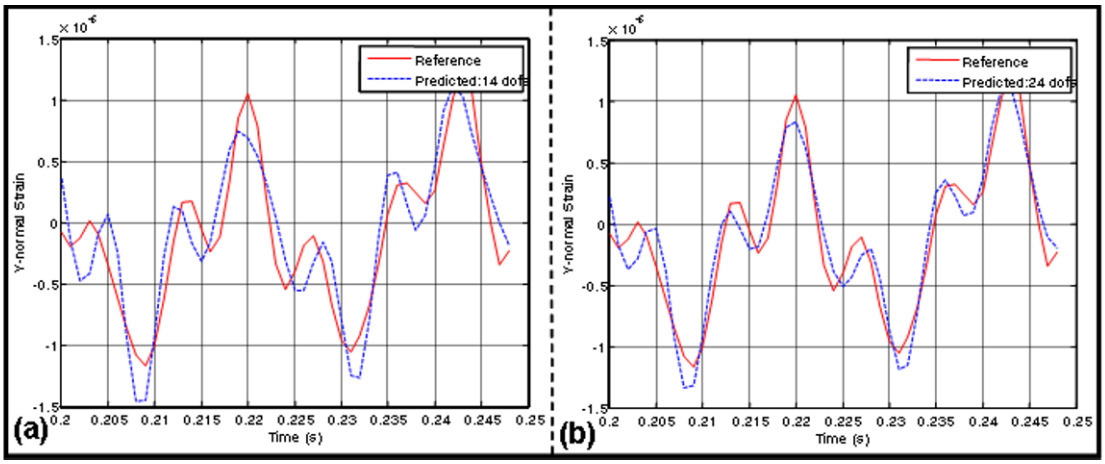

Figure 15: Strain response comparison at an interior location of box-beam by reference and predicted solutions using first six modes for expansion, (a) with 14 sensors, (b) with 24 sensors.

CONCLUSION

Using a limited set of measured responses, full field displacement can be obtained using an expansion procedure. The measured response can then be used in the finite element recovery process to obtain full field dynamic stress-strain due to any measured loading condition.

Several cases were investigated to show the accuracy and robustness of the expansion procedure. The expansion procedure will produce accurate results provided that there are a sufficient set of orthogonal mode shapes to span the space for the solution; this requires that a sufficient number of modes that participate in the response be included in the expansion process. Noise presents variation in the results but from the cases studied, significant noise did not seriously contaminate the results obtained. In terms of the limited set of measurement points, there must be sufficient number of measurement locations available for proper expansion. Use of redundant sensors can be an advantage from a practical perspective; however, use of more sensors does not satisfy the requirement for use of proper number of modes in expansion process.

REFERENCES

[1] Pingle, P., Avitabile, P., “Prediction of Full Field Dynamic Stress/Strain from Limited Sets of Measured Data”, Proceedings of the Twenty-Eight International Modal Analysis Conference, Jacksonville, FL, Feb 2010

[2] Chipman,C., “Expansion of Real Time Operating Data”, Master’s Thesis, University of Massachusetts Lowell, May 2009

[3] C.Chipman, P.Avitabile, “Expansion of Real Time Operating Data for Improved Visualization”, Proceedings of the Twenty-Sixth International Modal Analysis Conference, Orlando, FL, Feb 2008

[4] C.Chipman, P.Avitabile, “Expansion of Transient Operating Data”, Proceedings of the Twenty-Seventh International Modal Analysis Conference, Orlando, FL, Feb 2009

[5] Guyan, R.J., "Reduction of Stiffness and Mass Matrices", AIAA Journal, Vol. 3, No 2, 1965

[6] Paz, M, "Dynamic Condensation", AIAA Journal, Vol22, No 5, May 1984

[7] O'Callahan,J.C., Avitabile,P., Riemer,R., "System Equivalent Reduction Expansion Process", Seventh International Modal Analysis Conference, Las Vegas, Nevada, February 1989

[8] Kammer, DC, "A Hybrid Approach to Test Analysis Model Development for Large Space Structures", Journal of Vibration and Acoustics, Vol 113, July 1991

[9] Allemang,R.J. and Brown,D.L., "A Correlation Coefficient for Modal Vector Analysis", First International Modal Analysis Conference, Orlando, Florida, November 1982, pp. 110-116

[10] Van Zandt, T., “Development of Efficient Reduced Models for Multi-Body Dynamics Simulations of Helicopter Wing Missile Configurations,” Master’s Thesis, University of Massachusetts Lowell, April 2006.

[11] Pingle, P., "Prediction of Full-Field Dynamic Stress-Strain from Limited Sets of Measured Displacement Data", PhD. Thesis (submitted), University of Massachusetts Lowell, 2010.
[12] Avitabile,P., Piergentili,F., Lown,K., "Identifying Dynamic Loadings from Measured Response", Sound & Vibration, August 1999
[13] MATLAB R2008b – The MathWorks, Natick, Massachusetts
[14] Femap – Finite Element Modeling And Postprocessing, Version 9.3.1, Copyright © 2007 UGS Corp.

Limited Experimental Displacement Data used for obtaining Full-Field Dynamic Stress Strain Information

Pawan Pingle, Peter Avitabile
Structural Dynamics and Acoustic Systems Laboratory
University of Massachusetts Lowell
One University Avenue
Lowell, Massachusetts 01854

ABSTRACT

Full field displacement and full-field dynamic stress-strain information has been shown to be estimated accurately from limited sets of data using an expansion algorithm through analytical simulations. Experimental data is collected and used for the dynamic expansion process to predict dynamic stress-strain for a candidate structure. Experimental measurements are obtained in a controlled study using an impact excitation technique. Displacement data at limited locations is collected using dynamic photogrammetry and digital image correlation techniques. The full-field expanded displacement data is compared and validated with a reference solution. This full-field displacement data is then used to identify the dynamic stress-strain to show the usefulness of the technique.

NOMENCLATURE

Symbols:

$\{X_n\}$	full set displacement vector	$[U_a]^g$	generalized inverse of reduced shape matrix
$\{X_a\}$	reduced set displacement vector	$[U_n]$	expanded shape matrix
$[M_a]$	reduced mass matrix	$[T]$	transformation matrix.
$[M_n]$	expanded mass matrix	$[T_U]$	SEREP transformation matrix.
$[K_a]$	reduced stiffness matrix	$[REF_n]$	reference data at all degrees of freedom (dofs)
$[K_n]$	expanded stiffness matrix	$[RTO_a]$	real time operating data at measured dofs
$[U_a]$	reduced shape matrix	$[ERTO_n]$	expanded real time operating data at all dofs

INTRODUCTION

Generally, a structure is designed for many loading conditions including fatigue. The structure is considered to be safe under a certain number of loading cycles. But there are certain transient events that are difficult to model. These transient events can severely limit the structure's fatigue life such that the structure might fail in fatigue much below the expected designed life. Examples of such transient events could be sudden gust of wind on a turbine blade or a helicopter hard-landing or a barge striking a bridge. The main emphasis of this work is directed towards blade type structures but the techniques developed can be applied to a variety of different types of structures.

Continuous or periodic monitoring is required to assure the health of such structures to understand the effect of these types of transient events. Typically, only a handful of sensors are available for the evaluation of these rare, short-term events. This limited data does not always provide the details necessary in order to determine the effects of the events that occur, especially in terms of the overall fatigue usage for the system. Generally, a finite element model may be available but use of this limited data does not lend itself to easily integrate into the identification of the dynamic stress and the dynamic strain.

T. Proulx (ed.), *Linking Models and Experiments, Volume 2*, Conference Proceedings of the Society for Experimental Mechanics Series 5,
DOI 10.1007/978-1-4419-9305-2_14, © The Society for Experimental Mechanics, Inc. 2011

A newly developed real time operating data expansion technique [1-5] has been successfully used for the identification of more detailed information from limited sets of data. This expansion has mainly been used to augment the limited data acquired and allows for better overall visualization of these transient types of events. This technique has mainly been used for general response characteristics for structures.

In this work, these expansion techniques are further developed and extended in conjunction with the finite element mass and stiffness matrices to provide information at all of the finite element DOFs from these limited sets of measured data points. This allows for the identification of the dynamic stress and the dynamic strain to be identified from measured transient events, thereby enabling the estimation of fatigue accumulation or usage.

One way to predict the transient response and the associated dynamic stresses in the structure is to use the finite element analysis. An accurate model renders the finite element method of analyzing the dynamic stresses and strains extremely useful. But one of the challenges with the finite element analysis is correctly depicting the boundary conditions that the structure will undergo during operation. Also there is no accurate way to exactly represent the transient loads (for example, the wind loads) on the structure. Statistical and probabilistic approaches have to be used to estimate the forces that the structure undergoes during such transient events, but does not provide information due to specific events.

Finite element models have been used over the years to estimate the stresses induced in a component due to dynamic loads. Most of the work published in this area has been application oriented. Among such works, one which deals with the issue of dynamic stresses from a broader perspective using a modal analysis technique is presented in [6]. The failure of a mechanical component is examined by performing modal analysis using the finite element approach and then evaluating stresses in the component using a boundary element approach in [6]. Super-element method and global-local approach have also been used in the finite element modeling domain to enhance the accuracy of the models [7]. A finite element model is used as the base model to generate transient response of a vehicle body structure and then using the Modal Stress Method (for estimating global stress distribution) and the Component Mode Synthesis (for local stress time history), the fatigue life of the structure is estimated by Huang et al., [8]. Dynamic stresses in a structure have also been obtained from measured acceleration data using the normal mode analysis in [9]. In such a case, only a limited number of sensors provide the stress information, and are not always able to show critical stress concentration or accumulation.

From their inception in the early 80's, wind turbines have experienced fatigue problems. Virtually all the turbines built in California have experienced fatigue problems in sites with an average wind speed of 7 m/s or more. Blades have been repaired or replaced on most of the turbines. This led the wind energy community to study the fatigue life and probability of failure extensively [10, 11]. Several approaches have been developed [12], [13] and [14] to represent a structure's fatigue. Typically wind loads are estimated using the parametric or empirical modeling approaches [15]. Parametric models define the response, statistically with respect to the input conditions. Such models fit analytical distribution (Rayleigh or exponential fit) functions to the measured or the simulated data. The parameters of these distribution functions can be useful in defining the response/loads as a function of the input conditions. The end result then is a full statistical definition of the loads over all input conditions. The problem is that the Rayleigh distribution appears to be appropriate only for a single location on a single type of wind turbine (flatwise loads on vertical axis wind turbines). The exponential fit is rather complex in the sense that the starting point of the exponential fit is not very clear. Also as observed in [16], the exponential fit is not always the appropriate choice. The most prevalent alternative to parametric modeling is an empirical distribution of loads (a histogram describing frequency of occurrence of the modeled response quantity). For empirical models, the results of one ten-minute simulation for each wind speed bin are "cycle counted" and the number of cycles are multiplied by 20 year duration to extrapolate the fatigue loads to 20 years. According to [17], this method is flawed in at least two ways. First, it does not account for rare events and second, because the simulations do not capture accurate extreme statistics they do not estimate the peak load which will occur over the operating life of the machine.

A modal superposition method is used in [18] to resolve the forced vibration equation for a finite element model so as to use it to calculate the corresponding stress values. Estimating the damping values in the model can create problems in such a technique. Work has been done to evaluate the stress concentration regions and to estimate the stress-strain using different techniques. Dynamic forces and the stresses can be calculated [19] using a static model and a dynamic correction factor based on the modal accelerations at small number of the modal DOFs. Strain measurements taken at certain locations in a structure are used to analytically synthesize the frequency responses at those locations where no data was collected by Powell [20]. Using the stress-strain information, the decision on where to make structural modification is made. Blade element theory [21] is used to calculate the aerodynamic loads for small wind turbine blades. Using the load information

and a finite element model, the dynamic stresses are computed at the root region of the blades. Such work can only estimate the local stress, but the full-field information is not available.

The next section will describe the relevant theory required for understanding the proposed technique introduced for estimating dynamic stress-strain.

THEORY

The traditional design process relies on the general development of a finite element model, the assembly of the system matrices, the application of loads and the boundary conditions followed by the solution of the set of equations and the recovery of the stress-strain solution as shown in Figure 1. Along with being challenging to accurately depict the transient events, the traditional design process also has other issues, such as the actual loading is not known and the actual boundary conditions are not well understood.

Figure 1: Schematic Showing Normal Finite Element Model Development

For the approach considered in this work, the difference is that the actual application of the loads and the boundary conditions is not specifically performed. Rather, the sparse set of displacements, measured from an actual operating event, is used with a set of orthogonal expansion functions to obtain the full field displacement solution. This displacement solution is then used with the normal back substitution and recovery of the stress-strain solution in the finite element modeling process. This procedure is shown schematically in Figure 2 where the limited set of measurement DOFs are used with the expansion processes to obtain the full field displacement for the system.

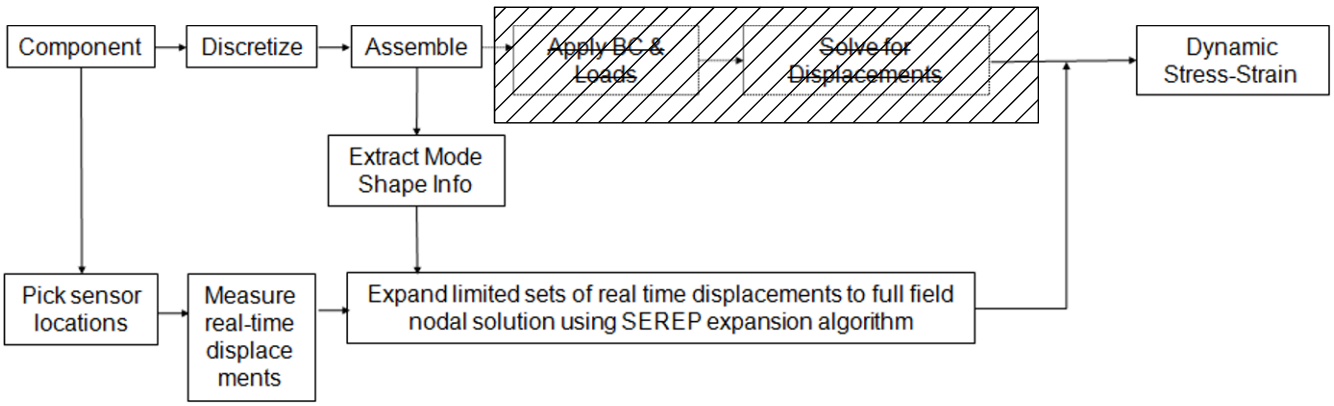

Figure 2: Schematic Showing Alternation Expansion/Solution Sequence

The full field displacement data is obtained from the limited sets of measured data using an expansion technique. Hence the expansion forms the basis of the proposed approach. A review of the model reduction/expansion techniques is presented in the next section.

MODEL REDUCTION

Model reduction is necessary in order to develop expansion approaches for modal data for the unmeasured translational DOF as well as for rotational DOF. For this work, the expansion is needed for augmenting the limited set of real-time operating data to provide a full field displacement solution. The reduction techniques are the basis of the expansion discussed in this work. These techniques have been presented in earlier work cited in the references; only summarizing equations are presented below. Several model reduction methods have commonly been used for expansion of measured data. Four common methods are Guyan [22], Dynamic Condensation [23], SEREP [24], and a Hybrid method [25]. In these methods, the relationship between the full set of degrees of freedom and a reduced set of degrees of freedom can be written as

$$\{X_n\}=[T]\{X_a\} \tag{1}$$

All of these methods require the formation of a transformation matrix that can project the full mass and stiffness matrices to a smaller size. The reduced matrices can be formulated as

$$[M_a]=[T]^T[M_n][T] \tag{2}$$

$$[K_a]=[T]^T[K_n][T] \tag{3}$$

For the specific work in this paper, only the SEREP method has been used for the expansion of mode shapes.
The System Equivalent Reduction Expansion Process (SEREP) produces reduced matrices for mass and stiffness that yield the exact frequencies and mode shapes as those obtained from the eigensolution of the full size matrix. The SEREP transformation is formed as

$$[T_U]=[U_n][U_a]^g \tag{4}$$

The SEREP transformation is developed with analytical mode shapes of the structure.

Equation 1 is used for expansion of real-time operating data and is written as

$$[ERTO_n]=[T][RTO_a] \tag{5}$$

CORRELATION TOOLS

The correlation tools utilized to compare the results of the expanded RTO [$ERTO_n$] and "reference time solution" [REF_n] are briefly discussed here in order to help clarify the differences between the techniques. Correlation tools such as, the Modal Assurance Criterion (MAC) [26] and the Time Response Assurance Criterion (TRAC) [27] will be used to verify the accuracy of the expanded RTO in each case. The MAC as used for this work will identify the correlation of the expanded real time operating displacement solution obtained with the reference solution. The MAC can be computed at each time step t to compare the transient displacement solution with time. The MAC is written as

$$MAC\_RTO=\frac{\left[\{REF_n\}^T\{ERTO_n\}\right]^2}{\left[\{REF_n\}^T\{REF_n\}\right]\left[\{ERTO_n\}^T\{ERTO_n\}\right]} \tag{6}$$

Similar to the MAC, the TRAC is a tool used to determine the degree of correlation between two time traces. For the cases presented here, the TRAC is the correlation for one DOF over all time for the expanded time data [$ERTO_n$] compared to the actual measured data [REF_n]. The TRAC is written as

$$TRAC\_RTO = \frac{\left[\{REF_n(t)\}^T \{ERTO_n(t)\}\right]^2}{\left[\{REF_n(t)\}^T \{REF_n(t)\}\right]\left[\{ERTO_n(t)\}^T \{ERTO_n(t)\}\right]} \tag{7}$$

The values produced by both the MAC and TRAC will range from 0 to 1; values approaching 1 indicate good correlation. A schematic is shown in Figure 3 showing the MAC and the TRAC correlations. Typically, the TRAC is comparison of the displacement - time response solutions (predicted and reference solutions) while the MAC is comparison between the deformed shape of the structure at each time instant as shown in Figure 3.

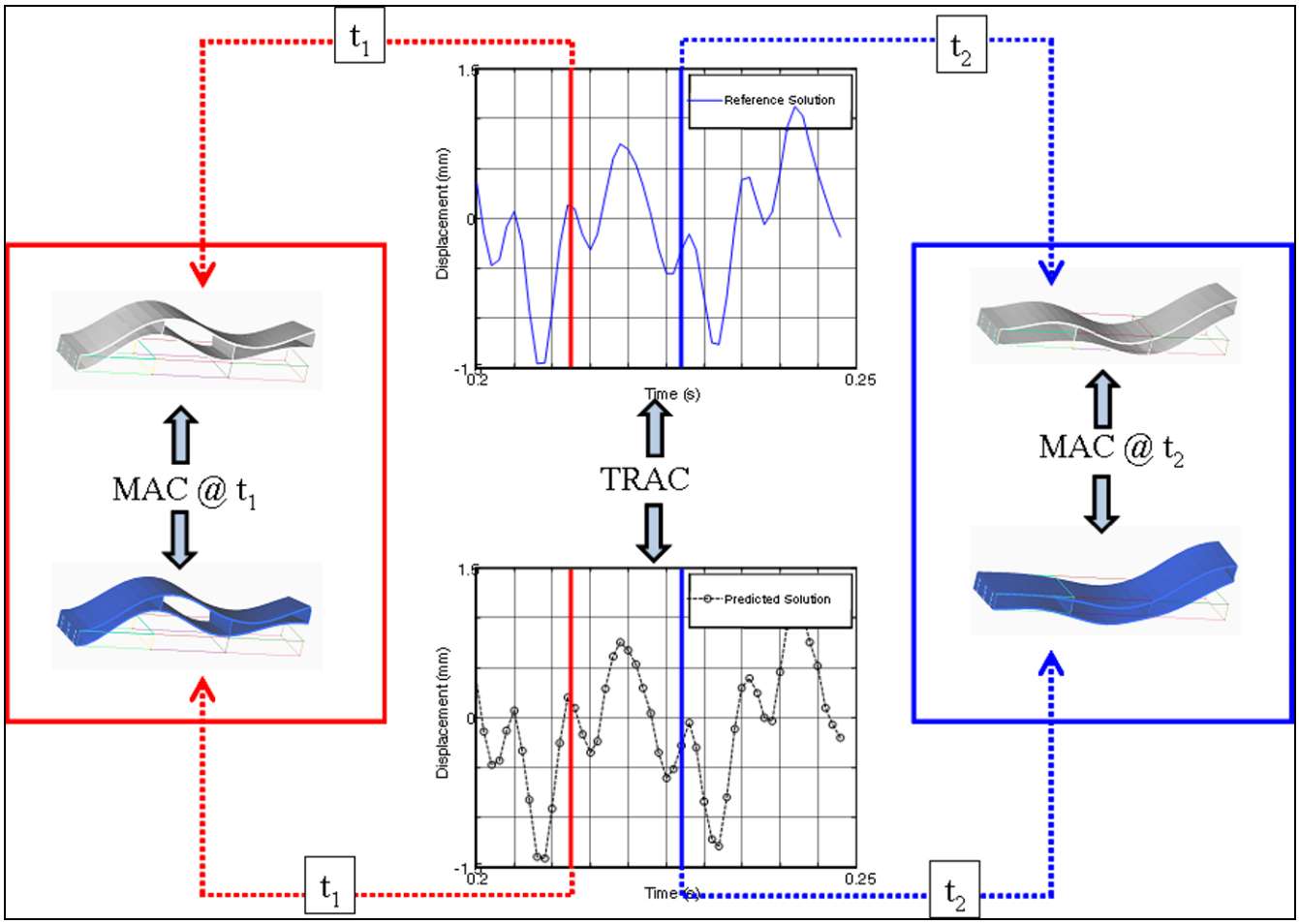

Figure 3: Schematic showing MAC and TRAC

MODEL DESCRIPTION

For this study, a simple structure (named as Base-Upright or BU), which has well correlated analytical and experimental modes from previous studies, was used. The structure was assembled from two aluminum plates. The structure was designed to be time-invariant, with well-spaced, directional modes that could be identified easily. Figure 4 shows the BU with the primary dimensions labeled. The base plate is 24 x 24 inches and rigidly bolted to the tied to the ground at the four corners using concrete anchors, while the upright is 24 x 30 inches. Both plates are 3/4" thick aluminum. The base plate and the upright are held together by 0.25 inch thick, 1.5 inch wide, 24 inch long steel L-brackets using 0.5 inch bolts.

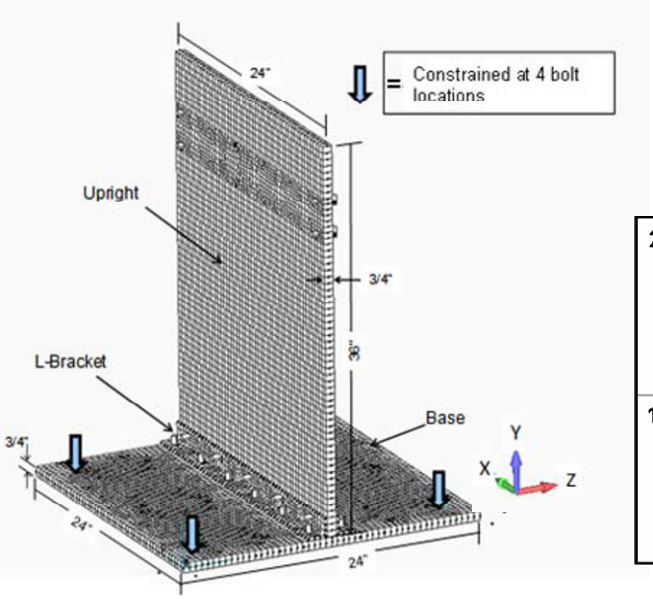

Figure 4: Base-Upright Structure used for Testing

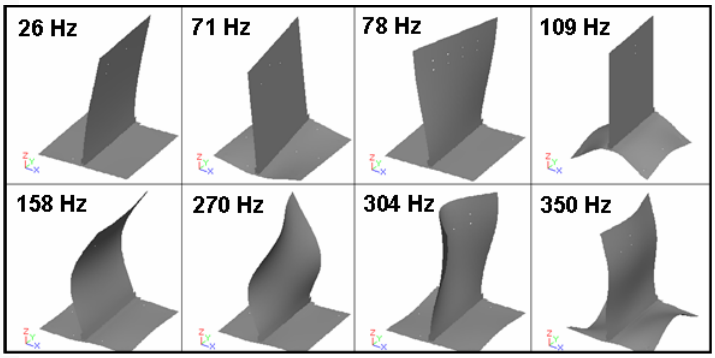

Figure 5: First 8 Mode Shapes of the BU Structure

A FEM of the BU is available and has been shown to be very well correlated to other measured test data from previous studies [29, 30]. The BU FEM was created using plate elements for all the components and has approximately 58,000 DOFs. Rigid links were used to tie the L-brackets to the plates along the two main, 24 inch edges of the L-brackets. Solid cylindrical elements were used at the bolt locations with the appropriate mass to mimic the effect of the bolts. The BU FEM was fixed at the four locations corresponding to the points tied to the ground in the actual structure. An eigensolution was performed on the BU FEM to determine the mode shape information. For reference, the analytical frequencies and mode shapes for the first 8 modes are shown in Figure 5.

The displacement data is recorded at 8 patches using digital image correlation (ARAMIS [34]) technique and at 8 target locations using dynamic photogrammetry (PONTOS [35]) technique as shown in Figure 6. The 8 targets used for PONTOS are located on top of the 8 ARAMIS patches. Both sets of data provide similar information and are provided for redundancy.

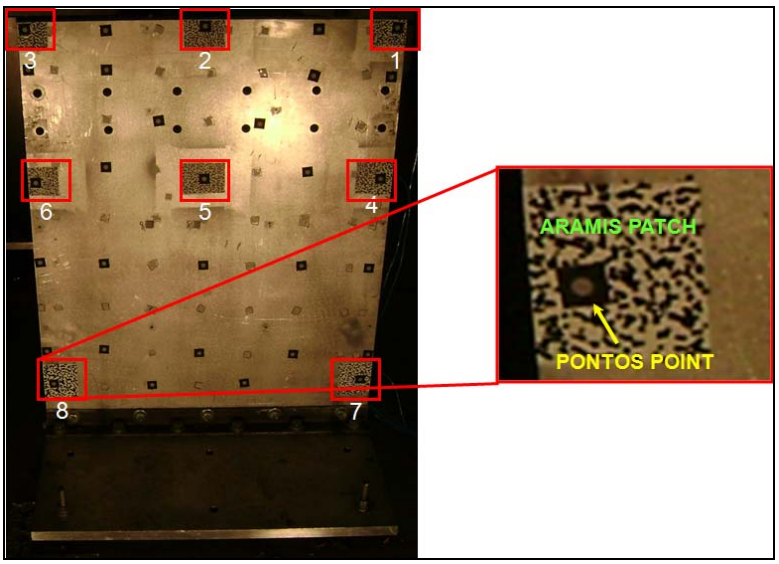

Figure 6: PONTOS Target Locations and ARAMIS Patches

An impact with a calibrated modal hammer was made at the top-right corner at Location 1 in Figure 6 of the Upright structure. The displacement data was collected at the same 8 target locations shown in Figure 6.

The displacement responses at 7 out of the 8 recorded locations were used to expand to 3112 finite element nodes using the expansion process. To identify the number of mode shapes required in the expansion process, an (Fast Fourier Transform) FFT was performed on a response measurement made at top-right corner of the Upright (one of the 8 measured locations). This location was chosen because all modes excited can be observed at that location. The results of the FFT are shown in top portion of Figure 7. The displacement response was collected for 4 seconds using 200 frames per second cameras that is, at 200Hz sample rate. So a maximum of 100Hz frequency data could be captured using DIC as seen in top portion of Figure 7. The bottom portion of the Figure 7 shows a typical frequency response of BU collected using Laser Doppler Vibrometer (LDV). The FFT collected using LDV gives a better interpretation of the higher modes of the BU.

The two out-of-plane modes, at 26 Hz and 78 Hz are mainly excited by the impact as seen from Figure 7. As seen from previous studies [1- 5], the expansion process should at least contain those modes excited by the forcing function for proper expansion. The first five modes of the Upright (which include the two out-of-plane modes excited by the impact) are used in this case for expansion purposes.

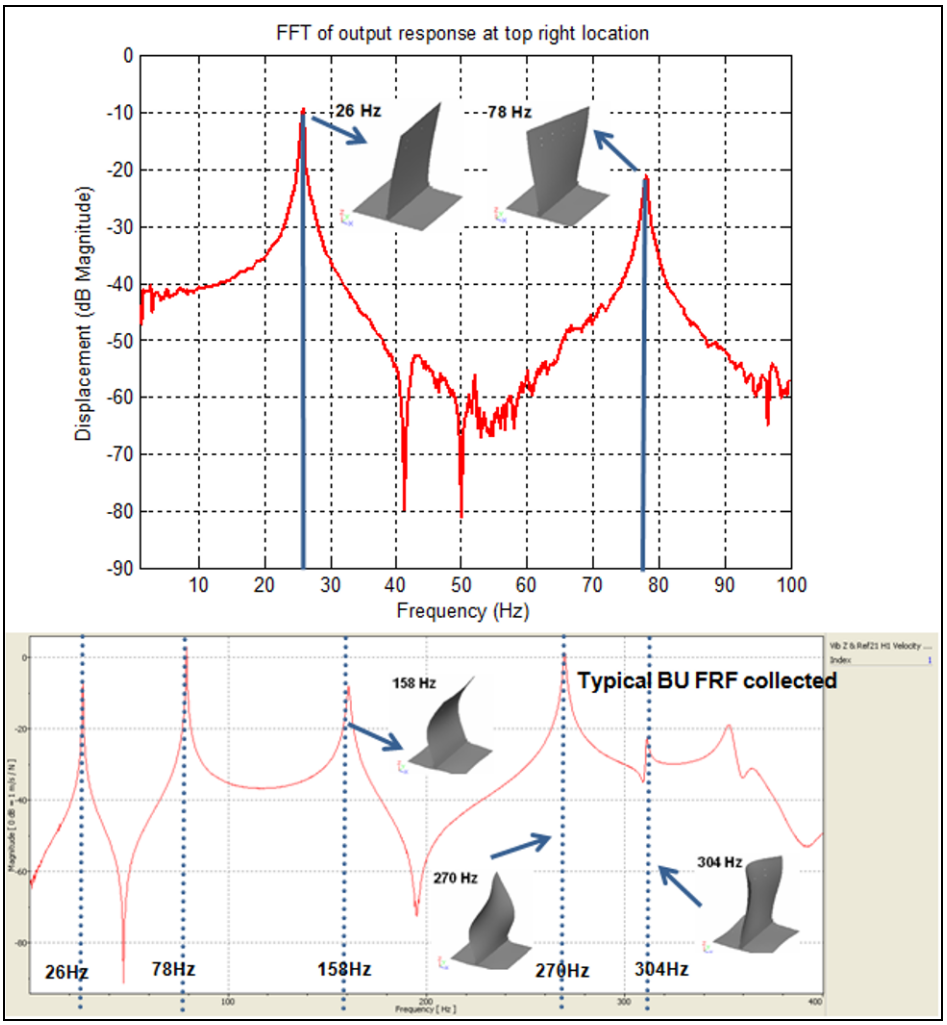

Figure 7: Details of the excitation force and response of the structure.

CASES STUDIED

CASE 1: DISPLACEMENT RESPONSE

There are three different sensor location configurations studied which compare displacements responses at three different locations in the BU structure. All the sensor configurations use 7 out of the 8 locations shown in Figure 6.

A. Sensor set-up A – uses locations 2, 3, 4, 5, 6, 7 and 8 for expansion.
B. Sensor set-up B – uses locations 1, 2, 3, 5, 6, 7 and 8 for expansion.
C. Sensor set-up C – uses locations 1, 2, 3, 4, 5, 6 and 8 for expansion.

For the first sensor configuration (Sensor set-up A), 2, 3, 4, 5, 6, 7 and 8 sensor displacement responses were used in expansion process to expand up to 3112 locations. The sensor 1 displacement response recorded experimentally was used for comparison with expanded solution. Note that the impact was made at the location 1 on the Upright structure, so location 1 will see the highest amplitude of response. The comparison of the expanded and the experimentally obtained response is shown in Figure 8a. The response was recorded for 4 seconds as shown. The responses predicted by the proposed technique compares well with the experimentally recorded response at the top-right location. For comparing the time responses, a TRAC was performed between the expanded solution and experimentally recorded response. A TRAC value of 98% was observed which show very good agreement between the two solutions.

The transient response comparison for initial time steps (where highest amplitude of response is observed) is shown in Figure 8b which is the first 0.5 sec of the response. As seen, the solution predicted by the proposed technique compares well with the experimentally recorded response. Note that the TRAC value increases from 98% to 100% because good correlation is observed for high Signal-to-Noise-Ratio (SNR) time period.

The second sensor configuration (Sensor set-up B) studied was using 1, 2, 3, 5, 6, 7 and 8 sensors excluding the 4th location. The comparison between expanded displacement response (which used the 7 sensors to expand to up to 3112 points in the Upright) and experimentally recorded displacement response at location 4 is made and shown in Figure 8c. The mode configuration used previously in the expansion process is used again in this case. Good correlation between the expanded and experimentally recorded displacement data set is observed. TRAC of up to 97 % is seen which means that the predicted solution is very similar to the experimentally recorded data set even though the comparison location at Location 4 was half-way to the fixed edge of the structure (where more noise in experimental data set is expected). Comparison for initial time period as seen in Figure 8d shows that even for mid-range SNR, the proposed technique does a good job of predicting accurate response. A TRAC of 99 % further substantiates the argument of accurate response prediction.

A third sensor configuration (Sensor set-up C) was studied where sensors 1, 2, 3, 4, 5, 6, and 8 were used excluding sensor 7 which is very close to the fixed edge of the structure. Higher noise and low SNR is expected. Figure 8e shows comparison between the predicted solution and experimentally recorded displacement response at location 7. As expected the experimental response is very noisy, especially for the time period from 2 to 4 seconds where the response dies out. A TRAC of 76% is observed for the time response comparison between the predicted and the experimental responses over the full range of 4 seconds. However, a TRAC value of 87% was obtained for the time responses at initial time steps where higher response was expected. A fairly good correlation is observed in Figure 8f between the experimental and the predicted responses.

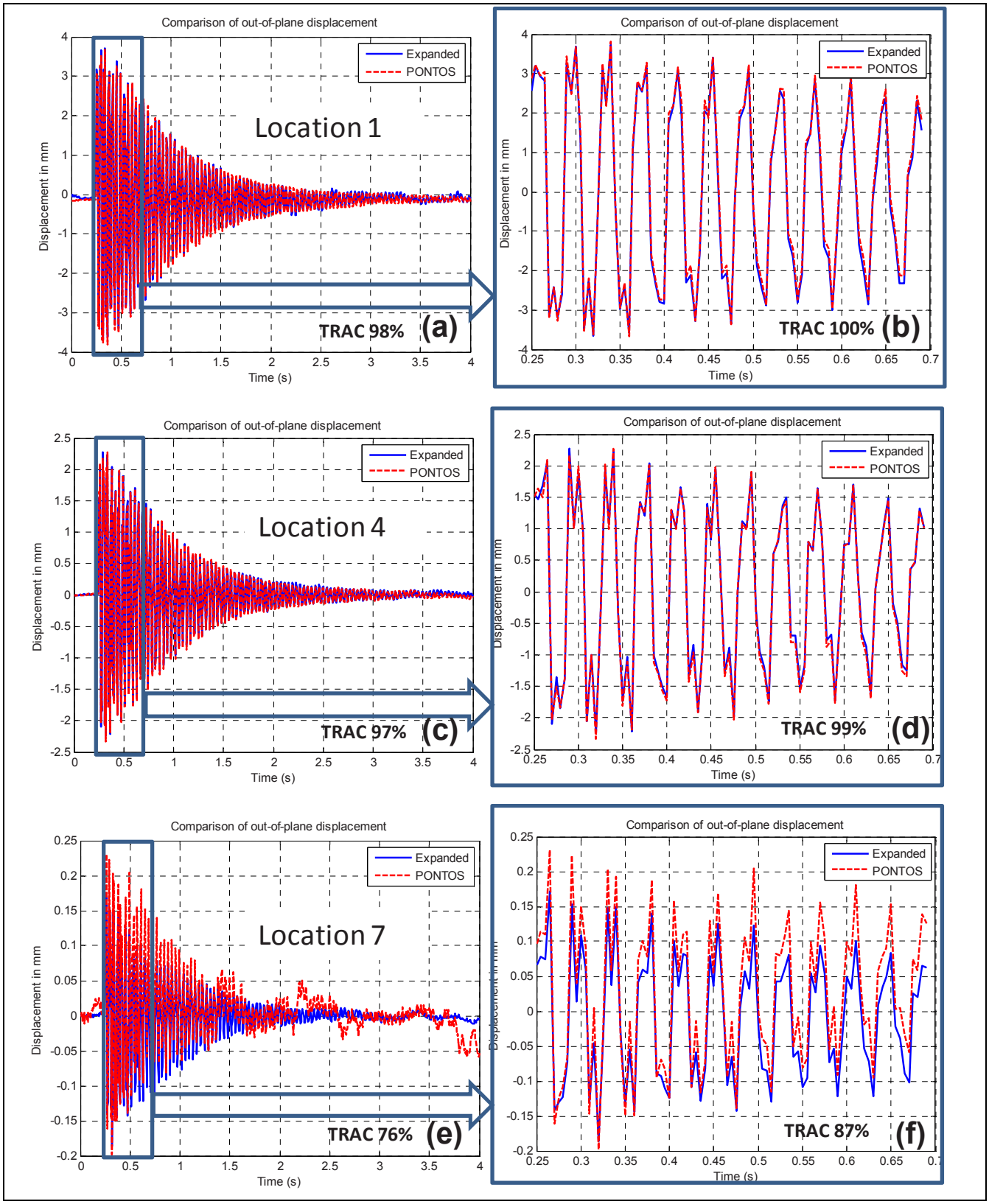

Figure 8: Overlay of the Displacement Responses (shown for complete and initial transient period) from Predicted Solution Using First Five Modes for Expansion and PONTOS at three different locations of the BU

For sensor configuration A, the output response at locations other than top right corner were also collected and compared with expanded results. Note however that the measurements used for comparison purposes were not included in expansion process. The output response comparison plots are shown in Figure 9 at five such locations. Notice that at all locations the TRAC correlation values are 99.9+% which indicates an excellent correlation of expanded data with measurements for the time period shown.

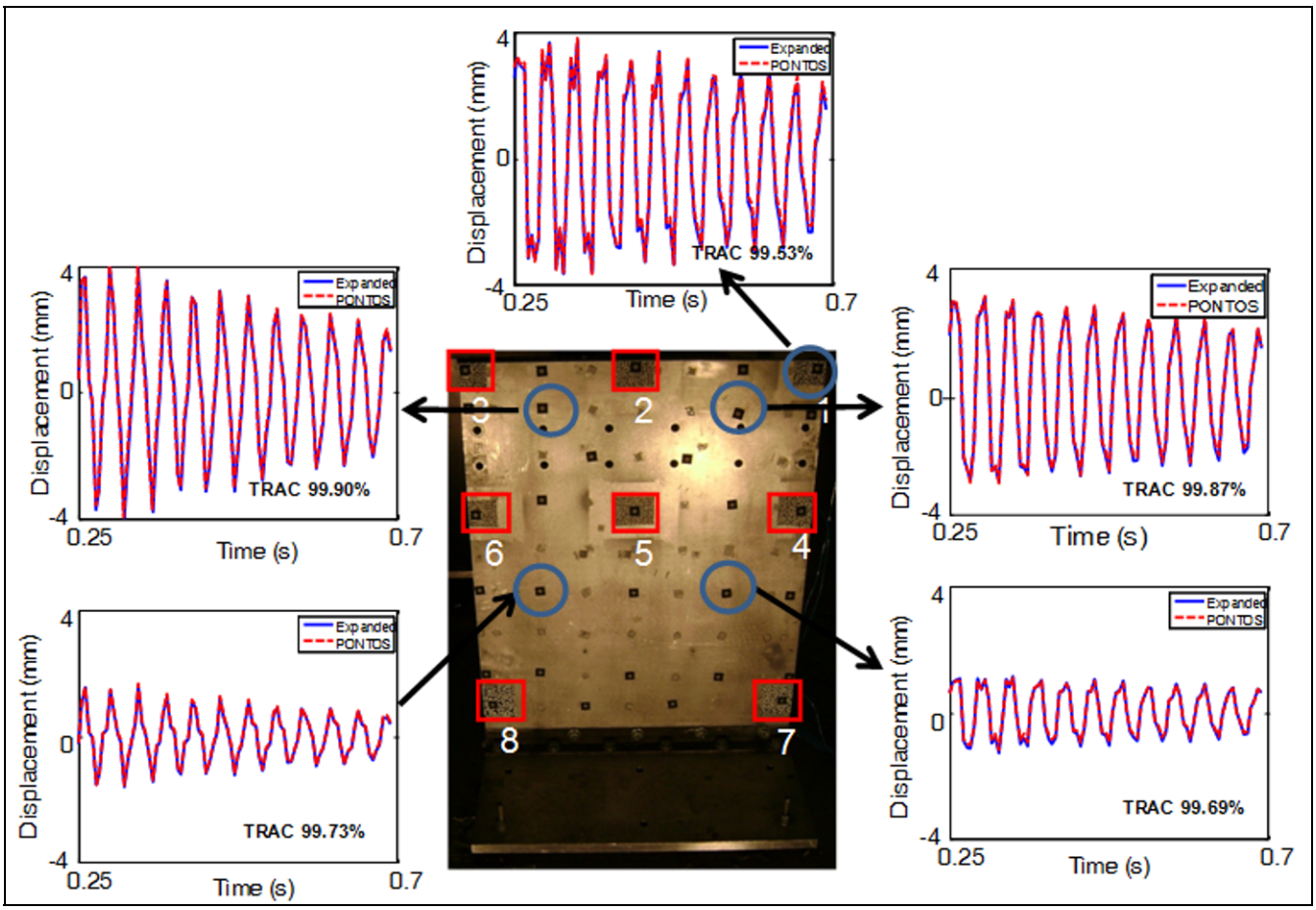

Figure 9: Overlay of the Displacement Responses from Predicted Solution Using First Five Modes for Expansion and PONTOS at Five Different Locations; expansion performed using sensor configuration A

With the sensor configuration B, the output response at locations other than location 4 were also collected and compared with the expanded results. Again the measurements used for comparison purposes were not included in the expansion process. The output response comparison plots are shown in Figure 10 at five such locations. Notice that at all but one location the TRAC correlation values are 99.9+% which indicates a very good correlation of expanded data with measurements for the time period shown. This confirms that even with 7 sensors, accurate prediction of response is possible using proposed methodology for up 3112 locations.

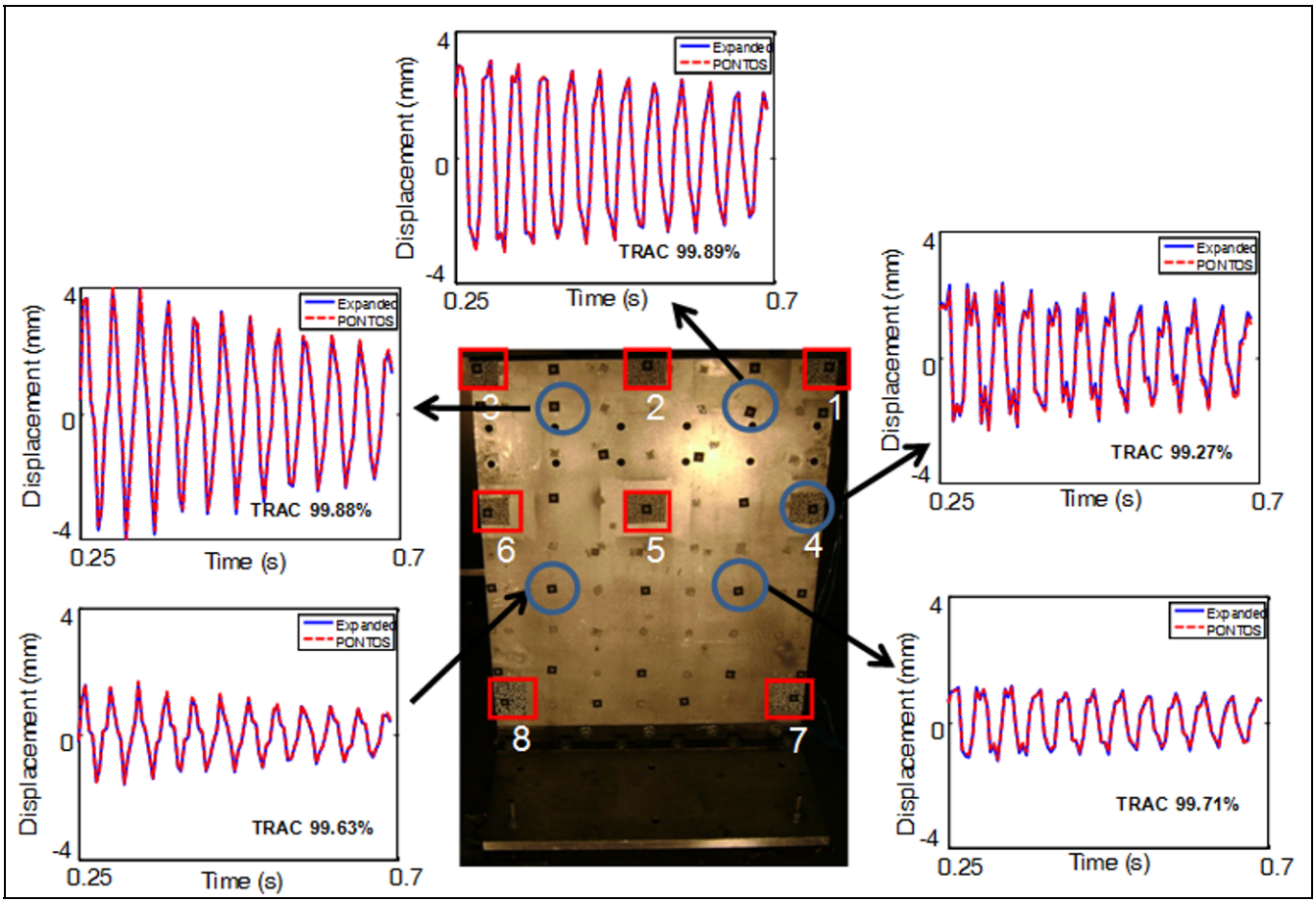

Figure 10: Overlay of the Displacement Responses from Predicted Solution Using First Five Modes for Expansion and PONTOS at Five Different Locations; expansion performed using sensor configuration B

Figure 11 shows the expanded output responses at five different locations in comparison with the reference experimental measurements for sensor configuration C. The measurements used for comparison purposes were not included in expansion process. Notice that at all locations except the location 7, the TRAC correlation values are 99.9+% which indicates a very good correlation of expanded data with measurements for the time period shown. For the 7th location, which is near to the fixed base of the structure, the displacement response is very small as compared to other locations as seen in Figure 11. The SNR is much smaller and hence the TRAC correlation drops to 87%.

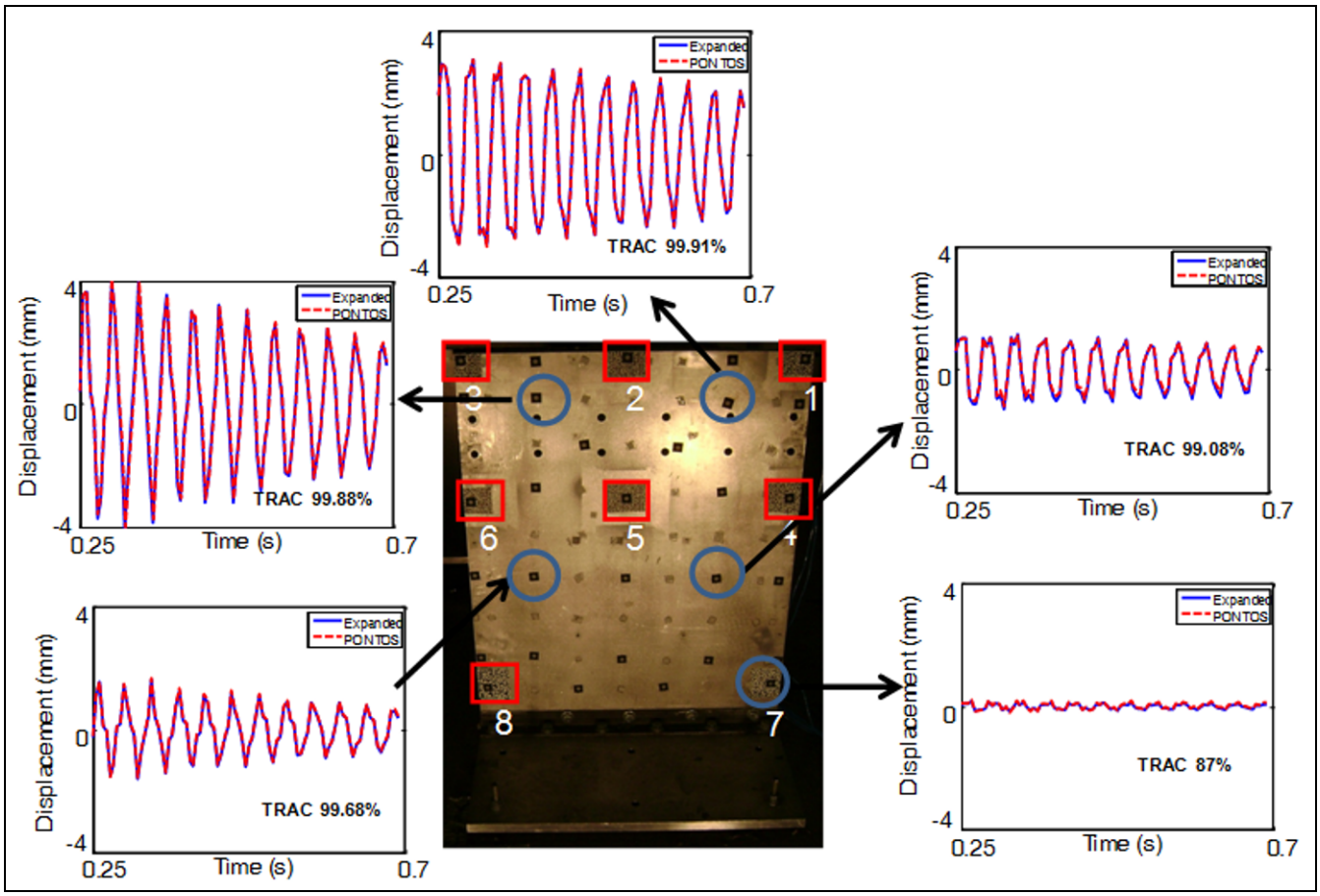

Figure 11: Overlay of the Displacement Responses from Predicted Solution Using First Five Modes for Expansion and PONTOS at Five Different Locations; expansion performed using sensor configuration C

CASE 2: STRAIN RESPONSE

The strain response is obtained from full-field expanded displacements for all the three sensor configurations discussed in Case 1 using strain recovery process outlined in [31]. The strain response has been calibrated for static load and discrete sine test.

Ideally for comparing the strain response obtained using the proposed methodology, the reference solution should be obtained experimentally. However, the minimum strain levels measured by using the DIC technique is 50 micro-strain. The maximum strain levels obtained in BU were well below the minimum strain levels that the DIC can measure accurately, even in regions where the highest strain resulted. So for comparison purposes, a FEM of the BU was used which has shown good correlation for previous studies has performed for the purpose of extracting mode shape information. The force pulse used for exciting the BU FEM was one of the impact force measurements made during the impact tests. The force pulse as shown in Figure 12 was discretized at every 0.0001 seconds. As seen in Figure 12, the impact on the BU was made at 0.25 seconds.

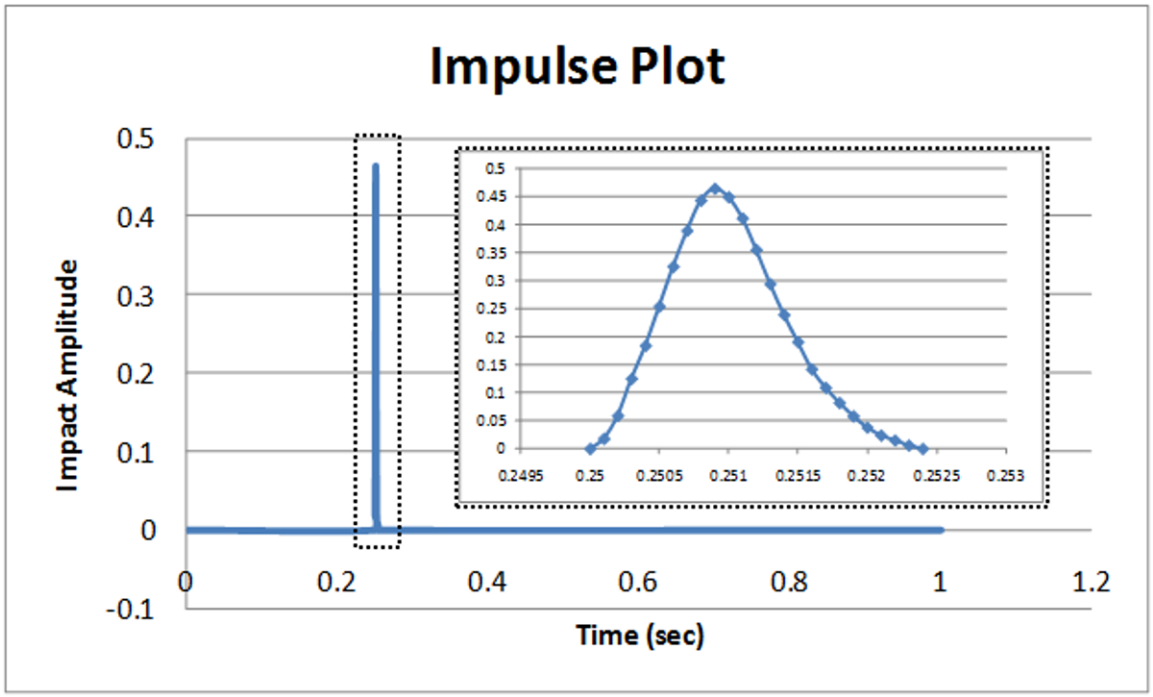

Figure 12: Force Pulse Used for BU Impact

A direct integration approach was used for obtaining the strain solutions for the FEM. The comparison between the FEA strain solution and the strain solution obtained using the proposed technique is made in Figures 13 a, c and e at locations 7, 8 and 4 respectively in the BU. The response shown is after the impact was made at 0.25 seconds for a sample time period of 0.15 seconds. The FEA transient solution was obtained for 400 steps with 0.001 seconds per step. The strain solution obtained from the proposed technique uses the full-field displacement solution. So the displacement sampling rate of 0.005 sec per sample also applies for the strain obtained from proposed technique. The FEA solution was performed at a finer time step to properly obtain an accurate numerical solution. This implies that the FEA and test data have different time increments. The FEA strain response had to be down-sampled to the response data points recorded during experimentation. The comparison of this down-sampled FEA strain solution with the predicted strain response using the expansion technique is shown in Figures 13 b, d and f for locations 7, 8 and 4 respectively.

The FEA solution shows contribution of higher order modes because the direct integration scheme was used to obtain the solution. However, a good overall agreement is observed between the predicted and FEA strain solutions for locations 7 and 8 which are higher strain regions in the structure as they are closer to the fixed base. Location 4, which is at the mid-level of the BU does not see as much strain in comparison to locations 7 and 8. There is a slight DC bias that appears on the data but the general trend is reasonable considering the lower level of strain observed at this location.

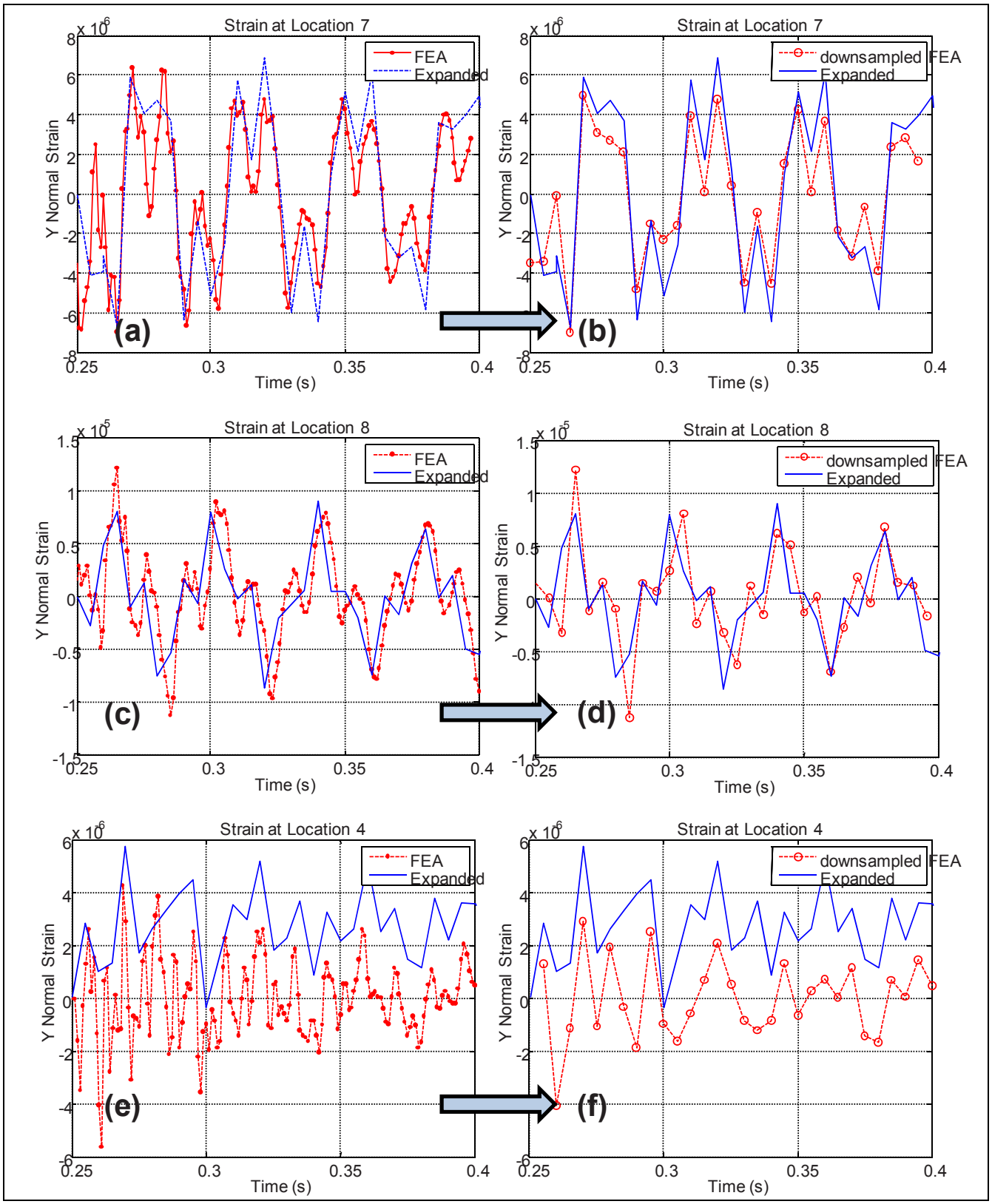

Figure 13: Comparison of strain response from FEA solution and predicted solution at Location 7, 8 and 4

Clearly, there is some small contribution of the higher order modes at the very start of the transient. In order to include more modes, additional measurement points would be required. However, this is not possible with the 8 target points selected. In order to understand the effect of using less number of modes for the response, a mode superposition solution was performed using only the first five modes used in the expansion process; this essentially truncates the effects of the higher order modes by using the modal superposition solution scheme. The results after using modal superposition scheme instead of the direct integration approach are shown in Figure 14. The down-sampled results have also been shown at two comparison locations (Location 7, and 8) in Figure 14. At locations 7 and 8, as seen from Figures 14 b and d, there is definite improvement observed in the correlation between the FEA strains and the strains predicted through the proposed approach because the effect of higher order modes is not observed in the FEA solution as only first five modes were used in the mode superposition solution scheme.

Location 4 was shown to provide excellent displacement response results as compared to the location 7. Note that the location 4 is nearer to the free edge of the BU structure, while the locations 7 and 8 are very near to the fixed edge of the BU structure. Invariably, higher displacement response and lower strain response will be observed at location 4 as compared to locations 7 and 8. The displacement response at location 7 was contaminated by experimental noise as observed in Case 1. Similarly, there is possibility of the strain response at location 4 to be contaminated by noise hence producing the discrepancies observed. However the locations 7 and 8 provide excellent strain response comparison, which validates the proposed methodology of estimating dynamic stress-strain experimentally.

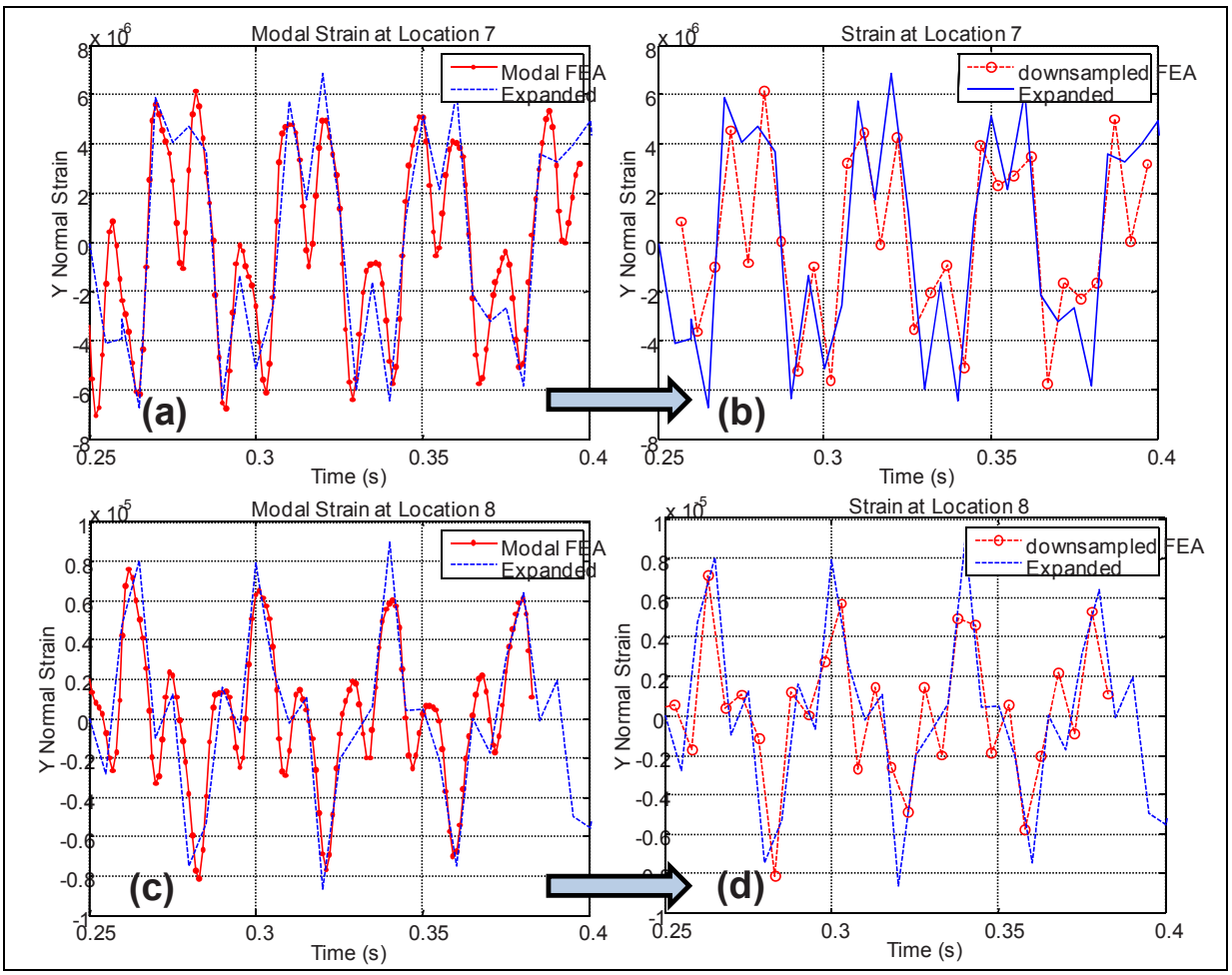

Figure 14: Comparison of strain response from FEA solution and predicted solution at Location 7 and 8

CONCLUSION

Using limited displacement measurements collected experimentally, accurate estimation of dynamic stress-strain was shown. The technique used to estimate dynamic stress strain was a full-field technique which involved use of expansion algorithm to obtain full-field displacements and then using the full-field displacements to obtain full-field dynamic stress-strain through stress recovery process. Dynamic stress-strain information at 3112 locations in the structure was successfully obtained from only 7 displacement measurements made experimentally due to impulsive excitation.

Several cases were investigated to show the accuracy and robustness of the expansion procedure. The expansion procedure will produce accurate results provided that there are a sufficient set of orthogonal mode shapes to span the space for the solution; this requires that a sufficient number of modes that participate in the response be included in the expansion process. Successful estimation of dynamic stress strain from limited experimental data was shown without the need for estimating the boundary conditions or loads.

REFERENCES

[1] Chipman, C., “Expansion of Real Time Operating Data”, Master’s Thesis, University of Massachusetts Lowell, May 2009

[2] Chipman, C., Avitabile, P., “Expansion of Real Time Operating Data for Improved Visualization”, Proceedings of the Twenty-Sixth International Modal Analysis Conference, Orlando, FL, Feb 2008

[3] Chipman, C., Avitabile, P., “Expansion of Transient Operating Data”, Proceedings of the Twenty- Seventh International Modal Analysis Conference, Orlando, FL, Feb 2009

[4] Pingle, P., Avitabile, P., “Prediction of Full Field Dynamic Stress/Strain from Limited Sets of Measured Data”, Proceedings of the Twenty-Eight International Modal Analysis Conference, Jacksonville, FL, Feb 2010

[5] Pingle, P., Avitabile, P., Niezrecki, C., “Real Time Operating Data Expansion for Dynamic Stress and Dynamic Strain Fatigue Accumulation”, The 7th International Workshop on Structural Health Monitoring, Stanford University, Stanford, CA, September 9-11, 2009

[6] Vandepitte, D., Sas, P., “Case study of fracture of a mechanical component due to resonance fatigue”, Mechanical Systems and Signal Processing, Volume 4, Issue 2, Pages 131-143, March 1990

[7] De Langhe, K., Vandepitte, D., Sas, P., “A combined dynamic-static finite element model for the calculation of dynamic stresses at critical locations”, Computers & Structures, Volume 65, Issue 2, Pages 241-254, October 1997

[8] Huang, L., Agarwal, H., Borowski, V., “Durability analysis of a vehicle body structure using modal transient methods”, Proceedings of the International Modal Analysis Conference - IMAC, v 1, p 407-414, 1997

[9] Tucchio, M., Epstein, H., Craney, III K., “An experimental-modal computational technique to find dynamic stresses”, Computers and Structures, Volume 24, Issue 4, Pages 559-569, 1986

[10] Kelly, N., Sutherland, H., "Damage Estimates from Long-Term Structural Analysis of a Wind Turbine in a U.S. Wind Farm Environment",1997 ASME Wind Energy Symposium, AIAA/ASME, pp. 170-179, 1997

[11] Veers, P., Sutherland, H., Ashwill, T., "Fatigue Life Variability and Reliability Analysis of a Wind Turbine Blade", Proceedings: Probabalistic Mechanics and Structural and Geothermal Reliability, Y.K. Lin ed., ASCE, July 1992

[12] Veers, P.,Lange, C., Wintersten, S., "FAROW: A Tool For Fatigue and Reliability of Wind Turbines", Proceedings of WindPower '93, AWEA, July 1993

[13] Lange, C., Kumar, S., "FITTING: A Subroutine to Fit Four Moment Probability Distributions to Data", SAND94-3039

[14] Manuel, L., Kashef, T., Winterstein, S., "Moment-Based Probability Modelling and Extreme Response Estimation The FITS Routine Version 1.2", SAND99-2985

[15] Manuel, L., Veers, P., Winterstein, S., "Parametric Models For Estimating Wind Turbine Fatigue Loads For Design", 2001 ASME Wind Energy Symposium, AIAA/ASME, 2001

[16] Veers, P., Winterstein, S., "Application of Measured Loads to Wind Turbine Fatigue and Reliability Analysis", 1997 ASME Wind Energy Symposium, AIAA/ASME, 1997

[17] Veers, P., Butterfield, S., "Extreme Load Estimation for Wind Turbines: Issues and Opportunities for Improved Practice”, 2001 ASME Wind Energy Symposium, AIAA/ASME, 2001

[18] Zhu, B., Xiao, J., “Study on calculation method and its application for dynamic stress of steam turbine blade”, American Society of Mechanical Engineers, Power Division (Publication) PWR, v 34, p 2/-, 1999

[19] Blelloch, P.(SDRC, United States), “Calculation of structural dynamic forces and stresses using mode acceleration”, Journal of Guidance, Control, and Dynamics, v 12, n 5, p 760-762, Sep-Oct 1989
[20] Powell, C., “Experimental Modal Analysis with Structural Modification Applied to System Stress Prediction”, Proceedings of the International Modal Analysis Conference & Exhibit, p 417, 1982
[21] Mahri, Z., Rouabah, M., “Calculation of dynamic stresses using finite element method and prediction of fatigue failure for wind turbine rotor”, WSEAS Transactions on Applied and Theoretical Mechanics, v 3, n 1, p 28-41, January 2008
[22] Guyan, R.J., "Reduction of Stiffness and Mass Matrices", AIAA Journal, Vol. 3, No 2, 1965
[23] Paz, M, "Dynamic Condensation", AIAA Journal, Vol22, No 5, May 1984
[24] O'Callahan,J.C., Avitabile,P., Riemer,R., "System Equivalent Reduction Expansion Process", Seventh International Modal Analysis Conference, Las Vegas, Nevada, February 1989
[25] Kammer, DC, "A Hybrid Approach to Test Analysis Model Development for Large Space Structures", Journal of Vibration and Acoustics, Vol 113, July 1991
[26] Allemang,R.J. and Brown,D.L., "A Correlation Coefficient for Modal Vector Analysis", First International Modal Analysis Conference, Orlando, Florida, November 1982, pp. 110-116
[27] Van Zandt, T., “Development of Efficient Reduced Models for Multi-Body Dynamics Simulations of Helicopter Wing Missile Configurations,” Master’s Thesis, University of Massachusetts Lowell, April 2006.
[28] Avitabile,P., Piergentili,F., Lown,K., “Identifying Dynamic Loadings from Measured Response”, Sound & Vibration, August 1999
[29] P.Pingle, P.Avitabile, “Comparison of 3D laser Vibrometer and Accelerometer Frequency Measurements”, Proceedings of the Twenty-Seventh International Modal Analysis Conference, Orlando, FL, Feb 2009
[30] Butland, A., “A Hybrid Component Model Synthesis Approach for System Modeling Applications”, Master’s Thesis, University of Massachusetts Lowell, 2008.
[31] Pingle, P., “Prediction of Full-Field Dynamic Stress-Strain from Limited Sets of Measured Displacement Data”, PhD. Thesis (submitted), University of Massachusetts Lowell, 2010.
[32] MATLAB R2008b – The MathWorks, Natick, Massachusetts
[33] Femap – Finite Element Modeling And Postprocessing, Version 9.3.1, Copyright © 2007 UGS Corp.
[34] ARAMIS, v. 6.0 User’s Manual, GOM mbH, Braunschweig, Germany, 2007
[35] PONTOS, User’s Manual, Revision A, GOM mbH, Braunschweig, Germany (2004)
[36] FEMtools 3.0 – Dynamic Design Solutions, Leuven, Belgium
[37] ABAQUS 6.5.1 © Dassault Systèmes, 2004

A Survey of Techniques to Estimate the Uncertainty in Material Parameters

Todd Simmermacher
Sandia National Laboratories
P. O. Box 5800
Albuquerque, NM 87185-0557

ABSTRACT

When estimating parameters for a material model from experimental data collected during a separate effects physics experiment, the quality of fit is only a part of the required data. Also necessary is the uncertainty in the estimated parameters so that uncertainty quantification and model validation can be performed at the full system level. The uncertainty and quality of fit of the data are many times not available and should be considered when fitting the data to a specified model. There are many techniques available to fit data to a material model and a few of them are presented in this work using a simple acoustical emission dataset. The estimated parameters and the affiliated uncertainty will be estimated using a variety of techniques and compared.

1. INTRODUCTION

In model validation and uncertainty quantification studies, uncertainty in model parameters such as Young's modulus and Poisson's ratio need to be characterized. Many times the uncertainty in these parameters is assumed to be uniformly distributed between two values that are chosen based upon expert opinion. A more quantitative and defendable estimate of the uncertainty in material parameters can be found through the analysis of data from material tests.

Material tests are used to identify parameters for constitutive models used in structural models. These material tests exercise the material over the load range, in terms of strain typically, of the environments that the model will be used to predict. A constitutive model is then fit to the data by calibrating the parameters of the model in either an ad hoc or formal optimization framework. It is these fitted parameters that are used in the structural model. A typical set of parameters are usually considered deterministic and are assumed to represent the mean of the data. A probabilistic model can be used to characterize the uncertainty in calculated responses from the full structural model by forward propagating the parametric uncertainty through the structural model. Using the collection of estimated parameters such as Young's modulus, a Kernel Density Estimator (KDE,[1]) is used to identify a probability density function (PDF) . The PDF is then used to generate samples of the parameter in a Monte Carlo ([2]), Latin Hypercube sampling (LHS) or other sampling techniques. In this work, a Bayesian technique [3] will be used to estimate the probabilistic model of the constitutive model parameters.

In this work, probabilistic models obtained using six techniques will be compared. The first four techniques use a traditional optimization procedure and the KDE to develop the probability model of the elastic parameters Young's modulus and Poisson's ratio. The fifth and sixth methods use a Bayesian technique to develop the probabilistic model of the elastic parameters.

2. DATA SET DESCRIPTION

The data being used for this analysis is described in [4]. The material was a syntactic carbon foam. The model required for the foam was a linear elastic model which has three parameters: density, Young's modulus and Poisson's ratio. The density can be estimated for a sample by measuring and weighing the samples. Estimating the Young's modulus and Poisson's ratio is the main objective of this paper.

The data to be fitted is acoustic data obtained from impact tests on the foam samples. The geometry of the test samples is given in Figure 1. The test was performed by dropping small steel spheres onto the sample and

T. Proulx (ed.), *Linking Models and Experiments, Volume 2*, Conference Proceedings of the Society for Experimental Mechanics Series 5,
DOI 10.1007/978-1-4419-9305-2_15, © The Society for Experimental Mechanics, Inc. 2011

measuring the resulting acoustic emissions. The time histories of the measured acoustic response were used to estimate the power spectral density (PSD) of the response. The peaks in the PSD were used to identify the approximate frequencies of the modes of the sample. Three frequencies were identified from the data. The test and model frequencies were correlated through comparisons between mode shapes calculated with approximate values for Young's modulus and Poisson's ratio as well as three dimensional laser based visualization of the measured mode shapes [4]. The identified frequencies and damping ratios for each sample are given in Table 1.

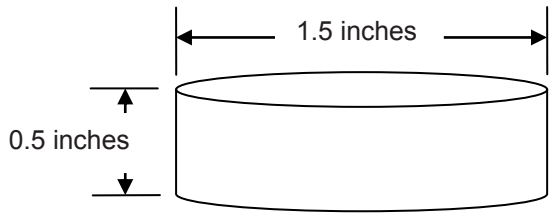

Figure 1 Geometry of Test Sample

Table 1 Experimental Frequencies Determined from Acoustic Emissions

Sample #	Mode 7		Mode 9		Mode 16		density
	modal freq (Hz)	Damping (%)	modal freq (Hz)	damping (%)	modal freq (Hz)	damping (%)	(lbf/in^3)
A	11,514	0.24	16,335	0.28	27,928	0.29	1.0995E-02
B	11,159	0.39	15,858	0.30	27,344	0.28	1.0885E-02
C	11,308	0.34	16,041	0.27	27,656	0.26	1.0931E-02
D	10,819	0.65	15,313	0.29	26,566	0.37	1.0595E-02
E	11,365	0.29	16,134	0.27	27,774	0.32	1.0994E-02
F	11,056	0.34	15,669	0.29	27,110	0.27	1.0812E-02
G	10,953	0.39	15,541	0.31	26,743	0.30	1.0809E-02
H	11,027	0.35	15,660	0.31	27,122	0.28	1.0828E-02
I	11,142	0.35	15,767	0.29	27,239	0.25	1.0799E-02
Mean	11,149	0.37	15,813	0.29	27,276	0.29	1.0850E-02

The model used for calculating the natural frequencies of the sample given a density, elastic modulus, and Poisson's ratio was developed using a finite element model and an empirical model mapping the parameters to the frequencies. Since the sample and consequently the model consist of only one material, the functional form of the natural frequencies can be given as

$$f_i = \sqrt{\frac{E}{\rho}} g_i(\nu) \tag{1}$$

where f_i is the i^{th} natural frequency, E and ρ are the Young's modulus and density, and g_i describes the functional variation of the natural frequency with Poisson's ratio. The specific form of g_i will be dependent on the geometry and boundary conditions of the sample. For the data used here, the geometry and boundary conditions were essentially unchanged between samples and therefore assumed constant. Small variations in the as-built dimensions of the sample were ignored in the frequency analysis.

To determine the function g_i, the geometry in Figure 1 was meshed using solid elements. The model was then run using an elastic modulus of 1 psi, a density of 1 lb/in^3, and for Poisson's ratios ranging from 0 to 0.45. The frequencies of interest were extracted from each run and tabulated. Some effort is required to insure that the same mode shape is tracked throughout the variation of Poisson's ratio. Many times the modes switch order so tracking modes by order was not successful. A plot of the resulting data is given in Figure 2.

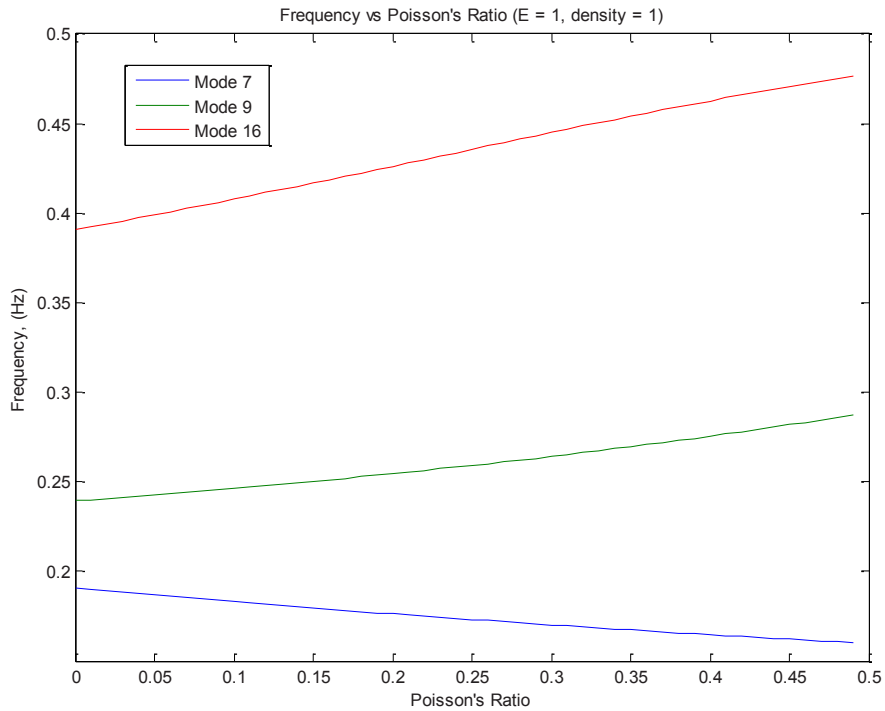

Figure 2 Variation of natural frequencies with Poisson's ratio.

Once the curves (Figure 2) were generated (and consequently, the form of $g_i(\rho)$ was established), Eq. (1) was used to evaluate the frequency given a value of Young's Modulus, density, and Poisson's ratio. This simplification produced a model that could be evaluated very quickly. A fast running model is extremely useful in uncertainty quantification where the model may have to be evaluated thousands of times. Many times, more general meta models or surrogate models are developed to represent the response measure of interest, ([3]) to expedite calculations.

3. OPTIMIZATION

Four optimization-based techniques for fitting the parameters of the model to the data were explored. The first technique was a least squares technique using only the first two frequencies in the cost function. The second was a least squares fit using all of the frequencies in a single optimization. The third technique is a least squares fit of the parameters individually for each sample. This optimization only uses two of the three available frequencies for the fitting. Statistics are derived from the collection of parameters from all of the fits. The final technique fits the parameters on each sample individually but uses all three frequencies for the fit. The statistics are derived from the collection of parameters from all of the fits similar to the second technique.

3.1. Two Mode Least Squares Fit

The first optimization technique to identify the elastic modulus and Poisson's ratio is to perform a least squares fit of all of the data using Eq. (1) to model the relationship between modes 7 and 9 and the elastic parameters. Two frequencies are the minimum number necessary since there are two parameters to estimate. The first two frequencies were chosen for the optimization because from Figure 2, it can be seen that the modes 9 and 16 are correlated with respect to Poisson's ratio and therefore would give poor estimates. The density used was an average of all of the densities given in Table 1. The variation of the density is small between samples. The cost function, e, used in the optimization is given by

$$e = \sum_{i=1}^{9} \left[\left(\frac{f_i^7 - f_{calc}^7}{f_{calc}^7} \right)^2 + \left(\frac{f_i^9 - f_{calc}^9}{f_{calc}^9} \right)^2 \right] \tag{2}$$

where f_i^j is the frequency of the j[th] mode of the i[th] dataset, and f_{calc}^j is the calculated frequency from Eq. (1) of the j[th] mode. The set of parameters that minimizes the cost function given in Eq. (9) are the optimal parameters.

The optimal values of the elastic parameters are given in Table 2. This estimate provides a point estimate of the elastic parameters

Table 2 Least Squares Estimated Elastic Parameters

Elastic Modulus	Poisson's Ratio	Fit Error
110,410 psi	0.173	0.006

3.2. Three Mode Least Squares Fit

The second optimization technique of estimating the values of the elastic parameters is similar to the first technique except that all three frequencies are used in the estimation process. The cost function used in the optimization is given by

$$e = \sum_{i=1}^{9} \left[\left(\frac{f_i^7 - f_{calc}^7}{f_{calc}^7} \right)^2 + \left(\frac{f_i^9 - f_{calc}^9}{f_{calc}^9} \right)^2 + \left(\frac{f_i^{16} - f_{calc}^{16}}{f_{calc}^{16}} \right)^2 \right] \tag{3}$$

The optimal values of the elastic parameters are given in Table 3. This estimate also provides a single estimate of the elastic parameters. The fit error on when using three frequencies is about twice the error than using two frequencies (Table 2) from each of the samples. This could indicate that mode 16 is either not as consistent with an elastic model as the first two modes or that there is more uncertainty in the identification of mode 16.

Table 3 Least Squares Estimated Elastic Parameters

Elastic Modulus	Poisson's Ratio	Fit Error
112,090 psi	0.199	0.013

3.3. Fitting Each Sample Individually

The third optimization technique used to identify the elastic modulus and Poisson's ratio is to perform an optimization to estimate the elastic parameters from modes 7 and 9 for each sample individually. The cost function for the optimization is similar to Eq. (2) and is given by

$$e = \left(\frac{f_i^7 - f_{calc}^7}{f_{calc}^7} \right)^2 + \left(\frac{f_i^9 - f_{calc}^9}{f_{calc}^9} \right)^2 \tag{4}$$

The density used was the actual density of the sample and therefore varied between samples. The optimal values of the elastic parameters are given in Table 4. The fit error is the frequency error between the frequency calculated using the optimized parameters for the sample and the experimentally measured frequency. Small errors in the prediction of the third mode indicates that the elastic model may in fact be appropriate.

Table 4 Estimated Elastic Parameters for Each Sample

Sample Number	Elastic Modulus (psi)	Poisson's Ratio	Fit Error for Mode 3
1	119,280	0.174	0.06%
2	111,120	0.176	0.11%
3	114,370	0.173	0.11%
4	101,230	0.170	0.16%
5	116,280	0.175	0.09%
6	108,030	0.172	0.13%
7	106,130	0.174	0.09%
8	107,860	0.175	0.13%
9	109,410	0.170	0.12%
Mean	110,410	0.173	0.11%

3.4. Fitting Each Sample Individually using Least Squares

The final optimization strategy identifies parameters for each sample individually, but uses all three frequencies for the fit. The cost function for this optimization is given as

$$e = \left(\frac{f_i^7 - f_{calc}^7}{f_{calc}^7} \right)^2 + \left(\frac{f_i^9 - f_{calc}^9}{f_{calc}^9} \right)^2 + \left(\frac{f_i^{16} - f_{calc}^{16}}{f_{calc}^{16}} \right)^2 \tag{5}$$

The results are given in Table 5. The estimated Poisson's ratio for all the samples is about 10% higher when all three frequencies are used than when only modes 7 and 9 are used to estimate the parameters. The fit error in the mode 16, however is much lower when all three frequencies are used rather than only estimating the parameters using modes 7 and 9. When all three frequencies are used, parameters that best match all three frequencies are estimated so the resulting error in the third mode would be expected to be lower.

Table 5 Estimated Elastic Parameters for Each Sample

Sample Number	Elastic Modulus (psi)	Poisson's Ratio	Fit Error for Third Mode
1	120,600	0.192	0.01%
2	112,780	0.201	0.02%
3	116,090	0.199	0.02%
4	103,080	0.201	0.03%
5	117,940	0.198	0.02%
6	109,850	0.200	0.02%
7	107,630	0.197	0.02%
8	109,710	0.204	0.02%
9	111,190	0.197	0.02%
Mean	112,100	0.199	0.02%

4. BAYESIAN ESTIMATION OF PARAMETERS

Bayesian techniques for determining probabilistic model parameters have been available for quite a while, however, most of the problem formulations have been analytically unsolvable. Only very special classes of problems could be solved. With the advent of the digital computer, a new surge of interest emerged and has grown into a very well developed technique. The use of Markov Chain Monte Carlo techniques has made Bayesian analysis accessible. A more complete background is provided in [3]. In parameter estimation for structural dynamics, the work presented here follows most closely the work performed in [5] and [6]. In [5] and [6], the authors used a Bayesian updating technique to determine a probabilistic model of the optimal parameters for a finite element model.

In the present work, Bayes theorem is used to estimate a probabilistic model for the elastic parameters Young's modulus and Poisson's ratio. The resulting models will be compared to those estimated using optimization theory from the previous section. The calibration parameters are given by

$$\theta = \{E, \nu, \log_{10}(\sigma)\} \tag{6}$$

where E is the Young's modulus, ν is the Poisson's ratio, and σ is the standard error yet to be defined. The updated or posterior probably density function is given by

$$p(\theta|\varepsilon) = p(\varepsilon|f,\theta)p(\theta) \tag{7}$$

where the likelihood is defined as

$$p(\varepsilon|f,\theta) = \prod_{i=1}^{9} \exp\left(\frac{1}{2\sigma^2}\left(\left(\frac{f_i^7 - f_{calc}^7}{f_{calc}^7}\right)^2 + \left(\frac{f_i^9 - f_{calc}^9}{f_{calc}^9}\right)^2\right)\right), \tag{8}$$

for the two frequency case and the three prior distributions are defined by

$$\theta^1 \sim u(1e5, 1.3e5)$$
$$\theta^2 \sim u(0, 0.45)$$
$$\theta^3 \sim u(-5, 5)$$

so that the distribution function $p(\theta)$ defined by

$$p(\theta) = u(1e5, 1.3e5)u(0, 0.45)u(-5, 5), \tag{9}$$

and $u(a,b)$ is the uniform probability density function defined between a and b. The frequencies are normalized in Eq. (7) to equally weight the three distinct modes; otherwise, the larger magnitude mode would get the most weight.

To evaluate Eq. (7), the Markov Chain Monte Carlo (MCMC) technique is used. When the MCMC technique reaches a stationary condition, the sequence of random numbers satisfy the PDF that is being evaluated. A detailed discussion on MCMC can be found in [2]. For this work, the slice sampler ([7]) as implemented in Matlab ([8]) is used to solve Eq. (7). A large (800,000) number of samples were generated using the MCMC technique. This large number of samples are only possible due to the fast running surrogate model defined by Eq. (1).

The marginal probability density functions for the estimates of each parameter are given in Figure 4. In addition to plotting the margin probability density functions, the assumed prior distribution from Eq. (9) is plotted to show the range and to compare the differences between the prior and the posterior PDF. The posterior distribution was estimated using the KDE estimator, [1].

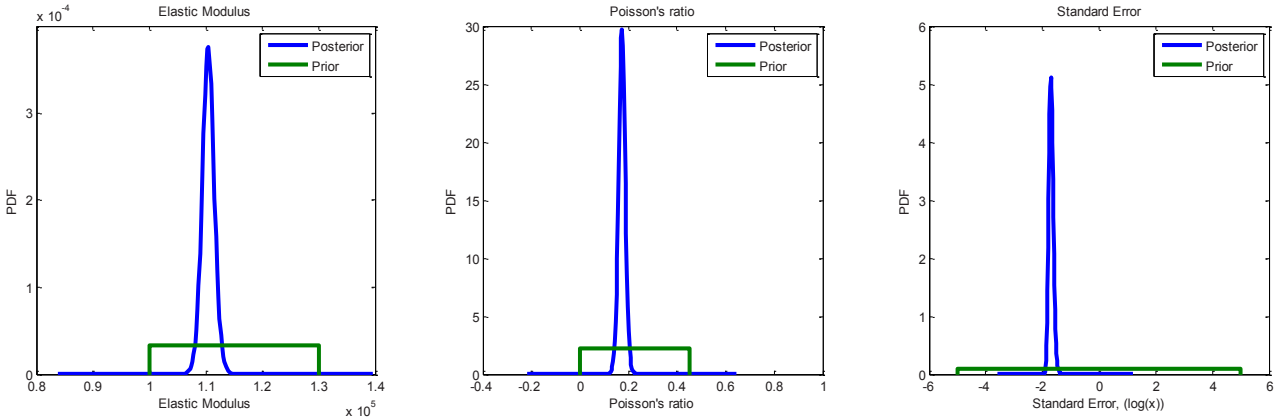

Figure 3 Probability density functions for Young's modulus, Poisson's Ratio, and standard error as calculated using Bayes theorem using two modes.

Finally, the same Bayesian technique was used but with all three frequencies for each sample included in the likelihood. The likelihood then becomes

$$p(\varepsilon|f,\theta)=\prod_{i=1}^{9}\exp\left(\frac{1}{2\sigma^2}\left(\left(\frac{f_i^7-f_{calc}^7}{f_{calc}^7}\right)^2+\left(\frac{f_i^9-f_{calc}^9}{f_{calc}^9}\right)^2+\left(\frac{f_i^{16}-f_{calc}^{16}}{f_{calc}^{16}}\right)^2\right)\right) \tag{10}$$

with the same priors as described in Eq. (9).

The results of the Bayesian analysis using Eq. (10) as a likelihood function are given in Figure 4. As was seen with the optimization results, the three frequency method results in PDFs that are slightly shifted, most notably in the distribution for the Poisson's ratio, when compared to the results with the two frequency likelihood function.

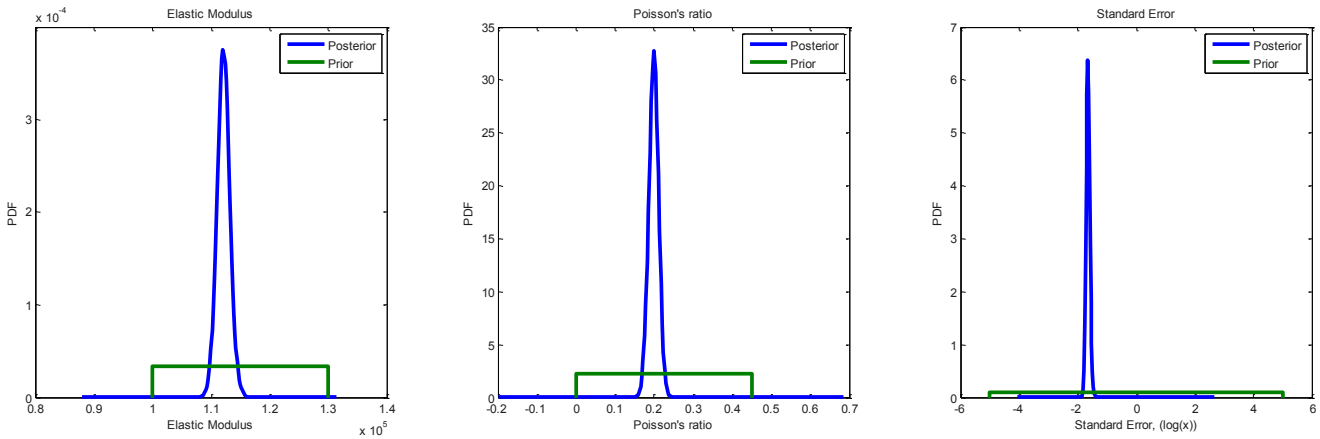

Figure 4 Prior and Posterior PDFs for Young's modulus, Poisson's ratio, and standard error from Bayesian updating using three modes.

5. COMPARISON OF RESULTS

The different techniques can be grouped into techniques that used two frequencies to estimate the elastic parameters and those techniques that used three frequencies for the estimation. Table 6 summarizes the three techniques of fitting elastic parameters used in this paper when two modes are used in the estimation. Table 7 summarizes the techniques for when three frequencies are used in the estimation. In both cases, the differences in the estimated parameters between the number of modes used in the fitting process is much greater than the differences in fitting techniques. As discussed above, when only two frequencies are used to fit the two elastic parameters, the estimated parameters will exactly reproduce the fitting data, and produce an error in the third

frequency. The error in predicting the third frequency represents the error due to noise, experimental errors, and errors due to the elastic model assumption. When three frequencies are used to estimate the parameters, these same errors exist, but the errors are spread over all three modes due to the least squares approach used here, producing a smaller error in the prediction of all three frequencies. The elastic parameters estimated using three frequencies will provide a more representative elastic model than will the parameters estimated using only two frequencies.

Table 6 Comparison of Optimal and Means of Elastic Parameters using two modes

Fit Method	Elastic Modulus	Poisson's Ratio
All Samples Least Squares (Table 2)	110,410 psi	0.173
Individual Samples Least Squares (Table 4)	110,410 psi	0.173
Bayesian	110,430 psi	0.173

Table 7 Comparison of Optimal and Means of Elastic Parameters using three modes

Fit Method	Elastic Modulus	Poisson's Ratio
All Samples Least Squares (Table 3)	112,100 psi	0.199
Individual Samples Least Squares (Table 5)	112,100 psi	0.199
Bayesian	112,120 psi	0.199

Probability density functions can be estimated using the posterior samples of the parameters obtained from the Bayesian calibration and from the optimizations where the elastic parameters were fit for each individual sample. KDEs were used to estimate the probability density functions of the parameters obtained with both the optimization and the Bayesian calibration. These KDEs are compared in Figure 5 and Figure 6 For the Young's modulus, the KDE representing the posterior distribution obtained from Bayesian calibration has a smaller variance than the optimization distribution. For Poisson's ratio, the trend is reversed with the PDF from the optimization results having the smaller variance.

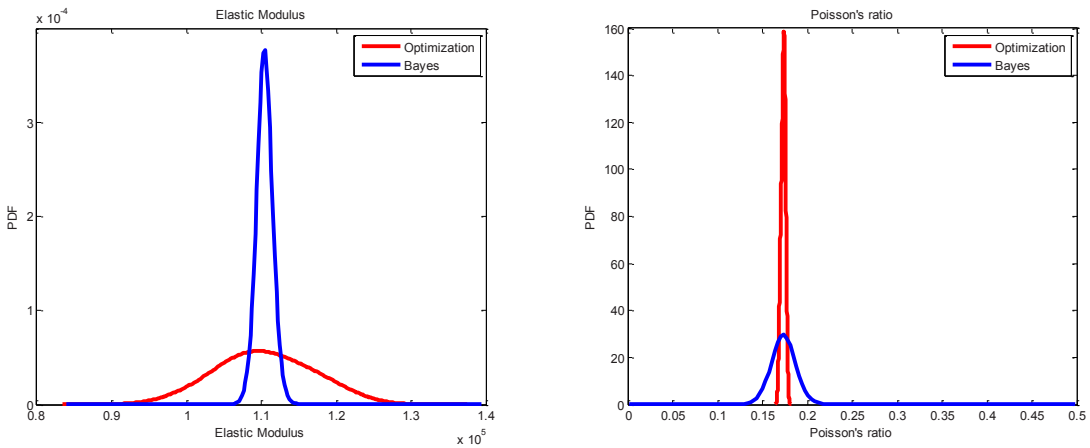

Figure 5 KDE comparisons for Young's modulus and Poisson's ratio using two frequencies for estimation.

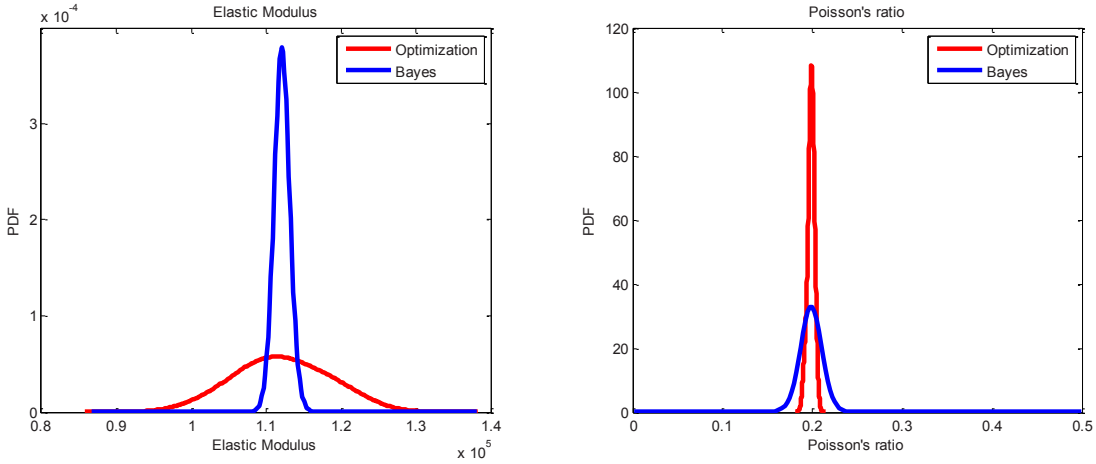

Figure 6 KDE comparisons for Young's modulus and Poisson's ratio using three frequencies for estimation.

Once the parameters for the elastic model and the standard error are calibrated using a Bayesian approach, the resulting samples can be forward propagated through the model to calculate the frequencies. The KDE of the frequencies can then be estimated. This provides an evaluation as to how well the estimation procedure performed. The standard error represents the error in the fit that is not consistent with the elastic model assumption, ([9]). These fit variations can be due to experimental uncertainty, measurement uncertainty, data fitting uncertainty, modeling assumptions such as linear elastic, and other epistemic sources. For the problem described in this paper, the error could also be due to the density. Here, the density was assumed to be the average of all the measured densities rather than using density as a design variable. The predicted first frequency with the error can be defined using Eq. (1) as

$$f_1(E,\nu,\sigma) = \left(1+10^{\sigma}\right)\sqrt{\frac{E}{\rho}}g_1(\nu) \tag{11}$$

The standard error is multiplied by the calculated frequency because of the manner in which the likelihood is normalized in Eq. (10). To calculate the PDFs shown in Figure 7, the parameters estimations from the Bayes procedure are evaluated in Eq. (11). The standard error is included by generating a Gaussian random variable with zero mean and a standard deviation equal to 10^{σ}. The PDF is then estimated using the KDE. In addition, frequency estimates can be generated using the prior. For this example, each of the elastic parameters are drawn from a uniform random distribution as defined by Eq. (9). Note that the estimate without the standard error does not fully cover the test data. This is because the data has some epistemic errors in them which is covered when the standard error, σ, is included.

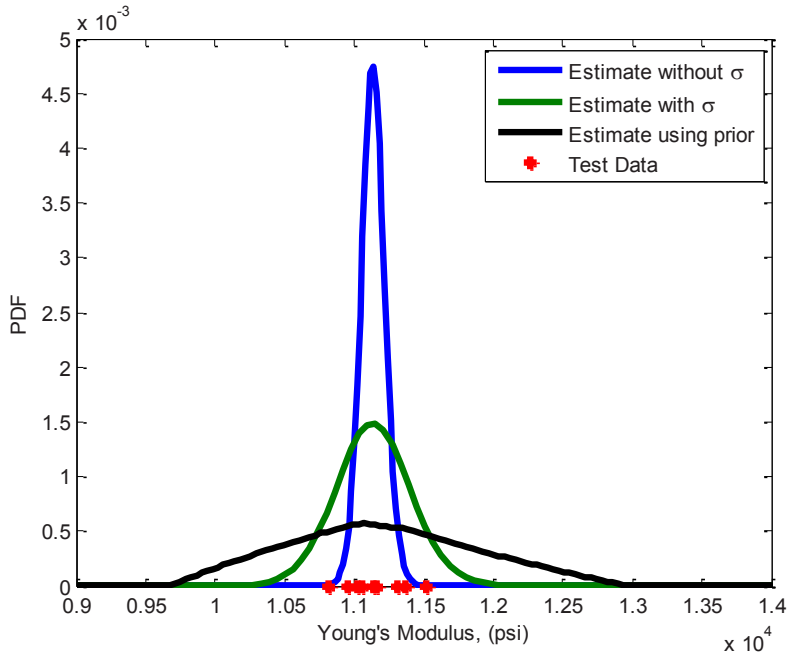

Figure 7 Probability density functions for the first frequency generated by back propagating estimated parameters.

The Bayesian technique of estimating parameters for a model has the advantage of producing estimates of PDFs for all of the estimated parameters as well as a PDF that can be used to assess the quality of fit of the parameters. In addition, using a parameterized prior such as a Johnson distribution (11), the variability in the PDF of the elastic parameters could also be explored by performing a series of Bayes estimations on a family of priors generated by varying the parameters of the Johnson distribution. This was not done in this work. Another advantage to the Bayesian technique is the ability to include prior information into the parameter estimation. If probability distribution functions already existed for a similar foam, those could be used as a prior instead of the uniform distribution.

The disadvantages to the Bayesian technique is the large number of runs necessary to generate the estimates of the PDFs. The only practical method to implement a Bayesian method is to have a very fast running model. Also, if there is little experimental data, the estimated distributions (posterior) for the elastic parameters will look like the assumed prior distributions. For a very large number of data points, the posterior distributions will approach the likelihood function.

6. CONCLUSIONS

A comparison of methods to fit the elastic parameters Young's modulus and Poisson's ratio from measured acoustic data is presented. Two different algorithms are used for estimating the parameters. The first is an optimization based least squares technique and the other is a Bayesian method. The parameters are fit using two different cost functions. The differences between the fit parameters are greater between the different cost functions than between the different algorithms. However, when the probability density functions are compared, the difference are most pronounce between algorithms with different trends for the Young's modulus and the Poisson's ratio. The analyses show that exploring different techniques when performing parameter estimations can provide a further characterization of the uncertainty.

7. ACKOWLEDGEMENTS

The author would like to thank Angel Urbina for his stimulating conversations and comments throughout the preparation of this paper.

Sandia is a multi-program laboratory operated by Sandia Corporation, a Lockheed Martin Company, for the United States Department of Energy's National Nuclear Security Administration under Contract DE-AC04-94AL85000.

8. REFERENCES

[1] Silverman, B. W., *Density Estimation for Statistics and Data Analysis*, Chapman and Hall, London, 1986.

[2] Robert, C. P., and Casella, G., *Monte Carlo Statistical Methods: Second Edition*, Springer Texts in Statistics: New York, 2004.

[3] Urbina, A., *Uncertainty Quantification and Decision Making in Hierarchical Development of Computational Models*, Ph. D. Dissertation, Vanderbilt University, 2009.

[4] Stasiunas, E. C., Simmermacher, T. W., "Development of a Constitutive Model For a Carbon Foam Material," *Proceedings of the International Modal Analysis Conference*, Feb, 2005.

[5] Marwala, T., Sibisi, S. , "Finite Element Model Updating Using Bayesian Framework and Modal Properties," *AIAA Journal of Aircraft*, Vol. 42, No 1, Pg 275 – 278, 2005.

[6] Hanson, K. M., and Hemez, F. ,"Bayesian Calibration of Material Models Based on Taylor Impact Tests," *Proceedings of the NECDC*, 2002.

[7] Neal, R, "Slice Sampling," *Annals of Statistics*, Vol. 31, No 3, pp 705-767, 2003.

[8] *Statistics Toolbox User's Guide*, The Mathworks, Inc. : Massachusetts, 2010.

[9] Kennedy, M. C. and O'Hagan, A. "Bayesian Calibration of Computer Models," *Journal of the Royal Statistical Society, Series B (Statistical Methodology)*, Vol. 63, No. 3, pp. 425-464, 2001.

[10] Johnson, N. L., "Systems of Frequency Curves Generated by Methods of Translation," *Biometrika Trust*, Vol. 36, No. ½, pp. 149-176, 1949.

Construction of DEM-base Traffic Model Using Optimal Velocity Model

Takayuki KOIZUMI, Nobutaka TSUJIUCHI, Ryota AKATSUKA
Department of Engineering, Doshisha University,
1-3, Tataramiyakodani, Kyotanabe-city, Kyoto, 610-0321, Japan

ABSTRACT

An environment is needed in which traffic can move smoothly, and traffic flow analysis is important in creating such an environment. Such analysis generally uses a micro-type traffic model. The micro model depicts an object (a car, a human, etc.) as a particle, and tracks the individual particles' behavior. However, this has been difficult because the objects exhibit complex behavior. Because the objects act with the individual resolves.

In this study, a Distinct Element Method (DEM)-base traffic model is constructed to aim the micro model depicting behavior characteristics in detail. DEM takes into account continuity and has received attention in the fields of micromeritics and terramechanics. In addition, the traffic model uses the Optimal Velocity (OV) model. The OV model is a method that calculates the optimal velocity from interparticle distance and accelerates or decelerates the particle. To validate the traffic model, experiment and simulation avoiding obstacles are carried out and the results are compared. As a result, the simulation showed similar behavior and velocity distribution to the experiment. Therefore, the effectiveness of the constructed traffic model could be confirmed.

1. INTRODUCTION

Traffic jams and congestion are generated in various places like roads, shopping malls, festivals, disaster areas, etc. Traffic jams and congestion cause mental stress and increase the incidence of traffic accidents. Thus, in designing environments in which people can move smoothly, traffic flow analysis is important.

Currently, use of the micro model in pursuing individual particle behavior is common in traffic flow analysis [1-6]. This model expresses an object, such as a car or person, as a particle. In this model, because the objects that become particles are capable of independent motion, the relation of action-reaction doesn't work between particles. A lot of other problems exist in expressing the behavior characteristics of an object in detail as a particle. In particular, when a pedestrian is targeted, free movement in any direction is possible. In addition, in showing a complex behavior characteristic that selects the moving pathway and the velocity from information that comes into sight, the analysis is very difficult. Therefore, we constructed a micro-type pedestrian model in which particle behaviors depict a pedestrian's behavior characteristics in detail, and analyzed the traffic flow.

A variety of micro models based on the Cellular Automata (CA) model have been proposed [1,2]. As CA model treats space discretely, the features can be calculated easily. However, there is a limit to the detailed expression of pedestrians' behavior characteristics because they exhibit unnatural behavior. On the other hand, with computer improvements, the Distinct Element Method (DEM) is paid attention to in the field of micromeritics and terramechanics [7]. DEM can express detailed behavior because DEM treats space continuously unlike the CA model. In this study, to aim micro-type pedestrian model depicting the behavior characteristics in detail, model-enhanced DEM is constructed. The acceleration computation of the particle modeled in this model incorporate the Optimal Velocity (OV) model [3,4]. The OV model calculates optimal velocity from distance between particles.

After that, the avoidance simulation, which takes into account the obstacle or other pedestrians, is done by using the DEM-base traffic model. In addition, an avoidance experiment similar to the simulations is done, and the effectiveness of the model is verified by comparing the results.

2. SYNOPSIS OF DEM-BASE TRAFFIC MODEL

To construct the DEM-base traffic model, the acceleration computation of the particle modeled in this model incorporates the OV model [3,4]. The OV model is a calculating method that requests the best particle velocity from the distance from a

T. Proulx (ed.), *Linking Models and Experiments, Volume 2*, Conference Proceedings of the Society for Experimental Mechanics Series 5,
DOI 10.1007/978-1-4419-9305-2_16, © The Society for Experimental Mechanics, Inc. 2011

particle forward, and accelerates and decelerates the particle. The acceleration of the particle located in x is given by Eq. (1):

$$\frac{d^2x}{dt^2} = \alpha\left(V(\Delta x) - \frac{dx}{dt} \right) \tag{1}$$

where α is known as the sensitivity, Δx is the interparticle distance, and $V(\Delta x)$ is known as the OV function. $V(\Delta x)$ is given by Eq. (2):

$$V(\Delta x) = \frac{v_{\max}}{2}\left(\tanh\left(\frac{\Delta x - d}{w} \right) + \tanh\left(\frac{d}{w} \right) \right) \tag{2}$$

where $v_{\max}$ is the maximum velocity, and d, w are the parameters. In this paper we choose $d = 0.47, w = 0.45$.

Next, we explain DEM [7]. DEM is a technique for not handling the structure as a continuum, but discretely analyzing it by modeling as individual particle elements.

In DEM, the acceleration of the particle is calculated by using a different method, and velocity dx/dt and position x are given in Eqs. (3) and (4):

$$\left.\frac{dx}{dt}\right|_{t+\Delta t} = \left.\frac{dx}{dt}\right|_{t} + \left.\frac{d^2x}{dt^2}\right|_{t+\Delta t} \Delta t \tag{3}$$

$$\left. x \right|_{t+\Delta t} = \left. x \right|_{t} + \left.\frac{dx}{dt}\right|_{t+\Delta t} \Delta t \tag{4}$$

In this way, as the acceleration at new time $t + \Delta t$ is integrated, displacement and the velocity at time $t + \Delta t$ are obtained. The movement tracks of the particle are computable by repeating this calculation by time step Δt.

In primary DEM, when the particle comes in contact with something, the contact force is calculated by using the Voigt model and the acceleration is given. However, it is necessary to calculate the acceleration of the particle in the noncontact state in the DEM-base traffic model. Then, the accelerometer calculation is done by using the above OV model in the traffic model.

The obstacle-avoiding algorithm by the DEM-base traffic model is described. This algorithm defines view area and affected area [5]. View area distinguishes the obstacle particle with the possibility of jamming in for the target direction of particle i. Affected area judges the particle to be actually influenced by the deceleration vector $\vec{v}_o$ in the area of view. Fig. 1 shows the view area and the affected area. r_i is radius of particle i in the figure.

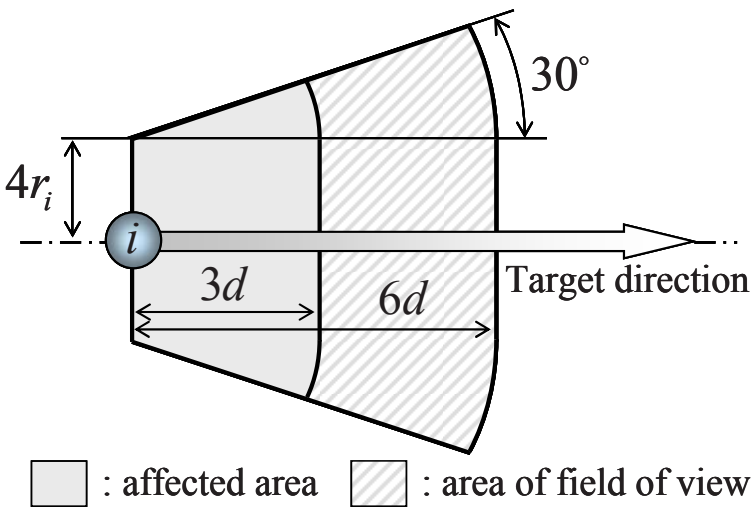

Fig. 1 View area and affected area

When the center of obstacle particle j doesn't exist in the view area, i doesn't receive influence from surrounding particles, and give maximum velocity $v_{i\max}$ in the target direction of i. On the other hand, when the center of particle j exists in the view area, velocities $|\vec{v}_{ni}|\cos\theta_{ni}, |\vec{v}_{nj}|\cos\theta_{nj}$ of the direction from i to j at t are obtained respectively (Fig. 2).

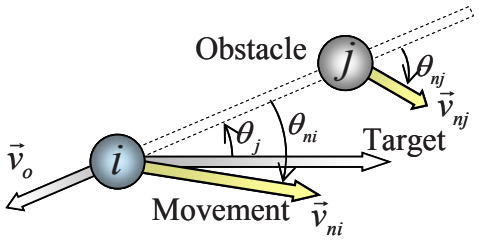

Fig. 2 Judgment of obstacle

In the case of $|\vec{v}_{ni}|\cos\theta_{ni} \le |\vec{v}_{nj}|\cos\theta_{nj}$, i is unaffected because i can't catch up with j. Then, i is given $v_{i\max}$ in the target direction. In the contrasting case of $|\vec{v}_{ni}|\cos\theta_{ni} > |\vec{v}_{nj}|\cos\theta_{nj}$, it is thought that there is a possibility of getting jammed up because i approaches j in the direction from i to j. Then, time Δt_{ij}, in which i and j come into contact with the direction from i to j, is requested by Eq. (5):

$$\Delta t_{ij} = \frac{|\vec{x}_i - \vec{x}_j| + r_i + r_j}{|\vec{v}_{ni}|\cos\theta_{ni} - |\vec{v}_{nj}|\cos\theta_{nj}} \tag{5}$$

Next, from the relation of the position and the velocity at t, position $\vec{x}_i', \vec{x}_j'$ of i, j at $t + \Delta t_{ij}$ are obtained respectively. It is judged from the $\vec{x}_i', \vec{x}_j'$ whether the center of j' exists in the affected area of i'.

When j' doesn't exist it (Fig.3(a)), it is assumed not to receive the influence of deceleration vector $\vec{v}_o$, because i is not intervened in particle j. Then, i is given $v_{i\max}$ in the target direction. On the other hand, when existing (Fig.3(b)), deceleration vector $\vec{v}_o$ acts on i because j jams in i.

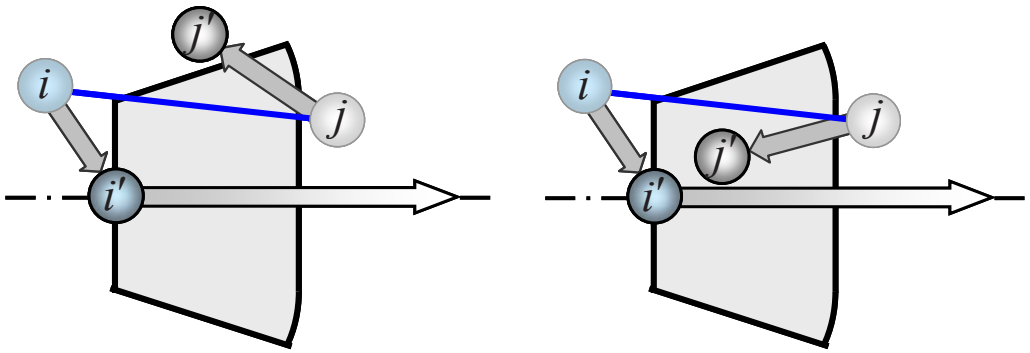

(a) $|\vec{v}_o| = 0$ **(b)** $|\vec{v}_o| \neq 0$

Fig. 3 Judgment of affected area

Deceleration $|\vec{v}_o|$ is requested from Eq. (6) by using the OV function of Eq. (2) (Fig. 4(a)).

$$|\vec{v}_o| = \alpha\left(V(\Delta x_{ij}) - |\vec{v}_{ni}|\cos\theta_{ni'}\right)\cdot\Delta t \quad \left(\Delta x_{ij} = \min\left(|x_i - x_j|, |x_i - x_{j'}|\right)\right) \tag{6}$$

In addition, by using $|\vec{v}_o|$, movement direction $\theta_{ni'}$ of the direction from i to j' at time $t + \Delta t$ is given by Eq. (7),

$$\theta_{ni'}\big|_{t+\Delta t} = \cos^{-1}\left(\frac{|\vec{v}_{ni}|\cos\theta_{ni'}\big|_t - |\vec{v}_o|}{v_{i\max}}\right)\cdot\frac{-\sin\theta_{j'}}{|\sin\theta_{j'}|} \tag{7}$$

and the movement velocity is given by expression (8) (Fig. 4(b)),

$$\begin{cases} |\vec{v}_{ni}| = v_{i\max} & \left(|\theta_{ni'} + \theta_{j'}| \le \dfrac{\pi}{6}\right) \\ |\vec{v}_{ni}| = v_{i\max}\cdot\cos\left(|\theta_{ni'} + \theta_{j'}| - \dfrac{\pi}{6}\right) & \left(|\theta_{ni'} + \theta_{j'}| > \dfrac{\pi}{6}\right) \end{cases} \tag{8}$$

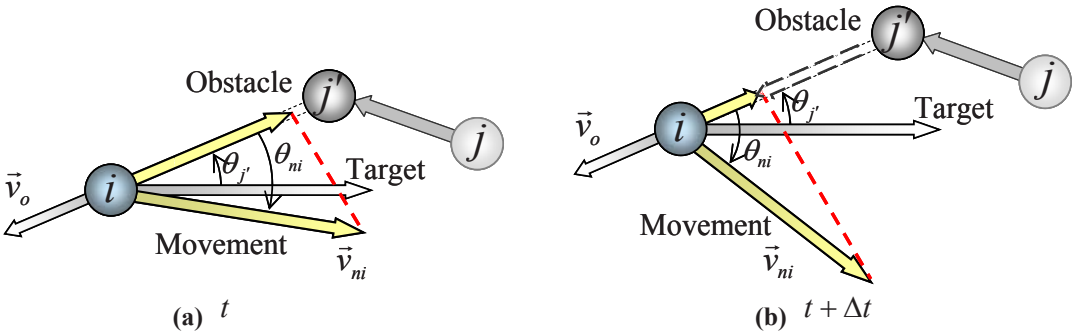

Fig. 4 Movement velocity vector

3. VALIDITY VERIFICATION OF THE DEM-BASE TRAFFIC MODEL

We simulated and experimented with avoiding obstacles and other pedestrians to verify the effectiveness of the constructed traffic model. The avoidance simulation and experiment were done in three types of conditions: (1) obstacle avoidance, (2) overtaking another pedestrian, and (3) avoiding an oncoming pedestrian. The avoidance simulation and experiment are described as follows.

3.1. AVOIDANCE SIMULATION

Table 1 shows initial X-Y coordinates of two particles, the direction of the target, and the maximum velocity in each condition. In this simulation, the particle radius was assumed to be 0.2 m, and the time step was assumed to be 1.0×10-4 s. In addition, the maximum velocity used was v_{max} =0.86 m/s, which was actually measured walking speed in this study.

Table 1 Parameter of avoidance simulation

Condition No.	X-Y coordinate ([m], [m])		Target direction		Maximum velocity (v_{max}) [m/s]	
	No. 1	No. 2	No. 1	No. 2	No. 1	No. 2
(1)	(-2,0)	(0,0)	X	0	0.86	0
(2)	(-2,0)	(-2,0)	X	X	0.86	0.43
(3)	(-2,0)	(2,0)	X	-X	0.86	0.86

3.2. AVOIDANCE EXPERIMENT

An avoidance experiment similar to the avoidance simulations was done. Fig. 5 shows the look of the experiment. By using a motion capture system, pedestrian behavior was measured with four markers attached to the test subject. Fig. 6 shows the attachment position of the markers. Then, the sampling frequency was assumed to be 200 Hz. The default position of test subjects and the target direction were determined as well as the simulation in each condition, and the test subjects were directed to walk in the target direction naturally. As the test subjects headed in the target direction, a walkway 3 m in width was set using colored cones (Fig.5).

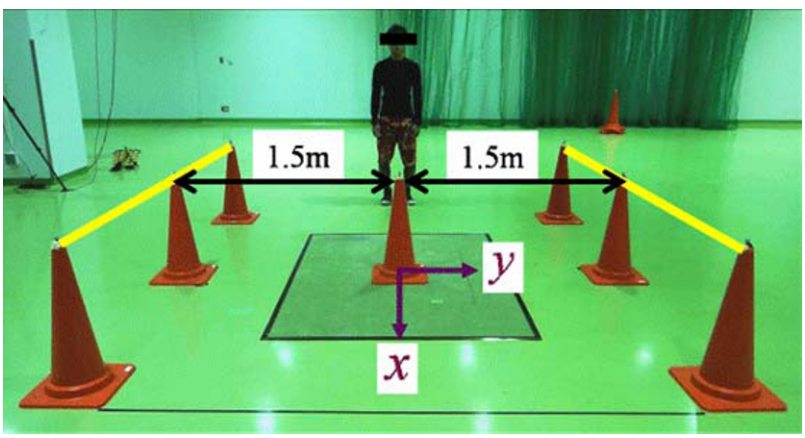

Fig. 5 Avoidance experiment (Condition No. 1)

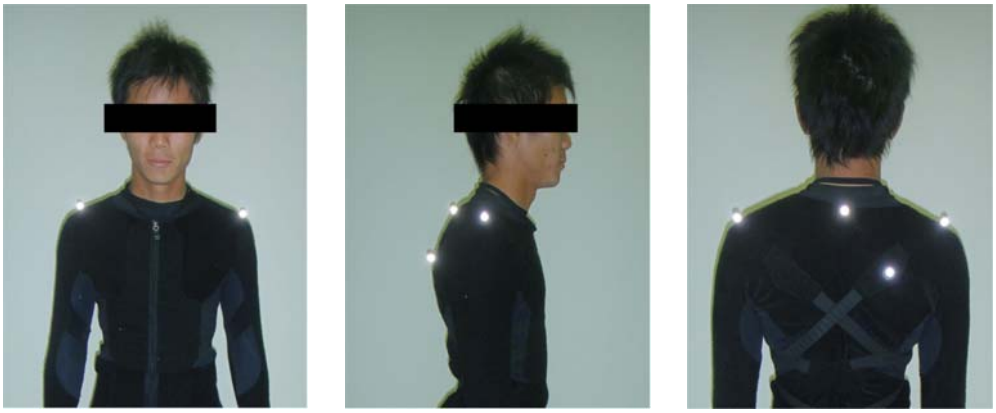

(a) Front side (b) Lateral side (c) Back side

Fig. 6 Attachment position of marker

3.3. RESULTS AND CONSIDERATIONS

The particle trajectories on the avoidance simulation in each condition are shown in Fig. 7 for five seconds. Particle No. 1 is white and No. 2 is black. Next, the subject's walking tracks in the avoidance experiment are shown in Fig. 8. From Figs. 7 and 8, the particle trajectories of the simulation correspond well to the walking tracks of the experiment. Also, each figure plots positional coordinates for a fixed time. As seen from the figures, the plot intervals have no variability. Therefore, particles are understood to move with constant velocity in both the simulation and the experiment. The above result shows that we successfully constructed the DEM-base traffic model depicting the behavior characteristics in detail.

Moreover, in the experiment, when the subject comes at about $|x|$=2 m after the experiment start, there is a tendency for the plot interval to narrow, and the walking speed decreases. This is because there was limited recognition range of the marker on the motion capture system, and the subject was directed to stop at $|x|$=2 m. On the other hand, it was set that the particles keep moving in the target direction in the simulation. However, it is thought that this difference doesn't greatly influence the result of avoiding the obstacle, because of after avoiding.

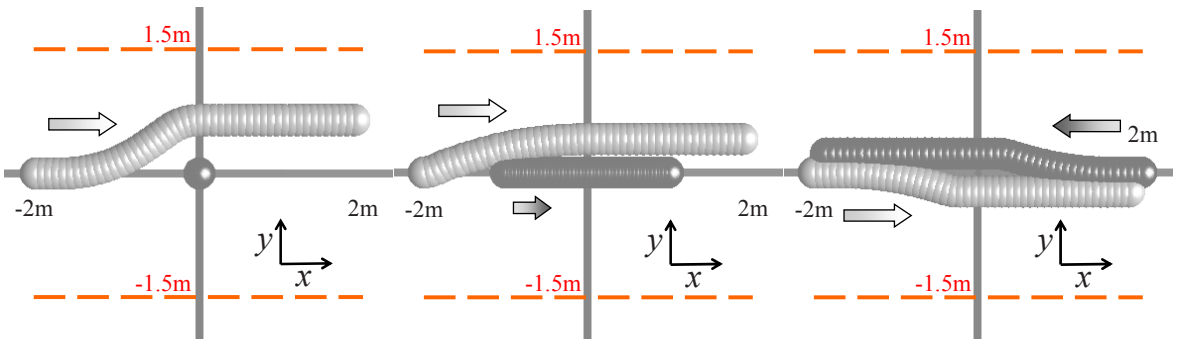

(a) Condition No. 1 (b) Condition No. 2 (c) Condition No. 3

Fig. 7 Orbital distribution (Avoidance simulation)

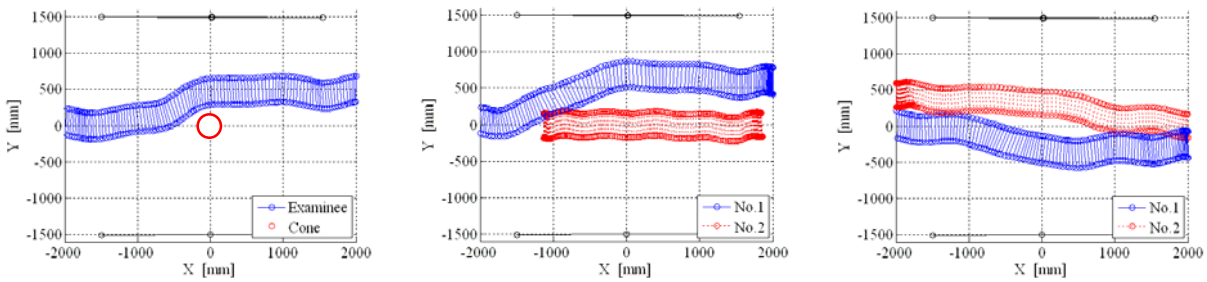

(a) Condition No. 1 (b) Condition No. 2 (c) Condition No. 3

Fig. 8 Orbital distribution (Avoidance experiment)

4. CONCLUSION

In this study, a DEM-base traffic model was constructed with invoking the OV model for DEM. As a result of a simulation of obstacle avoidance using the model, the behavior in the simulation agreed well with the experiments.

This model will introduce the influence of a wall in the future. In addition, the number of objects will be increased, the behavior characteristics in a crowd will be surveyed, and we will aim at the construction of a model depicting the behavior characteristics in detail.

REFERENCES

[1] K. Nishinari, Jammology Physics of Self-driven Particles Toward Solution of All Jams, 10th Annual Japanese -American Frontiers of Science Symposium, 2007.

[2] T. Tamaki, S. Yasue and E. Kita, Traffic Simulation Using Stochastic Velocity Model and CA (ITS), Information Processing Society of Japan Journal, vol.45, No.3, 858-869, 2004.

[3] M. Bando, K. Hasebe, A. Nakayama, A. Shibata and Y. Sugiyama, Dynamical Model of Traffic Congestion and Numerical Simulation, J. of Phys. Rev. E, Vol.51, No.2, 1035- 1042, 1995.

[4] M. Kuwahara and G.F. Newell, Queue Evolution on Freeways Leading to a Single Core City during the Morning Peak in Proceedings, 10th International Symposium on Transportation and Traffic Theory, 21-40, 1987.

[5] E. Harada, H. Gotoh and Y. Maruyama, Proposal of DEM-base Crowd Refuge Model with the Optimal Velocity Model, Japan Society of Civil Engineers, Vol.51, 553-558, 2007.

[6] D. Helbing and P. Molnar. Social Force Model for Pedestrian Dynamics. Phys. Rev. E, Vol.51, 4282-4286, 1995.

[7] P.A. Cundall, O.D.L. Strack, A Discrete Numerical Model for Granular Assemblies, Geotechnique, Vol.29, No.1, 47-65, 1979.

Confidence Intervals of Modal Parameters during Progressive Damage Test

Michael Döhler, Falk Hille, Xuan-Binh Lam, Laurent Mevel and Werner Rücker

Abstract In Operational Modal Analysis, the modal parameters (natural frequencies, damping ratios and mode shapes) obtained from Stochastic Subspace Identification (SSI) of a structure, are afflicted with statistical uncertainty. For evaluating the quality of the obtained results it is essential to know the respective confidence intervals of these figures. In this paper we present algorithms that automatically compute the confidence intervals of modal parameters obtained from covariance- and data-driven SSI of a structure based on vibration measurements. They are applied to the monitoring of the modal parameters of a prestressed concrete highway bridge during a progressive damage test that was accomplished within the European research project IRIS. Results of the covariance- and data-driven SSI are compared.

1 Introduction

Subspace-based linear system identification methods have been proven efficient for the identification of the eigenstructure of a linear multivariable system in many applications. In this paper, the main motivation is output-only structural identification in vibration mechanics, of a structure subject to ambient unmeasured vibrations. The obtained modal parameters (natural frequencies, damping ratios and mode shapes) are afflicted with a statistical uncertainty, e.g. due to measurement noise, unstationarities in the excitation, or measurement data that may not be long enough to assume convergence of the identification method. For evaluating the quality of the identified modal parameters it is essential to know the respective confidence intervals of these

Michael Döhler, Xuan-Binh Lam, Laurent Mevel
INRIA, Centre Rennes - Bretagne Atlantique, Campus de Beaulieu, F-35042 Rennes, France,
e-mail: michael.dohler@inria.fr, xuan.lam@inria.fr, laurent.mevel@inria.fr

Falk Hille, Werner Rücker
BAM Federal Institute for Material Research and Testing, Division Buildings and Structures, D-12200 Berlin, Germany, e-mail: falk.hille@bam.de, werner.ruecker@bam.de

T. Proulx (ed.), *Linking Models and Experiments, Volume 2*, Conference Proceedings of the Society for Experimental Mechanics Series 5,
DOI 10.1007/978-1-4419-9305-2_17, © The Society for Experimental Mechanics, Inc. 2011

figures, especially when evaluating changes in a system (e.g. due to damage) where identified modal parameters are compared.

The problem consists in quantifying the uncertainty related to the identified modal parameters of a structure subject to ambient unmeasured vibrations. In [9], an algorithm was derived to automatically compute confidence intervals in covariance driven SSI, based on [8]. In [4] and [5], some propositions were made that improve this algorithm in efficiency and generality. Using covariance driven SSI and data driven SSI with the Unweighted Principal Component Algorithm (UPC), the resulting algorithm is applied in this paper on the S101 Bridge in Austria to compute confidence intervals, together with an automated monitoring procedure, during the progressive damage test of the bridge.

2 Stochastic Subspace Identification

2.1 State Space Model

The mechanical system is supposed to be a stationary linear dynamical system

$$\begin{cases} M\ddot{\mathscr{Z}}(t)+C\dot{\mathscr{Z}}(t)+K\mathscr{Z}(t) = \nu(t) \\ Y(t) = L\mathscr{Z}(t) \end{cases},$$

with

- $\mathscr{Z}$: displacements of the degrees of freedom,
- M, C, K: mass, damping, stiffness matrices,
- t: continuous time,
- ν: excitation (Gaussien, zero-mean, white),
- L: observation matrix giving the observation Y.

The modal characteristics

- μ vibration modes or eigenfrequencies
- ψ_μ modal shapes or eigenvectors

are solutions of the following equation:

$$(M\mu^2+C\mu+K)\Psi_\mu = 0 \ , \ \psi_\mu = L\Psi_\mu .$$

We switch to the state space model in discrete time by sampling at the rate $1/\delta$ with

$$X_k = \begin{bmatrix} \mathscr{Z}(k\delta) \\ \dot{\mathscr{Z}}(k\delta) \end{bmatrix} \ , \ Y_k = Y(k\delta)$$

and get

$$\begin{cases} X_{k+1} = FX_k+V_k \\ Y_k = HX_k \end{cases} . \tag{1}$$

The modal characteristics (μ, ψ_μ) are given by the eigenstructure (λ, Φ_λ) of F:

$$e^{\delta\mu} = \lambda$$
$$\psi_\mu = \phi_\lambda \stackrel{\Delta}{=} H\Phi_\lambda$$

In the sequel the dimension of the observed output Y is much smaller than the dimension of the state X.

2.2 Identification Procedure

Knowing the output data Y_k at the time instants $k = 1, \ldots, N$, the eigenstructure (λ, ϕ_λ) of system (1) is identified with Stochastic Subspace Identification algorithms. In this work, the covariance driven approach [2, 7] and data driven approach with the Unweighted Principal Component algorithm [6, 7] are used.

For both approaches the parameters p and q are chosen as variables with $(p+1)r \geq qr \geq n$ with the desired model order n. Usually, $p+1 = q$ is set [1]. The data matrices

$$\mathscr{Y}_{p+1}^{+} \stackrel{\text{def}}{=} \begin{pmatrix} Y_{q+1} & Y_{q+2} & \vdots & Y_{N-p} \\ Y_{q+2} & Y_{q+3} & \vdots & Y_{N-p+1} \\ \vdots & \vdots & \vdots & \vdots \\ Y_{q+p+1} & Y_{q+p+2} & \vdots & Y_N \end{pmatrix}, \quad \text{and} \quad \mathscr{Y}_{q}^{-} \stackrel{\text{def}}{=} \begin{pmatrix} Y_q & Y_{q+1} & \vdots & Y_{N-p-1} \\ Y_{q-1} & Y_q & \vdots & Y_{N-p-2} \\ \vdots & \vdots & \vdots & \vdots \\ Y_1 & Y_2 & \vdots & Y_{N-p-q} \end{pmatrix} \quad (2)$$

are built, and, according to the method, a subspace matrix as follows:

- For the **covariance driven** approach, the subspace matrix

  $$\mathscr{H}_{p+1,q}^{\text{cov}} \stackrel{\text{def}}{=} \mathscr{Y}_{p+1}^{+} \mathscr{Y}_{q}^{-T}$$

  is built. It has the factorization property

  $$\mathscr{H}_{p+1,q}^{\text{cov}} = \mathscr{O}_{p+1} F \mathscr{C}_q$$

  with the matrix of observability

  $$\mathscr{O}_{p+1} = \begin{pmatrix} H \\ HF \\ \vdots \\ HF^p \end{pmatrix}$$

  and the matrix of controllability $\mathscr{C}_q$.

- For the Unweighted Principle Component algorithm of the **data driven** approach, the matrix

$$\mathscr{H}_{p+1,q}^{\text{data}} \stackrel{\text{def}}{=} \mathscr{Y}_{p+1}^{+} \mathscr{Y}_{q}^{-T} \left(\mathscr{Y}_{q}^{-} \mathscr{Y}_{q}^{-T} \right)^{-1} \mathscr{Y}_{q}^{-}$$

  is defined. It enjoys the factorization property

$$\mathscr{H}_{p+1,q}^{\text{data}} = \mathscr{O}_{p+1} \mathscr{X}_{q} \tag{3}$$

  into matrix of observability and Kalman filter state sequence. As $\mathscr{H}_{p+1,q}^{\text{data}}$ is usually a very big matrix and difficult to handle, a thin RQ decomposition of the data matrices is done at first:

$$\begin{pmatrix} \mathscr{Y}_{q}^{-} \\ \mathscr{Y}_{p+1}^{+} \end{pmatrix} = RQ = \begin{pmatrix} R_{11} & 0 \\ R_{21} & R_{22} \end{pmatrix} \begin{pmatrix} Q_1 \\ Q_2 \end{pmatrix}.$$

  Then, $\mathscr{H}_{p+1,q}^{\text{data}} = R_{21} Q_1$ follows and the subspace matrix is defined as

$$\mathscr{H}_{p+1,q}^{\text{data,R}} = R_{21},$$

  which enjoys also factorization property (3), but with a different matrix on the right side. See also [6] for further details.

In what follows, the superscripts of the subspace matrix $\mathscr{H}_{p+1,q}$ are skipped, as the identification procedure is the same for the covariance and data driven approach. Now we want to obtain the eigenstructure of the system (1) from a given matrix $\mathscr{H}_{p+1,q}$. The observability matrix $\mathscr{O}_{p+1}$ is obtained from a thin SVD of the matrix $\mathscr{H}_{p+1,q}$ and its truncation at the desired model order n:

$$\begin{aligned} \mathscr{H}_{p+1,q} &= U \, \Delta \, V^T \\ &= \begin{pmatrix} U_1 & U_0 \end{pmatrix} \begin{pmatrix} \Delta_1 & 0 \\ 0 & \Delta_0 \end{pmatrix} V^T, \\ \mathscr{O}_{p+1} &= U_1 \, \Delta_1^{1/2}. \end{aligned} \tag{4}$$

The observation matrix H is then found in the first block-row of the observability matrix $\mathscr{O}_{p+1}$. The state-transition matrix F is obtained from the shift invariance property of $\mathscr{O}_{p+1}$, namely

$$\mathscr{O}_{p}^{\uparrow}(H,F) = \mathscr{O}_{p}(H,F) \, F, \quad \text{where } \mathscr{O}_{p}^{\uparrow}(H,F) \stackrel{\text{def}}{=} \begin{pmatrix} HF \\ HF^2 \\ \vdots \\ HF^p \end{pmatrix}. \tag{5}$$

Of course, for recovering F, it is needed to assume that $\operatorname{rank}(\mathscr{O}_p) = \dim F$, and thus that the number $p+1$ of block-rows in $\mathscr{H}_{p+1,q}$ is large enough. The eigenstruc-

ture (λ, ϕ_λ) results from

$$\det(F - \lambda\, I) = 0,\;\; F\;\varphi_\lambda = \lambda\;\varphi_\lambda,\;\; \phi_\lambda = H\varphi_\lambda, \tag{6}$$

where λ ranges over the set of eigenvalues of F.

In practice, the truncation order of the SVD is increased from 1 to the maximal system order in Equation (4) to get a stabilization diagram of the obtained modes vs model order. This gives results for successive different but redundant models and modes that are common to many successive models can be distinguished from the spurious modes.

There are many papers on the used identification techniques. A complete description can be found in [2, 6, 7, 3], and the related references. A proof of non-stationary consistency of these subspace methods can be found in [3].

3 Confidence Interval Computation

The statistical uncertainty of the obtained modal parameters is necessary to assess the confidence one can have in these values, e.g. when comparing the modal parameters of different states of a structure. Modal parameters with little confidence (and hence large confidence intervals) are little useful for comparing structural states.

The uncertainties of the modal parameters at a chosen system order can be computed from the uncertainty of the subspace matrix by doing a sensitivity analysis, and the covariance of the subspace matrix $\Sigma_{\mathscr{H}}$ can be evaluated by cutting the sensor data into blocks on which instances of the subspace matrix are computed. It holds

$$\Delta f_j = \mathscr{J}_{f_j}\,\Delta(\mathrm{vec}\,\mathscr{H}),\quad \Delta d_j = \mathscr{J}_{d_j}\,\Delta(\mathrm{vec}\,\mathscr{H}),\quad \Delta\varphi_j = \mathscr{J}_{\varphi_j}\,\Delta(\mathrm{vec}\,\mathscr{H}),$$

with the frequencies f_j, damping ratios d_j and mode shapes φ_j, and their sensitivities $\mathscr{J}$ with respect to $\mathrm{vec}\,\mathscr{H}$. It follows

$$\mathrm{cov} f_j = \mathscr{J}_{f_j}\Sigma_{\mathscr{H}}\,\mathscr{J}_{f_j}^T,\quad \mathrm{cov} d_j = \mathscr{J}_{d_j}\Sigma_{\mathscr{H}}\,\mathscr{J}_{d_j}^T,\quad \mathrm{cov}\varphi_j = \mathscr{J}_{\varphi_j}\Sigma_{\mathscr{H}}\,\mathscr{J}_{\varphi_j}^T.$$

This offers a possibility to compute confidence intervals on the modal parameters at a certain system order without repeating the system identification. In [9] this algorithm was described in detail for the covariance-driven SSI.

In this paper, three extensions of the confidence interval computation of [9] are used:

- As the mode shapes are defined up to a complex constant, the confidence interval computation on them requires an additional constraint. In [9], the confidence intervals are computed with respect to one point of the mode shape that is normalized to value one, which results in a confidence interval of size zero of this point. In [4], the confidence intervals of the mode shapes are computed with respect to the maximal amplitude of deflection, which is applied in this paper.

- The sensitivity computation of $\mathscr{J}_{f_j}$, $\mathscr{J}_{d_j}$ and $\mathscr{J}_{\varphi_j}$ depends on the sensitivities of the singular vectors of $\mathscr{H}$. In [5], an efficient computation was derived, which is applied here.
- Also in [5], the computation of $\Sigma_{\mathscr{H}}$ was extended to the data driven UPC subspace matrix.

4 Modal Analysis of S101 Bridge during Progressive Damage Test

Within the European research project "Integrated European Industrial Risk Reduction System (IRIS)" the prestressed concrete bridge S01 was artificially damaged [10]. The damaging processes were accompanied with a permanent measurement of the static and dynamic behavior of the structure. With that action a complete record of monitoring data during a defined loss of structural integrity on a typical bridge structure could be provided to test and evaluate SHM methods and applications.

4.1 The S101 Bridge

The S101 was a prestressed concrete bridge from the early 1960th spanning over the 4-lane highway A1 in Austria. The structural system was a three-field frame with a 32 m wide mean field and two 12 m wide side fields. The superstructures cross section was designed as a 7.2 m wide post-tensioned double T-beam with varying heights (Figure 1).

During recurring technical inspections of the bridge several deficiencies as cracks and spellings have been found. Since the crack pattern correlated with the geometric properties of the prestressing a significant deficit of structural reliability was assumed. Because of the subsequent determined limited load bearing capacity it was decided to replace the structure.

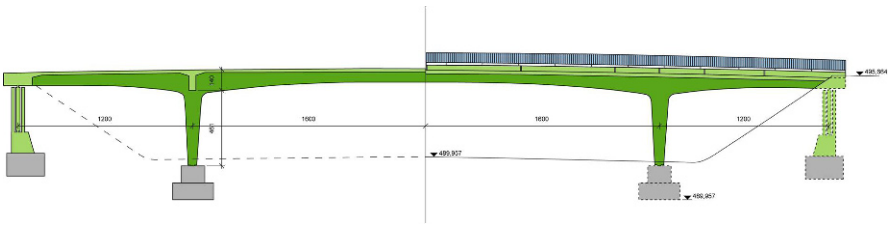

Fig. 1 System drawing of bridge S101 [10].

4.2 Measurement Description

The measurement campaign was carried out by the Austrian company VCE and the University of Tokyo [10]. For vibration measurement a BRIMOS measurement system containing a permanent sensor grid was used. The grid consisted out of 15 sensor locations on the bridge deck, see Figure 2, in each location three sensors for measurement in the bridge decks vertical, longitudinal and transversal direction. All in all, for vibration measurement 45 acceleration sensors were applied. Additionally, for verification of the static response of the structure to the damaging, the vertical displacement of the bridge deck was measured in three characteristic locations.

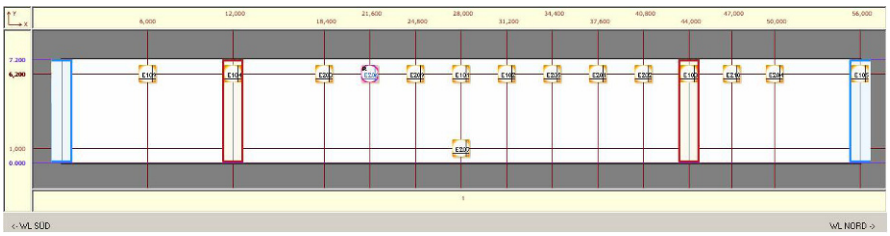

Fig. 2 Bridge deck with sensor grid for vibration measurement, on each location acceleration was measured in three directions [10].

The measurement took place with a sampling frequency of 500 Hz. All values were recorded permanently and stored in files with 165000 data points each. During the three days measurement campaign 714 data files each containing 48 channels were produced.

The damage test took place between the 10 and 13 December 2008. Because of the time in year and because of clouds the variation of the bridge temperature over the whole period of the test was minimal. During the test the highway beneath the bridge was open in one direction. Therefore dynamic excitations from moving trucks can be found in the signals. The second direction was closed for traffic because of construction work which in addition took place near the bridge. Perturbation of the measurement signals by the undergoing road construction work cannot be ruled out.

4.3 Damage Description

Prior to the demolition of the bridge a destructive damage test for measuring and investigating the structural behavior during damaging processes could be arranged and carried out. The campaign was planed and organized by VCE [10].

Two major damage scenarios were artificially induced. First, a significant damage on one of the four columns was reproduced by cutting through the column on its

Fig. 3 Destructive damaging; a) cutting through one of the columns, b) and c) successive intersecting of prestressing tendons [10].

A	First cut through column	G	Uplifting column
B	Second cut through column	H	Exposing cables and cut through first cable
C	Lowering column (first step)	I	Cut through second cable
D	Lowering column (second step)	J	Cut through third cable
E	Lowering column (third step)	K	Cut through fourth cable
F	Inserting steel plates		

Table 1 Damage scenarios during progressive damage test of S101 bridge.

lower end. With this action a change in the global structural system was to be implemented. After a second cut a 5 cm slice of the column was removed and the column was lowered for altogether 3 cm until the elastic ductility of the bridge structure was depleted (Figure 3).

Afterwards the column was uplifted again to its original position and secured there by steel plates. In a second damage scenario prestressing tendons of one of the beams were to be cut successively (Figure 3). Since the loss of prestressing by deterioration processes is a typical risk for existing RC bridges it was of specific interest to examine the sensitivity of damage identification routines to that kind of structural degradation. All in all three and a quarter of a wire bundle were cut through. Between each intersection pauses of several hours were kept to let the structural system change into a new state of equilibrium. For safety reasons the damaging process was stopped after 3.25 tendons were intersected. An overview of all introduced damages is given in Table 1.

4.4 System Identification Results before Destruction

In this paper, primary interest is in the identification of the first five modes in the frequency range [0–18 Hz]. For this, the data was downsampled from sampling rate 500 Hz by factor 8 and after a first examination only the sensors in vertical direction were chosen, as in this frequency range only vertical bending and torsional modes were present. System identification and confidence interval computation was done with the covariance and data driven SSI methods from Section 2.2 with parameters

$p+1=q=11$ at system orders $n=1,\ldots,70$. Confidence bounds were obtained by cutting the data into 100 blocks.

In Figure 4, the stabilization diagrams of the natural frequencies from both SSI methods are presented, where the confidence interval of each frequency is plotted as a horizontal bar. The obtained confidence bounds on the frequencies were used to clean the diagrams: Modes with frequencies having big confidence bounds are likely to be spurious and are erased. In this case, all modes with confidence bounds bigger than 2% of the frequency value were deleted.

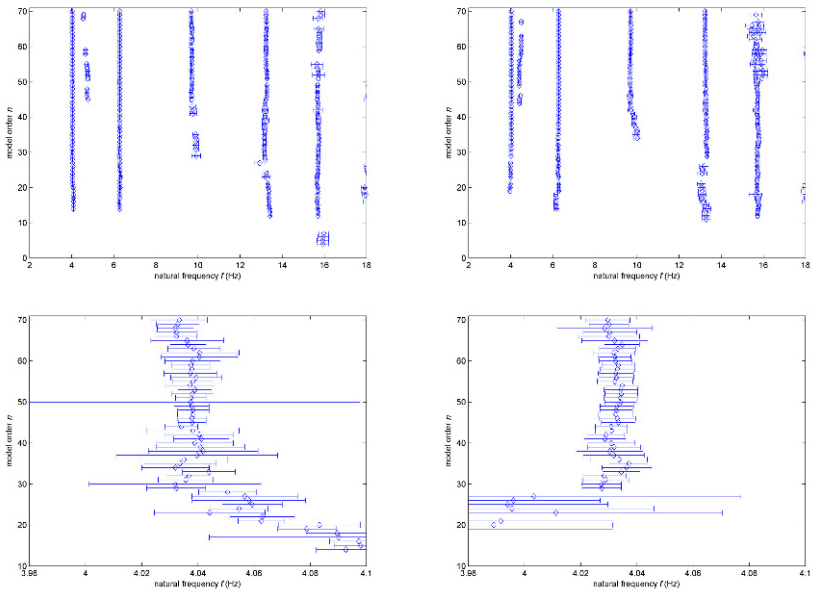

Fig. 4 Stabilization diagrams with covariance driven SSI (left) and data driven SSI (right) containing confidence intervals on the frequencies (top: full diagrams, bottom: zoom on first mode).

From the stabilization diagrams, the modes of the system are chosen. In Table 2, an overview of the obtained modal parameters and their confidence bounds at model order 40 is given. Note that all confidence bounds are relative values in percent, i.e. the standard deviation of a value divided by the value and multiplied by 100. For the mode shapes, only the relative confidence bound is displayed for the mode shape element of maximal amplitude.

Finally, the obtained mode shapes at the 14 sensors of one side of the bridge deck are displayed with their confidence bounds in Figure 5. From the 15th sensor on the other side of the bridge deck (see also Figure 2), information about the kind of the mode is obtained. So, modes 1, 3 and 5 are vertical bending modes and modes 2 and 4 are torsional modes.

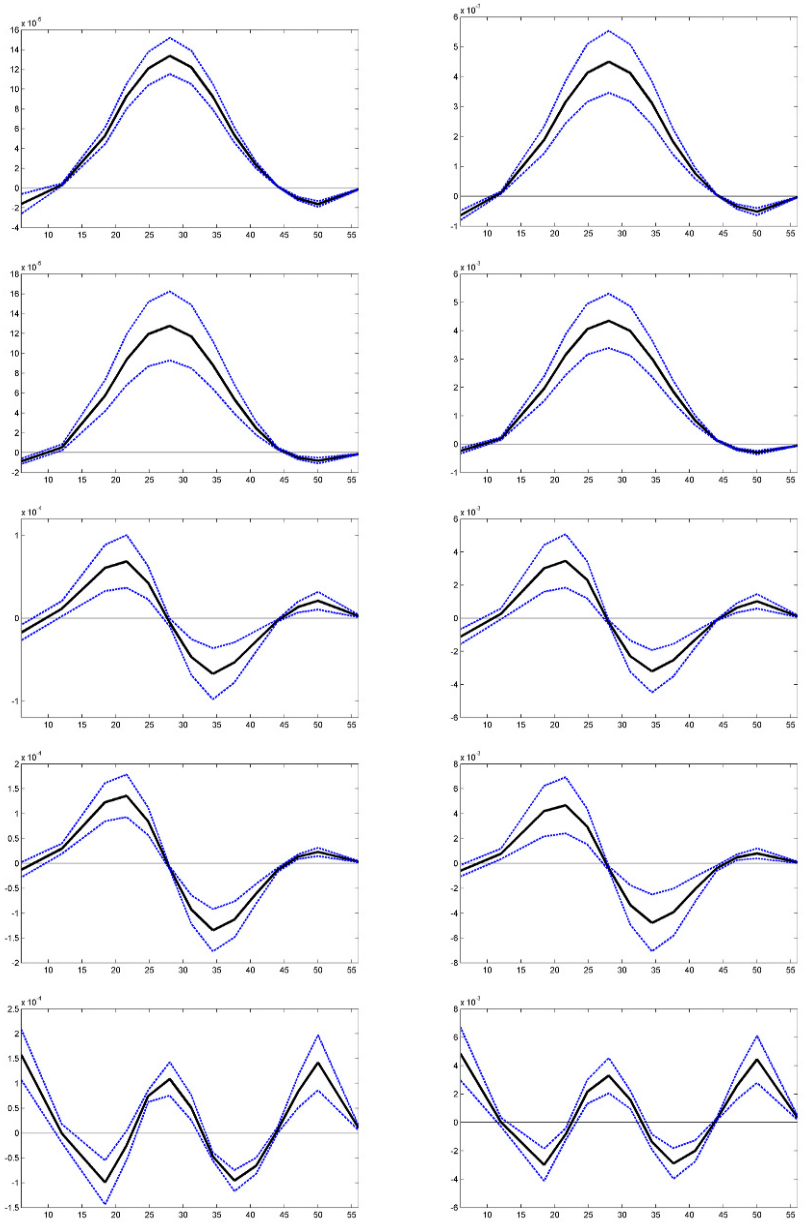

Fig. 5 First five mode shapes with their confidence bounds from covariance driven SSI (left) and data driven SSI (right).

	Covariance driven SSI					Data driven SSI (UPC)				
mode	f (in Hz)	$\tilde{\sigma}_f$	d (in %)	$\tilde{\sigma}_d$	$\tilde{\sigma}_{\varphi_{\max}}$	f (in Hz)	$\tilde{\sigma}_f$	d (in %)	$\tilde{\sigma}_d$	$\tilde{\sigma}_{\varphi_{\max}}$
1	4.039	0.34	1.1	23	13	4.031	0.21	1.3	22	22
2	6.292	0.19	0.6	52	27	6.282	0.11	0.7	19	22
3	9.730	3.42	3.0	92	47	9.872	1.17	2.1	32	46
4	13.19	0.67	1.3	73	31	13.31	0.38	1.4	22	48
5	15.72	0.70	1.8	20	32	15.73	0.39	1.8	19	39

Table 2 Overview of the estimated first 5 modes of S101 Bridge with natural frequencies f, their relative confidence bounds $\tilde{\sigma}_f = \sigma_f / f \cdot 100$, the damping ratios d, their relative confidence bounds $\tilde{\sigma}_d = \sigma_d / d \cdot 100$ and the relative confidence bounds of the mode shape element of maximal amplitude $\tilde{\sigma}_{\varphi_{\max}} = \sigma_{\varphi_{\max}} / \varphi_{\max} \cdot 100$.

To summarize the system identification results from covariance and data driven SSI, it can be said that both approaches give practically identical estimates in this test case when taking the obtained confidence bounds into account. However, the data driven approach seems to yield frequency and damping estimates that have lower confidence bounds than the covariance driven approach. Confidence bounds for the mode shape estimates are comparable for both approaches.

Confidence bounds are low on modes that seem to have stabilized in the stabilization diagram (e.g. on modes 1 and 2 at model order 40), while they are high on modes that have not stabilized yet (e.g. mode 3 at model order 40). Confidence bounds on frequency estimates are very low (lower than 1% on stabilized modes), while they are much higher on damping and mode shape estimates.

4.5 Monitoring during Progressive Damage Test

During the progressive damage test of the S101 Bridge, more than 700 datasets were available. Some of them contained erroneous data due to destruction work on the bridge or other influences that were deleted. On the left 680 datasets, an automated monitoring procedure was applied, that did the system identification and confidence interval computation automatically for each dataset. This means, that for each dataset a stabilization diagram was built with the SSI algorithms, containing model orders from 10 to 70. Then, the modes were chosen automatically using stabilization criteria such as thresholds for the damping estimates and confidence interval bounds, small frequency deviation between successive model orders, a minimum number of appearances of a frequency in the diagram and the MAC value between successive model orders.

The results of the frequency monitoring of all datasets are displayed in Figure 6 and the respective damage scenarios are explained in Table 1. Especially the frequency drop can be clearly seen when one column of the bridge was lowered before it was lifted up again (between A and G). This affected mainly the second, third and fourth mode, while the frequency changes in the first mode were less important. Es-

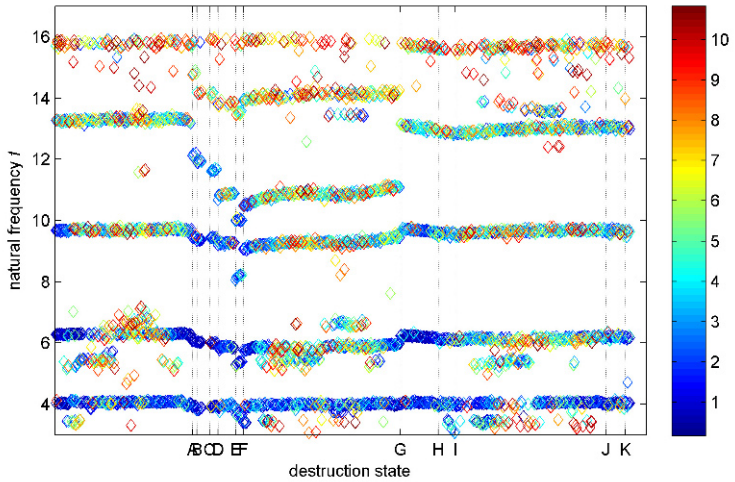

(a) covariance driven SSI

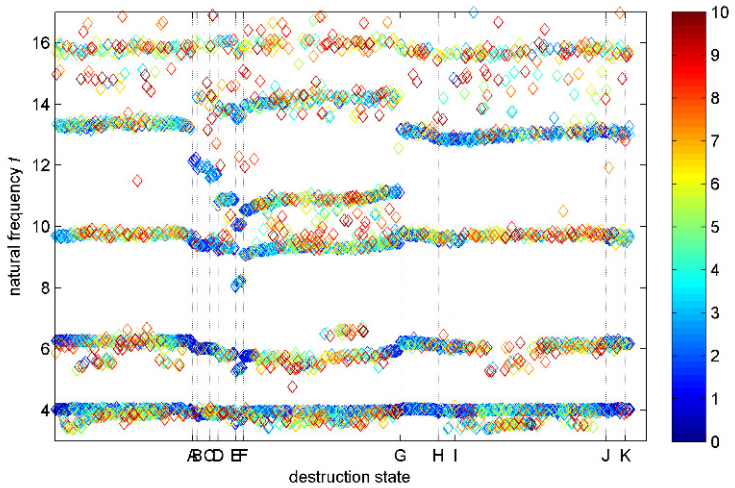

(b) data driven SSI (UPC)

Fig. 6 Natural frequencies with confidence bounds during progressive damage test of S101 Bridge (damage incidents from Table 1). The color bar indicates the confidence bound in percent of the obtained frequency.

pecially the change in the fourth mode is remarkable, as it split in two modes during the lowering of the column, with one lower and one higher frequency than before. The frequency changes in the fifth mode cannot be evaluated, as its uncertainty is very high compared to the other modes.

Also, the change in the frequencies when cutting the tendons (between G and K) is not significant. Only after the uplifting of the column and before cutting the first tendon (between G and H), some of the frequencies are dropping, probably due to the settling of the structural system after the uplifting. However, no significant change in the frequencies can be observed afterwards.

5 Conclusion

In this paper, confidence intervals on modal parameters during a progressive damage test were successfully computed with an improved algorithm. Using an automated monitoring procedure, the modal parameters of the S101 Bridge during this damage test were obtained completely automatically together with their confidence bounds. The artificially introduced damage scenarios "lowering of a column" could be clearly linked to changes in the natural frequencies, while "cutting the tendons" did not have a significant influence on the frequencies. It was shown that the confidence bounds on the modal parameters are essential when evaluating the changes in the modal parameters of the structure due to the introduced damages.

System identification results obtained by covariance and data driven SSI are very similar, with slightly lower confidence bounds for results obtained from data driven SSI with UPC.

Acknowledgments

This work was partially supported by the European project FP7-NMP CP-IP 213968-2 IRIS. We also thank VCE for providing the data from S101 Bridge.

References

1. Basseville, M., Benveniste, A., Goursat, M., Hermans, L., Mevel, L., van der Auweraer, H.: Output-only subspace-based structural identification: from theory to industrial testing practice. Journal of Dynamic Systems, Measurement, and Control **123**(4), 668–676 (2001)
2. Benveniste, A., Fuchs, J.J.: Single sample modal identification of a non-stationary stochastic process. IEEE Transactions on Automatic Control **AC-30**(1), 66–74 (1985)
3. Benveniste, A., Mevel, L.: Non-stationary consistency of subspace methods. IEEE Transactions on Automatic Control **AC-52**(6), 974–984 (2007)
4. Döhler, M., Lam, X.B., Mevel, L.: Confidence intervals on modal parameters in stochastic subspace identification. In: Proceedings of the 34th IABSE Symposium. Venice, Italy (2010)

5. Döhler, M., Mevel, L.: Robust subspace based fault detection. Tech. Rep. 7427, INRIA (2010). Submitted to 18th IFAC World Congress
6. van Overschee, P., De Moor, B.: Subspace Identification for Linear Systems: Theory, Implementation, Applications. Kluwer (1996)
7. Peeters, B., De Roeck, G.: Reference-based stochastic subspace identification for output-only modal analysis. Mechanical Systems and Signal Processing **13**(6), 855–878 (1999)
8. Pintelon, R., Guillaume, P., Schoukens, J.: Uncertainty calculation in (operational) modal analysis. Mechanical Systems and Signal Processing **21**(6) (2007)
9. Reynders, E., Pintelon, R., De Roeck, G.: Uncertainty bounds on modal parameters obtained from stochastic subspace identification. Mechanical Systems and Signal Processing **22**(4), 948–969 (2008)
10. VCE: Progressive damage test S101 Flyover Reibersdorf / draft. Tech. Rep. 08/2308, VCE (2009)

Identification of Material Properties of Composite Plates Utilizing Model Updating and Response Surface Techniques

Kenan Gurses, Bayindir Kuran, Caner Gencoglu
Mechanical Design Department
ROKETSAN A.S. PO Box 30, 06780, Elmadag, Ankara, Turkey

ABSTRACT

The identification of the material properties for the Carbon-Epoxy composite plates is presented. Modal testing is carried out on the manufactured plates to measure the natural frequencies and the mode shapes. The modal analyses are carried out for the sampled values of the orthotropic material properties. Samples are generated by utilizing the Central Composite Design technique. The natural frequencies and the mode shapes are predicted from the finite element analysis. Both quadratic response surfaces and artificial neural network (ANN) models are established for the residual between the predicted and the measured natural frequencies and the Modal Assurance Criteria (MAC). The accuracy of the response surface models is discussed. Sensitivities of the natural frequencies and the MAC for the significant modes are estimated. Sequential Quadratic Programming technique is utilized as the optimization method. The efficiencies of quadratic response surfaces and the ANNs are assessed.

INTRODUCTION

The tremendous amount of increase in the use of composite materials in almost all types of engineering structures has also attracted significant attention to the characterization of the composite materials. The material properties such as elastic and shear moduli and Poisson ratio of a composite structural component have to be supplied which is not an easy task. Although material properties of isotropic materials are well documented, elastic material properties of the composite materials necessitate special attention in experimental material characterization. The effective material properties strongly depend on the materials of the fiber and the matrix, ply orientations, laminate thickness and orientation sequence. Combinations of the fiber, matrix and lay-up parameters as well as manufacturing variations lead to carefully designed experimental techniques. Characterization tests can be carried out on test samples for the material to be characterized. The whole structure can also be tested to determine the stiffness parameters while the boundary conditions may sometimes not be fully simulated.

Recently, several studies on the characterization of the composite materials based on vibration tests have been published. Methods proposed in these studies are based on the correlation between the finite element and test models. The material properties of the composite structures are predicted through the optimization techniques in which several different objective functions utilizing natural frequencies and mode shapes are established. Cunha and Piranda [1] proposed a method for the determination of the

T. Proulx (ed.), *Linking Models and Experiments, Volume 2*, Conference Proceedings of the Society for Experimental Mechanics Series 5,
DOI 10.1007/978-1-4419-9305-2_18, © The Society for Experimental Mechanics, Inc. 2011

laminated composite tubes from modal tests. The objective function to be minimized is constructed based on the eigensolution residuals. Euler *et. al*. [2] presented a method that the orthotropic material properties are determined based on natural frequency correlations. Silva *et. al.* [3] proposed a model updating procedure based on the correlation between the analytical and experiment natural frequencies. They utilized a genetic algorithm to avoid the drawbacks of the gradient based optimization algorithms.

Finite element model updating has attracted significant interest in the area of structural dynamics. Several model updating methods have been proposed. The direct methods update the stiffness and mass matrices at one step in which physically meaningful corrections may sometimes not be reached. The iterative updating methods utilize the optimization procedures. These methods require the computation of the sensitivities of the finite element models. However, determination of the sensitivities for large finite element models may be computationally expensive. The establishment of a surrogate model for the modal response, on which updating procedure is based, can be practical from the computation effort perspective. The response surface method has been utilized in the field of optimization and reliability analysis. However, application in the filed of model updating is quite new. Chen and Chang [4] implemented the response surface method to correct the parameters of an H-shaped frame structure. They have used the natural frequencies for the correlation between the analytical and experimental models. Ren and Chen [5] proposed a modal updating procedure based on the response surface methodology. The proposed procedure employed the natural frequency residuals in the optimization algorithm. Cugnoni *et. al.* [6] presented an inverse method utilizing natural frequencies and mode shape data for characterization of the thick composite plates. Hwang *et. al.* [7] applied the genetic optimization algorithm to identify the elastic constants of composite plates by utilizing only natural frequency data.

This study summarizes the identification methodology based on the model updating and response surface methods. The natural frequencies and Modal Assurance Criteria functions are approximated by meta-models by which sensitivities with respect to the elastic constants can be evaluated with ease. Totally, 35 different sets of elastic constants are generated. Central Composite Design is implemented for the generation of the 25 which are utilized to generate the surrogate models. Latin Hypercube Sampling technique is employed for the remaining 10 sets which are utilized for the cross validation of the predicted results. The Sequential Quadratic Programming algorithm is implemented as the optimization method.

RESPONSE SURFACE TECHNIQUE

Response surface technique is a design of experiment methodology which gives estimate functions for the investigated behavior of a complex system. This method allows the designer to rapidly estimate the local response of a system by a close form formulation consists of interactions and higher order effects. By using response surface method, optimum design point can be approximated and critical parameters in the design can be determined. To obtain a response surface, the system is simulated/tested several times for different configurations and the response data of the system is collected. These data points are then used to fit a hyper surface to the performance of the examined system.

Quadratic Response Surfaces

In response surface methodology, if data follows a flat surface, a first order model is usually sufficient. If there is curvature in the data, a first order model would show a significant lack of fit and a higher order model must be used, such as:

$$y = a_0 + \sum_{i=1}^{k} a_i X_i + \sum_{\substack{i=1,j=2 \\ i<j}}^{k} a_{ij} X_i X_j + \sum_{i=1}^{k} a_{ii} X_i^2 \tag{1}$$

where y is the response of the system, Xi is the input variable vector and a are the constants of the close form response formulation [8-9].

Artificial Neural Networks

Neural network are computational models based on parallel structures with learning ability to generalize, to classify and to organize data. Neural networks are used to model multi input, multi output systems. Approximations of the system performance have been obtained in structural analysis [10-11]. Neural networks consist of single input single output elements so called the neurons, which are arranged parallel in layers. They are connected by synapses, which amplify or decrease the signals passing through them. The amplification factor for each connection is called as weight. The outputs of the neurons of one layer are inputs for the neurons on the next layer. The following three steps have to be followed to establish the neural network model of a system:

1. Selection of the network architecture: number of neurons in each layer, number of hidden layers, the type of transfer functions of neurons and the type of training algorithm (such as back propagation and Levenberg-Marquardt).
2. Training of the network such that SSE (Sum of Squared Errors) is minimized:

$$SSE = \sum_{i=1}^{k} \left\| y_i - \hat{y}_i \right\|^2 \tag{2}$$

where k is the number of training samples. y_i and $\hat{y}_i$ are the target value and the network output for the ith training sample, respectively.

3. Testing the network: Network model is tested against (input, output) pairs which are different from training pairs.

In this study, the structure of artificial neural network is the so called radial basis neural network. Consider the single radial basis neuron illustrated in **Figure 1**. Neuron receives the input vector $\vec{x}$ by the axons which do not have weights. The Euclidian norm is calculated between the input vector and a center vector $\vec{t}$ and the result is multiplied by the bias b. This product is passed through a non-linear radial basis activation function to get the output a. Output for the single neuron is expressed as

$$a = radbas\left(\left\| \vec{x} - \vec{t} \right\| b\right) \tag{3}$$

where the radial basis function illustrated in **Figure 2** is expressed as

$$radbas(n) = e^{-n^2} \tag{4}$$

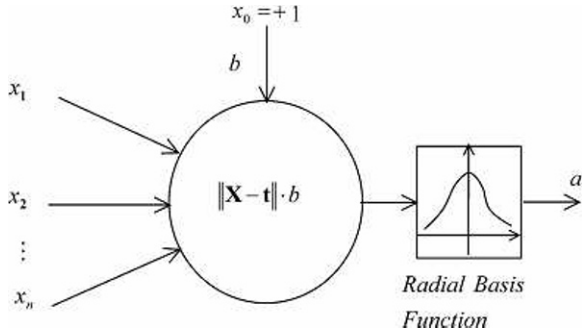

Figure 1: Single Radial Basis Neuron

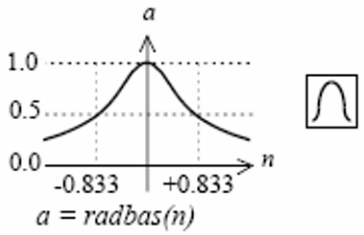

Figure 2: Radial Basis Function

Radial basis function networks have two layers: one hidden radial basis layer for inputs and a linear output layer.

METHODOLGY

In this study, the objective function includes residuals for the natural frequencies and Modal Assurance Criterion (MAC):

$$\Pi = A\sum_{i=1}^{m}\left|\frac{\omega_{ai} - \omega_{xi}}{\omega_{xi}}\right| + B\left(\sum_{i=1}^{m}\left|1 - MAC_{ii}\right|\right) \tag{5}$$

A and B are the weighting factors implemented in the optimization algorithm. ω_{ai} and ω_{xi} are the analytical and experimental natural frequencies for the i[th] mode, respectively. MAC_{ii} is the Modal Assurance Criterion (diagonal term) for the i[th] mode. m is the number of modes considered.

MAC for the i[th] mode can be defined as

$$MAC_{ii} = \frac{\left|\left\{\phi_i{}^x\right\}^T\left\{\phi_{im}{}^a\right\}\right|^2}{\left|\left\{\phi_i{}^x\right\}^T\left\{\phi_i{}^x\right\}\right|\left|\left\{\phi_i{}^a\right\}^T\left\{\phi_i{}^a\right\}\right|} \tag{6}$$

$\left\{\phi_i{}^x\right\}$ and $\left\{\phi_j{}^x\right\}$ are the i[th] and j[th] experimental eigenvectors and $\left\{\phi_{im}{}^a\right\}$ is the corresponding analytical eigenvectors for the master degrees of freedom (i.e. for the measured degrees of freedom).

The surrogate models for the objective functions are constructed and these approximate models are employed in the optimization algorithm. The lower and the upper bound for the input variables are given as

$50000\ \text{MPa} \leq E_{11} \leq 180000\ \text{MPa}$
$6000\ \text{MPa} \leq E_{22} \leq 20000\ \text{MPa}$
$0.15 \leq \nu_{12} \leq 0.45$
$3000\ \text{MPa} \leq G_{12} \leq 7000\ \text{MPa}$

The free-free boundary conditions of the composite plate are implemented in the analysis. First 5 natural frequencies and mode shapes are extracted by MSC.Nastran software package. 900 *Quad4* shell elements are generated along with 961 nodes. On the other hand, only 64 nodes designated in **Figure 3** are used during modal tests.

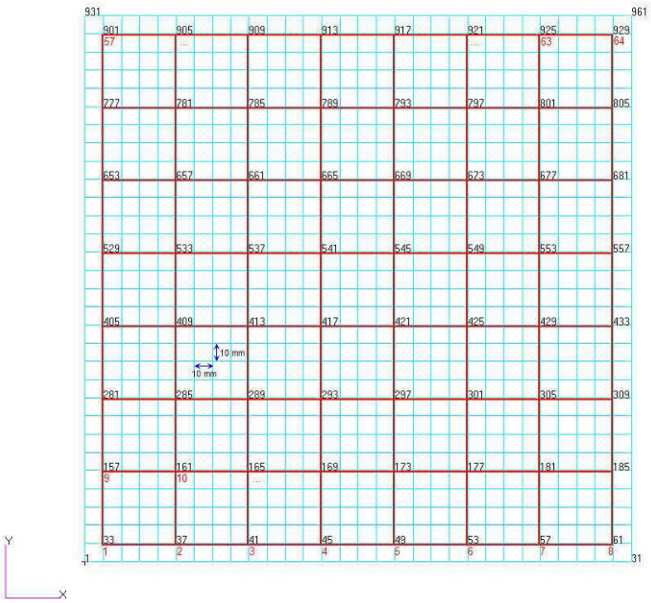

Figure 3: Finite Element and Experimental Models for the Free-Free Composite Plate

DESCRIPTION OF THE TEST ITEM AND TEST SETUP

The item used for modal test is a 300 mm by 300 mm composite plate. The thickness of the plate is 2.64 mm consisting of 12 equivalent carbon-epoxy layers with thickness 0.22 mm each. Carbon-epoxy layers are made of T-300 3K 2x2 Twill carbon fabric and UF-3369 epoxy resin. The orientation of the carbon fabric is 0-90 degrees and this orientation is the same for all layers. The average density of composite material ($\rho = 1482\ kg/m^3$) is calculated by measuring mass of the plate and dividing by the plate volume. The thickness uniformity of the plate is checked before the measurements.
The view of the test setup is given in **Figure 4**. The composite plate is suspended by 4 nylon yarns to simulate the free-free boundary conditions. Before the modal test is carried out, location of the excitation point and suspension points are determined utilizing the mode shapes obtained from finite element analysis. The plate is excited by roving the Impact Hammer (PCB model 086E80) over each 64 grid points and one accelerometer (DYTRAN model 3035BG) is mounted using wax on the 16^{th} grid point. For data acquisition, the measurement bandwidth is taken as 1024Hz which is enough to cover the first few modes of the composite plate. In order to provide 0.25Hz frequency resolution for FRF measurements, the time for each hammer hit is chosen as 4 seconds. To obtain one FRF data, 4 measurements are averaged. Windowing is not applied to the response signal since it was not required. In addition, H_v FRF estimator function is used.

The measurement data is gathered by *LMS SCADAS III-302VB* data acquisition system utilizing *LMS Test.Xpress* software. The data is transferred to the modal analysis software *Me-Scope VES* for modal parameter extraction.

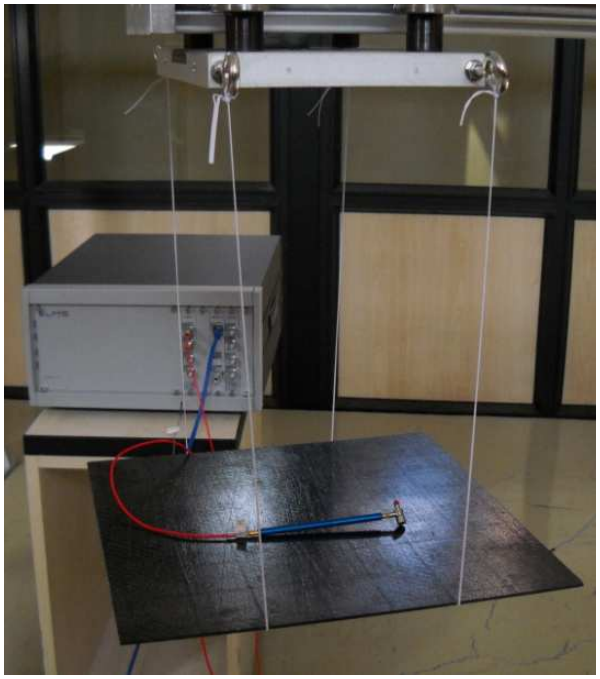

Figure 4: Experimental Setup

MODAL TEST RESULTS

The measurement data consists of 64 FRF data for 64 grid points which were collected using LMS Test.Xpress software. The FRF data is shown in **Figure 5** in overlaid form. Modal parameters are extracted using ME'Scope VES from the experimental FRF data.

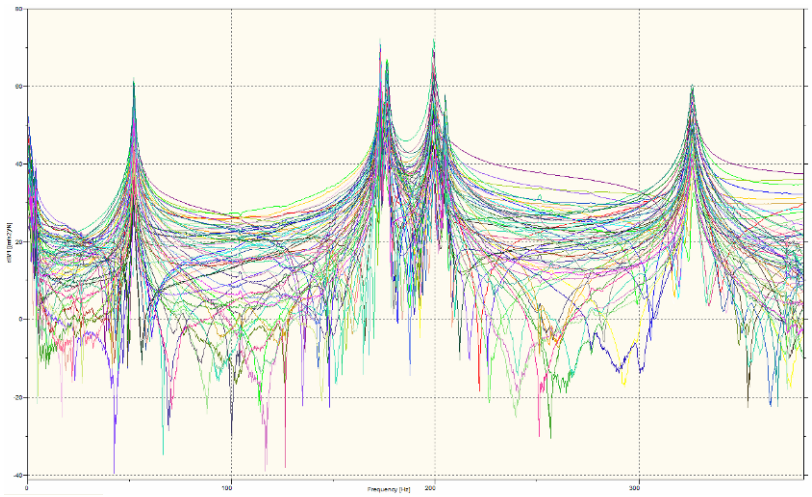

Figure 5: Experimental FRF Data of Grid Points (Overlaid)

Summation of all FRF data is calculated and for the extraction of the modal parameters the summation FRF curve is utilized. FRF summation curve is given on **Figure 6**.

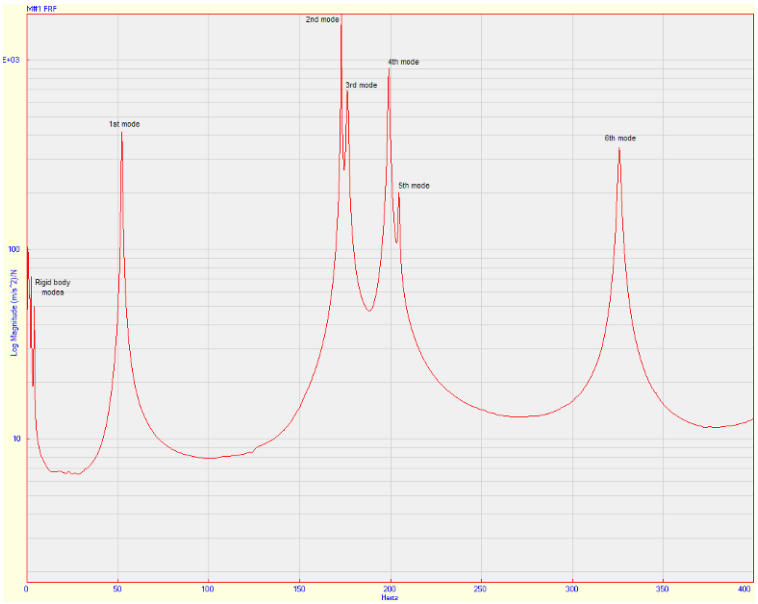

Figure 6: Summation FRF curve

Modal parameters obtained for the first five modes are given on **Table 1**. Note that the suspension frequencies of the plate are about 3 to 5 Hz which is approximately one tenth of the first elastic natural frequency of the plate. This ratio is enough to decouple the rigid body modes from the elastic modes of the plate.

Table 1: Experimental Mode Parameters

Mode #	Natural Frequency (Hz)	Structural Damping (η) %
1	52.35	0.52
2	173.07	0.08
3	176.37	0.19
4	199.24	0.21
5	204.80	0.18

First four mode shapes of the composite plate according to the experimental data are given in **Figure 7.**

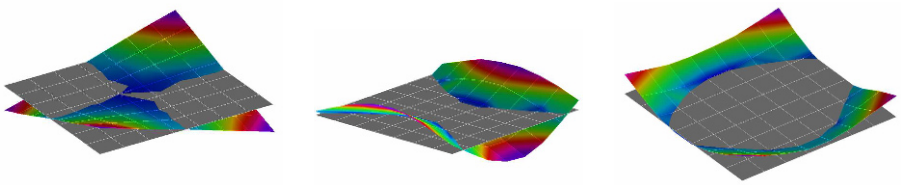

(a)1st mode **(b)2nd mode** **(c)3rd mode**

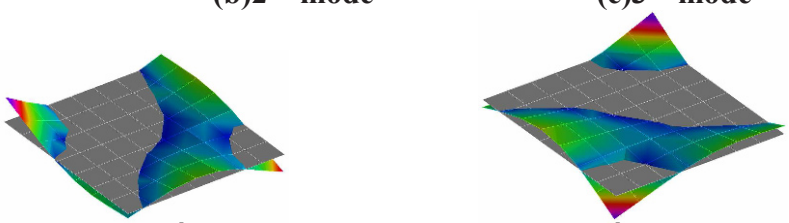

(d)4th mode **(e)5th mode**

Figure7: Experimental mode shapes

GENERATED SURROGATE MODELS

The elastic constants with the given bounds are first transformed into their associated coded forms to avoid ill-conditioning in computations [9]. The accuracy of the surrogate models is investigated by checking the Sum of Squared Errors (SSE) as well as performing Cross Validation study. The SSE values are given in **Table 2**. The natural frequencies for the validation data set are well predicted by both quadratic response surfaces and ANNs. On the other, ANN can regenerate the validation set of MAC data more accurately than the quadratic response surface model. Cross validation results are illustrated in **Figure 8**. The sensitivities of modal parameters with respect to changes in the elastic constants are also investigated. Sensitivity coefficients of the modal parameters which are the regression coefficients predicted are summarized in **Figure 9**. One can note that only MAC corresponding to the fourth mode is sensitive to Poisson constant. One additional note to address is that MAC values for the first three modes are not sensitive to elastic constants.

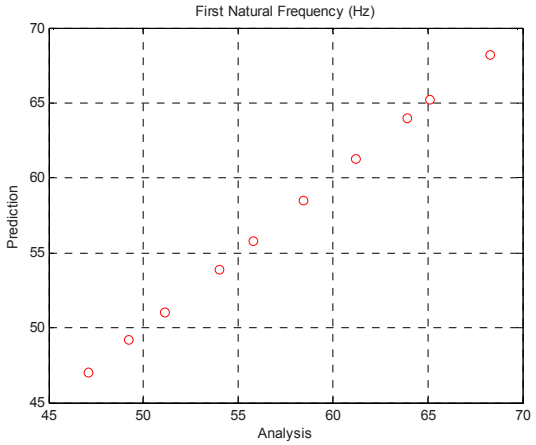

(a)

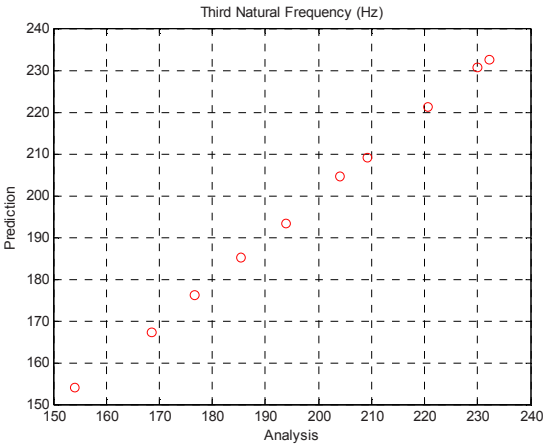

(c)

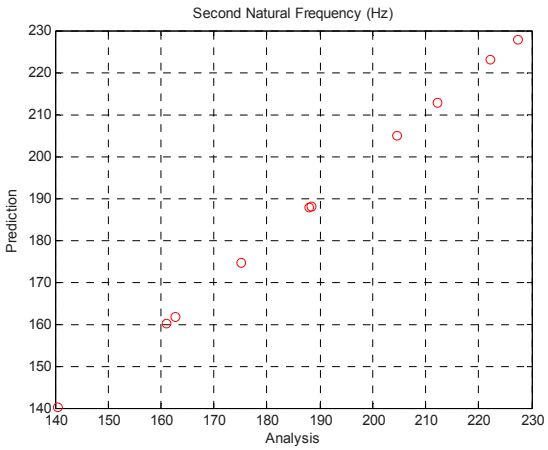

(b)

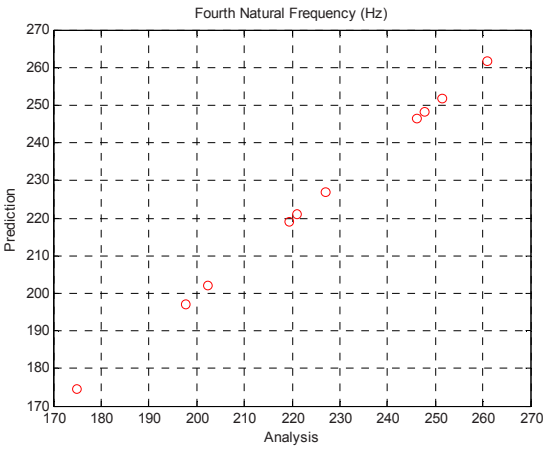

(d)

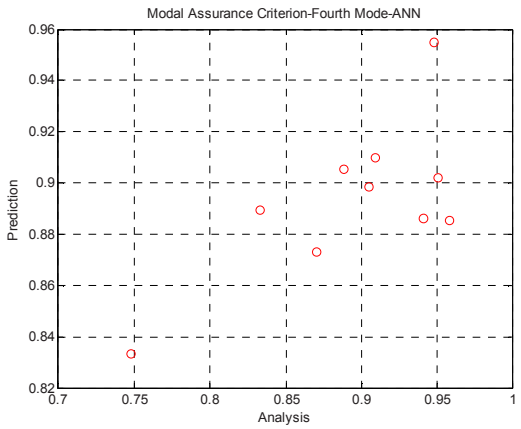

(e)

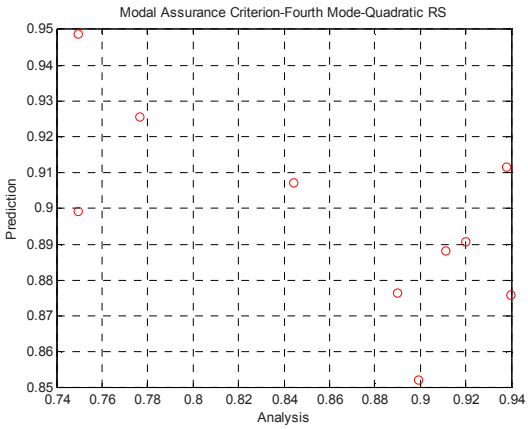

(f)

Figure 8. Cross Validation Results

Table 2. Sum of Squared Errors

	Quadratic Response Surfaces	Artificial Neural Networks
ω_1	0.0358	1.2e-25
ω_2	1.024	8.1e-23
ω_3	4.241	5.8e-23
ω_4	1.160	8.5e-24
MAC44	0.0846	0.0592

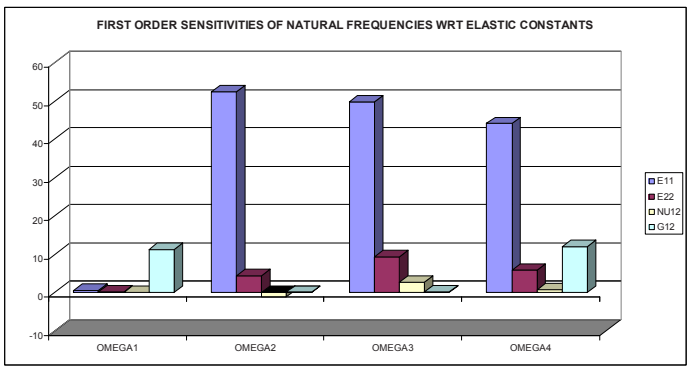

(a)

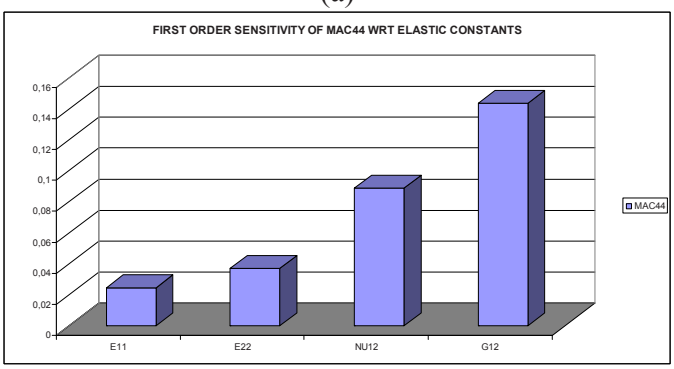

(b)

Figure 9.First Order Sensitivities of Modal Properties With Respect To Elastic Constants

DETERMINATION OF ELASTIC CONSTANTS

The material properties of the composite plate were calculated by an optimization algorithm which minimizes the differences between experimental and analytical modal parameters. The behavior of the system was modeled by artificial neural network model and quadratic response surface model separately and the optimization algorithm was executed for each model to calculate the material properties. The results for the quadratic response surface model and the artificial neural network model are tabulated in **Table 3**. Using these material properties, the natural frequencies of the composite plate are calculated by MSC. Nastran. The natural frequencies obtained for these material properties are given on **Table 4**.

Table 3: Material Properties Predicted

Stiffness Constants	Quadratic Res. Sur.	Art. Neural Networks
E_{11}	96420 MPa	96517 MPa
E_{22}	6582 MPa	7046 MPa
ν_{12}	0.2456	0.1983
G_{12}	4099 MPa	4129 MPa

Table 4: Natural Frequencies for the Optimized Solution

Mode #	QRS-Natural Freq.(Hz)	% Error	ANN-Natural Freq.(Hz)	% Error
1	52.49	0.27	52.68	0.63
2	174.0	0.54	174.67	0.92
3	177.81	0.82	177.96	0.9
4	204.79	2.78	205.30	3.04
5	204.79	0.005	205.30	0.24

The correlation plot between experimental natural frequencies and analytical natural frequencies and Modal Assurance Criterion calculated by utilizing neural network model and quadratic response surface model are presented on **Figure 10** and **Figure 11** respectively.

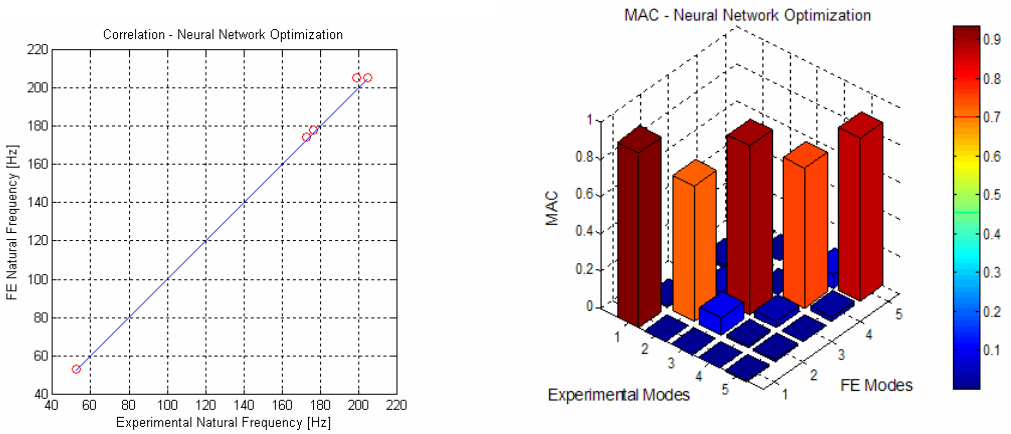

(a) Correlation Plot **(b)MAC Plot**

Figure 10: Correlation Plot and MAC Plot (Artificial Neural Network)

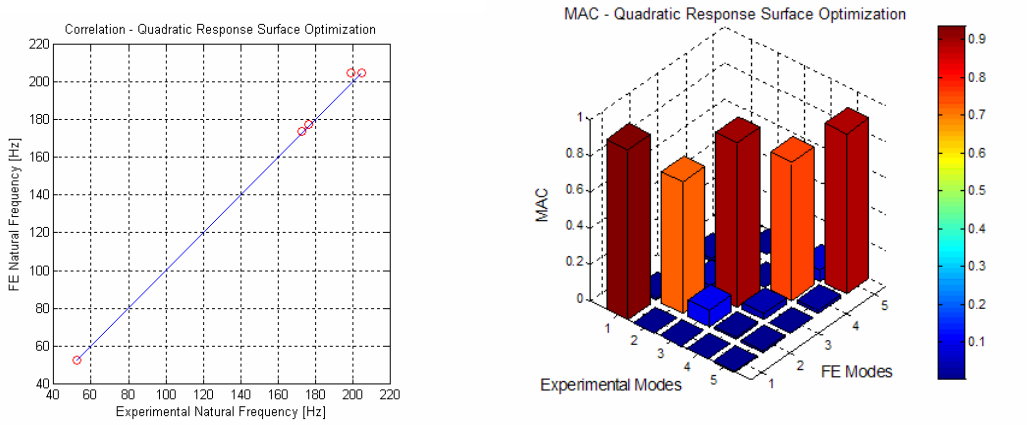

(a) Correlation Plot **(b)MAC Plot**

Figure 11: Correlation Plot and MAC Plot (Quadratic Response Surface)

Mode shapes generated using MSC. Nastran for predicted material properties are given in **Figure 12**.

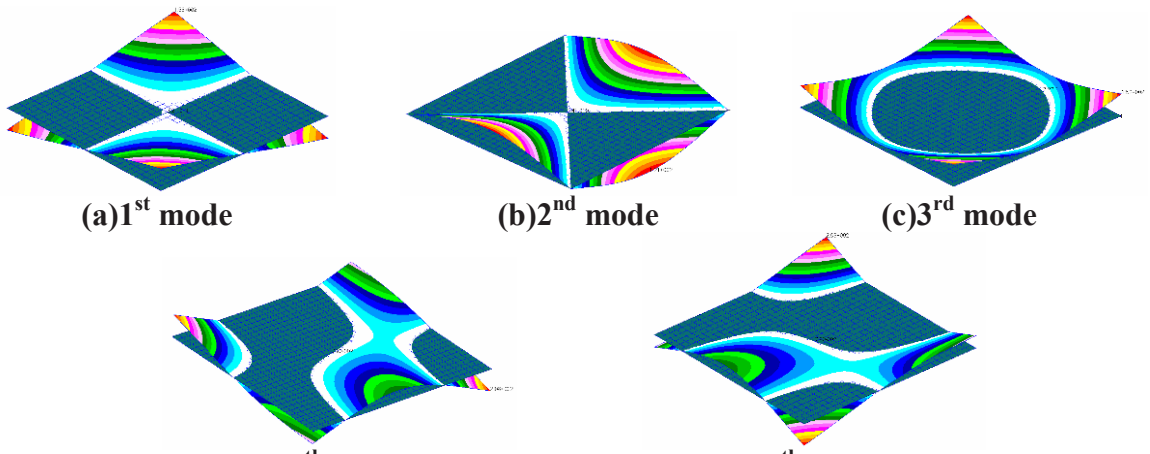

(a)1st mode **(b)2nd mode** **(c)3rd mode**

(d)4th mode **(e)5th mode**

Figure 12: Mode Shapes Generated Using MSC. Nastran

DISCUSSION

Comparing the natural frequencies obtained by using the material properties calculated using artificial neural network model and quadratic response surface model with the experimental natural frequencies, it can be stated that the results from the response surface model are closer to the experimental ones. The performance of quadratic response surface model comes out to be slightly better than the performance of artificial neural network model. Comparing the Modal Assurance Criterion and analytical mode shapes for the neural network model and the quadratic response surface model, one can see that the difference is not significant.

According to the analytical modal parameters, 4th and 5th modes are double modes, their natural frequencies are the same and one mode shape is obtained by rotating the other one 90 degrees about the normal of the plate. The analytical mode shapes and the experimental ones are similar; however the experimental natural frequencies of 4th and 5th modes are different. This difference can be resulted from manufacturing imperfections and dimensional errors.

CONCLUSION

In this study identification of material properties of a carbon-epoxy composite plate using model updating and response surface techniques is aimed. The modal parameters of the manufactured test plate were obtained by modal test. The natural frequencies and the mode shapes of the plate were also calculated using MSC. Nastran for 35 different material property sets. 25 of these property sets were generated by Central Composite Design technique and 10 sets were generated by Latin Hypercube Sampling technique. The experimental natural frequencies and mode shapes are used together with the analytical ones calculated by MSC. Nastran in order to obtain Modal Assurance Criterion (MAC) for each material property set. The objective function to be used in the optimization algorithm was composed using the MAC values together with natural frequencies. Quadratic response surface method and artificial neural network method are utilized separately to generate the approximate models for the behavior of the system. These two models are used separately in the optimization algorithm to obtain the material properties which yield the modal parameters closest to the experimental ones. Finally, to compare the performances of artificial neural network model and quadratic response surface model, the natural frequencies and mode shapes for resulting material properties are calculated and compared with the experimental modal parameters. It can be stated that the performance of quadratic response surface model is slightly better than the performance of artificial neural network model since its modal parameters are closer to the experimental modal parameters.

REFERENCES

[1]. Cunha J and Piranda J, Identification of Stiffness properties of Composite Tubes from Dynamic Tests, Experimental mechanics, Vo. 40, No. 2, 2000, pp. 211-218.
[2]. Euler E, Sol H., Dascotte E., Identification of Material Properties of Composite Beams: Inverse Method Approach, Proc. of 2006v SEM Annual Conference & exposition on Experimental and Applied Mechanics, June 2006, USA.
[3]. Silva M. F. T., Borges L. M. S. A., Rochinha F. A., Carvalho L. A. V., A Genetic Algorithm Applied to Composite Elastic Parameters Identification, Inverse Problems in Science and Engineering, Vol. 12, No.1, 2004, pp. 17-28.
[4]. Chen K. N., Chang C. T., Response Surface Method for Updating Dynamic Finite Element Models, Proc. of ESDA04, July 2004, Manchester UK.
[5]. Ren W. X., Chen H. B., Finite Element Model Updating in Structural Dynamics by Using the Response Surface Method, Engineering Structures, Vol. 32, Issue 8, 2010, pp.2455-2465.
[6]. Cugnoni J, Gmur T., Schorderet A., Inverse Method based on Modal Analysis for Characterizing the Constitutive Properties of Thick Composite Plate, Computers and Structures, Vol. 85, pp. 1310-1320, 2007.
[7]. Hwang S. F., Wu J. C., He R. S., Identification of Effective Elastic Constants of Composite Plates Based on a Hybrid Genetic Algorithm, Composite Structures, Vol. 90, pp. 217-224, 2009.
[8]. NIST/SEMATECH e-Handbook of Statistical Methods, June 11, from the World Wide Web: http://www.itl.nist.gov/div898/handbook/, 2006.
[9] Box, G. E. P., and K. B. Wilson, On the experimental attainment of optimum conditions, J. Roy. Stat. Soc., Ser. B, 13,1, 1951.
[10] Hajela, P. and Berke, L "Neural Networks in Structural Analysis and Design: An Overview", 41st AIAA/ASME/SAE/ASEE Joint Propulsion Conference & Exhibit, 10-13 July 2005, Tucson, Arizona.
[11] Swift, R. A. and Batill, S. M. "Application of Neural Network to Preliminary Structural Design", 32nd AIAA/ASME/ACSE/AHS/ASC Structural Dynamics and Materials Conference, 1991.

Globally enriched substructuring techniques for vibro-acoustic simulation

Umut Tabak and Daniel J. Rixen

Abstract The coupling between structures and internal and/or external acoustics in fluids is a common issue in many industrial design fields. Discretization of these kinds of problems results in a large number of equations which might sometimes impede a reasonable design time-line. Model reduction methods are used to efficiently reduce the system size and conduct analysis on the reduced problems. This research paper outlines some extensions of the standard Craig-Bampton method to strongly coupled vibroacoustic problems. Namely, the standard Craig-Bampton basis is enriched with the approximations of global mode representations, which are the outcomes of a new iterative solver that is being developed, namely *I*terative *R*educed *C*orrection *A*lgorithm, IRCA. An academic test example is considered to show the validity of the proposed substructuring schemes along with error comparisons on the frequency values.

1 Introduction

Coupling of elastic structures with the acoustics of light/heavy fluids is an important aspect in many design fields, such as aerospace and automotive industries. Prediction of this kind of coupled behaviour is commonly accomplished by the well known Finite Element Method [1] for interior problems. Exterior radiation problems are tackled either with Boundary Element [2] or Infinite Element methods [3]. Interaction of different physical domains often lead to unsymmetric system matrices [4], in particular when the different fields are described by different physical quantities.

Umut Tabak
Delft University of Technology, Mekelweg 2, 2628CD, Delft, The Netherlands, e-mail: u.tabak@tudelft.nl

Daniel J. Rixen
Delft University of Technology, Mekelweg 2, 2628CD, Delft, The Netherlands, e-mail: d.j.rixen@tudelft.nl

T. Proulx (ed.), *Linking Models and Experiments, Volume 2*, Conference Proceedings of the Society for Experimental Mechanics Series 5,
DOI 10.1007/978-1-4419-9305-2_19, © The Society for Experimental Mechanics, Inc. 2011

Selection of the nature of the unknown of the problem is thus important for the resulting matrix structure. For vibro-acoustics, this is the case when the problem is written in pressure perturbations for the fluid and displacements for the structure.

In this study, the classical displacement-pressure formulation is used. Some of the bottlenecks of these kinds of computations are the excessive computation times and the computer resources used for storage. Model order reduction techniques are well established in the structural field, such as the Craig-Bampton fixed interface [5] and Rubin free interface methods [6]. In the context of this research paper, we are concerned with the extension of the standard Craig-Bampton reduction method to the modelling of vibro-acoustic simulation of systems that are strongly coupled. Approximations of global representations are added to the basis representation to enrich the Craig-Bampton reduction space. These approximation vectors result from a new iterative solver, iterative reduced correction algorithm, that is still under development/improvement. In the context of the paper, a short theory overview and the common matrix equations are going to be provided in section 2.1. Section 2.2 will outline the symmetrization concept that is at the heart of the iterative algorithm. Section 2.3 will summarize the iterative correction algorithm. Section 3 will show the extension of the method to substructuring through the use of classical Craig-Bampton scheme. Section 4 will summarize the developed computational framework and includes a numerical example with results. In the last section, some discussions are provided.

2 Theoretical backgound and outline

2.1 Governing equations of the problem

For a formulation in terms of displacement u and nodal pressure perturbation p, the discretization of the governing differential equations for vibro-acoustics and of the coupling conditions on the interacting interfaces, results in (e.g. [4])

$$\begin{bmatrix} \mathbf{M}_s & \mathbf{0} \\ \mathbf{M}_{fs} & \mathbf{M}_f \end{bmatrix} \begin{bmatrix} \ddot{\mathbf{u}} \\ \ddot{\mathbf{p}} \end{bmatrix} + \begin{bmatrix} \mathbf{K}_s & \mathbf{K}_{sf} \\ \mathbf{0} & \mathbf{K}_f \end{bmatrix} \begin{bmatrix} \mathbf{u} \\ \mathbf{p} \end{bmatrix} = \begin{bmatrix} \mathbf{F}_s \\ \mathbf{F}_f \end{bmatrix}. \tag{1}$$

Fluids interacting with their surrounding structure couple through the continuity of the velocity on the interface and the equilibrium of the interface stresses/pressures, which results in the off-diagonal coupling blocks. A closed form relation exists between the off-diagonal coupling blocks, namely, $\mathbf{M}_{fs} = -\rho \mathbf{K}_{sf}^T$. With the use of this relation, one might write

$$\begin{bmatrix} \mathbf{M}_s & \mathbf{0} \\ -\mathbf{K}_{sf}^T & \frac{\mathbf{M}_f}{\rho} \end{bmatrix} \begin{bmatrix} \ddot{\mathbf{u}} \\ \ddot{\mathbf{p}} \end{bmatrix} + \begin{bmatrix} \mathbf{K}_s & \mathbf{K}_{sf} \\ \mathbf{0} & \frac{\mathbf{K}_f}{\rho} \end{bmatrix} \begin{bmatrix} \mathbf{u} \\ \mathbf{p} \end{bmatrix} = \begin{bmatrix} \mathbf{F}_s \\ \frac{\mathbf{F}_f}{\rho} \end{bmatrix}. \tag{2}$$

It is important to note that, from this point on, $\frac{\mathbf{M}_f}{\rho}$, $\frac{\mathbf{K}_f}{\rho}$ and $\frac{\mathbf{F}_f}{\rho}$ will be renamed $\mathbf{M}_f$, $\mathbf{K}_f$ and $\mathbf{F}_f$ respectively.

2.2 Symmetrization concept and its relation to reduction

Symmetrization approaches of the coupled vibro-acoustic problem defined in equation (2) exist and these are outlined in [7] and [8]. Therein, matrix scaling and eigenvector augmentation methods have been used to obtain symmetric formulations of the original unsymmetric coupled eigenvalue problem. In our work, we consider the post-multiplication approaches from [7] where the following post-transformation matrices are used[1] :

$$\tau = \begin{bmatrix} \mathbf{K}_s^{-1}\mathbf{M}_s & -\mathbf{K}_s^{-1}\mathbf{K}_{sf} \\ \mathbf{0} & \mathbf{I} \end{bmatrix}. \tag{3}$$

Applying then a change of variable

$$\begin{bmatrix} \mathbf{u} \\ \mathbf{p} \end{bmatrix} = \tau \begin{bmatrix} \tilde{\mathbf{u}} \\ \mathbf{p} \end{bmatrix}, \tag{4}$$

leads to the symmetric system

$$\begin{bmatrix} \mathbf{M}_s\mathbf{K}_s^{-1}\mathbf{M}_s & -\mathbf{M}_s\mathbf{K}_s^{-1}\mathbf{K}_{sf} \\ -\mathbf{K}_{sf}^T\mathbf{K}_s^{-1}\mathbf{M}_s & (\mathbf{M}_f + \mathbf{K}_{sf}^T\mathbf{K}_s^{-1}\mathbf{K}_{sf}) \end{bmatrix} \begin{bmatrix} \ddot{\tilde{\mathbf{u}}} \\ \ddot{\mathbf{p}} \end{bmatrix} + \begin{bmatrix} \mathbf{M}_s & \mathbf{0} \\ \mathbf{0} & \mathbf{K}_f \end{bmatrix} \begin{bmatrix} \tilde{\mathbf{u}} \\ \mathbf{p} \end{bmatrix} = \begin{bmatrix} \mathbf{F}_s \\ \mathbf{F}_f \end{bmatrix}. \tag{5}$$

The new system matrices are thus obtained by post-multiplication with τ. The new variable $\tilde{\mathbf{u}}$ can be interpreted as an acceleration.

The use of the post-multiplier matrix yields a symmetric system and will be useful to obtain real eigenvalues in the interaction problem of the reduced system (see the iterative correction algorithm in the next subsection). However, explicit construction of the symmetric system matrices given in (5) is not necessary in the implementation of the algorithm.

A common way to reduce the dynamic equations consists in representing the solution as a truncated series of modes of the full system. Using truncated left and right modal spaces one obtains the reduced problem

$$\phi^{L^T}\mathbf{M}_{system}\phi^R\ddot{\eta} + \phi^{L^T}\mathbf{K}_{system}\phi^R\eta = \phi^{L^T}\begin{bmatrix} \mathbf{F}_s \\ \mathbf{F}_f \end{bmatrix}, \tag{6}$$

which leads to a diagonal problem due to the orthogonality properties of the left and right eigenvectors. In the equations, superscript L represents the left eigenvectors, and the superscript R represents the right eigenvectors of the problem. The left and right modes are composed of a fluid and a structural part, namely

[1] This representation has an advantage for the forthcoming computations where the factorization of $\mathbf{K}_s$ is often available from the structural eigenvalue solver.

$$\phi^L = \begin{bmatrix} \phi_s^L \\ \phi_f^L \end{bmatrix}, \qquad \phi^R = \begin{bmatrix} \phi_s^R \\ \phi_f^R \end{bmatrix}. \tag{7}$$

The same kind of relation can be obtained by considering the symmetrization concept outlined above as

$$\phi^{sym^T} \mathbf{M}_{system} \tau \phi^{sym} \ddot{\eta} + \phi^{sym^T} \mathbf{K}_{system} \tau \phi^{sym} \eta = \phi^{sym^T} \begin{bmatrix} \mathbf{F}_s \\ \mathbf{F}_f \end{bmatrix}, \tag{8}$$

where τ is the post-symmetrization matrix provided in equation (3). It is worth mentioning the fact that since equation (8) is the symmetrized form of equation (6), its associated left and right eigenvectors are identical. Obviously $\phi^{sym} = \phi^R$ and that $\tau\phi^{sym} = \phi^L$. Further discussion on the relation between left and right eigenvectors can be found in Appendix A.

A common practice in the reduction approaches is to use an approximation space, **T**, which is also called the Ritz basis. If we want to find an approximation of the eigensolutions of the system, one can project the symmetrized eigenvalue problem onto this reduction space as

$$\mathbf{T}^T \left(\mathbf{K}_{system} \tau - \omega^2 \mathbf{M}_{system} \tau \right) \mathbf{T} \eta = 0, \tag{9}$$

which can also be written as

$$\mathbf{T}^T \left(\mathbf{K}_{system} - \omega^2 \mathbf{M}_{system} \right) \tau \mathbf{T} \eta = 0. \tag{10}$$

Equation (10) reveals an important result for the reduction and projection basis representations of the unsymmetric coupled problem, namely, one should always use different reduction and projection spaces on the right and left, respectively. This fact is also used in the explanation of the iterative correction algorithm in the following subsection.

2.3 Finding global enrichments: Iterative reduced correction algorithm, IRCA

The iterative correction algorithm is outlined in this subsection. The details might be found in [9]. The starting point for the algorithm is the uncoupled system modes. These modes are usually cheap to compute compared to solving the full coupled eigenvalue problem. Starting with the uncoupled system modes, the algorithm tries to converge to the system eigenpairs. The name of the algorithm comes from the fact that the corrections on one physical domain are computed by taking into account the effects of the other physical subdomain. In this way, the uncoupled starting modes are corrected iteratively to approximate the system response for the coupled problem. The steps of the algorithm are going to be outlined below.

Let us recall that the symmetrized vibro-acoustic problem (see previous section) is given as,

$$(\mathbf{M}_{system}\tau\ddot{\mathbf{x}} + \mathbf{K}_{system}\tau\mathbf{x}) = \mathbf{0}, \tag{11}$$

where τ is provided in equation (3).

Approximating the solution with Ritz vectors stored in $\mathbf{T}$ results in

$$\mathbf{x} = \mathbf{T}\eta. \tag{12}$$

The heart of the problem in model reduction studies is the selection of the proper ingredients for the projection matrix, $\mathbf{T}$. The iterative correction algorithm fills $\mathbf{T}$ with the uncoupled system modes and their corrections for the first iteration loop and updates the frequencies and modes simultaneously. Important correction vectors are selected on the basis of their relative contribution to the strain energy. The short general outline is presented next.

2.3.1 General outline

Let us call N the number of modes we want to find.

Step 1: Compute the first N structural and acoustic modes

$$\left(\mathbf{K}_s - \omega_s^2\mathbf{M}_s\right)\phi_s = \mathbf{0} \mapsto \omega_s^2, \phi_s, \tag{13}$$

$$\left(\mathbf{K}_f - \omega_f^2\mathbf{M}_f\right)\phi_f = \mathbf{0} \mapsto \omega_f^2, \phi_f. \tag{14}$$

Step2: Computation of the correction vectors

In the vibro-acoustic problem (2), we see that the uncoupled mechanical modes ($\mathbf{u} = \phi_u$, $\mathbf{p} = \mathbf{0}$) fully satisfy the mechanical equilibrium (second line of (2)), but not the acoustic balance (first equation of (2)). So let us use the acoustic balance to estimate the acoustical counterpart to ϕ_s as

$$\left(\mathbf{K}_f - \omega_s^2\mathbf{M}_f\right)\triangle_f^s = \omega_s^2\mathbf{K}_{sf}^T\phi_s, \tag{15}$$

where $\triangle_f^s$ is the acoustic correction to the mechanical mode. Obviously with this correction the mode $\mathbf{u} = \phi_s$, $\mathbf{p} = \triangle_f^s$ satisfies the acoustic balance, but no longer the mechanical equilibrium. But we hope that the correction so-computed gives valuable information on what behavior for the acoustics should be included in the reduction space.

Following the same reasoning for the purely acoustic modes we can compute structural corrections from the mechanical equilibrium:

$$\left(\mathbf{K}_s - \omega_f^2\mathbf{M}_s\right)\triangle_s^f = -\mathbf{K}_{sf}\phi_f. \tag{16}$$

It should be mentioned at this point that after the first iteration ω_f and ω_s represent the same values which are the eigenfrequencies of the coupled system representation. So that the mode vectors and eigenfrequencies are updated simultaneously.

Step 3: Energy based selection, transformation matrix and Gram-Schmidt orthogonalization

The importance of the corrections to properly approximate the coupled modes depends on the level of coupling and geometrical properties. In order to capture only important ingredients, computation of a relative strain energy based factor is proposed per physics. The factors are given as the ratio of the strain energy norm of the correction vectors with respect to their representative mode counterparts. Since in *IRCA*, at convergence, we expect that these correction vectors complement and correct the starting uncoupled basis vectors, we compare their energy norms to the energy norms of the modes from which these corrections are computed (see (15) and (16)). The importance of corrections can thus be estimated by

$$\varepsilon_p = \frac{\|\triangle_f^s\|_{\mathbf{K}_f}}{\|\phi_s\|_{\mathbf{K}_s}}, \tag{17}$$

$$\varepsilon_u = \frac{\|\triangle_s^f\|_{\mathbf{K}_s}}{\|\phi_f\|_{\mathbf{K}_f}}. \tag{18}$$

We select important correction vectors for the acoustic by setting $\varepsilon_p > 0.2$ and similarly, for the structural side, $\varepsilon_u > 0.2$. The comparison of the relative energy ratios with respect to the value 0.2 is based on current practical observation, however the driving idea is to choose the correction components that trigger important energy levels with respect to their sources. The other correction vectors that do not satisfy the selection criteria are not included in the basis. Note that the basis size is not fixed in this manner, but can vary between iterations.

After the energy based selection, the projection matrix $\mathbf{T}^c$ is formed with the selected correction vectors (c indicating that it will include the corrections computed in step 2) and is orthogonalized by the modified gram-schmidt orthogonalization algorithm to guarantee the linear independence of the vectors in the subspace where the best estimates of the eigenpairs will be searched for, namely,

$$\mathbf{T}^c = \begin{bmatrix} \phi_s & \mathbf{0} & \triangle_s^f & \mathbf{0} \\ \mathbf{0} & \phi_f & \mathbf{0} & \triangle_f^s \end{bmatrix}, \qquad \text{orth}(\mathbf{T}^c) \longrightarrow \mathbf{T}_\perp^c, \tag{19}$$

Step 4: Reduce system equations (interaction problem)

Using now the orthogonalized reduction basis, $\mathbf{T}_\perp^c$, to reduce the symmetrized eigenvalue problem, one can write the so-called interaction problem [12],

$$\underbrace{{\mathbf{T}_\perp^c}^T \mathbf{M}_{system} \tau \mathbf{T}_\perp^c}_{\mathbf{M}_{red}} \ddot{\eta} + \underbrace{{\mathbf{T}_\perp^c}^T \mathbf{K}_{system} \mathbf{T}_\perp^c}_{\mathbf{K}_{red}} \eta = \mathbf{0}. \tag{20}$$

The advantage on the use of these matrices is that they are reduced in size and symmetric. Thus they result in cheap computations and standard well-developed symmetric eigensolvers might be employed (QR for instance).

Step 5: Convergence check

A convergence check is performed with the previous eigenfrequencies, namely,

$$\varepsilon = \frac{\|\omega^j - \omega^{j-1}\|_2}{\|\omega^j\|_2}, \tag{21}$$

where ω^j is the set of approximate frequencies obtained at iteration j. The iteration is stopped if the frequency error estimate (21) is below the desired tolerance ε_{pre}. If not, the iteration continues by going to Step 2.

The remaining issue is to decide how to transform the current mode approximates to mono-physical modes needed to restart at Step 2 where corrections are computed. In this work, we take the first N approximate modes and split them into acoustic and structural parts.

The whole algorithm has just been outlined above. However in the context of this research paper, we are looking for some vectors (or pseudovectors) to be able to enrich the standard Craig-Bampton reduction space. To accomplish this task, one has two options in the context of IRCA. The first option is to stop IRCA iterations at a higher tolerance value than the preset tolerance value. The second option is to stop the iterations after a small iteration count (2 or 3, but which is essentially smaller than the iteration count on convergence) to end up with the enrichment vectors. These options are intended to limit the cost of computation of the correction vectors. However, it is still determined on user's choice.

3 Extension of the Craig-Bampton based substructuring to vibro-acoustic problems

Application of the Craig-Bampton method to vibro-acoustic problems has been illustrated in [10]. Extension of this reduction method with an enrichment is going to be outlined in this section. The degrees of freedom (dofs) are separated into interface and internal dofs. The interface dofs are denoted by "b" superscript and the internal dofs are denoted by the "i" superscript. The schematic representation of the problem is provided in Figure 1 on two components, A and B.

The source of the enrichment vectors are the outcomes of IRCA that has just been explained in the previous section. The partitioning of the dofs on the component level is represented by

$$\underbrace{\begin{bmatrix} \mathbf{M}^{bb} & \mathbf{M}^{bi} \\ \mathbf{M}^{ib} & \mathbf{M}^{ii} \end{bmatrix}}_{\mathbf{M}} \begin{bmatrix} \ddot{\mathbf{q}}^b \\ \ddot{\mathbf{q}}^i \end{bmatrix} + \underbrace{\begin{bmatrix} \mathbf{K}^{bb} & \mathbf{K}^{bi} \\ \mathbf{K}^{ib} & \mathbf{K}^{ii} \end{bmatrix}}_{\mathbf{K}} \begin{bmatrix} \mathbf{q}^b \\ \mathbf{q}^i \end{bmatrix} = \begin{bmatrix} \mathbf{F}^b \\ \mathbf{F}^i \end{bmatrix}. \tag{22}$$

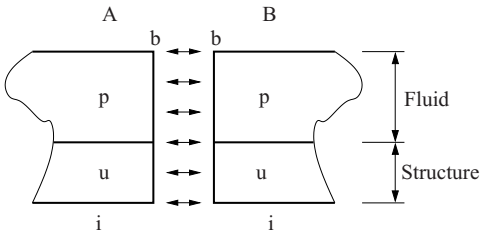

Fig. 1 Substructuring into two components

Note that, contrary to what was done in the previous section, here the partitioning is not done according to the physics. Thus a component can include both acoustic and mechanical degrees of freedom. The representation of the blocks in the matrices are provided in equations below for completeness :

$$\mathbf{M} = \begin{bmatrix} \begin{bmatrix} \mathbf{M}_s^{bb} & \mathbf{0} \\ -\mathbf{K}_{sf}^{bb\,T} & \mathbf{M}_f^{bb} \end{bmatrix} & \begin{bmatrix} \mathbf{M}_s^{bi} & \mathbf{0} \\ -\mathbf{K}_{sf}^{bi\,T} & \mathbf{M}_f^{bi} \end{bmatrix} \\ \begin{bmatrix} \mathbf{M}_s^{ib} & \mathbf{0} \\ -\mathbf{K}_{sf}^{ib\,T} & \mathbf{M}_f^{ib} \end{bmatrix} & \begin{bmatrix} \mathbf{M}_s^{ii} & \mathbf{0} \\ -\mathbf{K}_{sf}^{ii\,T} & \mathbf{M}_f^{ii} \end{bmatrix} \end{bmatrix}, \tag{23}$$

$$\mathbf{K} = \begin{bmatrix} \begin{bmatrix} \mathbf{K}_s^{bb} & \mathbf{K}_{sf}^{bb} \\ \mathbf{0} & \mathbf{K}_f^{bb} \end{bmatrix} & \begin{bmatrix} \mathbf{K}_s^{bi} & \mathbf{K}_{sf}^{bi} \\ \mathbf{0} & \mathbf{K}_f^{bi} \end{bmatrix} \\ \begin{bmatrix} \mathbf{K}_s^{ib} & \mathbf{K}_{sf}^{ib} \\ \mathbf{0} & \mathbf{K}_f^{ib} \end{bmatrix} & \begin{bmatrix} \mathbf{K}_s^{ii} & \mathbf{K}_{sf}^{ii} \\ \mathbf{0} & \mathbf{K}_f^{ii} \end{bmatrix} \end{bmatrix}. \tag{24}$$

The partitioning of the dofs follows accordingly

$$\begin{bmatrix} \mathbf{q}^{b\,T} & \mathbf{q}^{i\,T} \end{bmatrix} = \begin{bmatrix} \begin{bmatrix} \mathbf{u}_b{}^T & \mathbf{p}_b{}^T \end{bmatrix} & \begin{bmatrix} \mathbf{u}_i{}^T & \mathbf{p}_i{}^T \end{bmatrix} \end{bmatrix}. \tag{25}$$

In literature, different approaches have been used for the construction of the Craig-Bampton reduction basis. In [10], the authors use a partitioning approach which is different from the above, namely, they separate the structural and acoustic dofs and apply the standard Craig-Bampton method to this kind of partitioning while omitting some coupling terms in the constraint modes block of the basis. In the same work, they also propose a different approach which is similar to the ideas proposed in the previous section, namely, they use different right and left projection bases. These bases include different normal modes and constraint modes for right and left bases representations. In the current work, we follow the same ideas as in [10] and [11] for the constraint and vibration modes, besides we propose to add some pseudo-vectors to the basis or replace the fixed interface modes with these pseudo-vectors. These pseudo-vectors represent the global behaviour so they are expected to provide important information on how the neighbouring components

behave dynamically. This approach is expected to improve the computational results especially when strong coupling exist between components.

As will be detailed in the next subsections, there are several possible variants in using global modes. The first approach consists of using the vectors generated by IRCA in a standard Craig-Bampton basis to replace the fixed interface modes. The second approach is the same as the first approach however in this approach separate generalized dofs are not retained per component basis but the assembly of the generalized dofs is accomplished over one set of global generalized coordinates. In the third approach, one might select to use a combination of fixed interface modes and pseudo-vectors. These schemes are outlined in Sections 3.1, 3.2 and 3.3.

3.1 Replacing fixed interface modes by pseudo-vectors

The replacement of the fixed interface modes with pseudo-vectors is outlined in this subsection. The representation is provided starting from a standard Craig-Bampton basis. Use of the left and right projection ideas are provided in [11] and written as

$$\mathbf{T}_{cb,L}^{T} = \begin{bmatrix} \mathbf{I} & -\mathbf{K}_{bi}\mathbf{K}_{ii}^{-1} \\ \mathbf{0} & \phi_{i,L}^{T} \end{bmatrix}, \tag{26}$$

$$\mathbf{T}_{cb,R} = \begin{bmatrix} \mathbf{I} & \mathbf{0} \\ -\mathbf{K}_{ii}^{-1}\mathbf{K}_{ib} & \phi_{i,R} \end{bmatrix}. \tag{27}$$

In equations (26) and (27), the subscript R and L represents the right and left fixed interface modes, respectively. Similarly, subscript i represents the internal modes. For the right projection basis, one uses the pseudo-vectors, given by superscript P, in the second column instead of the fixed interface mode vectors, namely,

$$\begin{bmatrix} q_b \\ q_i \end{bmatrix} = \begin{bmatrix} \mathbf{I} & \phi_{b,R}^{P} \\ -\mathbf{K}_{ii}^{-1}\mathbf{K}_{ib} & \phi_{i,R}^{P} \end{bmatrix} \begin{bmatrix} \tilde{q}_b \\ \eta_i \end{bmatrix}. \tag{28}$$

It is important to note that this transformation does not provide interface connectors as in standard substructuring strategies since the boundary degrees of freedom have been transform in $\tilde{q}_b$. One thus needs an intermediate transformation to end up with the connector boundary dofs : using the first line of (28) to write

$$\tilde{\mathbf{q}}_b = \mathbf{q}_b - \phi_{b,R}^{P}\eta_i,$$

and substituting in the second line of (28) one finds the equivalent transformation

$$\begin{bmatrix} q_b \\ q_i \end{bmatrix} = \begin{bmatrix} \mathbf{I} & \mathbf{0} \\ -\mathbf{K}_{ii}^{-1}\mathbf{K}_{ib} & \left(\phi_{i,R}^{P} + \mathbf{K}_{ii}^{-1}\mathbf{K}_{ib}\phi_{b,R}^{P}\right) \end{bmatrix} \begin{bmatrix} q_b \\ \eta_i^{P} \end{bmatrix}. \tag{29}$$

The projection basis follows a similar reasoning. However, it deserves more attention because the ingredients are different: the constraint modes are not the direct transposes of the constraint modes in the right basis due to the unsymmetric nature of the component matrices. The left basis might be written following the left eigenvector problem and writing that basis in a Craig-Bampton like scheme,

$$\mathbf{T}_{cb,L}^{T} = \begin{bmatrix} \mathbf{I} & -\mathbf{K}_{bi}\mathbf{K}_{ii}^{-1} \\ \mathbf{0} & \left(\phi_{i,L}^{P\ T} + \phi_{b,L}^{P\ T}\mathbf{K}_{bi}\mathbf{K}_{ii}^{-1}\right) \end{bmatrix}. \tag{30}$$

To facilitate a numerically robust implementation, the modified mode vectors in equations (29) and (30) are orthogonalized with respect to the mass matrix.

3.2 Pseudo-vectors with unique global generalized dof

Use of global pseudo-vectors instead of the fixed interface modes has another advantage: since these modes are global to the system one can choose to associate them to a unique global degree of freedom on the system level. This operation might be summarized with a few matrix transformations. To exemplify the operations, we are going to consider a system that is divided into two components. Starting from the modal expansion where one set of generalized set of dofs are kept, the transformation equation might be written as

$$\begin{bmatrix} \mathbf{q}_b \\ \mathbf{q}_{i,1} \\ \mathbf{q}_{i,2} \end{bmatrix} = \begin{bmatrix} \mathbf{I} & \phi_b^P \\ -\mathbf{K}_{ii,1}^{-1}\mathbf{K}_{ib,1} & \phi_{i,1}^P \\ -\mathbf{K}_{ii,2}^{-1}\mathbf{K}_{ib,2} & \phi_{i,2}^P \end{bmatrix} \begin{bmatrix} \tilde{\mathbf{q}}_b \\ \eta^P \end{bmatrix}, \tag{31}$$

where $\mathbf{q}_b$ represents the common boundary dofs and $\mathbf{q}_{i,1}$ and $\mathbf{q}_{i,2}$ represents the internal dofs of component 1 and 2, respectively. To assemble the components, a transformation step is necessary using the first row of equation (31), namely, $\tilde{\mathbf{q}}_b = \mathbf{q}_b - \phi_b^P\eta$. Use of this relation results in

$$\begin{bmatrix} \mathbf{q}_b \\ \mathbf{q}_{i,1} \\ \mathbf{q}_{i,2} \end{bmatrix} = \begin{bmatrix} \mathbf{I} & \mathbf{0} \\ \left(-\mathbf{K}_{ii,1}^{-1}\mathbf{K}_{ib,1}\right) & \left(\phi_{i,1}^P + \mathbf{K}_{ii,1}^{-1}\mathbf{K}_{ib,1}\phi_b^P\right) \\ \left(-\mathbf{K}_{ii,2}^{-1}\mathbf{K}_{ib,2}\right) & \left(\phi_{i,2}^P + \mathbf{K}_{ii,2}^{-1}\mathbf{K}_{ib,2}\phi_b^P\right) \end{bmatrix} \begin{bmatrix} \mathbf{q}_b \\ \eta^P \end{bmatrix}, \tag{32}$$

indicating that component contributions of the amplitudes of the global modes can be assembled similarly to the interface degrees of freedom. This has an advantage in comparison to the conventional Craig-Bampton method, where the fixed interface modes are local to a component and thus generate separate degrees of freedom at the global level. With the just outlined scheme, the reduced system matrices are reduced one more level with respect to the conventional Craig-Bampton approach.

It is worth mentioning that when reducing the substructures on the component level, the same ideas outlined in Section 3.1 are used for the left and right projection spaces. The difference between the strategy proposed in this subsection and in the previous is only coming from the fact that the generalized dofs are also assembled globally with this scheme.

3.3 Enrichment of the reduction space with pseudo-vectors

The third improvement/enrichment approach is to include the pseudo-vectors into the reduction basis together with the fixed interface modes. The right reduction basis expansion is given as

$$\begin{bmatrix} \mathbf{q}_b \\ \mathbf{q}_i \end{bmatrix} = \begin{bmatrix} \mathbf{I} & \mathbf{0} & \phi^P_{b,R} \\ -\mathbf{K}_{ii}^{-1}\mathbf{K}_{ib} & \phi^{i,R} & \phi^P_{i,R} \end{bmatrix} \begin{bmatrix} \tilde{\mathbf{q}}_b \\ \eta_i \\ \eta^P_i \end{bmatrix}. \tag{33}$$

Following the similar reasoning of an intermediate transformation matrix from section 3.1, one can write

$$\begin{bmatrix} \mathbf{q}_b \\ \mathbf{q}_i \end{bmatrix} = \begin{bmatrix} \mathbf{I} & \mathbf{0} & \mathbf{0} \\ -\mathbf{K}_{ii}^{-1}\mathbf{K}_{ib} & \phi_{i,R} & \left(\phi^P_{i,R} + \mathbf{K}_{ii}^{-1}\mathbf{K}_{ib}\phi^P_{i,R}\right) \end{bmatrix} \begin{bmatrix} \mathbf{q}_b \\ \eta_i \\ \eta^P_i \end{bmatrix}. \tag{34}$$

For the projection basis, the modes that should be integrated into the basis are the left eigenvectors of the according problems. A mixture of fixed interface and global modes should be used. Taking these factors into account the left basis can be represented as

$$\mathbf{T}_{cb}^{L\ T} = \begin{bmatrix} \mathbf{I} & -\mathbf{K}_{bi}\mathbf{K}_{ii}^{-1} \\ \mathbf{0} & \phi^T_{i,L} \\ \phi^{P\ T}_{b,L} & \phi^{P\ T}_{i,L} \end{bmatrix}, \tag{35}$$

$$\mathbf{T}_{cb}^{L\ T} = \begin{bmatrix} \mathbf{I} & -\mathbf{K}_{bi}\mathbf{K}_{ii}^{-1} \\ \mathbf{0} & \phi^T_{i,L} \\ \mathbf{0} & \left(\phi^{P\ T}_{i,L} + \phi^{P\ T}_{b,L}\mathbf{K}_{bi}\mathbf{K}_{ii}^{-1}\right) \end{bmatrix}. \tag{36}$$

In order not to include linearly dependent vectors in the reduction basis, an orthogonalization through an interaction problem is accomplished for the vectors that are integrated into the left and right basis. Representing the mode vectors in the right basis as

$$\mathbf{Y}_R = \left[\phi^{i,R} \left(\phi^P_{i,R} + \mathbf{K}_{ii}^{-1}\mathbf{K}_{ib}\phi^P_{i,R}\right) \right], \tag{37}$$

and the mode set vectors in the left basis as

$$\mathbf{Y}_L^T = \begin{bmatrix} \phi_{i,L}^T \\ \left(\phi_{i,L}^{P\ T} + \phi_{b,L}^{P\ T}\mathbf{K}_{bi}\mathbf{K}_{ii}^{-1}\right) \end{bmatrix}, \tag{38}$$

one forms the interaction problem for the internal dofs of a component as

$$\mathbf{Y}^{L\,T}\left(\mathbf{K}^{ii} - \omega^2\mathbf{M}^{ii}\right)\mathbf{Y}^R\zeta = 0. \tag{39}$$

This reduced interaction problem is also unsymmetric and reveals left and right eigenvectors, namely $\mathbf{v}^L$ and $\mathbf{v}^R$. The recovery is accomplished over the left and right eigenvectors of the interaction problem. The mode set to be included into the basis is found by

$$\psi^L = \mathbf{Y}^L\mathbf{v}^L, \tag{40}$$

$$\psi^R = \mathbf{Y}^R\mathbf{v}^R. \tag{41}$$

The final form of the reduction and projection bases are given in a compact format as

$$\mathbf{T}_{cb}^{L\ T} = \begin{bmatrix} \mathbf{I} & -\mathbf{K}_{bi}\mathbf{K}_{ii}^{-1} \\ \mathbf{0} & \psi^{L\,T} \end{bmatrix}, \tag{42}$$

$$\mathbf{T}_{cb}^R = \begin{bmatrix} \mathbf{I} & \mathbf{0} \\ -\mathbf{K}_{ii}^{-1}\mathbf{K}_{ib} & \psi^R \end{bmatrix}. \tag{43}$$

4 Application and results

4.1 Computational framework and the model

An application code is being developed by the first author to test the above mentioned ideas. The finite element system matrices are generated in the commercial program ANSYS using the implemented fluid-structure coupling scheme [15]. The resulting matrices are extracted from the binary result files along with the boundary condition information. Partitioning operations are accomplished in Gmsh [16] and the related interface and internal dof information is found from the partitioned mesh structure of the model. According to the partitioning information, component matrices are built from the binary element matrix files of ANSYS. A MATLAB [17] interface to SLEPc/PETSc [18, 19] is created to solve sparse eigenvalue problems. This interface is used to solve the eigenvalue problems that are encountered in the course of this research paper.

For the test of ideas, a two-dimensional academic model is created. Namely, a structural beam is coupled to a closed fluid volume that is filled with water to simulate the strong coupling between the structure and the fluid. The structural properties of the beam are taken as follows: E = 71GPa, $\nu = 0.33$ and the density as 2800 kg/m^3. The speed of sound in water is taken as 1500 m/s and the density of water is

taken as 1000 kg/m^3. The finite element model consists of 5250 quadrilateral structural and fluid elements, namely FLUID29 and PLANE42 elements in ANSYS. The total model consists of 6616 degrees of freedom. The model is partitioned into two similar components for the conducted numerical tests. The interface lines contain both the fluid and structural degrees of freedom.

The test model is illustrated in Figure 2. The bold line represents the interface between the fluid and structure regions where the off-diagonal coupling blocks result from. The two ends of the beam are fixed for this problem.

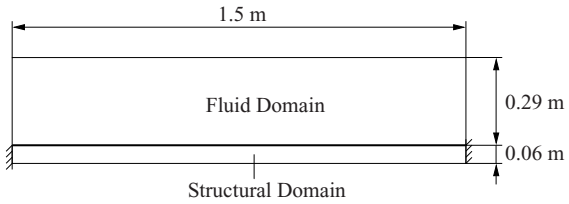

Fig. 2 Model of a rectangular cavity coupled to a beam

The discussed substructuring techniques in Sections 3.1, 3.2 and 3.3 are used to compute the reduced eigenfrequencies of the coupled system. We will start out the reduction studies with a modal basis where the structural variables, u, are expanded in the in-vacuo structural modes, $u = \phi_S \eta_S$, and the fluid variables, p, are also expanded in the rigid walled acoustic cavity modes, $p = \phi_F \eta_F$ [20]. Resulting in,

$$\begin{bmatrix} u \\ p \end{bmatrix} = \begin{bmatrix} \phi_S & \mathbf{0} \\ \mathbf{0} & \phi_F \end{bmatrix} \begin{bmatrix} \eta_S \\ \eta_F \end{bmatrix}. \tag{44}$$

This diagonal reduction and projection basis is used in order to show the improvement with respect to this basis. During the numerical tests, 30 mode vectors are kept in the bases. One exception is the implementation of the scheme of Section 3.3 where some combination of fixed interface and global modes are used.

4.2 Results

The results of the proposed schemes are presented in this subsection. All the presented results are based on a relative frequency error which is computed with respect to the frequencies that are found by ANSYS on the full coupled model.

Figure 3 represents the relative frequency error results of the proposed scheme in Section 3.1. The improvement on error levels by the use of IRCA vectors after some iterations are also indicated in the same result. For the current setting, 2 iterations are enough for IRCA to satisfy the tolerance criteria of 0.01 given by equation (21). The error levels marked with $\diamond$ represent the results obtained after 1 iteration of the

iterative algorithm. The improvement with respect to the uncoupled basis is fair. The error levels indicated by Δ represent the error levels obtained with the vectors that result from IRCA on the set tolerance level. The improvement on the latter is better for the considered number of mode vectors as one should expect. The application of the two-sided Craig-Bampton scheme outlined in Section 3.1 (equations 26 and 27) is also given for comparison purposes and labeled as tsCb.

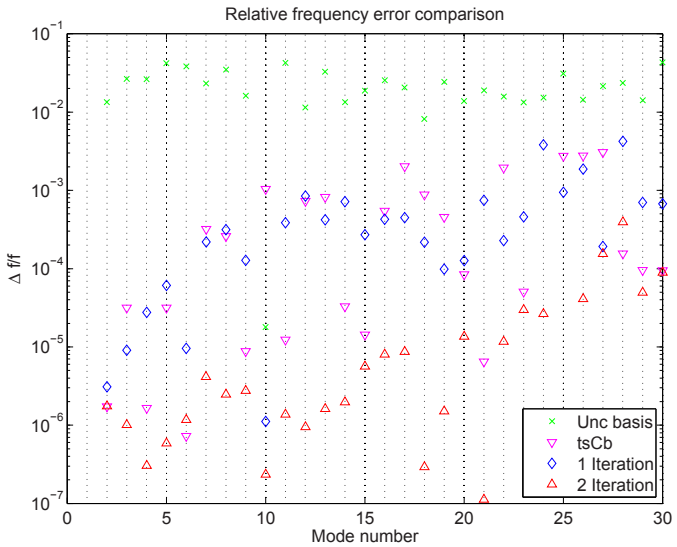

Fig. 3 Scheme section 3.1, 1 iteration vs. 2 iterations

Figure 4 reports the relative frequency error results of the proposed scheme in Section 3.2. As mentioned in the theoretical exposition, this scheme has the advantage of the assembly of the generalized dofs on the full reduced system level for the integration of the global modes into the reduction basis. The comparison of the current results with the two-sided Craig-Bampton scheme is also provided for these results. The results show fair accuracy for kept number of vectors in the reduction bases.

Figure 5 represents the relative frequency error results of the proposed scheme in Section 3.3. On this result figure, the combination of the mode vectors has been changed for comparison purposes. Namely, F mark in the legend represents the number of fixed interface modes, similarly the I mark represents the integrated number of global pseudo vectors into the reduction basis (e.g. 25F-5I represents the fact that 25 Fixed interface modes with 5 Irca modes are used in the mode block of the basis.). It should be mentioned that for this test, the ultimate results of the iterative correction algorithm is used. In general, increase of the global mode count results in a better accuracy.

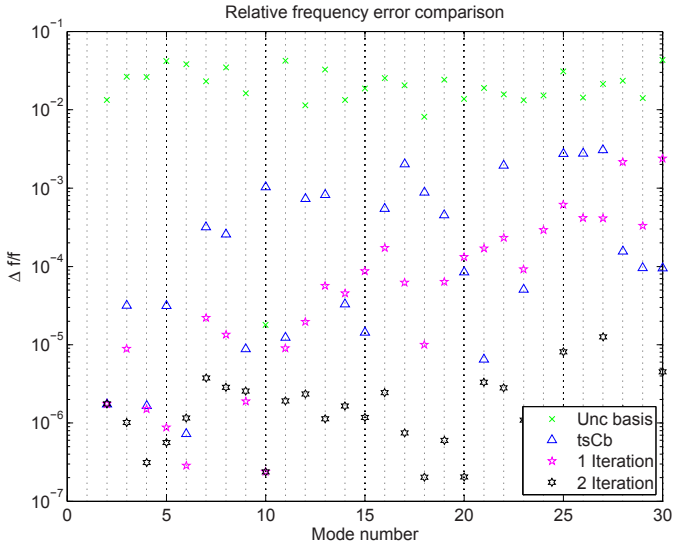

Fig. 4 Scheme section 3.2, 1 iteration vs. 2 iterations

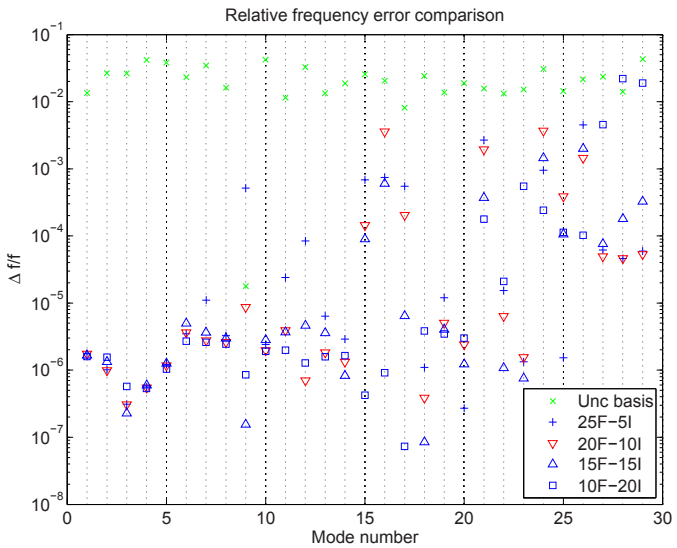

Fig. 5 Scheme section 3.3., integration of IRCA modes with fixed interface modes

5 Conclusion and discussion

In this paper, we proposed some computational schemes to extend the standard Craig-Bampton reduction method to coupled vibro-acoustic problems. The main

idea is to make use of some global information and integrate this information in the reduced representation. These enrichment vectors are computed from an iterative algorithm which at convergence represents the global mode approximations. The ultimate aim is not to compute global modes but some enrichment vectors which might provide important dynamic information on how the other components behave and how this might be reflected on the component level.

From the results presented here we can conclude that the proposed methods yield an acceptable accuracy level. However, there are important computational points to mention. Namely, the most important computational burden results from the computation of the correction vectors that are meant to complement the uncoupled system modes since expensive factorizations should be performed per physics due to the update of the operator matrices. Investigation of iterative solution methods in this respect might give a cure when the system sizes become exceedingly large.

Integration of the global mode vectors in the basis brings important information and has shown to improve the results on a large portion of the spectrum. Results also reveal that finding a trade-off when using a mix of the fixed interface modes with global pseudo modes is also significantly difficult. This is due to the fact that there is no mechanism to reveal some information on the coupling beforehand. This information is also dependent on the problem type, fluid which is in contact with the structure and geometry of the overall problem.

Acknowledgements This work is supported by the *Technologiestichting STW* of the Dutch Government and the authors gratefully acknowledge the means of support.

Appendix A: Relation of left and right eigenvector and the symmetrization concept

Let us consider the symmetrized vibro-acoustic problem and define its eigenvectors by

$$(\mathbf{K}_{system} - \omega^2 \mathbf{M}_{system}) \underbrace{\tau \phi^{sym}}_{\phi^R} = \mathbf{0} \tag{45}$$

The left eigenvector of this problem is, by symmetry, identical to $\phi^{\mathbf{sym}}$, namely $\phi^{\mathbf{sym}} = \phi^{\mathbf{L}}$. Consider now the non-symmetrized problem, the system exhibits left and right eigenvectors, which can be deduced from (45):

$$\phi^R = \tau \phi^{sym} = \begin{bmatrix} \mathbf{K}_s^{-1} \mathbf{M}_s \phi_s^L - \mathbf{K}_s^{-1} \mathbf{K}_{sf} \phi_f^L \\ \phi_f^L \end{bmatrix} \tag{46}$$

The left eigenvalue problem can be written as

$$\left(\begin{bmatrix} \mathbf{K}_s & \mathbf{K}_{sf} \\ \mathbf{0} & \mathbf{K}_f \end{bmatrix}^T - \omega^2 \begin{bmatrix} \mathbf{M}_s & \mathbf{0} \\ \mathbf{M}_{fs} & \mathbf{M}_f \end{bmatrix}^T \right) \begin{bmatrix} \phi_s^L \\ \phi_f^L \end{bmatrix} = 0 \tag{47}$$

which might also be written as

$$\left(\begin{bmatrix} \mathbf{K}_s & \mathbf{0} \\ {\mathbf{K}_{sf}}^T & \mathbf{K}_f \end{bmatrix} - \omega^2 \begin{bmatrix} \mathbf{M}_s & \mathbf{M}_{fs}^T \\ \mathbf{0} & \mathbf{M}_f \end{bmatrix} \right) \begin{bmatrix} \phi_s^L \\ \phi_f^L \end{bmatrix} = 0 \tag{48}$$

The first line of this equation yields

$$\begin{aligned} \phi_s^L &= \omega^2 \left(\mathbf{K}_s^{-1} \mathbf{M}_s \phi_s^L + \mathbf{K}_s^{-1} \mathbf{M}_{fs}^T \phi_f^L \right) \\ &= \omega^2 \left(\mathbf{K}_s^{-1} \mathbf{M}_s \phi_s^L - \mathbf{K}_s^{-1} \mathbf{K}_{sf} \phi_f^L \right) \end{aligned} \tag{49}$$

where we have used the relation $\mathbf{M}_{fs}^T = -\mathbf{K}_{sf}$ explained in section 2.1. Substituting this relation in (46) one finds

$$\phi^R = \begin{bmatrix} \frac{1}{\omega^2} \phi_s^L \\ \phi_f^L \end{bmatrix} \qquad \text{or} \qquad \phi^L = \begin{bmatrix} \omega^2 \phi_s^R \\ \phi_f^R \end{bmatrix} \tag{50}$$

which is inline with the proofs in [21] and [22].

References

1. Dhatt Gouri, Touzot Gilbert, The Finite Element Method Displayed, 1984, John Wiley and Sons, 1984
2. Wu T.W., Boundary Element Acoustics, Fundamentals and Computer Codes, WIT Press, 2000
3. Betess P., Infinite Elements, International Journal for Numerical Methods in Engineering, Vol.11, 53-64, 1977
4. Morand, H.J.P., Ohayon R., Fluid Structure Interaction, John Wiley and Sons, Masson, 1995
5. Craig R.R., Bampton M.C.C., Coupling of Substructures for Dynamic Analysis, AIAA Journal, vol.6(7), 1313-1319, 1968
6. Rubin S., Improved Component-Mode Representation for Structural Dynamic Analysis,AIAA Journal, vol.13(8), 995-1006, 1975
7. Felippa Carlos A., Symmetrization of the contained compressible-fluid vibration eigenproblem, Communications in Applied Numerical Methods, vol.1, 241-247, 1985
8. Felippa Carlos A., Symmetrization of the coupled eigenproblems by eigenvector augmentation, Communications in Applied Numerical Methods, vol.4(4), 561-563, 1988
9. Tabak Umut, Rixen Daniel J., Reduced iterative correction algorithm for coupled vibro-acoustic problems, Proceedings of ISMA 2010, International Conference on Noise and Vibration Engineering, 4685-4695, 2010
10. Maess Mathiass, Gaul Lothar, Component Mode Synthesis for Efficient Structure-Acoustic Simulation of Piping Systems, International Modal Analysis Conference XXIV, St.Louis, 2006.
11. Nactergaele Ph., Rixen D.J.,Steenhoek A.M., Efficient weakly coupled projection basis for the reduction of thermo-mechanical models, Journal of Computational and Applied Mathematics, Volume 234, Issue 7, 2010, Pages 2272-2278
12. Géradin M., Rixen D., Mechanical Vibrations. Theory and Application to Structural Dynamics,Wiley & Sons,2nd Ed, 1997
13. Craig R.R., Kurdila A., Fundamentals of Structural Dynamics, John. Wiley and Sons, 2006
14. Brechlin E., Gaul L., Two methodological improvements for component mode synthesis, International Conference on Noise and Vibration Engineering, ISMA2000, 2000

15. Programmer's Manual for Ansys, Ansys Release 11.
16. Geuzaine C. and Remacle J.-F., Gmsh: a three-dimensional finite element mesh generator with built-in pre- and post-processing facilities, International Journal for Numerical Methods in Engineering, Volume 79, Issue 11, 1309-1331, 2009
17. MATLAB, R2010b, www.mathworks.
18. Hernandez Vicente, Roman Jose E. and Vidal Vicente, SLEPc: A Scalable and Flexible Toolkit for the Solution of Eigenvalue Problems, ACM Transactions on Mathematical Software, 31(3), 351–362, 2005
19. PETSc user manual, Balay Satish and Buschelman Kris and Eijkhout Victor and Gropp William D. and Kaushik Dinesh and Knepley Matthew G. and McInnes Lois Curfman and Smith Barry F. and Zhang Hong, Argonne National Laboratory, ANL-95/11 - Revision 3.1, 2010
20. Wolf Joseph A. Jr., Modal Synthesis for Combined Structural-Acoustic Systems, AIAA Journal, 15(5), 7141-745, 1977,
21. Luo, Jianhui, Gea Hae Chang,Modal Sensitivity Analysis of Coupled Acoustic-Structural Systems, Journal of Vibration and Acoustics, vol.119, 545-550, 1997
22. Ma Zheng-Dong, Hagiwara Ichiro, Sensitivitity Analysis Methods for coupled structural-acoustic systems part I : Modal sensitivities, AIAA Journal, vol.29(10), 1787-1795, 1991

A Modal-Geometrical Selection Criterion for Master Nodes: Numerical and Experimental Testing

Elvio Bonisoli, Cristiana Delprete and Carlo Rosso
Politecnico di Torino, Corso Duca degli Abruzzi, 24 - 10129, Torino, Italy

ABSTRACT

Usually, the problem of master nodes selection characterizes both computational or experimental modal analyses and defines the numerical properties of reduced models that possess equivalent dynamic properties. Methodologies based on experience are normally used or heavy time-consuming numerical algorithms can be applied. In that paper, the Modal-Geometrical Selection Criterion (MoGeSeC) is applied to a crankshaft, both for an EMA (experimental modal analysis) and for a reduction procedure applied on progressive numerical models. Then the results are compared with other literature criteria and algorithms. The nodes suggested by MoGeSeC and other criteria are used for identification tools of the dynamic behaviour of the crankshaft. In that way MoGeSeC proves to be a very quick and accurate method because the nodes it selects depicts very well modal features of the tested component. The proposed criterion is also applied to the component in order to evaluate the reduced inertia and stiffness matrices and their numerical ill-conditioning is measured. Also in that case MoGeSeC provides the analyzer with a good instrument for identification processes.

NOMENCLATURE

A_{jk}	accelerance function in node *j*, due to a dynamic force acting in node *k*
$F_{0,k}$	amplitude of acting force in node *k*
j	imaginary operator
k_i	weight coefficients
m	order of the reduced model
n	number of degrees of freedom (dofs) of the starting model
r	number of considered modes in term $\mathbf{W}_m$
$\lambda_{\max}$, $\lambda_{\min}$	maximum and minimum eigenvalue
ξ_i	damping factor of mode *i*
ω	frequency of the acting force
ω_i	natural frequency of mode *i*
(x_i, y_i, z_i)	geometrical grid coordinates of node *i*
$\mathbf{f}(\mathbf{t})$	generalized forces set vector
$\mathbf{q}$	modal coordinates vector
$x(t)$, x_m , x_s	respectively generalized coordinates vector, master and slave subset
$\mathbf{W}$	weight function of the modal-geometrical selection criterion
$\mathbf{W}_g$	geometric term of the weight function
$\mathbf{W}_m$	modal term of the weight function
$\mathbf{M}$, $\mathbf{K}$	respectively mass and stiffness matrix
$\mathbf{M}_r$, $\mathbf{K}_r$	respectively mass and stiffness matrix of the reduced model
$\mathbf{Q}$	Fisher information matrix
$\mathbf{J}$	covariance matrix of error with truncated modal displacement base

T. Proulx (ed.), *Linking Models and Experiments, Volume 2*, Conference Proceedings of the Society for Experimental Mechanics Series 5,
DOI 10.1007/978-1-4419-9305-2_20, © The Society for Experimental Mechanics, Inc. 2011

$\mathbf{T}$	transformation matrix applied in the reduced technique
$\mathbf{\Phi}$, $\mathbf{\Phi}_m$, $\mathbf{\Phi}_s$	respectively complete eigenvector matrix, master and slave subset
$\mathbf{\Phi}_c$, $\mathbf{\Phi}_n$	respectively constraint and normal modes of Craig-Bampton reduction technique
$\mathbf{\Phi}_{m,gen}^{-1}$	generalized master subset eigenvector inverse matrix
$\boldsymbol{\omega}_r^2$	modal eigenvalues diagonal matrix

INTRODUCTION

In the experimental dynamic analysis, the selection of the points where the accelerometers have to be placed is a great problem. In the same way, when a model reduction is performed, it is not easy to define the master nodes. This is due to the deep relation between the nodes selection and the fundamental physical and dynamic properties of the body, in other words, the spatial incompleteness of the described degrees of freedom of a model and the modal model incompleteness of the dynamic behavior that the model represents could deeply change with respect to the nodes used for modal analysis or modal reduction. The places where sensors have to be put are usually selected on the basis of engineer's experience. It then becomes important to identify a method for choosing the master dofs that allow a good depiction of the dynamic behavior of the reduced model and an improvement of the numerical stability of modal matrices. Therefore, the objective of sensor placement strategy is to select locations that render the corresponding target mode shape partitions as linearly independent as possible and, at the same time, maximize the modal responses within the sensor data. These effective independence criteria (EI) are recommended by Friswell and Mottershead [1] for modal testing and modal updating.
Another criterion is based on modal kinetic energy estimations that can be used to help determine a good candidate node set. In [10] the proposal of a connection between these two influencing sensor placement methods has been analyzed.
In [12] different optimal sensor placement techniques, based on the maximization of the Fisher information matrix and the EI criteria or based on energetic approaches, such as the eigenvalue vector product (EVP), have been compared and applied on a bridge structure with the aim of maximizing the dynamic data information is depicted.

A complementary or alternative approach for master dofs selection in dynamic condensation approaches and optimal sensor placement techniques has to implement the following keypoints:

- integration of effective independence criteria and modal kinetic energy approaches in an adaptable and flexible formulation in order to maximize the modal description and the orthogonality properties and minimize the ill-conditioning of mass and stiffness matrices of the reduced model;
- selection of master dofs aside from the knowledge of a starting dynamic model and, therefore, with a very low computational cost; the approach has to reduce both analytical and experimental data, starting from the knowledge of the geometrical data of candidate node set and the modal properties;
- increment of model dofs and modal order by adding some auxiliary dofs to previously selected master nodes without iterative procedure in order to simplify the modelling process taking into account important nodes or the connection between sub-structures.

In order to validate the alternative approach named MoGeSeC (Modal-Geometrical Selection Criterion), in this paper, an extensive application of the proposed criterion is applied on a automotive component that possess rich dynamic properties, such as a crankshaft, and the results are compared with obtained from the EI criterion.

SELECTION CRITERIA OF MASTER NODES: MOGESEC AND EI

In order to maximize modal properties and eigenvector orthogonality and to reduce the ill-conditioning of the reduced model the Modal-Geometrical Selection Criterion of master dofs is here proposed and compared to the most used criterion called Effective Independence. A brief discussion on the mathematical basis of the two criteria is presented, then a comparison between the obtained results is conducted.

MODAL GEOMETRICAL SELECTION CRITERION

The basic idea of MoGeSeC is to consider both the geometrical and the modal features of the body. In fact the nodes selection has to consider both the disposition of nodes in the body volume and the modal shapes that have to be modelled or evaluated. If only geometrical or modal information are used, some important dynamic features could be underestimated. For example, considering just geometrical information, a torsional behaviour could be erased if the nodes are selected on a axis parallel to the rotational axis. In the same way, using only modal information, some areas of the body could be not represented in the model. Starting from this consideration, MoGeSeC selects the additional master dofs evaluating the maximum value of a weight function vector **W**, estimated for each physical node of the FE model or of all the possible experimental locations:

$$\mathbf{W} = \mathrm{diag}\left(\mathbf{W}_g\,\mathbf{W}_m^T\right) \tag{1}$$

where the geometrical vector $\mathbf{W}_g$ and the modal vector $\mathbf{W}_m$ are evaluated for each physical node p by means of expressions:

$$\begin{aligned} W_{g,p} &= \frac{1}{\max\left(\mathbf{W}_g\right)} \cdot 1 \Bigg/ \sum_{i=1}^{r}\left[\frac{1}{\left(x_p - x_i\right)^2 + \left(y_p - y_i\right)^2 + \left(z_p - z_i\right)^2}\right]^{k_1} \\ W_{m,p} &= \frac{1}{\max\left(\mathbf{W}_m\right)} \sum_{j=1}^{3(r+1)}\left[\Phi_{p,x}^{(j)\,2} + \Phi_{p,y}^{(j)\,2} + \Phi_{p,z}^{(j)\,2}\right]^{k_2} \end{aligned} \tag{2}$$

and the geometrical grid coordinates of the candidate p are $\left(x_p, y_p, z_p\right)$, while the geometrical grid coordinates of the r previously selected master nodes are $\left(x_i, y_i, z_i\right)$; the corresponding modal displacements of the candidate p for the j normalized modal shape are $\left(\Phi_{p,x}^{(j)}, \Phi_{p,y}^{(j)}, \Phi_{p,z}^{(j)}\right)$. Exponents k_1 and k_2 are weight parameters that allow flexibility to be increased. Both geometrical and modal terms are normalized to unit values.
It is possible to stress the following milestones of MoGeSeC methodology:

- actual physical nodes and the three coordinate displacements of the model are taken into account;
- as Matta and Kammer suggest in [8], [15], only translational generalized displacements are considered, because rotations are negligible;
- the reduced dynamic model should be able to replicate the modal properties of master nodes, such as representative model nodes or boundary connection nodes, and should be expanded by adding additional nodes without iterative procedures and by maintaining the previous ones;
- the aim of adding a new node is to improve numerical stability of matrices: this is done selecting the node with the furthest possible distance from the other master nodes and selection is also weighted with a high modal participation;
- the analytical expression for the geometrical term is based on a generalized gravitational force form; the sum of distances between the new candidates and the previously master nodes are evaluated through the power of parameter k_1 and the repeated choice of the same node is prevented;
- analogously, the sum of modal displacements of candidates is weighted through the power of parameter k_2; if k_2 is set equal to 1, the square norms sum of modal shapes is adopted;
- parameters k_1 and k_2 are arbitrarily set through applying the selection criterion to a wide number of case study models; they are initially set respectively to 2 and 1 and the parameter investigation for the optimal choice is discussed in some previous papers [19], [20]. In Figure 1 it may be evinced the local minimum for the function surface in the case of the first 150 modes of an exhaust pipeline; similar behaviour can be pointed out for the other considered models. For each model an optimal choice of k_1 and k_2 parameters can be done in the concurrence of surface minimum.

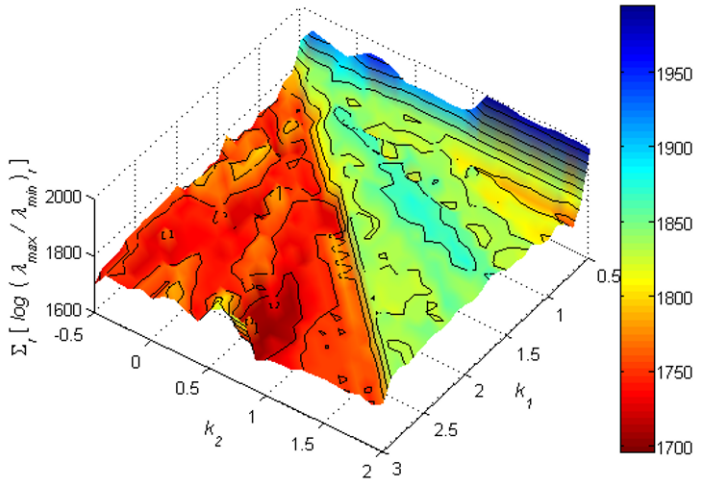

Figure 1 – Selection map of the weights k_1 and k_2 .

EFFECTIVE INDEPENDENCE METHOD

From among the numerous master nodes criteria and optimal sensor placement methods found in literature [7], [8], [9], [10], [11], [12], [13] the well-known effective iterative procedure based on the maximisation of the independence of modal properties is taken into account.

The effective independence method (EI) was developed to maximise both the spatial independence and signal strength of a number of targeted mode shapes. It has been implemented for optimal sensor location in modal identification of large structures [1], [11] and is based on the maximisation of the Fisher information matrix determinant **Q**. Estimating the covariance matrix of the error **J** to describe a generic configuration with the modal displacements, it results [12]:

$$\mathbf{J} = \mathbf{Q}^{-1} = \alpha \left[\mathbf{\Phi}^T \mathbf{\Phi}\right]^{-1} \tag{3}$$

where α is a constant.

The procedure is iterative: the methodology for selecting the best sensor placements is to unselect candidate sensor positions so that the determinant of the Fisher information matrix **Q** is maximised.

Although EI is an iterative technique and is rather computing-time consuming for complex FE models with respect to MoGeSeC, the results obtained with this approach give rise to an effective fairly uniform spacing for the sensor locations along the structure [12]. This objective is similar to the role of the geometrical vector term $\mathbf{W}_g$ of Equation (3) which allows the addition of physical nodes in a model geometrical area that respects as far as possible the other master nodes. Using just this information creates as main effect that EI can produce experimental setup not well distributed in the space occupied by the structure and a high sensitivity of ill-conditioning and mode-shapes identification for small error location of sensors. Pursuing independence properties, EI method can select sensor locations with low energy content, with a consequent possible loss of information. In order to overcome this limitation, the weighting of the mode-shape displacement is adopted in MoGeSeC by introducing the modal vector term $\mathbf{W}_m$. The aim of the methodology is to minimise the ill-conditioning and to improve numerical stability of mass and stiffness matrices of the reduced model. Therefore, the selection of added master nodes, based on relevant modal properties, is corrected by means of the geometrical vector term $\mathbf{W}_g$ in order to obtain an optimal distribution.

REDUCED MODELS

In order to determine a dynamic reduced model, an undamped linear multi-dof dynamic model of the whole system is considered. In the present paper dissipative terms, such as viscous damping or hysteretic effects, are neglected because the aim is preliminarily to focus on mechanical systems lightly damped or with proportional damping.

The equations of motion of the *n* generalized coordinates vector $\mathbf{x}(t)$ are described, in time domain, through the following well-known matrix expression:

$$\mathbf{M}\,\ddot{\mathbf{x}}(t)+\mathbf{K}\,\mathbf{x}(t)=\mathbf{f}(t) \tag{4}$$

where **M** and **K** are respectively the real and positive-definite symmetric mass matrix and the real and positive-semidefinite symmetric stiffness matrix obtained by a standard FE code; the system may be subject to a generalized force set vector $\mathbf{f}(t)$.

The *n* dofs **x** of the FE system may be generically partitioned in master $\mathbf{x}_m$ and slave $\mathbf{x}_s$ dofs. Each condensation criterion expresses the dofs **x** of the system as a function at least of the master dofs $\mathbf{x}_m$ and of a set of possible auxiliary non-physical dofs, as modal coordinates **q**:

$$\mathbf{x}=\begin{bmatrix}\mathbf{x}_m\\ \mathbf{x}_s\end{bmatrix}=\mathbf{T}\begin{bmatrix}\mathbf{x}_m\\ \mathbf{q}\end{bmatrix} \tag{5}$$

where **T** is the transformation matrix. Thus, Equation (5) can be rewritten as:

$$\begin{bmatrix}\mathbf{M}_{mm} & \mathbf{M}_{ms}\\ \mathbf{M}_{sm} & \mathbf{M}_{ss}\end{bmatrix}\begin{bmatrix}\ddot{\mathbf{x}}_m\\ \ddot{\mathbf{x}}_s\end{bmatrix}+\begin{bmatrix}\mathbf{K}_{mm} & \mathbf{K}_{ms}\\ \mathbf{K}_{sm} & \mathbf{K}_{ss}\end{bmatrix}\begin{bmatrix}\mathbf{x}_m\\ \mathbf{x}_s\end{bmatrix}=\begin{bmatrix}\mathbf{f}_m\\ \mathbf{0}\end{bmatrix} \tag{6}$$

where the mass and stiffness matrices of the reduced model, having $m < n$ dofs, are related to the transformation matrix **T** as:

$$\mathbf{M}_r=\mathbf{T}^T\mathbf{M}\,\mathbf{T} \quad \text{and} \quad \mathbf{K}_r=\mathbf{T}^T\mathbf{K}\,\mathbf{T}\,. \tag{7}$$

In the present paper, the applied reduction technique is the well-known Serep (System Equivalent Reduction Expansion Process) methodology [14], originally developed as an experimental modal technique able to identify equivalent dynamic systems.

The Serep technique is a low computational cost methodology because it only needs an ordinary modal analysis of the single sub-structure or an experimental modal identification. It permits flexible boundary conditions in sub-structuring problems to be taken into account, but it is also affected by a small numerical stability, due to the master nodes chosen for the reduction procedure. It is chosen in order to evaluate the performance of MoGeSeC in nodes selection because it tries to reduce the ill-conditioning of matrices.

In Serep approach [14] the relationship between master and slave dofs of the model is derived from the modal superposition:

$$\begin{bmatrix}\mathbf{x}_m\\ \mathbf{x}_s\end{bmatrix}=\begin{bmatrix}\mathbf{\Phi}_m\\ \mathbf{\Phi}_s\end{bmatrix}\mathbf{q} \tag{8}$$

where the eigenvector matrix $\mathbf{\Phi}$ is split into master (subscript *m*) and slave (subscript *s*) dofs and **q** is the modal coordinates vector.

The reduced model can be rewritten as:

$$\mathbf{M}_S\ \ddot{\mathbf{x}}_m + \mathbf{K}_S\ \mathbf{x}_m = \mathbf{f}_m\,. \tag{9}$$

where the mass and stiffness matrices are:

$$\begin{aligned} \mathbf{M}_S &= \mathbf{T}_S^T\,\mathbf{M}\,\mathbf{T}_S = \boldsymbol{\Phi}_{m,gen}^{-T}\ \boldsymbol{\Phi}_{m,gen}^{-1} \\ \mathbf{K}_S &= \mathbf{T}_S^T\,\mathbf{K}\,\mathbf{T}_S = \boldsymbol{\Phi}_{m,gen}^{-T}\ diag\left(\boldsymbol{\omega}_r^2\right)\boldsymbol{\Phi}_{m,gen}^{-1} \end{aligned}\,. \tag{10}$$

and $\boldsymbol{\omega}_r^2$ is the eigenvalues vector.

MODAL-PROPERTIES COMPARISON

The comparison of the two approach of sensor location are proposed with different targets:

- distribution in space of the selected nodes;
- modal identification results from experimental tests and comparison with respect to FE models;
- sensitivity of identified modal properties and robustness of reduced models from numerical or experimental data.

The comparison is carried on an engine component, it is the crankshaft of a 4 cylinder / 4 strokes diesel engine that is characterized by the following properties:

- it could be considered in a very simplified approach as a mono-dimensional (1D) object, as in the analytical method used for studying the torsional behaviour; so a basic idea of selecting very few nodes is to linearly distribute them along its axis, but master nodes selection outside axis is not so trivial for taking into account the bending behaviour;
- from a manufacturing point of view, it is obtained through casting and following turning and milling processes, it presents a plane of symmetry that could be slightly deformed by holes for lubricants and static balancing requirements;
- it has numerous bending modes in two different planes, interposed between several torsional and axial modes; rich dynamic properties are due to close modes effects in a quite reduced frequency area.

In Figure 2 and 3 the actual component and the corresponding model are shown.

Figure 2 – Actual crankshaft component.

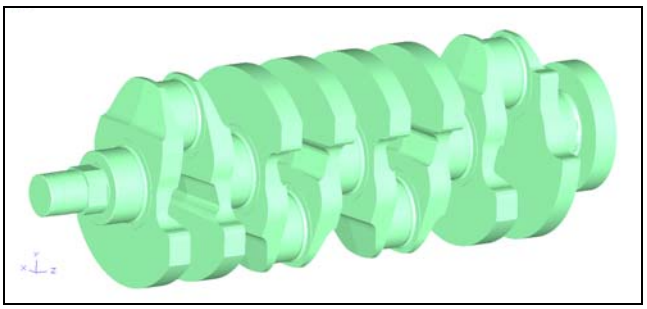

Figure 3 – Finite element model.

The FE model has been experimentally validated, through roving hammer impulse tests and MIMO (Multi Input Multi Output) modal identification technique in frequency domain [2]. The experimental tests are conducted for the case of free-free boundary conditions.
In Figure 4 the experimental test rig for the crankshaft case is shown.
The FE models of the components are described in Table 1.

Table 1 – FE model characteristics.

Fe model	# nodes	element type	# elements
Crankshaft	70570	Tetha10	309817

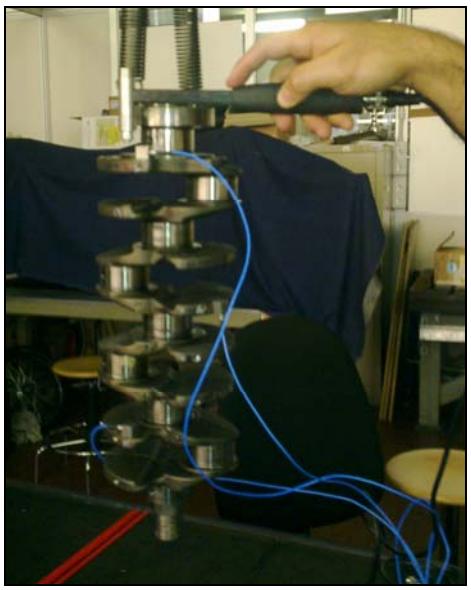

Figure 4 – Crankshaft test rig.

COMPARISON BETWEEN EI AND MOGESEC NODES

To measure the selection performance in the reduced models, two indexes are taken into account and the master nodes location is compared with respect to the spatial distribution of the model. The first index is the ill-conditioning parameter of matrices, i.e. the ratio $\lambda_{max}/\lambda_{min}$ between the maximum and minimum eigenvalues of both mass and stiffness matrices. The second one is the modal error estimation between experimentally identified and numerical results both on eigenfrequency and mode-shape by means of MAC index.
The sensor location for the crankshaft is evaluated in Figure 5, where the selected nodes of MoGeSeC (connected through blue lines) and EI (connected through red lines) are compared.
EI computational time is a key point, due to factorial increase of determinant evaluation and iterative nature of the approach, so the greater the number of sensor locations, the bigger, in a non linear manner, computational efforts become. MoGeSeC, instead, evaluated the sensor location in a direct computation and it is not iterative.
Globally the MoGeSeC approach demonstrates really good performance with very low computational cost, also comparing with other two selection approaches (Genetic Algorithm and Monte Carlo Algorithm) that are under investigation by the authors.

EIGENFREQUENCIES AND MODE-SHAPE COMPARISON

LMS TestLab software based on polyreference least-squares complex frequency-domain method is used in both MoGeSeC and EI technique [12]. Table 2 shows the comparison between numerical FE models and identified results. The relative error in eigenfrequencies between actual structure and FE model are minor than 8% for the first 7 modes and the mean values are similar and minor than 4% for both MoGeSeC and EI cases.
The first 7 identified and numerical mode shapes are reported for the crankshaft in Figure 7-12 respectively for MoGeSeC and EI approach with respect to FE results:

- orthogonality checks are shown in Figure 7 and 8, both MoGeSeC and EI produce good results, although also some low frequency modes present small coupling with maximum levels of about 30%. EI is evaluated better, but it is expected, due to the main selection idea of the method; anyway MoGeSeC maintains quite good result.
- MAC matrix between FE and identified modes obtained using respectively MoGeSeC or EI approach is the most significance comparison (Figure 9 and 10). The diagonal results are numerically listed in Table 2, where is shown also the mean value of MAC of the first 7 modes. Although EI results are good (mean value 81.8 %), MoGeSeC performance are excellent with a global increase of almost 5% (mean value 86.7 %).

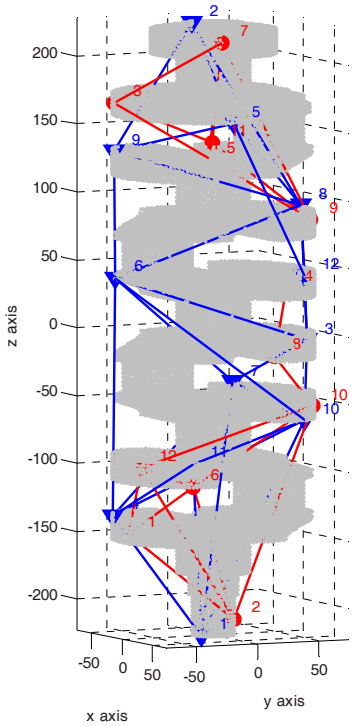

Figure 5 – Sensor location for the crankshaft.

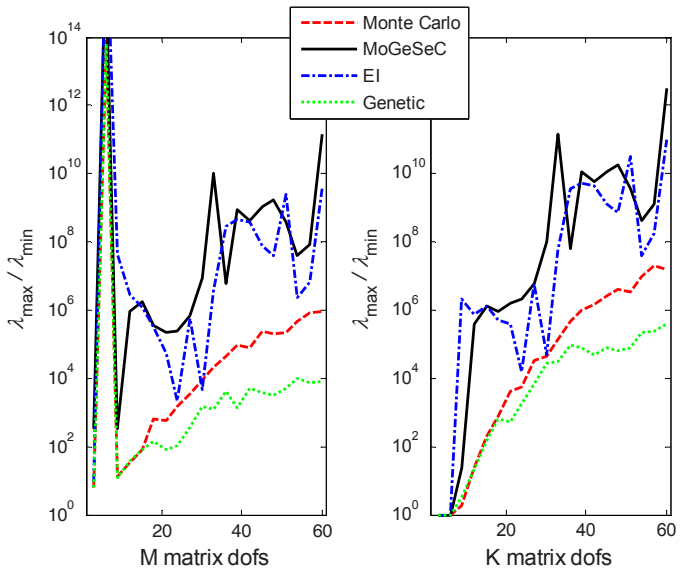

Figure 6 – Mass and stiffness matrices conditioning

Table 2 – FE model characteristics for crankshaft.

Mode	FEM	MoGeSeC			EI		
	Freq. [Hz]	MACFE/MOG	Freq. [Hz]	Error [%]	MACFE/EI	Freq. [Hz]	Error [%]
1	314.68	77.3	314,4	0,09	76.4	314.36	0.1
2	447.38	93.5	449,65	-0,51	77.8	450.27	-0.64
3	712.97	93.6	727,36	-1,98	82.2	728.06	-2.07
4	782.98	80.4	832,09	-5,9	79.4	829.38	-5.59
5	811.12	90.3	878,83	-7,7	88.1	878.64	-7.68
6	1030.39	88.0	1111,55	-7,3	89.7	1110.82	-7.24
7	1147.57	83.8	1190,09	-3,57	79.4	1190.37	-3.6
mean		86.7		-3.84	81.8		-3.82

- Mode shapes shown in Figure 11 and 12 demonstrate the comparison between numerical and identified results. It is evident that EI nodes are more concentrated on only a part of the structure, whilst they are more widespread in the MoGeSeC case; the spatial incompleteness introduced through the EI selection criterion is considered one of the main important task that it can be improved. It is highly reduced through MoGeSeC approach.

FREQUENCY RESPONSE COMPARISON

In Figures 13 and 14 the FRFs comparison is shown. The responses do not come from the analysis of the same excitation and measuring points, because the selected nodes are different with respect to the selection criterion. Modal superposition and proportional identified damping is applied. Eigenfrequencies are easily well identified, as confirmed in Table 2, with both approaches; also modal displacements are estimated in a more than satisfactory manner. Similar good identification are obtained, thus a global balance evaluation is considered.

NODE LOCATIONS COMPARISON

Figures 15 and 16 depicts the first six nodes selected by MoGeSeC (in blue) and by EI (in red). For both the colours, the lighter the colour of the area, the less the region is suitable for the sensor location, in the same manner, the darker the colour of the area, the more the node location is suitable for depicting model modal behaviour. The darker zone underlines where a node can be selected, so in the selection process the zone changes in lighter colour because it is yet selected. Dividing Figures 15 and 16 in a matrix, the rows represent the selection proceedings of the nodes starting from 1 to 6, the columns represent the two approaches, in particular the first (on the left) represents the geometric weight, the second depicts the modal contribution and the third is the balance of the two previous choices proposed by MoGeSeC. For EI just one images is reported for showing the selection results (fourth column). The third and the fourth columns have coloured dots that depict the nodes previously selected, so in the first row no nodes are shown, because selection process is at the first step.
There is a strong relationship between the analysed selection methods, as highlighted by the colour distribution. By observing the colour map, MoGeSeC appears to be very less sensitive to geometrical error in sensor location, in other words, displacements around the best location of sensor (selected by method) do not create a great change in the ill-conditioning of the reduced model. This is in accordance with the experience. EI shows a great sensitivity to the error in sensor location because it presents narrow good area nears worse, i.e. it does not univocally highlight positions that could be selected, in fact the images do not show uniform dark zones as in MoGeSeC results. In particular EI selects nodes without considering the body geometry, so it principally put the nodes on a part of the model, whereas MoGeSeC, considering the geometry, distributes the nodes across the whole external surface of the model, solution that is very easy and useful in experimental modal analysis.

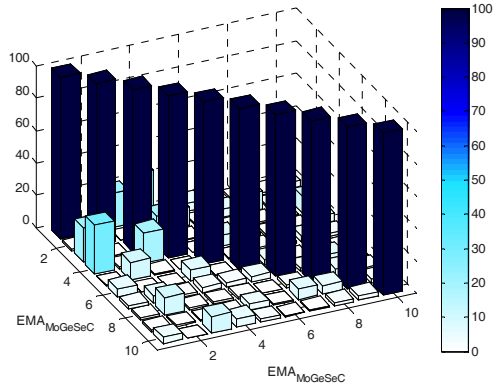

Figure 7 – MAC matrix (orthogonality property) of MoGeSeC modes for the crankshaft component.

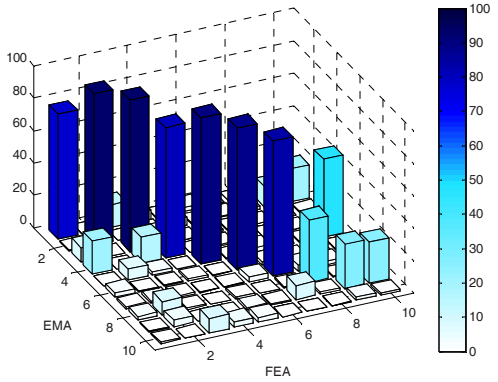

Figure 8 – MAC matrix between FEM modes and MoGeSeC modes for the crankshaft component.

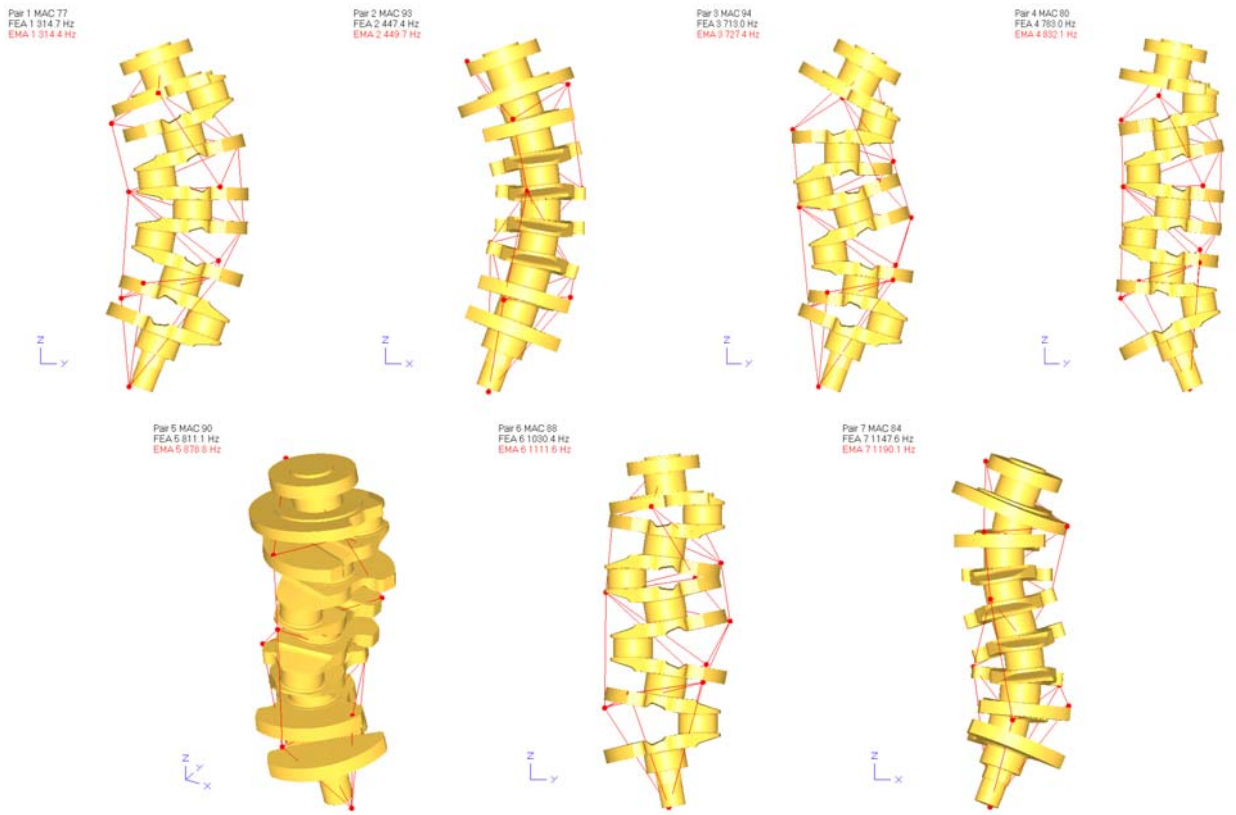

Figure 9 – Comparison of the first 7 crankshaft mode shapes between FE model and MoGeSeC reduced modes.

CONCLUSIONS

The numerical tests performed prove that MoGeSeC technique allows Serep methodology to reach a great numerical stability and a good agreement with the model or the actual object in a short time. MoGeSeC does not require a great computational effort in selecting the master nodes, it only needs information about the geometry and modal behavior of the structure. Such information can be provided by an FE model or by an experimental analysis. Finally, an important task of the proposed approach is its ability to distribute sensor locations and minimize spatial incompleteness of the identified mode-shapes.

The comparison with EI technique, based on the maximization of the independence of modal properties, demonstrates that the proposed methodology is an effective tool to minimize model ill-conditioning in dynamic condensation techniques and to define the number of sensors required and their location in experimental modal identifications. In particular, MoGeSeC provides a more distributed sensor placement that increases the modal shape rebuilt accuracy even with low sensor number.

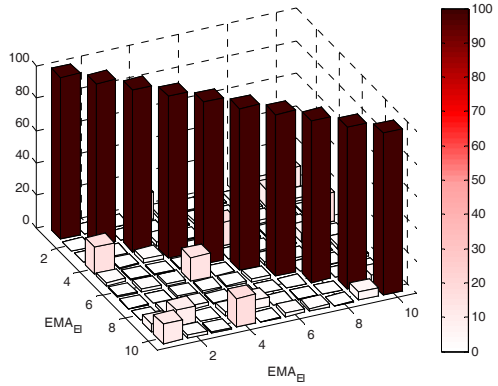

Figure 10 – MAC matrix (orthogonality property) of EI modes for the crankshaft component.

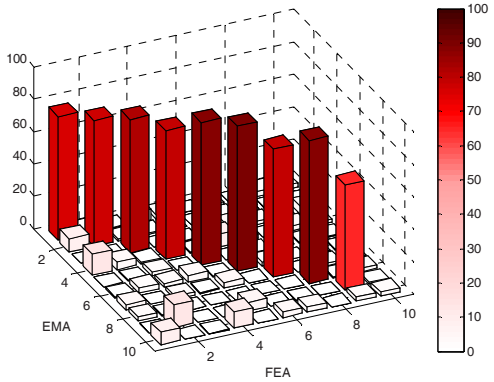

Figure 11 – MAC matrix between FEM modes and EI modes for the crankshaft component.

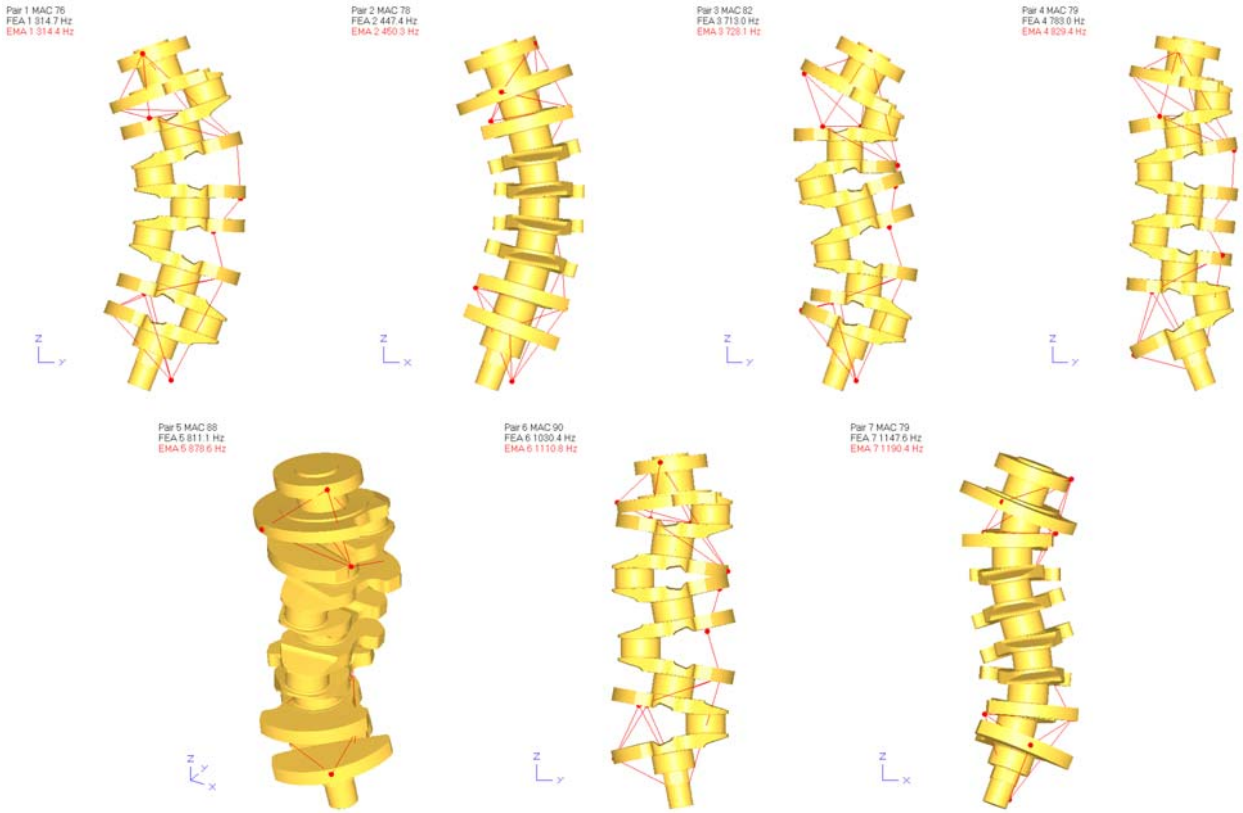

Figure 12 – Comparison of the first 7 crankshaft mode shapes between FE model and EI reduced modes.

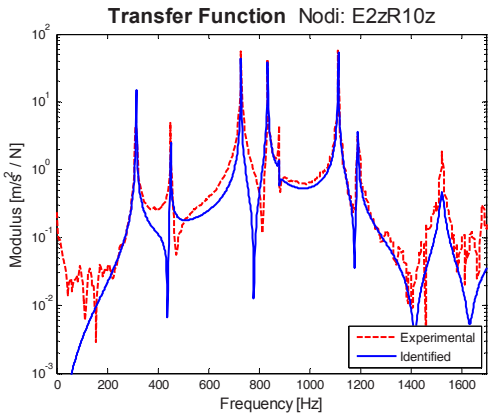

Figure 13 – Transfer function with MoGeSeC.

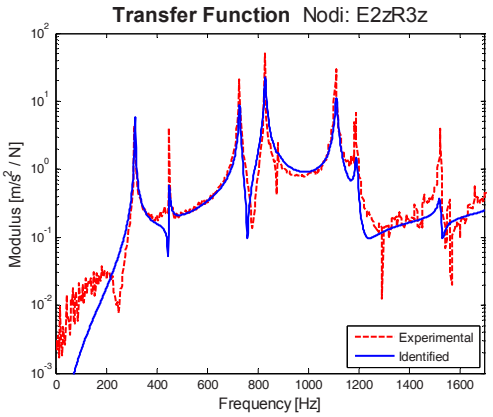

Figure 14 – Transfer function with EI technique.

BIBLIOGRAPHY

[1] M.I. Friswell, J.E. Mottershead, Finite Element Model Updating in Structural Dynamics, Dordrecht, Kluwer, 1995.

[2] Maia N., Silva, J., “Theoretical and Experimental Modal Analysis”, Research Studies Press Ltd., New York, ISBN 978-0863802089, 1997.

[3] J. Peck, I. Torres, A DMAP program for the selection of accelerometer locations in MSC/NASTRAN, in: Proc. 45th AIAA/ASME/ASCE/AHS/ASC Structures, Structural Dynamics and Materials Conference, Palm Springs, CA, USA, 2004, 19–22.

[4] J.N. Ramsden, J.R. Stoker, Mass condensation – A semi-automatic method for reducing the size of vibration problems, International Journal for Numerical Methods in Engineering 1 (1969) 333–349.

[5] B. Downs, Accurate reduction of stiffness and mass matrices for vibration analysis and a rationale for selecting master degree of freedom, ASME Journal of Mechanical Design 102 (1980) 412–416.

[6] N. Popplewell, A.W. Bertels, B. Arya, A critical appraisal of the eliminating technique, Journal of Sound and Vibration 31 (2) (1973) 213–233.

[7] V.N. Shah, M. Raymond, Analytical selection of masters for the reduced eigenvalue problem, International Journal of Numerical Methods in Engineering 18 (1982) 89–98.

[8] K.W. Matta, Selection of dofs for dynamic analysis, Journal of Pressure Vessel Technology 109 (1) (1987) 65–69.

[9] N.I. Grinenko, V.V. Mokeev, Problems of studying vibrations of structures by the finite element method, (English trans.), Prikladnaya Mekhanika 21 (1985) 231–235.

[10] W. Li, A degree selection method of matrix condensations for eigenvalue problems, Journal of Sound and Vibration 259 (2) (2003) 409–425.

[11] D.C. Kammer, R.D. Brillhart, Optimal sensor placement for modal identification using system-realization methods, Journal of Guidance, Control and Dynamics 19 (1996) 729–731.

[12] M. Meo, G. Zumpano, On the optimal sensor placement techniques for a bridge structure, Engineering Structures 27 (2005) 1488–1497.

[13] D.S. Li, H.N. Li, C.P. Fritzen, The connection between effective independence and modal kinetic energy methods for sensor placement, Journal of Sound and Vibration 305 (2007) 945–955.

[14] J. O’Callahan, P. Avitabile, R. Riemer, System equivalent reduction expansion process (SEREP), in: Proc. 7th IMAC, Las Vegas, Nevada, USA, 1989, 29–37.

[15] D.C. Kammer, M.L. Tinker, Optimal placement of triaxial accelerometers for model vibration tests, Journal of Mechanical Systems and Signal Processing 18 (2004) 29–41.

[16] R.J. Allemang, D.L. Brown, A correlation coefficient for modal vector analysis, in: Proc. 1st IMAC, Orlando, Florida, USA, 1982, 110–116.

[17] R.D. Henshell, J.H. Ong, Automatic masters for eigenvalue economization, Earthquake Engineering Structural Dynamics 3 (1975) 375–383.

[18] E. Bonisoli, C. Delprete, C. Rosso, “Comparison between dynamic condensation techniques in automotive application”, *SAE 2006 World Congress*, 2006, Detroit, Michigan, April 3-6, ISSN: 0148-7191, SAE Technical Paper 2006-01-1093, pp. 1-8.

[19] E. Bonisoli, C. Delprete, C. Rosso, “A modal-geometrical selection criterion in dynamic condensation techniques”, Proceedings of ESDA 2006, *8th Biennial ASME Conference on Engineering Systems Design and Analysis*, 2006, Torino, Italy, July 4-7, Paper ESDA2006-95469, pp. 1-8.
[20] E. Bonisoli, C. Delprete, C. Rosso, “Proposal of a modal-geometrical-based master nodes selection criterion in modal analysis”, *Mechanical Systems and Signal Processing*, April 2009, 23(3), ISSN: 0888-3270, DOI: 10.1016/j.ymssp.2008.05.012, pp. 606-620.
[21] R.J. Guyan, Reduction of stiffness and mass matrices, AIAA Journal 3 (2) (1965) 380.
[22] R.R. Craig, M.C.C. Bampton, Coupling of substructures for dynamic analyses, AIAA Journal 6 (7) (1968) 1313–1319.
[23] G.H. Golub, C.F. Van Loan, Matrix computations, North Oxford Academy, London, UK, 1986.

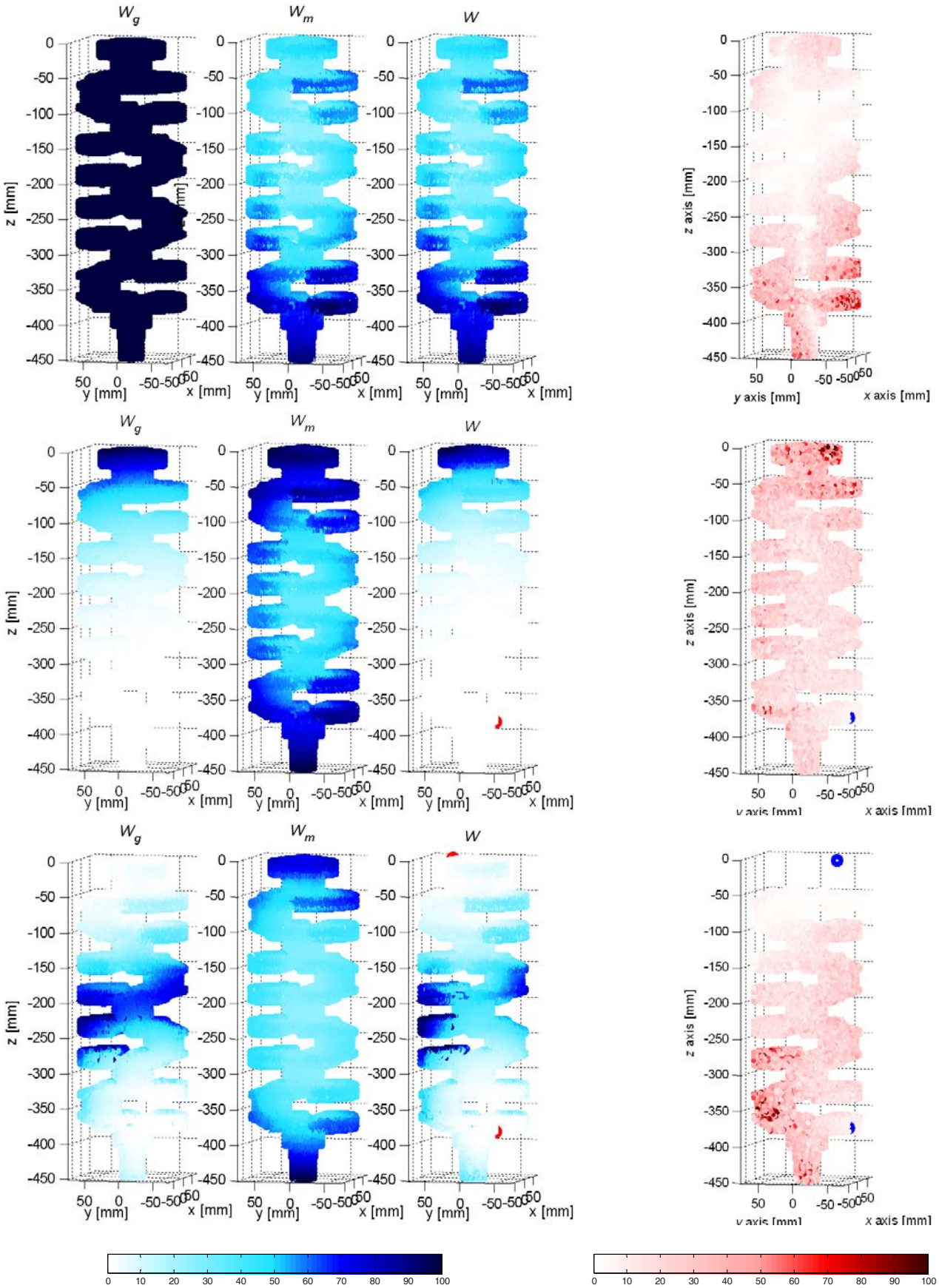

Figure 15: Comparison of selection map (MoGeSec on the left, EI on the right)

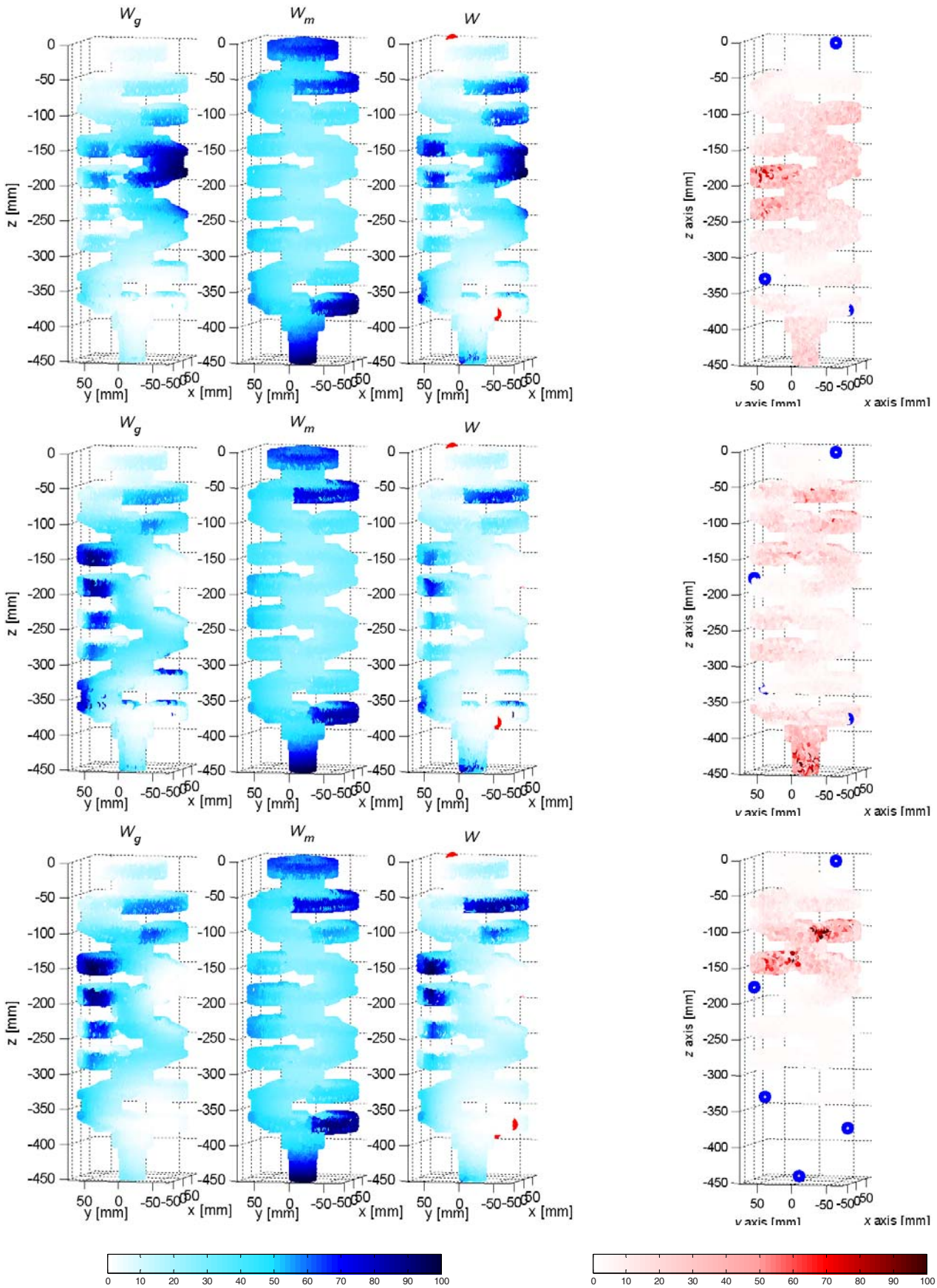

Figure 16: Comparison of selection map (MoGeSec on the left, EI on the right)

Robust optimization and quality control in spot welded structures

Q. I. Bhatti and M. Ouisse and S. Cogan

Abstract The performance characteristics (i.e., static, dynamic, crash, etc.) of a spot welded structure are strongly influenced by the number and the locations of the resistance spot welds. The design problem requires the number and locations of spot welds to be optimized so as to obtain reasonable trade-offs between manufacturing costs and structural performances. An optimization procedure is proposed which iteratively adds and removes spot welds in order to correct for approximations made in the iterative process. Moreover, a robustness indicator is formulated that allows to analyze the impact of the number of defective or broken spot welds on the system performance. This indicator provides a useful decision making tool for deciding both how many spot welds should be inspected following assembly as well as pointing to a small number of critical spot welds that should be reinforced. The proposed methodology will be illustrated on a full body-in-white structure.

1 Introduction

Resistance spot welding is one of the main manufacturing techniques for sheet metal structures and the automotive industry, for example, uses thousands of resistance spot welds (abbreviated RSW or spot weld) to assemble the body-in-white (BIW) for vehicles. Meanwhile, global competition pushes the automotive industry to re-

Q. I. Bhatti
FEMTO-ST Applied Mechanics, University of Franche-Comté, 24, rue de l'épitaphe, 25000 Besançon - France, e-mail: qamar.bhatti@femto-st.fr

M. Ouisse
FEMTO-ST Applied Mechanics, University of Franche-Comté, 24, rue de l'épitaphe, 25000 Besançon - France, e-mail: morvan.ouisse@univ-fcomte.fr

S. Cogan
FEMTO-ST Applied Mechanics, University of Franche-Comté, 24, rue de l'épitaphe, 25000 Besançon - France, e-mail: scott.cogan@univ-fcomte.fr

T. Proulx (ed.), *Linking Models and Experiments, Volume 2*, Conference Proceedings of the Society for Experimental Mechanics Series 5,
DOI 10.1007/978-1-4419-9305-2_21, © The Society for Experimental Mechanics, Inc. 2011

duce manufacturing cost and spot welds represent a significant contribution to the overall cost of the vehicle. Therefore, it is a worthwhile task to reduce the number of RSWs on the vehicle without compromising the performances. Due to mass production, even a small reduction in their number could lead to substantial reduction in the cost. However, the number and spatial distribution of spot welds has a significant impact on the structural performance criteria that must be taken into account by an analyst including the static, dynamic, and crash behaviors.

Currently, the numbers of spot welds and their locations are largely based on the designer's technical know-how and experience. However, this proves to be a daunting task for even the most experienced designers and problem has not been fully addressed by the research community. Some authors have examined the issue of improving the performance criteria by optimally relocating a fixed number of spot welds in the structure [2, 4, 5, 12, 13]. However, attempting to solve the optimization problem based on a fixed number of spot welds, where one is interested in finding the best locations, can pose two problems. First, this number may be too small and the solution may not be feasible even for the best distribution. Secondly, *a priori* defined number of RSWs may be too large and the overall production cost will be high due to the presence of redundant spot welds. This suggests that not only the locations but also the number of RSWs should be included in the optimization procedure as a variable to be determined. Thus, the aim should be to minimize the number of RSWs and find the best distribution of the existing number of RSWs simultaneously, so as to ensure an acceptable level of performance as dealt in [6–11].

Although simulation time for large and complex structures has been reduced over the years, the iterative nature of the discrete optimization problem still requires careful attention to calculation costs. Hence, in order to optimize the number of spot welds on the structures containing thousands of RSWs in a reasonable time, a simple decision making indicator is needed which can predict the contribution of the individual RSW towards the performance criteria. This indicator will not only be helpful to find the locations of the most influential RSWs but will also serve to indicate the redundant RSWs whose contributions towards the performance criteria are negligible. Bearing this in mind, we propose an optimization procedure which uses the elastic strain energy based indicator to remove the redundant spot welds and simultaneously, adds the new spot welds in the proximity of the most influential RSWs.

Another aspect of this study concerns the impact of uncertainty in the form of missing or defective RSWs on the structural performances. Indeed, when a BIW leaves the assembly line it is not unusual to find a small percentage of spot welds missing. Moreover, fatigue effects through the lifetime of the vehicle can lead to the breakage of spot welds. The important question to address here is just how many RSWs can be defective without compromising the specified performance criteria. In [3, 8], authors have used Monte Carlo (MC) simulations to study this problem under the assumption that each spot weld has equal chance of being defective or missing.

However, large number of analyses required for a meaningful MC simulation renders its use impractical. Hence, we propose a simple and less costly approach based on the impact of the most influential spot welds on the modal behavior. The objective is to plot a robustness curve showing the evolution of eigenfrequencies when progressively more influential spot welds are defective or missing. This robustness curve also serves as a useful decision making tool for deciding both how many spot welds should be inspected following assembly as well as pointing to a small number of critical spot welds that should be reinforced.

This presentation is organized as follows. In next section, optimization procedure is presented along with a brief description of decision making indicator for modal behavior. FE models are presented followed by optimization results. In sec 3 the issues related to robustness and quality control of a small percentage of influential spot welds are presented and finally, the conclusions of the study are drawn in the last section.

2 Spot weld optimization

2.1 Description of optimization procedure

A flowchart of the proposed optimization procedure is shown in the fig 1. The procedure will remove the redundant spot welds from the structure and simultaneously, will add the spot welds at the sensitive locations to the proximity of the most influential RSWs. This implies that either software has capability to create new spot welds when and where needed, or that a pool of candidate spot welds is already available in the numerical model which can be activated when needed. A decision making indicator presented later on will be used to rank the existing spot welds signifying their contribution to the performance criteria of interest.

2.2 Decision making indicator

The decision making indicators are the tools implemented in the spot welding optimization procedure to select the spot welds which are redundant and should be removed or those which are critical and should be reinforced. The indicators are used to correlate the contribution of individual spot welds to the target behavior and ideally should be easily calculated and lead to unambiguous choices. Two categories of indicators can be envisaged, namely *a priori* and *a posteriori*. The former are indicators which forecast in advance the influence of spot welds without removing them from the structure while the latter require the explicit removal of the spot welds from the structure. In practice, *a posteriori* indicators are very costly to evalu-

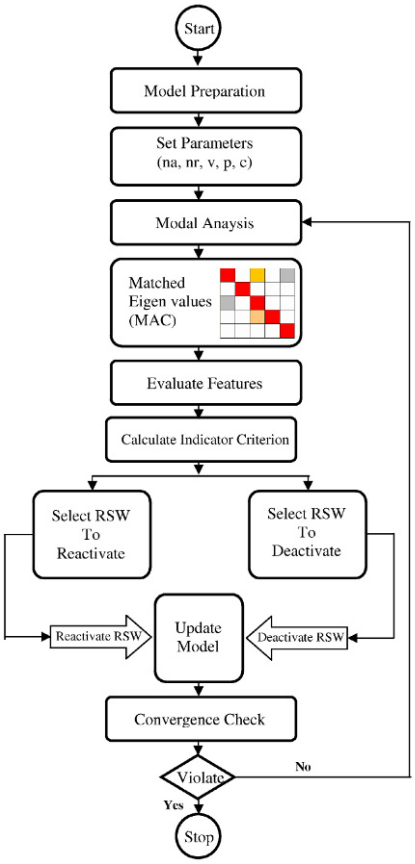

Fig. 1 Flowchart of the optimization procedure

ate since they require a large number of full model analyses while *a priori* indicators are generally far more efficient in terms of computational time.

Elastic strain energy of the elements is assumed to be very closely linked with the eigenfrequency shift, thus we decide to use *a priori* indicator based on elastic strain energy in spot weld and its adjacent shell elements. Additionally, the energy is normalized by the volume of the adjacent shell elements in order to remove the effect of their varying sizes. The indicator value for ith spot weld for mode k can be expressed as:

$$I_{i,k} = U_k^T K^{e,i} U_k + U_k^T K^{sh,i} U_k \frac{V_m^{sh,i}}{V_{tot}^{sh,i}}, \tag{1}$$

where $K^{e,i}$ is the stiffness matrix of ith RSW, $K^{sh,i}$ is the stiffness matrix of shell elements adjacent to ith RSW, U_k is the eigenvector k while $V_m^{sh,i}$ and $V_{tot}^{sh,i}$ are

respectively the mean volume and the total volume of shell elements adjacent to ith RSW.

2.3 Finite element model

The procedure is applied to a full body-in-white of a car. MSC.Nastran [1] FE model having approximately 1,000,000 dofs is meshed with 119498 CQUAD4 and 3459 CTRIA3 shell elements, 793 CHEXA solid elements and 14092 CLEAS1 spring elements as shown in fig 2(a). The subparts are assembled along 382 interfaces containing a total of 2612 active spot welds represented by CBUSH type FE spot weld model [8]. Initial spatial spot welds distribution and interfaces are shown in fig 2. The number of RSWs and eigenfrequencies of this design will be taken as references to calculate the relative shifts in frequencies and the increase or decrease in the number of RSWs.

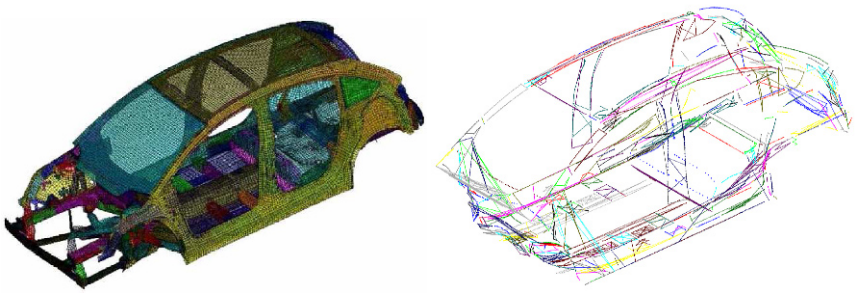

(a) (b)

Fig. 2 Body-in-white (**a**) finite element model (**b**) interface definitions (total interfaces: 382, total RSWs: 2612)

The optimization procedure requires new spot welds to be added in the structure, thus we created a pool of 1494 (57% of the original model) candidate RSWs uniformly along the different interfaces that can be added as required. Note that the RSWs removed during the optimization process will be placed in the pool of the candidate RSWs and will thus can be reactivated again if necessary.

2.4 Illustration

In this study, the objective is to minimize the number of spot welds while keeping the eigenfrequencies of the first torsion and bending modes higher than to those of the nominal design.

The first torsion and bending modes of the nominal design are shown in fig 3. MSC.Nastran is used to perform the modal analysis up to 65 Hz and takes almost 20 minutes on a Windows XP professional based computer having processor speed of 3.0 GHz with 2.0 GB RAM.

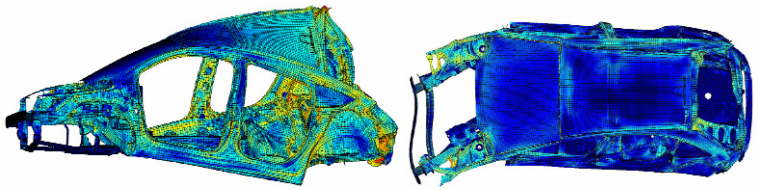

(a) (b)

Fig. 3 Modes shapes (**a**) torsion mode. (**a**) bending mode

Figure 4 shows the evolution of both eigenfrequencies during the optimization process. The procedure efficiently removed more than 14% of the total RSWs in only 6 iterations while both eigenfrequencies of the final design are better than those of the nominal design: 0.61% higher for mode 1 and 0.1% higher for mode 2. Note that the eigenfrequencies continue to improve despite of the fact that the total number of RSWs is decreasing. This is due to the addition of RSWs at the critical interfaces having higher influence. The final distribution of RSWs is shown in fig 5.

The proposed procedure is also designed to improve the robustness of the structure against defective or missing spot welds. This objective is achieved implicitly by sharing the loads of critical spot welds by adding the new spot welds at sensitive locations to their proximity. As a result, their indicator values will decrease, reflecting that if missing will produce less variations in the eigenfrequencies. To visualize this for the current illustration, we plotted the indicator values of first 270 spot welds of highest values for the nominal as well as the optimized designs in fig 6. Decreases in the indicator values of individual spot welds as well as in the mean values can clearly be observed. This means that optimized design is certainly now more robust against missing of spot welds and we will verify this fact in *a posteriori* robustness analysis in the next section.

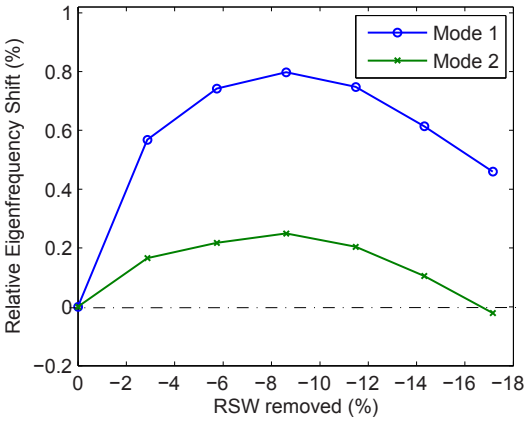

Fig. 4 Evolution of targeted eigenfrequencies during the optimization process

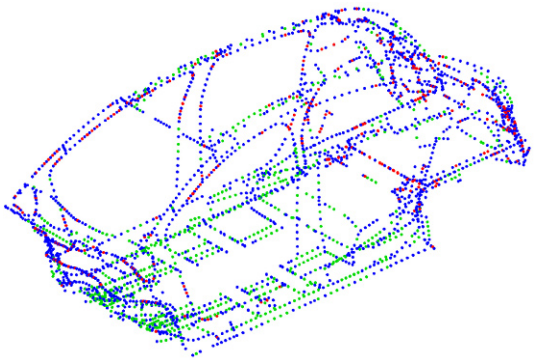

Fig. 5 Final distribution of the RSWs (blue: retained, green: removed, red: added)

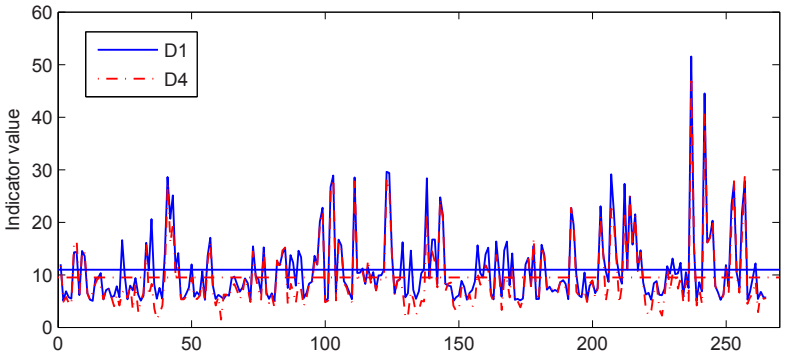

Fig. 6 Indicator values of first 270 spot welds of higher values (horizontal lines represent the mean values for these spot welds)

3 A posteriori robustness analysis and quality control methodology

In this work, we quantify the robustness as the worst case scenario among all possible design configurations due to uncertainty in term of defective or missing spot welds. The structure will be considered more robust which have low worst case variation due to missing of a specific number of spot welds. Alternatively, the structure is to be considered more robust which can afford to loose higher number of spot welds without compromising a specified critical performance limit.

As discussed earlier, while a MC simulation is potentially a straightforward way to quantity the robustness of a spot welded structure to defective or missing spot welds, large number of analyses required, renders its use impractical in the present context. Hence, we propose a simple and less costly approach based on an examination of the impact of the most influential spot welds on the performance criteria of interest. It has already been shown that the spot welds with higher indicator values have relatively stronger influence on the eigenfrequencies than the spot welds with lower indicator values [3, 8]. Therefore, they will be used to define a worst-case degradation curve as a function of an increasing number of missing of the most influential spot welds.

The goal is to draw the robustness curve showing the sensitivity of performance when the most influential spot welds are defective or missing. This robustness curve allows the impact of the number of defective or missing spot welds on the system performance to be analyzed in order to define a set of critical spot welds that should be quality controlled or reinforced. This curve also serves as a useful tool for deciding how many spot welds should be inspected following assembly while taking into account total number of RSWs and specific robustness level.

3.1 Procedure to obtain the robustness curve

The proposed procedure to obtain the robustness curve can briefly be described as follows:

1. all existing spot welds are ranked according to decreasing value of the indicator criteria,
2. a predefined number of spot welds of higher ranks are selected for removal,
3. an analysis is performed to evaluate the impact of removed spot welds on the modal behavior,
4. the indicator criteria is calculated for the remaining spot welds,
5. stop, if stopping criteria is met, otherwise, go to the first step.

3.2 Illustration

We applied the procedure on the nominal (2612 spot welds) and optimized (2238 spot welds) designs in order to quantify the robustness and analyze their relative behavior as a function of increasing number of missing of the most influential spot welds. The robustness curves were obtained due to missing of up to 100 spot welds by removing 10 spot welds of highest indicator values in each iteration. The number of RSWs removed in each iteration may be increased or decreased considering the trade-off between the total number of spot welds to be checked and the time required by one numerical analysis.

The robustness curves obtained for both modes are shown in fig 7 for both designs. The eigenfrequencies of the nominal design were taken as references to calculate the relative eigenfrequency shifts. The curves illustrate that optimized design is relatively less sensitive to the missing of spot welds despite of the fact that it contains 14% less number of spot welds. In other words, it can afford to loose more number of most influential spot welds before violating a specified level of degradation in the eigenfrequencies: for example to observe a 6.0% relative eigenfrequency shift for mode 1, optimized design can loose up to 100 most influential spot welds while nominal design requires only 40 spot welds. This gain in robustness is achieved in the optimization process by adding the spot welds on the sensitive regions in the proximity of critical spot welds. In turn, impact of the critical spot welds decreased, reflected by the decreases in indicator values of these critical spot welds as observed in fig 6.

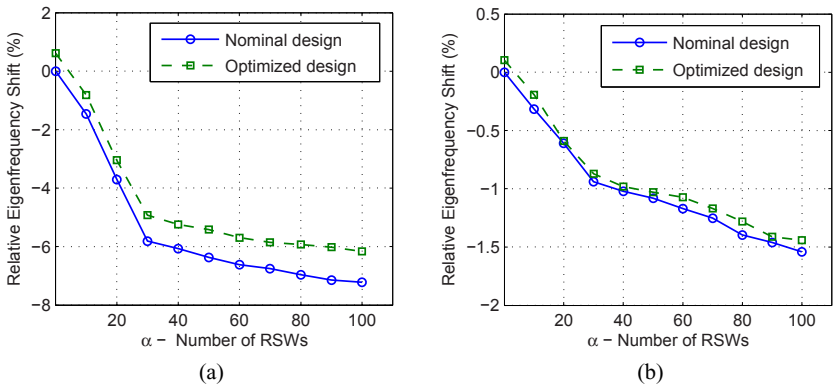

Fig. 7 Robustness curves for two modes (**a**) mode 1 (**b**) mode 2

However, note that most of the degradations in the eigenfrequencies are due to only the first 30 RSWs for both designs. This implies that these are the most critical RSWs and need special attention of the designer. This is a valuable feedback and designer can use this auxiliary information in various ways such as:

- design of a small number of critical spot welds can be modified to improve their performance characteristics,
- subparts joined by the critical spot welds can be redesigned to absorb their adverse impact,
- most critical spot welds may be quality controlled to ensure their effective presence.

3.3 Effect of quality control on robustness

As noted that after optimization, there still remains few spot welds if missing can cause large variations in the performance criteria. Hence, to take an advantage of the information obtained by robustness curves, we propose a quality control of limited number of spot welds in order to guarantee the robustness of the population of identical structures within acceptance level due to missing of remaining uncontrolled spot welds.

Let us assume that first 20 spot welds identified while obtaining the robustness curves for optimized design are quality controlled and thus effectively present on the structure. The procedure was applied again to obtain the robustness curves for the remaining uncontrolled spot welds. New robustness curves along with the initial curves without quality control of spot welds are shown in fig 8 for both modes. See the remarkable improvement in robustness as up to 3 times lower worst case variations are observed now for mode 1 up to missing of 100 most influential spot welds.

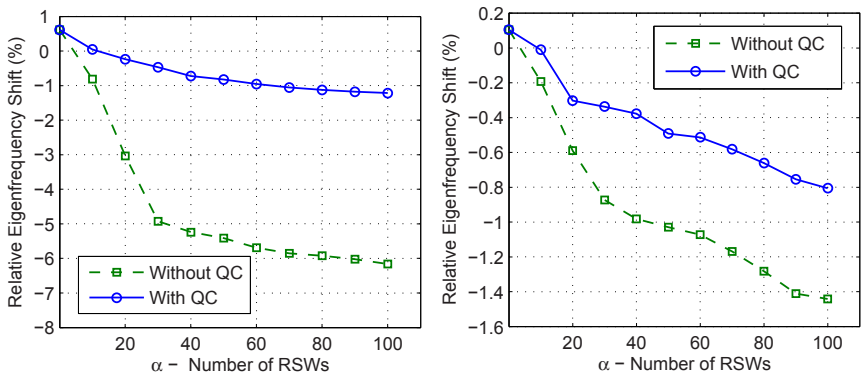

Fig. 8 Robustness curves for two modes after quality control of 20 RSWs (**a**) mode 1. (**b**) mode 2

To further very the methodology, we performed the MC simulations with strain-weighted selection scheme [8] without and with quality control of 20 spot welds for optimized design. 75 samples with 100 missing spot welds have been used for each simulation. Their scatter clouds are shown in fig 9 along with worst case variations obtained by our proposed procedure for missing of the same number of spot welds.

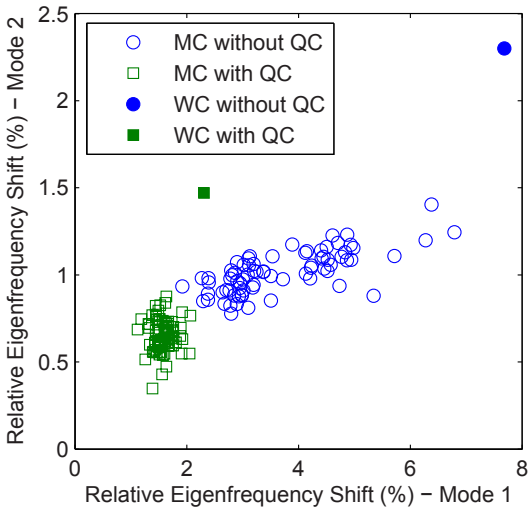

Fig. 9 Scatter clouds of MC simulations along with worst case variations

Results confirm firstly, effectiveness of quality control methodology to guarantee the impact of failure in the remaining uncontrolled spot welds within acceptable level: spread of eigenfrequencies shifts are much smaller for quality controlled spot welds formulation, secondly, procedure proposed to obtain robustness curve is efficient as well as accurate: 10 analyses required to find the worst case variations while 75 analyses for MC simulations are unable to find the worst case variations of the same degree.

Nevertheless, the important question lies in finding an acceptable compromise between robustness and the cost of controlling additional spot welds following assembly or the cost of reinforcing critical spot welds to avoid failure during the lifetime of the vehicle.

To answer this question, the behavior of missing of uncontrolled spot welds on the eigenfrequency is analyzed as a function of the number of quality controlled spot welds for optimized design up to relative eigenfrequency shift of 1.0% for mode 1. Maximum 40 spot welds are considered for quality control. Curves in fig 10 show that the design is becoming less sensitive to missing spot welds as the number of quality controlled spot welds increases. These curves show that there is no gain in robustness in case of controlling 10 spot welds but the robustness increases rapidly above this number.

In conclusion, an analyst can use this approach to select the design taking into account trade-offs between the total number of spot welds, the impact of missing spot welds, and the number of quality controlled spot welds to ensure a specific level of satisfaction.

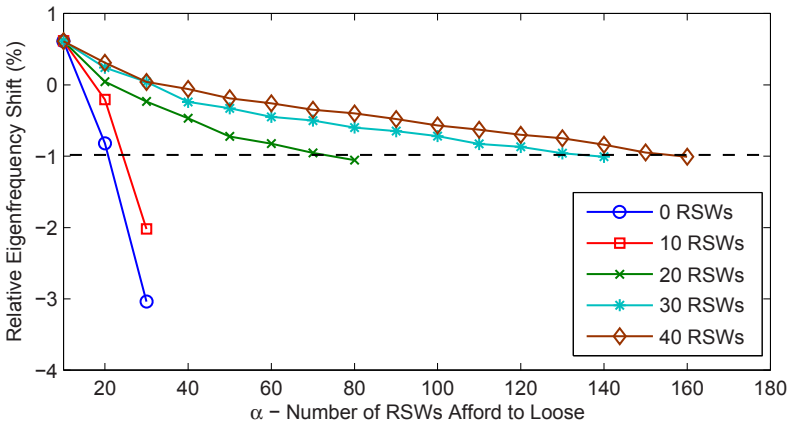

Fig. 10 Effect of increased number of quality controlled RSWs

4 Conclusions

An optimization procedure is presented which iteratively adds and removes spot welds to find the optimal distribution as well as the number of spot welds needed to improve the performance characteristics of interest. Meanwhile, the structural performances can be undermined by the presence of defective or missing spot welds due to manufacturing defects or fatigue. A simple approach is formulated to analyze the impact of the number of defective or missing spot welds on the system performance with the goal of replacing the more cost intensive sampling based approaches found in the literature. This approach can not only provide a measure of robustness but also could serve as a useful tool to provide insight into the most influential spot welds as well as for deciding how many spot welds should be inspected following assembly. The analyst can then ensure a specific level of robustness either by quality controlling or redesigning of these small number of spot welds.

Acknowledgements

The authors would like to thank PSA Peugeot-Citroën for providing the finite element model of the body-in-white.

References

[1] MSC.Nastran, version 2004 edn. MSC (2004)
[2] Chae, S.W., Kwon, K.Y., Lee, T.S.: An optimal design system for spot welding locations. Finite Elements in Analysis and Design **38**(3), 277 – 294 (2002)
[3] Donders, S., Brughmans, M., Hermans, L., Liefooghe, C., der Auweraer, H.V., Desmet, W.: The robustness of dynamic vehicle performance to spot weld failures. Finite Elements in Analysis and Design **42**(8-9), 670 – 682 (2006)
[4] Eom, J.S., Ju, B.H., Choi, N., Park, J.M., Lee, B.C., Byun, H.B.: Optimization on the spot welded configuration of vehicle components considering the structural performance. Key Engineering Materials **362-328**, 957–962 (2006)
[5] Ertas, A.H., Sonmez, F.O.: Optimization of spot-weld joints. Proceedings of the Institution of Mechanical Engineers, Part C: Journal of Mechanical Engineering Science **223**(3), 545–555 (2009)
[6] Hasegawa, H., Sasaki, H., Uehara, H., Kawamo, K.: Optimization of spot-weld positions for vehicle design by using hybrid meta-heuristics. International journal of vehicle design **43**(1-4), 151–172 (2007)
[7] Liao, Y.G.: Optimal design of weld pattern in sheet metal assembly based on a genetic algorithm. The International Journal of Advanced Manufacturing Technology **26**(5), 512 – 516 (2005)
[8] Ouisse, M., Cogan, S.: Robust design of spot welds in automotive structures: A decision-making methodology. Mechanical Systems and Signal Processing **24**(4), 1172 – 1190 (2010)
[9] Puchner, K., Dannbauer, H., Meise, M.: Spot weld optimization regarding stiffness and fatigue using standard software. SAE 2006 World Congress and Exhibition, Detroit, MI, USA (2006)
[10] Wang, L., Levia, J.P., Basu, P.K.: Design optimization of automobile welds. International journal of vehicle design **31**(4), 377–391 (2003)
[11] Xiang, Y., Wang, Q., Fan, Z., Fang, H.: Optimal crashworthiness design of a spot-welded thin-walled hat section. Finite Elements in Analysis and Design **42**(10), 846 – 855 (2006)
[12] Yamaguchi, A., Wakana, G., Obayashi, K., Okabe, T., Muller-Bechtel, M.: Spot-weld layout optimization for body stiffness by topology optimization. SAE International technical paper no. 2008-01-0878 (2008)
[13] Zhang, Y., Taylor, D.: Optimization of spot-welded structures. Finite Elements in Analysis and Design **37**(12), 1013 – 1022 (2001)

Interface Reduction in the Dual Craig-Bampton method based on dual interface modes

Daniel J. Rixen

Abstract In this paper we propose an interface reduction technique in order to obtain a system of low order for structural problems on which the Dual Craig-Bampton substructuring technique has been applied. In order to develop this strategy we first rewrite the Dual Craig-Bampton method in a new form, where attachment modes are used instead of residual attachment modes. Then it is shown that the interface problem obtained with only static attachment modes can provide essential information on the interface behavior. Those interface modes can be used to efficiently reduce the interface problem in a way dual to the interface reduction technique commonly used for the standard Craig-Bampton approach. The method is applied to two problems: a space frame and a two-dimensional academic solid problem. It is shown that good accuracy can be obtained with the method even for low order reduced systems. We also discuss the physical meaning of the interface modes which can be associated to negative eigenvalues.

1 Introduction

The Craig-Bampton substructuring method [3] is one of the most common methods used in structural dynamics to reduce the order of a large model. In [12] a version of the Craig-Bampton method using dually assembled substructures and free interface modes was proposed. It was shown that such method can present some advantages although its application requires non-classical assembly and solution techniques.

The major bottleneck of substructuring techniques is that, as the number of substructure increases, the number of interface degrees of freedom grows unnecessarily. In the standard Craig-Bampton method the interface can be reduced by considering

Daniel J. Rixen
Delft University of Technology, faculty 3mE, Engineering Dynamics, mekelweg 2, 2628CD Delft, The Netherlands e-mail: d.j.rixen@tudelft.nl

T. Proulx (ed.), *Linking Models and Experiments, Volume 2*, Conference Proceedings of the Society for Experimental Mechanics Series 5,
DOI 10.1007/978-1-4419-9305-2_22, © The Society for Experimental Mechanics, Inc. 2011

interface modes obtained from the statically condensed problem [4]. In this paper we propose a similar method, but now suitable for the Dual Craig-Bampton method.

In section 2 we shortly recall the Dual Craig-Bamtpon method and in section 3 we propose an alternative, but equivalent, formulation of that substructuring method. In section 4 the concept of interface modes for the dual interface problem is introduced in order to reduce the interface problem. The method is then tested on two problems in sections 5 and 6. In section 7 we go deeper in the discussion of modes with interface incompatibility and interface modes. We conclude with some general remarks and an outlook on further research in section 8.

2 The Dual Craig-Bampton in a nuttshell

The Dual Craig-Bampton method was proposed in [12] as a Dual version of the classical Craig-Bampton substructuring technique [3]. Here we shortly recall the method and introduce the notations used in this paper.

Let us consider the linear dynamic equations for a structure

$$\mathbf{M}_a\ddot{\mathbf{u}}_a + \mathbf{K}_a\mathbf{u}_a = \mathbf{f}_a(t) \tag{1}$$

where $\mathbf{M}_a$, $\mathbf{K}_a$, $\mathbf{u}_a$ and $\mathbf{f}_a$ are respectively the global (assembled) mass and stiffness matrix, and the associated displacements and applied forces.

Assume that the problem is decomposed in N^s non-overlapping substructures, the dynamic equilibrium equations can be locally expressed by

$$\begin{cases} \mathbf{M}^{(s)}\ddot{\mathbf{u}}^{(s)} + \mathbf{K}^{(s)}\mathbf{u}^{(s)} + \begin{bmatrix} \mathbf{b}^{(s)^T}\boldsymbol{\lambda} \\ \mathbf{0} \end{bmatrix} = \mathbf{f}^{(s)} \qquad s = 1,\ldots N_s \\ \sum_{s=1}^{N_s} \mathbf{b}^{(s)}\mathbf{u}_b^{(s)} = \mathbf{0} \end{cases} \tag{2}$$

where the superscript $\star^{(s)}$ indicates that the quantity belongs to substructure s, and where $\mathbf{b}^{(s)}$ is a signed Boolean matrix such that the second equation in (2) represents the equality of displacements on the interface (i.e. the interface compatibility condition). $\mathbf{u}_b$ is the restriction of the displacement degrees of freedom (dofs) to the boundary (interface) and $\boldsymbol{\lambda}$ represent the Lagrange multipliers associated to the interface compatibility condition such that $\mathbf{b}^{(s)^T}\boldsymbol{\lambda}$ are the interface internal forces. Let us also use the block diagonal notation

$$\mathbf{M} = \begin{bmatrix} \mathbf{M}^{(1)} & & \mathbf{0} \\ & \ddots & \\ \mathbf{0} & & \mathbf{M}^{(N_s)} \end{bmatrix} \qquad \mathbf{K} = \begin{bmatrix} \mathbf{K}^{(1)} & & \mathbf{0} \\ & \ddots & \\ \mathbf{0} & & \mathbf{K}^{(N_s)} \end{bmatrix} \tag{3}$$

$$\mathbf{u} = \begin{bmatrix} \mathbf{u}^{(1)} \\ \vdots \\ \mathbf{u}^{(N_s)} \end{bmatrix} \qquad \mathbf{f} = \begin{bmatrix} \mathbf{f}^{(1)} \\ \vdots \\ \mathbf{f}^{(N_s)} \end{bmatrix}$$

$$\mathbf{B} = \begin{bmatrix} \mathbf{B}^{(1)} & \cdots & \mathbf{B}^{(N_s)} \end{bmatrix} \qquad \mathbf{B}^{(s)} = \begin{bmatrix} \mathbf{b}^{(s)} \\ \mathbf{0} \end{bmatrix}$$

so that the dynamic equilibrium of a substructured system can be written as

$$\begin{bmatrix} \mathbf{M} & \mathbf{0} \\ \mathbf{0} & \mathbf{0} \end{bmatrix} \begin{bmatrix} \ddot{\mathbf{u}} \\ \lambda \end{bmatrix} + \begin{bmatrix} \mathbf{K} & \mathbf{B}^T \\ \mathbf{B} & \mathbf{0} \end{bmatrix} \begin{bmatrix} \mathbf{u} \\ \lambda \end{bmatrix} = \begin{bmatrix} \mathbf{f} \\ \mathbf{0} \end{bmatrix} \tag{4}$$

The solution of the dynamic equilibrium for a substructure (second set of equations in (4)) can be found in the form

$$\mathbf{u}^{(s)} = \mathbf{u}^{(s)}_{stat} + \sum_{r=1}^{n^{(s)}-m^{(s)}} \theta_r^{(s)} \eta_r^{(s)} \tag{5}$$

where $n^{(s)}$ is the dimension of the local problem, $\theta_r^{(s)}$ are the free interface modes number of substructure s solution of

$$\left(\mathbf{K}^{(s)} - \omega_r^2 \mathbf{M}^{(s)}\right) \theta_r^{(s)} = \mathbf{0} \tag{6}$$

and where the quasi-static solution $\mathbf{u}^{(s)}_{stat}$ is given by

$$\mathbf{u}^{(s)}_{stat} = -\mathbf{K}^{(s)^+} \mathbf{B}^{(s)^T} \lambda + \sum_{i=1}^{m^{(s)}} \mathbf{R}_i^{(s)} \alpha_i^{(s)} \tag{7}$$

In this last equation $\mathbf{K}^{(s)^+}$ is a pseudo-inverse in case the substructure are floating, hence when $m^{(s)}$ local rigid body modes $\mathbf{R}_i^{(s)}$ exist (see e.g. [7]). If the substructure has no rigid body modes when disconnected from its neighbors, $\mathbf{K}^{(s)^+} = \mathbf{K}^{(s)^{-1}}$ is simply the inverse of $\mathbf{K}$. Defining the projector

$$\mathbf{P}^{(s)} = \mathbf{I} - \mathbf{M}^{(s)} \mathbf{R}^{(s)} \mathbf{R}^{(s)^T} \quad \text{such that} \quad \mathbf{R}^{(s)^T} \mathbf{P}^{(s)} = \mathbf{0} \quad , \quad \mathbf{P}^{(s)} \mathbf{M}^{(s)} \mathbf{R}^{(s)} = \mathbf{0} \tag{8}$$

we can compute a generalized inverse where the rigid body modes have been filtered out, namely

$$\mathbf{G}^{(s)} = \mathbf{P}^{(s)^T} \mathbf{K}^{(s)^+} \mathbf{P}^{(s)} \tag{9}$$

so that the quasi-static solution can also be written as

$$\mathbf{u}^{(s)}_{stat} = -\mathbf{G}^{(s)} \mathbf{B}^{(s)^T} \lambda + \sum_{i=1}^{m^{(s)}} \mathbf{R}_i^{(s)} \alpha_i^{(s)} \tag{10}$$

Assuming now that the solution in the substructure is represented in an approximate way by using only the first $n_\theta^{(s)}$ internal modes, one writes

$$\mathbf{u}^{(s)} \simeq -\mathbf{G}^{(s)}\mathbf{B}^{(s)^T}\lambda + \mathbf{R}^{(s)}\alpha^{(s)} + \Theta^{(s)}\eta^{(s)} \tag{11}$$

where $\Theta^{(s)}$ is a matrix containing in its column the first $n_\theta^{(s)}$ internal modes of the substructure.

Instead of using the so-called attachment modes $\mathbf{G}^{(s)}$ representing the static response to interface forces, it is common to use the residual attachment modes (see for instance the MacNeal and the Rubin methods [11, 14]). To find the residual flexibility, we observe that the flexibility has as spectral expansion

$$\mathbf{G}^{(s)} = \sum_{r=1}^{n^{(s)}-m^{(s)}} \frac{\theta_r^{(s)}\theta_r^{(s)^T}}{\omega_r^{(s)^2}} \tag{12}$$

so that the dynamic response of a substructure can be equivalently approximated by

$$\mathbf{u}^{(s)} = -\mathbf{G}_{res}^{(s)}\mathbf{B}^{(s)^T}\lambda + \mathbf{R}^{(s)}\alpha^{(s)} + \Theta^{(s)}\eta^{(s)} \tag{13}$$

where

$$\mathbf{G}_{res}^{(s)} = \sum_{r=n_\theta^{(s)}+1}^{n^{(s)}-m^{(s)}} \frac{\theta_r^{(s)}\theta_r^{(s)^T}}{\omega_r^{(s)^2}} = \mathbf{G}^{(s)} - \sum_{r=1}^{n_\theta^{(s)}} \frac{\theta_r^{(s)}\theta_r^{(s)^T}}{\omega_r^{(s)^2}} \tag{14}$$

Using the block diagonal notations we can write

$$\mathbf{u} = -\mathbf{G}_{res}\mathbf{B}^T\lambda + \mathbf{R}\alpha + \Theta\eta \tag{15}$$

where

$$\mathbf{G}_{res} = \begin{bmatrix} \mathbf{G}_{res}^{(1)} & & \mathbf{0} \\ & \ddots & \\ \mathbf{0} & & \mathbf{G}_{res}^{(N_s)} \end{bmatrix} \qquad \mathbf{R} = \begin{bmatrix} \mathbf{R}^{(1)} & & \mathbf{0} \\ & \ddots & \\ \mathbf{0} & & \mathbf{R}^{(N_s)} \end{bmatrix} \qquad \Theta = \begin{bmatrix} \Theta^{(1)} & & \mathbf{0} \\ & \ddots & \\ \mathbf{0} & & \Theta^{(N_s)} \end{bmatrix}$$

$$\alpha = \begin{bmatrix} \alpha^{(1)} \\ \vdots \\ \alpha^{(N_s)} \end{bmatrix} \qquad \eta = \begin{bmatrix} \eta^{(1)} \\ \vdots \\ \eta^{(N_s)} \end{bmatrix}$$

The approximation (13) can be written in matrix form as

$$\begin{bmatrix}\mathbf{u}\\ \lambda\end{bmatrix} = \begin{bmatrix} \mathbf{R}^{(1)}\ \Theta^{(1)} & & \mathbf{0} & -\mathbf{G}_{res}^{(1)}\mathbf{B}^{(1)^T} \\ & \ddots\ \ddots & & \vdots \\ \mathbf{0} & & \mathbf{R}^{(N_s)}\ \Theta^{(N_s)} & -\mathbf{G}_{res}^{(N_s)}\mathbf{B}^{(N_s)^T} \\ \mathbf{0} & \cdots & \mathbf{0} & \mathbf{I} \end{bmatrix} \begin{bmatrix} \alpha^{(1)} \\ \eta^{(1)} \\ \vdots \\ \alpha^{(N_s)} \\ \eta^{(N_s)} \\ \lambda \end{bmatrix}$$

$$= \begin{bmatrix} \mathbf{R} & \Theta & -\mathbf{G}_{res}\mathbf{B}^T \\ \mathbf{0} & \mathbf{0} & \mathbf{I} \end{bmatrix} \begin{bmatrix} \alpha \\ \eta \\ \lambda \end{bmatrix} = \mathbf{T}_{dual} \begin{bmatrix} \alpha \\ \eta \\ \lambda \end{bmatrix} \tag{16}$$

Finally using this approximation to reduce the dual dynamic equations (4), one finds the reduced system

$$\tilde{\mathbf{M}} \begin{bmatrix} \ddot{\alpha} \\ \ddot{\eta} \\ \ddot{\lambda} \end{bmatrix} + \tilde{\mathbf{K}} \begin{bmatrix} \alpha \\ \eta \\ \lambda \end{bmatrix} = \mathbf{T}_{dual}^T \begin{bmatrix} \mathbf{f} \\ \mathbf{0} \end{bmatrix} \tag{17}$$

where the reduced matrices are

$$\tilde{\mathbf{M}} = \mathbf{T}_{dual}^T \begin{bmatrix} \mathbf{M} & \mathbf{0} \\ \mathbf{0} & \mathbf{0} \end{bmatrix} \mathbf{T}_{dual} = \begin{bmatrix} \mathbf{I} & \mathbf{0} & \mathbf{0} \\ \mathbf{0} & \mathbf{I} & \mathbf{0} \\ \mathbf{0} & \mathbf{0} & \mathbf{M}_{res} \end{bmatrix} \tag{18}$$

$$\tilde{\mathbf{K}} = \mathbf{T}_{dual}^T \begin{bmatrix} \mathbf{K} & \mathbf{B}^T \\ \mathbf{B} & \mathbf{0} \end{bmatrix} \mathbf{T}_{dual} = \begin{bmatrix} \mathbf{0} & \mathbf{0} & \mathbf{R}^T\mathbf{B}^T \\ \mathbf{0} & \Omega^2 & \Theta^T\mathbf{B}^T \\ \mathbf{B}\mathbf{R} & \mathbf{B}\Theta & -\mathbf{F}_{res} \end{bmatrix} \tag{19}$$

where

$$\mathbf{F}_{res} = \mathbf{B}\mathbf{G}_{res}\mathbf{B}^T = \sum_{s=1}^{N_s} \mathbf{B}^{(s)}\mathbf{G}_{res}^{(s)}\mathbf{B}^{(s)^T} \tag{20}$$

$$\mathbf{M}_{res} = \mathbf{B}\mathbf{G}_{res}\mathbf{M}\mathbf{G}_{res}\mathbf{B}^T = \sum_{s=1}^{N_s} \mathbf{B}^{(s)}\mathbf{G}_{res}^{(s)}\mathbf{M}^{(s)}\mathbf{G}_{res}^{(s)}\mathbf{B}^{(s)^T} \tag{21}$$

The reduced form (17) was first introduced in [12] and was named the Dual Craig-Bampton method since the form highly resembles the classical Craig-Bampton method, but now using free interface modes and using a dual assembly procedure. Note that the reduction basis (16) is identical to what is used in the MacNeal and Rubin methods [11, 14], but here we obtain a nice block diagonal form of the reduced matrices since, contrary to the latter methods, we consider the dually assembled problem. This implies that not only the equilibrium equations are weakened by the reduction, but also the interface compatibility. Let us note that the reduced form (17) can be computed by first reducing the operators per substructures, then assemble the different components in the global $\tilde{\mathbf{K}}$ and $\tilde{\mathbf{M}}$.

Finally let us note that, in order to improve the reduction efficiency, one can use so-called truncation augmentation of the local basis as explained in [13].

3 An alternative formulation of the Dual Craig-Bampton

As recalled in the previous section, the Dual Craig-Bampton as proposed earlier in [12] uses the residual attachment modes. This leads to the reduced matrices (19, 18) where the coupling between attachment modes and internal modes appears in the reduced stiffness matrix $\tilde{\mathbf{K}}$. In this paper dealing with interface reduction, we will see that it might be more appropriate to use an other equivalent form of the Dual Craig Bampton. To this end we use attachment modes $\mathbf{G}^{(s)}$ (9) and not the residual ones $\mathbf{G}^{(s)}_{res}$ (14).

Thus the approximation is now written as

$$\begin{bmatrix}\mathbf{u}\\ \lambda\end{bmatrix} = \begin{bmatrix} \mathbf{R}^{(1)} & \Theta^{(1)} & & \mathbf{0} & -\mathbf{G}^{1}\mathbf{B}^{(1)^T} \\ & \ddots & \ddots & & \vdots \\ \mathbf{0} & & \mathbf{R}^{(N_s)} & \Theta^{(N_s)} & -\mathbf{G}^{N_s}\mathbf{B}^{(N_s)^T} \\ \mathbf{0} & \cdots & & \mathbf{0} & \mathbf{I} \end{bmatrix} \begin{bmatrix} \alpha^{(1)} \\ \eta^{(1)} \\ \vdots \\ \alpha^{(N_s)} \\ \eta^{(N_s)} \\ \lambda \end{bmatrix} \tag{22}$$

$$= \begin{bmatrix} \mathbf{R} & \Theta & -\mathbf{G}\mathbf{B}^T \\ \mathbf{0} & \mathbf{0} & \mathbf{I} \end{bmatrix} \begin{bmatrix} \alpha \\ \eta \\ \lambda \end{bmatrix} \tag{23}$$

$$= \bar{\mathbf{T}}_{dual} \begin{bmatrix} \alpha \\ \eta \\ \lambda \end{bmatrix} \tag{24}$$

When only a small number of vibration modes are considered (typically the lowest modes in Θ), this representation is an approximation yielding a reduction basis. Using this reduction basis to transform the system we find the following reduced problem

$$\bar{\mathbf{M}} \begin{bmatrix} \ddot{\alpha} \\ \ddot{\eta} \\ \ddot{\lambda} \end{bmatrix} + \bar{\mathbf{K}} \begin{bmatrix} \alpha \\ \eta \\ \lambda \end{bmatrix} = \bar{\mathbf{T}}^T_{dual} \begin{bmatrix} \mathbf{f} \\ \mathbf{0} \end{bmatrix} \tag{25}$$

where the reduced matrices are now

$$\bar{\mathbf{M}} = \bar{\mathbf{T}}^T_{dual} \begin{bmatrix} \mathbf{M} & \mathbf{0} \\ \mathbf{0} & \mathbf{0} \end{bmatrix} \bar{\mathbf{T}}_{dual} \tag{26}$$

$$= \begin{bmatrix} \mathbf{R}^T\mathbf{M}\mathbf{R} & \mathbf{0} & -\mathbf{R}^T\mathbf{M}\mathbf{G}\mathbf{B}^T \\ \mathbf{0} & \Theta^T\mathbf{M}\Theta & -\Theta^T\mathbf{M}\mathbf{G}\mathbf{B}^T \\ -\mathbf{B}\mathbf{G}\mathbf{M}\mathbf{R} & -\mathbf{B}\mathbf{G}\mathbf{M}\Theta & \mathbf{B}\mathbf{G}\mathbf{M}\mathbf{G}\mathbf{B}^T \end{bmatrix} = \begin{bmatrix} \mathbf{I} & \mathbf{0} & \mathbf{0} \\ \mathbf{0} & \mathbf{I} & -\Omega^{-2}\Theta^T\mathbf{B}^T \\ \mathbf{0} & -\mathbf{B}\Theta\Omega^{-2} & \mathbf{M}_I \end{bmatrix}$$

$$\bar{\mathbf{K}} = \bar{\mathbf{T}}^T_{dual} \begin{bmatrix} \mathbf{K} & \mathbf{B}^T \\ \mathbf{B} & \mathbf{0} \end{bmatrix} \bar{\mathbf{T}}_{dual} \tag{27}$$

$$= \begin{bmatrix} \mathbf{0} & \mathbf{0} & \mathbf{R}^T\mathbf{B}^T \\ \mathbf{0} & \Theta^T\mathbf{K}\Theta & -\Theta^T\mathbf{K}\mathbf{G}\mathbf{B}^T + \Theta^T\mathbf{B}^T \\ \mathbf{B}\mathbf{R} & -\mathbf{B}\mathbf{G}\mathbf{K}\Theta + \mathbf{B}\Theta & \mathbf{B}\mathbf{G}\mathbf{K}\mathbf{G}\mathbf{B}^T - 2\mathbf{B}\mathbf{G}\mathbf{B}^T \end{bmatrix} = \begin{bmatrix} \mathbf{0} & \mathbf{0} & \mathbf{R}^T\mathbf{B}^T \\ \mathbf{0} & \Omega^2 & \mathbf{0} \\ \mathbf{B}\mathbf{R} & \mathbf{0} & -\mathbf{F}_I \end{bmatrix}$$

where

$$\mathbf{F}_I = \sum_{s=1}^{N_s} \mathbf{B}^{(s)}\mathbf{G}^{(s)}\mathbf{B}^{(s)^T} = \mathbf{B}\mathbf{G}\mathbf{B}^T \tag{28}$$

$$\mathbf{M}_I = \sum_{s=1}^{N_s} \mathbf{B}^{(s)}\mathbf{G}^{(s)}\mathbf{M}^{(s)}\mathbf{G}^{(s)}\mathbf{B}^{(s)^T} = \mathbf{B}\mathbf{G}\mathbf{M}\mathbf{G}\mathbf{B}^T \tag{29}$$

Let us summarize both formulations:

$$\begin{bmatrix} \mathbf{I} & \mathbf{0} & \mathbf{0} \\ \mathbf{0} & \mathbf{I} & \mathbf{0} \\ \mathbf{0} & \mathbf{0} & \mathbf{M}_{res} \end{bmatrix} \begin{bmatrix} \ddot{\alpha} \\ \ddot{\eta} \\ \ddot{\lambda} \end{bmatrix} + \begin{bmatrix} \mathbf{0} & \mathbf{0} & \mathbf{R}^T\mathbf{B}^T \\ \mathbf{0} & \Omega^2 & \Theta^T\mathbf{B}^T \\ \mathbf{B}\mathbf{R} & \mathbf{B}\Theta & -\mathbf{F}_{res} \end{bmatrix} \begin{bmatrix} \alpha \\ \eta \\ \lambda \end{bmatrix} = \mathbf{T}_{dual}^T \begin{bmatrix} \mathbf{f} \\ \mathbf{0} \end{bmatrix} \tag{17}$$

$$\begin{bmatrix} \mathbf{I} & \mathbf{0} & \mathbf{0} \\ \mathbf{0} & \mathbf{I} & -\Omega^{-2}\Theta^T\mathbf{B}^T \\ \mathbf{0} & -\mathbf{B}\Theta\Omega^{-2} & \mathbf{M}_I \end{bmatrix} \begin{bmatrix} \ddot{\alpha} \\ \ddot{\eta} \\ \ddot{\lambda} \end{bmatrix} + \begin{bmatrix} \mathbf{0} & \mathbf{0} & \mathbf{R}^T\mathbf{B}^T \\ \mathbf{0} & \Omega^2 & \mathbf{0} \\ \mathbf{B}\mathbf{R} & \mathbf{0} & -\mathbf{F}_I \end{bmatrix} \begin{bmatrix} \alpha \\ \eta \\ \lambda \end{bmatrix} = \bar{\mathbf{T}}_{dual}^T \begin{bmatrix} \mathbf{f} \\ \mathbf{0} \end{bmatrix} \tag{25}$$

Remarks

1. Let us note that although the reduced matrices are different, the approximations are based on identical subspaces and hence the results obtained with the formulations (17) and (25) are identical. It is however noteworthy that when the residual attachment modes are used, the coupling between the attachment modes on the vibration modes Θ appears in the reduced stiffness, see (17), whereas when the non-residualized attachment modes are used, the coupling appears in the mass matrix, see (25).
2. In the reduced stiffness matrix (27) we observe a coupling between the attachment modes and the rigid body modes. This can be explained by the fact that the rigid body modes must be considered as part of the static solutions as explained before, so that the block
$$\begin{bmatrix} \mathbf{0} & \mathbf{R}^T\mathbf{B}^T \\ \mathbf{B}\mathbf{R} & \mathbf{F}_I \end{bmatrix}$$
must be seen as the dually assembled statically condensed flexibility, similar to the statically condensed (Guyan) stiffness matrix in the classical Craig-Bampton method. It then becomes clear that the form (25) is the true counterpart of the classical Craig-Bampton.

3. Let us stress again that exactly like in the original formulation(17) of the Dual Craig-Bampton, the last set of equations in (25) represent a weakened compatibility condition. This can be seen from the fact that this last set of equation originates from

$$\begin{bmatrix} -\mathbf{BG} & \mathbf{I} \end{bmatrix} \begin{bmatrix} \text{Substructure equilibrium equations} \\ \text{Interface compatibility} \end{bmatrix}$$

   Thus the weak compatibility condition imposed in the reduced method can be interpreted as follows. The local equilibrium is only satisfied weakly do to the approximation of the local dofs, resulting in a force error $res_{\mathbf{f}}$ on the substructure. If that force error would be applied to the substructure, static displacements $res_{\mathbf{u}} = \mathbf{G}\, res_{\mathbf{f}}$ would result. Then the weak compatibility states that the compatibility error on the interface can be as big as the incompatibility of $res_{\mathbf{u}}$ on the interface.
4. For the original formulation (17) it can easily be verified that setting $\mathbf{M}_{res} = 0$ would enforce exact interface compatibility and in that case the Dual Craig-Bampton is equivalent to the MacNeal method [12]. For the new form (25) such an equivalence can not be found. However one can verify that if all modes are included in Θ (in which case the method is a mere transformation but not a reduction) the exact compatibility is retrieved: the last set of equations in (25) can be written as

$$\mathbf{B}\left(-\Theta\Omega^{-2}\ddot{\eta} + \mathbf{GMGB}^T\ddot{\lambda} + \mathbf{R}\alpha - \mathbf{GB}^T\lambda\right) = -\mathbf{BGf}$$

   When Θ contains all modes, $\mathbf{G} = \Theta\Omega^{-2}\Theta^T$ and we can write

$$\mathbf{B}\left(-\Theta\Omega^{-2}\ddot{\eta} + \Theta\Omega^{-4}\Theta^T\mathbf{B}^T\ddot{\lambda} + \mathbf{R}\alpha - \mathbf{GB}^T\lambda\right) = -\mathbf{B}\Theta\Omega^{-2}\Theta^T\mathbf{f}$$

   or

$$\mathbf{B}\Theta\Omega^{-2}\left(-\ddot{\eta} + \Omega^{-2}\Theta^T\mathbf{B}^T\ddot{\lambda} + \Theta^T\mathbf{f}\right) + \mathbf{B}\left(\mathbf{R}\alpha - \mathbf{GB}^T\lambda\right) = 0$$

   Taking in account the modal equilibrium equations corresponding to the first set of equations in (25),

$$\mathbf{B}\Theta\Omega^{-2}\left(\Omega^2\eta\right) + \mathbf{B}\left(\mathbf{R}\alpha - \mathbf{GB}^T\lambda\right) = \mathbf{Bu} = 0$$

   concluding the verification that when all modes are included, exact compatibility is satisfied.
5. The fact that a weak compatibility is allowed in the Dual Craig-Bampton implies that the infinite eigenvalues related to the Lagrange multipliers λ in the non-reduced problem (2) are no becoming finite. Since those eigenvalues are related to the compatibility constrained it can be showed that they are negative. In practice those negative eigensolutions will appear only in the higher spectrum is the reduction space is rich enough. Also using so-called model truncation

augmentation modes helps rejecting those spurious eigensolutions to the higher frequencies [13].

6. Here we have chosen to use $\mathbf{G}$ as attachment modes. One could also have chosen to use $\mathbf{K}^+$ instead. In that case the attachment modes would not have been $\mathbf{M}$-orthogonal to the rigid-body modes $\mathbf{R}$, which would have introduced an additional coupling term between rigid body modes and attachment modes in the reduced mass matrix $\bar{\mathbf{M}}$ (see (26)).
7. Finally let us note that in this new formulation (25), the statically condensed part of the reduced matrices, namely the parts pertaining to the attachment and rigid-body modes, do not change when the approximation space is enriched with vibration modes Θ. Thus was not the case in the original formulation. This will simplify the application of interface reduction as explained in the next section.

4 Interface modes to reduce the interface problem

One of the major bottlenecks of substructuring techniques is that as the number of substructure increases, the size of the interface problem, namely the number of interface dofs λ in the case of the Dual Craig-Bampton, also increases so that for a large number of substructure the reduced problem has not significantly less dofs than the original problem. This issue is not proper to the dual approach but is known to be an issue for any substructuring method. For the classical (primal) Craig-Bampton method an interface reduction method was proposed in [4], and was further analyzed in [1, 2]. The technique proposed in [4] consists in representing the interface dofs (the displacements for the classical Criag-Bampton) in terms of a reduced number of modes. The modes to represent the interface behavior is usually obtained by solving the statically condensed problem, i.e. a Guyan reduction of the system equivalent to a Craig-Bampton with no internal modes. This method was applied and modified in [9]. An a posteriori error analysis of the Craig-Bampton method with interface reduction and an adaptive enrichment of the reduction basis was proposed in [10].

In order to reduce the interface problem for the Dual Craig Bampton, let us consider the case where no vibration modes are included in the reduction basis, namely we consider only the static modes so that the approximation writes

$$\begin{bmatrix} \mathbf{u} \\ \lambda \end{bmatrix} = \begin{bmatrix} \mathbf{R} & -\mathbf{G}\mathbf{B}^T \\ \mathbf{0} & \mathbf{I} \end{bmatrix} \begin{bmatrix} \alpha \\ \lambda \end{bmatrix} = \mathbf{T}_{dual,stat} \begin{bmatrix} \alpha \\ \lambda \end{bmatrix} \tag{30}$$

so that the reduction of the dual problem leads to

$$\begin{bmatrix} \mathbf{I} & \mathbf{0} \\ \mathbf{0} & \mathbf{M}_I \end{bmatrix} \begin{bmatrix} \ddot{\alpha} \\ \ddot{\lambda} \end{bmatrix} + \begin{bmatrix} \mathbf{0} & \mathbf{R}^T\mathbf{B}^T \\ \mathbf{B}\mathbf{R} & -\mathbf{F}_I \end{bmatrix} \begin{bmatrix} \alpha \\ \lambda \end{bmatrix} = \mathbf{T}_{dual,stat}^T \mathbf{f} \tag{31}$$

Clearly in this case it does not matter if we consider the first or second variant of the Dual Craig-Bampton (25) or (25) since when no vibration modes are included $\mathbf{G}_{res} = \mathbf{G}$. Similar to the procedure proposed in [4] for the primal Craig-Bampton,

let us consider the eigensolutions of the statically condensed dual problem derived from (31):

$$\left(-\mu_k^2 \begin{bmatrix} \mathbf{I} & \mathbf{0} \\ \mathbf{0} & \mathbf{M}_I \end{bmatrix} + \begin{bmatrix} \mathbf{0} & \mathbf{R}^T\mathbf{B}^T \\ \mathbf{BR} & -\mathbf{F}_I \end{bmatrix}\right) \begin{bmatrix} \mathbf{x}_{\alpha_k} \\ \mathbf{x}_{\lambda_k} \end{bmatrix} = \mathbf{0} \tag{32}$$

The eigenvectors of this problem will form a basis to represent the interface dynamics. Note that those eigenvectors include not only the interface force modes $\mathbf{x}_{\lambda_k}$ but also the associated rigid body displacements necessary to guarantee the self-equilibrium of the interface forces with the inertia forces in the substructures. Due to the symmetry of the statically-condensed dual interface problem, the eigensolutions satisfy the orthogonality properties

$$\begin{bmatrix} \mathbf{X}_\alpha^T & \mathbf{X}_\lambda^T \end{bmatrix} \begin{bmatrix} \mathbf{I} & \mathbf{0} \\ \mathbf{0} & \mathbf{M}_I \end{bmatrix} \begin{bmatrix} \mathbf{X}_\alpha \\ \mathbf{X}_\lambda \end{bmatrix} = \mathbf{I} \qquad \begin{bmatrix} \mathbf{X}_\alpha^T & \mathbf{X}_\lambda^T \end{bmatrix} \begin{bmatrix} \mathbf{0} & \mathbf{R}^T\mathbf{B}^T \\ \mathbf{BR} & -\mathbf{F}_I \end{bmatrix} \begin{bmatrix} \mathbf{X}_\alpha \\ \mathbf{X}_\lambda \end{bmatrix} = \mu^2 \tag{33}$$

where $\mathbf{X}_\alpha$, $\mathbf{X}_\lambda$ contain in their columns the eigenvectors of (32) and where μ^2 is a diagonal matrix containing the associated eigenvalues. In these relations we have assumed that the eigenvectors have been normalized with respect to reduced mass matrix. Note that due to the weak compatibility imposed in this statically condensed problem, there will be as many positive eigenvalues as there are rigid body modes in $\mathbf{R}$ and as many negative eigenvalues as there are effective Lagrange multipliers. Non-effective Lagrange multipliers, namely those related to possibly redundant compatibility conditions (as encountered sometimes on corners) will generate zero eigenvalues. Since the compatibility is very weak in this statically condensed problem, one typically finds positive and negative eigenvalues with low absolute values.

The strategy now consists in considering only a small number of interface modes to approximate the interface dynamics. For that we choose the n_{stat} modes corresponding to the *eigenvalues μ_k with the lowest absolute value*. Storing those lowest eigensolutions in $\tilde{\mathbf{X}}_\alpha$, $\tilde{\mathbf{X}}_\lambda$ and $\tilde{\mu}^2$, we propose to modify the approximations in the Dual Craig-Bampton by applying a second reduction step so that

$$\begin{bmatrix} \alpha \\ \eta \\ \lambda \end{bmatrix} \simeq \begin{bmatrix} \mathbf{0} & \tilde{\mathbf{X}}_\alpha \\ \mathbf{I} & \mathbf{0} \\ \mathbf{0} & \tilde{\mathbf{X}}_\lambda \end{bmatrix} \begin{bmatrix} \eta \\ \tilde{\lambda} \end{bmatrix} = \mathbf{T}_I \begin{bmatrix} \eta \\ \tilde{\lambda} \end{bmatrix} \tag{34}$$

Applying now this reduction to the reduced system (25) leads to

$$\begin{bmatrix} \mathbf{I} & -\Omega^{-2}\Theta^T\mathbf{B}^T\tilde{\mathbf{X}}_\lambda \\ -\tilde{\mathbf{X}}_\lambda^T\mathbf{B}\Theta\Omega^{-2} & \mathbf{I} \end{bmatrix} \begin{bmatrix} \ddot{\eta} \\ \ddot{\tilde{\lambda}} \end{bmatrix} + \begin{bmatrix} \Omega^2 & \mathbf{0} \\ \mathbf{0} & \tilde{\mu}^2 \end{bmatrix} \begin{bmatrix} \eta \\ \tilde{\lambda} \end{bmatrix} = \mathbf{T}_I^T\bar{\mathbf{T}}_{dual}^T\mathbf{f} \tag{35}$$

Once this reduced problem is solved, the physical dofs can be reconstructed by applying to back transformation

$$\begin{bmatrix} \mathbf{u} \\ \lambda \end{bmatrix} = \bar{\mathbf{T}}_{dual} \mathbf{T}_I \begin{bmatrix} \eta \\ \tilde{\lambda} \end{bmatrix} = \begin{bmatrix} \Theta & \left(\mathbf{R}\tilde{\mathbf{X}}_\alpha - \mathbf{G}\mathbf{B}^T\tilde{\mathbf{X}}_\lambda\right) \\ \mathbf{0} & \tilde{\mathbf{X}}_\lambda \end{bmatrix} \begin{bmatrix} \eta \\ \tilde{\lambda} \end{bmatrix} \tag{36}$$

5 Numerical example of a truss frame

To illustrate the Dual Craig-Bampton method with interface reduction, let us consider the truss frame used in [12, 13] and depicted in figure 1. The frame is composed of repeated cells, each cell having dimension $0.35 \times 0.35 \times 0.5$ m. The outer beams of the cells have a hollow circular cross-section (outside/inside diameters are 0.02 m and 0.018 m). The diagonal members inside the cells have plain circular section of diameter 0.008 m. We consider five substructures for this system, one per arm and one for the central part. The arms are connected to the central part through 12 points: 4 points at the center of the faces of the central part, and 8 points it the vertices. The dofs of on the mid-face points must be connected only with one neighbor, whereas the vertices have two neighbors and thus two Lagrange multipliers are needed for those dofs. Therefore the compatibility conditions defined by $\mathbf{B}$ requires $4 \times 6 + 8 \times 6 \times 2 = 120$ Lagrange multipliers λ. For practical implementation reasons, we treat all substructures in an equal way and therefore redundant constraints are defined on the vertices by stating the equality between dofs for all combination of neighbors. This leads to using 3 Lagrange multipliers for the dofs on the vertices. So in our implementation we will have $4 \times 6 + 8 \times 6 \times 3 = 168$ Lagrange multipliers, out of which 48 are redundant.

By trial and error, we have chosen the minimal number of modes per substructure such that, without interface reduction, the first 30 eigenfrequencies computed for the Dual Craig-Bampton have an absolute relative error of no more than 1.5 % when compared to the eigenfrequencies of the non-reduced problem. We find that to have

$$\max_{k=1\ldots30} \frac{\left|\omega_{full_j} - \omega_{DCB_j}\right|}{\omega_{full_j}} < 1\%$$

we need must take 29 modes in the arms of the frame that are not attached to the ground, 27 modes in the arm attached to the ground, and 1 mode for the central part. Since the total number of rigid body modes for the substructures is $4 \times 6 = 24$ and since there are 120 effective Lagrange multipliers, the effective size of the reduced model is $3 \times 29 + 27 + 1 + 24 + 120 = 259$.

Applying now the interface reduction as proposed in the previous section, we find by trial and error that a minimum of 74 interface modes. So the effective size of the reduced system is now 213. The relative frequency errors are plotted in figure 2. Note that the first negative eigenvalue for the Dual Craig- Bampton appears for mode 115 in the case no interface reduction is applied, and for mode 111 in case of interface reduction.

Let us note in figure 2 that for some frequencies the error decreases when interface reduction is applied (see for instance errors on frequencies of modes 4, 5,

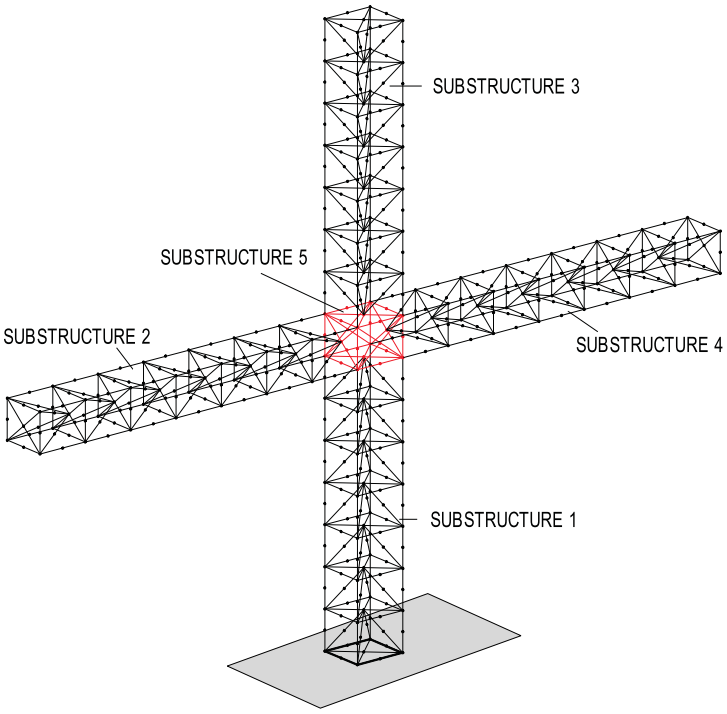

Fig. 1 An example truss frame structure

16-19) . This is counter-intuitive since one would expect errors to be the lowest when no interface reduction is present. Nevertheless since the reduction technique used here is reducing a problem written in primal and dual variables (deriving from a saddle point variatonal problem) the convergence is not guaranteed to be monotonic.

6 Numerical example of two-dimensional solid

In the truss frame example of the previous section, applying interface reduction did not significantly decrease the dimension of the reduced system since for that problem the interface includes a relatively small number of degrees of nodes compared to the internal nodes of the substructures.

Let us now consider the problem of plane-stress two-dimensional square decomposed in 9 substructures as illustrated in figure 3. Each substructure is discretized by 10×10 linear four-noded finite element. The structure is clamped in both directions on one side.

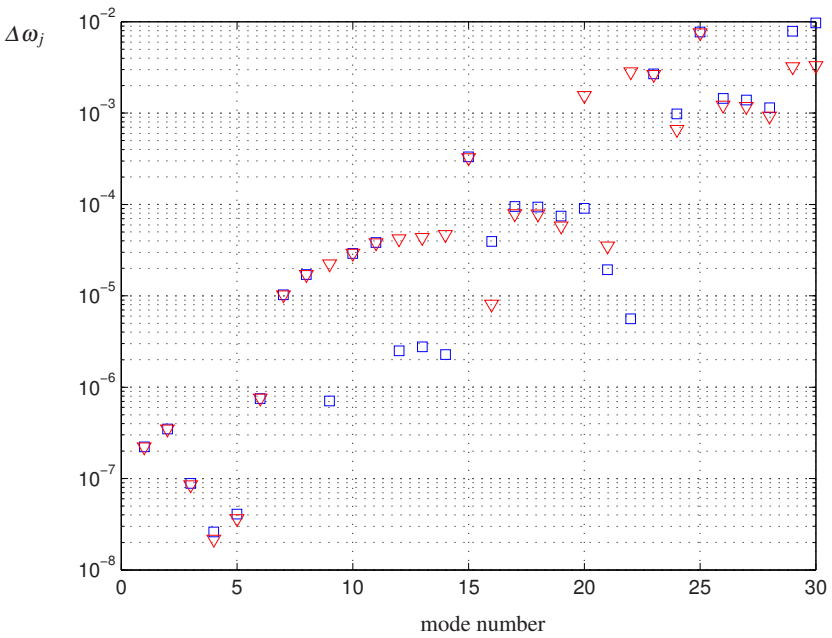

Fig. 2 Truss frame: relative frequency error $\Delta\omega_j = \frac{|\omega_{full_j} - \omega_{DCB_j}|}{\omega_{full_j}}$ for the Dual Craig-Bampton with (red triangles) and without interface reduction (blue squares).

In order for the first 30 eigenfrequencies to have a relative error of maximum 1% (as in the previous example), one requires 10 vibration modes per substructures (this is determined by trial and error when no interface reduction is applied). We then look for the number of interface modes needed to maintain an maximum relative error of 1%. This is achieved with 62 interface modes. The results are depicted in figure 4.

For this case we note that the interface reduction significantly decreases the dimension of the reduced problem. Indeed, since there are 252 interface compatibility constraints[1] the effective dimension of the reduced problem is 360 without interface reduction, and 128 after interface reduction. Note that with 128 generalized degrees of freedom w are able to approximate accurately 30 modes, which shows the efficiency of the Dual Craig-Bampton with interface reduction.

[1] In our implementation we use 276 Lagrange multipliers since all redundant compatibility conditions are consider for simplicity at corners.

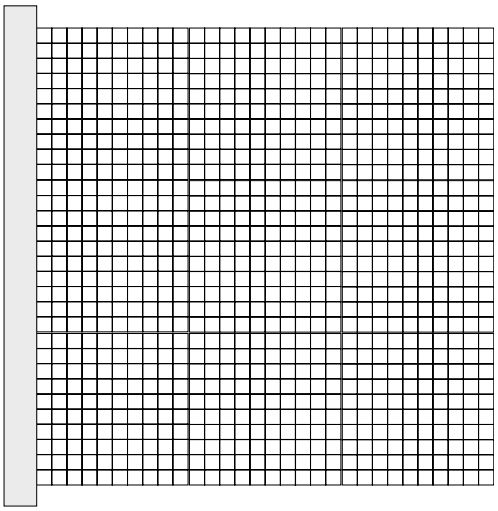

Fig. 3 A two-dimensional solid problem decomposed in 9 substructures

7 Interpretation of static modes of the dual interface problem

In the Dual Craig-Bampton, interpretation of modes and frequencies is a bit different from normal reduction techniques and we will further discuss this point here.

If we consider again the initial dually assembled problem before reduction, equation (1), there exist $2N_\lambda$ infinite eigenvalues related to the "dynamics" of the Lagrange multipliers.[2] This can be understood by the fact that the Lagrange Multipliers have associated coefficients in K_a, but they have no contribution to the mass M_a. See [6] for further details.

In the Dual Craig-Bampton approach the compatibility condition is weakened, which had as consequence to introduce contribution of the Lagrange multipliers to the reduced mass matrix (see section 3). The infinite eigenvalues of the original system therefore become finite and have negative values due to the fact that the dually assembled problem originates from a saddle point problem (one could say that the problem is positive definite for the physical displacements, and negative definite for the Lagrange multipliers). Hence it is understood that the modes associated to negative eigenvalues of the reduced system will be related to strong incompatibilities.

To illustrate this discussion, we show in figure 5 the modes 1, 2 and 30 obtained with the Dual Craig Bampton method (without interface reduction and with 10 vibration modes per substructure). Clearly we see that the first modes are the correct modes of the system. The last mode, mode 30, looks fine: this mode had an accurate frequency (see previous section), but slight incompatibilities appear at some location on the interface. As a matter of fact, its MAC when compared to mode 30 of the non-reduced problem is about 0.8.

[2] Here we assume that no redundant constraints are in the equations. If this would be the case, then one has as many zero frequencies as there are redundant constraints in **B**.

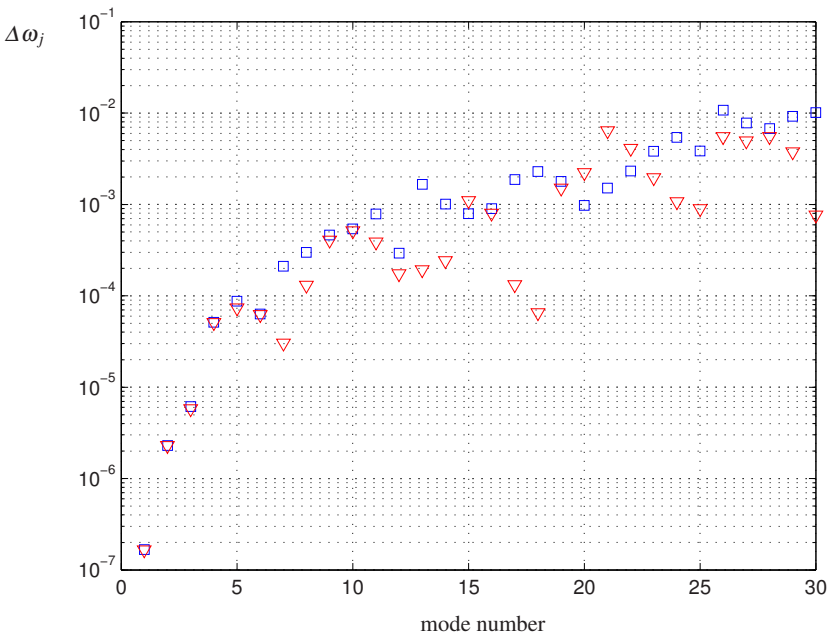

Fig. 4 Two-dimensional solid: relative frequency error $\Delta\omega_j = \frac{\left|\omega_{full_j} - \omega_{DCB_j}\right|}{\omega_{full_j}}$ for the Dual Craig-Bampton with (red triangles) and without interface reduction (blue squares).

Figure 6 represents again mode 30, but with and without interface reduction (as explained in the previous section). One can clearly see that the interface reduction allows even some more incompatibility on the interface, but without significantly changing the associated frequency nor the MAC number.

In figure 7 we show the first six modes obtained from the statically condensed interface problem (32), namely

$$\mathbf{T}_{dual,stat} \begin{bmatrix} \mathbf{X}_\alpha \\ \mathbf{X}_\lambda \end{bmatrix}$$

Clearly the first 3 modes resemble strongly the true modes of the system. Mode 4 however exhibits very large interface incompatibility and has a negative eigenvalue. This indicates that mode 4 is a mode of which the Lagrange multiplier part $\mathbf{x}_{\lambda_k}$ plays an important role in provide compatibility and need therefore to be include in the reduction basis of the interface.

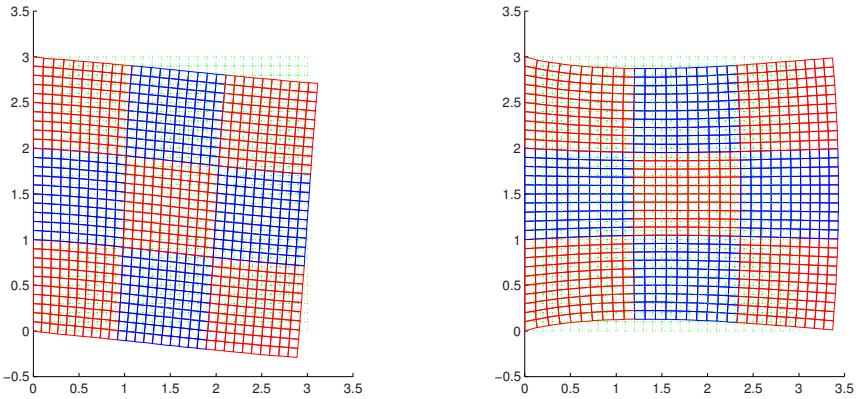

Mode 1 (MAC=1.0,$\Delta\omega = -1.6e-7$) Mode 2 (MAC=1.0,$\Delta\omega = -2.3e-6$)

Fig. 5 Modes 1,2 obtained by the Dual Craig-Bampton method (no interface reduction).

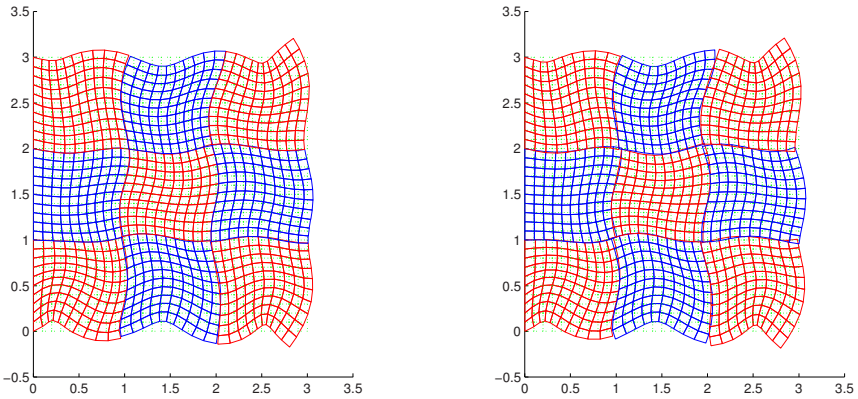

Mode 30 (MAC=0.75,$\Delta\omega = -1.2e-2$) Mode 30,(MAC=0.79,$\Delta\omega = -7.6e-4$) with interface reduction)

Fig. 6 Modes 30 obtained by the Dual Craig-Bampton method (without and with interface reduction).

8 Conclusion and outlook

In this paper we have proposed an interface reduction technique for the Dual Craig-Bampton method. The interface modes describe amplitudes of rigid-body modes and interface forces which can be used to further reduce the Dual Craig-Bampton matrices. The strategy proposed here can be seen as fully dual to the interface reduction of the classical Craig-Bampton using interface modes from the statically reduced problem.

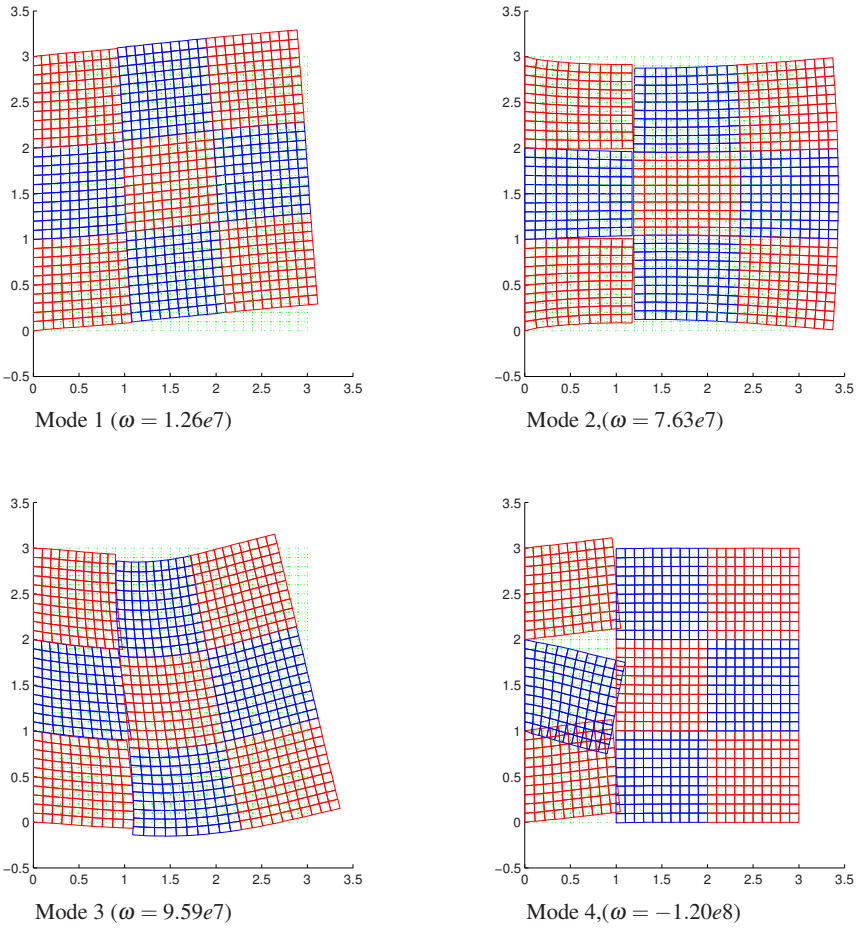

Fig. 7 Modes 1, 2, 3, 4 of the statically condensed dual interface problem (32).

We have shown in two examples that the method allows reducing the system to a small number of degrees of freedom while keeping good accuracy on the frequencies of the system.

We note that one of the major cost in the interface reduction strategy proposed here resides in the solution of the statically condensed interface problem (32). In particular the factorization of $\mathbf{F}_I$ implies a significant computational cost. Nevertheless several options exist to reduce that cast by approximating the interface operators and find approximate interface modes. In particular the large know-how present in the field of parallel computing can be used to approximate the inverse of the interface flexibility. One could approximate that operator by a projected Dirichlet operator like it is done in the Dirichlet preconditioner of the FETI method. One could also

reduce the interface problem before performing the Daul Craig-Bampton projection if we compute interface modes for using for instance the approximation proposed in [5]. Further approximation of the interface operator could also be derived from [8]. This will be investigated in our future work.

References

1. Bourquin, F.: Component mode synthesis and eigenvalues of second order operators: Discretization and algorithm. RAIRO Mathematical Modelling and Numerical Analysis **26**(3), 385–423 (1992)
2. Bourquin, F.: A domain decomposition method for the eigenvalue problem in elastic multistructures. In: Ciarlet, Trabucho, V. Eds. (eds.) Asymptotic Methods for Elastic Structures, pp. 16–29. Walter de Gruyter & Co. (1995)
3. Craig, R., Bampton, M.: Coupling of substructures for dynamic analysis. AIAA Jnl. **6**(7), 1313–1319 (1968)
4. Craig, R., Chang, C.: Substructure coupling for dynamic analysis and testing. Tech. Rep. CR-2781, NASA (1977)
5. Cros, J.M.: Parallel modal synthesis in structural dynamics. Contemporary Mathematics **218**, 492–499 (1998). Tenth International Conference on Domain Decomposition Methods, Boulder, CO, August 1997
6. Farhat, C., Crivelli, L., Gradin, M.: Implicit time integration of a class of constrained hybrid formulations–part i: Spectral stability theory. Computer Methods in Applied Mechanics and Engineering **125**(1-4), 71 – 107 (1995). DOI DOI: 10.1016/0045-7825(95)00783-W. URL http://www.sciencedirect.com/science/article/B6V29-3XX6TYH-5/2/c3b587b83a9a27ae0cebfd0353517118
7. Farhat, C., Rixen, D.: Encyclopedia of Vibration, chap. Linear Algebra, pp. 710–720. Academic Press (2002). Isbn 0-12-227085-1
8. Garvey, S., Penny, J., Gilbert, A.: The reduction of computation effort in kron's method for eigenvalue and response analysis of large structures. Jnl. Comp. Struct. **34**(4), 593–602 (1990)
9. Herrmann, J., Maess, M., Gaul, L.: Substructuring including interface reduction for the efficient vibro-acoustic simulation of fluid-filled piping systems. Mechanical Systems and Signal Processing **24**(1), 153 – 163 (2010). DOI DOI: 10.1016/j.ymssp.2009.05.003. URL http://www.sciencedirect.com/science/article/B6WN1-4W91PTV-2/2/13c6d4dc7f1ca7f307997052971a1d9a
10. Jakobsson, H., Bengzon, F., Larson, M.G.: Adaptive component mode synthesis in linear elasticity. International J. Numer. Methods Engineering (2010 (submitted))
11. MacNeal, R.: A hybrid method of component mode synthesis. Jnl. Comp. Struct. **1**(4), 581–601 (1971)
12. Rixen, D.: A dual craig-bampton method for dynamic substructuring. Jnl. Comp. Math. **168**(1-2), 383–391 (2004)
13. Rixen, D.J.: Dual craig-bampton with enrichment to avoid spurious modes. In: IMAC-XXVII: International Modal Analysis Conference, Orlando, FL. Society for Experimental Mechanics, Bethel, CT (2009)
14. Rubin, S.: Improved component-mode representation for structural dynamic analaysis. AIAA Jnl. **13**(8), 995–1006 (1975)

A Truly Hybrid Approach to Substructuring Problems Using Mixed Assembly and Implicit Solving Strategies

S.N. Voormeeren, P.L.C. van der Valk and D.J. Rixen

Abstract In recent years, the structural dynamic community showed a renewed interest in component coupling (i.e. dynamic substructuring) and decoupling techniques for structural dynamic analysis of assembled systems. Especially for hybrid problems, where some component models are obtained from experimental data and others from numerical modeling, these techniques offer interesting possibilities. However, since measured models are generally expressed in terms of flexibility and numerical models in terms of stiffness, model inversions are needed at least at the component interfaces. This leads to increased computational effort and/or amplification of measurement errors.
To avoid the inversions of the component models, a truly hybrid approach to coupling and decoupling problems is proposed in this paper. Using a mixed assembly methodology derived from a so-called "three field formulation", stiffness type components can be directly assembled to flexibility based subsystems. Then only the interface problem remains to be solved. In part one of this paper the theoretical derivation of the proposed methodology is addressed. Furthermore, we outline the differences with respect to the existing methods.

1 Introduction

1.1 Dynamic Substructuring

Dynamic substructuring (DS) techniques have been well established over the past decades. These techniques consist in constructing the structural dynamic model of a large and complex system by assembling the dynamic models of its simpler components (also called subsystems or substructures). In recent years, the structural dynamic community showed a renewed interest in these substructure coupling techniques, especially in the context of experimental applications. Since the application of the DS methodology using experimental models is usually performed in the frequency domain, using component frequency response function (FRF) matrices, these techniques are often termed *frequency based substructuring* (FBS).

In FBS, two classes of problems can be distinguished. In the first class the coupling problem is considered, where the dynamics of a system are obtained by assembly of the dynamic models of its components. This *coupling* problem is sometimes also referred to as the "forward" problem. The second class of problems considers the reverse case, namely how a substructure model can be found from the assembled system. This *decoupling* problem is sometimes also referred to as "backward" analysis. In this paper we will focus only on the coupling problem in dynamic substructuring.

An experimental FBS analysis consists in finding the structural dynamic behavior of a system composed of multiple components, where at least one component model is derived experimentally. This is sometimes also called "hybrid" analysis. Although the basic theory of dynamic substructuring has been formulated decades ago, successful application of experimental FBS techniques is often limited to relatively simple systems. Application to complex real-life engineering structures is often hindered by the method's notorious sensitivity to experimental errors.

Corresponding author: Sven Voormeeren
Delft University of Technology, Mekelweg 2, 2628CD Delft, the Netherlands
e-mail: s.n.voormeeren@tudelft.nl

T. Proulx (ed.), *Linking Models and Experiments, Volume 2*, Conference Proceedings of the Society for Experimental Mechanics Series 5,
DOI 10.1007/978-1-4419-9305-2_23, © The Society for Experimental Mechanics, Inc. 2011

1.2 Problem Description

Over the last decades, research has revealed that many aspects have caused the failing of FBS methods on complex structures. Some of the classic issues are described below, although it should be noted that this overview is by no means exhaustive:

Rotational degrees of freedom A lot has been written on the importance of rotational degrees of freedom in dynamic substructuring [7, 18, 9]. The measurement of rotations and torques is however very difficult in practice, so rotational DoF are often neglected. The influence of omitting the rotational information strongly depends on the component's interface flexibility [4]. To overcome this issue one can either put efforts in measuring the rotational DoF [20] or expand translational data to reconstruct the rotational responses [21, 22]. In particular, if one assumes that the interface has only local rigid motions one can construct its response from a minimum of 6 coupling DoF at three nodes. This approach only yields good results up to frequencies where local deformation starts to take place.

Continuity of interface In many practical situation the interface between substructures is in fact a continuous surface or curve. Measurements however can usually only be performed on a limited number of discrete points. In that case one can reconstruct the interface continuous behavior using expansion strategies. The simplest method is to consider a rigid behavior around measured points, but more advanced methods such as the SEREP method [21] can be used to include static deformations obtained from a local finite element model of the interface. Such a local finite element model can also be used to include local dynamic modes in the expansion of the interface measurement points [6]. Recently, the experimental community successfully started using these kind of multiple point connections [23, 19, 2, 15].

Dynamics of joints Dynamic substructuring methods are sensitive to the coupling mechanisms taking place at the subsystem interfaces. Usually the coupling between the subsystems is either modeled as exact or with linear flexible joints. In many engineering structures, however, people found nonlinear coupling mechanisms between substructures, originating for instance from friction between bolted parts. Efforts are made to develop nonlinear models to account for such mechanisms [8, 10].

The issues described above need to be taken into account in any FBS application to avoid making systematic errors. The type of error that we will focus on in this work however, is more general of nature and currently seems to be the biggest bottleneck in FBS: random experimental errors. When performing dynamic substructuring using experimental data, measurement errors affect the response of the coupled system. These errors originate for instance from measurement noise, collocation errors, added mass effects, etcetera. Since all these errors have a more or less random perturbation effect on the measured FRFs, we will here designate all these sources as "experimental error".

If the FRFs are polluted with measurement errors the coupling results will be erroneous. The severity of the error in the assembled FRF matrices strongly depends on which FRFs of the subsystems are affected by the measurement errors. The measured interface FRF matrix for example needs to be inverted in the usual FBS methods. Due to the matrix inversion, small measurement errors can be significantly amplified, resulting in large errors in the FRFs of the coupled system. Research showed that this is especially problematic around the eigenfrequencies of the components [16, 28, 26], where small errors are greatly amplified. To improve the robustness of FBS a lot of effort has therefore been spend on filtration techniques, using for instance singular value decomposition to make the inversion less sensitive to small perturbations on the matrix entries [12, 3, 17, 5].

1.3 Paper Outline

In this work we take a different approach to overcome the problem outlined above. Instead of developing ways to improve the current FBS methods, we try to develop an "inverse free" FBS method that aims to avoid the sensitive matrix inversions. From a so-called three-field approach to assembly of substructure models, we will develop a procedure for "mixed" assembly of FRF matrices. That is, a method which allows stiffness and flexibility representations of substructure models to be directly assembled without first having to invert (one of) the models to obtain a common representation. The underlying idea is that each substructuring model involved in the assembly can be expressed in its "natural" form, so (condensed) dynamic stiffness FRFs for models derived from finite element (FE) or analytic models and receptance FRFs for models obtained from experiments. To this end, the next section presents a general framework for substructure assembly. The resulting "mixed" assembly approach forms a starting point for the new FBS method.

The key to an alternative FBS method is not only in the mixed assembly however; the strategy for solving the assembled equations is equally important. This aspect is treated in section 3. In section 4 the method is applied to an academic case study, which includes an analysis of the method's sensitivity and comparison to existing FBS methods. The paper is ended by some conclusions and recommendations in section 5.

2 A General Framework for Substructure Assembly

This section addresses an important aspect of dynamic substructuring, namely the assembly of component models to obtain the structural dynamic model of the total system. Traditionally one uses in FBS either so-called "primal" or "dual" approaches, as outlined in [14]. However, in order to derive the "inverse free" FBS method we need a third option: "mixed assembly". In this section, we will present a general framework for substructure assembly which allows to derive this mixed assembly method.

In general, structural dynamic component models in the frequency domain can be expressed either in terms of stiffness or flexibility. The former can be the case for dynamic stiffness FRF matrices (possibly condensed) originating from finite element (FE) models, while the latter is the case for experimentally obtained receptance models (where a force is applied and dynamic responses are measured) or models synthesized from analytical mode shapes.[1] Hence, the substructure DoF vector either contains displacement DoF or force DoF. Given the different representations of the substructure models, three assembly cases can be distinguished:

1. Assembly of displacements to displacements: "stiffness assembly".
2. Assembly of forces to forces: "flexibility assembly".
3. Assembly of displacements to forces: "mixed assembly".

These three cases are illustrated in figure 1 and will be treated in detail in the subsequent sections, where we will use a so called three field variational formulation to derive the required assembly procedures. Such an approach is needed to tackle the mixed assembly problem; for the more straightforward cases of dynamic stiffness and receptance assembly a two field formulation is already sufficient.

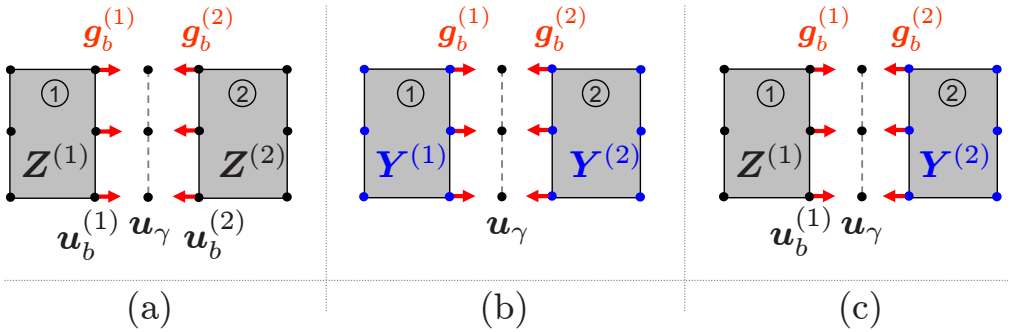

Fig. 1: Three different assembly cases

2.1 Dynamic Stiffness Assembly

In this section we treat the assembly of components expressed in terms of dynamic stiffness. We start from the linear, discrete and possibly condensed dynamic stiffness form of the equations of motion of a substructure s connected to other substructures:

$$\boldsymbol{Z}^{(s)}(\omega)\boldsymbol{u}^{(s)}(\omega) = \boldsymbol{f}^{(s)}(\omega) + \boldsymbol{g}^{(s)}(\omega) \tag{1}$$

Here $\boldsymbol{Z}^{(s)}$ denotes the substructure's dynamic stiffness matrix, $\boldsymbol{u}^{(s)}$ the vector of displacement degrees of freedom, $\boldsymbol{f}^{(s)}$ the external excitation vector and $\boldsymbol{g}^{(s)}$ the vector of connection forces felt from connected substructures. Note that in the subsequent discussion we will omit the explicit frequency dependence for clarity. We partition the subsystem DoF and the associated matrices in an internal $_i$ and boundary $_b$ part and write the DoF vector and vector of connection forces as:

$$\boldsymbol{u}^{(s)} = \begin{bmatrix} \boldsymbol{u}_i^{(s)} \\ \boldsymbol{u}_b^{(s)} \end{bmatrix} \quad , \quad \boldsymbol{g}^{(s)} = \begin{bmatrix} \boldsymbol{0} \\ \boldsymbol{g}_b^{(s)} \end{bmatrix}$$

[1] Note that a FE model can often easily be used to obtain a receptance FRF matrix of the structure by simple performing a model analysis and synthesizing the FRFs. However, when the model contains frequency dependent behavior, for example from viscoelastic effects, the identification of mode shapes is impossible and one either has to work directly with the dynamic stiffness model or invert it at every frequency to obtain the receptance matrix.

By definition the vector of connection forces $\boldsymbol{g}$ is zero at the internal subsystem DoF. Between the substructures we can define the intermediate interface displacement field $\boldsymbol{u}_\gamma$, to govern the compatibility of substructural displacements at the interface. This condition then writes:

$$\boldsymbol{u}_b^{(s)} - \boldsymbol{L}_b^{(s)} \boldsymbol{u}_\gamma = \boldsymbol{0} \tag{2}$$

Here $\boldsymbol{L}_b^{(s)}$ is a Boolean matrix localizing the DoF from the global intermediate displacement field corresponding to the substructure boundary DoF. As a result, we end up with a three field formulation of the substructuring problem, having as independent unknowns the substructure DoF field $\boldsymbol{u}^{(s)}$, the field of interface connection forces $\boldsymbol{g}_b^{(s)}$ and the intermediate interface displacement field $\boldsymbol{u}_\gamma$. Taking a variational approach we can now obtain the assembled equations. To this end, we can set up the Lagrangian of this problem as:

$$\mathscr{L}\left(\boldsymbol{u}^{(s)}, \boldsymbol{g}_b^{(s)}, \boldsymbol{u}_\gamma\right) = \sum_s \left(\frac{1}{2} \boldsymbol{u}^{(s)^T} \boldsymbol{Z}^{(s)} \boldsymbol{u}^{(s)} - \boldsymbol{f}^{(s)^T} \boldsymbol{u}^{(s)} + \boldsymbol{g}_b^{(s)^T} \left(\boldsymbol{L}_b^{(s)} \boldsymbol{u}_\gamma - \boldsymbol{u}_b^{(s)} \right) \right) \tag{3}$$

For the sake of simplicity we will now consider the assembly problem for two substructures only ($s = 1, 2$), although the concepts presented can be easily generalized to the assembly of an arbitrary number of components. This situation is depicted in figure 1 (a). To find the assembled equations we take the variation with respect to the free variables to find the equations of motion of the assembly of two components:

$$\begin{bmatrix} \boldsymbol{Z}_{ii}^{(1)} & \boldsymbol{Z}_{ib}^{(1)} & \boldsymbol{0} & \boldsymbol{0} & \boldsymbol{0} & \boldsymbol{0} & \boldsymbol{0} \\ \boldsymbol{Z}_{bi}^{(1)} & \boldsymbol{Z}_{bb}^{(1)} & \boldsymbol{0} & \boldsymbol{0} & -\boldsymbol{I} & \boldsymbol{0} & \boldsymbol{0} \\ \boldsymbol{0} & \boldsymbol{0} & \boldsymbol{Z}_{ii}^{(2)} & \boldsymbol{Z}_{ib}^{(2)} & \boldsymbol{0} & \boldsymbol{0} & \boldsymbol{0} \\ \boldsymbol{0} & \boldsymbol{0} & \boldsymbol{Z}_{bi}^{(2)} & \boldsymbol{Z}_{bb}^{(2)} & \boldsymbol{0} & -\boldsymbol{I} & \boldsymbol{0} \\ \boldsymbol{0} & -\boldsymbol{I} & \boldsymbol{0} & \boldsymbol{0} & \boldsymbol{0} & \boldsymbol{0} & \boldsymbol{L}_b^{(1)} \\ \boldsymbol{0} & \boldsymbol{0} & \boldsymbol{0} & -\boldsymbol{I} & \boldsymbol{0} & \boldsymbol{0} & \boldsymbol{L}_b^{(2)} \\ \boldsymbol{0} & \boldsymbol{0} & \boldsymbol{0} & \boldsymbol{0} & \boldsymbol{L}_b^{(1)^T} & \boldsymbol{L}_b^{(2)^T} & \boldsymbol{0} \end{bmatrix} \begin{bmatrix} \boldsymbol{u}_i^{(1)} \\ \boldsymbol{u}_b^{(1)} \\ \boldsymbol{u}_i^{(2)} \\ \boldsymbol{u}_b^{(2)} \\ \boldsymbol{g}_b^{(1)} \\ \boldsymbol{g}_b^{(2)} \\ \boldsymbol{u}_\gamma \end{bmatrix} = \begin{bmatrix} \boldsymbol{f}_i^{(1)} \\ \boldsymbol{f}_b^{(1)} \\ \boldsymbol{f}_i^{(2)} \\ \boldsymbol{f}_b^{(2)} \\ \boldsymbol{0} \\ \boldsymbol{0} \\ \boldsymbol{0} \end{bmatrix} \tag{4}$$

In the above equations we can recognize the fifth and sixth equations as the compatibility conditions, governing the compatibility between the $\boldsymbol{u}_b^{(s)}$ and $\boldsymbol{u}_\gamma$. The last row is the equilibrium condition on the interface, stating that the sum of the substructure connection forces must be zero. Note that when starting from this three-field formulation, we only required compatibility at the substructure interfaces; the equilibrium conditions followed naturally from the compatibility condition. The above assembled equations of motion still contain the full three fields, which is inefficient for most analyses from a computational point of view. Therefore, it is desired to simplify the equations. In essence two ways exist to do this, namely so called *primal* or *dual* assembly, as discussed next.

2.1.1 Dual Assembly

In dual assembly, one eliminates the interface connection force fields by realizing that the interface forces should be equal and opposite to satisfy the interface equilibrium. To *a priori* satisfy this condition, we can introduce a unique field of interface forces λ, as follows:

$$\boldsymbol{g}_b^{(s)} = -\boldsymbol{B}_b^{(s)^T} \lambda$$

Here $\boldsymbol{B}_b^{(s)}$ is a signed Boolean matrix acting on the substructure interface DoF and λ corresponds physically to the interface force intensities. Note that the minus sign is chosen to stress the fact that whereas $\boldsymbol{g}_b^{(s)}$ was seen as an external force for the substructure, λ is considered an internal force. Due to the construction of the Boolean matrices it holds that [14]:

$$\sum_s \boldsymbol{B}_b^{(s)} \boldsymbol{L}_b^{(s)} = \boldsymbol{0} \tag{5}$$

Hence this choice for the interface connection forces satisfies the interface equilibrium for any λ. This choice gives rise to the following transformation:

$$\begin{bmatrix} \boldsymbol{u}_i^{(1)} \\ \boldsymbol{u}_b^{(1)} \\ \boldsymbol{u}_i^{(2)} \\ \boldsymbol{u}_b^{(2)} \\ \boldsymbol{g}_b^{(1)} \\ \boldsymbol{g}_b^{(2)} \\ \boldsymbol{u}_\gamma \end{bmatrix} = \begin{bmatrix} \boldsymbol{I} & \boldsymbol{0} & \boldsymbol{0} & \boldsymbol{0} & \boldsymbol{0} & \boldsymbol{0} \\ \boldsymbol{0} & \boldsymbol{I} & \boldsymbol{0} & \boldsymbol{0} & \boldsymbol{0} & \boldsymbol{0} \\ \boldsymbol{0} & \boldsymbol{0} & \boldsymbol{I} & \boldsymbol{0} & \boldsymbol{0} & \boldsymbol{0} \\ \boldsymbol{0} & \boldsymbol{0} & \boldsymbol{0} & \boldsymbol{I} & \boldsymbol{0} & \boldsymbol{0} \\ \boldsymbol{0} & \boldsymbol{0} & \boldsymbol{0} & \boldsymbol{0} & -\boldsymbol{B}_b^{(1)^T} & \boldsymbol{0} \\ \boldsymbol{0} & \boldsymbol{0} & \boldsymbol{0} & \boldsymbol{0} & -\boldsymbol{B}_b^{(2)^T} & \boldsymbol{0} \\ \boldsymbol{0} & \boldsymbol{0} & \boldsymbol{0} & \boldsymbol{0} & \boldsymbol{0} & \boldsymbol{I} \end{bmatrix} \begin{bmatrix} \boldsymbol{u}_i^{(1)} \\ \boldsymbol{u}_b^{(1)} \\ \boldsymbol{u}_i^{(2)} \\ \boldsymbol{u}_b^{(2)} \\ \boldsymbol{\lambda} \\ \boldsymbol{u}_\gamma \end{bmatrix} \tag{6}$$

Substituting this transformation in the three-field assembled equations of motion (4) replaces the local connection forces by the unique global field $\boldsymbol{\lambda}$, satisfying the interface equilibrium condition. To end up with a symmetric system one can use the above transformation to subsequently pre-multiply the equations. This eliminates the intermediate displacement field $\boldsymbol{u}_\gamma$, due to the relation between the Boolean matrices in (5). The procedure is illustrated in figure 2 and the simplified assembled equations become:

$$\begin{bmatrix} \boldsymbol{Z}_{ii}^{(1)} & \boldsymbol{Z}_{ib}^{(1)} & \boldsymbol{0} & \boldsymbol{0} & \boldsymbol{0} \\ \boldsymbol{Z}_{bi}^{(1)} & \boldsymbol{Z}_{bb}^{(1)} & \boldsymbol{0} & \boldsymbol{0} & \boldsymbol{B}_b^{(1)^T} \\ \boldsymbol{0} & \boldsymbol{0} & \boldsymbol{Z}_{ii}^{(2)} & \boldsymbol{Z}_{ib}^{(2)} & \boldsymbol{0} \\ \boldsymbol{0} & \boldsymbol{0} & \boldsymbol{Z}_{bi}^{(2)} & \boldsymbol{Z}_{bb}^{(2)} & \boldsymbol{B}_b^{(2)^T} \\ \boldsymbol{0} & \boldsymbol{B}_b^{(1)} & \boldsymbol{0} & \boldsymbol{B}_b^{(2)} & \boldsymbol{0} \end{bmatrix} \begin{bmatrix} \boldsymbol{u}_i^{(1)} \\ \boldsymbol{u}_b^{(1)} \\ \boldsymbol{u}_i^{(2)} \\ \boldsymbol{u}_b^{(2)} \\ \boldsymbol{\lambda} \end{bmatrix} = \begin{bmatrix} \boldsymbol{f}_i^{(1)} \\ \boldsymbol{f}_b^{(1)} \\ \boldsymbol{f}_i^{(2)} \\ \boldsymbol{f}_b^{(2)} \\ \boldsymbol{0} \end{bmatrix} \tag{7}$$

The above system is called the *dual* assembled system, since the unknowns defining the interface problem are forces which are mathematically dual to the original displacement unknowns. As a result, the compatibility condition is present explicitly in the assembled equations of motion, i.e. the last row in eq. (2.2). In a practical setting however, where measured receptance matrices are used to describe the component dynamics, this form of the assembled equations is not very relevant. One can therefore transform the above equation (2.2) to a receptance form by eliminating the Lagrange multipliers. The resulting expression is the well known LM FBS method for assembly of receptance FRF matrices [13, 14].

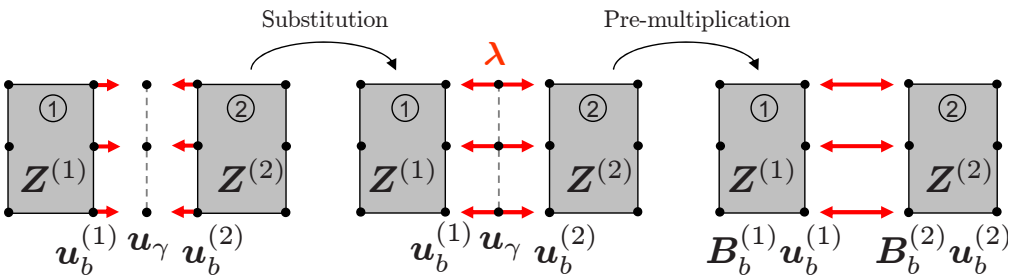

Fig. 2: Simplification of the three-field formulation for stiffness assembly according to dual assembly.

2.1.2 Primal Assembly

Another way to obtain a simplified expression for the assembled system (4) can be obtained by realizing that the compatibility condition can be *a priori* satisfied by choosing a unique set of substructure interface DoF as:

$$\boldsymbol{u}_b^{(s)} = \boldsymbol{L}_b^{(s)} \boldsymbol{u}_\gamma$$

This choice gives the following transformation:

$$\begin{bmatrix} \boldsymbol{u}_i^{(1)} \\ \boldsymbol{u}_b^{(1)} \\ \boldsymbol{u}_i^{(2)} \\ \boldsymbol{u}_b^{(2)} \\ \boldsymbol{g}_b^{(1)} \\ \boldsymbol{g}_b^{(2)} \\ \boldsymbol{u}_\gamma \end{bmatrix} = \begin{bmatrix} \boldsymbol{I} & \boldsymbol{0} & \boldsymbol{0} & \boldsymbol{0} & \boldsymbol{0} \\ \boldsymbol{0} & \boldsymbol{0} & \boldsymbol{0} & \boldsymbol{0} & \boldsymbol{L}_b^{(1)} \\ \boldsymbol{0} & \boldsymbol{I} & \boldsymbol{0} & \boldsymbol{0} & \boldsymbol{0} \\ \boldsymbol{0} & \boldsymbol{0} & \boldsymbol{0} & \boldsymbol{0} & \boldsymbol{L}_b^{(2)} \\ \boldsymbol{0} & \boldsymbol{0} & \boldsymbol{I} & \boldsymbol{0} & \boldsymbol{0} \\ \boldsymbol{0} & \boldsymbol{0} & \boldsymbol{0} & \boldsymbol{I} & \boldsymbol{0} \\ \boldsymbol{0} & \boldsymbol{0} & \boldsymbol{0} & \boldsymbol{0} & \boldsymbol{I} \end{bmatrix} \begin{bmatrix} \boldsymbol{u}_i^{(1)} \\ \boldsymbol{u}_i^{(2)} \\ \boldsymbol{g}_b^{(1)} \\ \boldsymbol{g}_b^{(2)} \\ \boldsymbol{u}_\gamma \end{bmatrix}$$

Again, this transformation is substituted in (4) thereby eliminating the substructure boundary DoF sets $\boldsymbol{u}_b^{(s)}$ and satisfying the interface compatibility condition. Pre-multiplication is then needed to obtain a symmetric system of equations. Using again the relation between the Boolean matrices $\boldsymbol{L}_b$ and $\boldsymbol{B}_b$ in eq. (5), we see that by doing so the equilibrium condition is also satisfied and drops out of the equation. The procedure is illustrated in figure 3 and results in the following expression for the assembled system:

$$\begin{bmatrix} \boldsymbol{Z}_{ii}^{(1)} & \boldsymbol{0} & \boldsymbol{Z}_{ib}^{(1)}\boldsymbol{L}_b^{(1)} \\ \boldsymbol{0} & \boldsymbol{Z}_{ii}^{(2)} & \boldsymbol{Z}_{ib}^{(2)}\boldsymbol{L}_b^{(2)} \\ \boldsymbol{L}_b^{(1)^T}\boldsymbol{Z}_{bi}^{(1)} & \boldsymbol{L}_b^{(2)^T}\boldsymbol{Z}_{bi}^{(2)} & \boldsymbol{L}_b^{(1)^T}\boldsymbol{Z}_{bb}^{(1)}\boldsymbol{L}_b^{(1)} + \boldsymbol{L}_b^{(2)^T}\boldsymbol{Z}_{bb}^{(2)}\boldsymbol{L}_b^{(2)} \end{bmatrix} \begin{bmatrix} \boldsymbol{u}_i^{(1)} \\ \boldsymbol{u}_i^{(2)} \\ \boldsymbol{u}_\gamma \end{bmatrix} = \begin{bmatrix} \boldsymbol{f}_i^{(1)} \\ \boldsymbol{f}_i^{(2)} \\ \boldsymbol{L}_b^{(1)^T}\boldsymbol{f}_b^{(1)} + \boldsymbol{L}_b^{(2)^T}\boldsymbol{f}_b^{(2)} \end{bmatrix} \tag{8}$$

The above equations form the so called *primal* assembled system; the most compact form of the assembled equations of motion using a minimum number of DoF. Note that this type of assembly is the way individual elements are classically assembled in a finite element method. However, as we noted previously regarding the dual form of the assembled equations, the above equation (8) usually needs to be inverted to a receptance form to be useful in an experimental FBS analysis. The resulting expression for the assembled receptance matrix is in the literature commonly termed the "impedance coupling" method [11, **?**, 14].

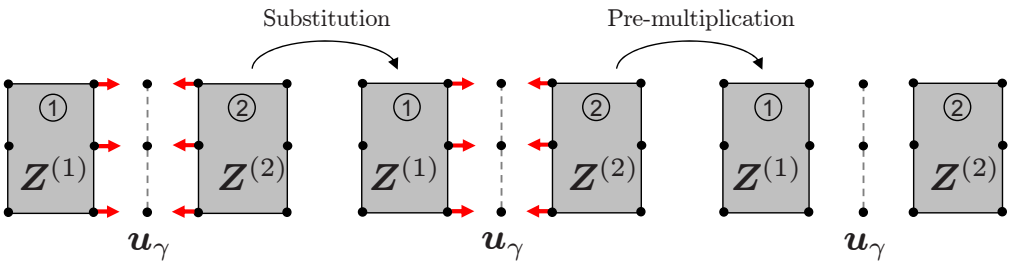

Fig. 3: Simplification of the three-field formulation for stiffness assembly according to primal assembly.

2.1.3 A mix of both: Dirichlet-Neumann assembly

In addition to the primal and dual assembly methods treated above, the assembled equations in (4) can also be simplified by combining both methods, that is, by choosing both a unique set of interface DoF and interface forces. Thereby, both the equilibrium and compatibility condition on the interface are satisfied *a priori*. This gives rise to the following transformation:

$$\begin{bmatrix} \boldsymbol{u}_i^{(1)} \\ \boldsymbol{u}_b^{(1)} \\ \boldsymbol{u}_i^{(2)} \\ \boldsymbol{u}_b^{(2)} \\ \boldsymbol{g}_b^{(1)} \\ \boldsymbol{g}_b^{(2)} \\ \boldsymbol{u}_\gamma \end{bmatrix} = \begin{bmatrix} \boldsymbol{I} & \boldsymbol{0} & \boldsymbol{0} & \boldsymbol{0} \\ \boldsymbol{0} & \boldsymbol{0} & \boldsymbol{0} & \boldsymbol{L}_b^{(1)} \\ \boldsymbol{0} & \boldsymbol{I} & \boldsymbol{0} & \boldsymbol{0} \\ \boldsymbol{0} & \boldsymbol{0} & \boldsymbol{0} & \boldsymbol{L}_b^{(2)} \\ \boldsymbol{0} & \boldsymbol{0} & -\boldsymbol{B}_b^{(1)^T} & \boldsymbol{0} \\ \boldsymbol{0} & \boldsymbol{0} & -\boldsymbol{B}_b^{(2)^T} & \boldsymbol{0} \\ \boldsymbol{0} & \boldsymbol{0} & \boldsymbol{0} & \boldsymbol{I} \end{bmatrix} \begin{bmatrix} \boldsymbol{u}_i^{(1)} \\ \boldsymbol{u}_i^{(2)} \\ \boldsymbol{\lambda} \\ \boldsymbol{u}_\gamma \end{bmatrix}$$

Substitution of this transformation in the three field assembled equations of motion in (4) simultaneously introduces the interface force field $\boldsymbol{\lambda}$ and eliminates the substructure boundary DoF $\boldsymbol{u}_b^{(s)}$, as illustrated in figure 4. This gives:

$$\begin{bmatrix} \boldsymbol{Z}_{ii}^{(1)} & \boldsymbol{0} & \boldsymbol{0} & \boldsymbol{Z}_{ib}^{(1)}\boldsymbol{L}_b^{(1)} \\ \boldsymbol{Z}_{bi}^{(1)} & \boldsymbol{0} & -\boldsymbol{B}_b^{(1)^T} & \boldsymbol{Z}_{bb}^{(1)}\boldsymbol{L}_b^{(1)} \\ \boldsymbol{0} & \boldsymbol{Z}_{ii}^{(2)} & \boldsymbol{0} & \boldsymbol{Z}_{ib}^{(2)}\boldsymbol{L}_b^{(2)} \\ \boldsymbol{0} & \boldsymbol{Z}_{bi}^{(2)} & -\boldsymbol{B}_b^{(2)^T} & \boldsymbol{Z}_{bb}^{(2)}\boldsymbol{L}_b^{(2)} \end{bmatrix} \begin{bmatrix} \boldsymbol{u}_i^{(1)} \\ \boldsymbol{u}_i^{(2)} \\ \boldsymbol{\lambda} \\ \boldsymbol{u}_\gamma \end{bmatrix} = \begin{bmatrix} \boldsymbol{f}_i^{(1)} \\ \boldsymbol{f}_b^{(1)} \\ \boldsymbol{f}_i^{(2)} \\ \boldsymbol{f}_b^{(2)} \end{bmatrix}, \tag{9}$$

where three lines of zeros have dropped out of the equation, resulting in a square system of equations. As can be seen this expression for the assembled system is non symmetric, therefore in practice this form of the assembled equations is often not very useful. Pre-multiplication with this transformation matrix does solve this, as it eliminates the Lagrange multipliers and results in the primal assembled system obtained in (8). The reason we still show this type of assembly is that a similar transformation is used in the case of mixed assembly. Note that the name of this type of assembly refers to the way the assembled system can be solved, namely using the Gauss-Seidel method. This leads to so-called Dirichlet-Neumann iterations known from domain decomposition theory [27].

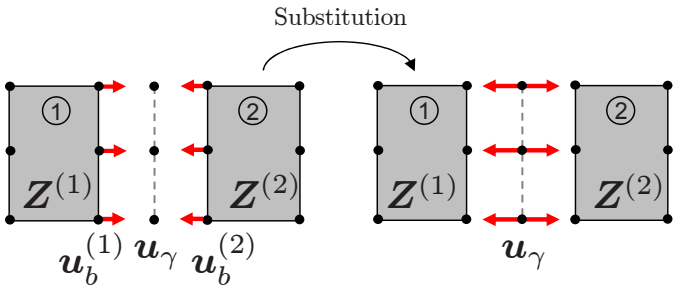

Fig. 4: Simplification of the three-field formulation for stiffness assembly using to Dirichlet-Neumann assembly.

2.2 Receptance Assembly

In this section we will address the assembly of two subsystems expressed in terms of flexibility. These substructure models can for example result from direct measurements or a modal synthesis from an FE model or measurement. For such systems, the equations of motion are as follows:

$$\boldsymbol{u}^{(s)}(\omega) = \boldsymbol{Y}^{(s)}(\omega)\left(\boldsymbol{f}^{(s)}(\omega) + \boldsymbol{g}^{(s)}(\omega)\right) \tag{10}$$

The true degrees of freedom for this problem are not the displacements $\boldsymbol{u}$, but the unknown coupling forces $\boldsymbol{g}$. Hence we can write the equations of motion as:

$$\boldsymbol{Y}^{(s)}\boldsymbol{g}^{(s)} = \boldsymbol{u}^{(s)} - \boldsymbol{Y}^{(s)}\boldsymbol{f}^{(s)} = \boldsymbol{u}^{(s)} - \boldsymbol{p}^{(s)}$$

Here the vector $\boldsymbol{p}$ can be interpreted as a displacement excitation vector resulting from the externally applied forces. However, since by definition $\boldsymbol{g}$ is only non-zero at the boundary DoF, the problem reduces to the interface DoF:

$$\boldsymbol{Y}_{bb}^{(s)}\boldsymbol{g}_b^{(s)} = \boldsymbol{u}_b^{(s)} - \boldsymbol{p}_b^{(s)}$$

This indicates that in order to assemble receptance FRF models, only information at the interface DoF is needed. Mathematically, this is due to fact that the receptance FRF matrix is the inverse of the dynamic stiffness matrix and thereby implicitly a "condensed" matrix. In contrast to the dynamic stiffness matrix, the receptance matrix is therefore not a sparse matrix but is in general non-zero at all of its entries. Physically, this means that every single receptance FRF contains all of the structure's dynamics and as a result, the interface receptance FRFs are sufficient for an FBS analysis. In case one is also interested in the responses at internal points in the structure after assembly, these responses can be reconstructed once the interface behavior is computed.

Based on the above equation we can now set up the Lagrangian of the receptance assembly problem as:

$$\mathscr{L}\left(\boldsymbol{g}_b^{(s)}, \boldsymbol{u}_b^{(s)}, \boldsymbol{u}_\gamma\right) = \sum_s \left(\frac{1}{2}\boldsymbol{g}_b^{(s)^T}\boldsymbol{Y}_{bb}^{(s)}\boldsymbol{g}_b^{(s)} + \boldsymbol{p}_b^{(s)^T}\boldsymbol{g}_b^{(s)} + \boldsymbol{g}_b^{(s)^T}\left(\boldsymbol{L}_b^{(s)}\boldsymbol{u}_\gamma - \boldsymbol{u}_b^{(s)}\right)\right) \tag{11}$$

As before we now consider the assembly of two subsystems for the sake of illustration, as shown schematically in figure 1 (b). Taking again the variation of this expression to the free variables, one obtains the assembled equations of motion as:

$$\begin{bmatrix} \boldsymbol{Y}_{bb}^{(1)} & \boldsymbol{0} & \boldsymbol{L}_b^{(1)} \\ \boldsymbol{0} & \boldsymbol{Y}_{bb}^{(2)} & \boldsymbol{L}_b^{(2)} \\ \boldsymbol{L}_b^{(1)^T} & \boldsymbol{L}_b^{(2)^T} & \boldsymbol{0} \end{bmatrix} \begin{bmatrix} \boldsymbol{g}_b^{(1)} \\ \boldsymbol{g}_b^{(2)} \\ \boldsymbol{u}_\gamma \end{bmatrix} = \begin{bmatrix} -\boldsymbol{p}_b^{(1)} \\ -\boldsymbol{p}_b^{(2)} \\ \boldsymbol{0} \end{bmatrix} \tag{12}$$

Note that although we started from a three field formulation, the above equation is actually the dual assembled form for flexibility type of substructures, as can be seen by comparing eqs. (12) and (2.2). In contrast to the dynamic stiffness assembly of the previous section, here the dual DoF are the interface connection forces, while the intermediate interface displacements constitute the unique field. The compatibility conditions for the components are stated implicitly in the first and second rows; in case some form of filtering is applied to the FRFs (e.g. modal synthesis and truncation), compatibility is required in a weakened form only. The third row can be recognized as the equilibrium condition.

From the above set of assembled equations, the only simplification to be made is to go to a true primal system as in the previous section. As in the dual assembly of the previous section, we again choose the interface forces in the form:

$$\boldsymbol{g}_b^{(s)} = -\boldsymbol{B}_b^{(s)^T} \lambda \tag{13}$$

As before, this gives the following transformation:

$$\begin{bmatrix} \boldsymbol{g}_b^{(1)} \\ \boldsymbol{g}_b^{(2)} \\ \boldsymbol{u}_\gamma \end{bmatrix} = \begin{bmatrix} -\boldsymbol{B}_b^{(1)^T} & \boldsymbol{0} \\ -\boldsymbol{B}_b^{(2)^T} & \boldsymbol{0} \\ \boldsymbol{0} & \boldsymbol{I} \end{bmatrix} \begin{bmatrix} \lambda \\ \boldsymbol{u}_\gamma \end{bmatrix}$$

Again, we first substitute the above transformation in eq. (12). This introduces the unique interface force field λ and eliminates the $\boldsymbol{g}_b^{(s)}$, hence the equilibrium condition is satisfied. Pre-multiplication then eliminates the interface displacement field (illustrated in figure 5) and gives the primal assembled system in terms of the unknown interface force intensities λ only:

$$\left(\boldsymbol{B}_b^{(1)}\boldsymbol{Y}_{bb}^{(1)}\boldsymbol{B}_b^{(1)^T} + \boldsymbol{B}_b^{(2)}\boldsymbol{Y}_{bb}^{(2)}\boldsymbol{B}_b^{(2)^T}\right)\lambda = -\left(\boldsymbol{B}_b^{(1)}\boldsymbol{p}_b^{(1)} + \boldsymbol{B}_b^{(2)}\boldsymbol{p}_b^{(2)}\right)$$

It should be noted that this exactly the same expression as would be obtained from the elimination of the Lagrange multipliers in . When this expression for λ, combined with eq. (13), is then used in the subsystem models (10), one essentially ends up with the assembled equation as found from the LM FBS method.

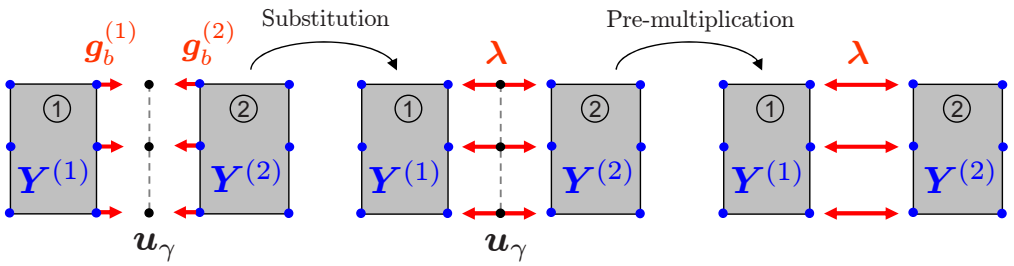

Fig. 5: Simplification of the three-field formulation of the flexibility assembly case.

2.3 Mixed Assembly

In this section we consider the case of mixed assembly, where one subsystem is expressed in dynamic stiffness form while the other is represented using receptance FRFs. This is for instance the case when directly assembling an FE model (possibly with frequency dependent behavior) and a measured component model. To derive the assembled equations of motion in this case,

one simply combines the Lagrangians found earlier for the stiffness and flexibility assembly cases in eqs. (3) and (11) and takes their variation.

Let us consider the case where we want to assemble substructure 1, expressed in dynamic stiffness form, with component 2, which has a receptance representation. This is schematically shown in figure 1 (c). The following three field assembled equations are then found from a variational approach:

$$\begin{bmatrix} \boldsymbol{Z}_{ii}^{(1)} & \boldsymbol{Z}_{ib}^{(1)} & \boldsymbol{0} & \boldsymbol{0} & \boldsymbol{0} \\ \boldsymbol{Z}_{bi}^{(1)} & \boldsymbol{Z}_{bb}^{(1)} & -\boldsymbol{I} & \boldsymbol{0} & \boldsymbol{0} \\ \boldsymbol{0} & -\boldsymbol{I} & \boldsymbol{0} & \boldsymbol{0} & \boldsymbol{L}_b^{(1)} \\ \boldsymbol{0} & \boldsymbol{0} & \boldsymbol{0} & \boldsymbol{Y}_{bb}^{(2)} & \boldsymbol{L}_b^{(2)} \\ \boldsymbol{0} & \boldsymbol{0} & \boldsymbol{L}_b^{(1)^T} & \boldsymbol{L}_b^{(2)^T} & \boldsymbol{0} \end{bmatrix} \begin{bmatrix} \boldsymbol{u}_i^{(1)} \\ \boldsymbol{u}_b^{(1)} \\ \boldsymbol{g}_b^{(1)} \\ \boldsymbol{g}_b^{(2)} \\ \boldsymbol{u}_\gamma \end{bmatrix} = \begin{bmatrix} \boldsymbol{f}_i^{(1)} \\ \boldsymbol{f}_b^{(1)} \\ \boldsymbol{0} \\ \boldsymbol{p}_b^{(2)} \\ \boldsymbol{0} \end{bmatrix} \tag{14}$$

In this equation, the third row is the compatibility condition for component 1 while the fourth row can be recognized as the (possibly weakened) compatibility condition for component 2. The fifth row constitutes the equilibrium condition.

As in the previous sections, the three field assembled equations of motion can be simplified to find a more compact expression. However, since we are considering mixed assembly, we cannot simply apply the primal or dual assembly methods of the previous sections. Instead, we should also mix the transformations. First it should be realized that in the case of mixed assembly we need *both* a unique interface displacement $\boldsymbol{u}_\gamma$ field and unique interface force field λ to facilitate the interaction between the force and displacement DoF of both substructures. One can then devise a transformation in the form:

$$\begin{bmatrix} \boldsymbol{u}_i^{(1)} \\ \boldsymbol{u}_b^{(1)} \\ \boldsymbol{g}_b^{(1)} \\ \boldsymbol{g}_b^{(2)} \\ \boldsymbol{u}_\gamma \end{bmatrix} = \begin{bmatrix} \boldsymbol{I} & \boldsymbol{0} & \boldsymbol{0} \\ \boldsymbol{0} & \boldsymbol{L}_b^{(1)} & \boldsymbol{0} \\ \boldsymbol{0} & \boldsymbol{0} & -\boldsymbol{B}_b^{(1)^T} \\ \boldsymbol{0} & \boldsymbol{0} & -\boldsymbol{B}_b^{(2)^T} \\ \boldsymbol{0} & \boldsymbol{I} & \boldsymbol{0} \end{bmatrix} \begin{bmatrix} \boldsymbol{u}_i^{(1)} \\ \boldsymbol{u}_\gamma \\ \lambda \end{bmatrix}$$

This transformation corresponds to primal assembly for the first structure as in the previous section, whereas the second component is subject to Dirichlet-Neumann assembly as outlined in section 2.1.3. Substitution of this transformation in eq. (14) introduces both the unique interface force field and eliminates $\boldsymbol{u}_b^{(2)}$. Pre-multiplication is needed only for the sake of symmetry and gives the mixed assembled system:

$$\begin{bmatrix} \boldsymbol{Z}_{ii}^{(1)} & \boldsymbol{Z}_{ib}^{(1)}\boldsymbol{L}_b^{(1)} & \boldsymbol{0} \\ \boldsymbol{L}_b^{(1)^T}\boldsymbol{Z}_{bi}^{(1)} & \boldsymbol{L}_b^{(1)^T}\boldsymbol{Z}_{bb}^{(1)}\boldsymbol{L}_b^{(1)} & \boldsymbol{L}_b^{(1)^T}\boldsymbol{B}_b^{(1)^T} \\ \boldsymbol{0} & -\boldsymbol{B}_b^{(2)}\boldsymbol{L}_b^{(2)} & -\boldsymbol{B}_b^{(2)}\boldsymbol{Y}_{bb}^{(2)}\boldsymbol{B}_b^{(2)^T} \end{bmatrix} \begin{bmatrix} \boldsymbol{u}_i^{(1)} \\ \boldsymbol{u}_\gamma \\ \lambda \end{bmatrix} = \begin{bmatrix} \boldsymbol{f}_i^{(1)} \\ \boldsymbol{L}_b^{(1)^T}\boldsymbol{f}_b^{(1)} \\ -\boldsymbol{B}_b^{(2)}\boldsymbol{p}_b^{(2)} \end{bmatrix} \tag{15}$$

Note that, as expected, the above mixed assembled system is symmetric, since we know that:

$$\sum_s \boldsymbol{B}_b^{(s)}\boldsymbol{L}_b^{(s)} = \sum_s \left(\boldsymbol{L}_b^{(s)^T}\boldsymbol{B}_b^{(s)^T}\right)^T = \boldsymbol{0}$$

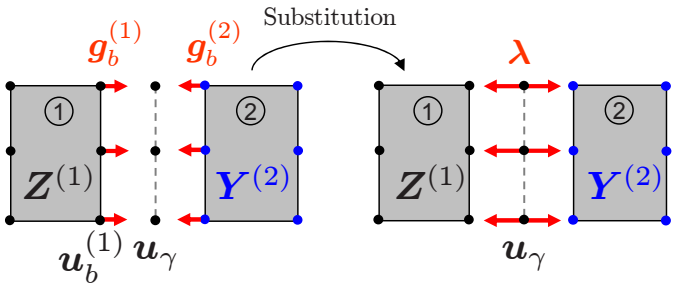

Fig. 6: Simplification of the three-field formulation of the mixed assembly case.

For the sake of illustration, let us now simplify the above assembled equations for the case where the boundary DoF of both substructures are ordered equally. In this case $\boldsymbol{L}_b^{(1)}$, $\boldsymbol{L}_b^{(2)}$ and $\boldsymbol{B}_b^{(2)}$ are identity matrices, while $\boldsymbol{B}_b^{(1)}$ is minus identity. If we reorder the DoF sets such that the Lagrange multipliers are associated to component 1 and the interface displacement field is associated to component 2, we can write the assembled equations of motion according to:

$$\begin{bmatrix} \boldsymbol{Z}_{ii}^{(1)} & \boldsymbol{Z}_{ib}^{(1)} & \boldsymbol{0} \\ \boldsymbol{Z}_{bi}^{(1)} & \boldsymbol{Z}_{bb}^{(1)} & -\boldsymbol{I} \\ \boldsymbol{0} & -\boldsymbol{I} & -\boldsymbol{Y}_{bb}^{(2)} \end{bmatrix} \begin{bmatrix} \boldsymbol{u}_i^{(1)} \\ \boldsymbol{u}_\gamma \\ \boldsymbol{\lambda} \end{bmatrix} = \begin{bmatrix} \boldsymbol{f}_i^{(1)} \\ \boldsymbol{f}_b^{(1)} \\ -\boldsymbol{p}_b^{(2)} \end{bmatrix} \tag{16}$$

From the above equation one can clearly see the way the two systems interact. In addition to the external excitations, component 2 is excited by interface displacements from component 1 through its boundary DoF, while component 1 feels and additional forces from component 2 through its interface.

The mixed assembly expression in (15) will form the basis for the alternative "inverse free" FBS method, although we could also take eq. (12) as a starting point. The mixed assembly expression is somewhat more general in the sense that it can also handle frequency dependent properties in the dynamic stiffness matrix. For cases in which we deal with measured receptance FRF matrices only, or the FE modeled substructures can be converted to receptance FRFs (e.g. through modal synthesis), one could however also start from (12). The method for solving the assembled equations outlined in the next section is equally valid for both representations.

3 Solving the Assembled Equations

As can be seen from section 2, the system that has to be solved (i.e. eq. 15) contains a dynamic stiffness part, a receptance part and a number of off-diagonal coupling terms. From this system of coupled subsystem equations we, in general, want to find a set of assembled eigenfrequencies and modes or a set of coupled FRFs. One approach would be to either transform the mixed equations into a stiffness or flexibility form, but in order to do so we eventually need to invert the flexibility matrix of the interface of the measured system. This will then result in exactly the same sensitivity to measurement errors as found with the classical experimental substructuring techniques.

Another approach would be to try to obtain the eigenfrequencies and modes directly from the mixed assembled of equations. One such method was first presented Wittrick and Williams in the 1970's [29]. With this method, which will be explained in this section, one is able to determine the natural undamped frequencies of any linearly elastic structure if either its dynamic stiffness or receptance FRF matrix is known.

3.1 Identification of Eigenfrequencies

For the readers' general understanding, the concept and basic algorithm of the method will be briefly described in this section. The algorithm is based on a theorem postulated by Rayleigh his classic work on the *Theory of Sound* [25]:

> "If one constraint is imposed upon a linearly elastic structure, whose natural frequencies of vibration, arranged in ascending order of magnitude, are ω_r, the natural frequencies $\tilde{\omega}_r$ of the constrained structure are such that: $\omega_r < \tilde{\omega}_r < \omega_{r+1} \quad r = 1,2,3,..$".

This can be reformulated as:

> "If one constraint is removed from a structure, the number of natural frequencies which lie below some fixed chosen frequency either remains unchanged ore increases by one".

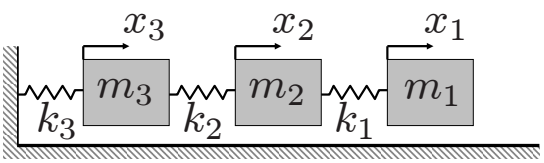

Fig. 7: mass & spring model

This reasoning has been illustrated using figures 7 and 8. Figure 7 is a simple three DoF mass - spring system and in figure 8 three different plots are shown where the solid lines represent the driving point FRFs of:

- x_1 with both x_2 and x_3 constrained,
- x_2 with x_1 unconstrained and x_3 constrained,
- x_3 with both x_1 and x_2 unconstrained.

The theorem stated above can also be easily verified from figure 8.

The method devised by Wittrick and Williams uses the number of negative eigenvalues of the dynamic stiffness matrix at a certain frequency ω_j to determine the number of natural frequencies of the dynamic system which can be found below this particular frequency. In their work, the number of negative eigenvalues of the matrix is called its *sign count* $s(\boldsymbol{Z}(\omega_j))$. In order to compute the sign count of the matrix, we let Z_r be the leading principle minor of order r of $\boldsymbol{Z}(\omega_j)$, i.e. the determinant of the $r \times r$ matrix formed by the first r rows and columns of $\boldsymbol{Z}(\omega_j)$ and the zeroth order minor Z_0 is set to $+1$. Physically, one can understand this as fully constraining the system and releasing one DoF at a time and computing the determinant of these constrained systems. The resulting sequence of determinants of a growing system is called a Sturm sequence. Now it is known that the number of changes of sign between consecutive members of the Sturm sequence:

$$\{Z_0, Z_1, Z_2, \ldots, Z_n\}$$

is equal to the number of natural frequencies of the system below ω_j). So, using this sequence one can determine at which frequencies the sign count changes and thus find the natural frequencies of the system. This procedure is visualized in figure 8, where the development of the thee leading principle minors is plotted. It can be shown that the sign count of the dynamic stiffness matrix $\boldsymbol{Z}(\omega)$ is equal to that of its inverse, the receptance matrix $\boldsymbol{Y}(\omega)$ [29]. In order to show that this method can

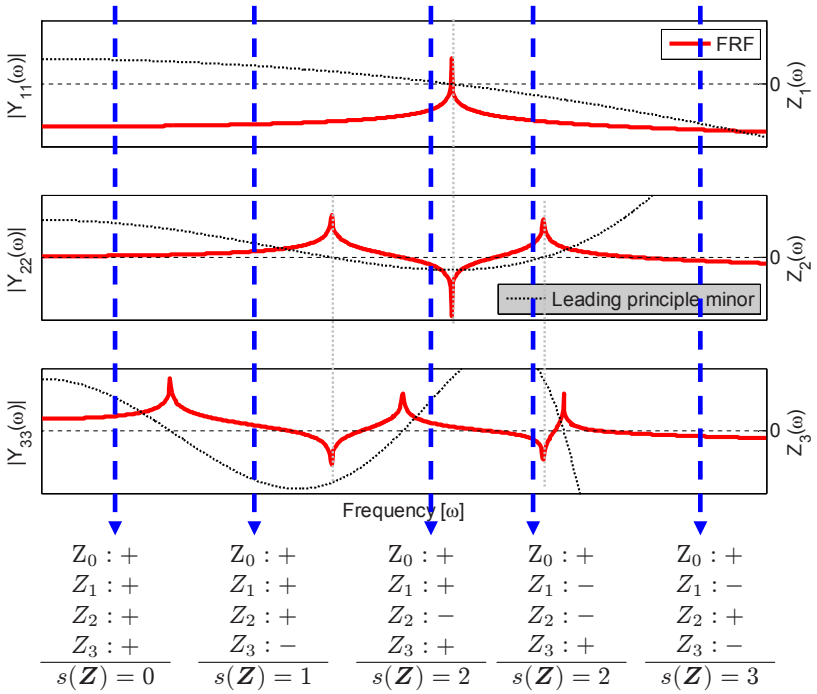

Fig. 8: Computing the sign count

also be used to compute the natural frequencies of the mixed assembled system (15), the dynamic system of figure 7 is used again as an example. The first subsystem A, consisting of m_1,m_2,k_1 and k_2 is still in the form of a dynamic stiffness matrix:

$$\boldsymbol{Z}_A(\omega) = \left[\begin{bmatrix} k_1 & -k_1 & 0 \\ -k_1 & k_1+k_2 & -k_2 \\ 0 & -k_2 & k_2 \end{bmatrix} - \omega^2 \begin{bmatrix} m_1 & 0 & 0 \\ 0 & m_2 & 0 \\ 0 & 0 & 0 \end{bmatrix} \right] \tag{17}$$

Subsystem B, consisting of m_3 and k_3 is now in the form of a receptance matrix:

$$\boldsymbol{Y}_B(\omega) = \left[k_3 - \omega^2 m_3\right]^{-1}; \tag{18}$$

Using the assembly techniques of section 2, the two subsystems can be assembled directly:

$$\begin{aligned} &\boldsymbol{H}(\omega) = \begin{bmatrix} \boldsymbol{Z}_A(\omega) & \boldsymbol{L}^T\boldsymbol{B}^T \\ \boldsymbol{B}\boldsymbol{L} & -\boldsymbol{Y}_B(\omega) \end{bmatrix} \\ &\text{where: } \boldsymbol{B}\boldsymbol{L} = \begin{bmatrix} 0 & 0 & 1 \end{bmatrix} = \left[\boldsymbol{L}^T\boldsymbol{B}^T\right]^T, \end{aligned} \tag{19}$$

with the associated DoF vector:

$$\boldsymbol{q} = \begin{bmatrix} u_1 & u_2 & u_\gamma & \lambda \end{bmatrix}^T \tag{20}$$

Now, applying the same kind of reasoning for computing the sign count as before, a Sturm sequence has to be build by releasing one constraint at a time and computing the minor of the matrix thereby obtained. From figure 9 we see that the first two principle leading minors are exactly the same as before, as expected. The third shows only one zero crossing, which comes from the fact that by "constraining" λ, the leading principle minor of $\boldsymbol{Z}_A$ is computed, which has one rigid body mode and one natural frequency at infinity. The fourth principle leading minor shows four zero crossings, which are related to the three natural frequencies (indicated by the black markers) of the structure and to the natural frequency of subsystem B (indicated by the starred marker). Clearly, the sign count computed in this way is incorrect and this is due to two reasons. First of all, one should

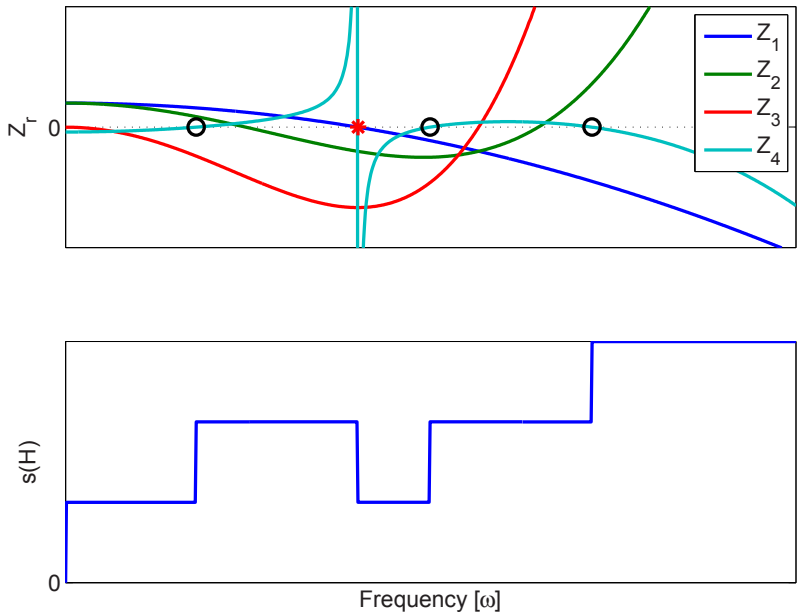

Fig. 9: Computing the sign count

only apply and release constraints on u (and not on λ) when computing the Sturm sequence. Thus Z_3 should not be within the Sturm sequence to compute the sign count of $\boldsymbol{H}(\omega)$. Second of all, the last leading principle minor of $\boldsymbol{H}(\omega)$ is equal to [24]:

$$Z_4 = \det\left(\boldsymbol{H}(\omega)\right) = \det\left(\boldsymbol{Y}_B(\omega)\right)\det\left(\boldsymbol{Z}_A(\omega) + \boldsymbol{L}^T\boldsymbol{B}^T\boldsymbol{Y}_B(\omega)^{-1}\boldsymbol{B}\boldsymbol{L}\right) \tag{21}$$

So it can be seen that the zero crossing related to the natural frequency of subsystem B will always be present in the leading principle minor Z_4 and that the second term in equation 21 is in fact a primal assembly of the interface stiffness' of the two subsystems. In order to avoid the zero crossing due to the natural frequency of subsystem B, an alternative minor is used in the Sturm sequence (Z_1,Z_2,Z_{c3}):

$$Z_{c3} = \det\left(\boldsymbol{H}(\omega)\right)\det\left(\boldsymbol{Y}_B(\omega)\right)^{-1} = \det\left(\boldsymbol{Z}_A(\omega) + \boldsymbol{L}^T\boldsymbol{B}^T\boldsymbol{Y}_B(\omega)^{-1}\boldsymbol{B}\boldsymbol{L}\right) \tag{22}$$

If the sign count algorithm is applied to this new Sturm sequence, the correct results are obtained, as can be seen in figure 10.

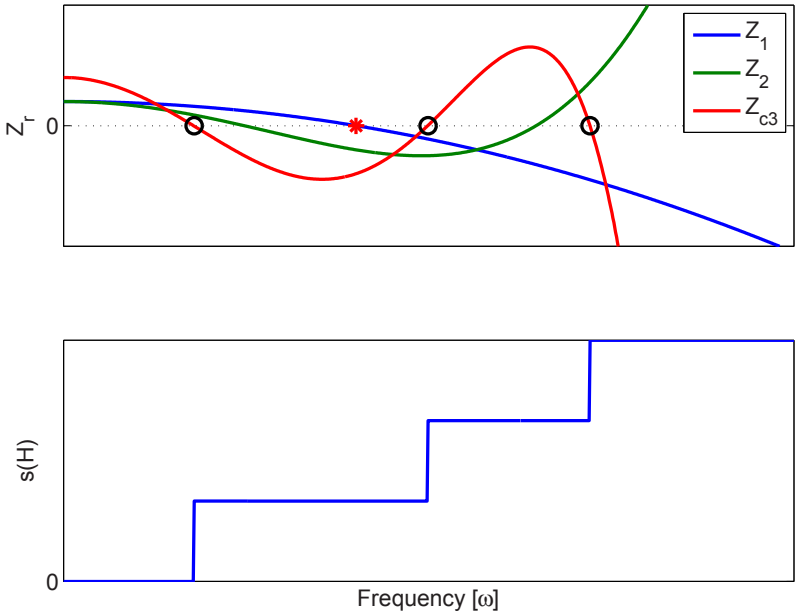

Fig. 10: Computing the sign count

3.2 Identification of Eigenmodes

Using the natural frequencies of the assembled system obtained using the sign count method, the corresponding eigenmodes can also be identified. At an eigenfrequency of the assembled system, the following holds:

$$\boldsymbol{H}(\omega_r)\boldsymbol{q} = \boldsymbol{0}, \quad \text{for } r = 1,2,\ldots,n \tag{23}$$

Since the sign count approximates the location of the eigenfrequency and is limited by the frequency resolution, (23) will most likely not hold exactly:

$$\boldsymbol{H}(\omega_r)\boldsymbol{q} = \boldsymbol{\varepsilon}, \quad \text{for } r = 1,2,\ldots,n \ , \tag{24}$$

where $||\varepsilon|| << 1$. This equation is solved by performing an eigenvalue analysis on $\boldsymbol{H}(\omega_r)$ and selecting the eigenmode ($\boldsymbol{x}_1$) corresponding to the lowest eigenvalue μ_1 as the mode shape ϕ_r corresponding to the eigenfrequency ω_r:

$$\begin{aligned} &(\boldsymbol{H}(\omega_r) - \mu_1 \boldsymbol{I})\,\boldsymbol{x}_1 = \boldsymbol{0}, \qquad \mu_1 < \mu_2 < \ldots < \mu_n \\ &\text{then: } \phi_r = \boldsymbol{x}_1 \end{aligned} \tag{25}$$

However, the mode shapes identified in this way have an arbitrary scaling factor and also include a number of interface force terms λ. In order to synthesize the receptance FRFs of the assembled structure, the interface force entries have to expanded to the subsystem responses and the mode shapes have to be mass normalized. One way of doing this is to compute the driving point FRF of the structure, by taking the inverse of $\boldsymbol{H}(\omega)$ at a limited number of points around the natural frequencies. Then, by using the normal mode model (26), the unknown real scalars a_r can be determined in a least squares sense.

$$\boldsymbol{Y}_{jj}(\omega) = \sum_{r=1}^{n} \frac{a_r^2 \phi_{j,r} \phi_{j,r}^T}{-\omega^2 + \omega_r^2 + 2i\zeta_r \omega \omega_r} \tag{26}$$

Note that this scaling scheme could be very sensitive to the estimates of the modal damping ζ_r and the frequency resolution.

3.3 Some Comments

During the research that preceded this paper, other approaches towards an inverse-free FBS method have also been investigated. For example, we have tried solving the LM FBS equations using an iterative Conjugate Gradient approach in order to avoid direct computation of the inverse of the interface flexibility matrices. Furthermore, we attempted to directly invert the mixed assembled equations in eq. (15). After performing Monte Carlo simulations on these variants (see next section), it turned out that they all showed exactly the same sensitivity to errors as the classic FBS methods. The reason is that essentially the same equations are solved, albeit in a different way, and errors propagate and amplify regardless of the exact method used to solve the equations. Hence, we concluded that a truly different approach to solving the equations was needed, which did not involve computing any inverse, whether explicitly or implicitly.

The trick of the proposed method is not in the fact that it completely avoids solving/inverting the system matrices, since a partial factorization of the assembled equations is still required for the computation of the sign count and inversion of the mixed assembled matrix is still needed at some frequencies for the mode scaling. The key feature however is that the results of these computations are not used directly in further computations. This is in contrast to normal FBS methods, where the inverted (interface) FRF matrices are used to calculate the total assembled FRF matrix. It is through those computations that the sensitivity to measurement errors is propagated to all the FRFs. We therefore hypothesize that in the current approach, the propagation of errors is limited. Whether this is indeed the case will be investigated in the next section.

4 Case Study

In this section the results of a case study are presented. The simple problem used for this study is shown in figure 11 and consists of two lightly damped mass-spring-damper systems (modal damping $< 1\%$). Subsystem A has 7 degrees of freedom, subsystem B possesses 4 DoF and the systems are coupled at a 2 DoF interface. When combined the system AB is formed. The system parameters are listed in table 1; Rayleigh damping is added ($\boldsymbol{C} = \alpha \boldsymbol{M} + \beta \boldsymbol{K}$) with $\alpha = 0.01$ and $\beta = 0$.

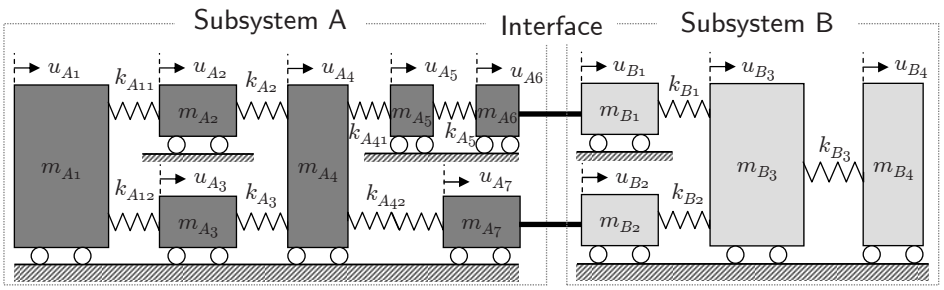

Fig. 11: Simple system used for case study.

Component A is assumed to be modeled analytically and hence will be expressed in a dynamic stiffness format. We imagine subsystem B to be modeled experimentally and as a result is expressed in the receptance FRF format. In the remainder of this section we will perform several analyses on this simple system to illustrate the method laid out in the previous two sections. First, in the next subsection we will take the nominal system models (i.e. without any perturbations due to "measurement errors") and identify the eigenfrequencies and -modes and synthesize the assembled FRF. Thereafter we will perform a sensitivity analysis using the Monte Carlo method in order to determine whether the proposed alternative FBS methodology is indeed less sensitive to measurement errors than the traditional methods.

4.1 Calculation of Assembled Modes and FRFs

Using the sign counting method described in the previous section, the first analysis of the mixed form of the assembled system (i.e. eq. (15)) was to identify its eigenfrequencies. Obviously, the accuracy with which one can determine these eigenfrequencies is limited by the frequency resolution of the model/measurement of the subsystems. Therefore, we performed an analysis with

System parameters			
Mass [kg]	Stiffness [N/m]	Mass [kg]	Stiffness [N/m]
$m_{A1} = 10$	$k_{A11} = 2 \cdot 10^3$	$m_{B1} = 2$	$k_{B1} = 1 \cdot 10^3$
$m_{A2} = 3$	$k_{A12} = 2 \cdot 10^3$	$m_{B2} = 4$	$k_{B2} = 1 \cdot 10^3$
$m_{A3} = 3$	$k_{A2} = 1 \cdot 10^3$	$m_{A3} = 8$	$k_{B3} = 2 \cdot 10^3$
$m_{A4} = 6$	$k_{A3} = 1 \cdot 10^3$	$m_{B4} = 5$	
$m_{A5} = 2$	$k_{A41} = 0.5 \cdot 10^3$		
$m_{A6} = 2$	$k_{A42} = 1 \cdot 10^3$		
$m_{A7} = 4$	$k_{A5} = 0.2 \cdot 10^3$		

Table 1: Parameters of mass-spring systems

both 100 and 500 frequency points, corresponding to a frequency resolution of 0.5Hz and 0.1Hz respectively, on the interval from 0 to 50 Hz. The results are listed in table 2 below and are pretty satisfactory, with errors on the identified frequencies limited to 3% with respect to the true eigenfrequencies. As expected, the higher frequency resolution analysis gave slightly more accurate results.

Mode no.	**True freq.** [Hz]	**Identified freq.** $\Delta f = 0.5Hz$ [Hz]	**Difference** [%]	**Identified freq.** $\Delta f = 0.1Hz$ [Hz]	**Difference** [%]
ω_1	0	0	0	0	0
ω_2	7.02	7.25	3.3	7.05	0.5
ω_3	15.26	15.25	-0.1	15.25	-0.1
ω_4	16.21	16.25	0.2	16.25	0.2
ω_5	19.53	19.75	1.1	19.55	0.1
ω_6	24.70	24.75	0.2	24.65	-0.2
ω_7	28.67	28.75	0.3	28.65	-0.1
ω_8	30.69	30.75	0.2	30.65	-0.1
ω_9	39.58	39.75	0.4	39.55	-0.1

Table 2: Identified eigenfrequencies of assembled system

With the eigenfrequencies identified, the next step is to obtain the associated mode shapes in the way described in the previous section. As for the frequencies, the accuracy of the identified mode shapes is dependent on the frequency resolution of the models. Using the same two frequency resolutions as for the identification of the eigenfrequencies, the corresponding mode shapes are identified and compared to the true mode shapes using the MAC criterion [1]. The results are shown in figure 12. For the case of the coarse frequency spacing of 0.5 Hz, it can be seen that the results are not so good for the closely spaced modes. Increasing the frequency resolution to 0.1Hz solves this problem and all the modes are accurately identified; all MAC values are larger than 0.99 with respect to the true mode shapes obtained analytically.

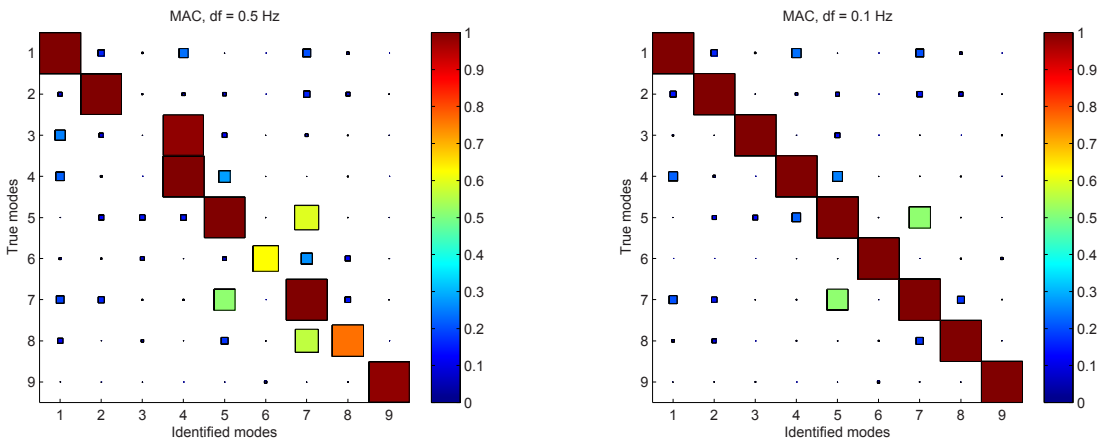

Fig. 12: MAC values for identified modes with frequency resolution of 0.5 Hz (left) and 0.1 Hz (right)

Next, we take the results obtained from the case with highest frequency resolution and try to synthesize the receptance FRFs of the assembled system. The difficulty with doing so is that no damping values are obtained from the procedure outlined in the previous section. Hence, the modal damping values are estimated at the average of the modal damping values of the true system. One of the resulting FRFs (a driving point FRF at DoF 7) is shown in figure 13. It can be seen that the synthesized assembled FRF closely resembles the true FRF of system *AB*, apart from some small discrepancies around resonances and anti-resonances. As explained, these are due to the incorrect damping values and some inaccuracies in the scaling of the mode shapes.

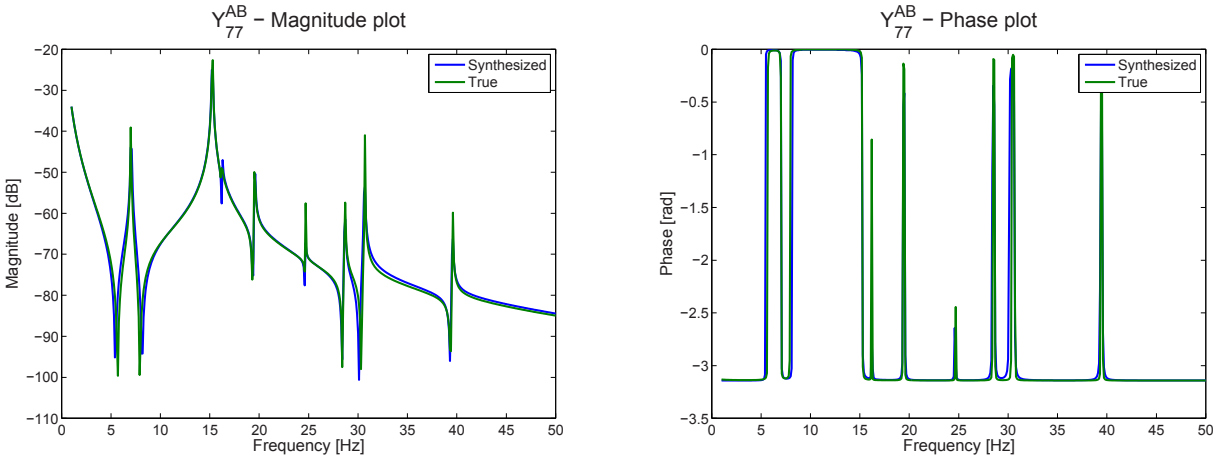

Fig. 13: Synthesized vs. true assembled FRF

4.2 Sensitivity of Assembled FRFs

Now that it was shown in the previous subsection that the proposed method is indeed capable of predicting the assembled mode shapes and FRFs, the question that remains is whether it is more robust than the conventional FBS methods when random measurement errors are present in the subsystem models. To quantify the sensitivity of the approach, a sensitivity analysis was performed in the form of Monte Carlo simulations. To that end, the receptance FRF matrix of component *B*, which was imagined to originate from measurements, was perturbed with a normally distributed random error with a standard deviation of $\pm 2\%$ on the magnitude and ± 2 deg on the phase of the original FRF. This perturbed receptance matrix was then used in the assembly and identification procedures outlined in sections 2 and 3. This was done for a thousand different perturbations and subsequently the mean and standard deviation of the assembled FRFs were calculated to obtain the sensitivity of the approach. The same perturbed FRF matrices of *B* were also used in the LM FBS method, in order to compare sensitivities. Note that the dynamic stiffness matrix of substructure *A* was not perturbed, as this component was assumed to be the analytical component in the assembly.

The results of the sensitivity analysis are shown in figures 14 and 15 for the same assembled FRF considered above, the driving point FRF at DoF 7. From figure 14 it can be seen that the proposed alternative FBS method seems to perform slightly better than the LM FBS method, since the maximum standard deviation is lower. From a more detailed inspection of this figure, we see that the two methods behave quite differently. Where the LM FBS method (and in fact all classic FBS methods [28]) have the largest sensitivity around the eigenfrequencies of the subsystems, the alternative FBS method seems to suffer from this problem to a lesser extent. In fact, it seems to be most sensitive around the global anti-resonances.

The effect of the sensitivities is shown in figure 15, where the average FRF is plotted in black and the 95% confidence interval is shown as a gray band around the FRF. One can see that the alternative FBS method indeed shows the largest uncertainty around its anti-resonances, which is also reflected by the fact that the magnitude at these frequencies is not synthesized entirely correctly (see for instance the first anti-resonance). However, where the LM FBS shows a big sensitivity around 16 Hz, possibly leading to spurious peaks in the assembled FRF, the alternative FBS method shows much smaller uncertainty.

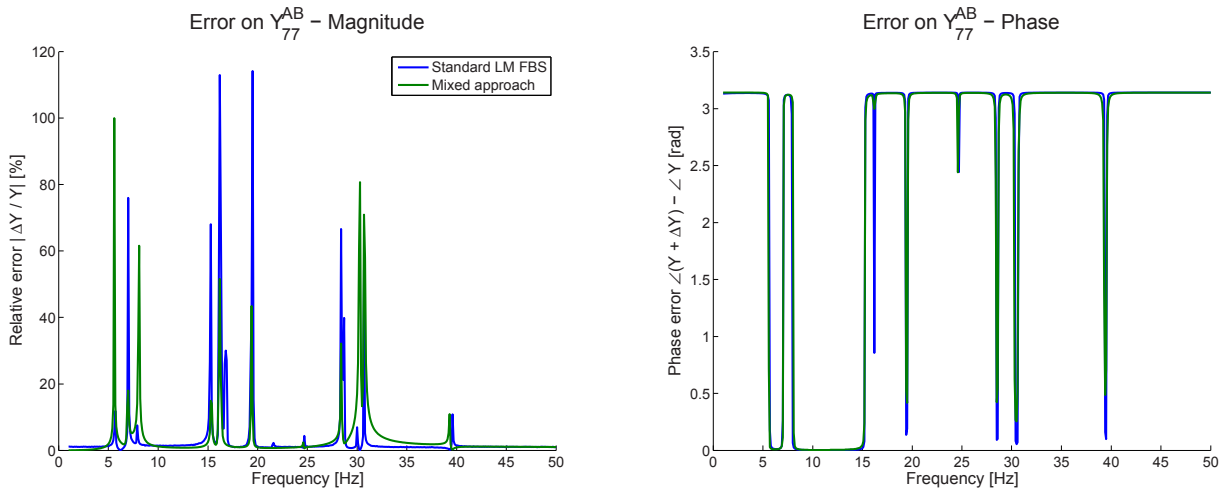

Fig. 14: Standard deviations found from sensitivity analysis

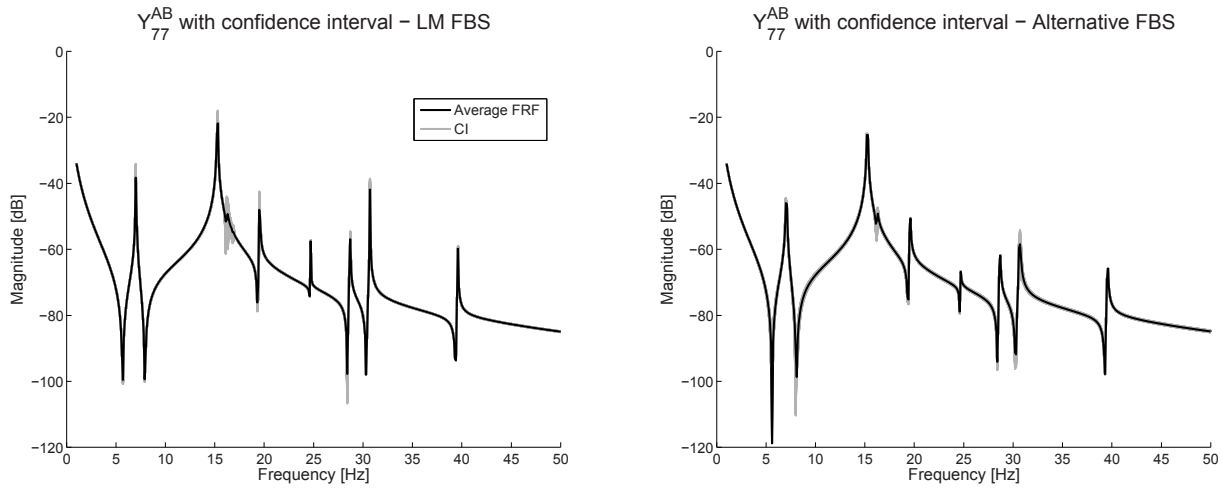

Fig. 15: Assembled FRFs obtained with LM FBS (left) and alternative FBS (right) and their confidence intervals

5 Conclusions & Recommendations

In this paper we presented a first attempt to develop an alternative method for experimental frequency based substructuring. Since the traditional FBS methods suffer from large sensitivity to measurement errors due to the inversion of the interface flexibility FRFs, the aim of this work was to derive an "inverse free" methodology for FBS. To this end, a framework for the assembly of substructure FRF models was presented in section 2. This framework allowed to derive a "mixed assembly" procedure, in which dynamic stiffness and receptance FRFs can be directly coupled without inversion. However, in order to actually solve the mixed assembled models in an inverse free manner, additional procedures were needed. Section 3 therefore presented an algorithm known as "sign counting" which allows to locate the eigenfrequencies of the assembled structure. Based on this information the assembled mode shapes could be extracted and, if needed, the assembled receptance FRFs reconstructed.

A case study on a simple academic system in section 4 was used to illustrate the methodology. This showed that the method indeed is able to identify the modes and frequencies of the assembled system accurately. However, due to a lack of information on damping and difficulties with scaling the mode shapes, reconstructing the assembled receptance FRFs is somewhat more tricky. Nonetheless, reasonably accurate results could still be obtained.

For the method to be truly promising, we needed to asses its sensitivity to measurement errors. Using Monte Carlo simulations with randomly distributed errors on the subsystem FRFs, the sensitivity of the method could be quantified and compared to classic FBS methods. The results indicated that the alternative FBS method seems indeed to be less sensitive to errors in the subsystem descriptions. In contrast to the classic FBS methods the proposed method seems most sensitive around anti-resonances, but seems to suffer less from spurious modes around the subsystem resonances.

However, in order to apply the proposed alternative FBS methodology successfully to an experimental problem there are still a few bottlenecks that we feel need to be tackled:

- Obtaining accurate values for the damping of the assembled system
- Scaling of the identified mode shapes
- Distinguishing between closely spaced modes and measurement artifacts in the sign counting algorithm

Finally, it might be very interesting to apply the proposed methodology to substructure decoupling problems, which are even more sensitive to measurement errors than "normal" (i.e. coupling) FBS problems.

References

1. Allemang, R., Brown, D.: A Correlation Coefficient for Modal Vector Analysis. In: Proceedings of the International Modal Analysis Conference, pp. 110–116. Society for Experimental Mechanics (1982)
2. Allen, M., Mayes, R.: Comparison of FRF and Modal Methods for Combining Experimental and Analytical Substructures. In: Proceedings of the Twentyfifth International Modal Analysis Conference, Orlando, FL. Society for Experimental Mechanics, Bethel, CT (2007)
3. Bregnant, L., Otte, D., Sas, P.: FRF Substructure Synthesis. Evaluation and Validation of Data Reduction Techniques. In: Proceedings of the Twentieth International Conference on Noise & Vibration Engineering (ISMA). Katholieke Universiteit Leuven, Leuven, BE (1995)
4. Campbell, R., Hambric, S.: Application of Frequency Domain Substructure Synthesis Technique for Plates loaded with Complex Attachments. Tech. rep., Pennsylvania State University Park Applied Research Lab (2004)
5. Carne, T.G., Dohrmann, C.R.: Improving Experimental Frequency Response Function Matrices for Admittance Modeling. In: Proceedings of the Twenty Fourth International Modal Analysis Conference, St. Louis, MO. Society for Experimental Mechanics, Bethel, CT (2006)
6. Corus, M., Balmes, E., Nicolas, O.: Using Model Reduction and Data Expansion Techniques to Improve SDM. Mechanical Systems and Signal Processing **20**, 1067–1089 (2006)
7. Duarte, M., Ewins, D.: Some Insights into the Importance of Rotational Degrees of Freedom and Residual Terms in Coupled Structure Analysis. In: Proceedings of the Thirteenth International Modal Analysis Conference, Nashvill, TN, pp. 164–170. Society for Experimental Mechanics, Bethel, CT (1995)
8. Ferreira, J., Ewins, D.: Multi-Harmonic Nonlinear Receptance Coupling Approach. In: Proceedings of the Fifteenth International Modal Analysis Conference, Orlando, FL, pp. 27–33. Society for Experimental Mechanics, Bethel, CT (1997)
9. Gialamas, T., Tsahalis, D., Bregant, L., Otte, D., van der Auweraer, H.: Substruturing by means of FRFs. Some Investigations on the Significance of Rotational DOFs. In: Proceedings of the Fourteenth International Modal Analysis Conference, Dearborn, MI, pp. 619–625. Society for Experimental Mechanics, Bethel, CT (1996)
10. Hunter, N., Paez, T.: Nonlinear Behavior of a 45 Degree Bolted Lap Joint. In: Proceedings of the Twentyfourth International Modal Analysis Conference, St. Louis, MO. Society for Experimental Mechanics, Bethel, CT (2006)
11. Imregun, M., Robb, D.: Structural Modification via FRF Coupling using Measured Data. In: Proceedings of the Tenth International Modal Analysis Conference, San Diego, CA, pp. 1095–1099. Society for Experimental Mechanics, Bethel, CT (1992)
12. Imregun, M., Robb, D., Ewins, D.: Structural modification and coupling dynamic analysis using measured frf data. In: Proceedings of the Fifth International Modal Analysis Conference, London, UK, pp. 1136–1141. Society for Experimental Mechanics, Bethel, CT (1987)
13. de Klerk, D., Rixen, D., de Jong, J.: The Frequency Based Substructuring (FBS) Method Reformulated According to the Dual Domain Decomposition Method. In: Proceedings of the Twenty Fourth International Modal Analysis Conference, St. Louis, MO. Society for Experimental Mechanics, Bethel, CT (2006)
14. de Klerk, D., Rixen, D., Voormeeren, S.: General Framework for Dynamic Substructuring: History, Review and Classification of Techniques. AIAA Journal **46**(5), 1169–1181 (2008)
15. de Klerk, D., Rixen, D., Voormeeren, S., Pasteuning, F.: Solving the RDoF Problem in Experimental Dynamic Substructuring. In: Proceedings of the Twenty Sixth International Modal Analysis Conference, Orlando, FL. Society for Experimental Mechanics, Bethel, CT (2008). Paper no. 129
16. de Klerk, D., Voormeeren, S.: Uncertainty Propagation in Experimental Dynamic Substructuring. In: Proceedings of the Twenty Sixth International Modal Analysis Conference, Orlando, FL. Society for Experimental Mechanics, Bethel, CT (2008). Paper no. 133
17. Lim, T., Li, J.: A Theoretical and Computational Study of the FRF-Based Substructuring Technique applying enhanced Least Square and TSVD Approaches. Journal of Sound and Vibration **231**, 1135–1157 (2000)
18. Liu, W., Ewins, D.: The Importance Assessment of RDOF in FRF Coupling Analysis. In: Proceedings of the Seventeenth International Modal Analysis Conference, Orlando, FL, pp. 1481–1487. Society for Experimental Mechanics, Bethel, CT (1999)
19. Mayes, R., Stasiunas, E.: Combining Lightly Damped Experimental Substructures with Analytical Substructures. In: Proceedings of the Twentyfifth International Modal Analysis Conference, Orlando, FL. Society for Experimental Mechanics, Bethel, CT (2007)
20. Montalvao, D., Ribeiro, A., Maia, N., Silva, J.: Estimation of the Rotational Terms of the Dynamic Response Matrix. Shock and Vibration **11**, 333–350 (2004)
21. O'Callahan, J., Avitabile, P., Riemer, R.: System Equivelant Reduction Expansion Process (SEREP). In: Proceedings of the Seven International Modal Analysis Conference, Las Vegas, NV, pp. 29–37. Society for Experimental Mechanics, Bethel, CT (1989)
22. O'Callahan, J., Lieu, I., Chou, C.: Determination of Rotational Degrees of Freedom for Moment Transfers in Structural Modifications. In: Proceedings of the Third International Modal Analysis Conference, Orlando, FL, pp. 465–470. Society for Experimental Mechanics, Bethel, CT (1985)
23. Pasteuning, F.: Experimental Dynamic Substructuring and its Application in Automotive Research – Substructure modelling, measurement and connectivity. Master's thesis, Delft University of Technology, Faculty of Mechanical, Maritime and Materials Engineering, Department of Precision and Microsystems Engineering (2007)

24. Petersen, K.B., Pedersen, M.S.: The matrix cookbook (2008). URL http://matrixcookbook.com
25. Rayleigh, J.: The Theory of Sound. Dover Publications (1896)
26. Rixen, D.: How measurement inaccuracies induce spurious peaks in Frequency Based Substructuring. In: Proceedings of the Twenty Sixth International Modal Analysis Conference, Orlando, FL. Society for Experimental Mechanics, Bethel, CT (2008). Paper no. 87
27. Tosseli, A., Widlund, O.: Domain Decomposition Methods – Algorithms and Theory, vol. 34. Springer (2004)
28. Voormeeren, S., de Klerk, D., Rixen, D.: Uncertainty Quantification in Experimental Frequency Based Substructuring. Mechanical Systems and Signal Processing **24**(1), 106–118 (2010). Doi:10.1016/j.ymssp.2009.01.016
29. Wittrick, W., Williams, F.: A General Algorithm for Computing Natural Frequencies of Elastic Structures. Quart. Journ. Mech. and Applied Math. **XXIV**, 263–284 (1971)

Model updating methodologies for multibody simulation models: application to a full-scale wind turbine model

Simone Manzato, Bart Peeters, Alessandro Toso, Herman Van der Auweraer
LMS International
Interleuvenlaan 68
B-3001 Leuven, Belgium

Richard Osgood
National Renewable Energy Laboratory
National Wind Technology Center – MS 3911
1617 Cole Blvd.
Golden, CO 80401, USA

ABSTRACT
In the industrial environment, the request for accurate models able to predict the behavior of a structure in different operating conditions is continuously increasing. To analyze the dynamic performances of complex mechanisms, multibody models are widely used, in particular if control laws for these systems need to be defined and tested. Wind turbines represent a typical application in which multibody models are used for control laws development. In this paper, an Experimental Modal Analysis campaign on the CART-3 wind turbine is used as reference to update a tailored multibody model. Standard model updating techniques based on mode shapes and natural frequencies are adapted to be used in a professional CAE environment. The results obtained show a big influence of the correlation indices selected to drive the updating phase.

1. INTRODUCTION

In modern analysis of structural dynamics, an always increasing effort is devoted to the derivation of accurate and reliable models which can be used to simulate the real behavior of the system and optimize its performances. By using experimental data measured on the actual structure, parameter identification and model updating techniques can be applied to refine, correct or update a numerical model [1,2]. However, when applying these techniques, it must be remembered that both the numerical and experimental models are subjected to different types of errors. While numerical models are limited by the assumptions introduced to represent the behavior of the real structure, experimental results can be considered valid only for the test conditions and the amount of information is limited by the number and nature of measured points. Other errors can be due to insufficient excitation, response bandwidth or assumptions introduced during the processing of the results [3,4].

Historically, structural identification and model updating techniques were developed to improve the accuracy of Finite Element models, which are nowadays an industrial standard to simulate and analyze the static and dynamic behavior of mechanical systems. An overview of the more common methods for model updating is given in [1,2,5]. In most applications, the correlation between experimental and numerical models is performed by comparing the natural frequencies and the mode shapes or the Frequency Response Functions. Natural frequencies are usually compared in terms of error between the numerical and experimental values. Common correlation indices developed to compare mode shapes or Frequency Response Function are the Modal Assurance Criterion (MAC) and Frequency Response Assurance Criterion (FRAC), to compare each numerical vector with all the experimental one, and the CoOrdinate Modal Assurance Criterion (COMAC) and the Response Vector Assurance Criterion (RVAC) to compare all the response values at each degree of freedom (COMAC) or natural frequency (RVAC).

Once the correlation between the models is defined, different techniques can be applied to estimate the value of the parameters of the model or to improve them with model updating techniques. By using direct methods, the elements in the stiffness and mass matrices can be updated in a one-step procedure. The main drawback of this technique is that the noise and inaccuracies in the experimental results are exactly reproduced in the numerical model. Moreover, the updated model won't maintain the structural connectivity and the corrected parameters could be not physically meaningful. To overcome these limitations, iterative methods were developed, which are usually posed as optimization problems and make use of the

T. Proulx (ed.), *Linking Models and Experiments, Volume 2*, Conference Proceedings of the Society for Experimental Mechanics Series 5,
DOI 10.1007/978-1-4419-9305-2_24, © The Society for Experimental Mechanics, Inc. 2011

sensitivity of the parameters to update the model. The error between analytical and experimental results is set as an objective function to be minimized by changing a set of physical parameters in the numerical model. Usually, structural model parameter estimation problems based on measured data are often formulated as weighted least-squares problems. To enhance the convergence rate and simplify the optimization, modal metrics, measuring the residuals between measured and model predicted modal data, are built up into a single metric formed as a weighted average of the multiple modal metrics. However, the values assigned to the weights cannot be known a priori and strongly influence the results of the optimization [4]. For these reasons, parameter identification has been also formulated as a multi-objective problem, allowing the minimization of the multiple modal metrics but eliminating the need for using arbitrary weighting factors. The set of multiple optimal solutions will results in a Pareto front from which the user will select the more adequate.

Developing models using the Multibody Simulation (MBS) approach allows the designer to analyze the behavior of complex mechanisms working in a multiphysic environment. Besides analyzing the kinematic and dynamic behavior of the system, they can be integrated with other simulation tools to study, e.g., the durability, aerodynamic, or acoustic performances. They are also widely used to test and design control strategies and more in general to develop mechatronic systems. To take into account for flexibility in a multibody model, three approaches are available. The first one consists in modeling the flexible bodies using the FE method, reduce them using Component Mode Synthesis and linking them to the structure using joints and constraints [6]. For such models, the model updating techniques described above can be directly applied. Another approach is to write the equations of motion of the bodies using a finite element coordinate system approach, in which flexibility is directly taken into account [7]. The last approach deals with purely rigid bodies connected using massless elastic force elements. Using this method has clearly some limitations, since it can be applied only to relatively simple geometries and the accuracy depends on the number of elements used to discretize the component, but on the other hand it allows reducing the complexity of the structure and making it computationally lighter. If model updating is to be applied to this class of models, no dedicated methods were developed.

The aim of this study is the development of a methodology to update multibody model with experimental data, using as automation tool a commercial optimization environment. The method is developed to be as general as possible, and will be here applied to a full scale wind turbine model with unknown blade properties and for which experimental modal analysis results are available. Modeling wind turbine with multibody simulation tools is very important, being possible to analyze the response of the structure to dynamic loads, such as aerodynamic and gravitational forces, varying with time as the blades rotate [8]. An accurate determination of the modes and natural frequencies in different operating conditions is mandatory to obtain an adequate insight of the system dynamics and optimize the performances by separating the turbine natural frequencies from the rotor speed's harmonics. Another common solution for reducing dynamic loads is the definition of control laws to actively damp component vibrations. In order to design efficient controls, the model must accurately predict the dynamic behavior for a wide range of operating conditions.

The paper is organized as follows: in section 2, the proposed model updating methodology based on modal data and the correlation indices selection are presented. Section 3 will describe the CART3 wind turbine, the experimental campaign and the multibody modeling. Section 4 and 5 will then present the obtained results for the single and multi-objective optimization problems. Finally some conclusion will be drawn.

2. MODEL UPDATING BASED ON MODAL DATA

In this paper, a methodology to update multibody simulation models based on modal data is presented. The results of an Experimental Modal Analysis campaign on a structure consist of the FRFs between the input and the output points, which can be processed to obtain the natural frequencies and mode shapes. Let define

$$D = \left\{ \underline{\omega} = \{\omega_1, \omega_2, ..., \omega_N\} \in C^N, \underline{\underline{\Psi}} = \left\{ \underline{\psi}_1, \underline{\psi}_2, ..., \underline{\psi}_N \right\} \in C^{N \times M} \right\} \quad (1)$$

the set of measured modal data from a structure, consisting of natural frequencies ω and modal matrix Ψ, with N the number of identified modes observed at M degrees of freedom. Usually modal parameters are considered to be real, but for generality they will be considered here as complex.

Obtaining the modal parameters for a multibody model is not as straightforward as for finite elements models: the model needs to be linearized at a given instant in time and the state space formulation derived, where the state variables are the degrees of freedom (DOF) of each body, considered in its center of gravity. Being q the vector of the generalized coordinates and M the generalized mass matrix, the equation of motion can be written as:

$$\underline{\underline{M}}\,\underline{\ddot{q}} = f\left(\underline{q}, \underline{\dot{q}}, t\right) \quad (2)$$

At the selected instants in time, the model is frozen and perturbed around its configuration to obtain the state space formulation:

$$\begin{cases} \dot{\underline{x}} = \underline{\underline{A}}\,\underline{x} + \underline{\underline{B}}\,\underline{u} \\ \underline{y} = \underline{\underline{C}}\,\underline{x} + \underline{\underline{D}}\,\underline{u} \end{cases} \tag{3}$$

where $\underline{x} = \left(\underline{q}, \dot{\underline{q}}\right)$ is the vector of the states. The modal data are now the eigenvalues and eigenvectors of the A matrix in equation 3. Usually, some outputs points need to be defined on the multibody model on the locations where the sensors on the actual structure were positioned. The relation between the states and the outputs is expressed by the C matrix in equation 3 hence, by multiplying the modal matrix for the C matrix, the mode shapes can be projected from the generalized coordinates to the output points, allowing a direct comparison with the experimental results. Being $\underline{\underline{\tilde{\Psi}}}$ the modal matrix obtained from the multibody model and referred to the generalized coordinates, the modal vectors referred to the output points are:

$$\underline{\underline{\tilde{\Psi}}}_m = \underline{\underline{C}} \times \underline{\underline{\tilde{\Psi}}} \tag{4}$$

Given a set of uncertain parameters $\underline{\delta}$ of the multibody model that need to be updated, the numerical modal set can be expressed as:

$$\tilde{\mathrm{D}}(\underline{\delta}) = \left\{ \underline{\tilde{\omega}}(\underline{\delta}) \in \mathrm{C}^{\mathrm{N_m}}, \underline{\underline{\tilde{\Psi}}}_m(\underline{\delta}) \in \mathrm{C}^{\mathrm{N_m \times M}} \right\} \tag{5}$$

By properly comparing equation 1 with equation 5, the correlation between the experimental and numerical models can be evaluated. To compare the mode shapes, the well-known Modal Assurance Criterion is applied:

$$\mathrm{MAC}_{\mathrm{i,k}} = \frac{\left| \underline{\tilde{\Psi}}_{\mathrm{i}}^{\mathrm{H}} \underline{\Psi}_{\mathrm{k}} \right|^2}{\left[\underline{\tilde{\Psi}}_{\mathrm{i}}^{\mathrm{H}} \underline{\tilde{\Psi}}_{\mathrm{i}} \right] \left[\underline{\Psi}_{\mathrm{k}}^{\mathrm{H}} \underline{\Psi}_{\mathrm{k}} \right]} \begin{matrix} \mathrm{i} = 1, \mathrm{N_m} \\ \mathrm{k} = 1, \mathrm{N} \end{matrix} \tag{6}$$

Where N is the number of modes identified from the experimental results and N_m the number of calculated mode shapes. By analyzing the MAC matrix, the pairs of modes with the higher correlation are identified and the errors between the corresponding natural frequencies are evaluated as follows:

$$\varepsilon_{\mathrm{k}} = \left| \frac{\omega_k - \tilde{\omega}_k}{\omega_k} \right|, \mathrm{k} = 1, \mathrm{N} \tag{7}$$

In this study, the problem of identifying the model parameter values $\underline{\delta}$ that give the best fit with the experimental results set D is formulated as an optimization problem. Due to the non-linear relation between the parameters and the modal response of the model, many local extrema could exist for the chosen objective function. To prevent the convergence toward one of those local points, gradient-based algorithm should be avoided; by using evolutionary-based algorithms, on the contrary, the robustness of the solution can be guaranteed.
Depending on the combination of the correlation indices in equations (6) and (7), different optimization problems can be defined. Initially, a single-objective optimization problem is defined, by using the objective function:

$$J_1(\delta) = \sum_{i=1}^{N} \left(w_1 \cdot (1 - MAC_i) + w_2 \varepsilon_i \right) \tag{8}$$

In equation (8), i identifies the pairs of more correlated modes in term of MAC values and w_1 and w_2 are the weights for the two indices. The solution of a single-objective optimization problem is relatively fast, but the main disadvantage is that it strongly depends on the values assigned to the weights. The weights should be selected with respect to the adequacy of the numerical model and the accuracy of the experimental data obtained. Hence, their selection cannot be made a priori since modeling and measurement errors cannot be easily estimated and their selection must rely on the analyst's experience [4]. The definition of the parameter identification as a multi-objective problem eliminates the need of arbitrary weighting factors. Another advantage is that all admissible solutions in the parameter space are obtained which constitute model trade-off in fitting the different modal properties. The solution of the optimization problem results in a Pareto front, which is a collection of points in the design space that represent a limit beyond which the design cannot be improved without causing degradation in one of the other objectives [9]. Points belonging to the Pareto frontier are usually called dominating solutions; the concept of Pareto dominance of point A over point B can be defined as follow:

$$A \underset{P}{\succ} \mathrm{B} \Leftrightarrow \left(\forall_i : F_i(A) \le F_i(B) \right) \cap \left(\exists_j : F_j(A) < F_j(B) \right) \tag{9}$$

The analyst can at this point select the solution on the front which better satisfies the specific problem. For the multi-objective optimization problem, the objectives are here defined by splitting the terms in equation (8) and considering each contribution separately:

$$J_{\psi}(\delta) = \sum_{i=1}^{N} MAC_i \quad ; J_{\omega}(\delta) = \sum_{i=1}^{N} \varepsilon_i \tag{10}$$

By choosing the two objective functions as in equation (10), the solutions in the Pareto front will result in a trade-off between the overall fit in modal frequencies and the overall fit in the mode shapes.

3. THE CART3 WIND TURBINE

In this paper, the model updating methodology will be applied to the 3-bladed Control Advance Research Turbine (CART-3), located at the NREL test facility in Boulder, Colorado. This turbine is a Westinghouse model WWG-0600, modified in order to obtain a simple aerodynamic behavior and allow designers to focus on control strategies. The control laws are designed using a multibody model of the turbine [10,11]. To improve the model, a test campaign on the turbine in parked condition was performed within a collaboration between LMS International and NREL, using both Experimental Modal Analysis (EMA) and Operational Modal Analysis (OMA) techniques [12]. For a preliminary correlation and to verify the applicability of the proposed methodology, only the EMA results in terms of natural frequencies and mode shapes will be here used. The identified natural frequencies are presented in Table 1. A detailed description of the test campaign can be found in [13].

Table 1: Identified mode shapes from the Experimental Modal Analysis test campaign

MODE	DESCRIPTION	FREQUENCY [Hz]	MODE	DESCRIPTION	FREQUENCY [Hz]
1	Tower fore-aft	0.86	9	2nd rotor asym. flap	6.44
2	Tower side-to-side	0.88	10	2nd rotor asym. flap	6.56
3	1st rotor asym. flap	1.45	11	2nd rotor sym. flap	6.89
4	1st rotor asym. flap	1.51	12	2nd rotor asym. flap	6.96
5	1st rotor sym. flap	1.85	13	2nd tower fore-aft	7.16
6	1st rotor asym. lag	2.97	14	3rd rotor asym. flap	9.44
7	1st rotor asym. lag	3.06	15	3rd rotor asym. flap	9.89
8	2nd rotor asym. flap	4.14	(-)	(-)	(-)

The numerical model of the wind turbine is built using the commercial multibody software LMS Virtual.Lab Motion. The model is built using rigid bodies. The connections between different components of the mechanism are modeled using rigid joints, while to model the flexibility of the tower and the blades the bodies are connected with massless elastic force elements. In this model, the Euler-Bernoulli linear beam force element available in Virtual.Lab Motion is used. According to NREL's instructions, the tower is modeled using the data in [10]. Being the data obtained from a parked-condition test, the nacelle is rigidly connected to the tower and, together with the transmission and the electrical components, is modeled as a single rigid body. The hub, rigidly attached to the tower, is modeled also a rigid body, but its inertia contributions are kept separated from those of the nacelle. Usually, blade properties are listed in a table such as the one in [10], where all parameters are described at different locations along the pitch axis of the blade. For these specific blades, only the mass and directional stiffness properties were identified, without any detailed information about the body inertias and the gravitational and elastic centre locations. Since these parameters are mandatory to create a multibody model, an approximation is introduced and the model is built assuming the blade as a straight cantilevered beam, with the elastic and gravitational axis located along the pitch axis. The parameter identification methodology will then try to update the inertia and stiffness parameters to match the experimental results. Figure 1 shows the multibody model of the wind turbine created in Virtual.Lab Motion and figure 2 a screenshot of the mode shapes animation tool; figure 3 focuses then on the modeling of the blade, with the lumped element used to model the inertia and stiffness properties of each section. After building the model, the initial correlation between experimental and numerical model is investigated. Due to the limited number of sensors used to identify the blade dynamic behavior and the small number of bodies used to build the flexible multibody model, only the lower order modes will be used to drive the updating phase. In particular, together with the fore-aft tower bending mode (see table 1), only the 1st order flap and lag modes of the rotor are included. The tower side-to-side mode is found to be highly non-mono-phase, resulting in a complex behavior difficult to be matched; hence, it is decided not to consider it as a reference. The components of the vector which cause this behavior are the nodes on the non-vertical blades; it was verified that excluding those components, the MAC value was relatively high and the visualization of the mode satisfactory. The initial correlation between each pair of modes in terms of the indices defined in equations 6 and 7 are listed in table 2.

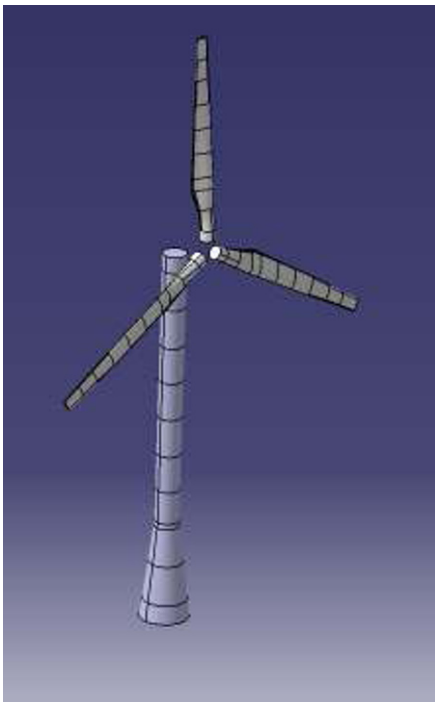

Fig. 1 CART3 wind turbine multibody model

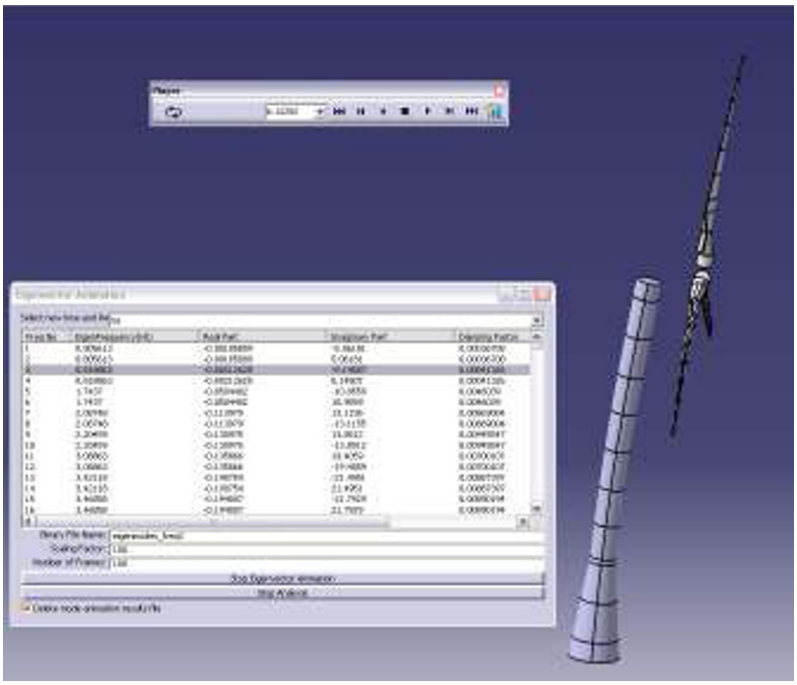

Fig. 2 Example of mode shape animation in Virtual.Lab Motion

Fig. 3 detail of the blade multibody modeling

Table 2: initial values of correlation indices between numerical and experimental results

MODE # EXP/NUM	MAC	ε
1/1	0.8565	0.0229
2/2	0.9530	0.1735
3/3	0.8603	0.2441
4/4	0.8823	0.0513
5/6	0.9393	0.0157
6/5	0.7543	0.0714
SUM	5.243	0.5789

4. SINGLE-OBJECTIVE OPTIMIZATION RESULTS

Firstly, the model updating based on a single-objective optimization is performed. The problem is formulated as the minimization of the objective function in equation (8), without taking into account any weight between the two indices. Assuming that the tower properties listed in [10] are correct, the identification will focus on the structural parameters of the nacelle, the hub and the blade. For the nacelle and the hub, considered as purely rigid bodies and connected rigidly to the remaining of the structure, the parameters considered are the mass and rotational inertia values. For the blades, due to the high number of uncertainties, the stiffness of the beam elements in the flap and lag direction and the inertia properties of each body will be considered as design variable to be modified. In total, 75 structural parameters need to be updated. Due to the dimension of the problem, the optimization will be performed in two consecutive steps: a first one, where the nacelle and hub properties are updated together with the blade stiffness; in the second, the previous parameters will be frozen at their optimal values and the inertia parameters of the bodies of the blade will be considered. It must be noted that despite the blades are 3,

the multibody model is built parametrically and they are related to the same file, being then possible to define the parameters just once.
Since the modal parameters are not a direct output of Virtual.Lab Motion, the state space matrices need to be extracted from the results file, and then the procedure shown in section 2 can be applied by defining a Matlab script. To automate the process and run the optimization, the commercial software Noesis Optimus is used. The workflow created with the different tasks that need to be performed for each design is shown in figure 4.

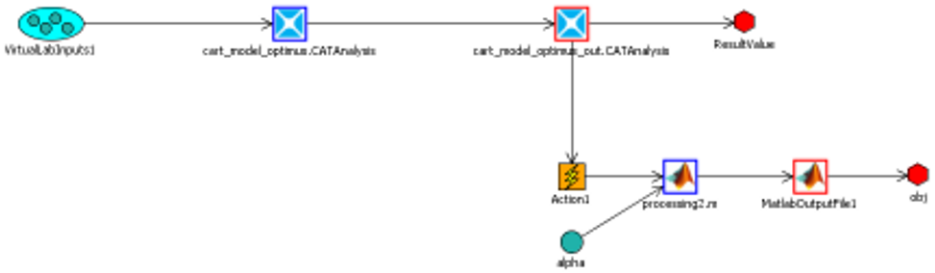

Fig. 4 process automation in Noesis Optimus

The algorithm selected to optimize the model is the Self Adaptive Evolution algorithm available in the software, which is based on genetic evolution techniques. The total number of design evaluated during the first optimization is 4200, coming from 30 generations of 140 individuals each; the number of parents, that is the number of optimal points from the previous generations used to evaluate the new individuals is set to 28. For the second optimization run, 20 generations of 200 individuals are evaluated (with 40 parents per new population), resulting in a total of 4000 design evaluations. The results after each of the two runs are shown in table 3.

Table 3: results for the single objective optimization

MODE # EXP/NUM	**1ST RUN**		**2ND RUN**	
-	MAC	ε	MAC	ε
1/1	0.8696	0.0034	0.8698	0.0026
2/2	0.9537	0.0028	0.9535	7.34E-5
3/3	0.8479	0.0259	0.8536	0.0317
4/4	0.8543	0.1282	0.8582	0.121
5/6	0.9325	0.0106	0.9328	0.0215
6/5	0.7649	0.0780	0.7667	0.0718
SUM	5.223	0.249	5.2345	0.2487

By comparing the results in table 3 with table 2, it can be seen how the MAC values are not changing too much. On the other hand, there are significant changes in the errors between the natural frequencies. In particular, the errors between the frequencies of the first three correlated modes are significantly reduced already after the first optimization run. A different trend can be observed for the forth modes, where the error between the corresponding modes is drastically increased after the first run and then reduced after the second, but still showing a bigger value if compared with the original. For the last two modes, the errors remain more or less constant. The reason for this behavior is probably related to the choice of the objective function. It is a trade off between the MAC values and error between natural frequencies for all the modal data considered. Moreover, by assigning no weights to the correlation indices used, they are given the same importance. The result is that the optimum point found by applying this methodology shows a better overall behavior, not guarantying an increased correlation for all the indices used. By analyzing the results of the optimization, it is observed that only few of the parameters considered in the two run show a significant correlation with the objective function, partially explaining the limited improvement obtained.

5. MULTI-OBJECTIVE OPTIMIZATION RESULTS

To verify the influence of the weights on the results, a multi-objective optimization is also performed. In this case, all the parameters are considered at once, resulting in a relatively big design space. Between the different algorithms available, the Non-dominated Sorting Differential Evolution (NSDE) is selected [9]. The advantage of this algorithm is that it creates a Pareto front with uniformly distributed points and assigns weights to the objectives with respect to the location of the point in the front. For this problem, all the variables are considered together and with the same ranges defined for the single-objective problem. Starting from the original model, an initial random population of 256 individuals is considered; after this, 35 new

populations of 150 individuals each are considered. The Pareto front resulting from the optimization is shown in figure 5, where goal 1 on the x axis is J_ω and goal 2 is J_ψ (see equation 10).

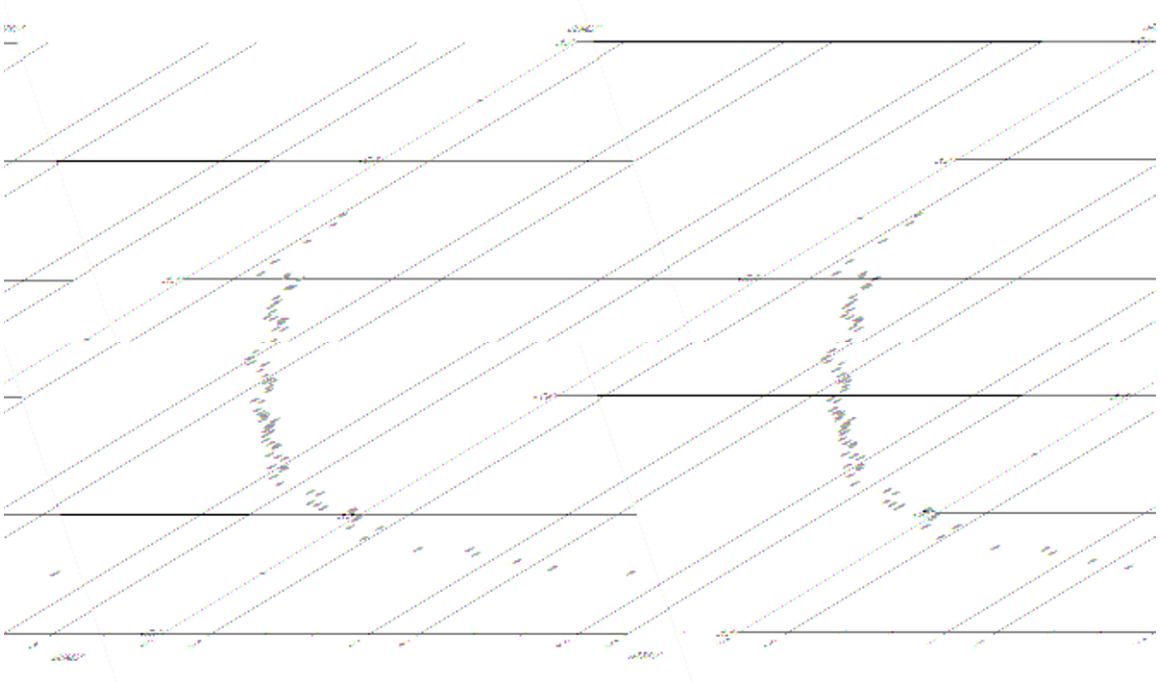

Fig. 5 Pareto front for the multi-objective optimization problem

By observing the front, it can be seen how the non-dominated points present a small variation of the MAC values; on the other end, the values of the objective function representing the errors between the natural frequencies are distributed in a wider range. Table 4 shows the results obtained by selecting 4 points along the Pareto front; the location on the front gives the relative weights for the two objective function considered.

Table 4: results of the multi-objective optimization for a set of optimal points with different weights

MODE # EXP/NUM	**w(J_ψ)=0 w(J_ω)=1**		**w(J_ψ)=0.09 w(J_ω)=0.91**		**w(J_ψ)=0.28 w(J_ω)=0.72**		**w(J_ψ)=0.55 w(J_ω)=0.45**	
-	MAC	ε	MAC	ε	MAC	ε	MAC	ε
1/1	0.8676	0.0024	0.8644	0.0438	0.8425	0.0461	0.828	0.05
2/2	0.9527	0.0036	0.9472	0.0005	0.9483	0.1992	0.9364	0.37
3/3	0.8533	0.0047	0.8756	0.0654	0.8950	0.3852	0.9279	0.754
4/4	0.8571	0.0979	0.8695	0.0714	0.9007	0.1917	0.9437	0.512
5/6	0.9282	0.0337	0.9276	0.1399	0.9351	0.1519	0.9339	0.21
6/5	0.7867	0.0712	0.8112	0.0041	0.8463	0.0071	0.889	0.0614
SUM	5.2456	0.2558	5.2955	0.3251	5.368	0.982	5.459	1.958

By comparing the results in table 4 with that on table 3 for the single objective optimization and the original design in table 2, it is immediately clear how bigger improvements can be obtained for the error between the natural frequencies than for the MAC values. By considering a weight of 1 for the error between the natural frequencies and 0 for the MAC, a relatively good result can be obtained, that is relatively similar to the one of the single objective optimization. By using a higher weight associated to the MAC values, some improvement can be obtained, but on the other hand the error between natural frequencies is significantly increased, leading to non-acceptable solutions. The better solution can probably be considered the one with w(J_ψ)=0.09 and w(J_ω)=0.91, where both objective function are improved with the respect to the original design and the single objective optimization results.

By processing the results, both in the single and in the multi-objective optimization run, a very low correlation between the design variables and the objective functions is observed. Besides the modeling approximation discussed in section 3, the relatively high number of design parameters to be optimized at once and the formulation of the objective functions can both be reasons for this behavior. By the way, the optimal solutions selected in the two cases show some improvements with

respect to the original one, increasing the correlation between the multibody model and the experimental modal results. Figure 6 shows a comparison between some of the experimental and numerical mode shapes.

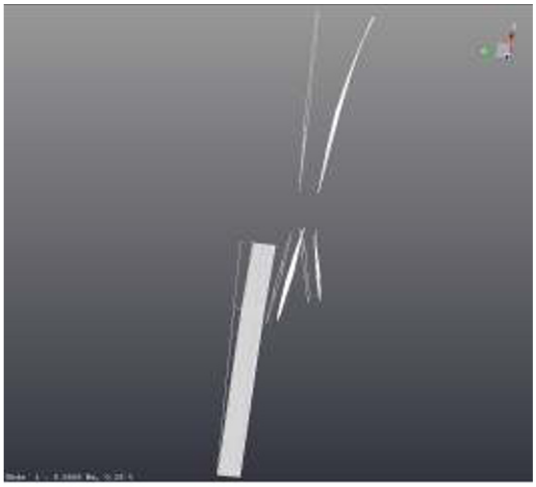

a) Tower fore-aft bending experimental

b) Tower fore-aft bending numerical

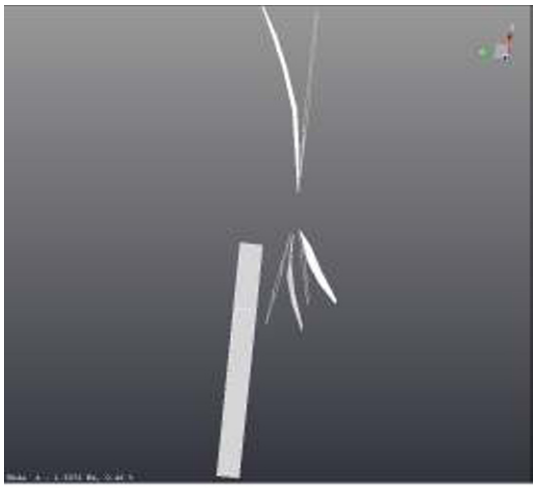

c) 1st rotor flap asymmetric experimental

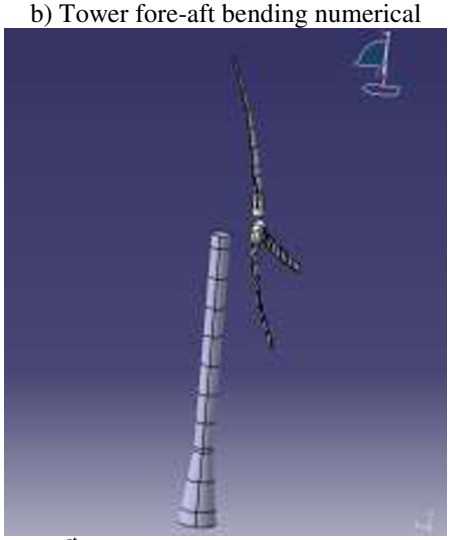

d) 1st rotor flap asymmetric numerical

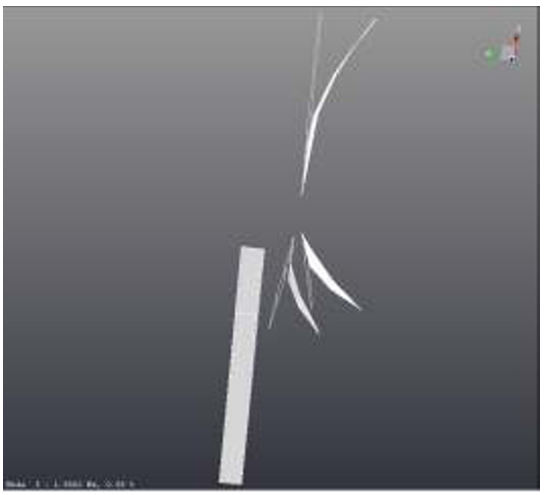

e) 1st rotor flap symmetric experimental

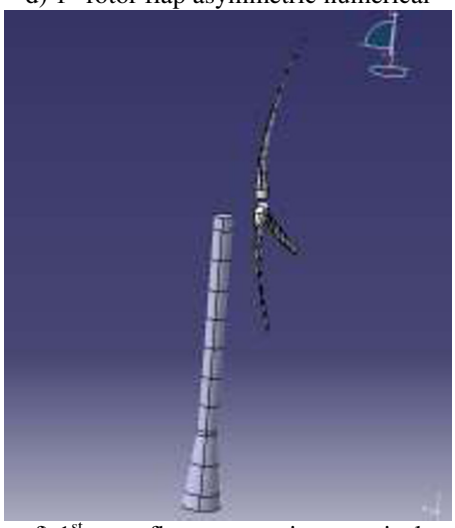

f) 1st rotor flap symmetric numerical

Fig. 6 Comparison between some of the experimental and numerical mode shapes

6. CONCLUSIONS

This paper presents a methodology to update multibody simulation models using experimental modal data. The proposed methodology is based on common updating and parameter identification techniques developed specifically for Finite Element Models, modified to be used with commercial multibody software such as LMS Virtual.Lab Motion. The reference data used for the updating are the modal vectors and natural frequencies identified on the actual structure after performing an Experimental Modal Analysis campaign. To correlate the numerical and experimental model, different correlation indices can be defined: in this case, the Modal Assurance Criterion and the relative error between the natural frequencies are selected. To perform the updating, a single objective optimization problem can be defined, by combining the two correlation indices into a single objective function. Despite being possible to use standard optimization techniques, when combining different indices some weights need to be defined, influencing significantly the results that could be obtained. To solve this problem, multi-objective optimization techniques can be applied, considering separately each correlation indices. The optimal solution will be distributed along a Pareto front, where weights are automatically assigned to each objective function for all the points depending on their location on the front.

The proposed methodology is applied to a full scale multibody model of the NREL CART3 wind turbine. Both the single objective and multi-objective optimization problems are applied to try to identify the unknown parameters and update the model. Due to missing information about the model, some geometrical and structural approximation is introduced to build the numerical model. The tower and the blades are modeled as flexible using a lumped-parameter approach, while the nacelle, generator and drive-train are modeled as a single rigid body since the measurement campaign has been performed with the turbine in parked conditions. The two optimization problems are both solved using Genetic Algorithms, to prevent convergence towards local extrema and increase the robustness of the search. The optimal point obtained from the single objective optimization shows a significant reduction in the errors between natural frequencies, while the MAC remains constant. In the multi-objective optimization, the points on the front represent different trade-off solutions, depending on the weights assigned to the objectives. Lower variation of the MAC can be observed, and to obtain some improvement big error between natural frequencies need to be accepted. Hence, a solution which showed both an increase in MAC and a reduction in the natural frequencies index is selected, showing similar results to the one obtained from the single-objective problem.

The main advantage of the proposed methodology is its flexibility and the possibility to apply it to a general multibody model for which experimental modal analysis are available. Moreover, depending on the data available, it can be modified to tackle with the specific problem. Great attention should be given to the selection of the correlation indices and the objective functions, since the selection can greatly influence the results that could be obtained.

ACKNOLEDGEMENTS

The work presented in this paper was performed within the 6th framework of the Marie Curie Host Fellowships Smart Structures (A Computer-Aided Engineering Approach to Smart Structures) project (MRTN-CT-2006-035559). The authors would like to thank the European Commission for the grant received.

REFERENCES

[1] Friswell M.I. and Mottershead J.E., Finite Element Model Updating in Structural Dynamics, Kluwer Academic Publisher, 1995.

[2] Mottershead J.E. and Friswell M.I., Model updating in structural dynamics: A survey, Journal of Sound and Vibrations, 167(2), 347-375, 1993.

[3] Jaishi B. and Ren W., Finite element model updating based on eigenvalue and strain energy residuals using multiobjective optimization technique, Mechanical Systems and Signal Processing, 21, 2295-2317, 2007.

[4] Christodoulou K. and Papadimitrou C., Structural identification based on optimally weighted modal residual, Mechanical Systems and Signal Processing, 21(1), 4-23, 2007.

[5] Heylen W., Lammens S. and Sas P., Modal Analysis Theory and Testing, Katholieke Universiteit Leuven, Department Werktuigkunde, Leuven, 1997.

[6] Craig R.R. and Bampton M.C.C., Coupling of substructures for dynamic analysis, AIAA Journal, 6, 1313-1319, 1968.

[7] Brüls O., Fisette P. and Verlinden O., Computer-Aided analysis of rigid and flexible multibody system, GraSMech Course 2009-2010 material, Université Catholique de Louvain, 2010.

[8] Griffith T.D., Carne T.G. and Paquette J.A., Modal testing validation of blade models, Wind Engineering, 32(2), 91-102, 2008.

[9] Noesis Solutions, Optimus Rev. 9 Theory Manual, Leuven, Belgium, 2009.

[10] Stol K.A., Geometry and structural properties for the controls advanced research turbine (CART) from model tuning, NREL/SR-500-32087, Colorado, USA, 2004.

[11] Wright A.D., Fingersh L.J., and Stol K.A., Designing and testing controls to mitigate tower dynamic loads in the controls advanced research turbine, 45th AIAA Aerospace Sciences Meeting and Exhibit,Wind Energy Symposium, Reno, Nevada, USA, 2007.

[12] Manzato S., Peeters B., Osgood R. and Luczak M., Wind Turbine Model Validation by Full-Scale Vibration Test, Proceedings of the European Wind Energy Conference(EWEC) 2010, Warsaw, PL, 2010.
[13] Osgood R., Bir G., Mutha H., Peeters B., Luczak M. and Sablon G., Full-scale modal wind turbine test: comparing shaker excitation with wind excitation, Proceedings of IMAC 28, Jacksonville, FL, USA, February 2010.

DOF Reduction Strategy for Large Order Finite Element Models

Robert N. Coppolino, CTO
Measurement Analysis Corporation
23850 Madison Street
Torrance, California 90505

ABSTRACT

State-of-the-art technologies in computation and software have led to ever increasing size of finite element models, simply because this is possible. While it is arguable that "degree-of-freedom" proliferation is unnecessary, there are some potential benefits to be realized, namely (1) commonality of stress and dynamic models and (2) employment of finite element models in the mid- and high-frequency ranges (normally the domain of statistical energy analysis). The conventional approach to Test Analysis Model (TAM) definition for modal testing is based on Guyan Reduction. The strategy encounters severe difficulties (due to Boussinesq type singularities) when shell and 3-D elasticity elements are used to build a finite element model (FEM). This paper describes a "load-patch" variation of Guyan Reduction that alleviates 3-D problematic singularities. Two illustrative examples are used to demonstrate advantages and benefits of the new TAM definition procedure.

1. INTRODUCTION

Finite element models of modern structural systems, such as aircraft, spacecraft, and automobiles, are typically composed of thousands to millions of grid points due to the sophistication of commercial CAE software products and mechanical (static and dynamic) fidelity requirements[1,2]. During the 1960's model order reduction methods, based on the Rayleigh-Ritz method[3] were introduced for computation of "large order" system normal modes. The two prominent reduction methods that are popular to this day are (1) Guyan Reduction[4] and the Craig-Bampton method[5]. In the decade that followed, iterative methods[6,7] that treated large, sparse eigenvalue problems, were developed and became widely accepted. While mathematical methods for treating very large order dynamic finite element models are quite mature, the need for reduced order models (commonly called Test-Analysis Models or TAMs) persists in modal testing applications[8]. This is due to the fact that models of an order consistent with modal test instrumentation are required (predominantly in aerospace applications) for test data quality evaluation and test-analysis correlation. The most widely accepted method employed for definition of TAMs is Guyan Reduction.

For many years following the introduction of Guyan Reduction in 1965, finite element models were typically composed of one- and two-dimensional finite elements based upon technical theory (e.g., beams, plates and shells). Static deflection shape functions produced by application of point loads (the basis of Guyan Reduction) were typically smooth and "sensible". Increasing utilization of three dimensional finite elements in structural dynamic models in recent years has led to a critical difficulty in the development of TAMs due to poorly defined shape functions. The present paper formally introduces a "new" model order reduction approach that is based upon application of distributed load patches to define reasonable deflection shape functions (Note that "new" is deliberately placed in quotes by the author, since it is believed that the load patch method has been used by others in a variety of applications, without being "formalized" as a general reduction strategy). This "new" reduction procedure, while conceptually similar to Guyan Reduction, produces accurate, consistent TAMs when one-, two- and three-dimensional finite elements are employed to define the dynamic finite element model.

T. Proulx (ed.), *Linking Models and Experiments, Volume 2*, Conference Proceedings of the Society for Experimental Mechanics Series 5,
DOI 10.1007/978-1-4419-9305-2_25, © The Society for Experimental Mechanics, Inc. 2011

2. NOMENCLATURE

Matrices and Vectors:

$\{F\}$	Force Vector (Eq. 1)	$[T_\Psi]$	Reduction Transformation (Eq. 16)
$[\mathrm{I}]$	Identity Matrix (Eq. 2)	$\{U\}$	Displacement vector (Eq. 1)
$[K]$	Stiffness Matrix (Eq. 1)	$\{q\}$	Modal displacement vector (Eq. 7)
$[M]$	Mass Matrix (Eq. 1)	$[\Phi]$	Modal matrix (Eq. 7)
$[P]$	Modal Participation Matrix (Eq. 10)	$[\Psi]$	Load Patch Transformation (Eq. 13)
$\{Q\}$	Generalized Force Vector (Eq. 9)	$[\lambda]$	Eigenvalue Matrix (Eq. 8)

Variables:

E_Φ	Modal Coherence Metric (Eq. 18)	ω	frequency (radians/sec) (Eq. 11)

Subscripts:

A	Approximate (Eq. 18)	n	Normal Mode (Eq. 10)
CB	Craig-Bampton (Eq. 8)	o	Omitted (Eq. 1)
E	Exact (Eq. 18)	Ψ	Load Patch (Eq. 13)
a	Analysis (Eq. 1)		

3. COVENTIONAL ORDER REDUCTION STRATEGIES

While many authors have developed and refined dynamic finite element model reduction procedures since the late 1960s, two related strategies retain the broadest acceptance. They are (a) Guyan Reduction[4] and (b) the Craig-Bampton Method[5].

3.1 GUYAN REDUCTION

The underlying idea that defines Guyan Reduction is static condensation…and Guyan's monumental formulation was published as a one-half page technical note! The degrees of freedom describing a structural dynamic system are first separated into "analysis" and "omitted" subsets, which lead to the partitioned matrix equations (ignoring damping)

$$\begin{bmatrix} \overline{M}_{aa} & M_{ao} \\ M_{oa} & M_{oo} \end{bmatrix} \begin{Bmatrix} \ddot{U}_a \\ \ddot{U}_o \end{Bmatrix} + \begin{bmatrix} \overline{K}_{aa} & K_{ao} \\ K_{oa} & K_{oo} \end{bmatrix} \begin{Bmatrix} U_a \\ U_o \end{Bmatrix} = \begin{Bmatrix} \overline{F}_a \\ F_o \end{Bmatrix} \tag{1}$$

If only the "analysis" partition of the mass matrix were non-zero, and external forces were only applied to "analysis" degrees of freedom, the relationship between "analysis" and "omitted" degrees of freedom would be

$$\begin{Bmatrix} U_a \\ U_o \end{Bmatrix} = \begin{bmatrix} \mathrm{I}_{aa} \\ -K_{oo}^{-1} K_{oa} \end{bmatrix} \{U_a\} \tag{2}$$

In that situation, the reduction transformation in equation 2 would be exact. However, when the "omit" partitions are non-zero, the reduction transformation is approximate (its columns are Rayleigh-Ritz shape functions).

Application of the reduction transformation, in a symmetric manner following the Rayleigh-Ritz method yields, respectively, the (statically exact) reduced stiffness matrix and (dynamically approximate) mass matrix

$$[K_{aa}] = \begin{bmatrix} \mathrm{I}_{aa} & -K_{ao}K_{oo}^{-1} \end{bmatrix} \cdot \begin{bmatrix} \overline{K}_{aa} & K_{ao} \\ K_{oa} & K_{oo} \end{bmatrix} \cdot \begin{bmatrix} \mathrm{I}_{aa} \\ -K_{oo}^{-1} K_{oa} \end{bmatrix} = [\overline{K}_{aa}] - [K_{ao}K_{oo}^{-1}K_{oa}] \tag{3}$$

$$\left[M_{aa}\right]=\left[\mathrm{I}_{aa} \quad -K_{ao}K_{oo}^{-1}\right]\cdot\begin{bmatrix}\overline{M}_{aa} & M_{ao}\\ M_{oa} & M_{oo}\end{bmatrix}\cdot\begin{bmatrix}\mathrm{I}_{aa}\\ -K_{oo}^{-1}K_{oa}\end{bmatrix}. \tag{4}$$

The reduced (approximate) applied force vector is

$$\left\{F_a\right\}=\left\{\overline{F}_a\right\}-\left[K_{ao}K_{oo}^{-1}\right]\left\{F_o\right\} \tag{5}$$

It should be noted that the reduction transformation matrix columns (in equation 2) are physically consistent with normalized deflection shapes associated with application of individual unit "analysis" set loads. This central idea in Guyan Reduction is the primary motivating principal employed in development of the "new" method to be discussed later in this paper.

3.2 CRAIG-BAMPTON MODELS

The Craig-Bampton method, while one of the earliest systematic approaches for component mode synthesis (CMS), continues to be the most widely applied CMS strategy. The matrix equations for of a single Craig-Bampton component are a logical extension to Guyan Reduction. The degrees of freedom describing a component dynamic system are first separated into "boundary-analysis" and "interior-omitted" subsets, which lead to the partitioned matrix equations (ignoring damping)

$$\begin{bmatrix}\overline{M}_{aa} & M_{ao}\\ M_{oa} & M_{oo}\end{bmatrix}\begin{Bmatrix}\ddot{U}_a\\ \ddot{U}_o\end{Bmatrix}+\begin{bmatrix}\overline{K}_{aa} & K_{ao}\\ K_{oa} & K_{oo}\end{bmatrix}\begin{Bmatrix}U_a\\ U_o\end{Bmatrix}=\begin{Bmatrix}\overline{F}_a\\ F_o\end{Bmatrix}. \tag{6}$$

By augmenting the Guyan Reduction transformation (equation 2) with a truncated set of "boundary-fixed" modes, the Craig-Bampton reduction transformation is defined as,

$$\begin{Bmatrix}U_a\\ U_o\end{Bmatrix}=\begin{bmatrix}\mathrm{I}_{aa} & 0_{an}\\ -K_{oo}^{-1}K_{oa} & \Phi_{on}\end{bmatrix}\begin{Bmatrix}U_a\\ q_n\end{Bmatrix}. \tag{7}$$

Application of the reduction transformation, in a symmetric manner following the Rayleigh-Ritz method yields, respectively, the Craig-Bampton component reduced stiffness and mass matrices,

$$\left[K_{CB}\right]=\begin{bmatrix}K_{aa} & 0_{an}\\ 0_{na} & \lambda_{nn}\end{bmatrix},\ \left[M_{CB}\right]=\begin{bmatrix}M_{aa} & P_{an}\\ P_{na} & \mathrm{I}_{nn}\end{bmatrix}, \tag{8}$$

and the reduced (approximate) applied force vector,

$$\begin{Bmatrix}F_a\\ Q_n\end{Bmatrix}=\begin{Bmatrix}\left\{\overline{F}_a\right\}-\left[K_{ao}K_{oo}^{-1}\right]\left\{F_o\right\}\\ \left[\Phi_{on}^{T}\right]\left\{F_o\right\}\end{Bmatrix}. \tag{9}$$

3.3 REDUCED MODEL "ENHANCEMENTS"

One may attempt to define an enhancement of the Guyan Reduction method based on a frequency domain solution of the Craig-Bampton component equations,

$$\begin{bmatrix}M_{aa} & P_{an}\\ P_{na} & \mathrm{I}_{nn}\end{bmatrix}\begin{Bmatrix}\ddot{U}_a\\ \ddot{q}_n\end{Bmatrix}+\begin{bmatrix}K_{aa} & 0_{an}\\ 0_{na} & \lambda_{nn}\end{bmatrix}\begin{Bmatrix}U_a\\ q_n\end{Bmatrix}=\begin{Bmatrix}F_a\\ Q_n\end{Bmatrix}, \tag{10}$$

resulting in the modified, frequency dependent reduced mass and stiffness matrices and applied force vector,

$$\left[\tilde{M}_{aa}(\omega)\right]=\left[M_{aa}\right]+\omega^2\left[P_{an}\right]\left[\lambda_{nn}-\omega^2\mathrm{I}_{nn}\right]^{-1}\left[P_{na}\right],\ \left[\tilde{K}_{aa}(\omega)\right]=\left[K_{aa}\right], \tag{11}$$

$$\left\{\tilde{F}_a(\omega)\right\}=\left\{F_a\right\}+\omega^2\left[P_{an}\right]\left[\lambda_{nn}-\omega^2\mathrm{I}_{nn}\right]^{-1}\left\{Q_n\right\}. \tag{12}$$

The above frequency dependent reduced mass matrix suggests that any physically consistent enhancement to Guyan Reduction cannot be expressed as a constant matrix, although the IMS method[9] does provide an approximation of that effect. Whenever a conventional TAM mass matrix is required (especially in support of a modal test), the most effective strategy for determination of an appropriate analysis set is described in Reference 8 or closely related methodologies.

4. NEW REDUCTION STRATEGY CIRCUMVENTING GUYAN REDUCTION LIMITATIONS

When the Guyan Reduction method was introduced in 1965, the majority of matrix structural dynamic models were assembled using finite elements based on technical theories (e.g., beams, plates and shells). Deformation shapes for technical theory based structural models, subjected to point loads, are generally smooth resulting in "well-behaved" Rayleigh-Ritz shape functions. As finite element technology continued to evolve, elements based on 3-D elasticity theory matured to the point that many of today's highly refined finite element models incorporate 3-D elastic elements. Dynamic models using 3-D elastic elements are generally quite accurate and effective, except for situations in which reduced models are required (e.g., preparation of test-analysis models or TAMs). Since highly refined 3-D elastic models closely follow exact mathematical behavior, deformations associated with point loads are extreme (infinite in the limit, as in the case of the Boussinesq problem[10]), producing Rayleigh-Ritz shape functions that do not resemble normal modes. Thus application of Guyan Reduction on dynamic models composed of 3-D elements, as well as several types of one and two dimensional elements, is inappropriate.

4.1 LOAD PATCH STRATEGY

Prior to the introduction of the finite element method, investigators defined Rayleigh-Ritz shape functions as any admissible linearly independent shape functions. A common practice was utilization of deflection patterns based on deflections due to distributed static load patterns. The alternative reduction strategy, presented herein, borrows from this earlier common practice and formalizes a systematic procedure[11] that has advantages to be demonstrated.

Consider the general distribution of static loads described by the matrix equation,

$$\left\{F\right\}=\begin{bmatrix}\Psi_{11} & 0 & \ldots & 0\\ 0 & \Psi_{22} & \ldots & 0\\ \ldots & \ldots & \ldots & \ldots\\ 0 & 0 & \ldots & \Psi_{kk}\end{bmatrix}\begin{Bmatrix}F_1\\ F_2\\ \ldots\\ F_k\end{Bmatrix}=\left[\Psi\right]\left\{F_\psi\right\}, \tag{13}$$

where the individual load patches, $[\Psi_{ii}]$, represent unit load patterns (over each specific geometric patch) that are mathematically the transposes of rigid body deflection patterns. The static displacement due to the above defined loading is

$$\left\{U\right\}=\left[K\right]^{-1}\left\{F\right\}=\left[K^{-1}\Psi\right]\left\{F_\psi\right\}. \tag{14}$$

Pre-multiplication of this result by the transpose of unit loadings yields,

$$\left\{U_\psi\right\}=\left[\Psi\right]^T\left[K\right]^{-1}\left\{F\right\}=\left[\Psi^T K^{-1}\Psi\right]\left\{F_\psi\right\},\quad \left\{F_\psi\right\}=\left[\Psi^T K^{-1}\Psi\right]^{-1}\left\{U_\psi\right\}. \tag{15}$$

The above generalized displacements are mathematically the average 6-DOF displacements at the geometric centroid of each load patch. Substitution of this result into equation 14 yields the (load patch based) "Guyan Reduction" transformation,

$$\{U\} = \left[K^{-1}\Psi\right]\left[\Psi^T K^{-1}\Psi\right]^{-1}\{U_\psi\} = [T_\psi]\{U_\psi\}. \tag{16}$$

Finally, the load patch based "Guyan Reduction" stiffness and mass matrices are

$$[K_{\psi\psi}] = [T_\psi]^T[K][T_\psi] = \left[\Psi^T K^{-1}\Psi\right]^{-1}, \quad [M_{\psi\psi}] = [T_\psi]^T[M][T_\psi]. \tag{17}$$

It should be noted that, in the limiting case of concentrated, point patch loads, the present formulation reduces to Guyan Reduction.

The qualities associated with this alternative reduction strategy are demonstrated with two basic examples in the following sections.

4.2 STRETCHED STRING EXAMPLE

Consider a stretched string of length (L=72") and tension (T=9.85x10^{7}xρA), which is modeled by 400 "string" elements. Vibration modes associated with (a) exact system analysis, (b) Guyan Reduction (reduced to four analysis degrees of freedom) and (c) the alternative reduction strategy (reduced using load patches) are summarized in Figures 1 and 2.

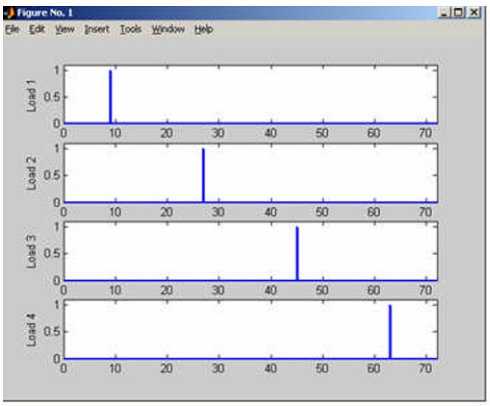

Guyan Reduction Unit Point Loads

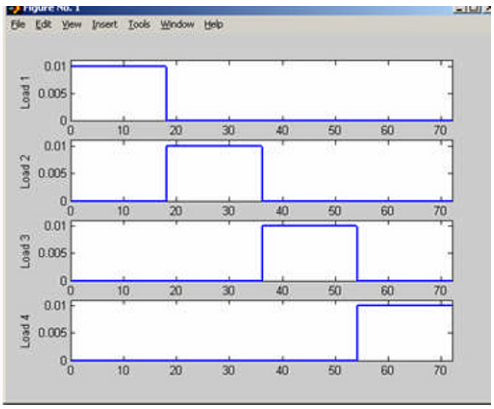

New Reduction Unit Load Patches

Figure 1: Stretched String Example Load Patterns for Model Order Reduction to Four Degrees of Freedom

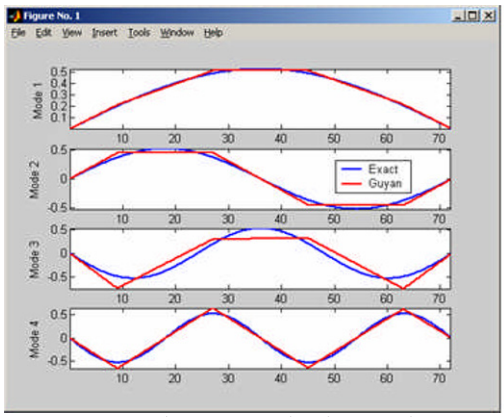

Exact and Guyan Reduction Modes

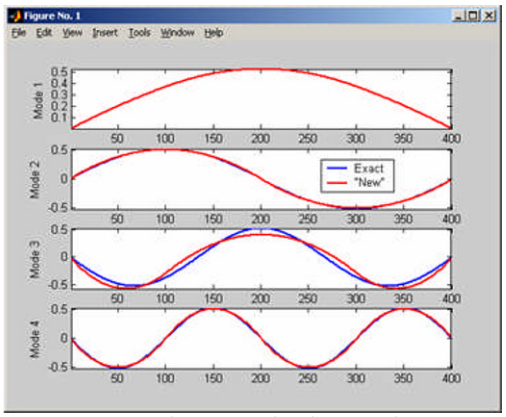

Exact and New Reduction Modes

Figure 2: Comparison of the First Four Stretched String Mode Shapes Computed via Reduction to 4 DOF

The limitations associated with Guyan Reduction, for this example, are clearly illustrated by the straight segment mode shapes associated with point unit loads. In contrast, modes associated with distributed unit patch loads more closely follow the exact mode shapes, indicating the advantage of the new reduction strategy. A quantitative comparison of modal frequency and mode shape errors associated with Guyan Reduction and the new reduction strategy is provided in Figure 3.

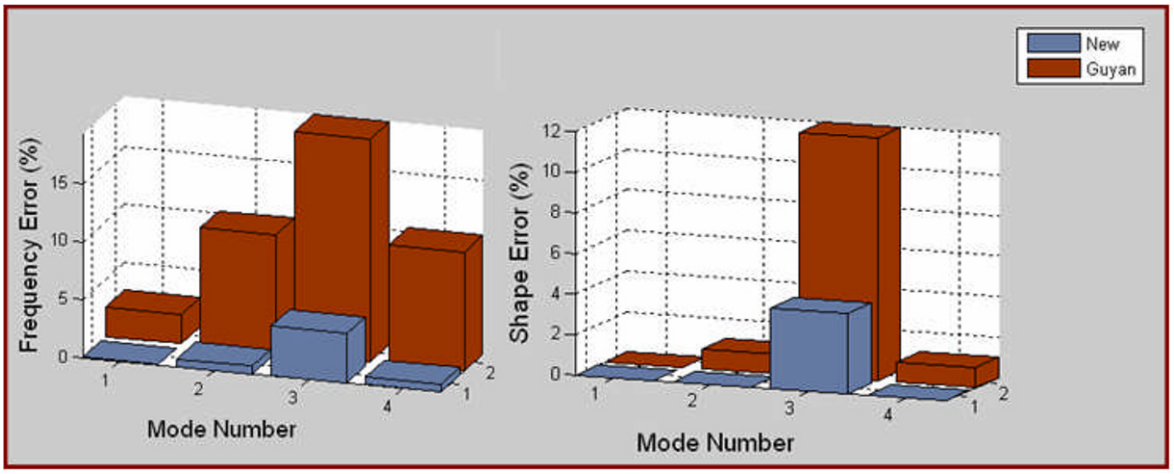

Natural Frequency Errors Mode Shape Errors

Figure 3: Comparison of Natural Frequency and Mode Shape Errors Associated with Reduction to 4 DOF

It should be noted that the mode shape error is based on the modal coherence metric (for mode "i"),

$$(E_{\Phi})_i = 1 - \left[\{\Phi_E\}_i^T [M] \{\Phi_A\}_i\right]^2 \tag{18}$$

The accuracies of the two reduction strategies for the 400 element stretched string model reduced to 16 analysis degrees of freedom are summarized in Figure 4.

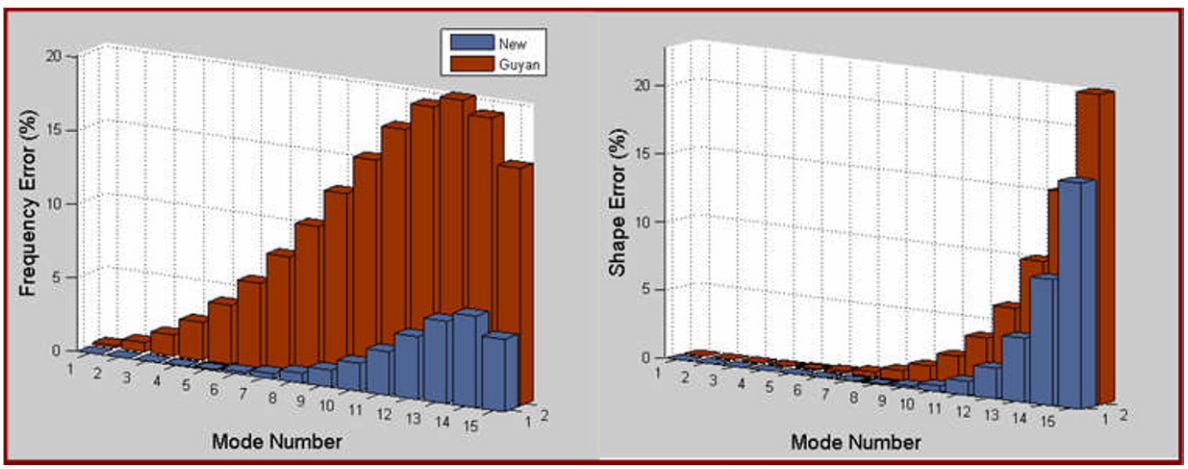

Natural Frequency Errors Mode Shape Errors

Figure 4: Comparison of Natural Frequency and Mode Shape Errors Associated with Reduction to 16 DOF

4.3 BRANCHED SHELL EXAMPLE

The shell structure, shown below in Figure 5, serves as the second illustrative example in this paper. It consists of five substructures, namely (1) a lower cylindrical skirt (fully fixed at its base), (2) a lower hemispherical bulkhead, (3) lower cylindrical section, (4) upper cylindrical section, and (5) upper hemispherical bulkhead. The overall dimensions of the aluminum structure are length, L=100 inches, radius, R=20 inches, and wall thickness, h=0.4 inches.

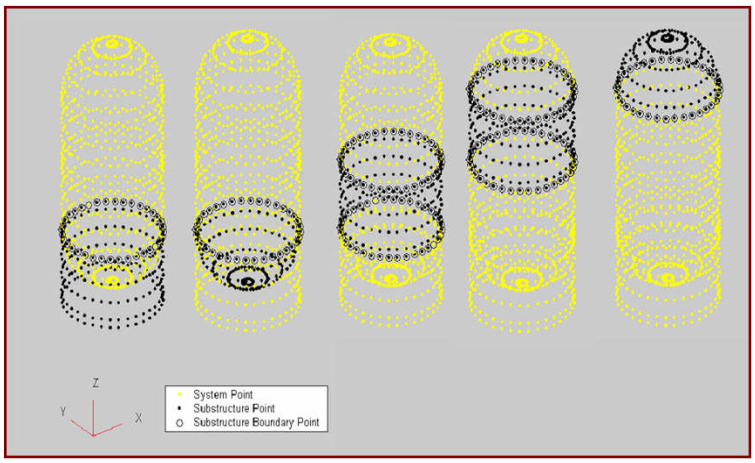

Figure 5: Multi-Segmented Shell Structure

The new reduction strategy is applied to this 6480 DOF shell finite element model by application of unit body loads (following equation 13) at each of the individual "ring" stations. An interesting result of the selected unit load patterns is a reduction of displacement DOFs to centerline grid points (following equation 16) as illustrated in Figure 6. The reduced model consisting of 27 centerline DOFs, with a fixed base, may serve as a test-analysis model (TAM). Also depicted in Figure 6 are (a) a typical accelerometer arrangement that may be employed to construct an effective centerline 6 DOF displacement array, and (b) the (consistent) rigid body mass matrix associated with the reduced model.

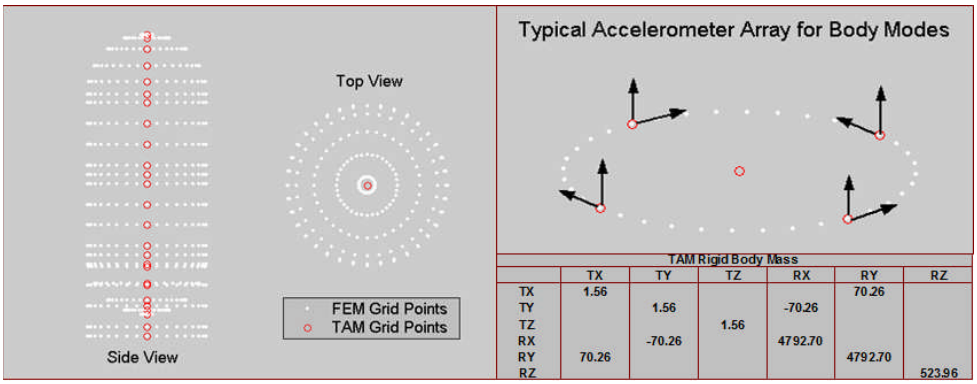

Figure 6: Reduced Centerline Shell Structure Model with Related TAM Information

Computed modes for both the exact and reduced shell models, summarized in Figure 7, indicate several key features associated with the new reduction method (when it is applied to shell structural dynamics), namely (a) overall body mode frequency and mode shapes of the reduced model are essentially exact, and (b) shell breathing modes are automatically not computed by the reduced model.

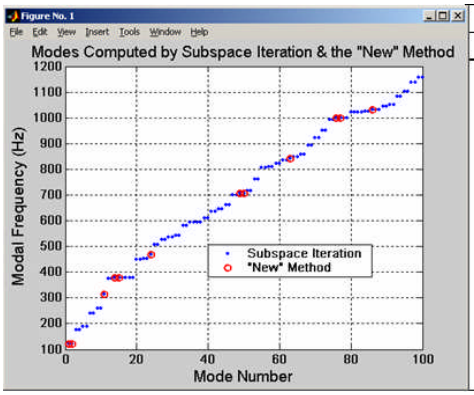

Full Model		Load Patch		
Mode	Freq (Hz)	Mode	Freq (Hz)	COR
1	122.20	1	122.20	100
2	122.20	2	122.20	100
11	315.24	3	315.24	100
14	377.21	4	377.21	100
15	377.21	5	377.21	100
24	467.77	6	467.92	100
49	706.65	7	706.84	100
50	706.65	8	706.85	100
63	841.31	9	841.35	100
76	997.48	10	999.12	100
77	997.50	11	999.14	100
86	1029.90	12	1046.30	99

Figure 7: Exact and Reduced Model Modes of the Shell Structure

5. CONCLUSIONS

While Guyan continues to be widely utilized for definition of test-analysis models (TAMs), modern 3-D elastic and other advanced models have introduced serious deficiencies in its application. Specifically, inappropriate Rayleigh-Ritz trial vectors result from implied point unit loads associated with Guyan Reduction. This paper introduces a new, systematic strategy for definition of reduced finite element structural dynamic models, employing trial vectors associated with distributed load patches. The new method closely follows the Guyan Reduction principle and it appears to produce more accurate reduced models in situations that are both appropriate and problematic for classical Guyan Reduction.

A key feature of the new method is its natural definition of centroidal, "average" displacements associated with systematically defined, distributed load patches. This feature leads to definition of straightforward TAMs that should be especially advantageous in test-analysis correlation evaluations of shell-type structures. In addition, in the case of a symmetric shell-type structure, the new reduction strategy permits computation of accurate (almost exact) overall body modes, while ignoring the many breathing modes (in the same frequency band as body modes),

The new load-patch reduction method must be subjected to further studies and evaluations in order to uncover the extent and limitations of its utility.

REFERENCES

[1] Harris' Shock and Vibration Handbook, 6th Ed, A. Piersol and T. Paez (Ch. 23, R. Coppolino), McGraw-Hill, 2010
[2] The Finite Element Method: Its Basis and Fundamentals, 6th Ed, O. Zienkiewicz, R. Taylor, and J. Zhou, Elsevier,2005
[3] "Über eine neue Methode zur Lösung gewisser Variationsprobleme der mathematischen Physik", W. Ritz, J. reine angew. Math. 135, 1-61, 1908.
[4] "Reduction of Stiffness and Mass Matrices", R. Guyan, AIAA Journal, Vol. 3, 1965
[5] "Coupling of Substructures for Dynamic Analysis", R. Craig and M. Bampton, AIAA Journal, Vol. 6, July 1968
[6] "Large Eigenvalue Problems in Dynamic Analysis", K-J Bathe and E. Wilson, ASCE J. Eng. Mech. Div 98(6), 1972
[7] The Lanczos Method Evolution and Application, L. Komzsik, Cambridge University Press, 1987
[8] "Automated Response DOF Selection for Mapping of Experimental Normal Modes", R. Coppolino, IMAC XVI, 1998
[9] "A Procedure for an Improved Reduced System (IRS) Model, J. O'Callahan, IMAC VII, 1989
[10] History of Strength of Materials, S. Timoshenko, Dover Publications, 1983
[11] Conversations, during the mid 1980's, with Robert T. Lahey, who had previously developed and applied a load patch procedure at Lockheed Aircraft Company.

Understanding Large Order Finite Element Model Dynamic Characteristics

Robert N. Coppolino, CTO
Measurement Analysis Corporation
23850 Madison Street
Torrance, California 90505

ABSTRACT

State-of-the-art technologies in computation and software have led to ever increasing size of finite element models, simply because this is possible. While it is arguable that "degree-of-freedom" proliferation is unnecessary, there are some potential benefits to be realized, namely (1) commonality of stress and dynamic models and (2) employment of finite element models in the mid- and high-frequency ranges (normally the domain of statistical energy analysis). When large order finite element models are developed using appropriate wavelength-based rules, they are valid for high frequency, high modal density dynamic analysis. Such models do not suffer from the need for simplifying and/or "smearing" assumptions used in statistical energy analysis (SEA). This paper describes energy-based metrics that clearly identify the characteristics of normal modes, of large-order models. In addition, a modal filtering method, that employs shape function classes (e.g. overall body and bulge shapes) and modal coherence analysis, identifies "target" modes of interest which are a subset of a very large set of overall body, local and breathing modes. Illustrative models are used to demonstrate the procedures.

1. INTRODUCTION

Finite element models of modern structural systems, such as aircraft, spacecraft, and automobiles, are typically composed of thousands to millions of grid points due to the sophistication of commercial CAE software products and mechanical (static and dynamic) fidelity requirements[1,2]. The level of complexity in modern dynamic system models has produced a challenge to engineering understanding of the character and classification of normal modes. Sophisticated geometric displays of normal modes provide the engineer with an intuitive, subjective impression of their character. However, they fail to define objective, quantitative metrics to clearly characterize normal modes.

Since the 1960's, the aerospace industry has developed and utilized mathematical tools that logically segment complex dynamic systems. The Craig-Bampton[3] and Benfield-Hruda[4] methods of component mode synthesis (CMS) are leading examples of procedures that have permitted effective analysis of complex dynamic systems (ahead of the great advances in computational hardware subsequent to the 1960s). Moreover, these methods yielded effective metrics for characterizing normal modes, utilizing quantities such as modal kinetic energy, modal strain energy, and modal participation and effective mass[1]. Component mode synthesis and its mode characterization metrics are quite straightforward when applied to branched, beam-like aerospace structures. They tend, however, to become awkward with structures that have highly distributed component interfaces (as in the case of automobile structures). Finally, it is noted that component mode synthesis may not be used at all on large-order finite element models, leaving the engineer with a more acute need for quantitative normal mode metrics.

Regardless of the engineer's choice of dynamic analysis strategy (CMS or complete system), the structural system is always composed of distinct subsystems (e.g., fuselage, wings, vertical and horizontal stabilizers, engines, …). In addition, individual normal modes often have dominant directional activity (e.g., surge, sway, heave, roll, pitch, and yaw). Segmentation of modal kinetic and strain energies by directions and physical components are exploited in this paper to yield clear metrics for "naming" of normal modes.

Another difficulty encountered in the analysis of shell-type aerospace structures is the result of the presence of many local shell breathing modes in the same frequency band as dominant body modes. Employment of modal effective mass as a metric provides one approach for discrimination of the two modal classes. A new, more effective means for mode discrimination, based on modal coherence with respect to "shape families", is introduced and demonstrated in this paper.

T. Proulx (ed.), *Linking Models and Experiments, Volume 2*, Conference Proceedings of the Society for Experimental Mechanics Series 5,
DOI 10.1007/978-1-4419-9305-2_26, © The Society for Experimental Mechanics, Inc. 2011

2. NOMENCLATURE

Matrices and Vectors:

$\{F\}$	Force (Eq. 1)	$\{R_{Bodies,n}\}_n$	Residual flexible body deformation (Eq. 14)
$[K]$	Stiffness (Eq. 1)	$\{SE\}_n$	Modal strain energy (Eq. 11)
$[\overline{K}_{bb}]$	Craig-Bampton boundary stiffness (Eq. 5)	$[\Phi]$	Modal matrix (Eq. 2)
$\{KE\}_n$	Modal kinetic energy (Eq. 10)	$[\Psi_{Body,i}]$	Rigid body matrix for Body "*i*" (Eq. 14)
$[M]$	Mass (Eq. 1)	$[\Psi_{ib}]$	Craig-Bampton "constraint modes" (Eq. 4)
$[\overline{M}_{bb}]$	Craig-Bampton boundary mass (Eq. 5)	$\{u\}$	Displacement vector (Eq. 1)
$[Meff]_n$	Modal effective mass (Eq. 8)	$\{q\}$	Modal displacement vector (Eq. 2)
$[P]$	Modal participation factor (Eq. 5)	$\{\varphi_{Body.i}\}_n$	Body modal coefficient vector (Eq. 14)

Variables:

$COH_{Bodies,n}$	Modal coherence (Eq. 17)	i	Imaginary unit (Eq. 1)
f	Circular frequency	η	Structural damping coefficient (Eq. 1)
$h_n(f)$	Modal frequency response (Eq. 6)	λ	Eigenvalue (Eq. 2)

Subscripts:

B	Number of "bodies"	b	"boundary", or "body"
RX, RY, RZ	Global rotational coordinates	e	"external"
Tot	"Total"	i	"internal"
N	Number of modes	n	"mode" number
TX, TY, TZ	Global translation coordinates	q	"interior" modes

3. DESIGN OF RELEVANT FINITE ELEMENT MODELS

Finite element models that faithfully simulate dynamic response, loads and stresses associated with anticipated dynamic environments must be designed to (a) produce accurate system modes and/or frequency response over the frequency band of interest, and (b) accurately predict redundant load paths and peak local stresses that define structural safety margins. The above two requirements may be employed to define a unified dynamic-stress model or separate dynamic and stress models (a common practice in the aerospace industry).

3.1 DYNAMIC FIDELITY REQUIREMENTS

In order to develop a relevant dynamic model, general requirements should be addressed based on

1. Frequency band width 0<f<f*, and intensity (F*) of anticipated dynamic environments.
2. General characteristics of structural or mechanical components.

Dynamic environments are generally (a) harmonic, (b) transient, (c) impulsive or (d) random. For all categories, the cut-off frequency (f*) is reliably determined by shock response spectrum analysis[1]. The overall intensity level of a dynamic environment is described by the peak amplitude for harmonic, transient and impulsive events, or by the statistical amplitude (e.g., mean plus a multiple of the standard deviation) for a long duration random environment. With the cut-off frequency (f*) established, the shortest relevant wavelength (L) of forced vibration for components in a structural assembly may be calculated. For finite element modeling, the quarter wavelength (L/4) is of particular interest, since it is a rough estimate of the grid spacing needed to characterize system dynamics at the cut-off frequency. Note that the actual grid spacing requirement is a function of the specific elements being used. Grid spacing (quarter wavelength) guidelines, for typical structural components, are summarized in Table 1.

Component	Mode Type	Quarter Wavelength (L/4)	Additional Data
String	Lateral	$(\sqrt{T/\rho A})/(4f^*)$	T=tension, A=area, ρ = mass density
Rod	Axial	$(\sqrt{E/\rho})/(4f^*)$	E = elastic modulus
Rod	Torsion	$(\sqrt{G/\rho})/(4f^*)$	G = shear modulus
Beam	Bending	$(\pi/2)(EI/\rho A)^{1/4}/\sqrt{2\pi f^*}$	EI = flexural stiffness
Membrane	Lateral	$(\sqrt{N/\rho h})/(4f^*)$	N = stress resultant
Plate	Bending	$(\pi/2)(D/\rho h)^{1/4}/\sqrt{2\pi f^*}$	D=flexural stiffness, h=thickness
3-D Elastic	Dilational	$(\sqrt{E/\rho})/(4f^*)$	
3-D Elastic	Shear	$(\sqrt{G/\rho})/(4f^*)$	
Acoustic	Dilational	$(\sqrt{B/\rho})/(4f^*)$	B=Bulk Modulus

Table 1: Grid Spacing Guidelines for Typical Structural Components

3.2 STRESS FIDELITY REQUIREMENTS

Accurate modeling of stress concentrations, for a unified dynamic-stress model, may be addressed by employment of adaptive mesh refinement[2], or by utilization of documented stress concentration formulae[5]. If mesh refinement is utilized, the number of model degrees of freedom may increase substantially, imposing undue computational resource penalties on a model that had been appropriately designed for study of dynamic response and loads. If localized stress concentrations do not affect a model's dynamics fidelity, it is prudent to recover detailed stresses by employing (a) stress concentration formulae and/or (b) separate, detailed local or global "stress" finite element models (designed using adaptive mesh refinement).

3.3 ILLUSTRATIVE EXAMPLE SHELL STRUCTURE [3]

The shell structure, shown below in Figure 1, serves as an illustrative example system throughout this paper. It consists of five substructures, namely (1) a lower cylindrical skirt (fully fixed at its base), (2) a lower hemispherical bulkhead, (3) lower cylindrical section, (4) upper cylindrical section, and (5) upper hemispherical bulkhead. The overall dimensions of the aluminum structure are length, L=100 inches, radius, R=20 inches, and wall thickness, h=0.4 inches. It should be noted that this illustrative example structure does not represent a realistic design. The rather high thickness-to-radius ratio, h/R=1/50, was selected to produce less shell breathing modes in the base frequency band (f < 2000 Hz) than typical aerospace systems, while including modes of sufficient complexity to illustrate key aspects of quantitative normal mode metrics.

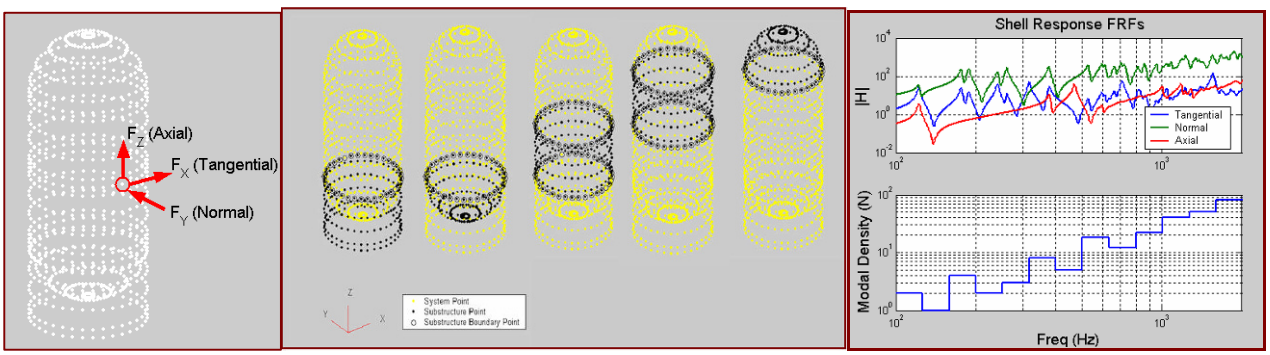

Shell with Applied Forces | Shell Structure Component Breakdown | FRFs and Modal Density Distribution

Figure 1: Illustrative Example Shell Structure (Modal Density, N = number of modes per 1/3 octave band)

4. MODAL CHARACTERIZATION METRICS

The fundamental set of matrix equations describing forced response of a linear structural dynamic FEM (with structural damping) are

$$[M]\{\ddot{u}\}+1+i\eta)[K]\{u\}=\{F_e(t)\}. \tag{1}$$

For the case of undamped free vibration, the orthonormal mode transformation and properties with respect to system mass and stiffness are

$$\{u\}=[\Phi]\{q\}\ ,[\Phi]^T[M][\Phi]=[\mathrm{I}],\ [\Phi]^T[K][\Phi]=[\lambda]. \tag{2}$$

4.1 MODAL PARTICIPATION FACTORS AND MODAL EFFECTIVE MASS (CRAIG-BAMPTON MODEL)

In the case of a supported (e.g., base-fixed) system, the displacement degrees of freedom are partitioned into interior (or free) and boundary (or fixed) degree of freedom subsets, as shown below:

$$\begin{bmatrix} M_{ii} & M_{ib} \\ M_{bi} & M_{bb} \end{bmatrix}\begin{Bmatrix} \ddot{u}_i \\ \ddot{u}_b \end{Bmatrix}+(1+i\eta)\begin{bmatrix} K_{ii} & K_{ib} \\ K_{bi} & K_{bb} \end{bmatrix}\begin{Bmatrix} u_i \\ u_b \end{Bmatrix}=\begin{Bmatrix} F_i(t) \\ F_b(t) \end{Bmatrix} \tag{3}$$

The Craig-Bampton[3] modal transformation describes the interior degrees of freedom in terms of boundary fixed modes and "constraint modes" associated with unit boundary displacements.

$$\begin{Bmatrix} u_i \\ u_b \end{Bmatrix}=\begin{bmatrix} \Phi_{iq} & -K_{ii}^{-1}K_{ib} \\ 0_{bq} & \mathrm{I}_{bb} \end{bmatrix}\begin{Bmatrix} q \\ u_b \end{Bmatrix}=\begin{bmatrix} \Phi_{iq} & \Psi_{ib} \\ 0_{bq} & \mathrm{I}_{bb} \end{bmatrix}\begin{Bmatrix} q \\ u_b \end{Bmatrix} \tag{4}$$

It should be noted that when the boundary is statically determinate, the "constraint modes" are rigid body vectors, referenced at the boundary. When the above transformation is applied, the resulting Craig-Bampton component dynamic equations are

$$\begin{bmatrix} \mathrm{I}_{qq} & P_{qb} \\ P_{bq} & \overline{M}_{bb} \end{bmatrix}\begin{Bmatrix} \ddot{q} \\ \ddot{u}_b \end{Bmatrix}+(1+i\eta)\begin{bmatrix} \omega_q^2 & 0_{ib} \\ 0_{bi} & \overline{K}_{bb} \end{bmatrix}\begin{Bmatrix} q \\ u_b \end{Bmatrix}=\begin{bmatrix} \Phi_{iq}^T & 0_{qb} \\ \Psi_{ib}^T & \mathrm{I}_{bb} \end{bmatrix}\begin{Bmatrix} F_i(t) \\ F_b(t) \end{Bmatrix}, \tag{5}$$

The boundary mass and stiffness matrix partitions reduce to (a) the 6X6 rigid body mass matrix and (b) a null 6X6 boundary stiffness matrix, respectively, if the boundary is statically determinate. It is of interest to consider the response of such a system to simple harmonic boundary accelerations. The modal accelerations, in this situation are:

$$\ddot{q}_n(f)=-h_n(f)[P_{nb}]\{\ddot{u}_b(f)\}\ ,\qquad h_n(f)=\frac{-(f/f_n)^2}{1+i\eta_n-(f/f_n)^2} \tag{6}$$

And the boundary reaction loads, for a statically determinate boundary, are:

$$\{F_b(f)\}=\left[\overline{M}_{bb}-\sum_{n=1}^{N}[P_{bn}P_{nb}]h_n(f)\right]\{\ddot{u}_b(f)\} \tag{7}$$

The modal participation products are called modal effective mass matrices (one per mode), which when summed are approximately the total system rigid body mass (equal only if the boundary is massless). Modal effective mass is a modal metric that indicates direction of modal activity as well as degree with which the boundary reacts to modal response.

$$[Meff]_n=[P_{bn}][P_{nb}]\ ,\ \sum_{n=1}^{N}[Meff]_n\approx[\overline{M}_{bb}] \tag{8}$$

4.2 KINETIC ENERGY AND STRAIN ENERGY

The distributions of kinetic and strain energies in one particular mode are the following respective term-by term products:

$$\{KE\}_n = \{[M]\{\Phi\}_n\} \otimes \{\Phi\}_n \quad , \quad KE_{TOT,n} = \sum_{i=1}^{DOF} KE_{in} = 1 \tag{10}$$

$$\{SE\}_n = \{[K]\{\Phi\}_n\} \otimes \{\Phi\}_n \quad , \quad SE_{TOT,n} = \sum_{i=1}^{DOF} SE_{in} = \lambda_n \tag{11}$$

The individual terms in each of these "energy" vectors are directly associated with the dynamic system degrees of freedom. As such, they provide appropriately weighted metrics for kinetic and strain energy distributions that are not indicated by the geometric modes shape (e.g., "heavier" degrees of freedom have greater kinetic energy than "lighter" degrees of freedom with equivalent modal displacements). Further insight into the character of individual modes is gained by summations of subgroups.

4.3 CLASSIFICATION BY ENERGY ACTIVITY DIRECTION

Modal kinetic and strain energy grouped sums, partitioned by global direction yield the direction of overall modal activity for a particular mode. These metrics are not weighted by level of boundary reaction (as is the case for modal effective mass).

$$\begin{aligned} \{KE\}_n &\Rightarrow \sum\{KE_{TX}\}_n, \sum\{KE_{TY}\}_n, \sum\{KE_{TZ}\}_n, \sum\{KE_{RX}\}_n, \sum\{KE_{RY}\}_n, \sum\{KE_{RZ}\}_n \\ \{SE\}_n &\Rightarrow \sum\{SE_{TX}\}_n, \sum\{SE_{TY}\}_n, \sum\{SE_{TZ}\}_n, \sum\{SE_{RX}\}_n, \sum\{SE_{RY}\}_n, \sum\{SE_{RZ}\}_n \end{aligned} \tag{12}$$

4.4 CLASSIFICATION BY COMPONENT ENERGY DISTRIBUTION

Modal kinetic and strain energy grouped sums, partitioned by subsystem component yield the distribution of component activity for a particular mode. It should be noted that the component kinetic and strain energies are not necessarily distributed in the same manner as one another.

$$\begin{aligned} \{KE\}_n &\Rightarrow \sum\{KE_1\}_n, \sum\{KE_2\}_n, \sum\{KE_3\}_n, \ldots\ldots \\ \{SE\}_n &\Rightarrow \sum\{SE_1\}_n, \sum\{SE_2\}_n, \sum\{SE_3\}_n, \ldots\ldots \end{aligned} \tag{13}$$

4.5 ILLUSTRATIVE EXAMPLE MODAL METRICS

Classification of system modes for the illustrative example shell structure in accordance with energy distributions and modal effective mass is provided for a selected subset of modes in Table 2

Mode	Description	FREQ (Hz)	Kinetic Energy (%)					Strain Energy (%)					Kinetic Energy (%)			Modal Effective Mass (%)					
			SKIRT	DOME1	SHELL1	SHELL2	DOME2	SKIRT	DOME1	SHELL1	SHELL2	DOME2	X	Y	Z	X	Y	Z	RX	RY	RZ
1	Y-Bending	122.21			11	36	51	65		27	8			96	4		62		98		
2	X-Bending	122.21			11	36	51	65		27	8		96		4	62				98	
3	Shell N=3S	176.16			46	51		14	7	35	41	3	50	50							
11	RZ-Torsion	316.86	4	6	22	43	26	59		31	9		50	50							82
14	Y-Bending	377.59	12	36	28	9	16	67	5	15	11	2		91	9		30				
15	X-Bending	377.62	12	36	28	9	16	67	5	15	11	2	91		9	30					
24	Z-Axial	469.44	3	7	18	35	37	56		29	11	3			99			81			
25	Skirt N=5S	506.51	96		2			85	12				50	50							
													Meff Partial Sum (%)			91	91	81	98	98	82

Table 2: Selected Modes of the Example Shell Structure (Metrics>1% shown)

The general characteristics of the first two overall "Y" and "X" bending modes are indicated by directional kinetic energies and modal effective masses. Moreover, the general increase in component kinetic energies for these modes with height above the base indicates overall activity distribution. Distribution of interior structural loading for the first two bending modes correctly indicates highest loads occurring in the skirt. Characteristics of the other overall body modes (11, 14, 15 24) are also clearly revealed by kinetic energy, strain energy and modal effective mass distributions.

The self-equilibrating nature of shell breathing in modes 3 and 25 is clearly indicated by the absence of modal effective mass. Graphical illustrations indicating the character of the fundamental (Y) bending mode and the lowest frequency shell breathing mode are provided in Figure 2. Kinetic (KE) and strain or potential energy (PE) distributions are indicated in "pie" format.

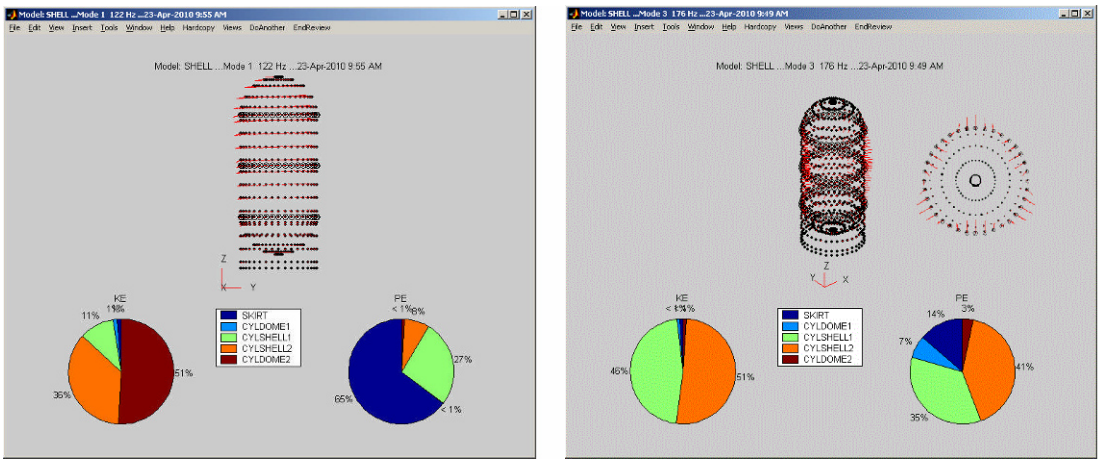

Mode 1: Y-Bending Mode 3: Cylinder n=3 Breathing

Figure 2: Graphical Illustration of the Character of Two System Modes

The modal metrics, based on kinetic energy and strain energy distributions (in accordance with direction and component activity) and modal effective mass, have been shown to clearly and quantitatively characterize modes of the illustrative example system. Most of the system modes are dominated by shell breathing activity; a few system modes are characterized by overall body bending, axial and torsional deformation. Often only the overall body modes are of interest, since they are generally the primary contributors to critical system dynamic loads. The modal filtering metric introduced below provides the means for focusing on overall body modes.

4.6 CLASSIFICATION BY "BODY" MODE SHAPE FAMILIES

The modal deformation of a dynamic finite element system may be arbitrarily segmented into selected subsystems (or bodies). In the case of the illustrative example shell structure, a "body" is designated as a ring of grid points for one of the five component shells at a particular axial location. Consider transformation, depicted in Equations 14 and 15, that relates the modal deformation of designated "bodies" to rigid body motions ($\Psi_{Body,i}$) and "residual" flexible body deformations ($R_{Body,i}$).

$$\begin{Bmatrix} \Phi_{Body,1} \\ \Phi_{Body,2} \\ \dots \\ \Phi_{Body,B} \end{Bmatrix}_n = \begin{bmatrix} \Psi_{Body,1} & 0 & \dots & 0 \\ 0 & \Psi_{Body,2} & \dots & 0 \\ 0 & \dots & \dots & 0 \\ 0 & 0 & 0 & \Psi_{Body,B} \end{bmatrix} \begin{Bmatrix} \varphi_{Body,1} \\ \varphi_{Body,2} \\ \dots \\ \varphi_{Body,B} \end{Bmatrix}_n + \begin{Bmatrix} R_{Body,1} \\ R_{Body,2} \\ \dots \\ R_{Body,B} \end{Bmatrix}_n \tag{14}$$

$$\{\Phi\}_n = [\Psi_{Bodies}]\{\varphi_{Bodies}\}_n + \{R_{Bodies}\}_n \tag{15}$$

Note that the defined transformation is not a constraint; it is merely a means of discriminating classes of deformation in a system mode. By employing a mass-weighted linear least squares fit that orthogonalizes local rigid body and flexible body deformations, the coefficients of the "rigid bodies" transformation are determined and the flexible body deformations are,

$$\{\varphi_{Bodies}\}_n = \left[\Psi_{Bodies}^T M \Psi_{Bodies}\right]^{-1}\left[\Psi_{Bodies}^T M \Phi_n\right], \ \{R_{Bodies}\}_n = \{\Phi\}_n - [\Psi_{Bodies}]\{\varphi_{Bodies}\}_n . \tag{16}$$

The degree of purity of overall body motion in a system mode is quantified as the "body" mode coherence

$$COH_{Bodies,n} = 1 - \{R_{Bodies}\}_n^T [M] \{R_{Bodies}\}_n \tag{17}$$

4.7 ILLUSTRATIVE EXAMPLE IDENTIFICATION OF "BODY" MODES

The above defined metric for quantification of overall body mode coherence is applied to the illustrative example system modes resulting in the following result.

Mode	Freq (Hz)	Type	Modal Effective Mass (%)						Body Shape
			X	Y	Z	RX	RY	RZ	Coherence (%)
1	122.21	Bending-TX		62		98			100
2	122.21	Bending-TY	62				98		100
3 to 10		Breathing							0
11	316.86	Torsion-RZ						82	100
12 to 13		Breathing							0
14	377.59	Bending-TY		30					100
15	377.62	Bending-TX	30						100
16 to 23		Breathing							0
24	469.44	Axial-TZ			81				100
25 to 48		Breathing							0
49	706.65	Bending-TY		1					100
50	706.65	Bending-TX	1						100
51 to 62		Breathing							0
63	841.31	Torsiion-RZ						10	100
64 to 75		Breathing							0
76	997.48	Bending-TY							100
77	997.50	Bending-TX							100
78 to 85		Breathing							0
86	1029.90	Axial-TZ			8				99
			92	92	89	98	98	92	

Table 3: Identification of Overall Body Modes using "Body" Mode Coherence

The "body" mode coherence modal filter automatically separates the overall body modes from shell breathing modes, even for modes that have minimal modal effective mass. Note that shell breathing modes have "zero" coherence. This metric provides greater effectiveness than the modal effective mass metric that is generally used to identify body modes that produce significant base reaction loads (and consequently fails to designate self-equilibrating body modes).

5. CONCLUSIONS

Finite element models of modern structural systems, such as aircraft, spacecraft, and automobiles, are typically composed of thousands to millions of grid points due to the sophistication of commercial CAE software products and mechanical (static and dynamic) fidelity requirements. The level of complexity in modern dynamic system models has produced a challenge to engineering understanding of the character and classification of normal modes. While geometric displays of normal modes provide the engineer with an intuitive, subjective impression of their character, they fail to define objective, quantitative metrics to clearly characterize normal modes.

This paper described and demonstrated a variety of modal metrics, often employed in aerospace applications to quantitatively characterize normal modes on the basis of kinetic and strain energy distributions and modal effective mass. The energy based metrics were segmented into rationally defined components (rather than the system model's grid points) that clearly indicate modal activity distributions. Overall direction of modal activity was also clearly defined based on directionally summed kinetic energy components and modal effective mass.

A new metric for characterizing and filtering system modes, based on shape function families, was introduced. This shape family metric appears to effectively segregate overall body modes and breathing modes of shell-type structures, without the use of tedious mode-by-mode graphical reviews.

REFERENCES

[1] Harris' Shock and Vibration Handbook, 6th Ed, A. Piersol and T. Paez (Ch. 23, R. Coppolino), McGraw-Hill, 2010
[2] The Finite Element Method: Its Basis and Fundamentals, 6th Ed, O. Zienkiewicz, R. Taylor, and J. Zhou, Elsevier,2005
[3] "Coupling of Substructures for Dynamic Analysis", R. Craig and M. Bampton, AIAA Journal, Vol. 6, July 1968
[4] "Vibration Analysis of Structures by Component Mode Substitution", W. Benfield and R. Hruda, AIAA Journal, Vol. 9, July 1971
[5] Peterson's Stress Concentration Factors, 3rd Ed, W. Pilkey and D. Pilkey, Wiley, 2008

FEM Sensitivity Method for Uncertainty and Reconciliation Analyses

Robert N. Coppolino, CTO
Measurement Analysis Corporation
23850 Madison Street
Torrance, California 90505

ABSTRACT

Parametric variation of large order finite element models is required for evaluation of uncertainty and test-analysis reconciliation analyses. Established procedures for computation of modal frequency and mode shape derivatives are widely used in such studies. While modal derivatives accurately describe sensitivities for small parametric changes, they may be ineffective when modal frequencies are closely spaced or repeated. Over the past decade, an alternative modal sensitivity procedure has been employed for modal test-analysis reconciliation, without rigorous proof of its validity. This procedure, based on definition of residual shape functions that augment baseline system mode shapes, produces reduced mass and stiffness (sensitivity) matrices. The resultant sensitivity formulation is extremely effective for computation of altered system modes associated with large parametric variations, regardless of the presence of closely-spaced or repeated modal frequencies. This paper provides a rigorous validity proof of the alternative modal sensitivity formulation. Residual shape functions are similar to well-known quasi-static residual vectors for both localized and highly distributed model changes. A simple illustrative example is provided to demonstrate effectiveness of the technique.

1. INTRODUCTION

Efficient computation of structural dynamic modal frequency and mode shape sensitivities associated with variation of physical stiffness and mass parameters is essential for (1) practical design sensitivity and uncertainty studies and (2) reconciliation of finite element models with modal test data. Sensitivity analysis procedures fall in two distinct categories, namely (a) modal derivatives for small parametric variation and (b) altered system modes associated with "large" parametric variation. The latter category is generally applicable to modal testing, which often requires significant local parameter changes at joints to effect FEM-test reconciliation[1]. However, many investigators and commercial software packages employ estimated modal derivatives in optimization strategies, which address FEM-test reconciliation objectives.

Since the 1960's, methods for computation of modal frequency and mode shape derivatives have evolved. Fox and Kapoor[2] introduced an exact derivative formulation that required knowledge of all modes of the original system; application of the procedure when a truncated set of modes was employed produced compromised derivatives. In response to this difficulty, Nelson[3] derived an exact formulation for computation of mode shape derivatives for truncated mode sets. Efforts to refine and extend application of mode shape derivatives for finite parameter change sensitivity computations have been pursued by many investigators (including the present author). However, the need for modal frequency and mode shape sensitivities that map over very large ranges for multiple parameters suggests alternative Rayleigh-Ritz strategies.

The Rayleigh-Ritz method, actually introduced by Ritz[4], is one of the most significant developments in analytical mechanics of the past century. This method provides a logical energy formulation for consistent reduction of mass and stiffness matrices employing a set of trial vectors as a reduction transformation. Effectiveness and accuracy of the reduction process depends on selection of an appropriate trial vector set. When a truncated set of baseline system mode shapes is used as the trial vector set, the Rayleigh-Ritz method often produces poor estimates for the altered system[5]. Augmentation of the truncated baseline system mode shapes with appropriately defined additional vectors, however, has been found to produce extremely accurate altered system modal frequencies and mode shapes. Quasi-static residual vectors[6], appended to a truncated set of mode shapes, were found to produce extremely accurate modes for offshore oil platform models subjected to localized alterations[7]. This paper introduces a new procedure for selection of augmented trial vectors that is appropriate for structures that are subjected to highly distributed, as well as localized, alterations.

T. Proulx (ed.), *Linking Models and Experiments, Volume 2*, Conference Proceedings of the Society for Experimental Mechanics Series 5,
DOI 10.1007/978-1-4419-9305-2_27, © The Society for Experimental Mechanics, Inc. 2011

2. NOMENCLATURE

Matrices:

[*A*]	Generalized mass (equation 24)	[ΔK]	Stiffness alteration
[*COR*]	Cross-orthogonality (equation 3)	[ΔM]	Mass alteration
[*I*]	Identity	[Φ]	Mode shapes
[*K*]	Stiffness	[Γ]	Unit loads (equation 9)
[*M*]	Mass	[Ψ]	Trial vectors
[*OR*]	Orthogonality (equation 4)	[Δk]	Generalized stiffness alteration (equation 7)
[U]	Physical displacement	[Δk]	Generalized mass alteration (equation 7)
[*k*]	Generalized stiffness (equation 6)	[ϕ]	Generalized mode shape (equation 5)
[*m*]	Generalized mass (equation 6)	[λ]	Eigenvalues (equation 1), (2π x frequency)^2
[*q*]	Generalized displacement (equation 33)		

Variable and subscripts:

p	Structural alteration parameter (equation 2)

H	High frequency mode shapes	*a*	Boundary partition (equation 31)
L	Low frequency mode shapes	*n*	Interior partition mode shape (equation 33)
O	Baseline system (eq. 1), interior partition (eq. 31)	ρ	Residual (equation 12)
S	"Static" (equation 9)		

3. SENSITIVITY ANALYSIS STRATEGIES

The present discussion focuses on Rayleigh-Ritz procedures that address structural sensitivities due to stiffness and mass alterations described by large (as opposed to small) parametric variations. Therefore formulations that address computation of eigenvalue and mode shape derivatives are not considered.

3.1 EXACT MODAL ANALYSIS OF BASELINE AND ALTERED STRUCTURES

The matrix equations describing exact free vibration of baseline and altered structures, respectively, are

$$[K_O][\Phi_O] - [M_O][\Phi_O][\lambda_O] = [0] \tag{1}$$

and

$$[K_O + p \cdot \Delta K][\Phi] - [M_O + p \cdot \Delta M][\Phi][\lambda] = [0] \tag{2}$$

It is implicitly assumed that the stiffness and mass changes scale linearly with respect to the parameter, *p*. Therefore, changes in "beam" depth may not be directly applied, since the axial stiffness (AE) scales linearly with depth and the flexural stiffness (EI) scales as the cube of depth. The appropriate formulation for equation 2 permits linear sensitivity of "AE" and "EI" separately.

The relationship between mode shapes of the baseline and altered structures is expressed as the cross-orthogonality of orthonormal mode shape sets,

$$[COR] = [\Phi_O^T][M_0][\Phi] \tag{3}$$

where

$$[OR_o] = [\Phi_O^T][M_0][\Phi_0] = [\mathrm{I}_o] \quad , \quad [OR] = [\Phi^T][M_0][\Phi] = [\mathrm{I}]. \tag{4}$$

3.2 TRUNCATED MODE SET APPROXIMATION

The most fundamental Rayleigh-Ritz approximation, commonly used in structural dynamics modification[5], employs a truncated set of low frequency eigenvalues as the reduction transformation described by

$$[\Phi] = [\Phi_{OL}][\varphi], \tag{5}$$

where the reduced baseline structure stiffness and mass matrices, respectively, are

$$[k_O] = [\Phi_{OL}^T K_O \Phi_{OL}] = [\lambda_{OL}] \ , \ [m_O] = [\Phi_{OL}^T M_O \Phi_{OL}] = [\mathrm{I}_{OL}], \tag{6}$$

the reduced stiffness and mass sensitivity matrices, respectively, are

$$[\Delta k] = [\Phi_{OL}^T \Delta K \Phi_{OL}] \ , \ [\Delta m] = [\Phi_{OL}^T \Delta M \Phi_{OL}], \tag{7}$$

and the reduced altered structure free vibration equation is

$$[\lambda_{OL} + p \cdot \Delta k][\varphi] - [\mathrm{I}_{OL} + p \cdot \Delta m][\varphi][\lambda] = [0]. \tag{8}$$

A well-known result of this type of trial vector reduction strategy is that the approximate altered structure eigenvalues are generally higher than results for the exact solution, and the approximate mode shapes do not closely follow the exact shapes when parametric alterations are large.

3.3 RESIDUAL VECTOR AUGMENTATION (FOR LOCAL ALTERATIONS)

The static displacements for a baseline structure subjected to unit loads (at physical degrees of freedom where the structure is to be altered) described by the columns of a load array, [Γ], are the solutions of

$$[K_O][U_S] = [\Gamma], \tag{9}$$

A low frequency modal approximation of static displacements for the above system employs the transformation,

$$[U_{SL}] = [\Phi_{OL}][q_L], \tag{10}$$

resulting in the approximate static displacements,

$$[q_L] = [\lambda_L^{-1}][\Phi_{OL}^T][\Gamma] \ , \ [U_{SL}] = [\Phi_{OL} \lambda_L^{-1} \Phi_{OL}^T][\Gamma], \tag{11}$$

The difference between the exact and approximate static solutions defines MacNeal's[6] quasi-static residual vectors,

$$[\Psi_\rho] = [U_S] - [U_{SL}] = [K_O^{-1} - \Phi_{OL} \lambda_L^{-1} \Phi_{OL}^T][\Gamma] \equiv [\Phi_{OH} \lambda_H^{-1} \Phi_{OH}^T][\Gamma], \tag{12}$$

which have been mathematically proven to be the quasi-static displacements associated with all of the high-frequency mode shapes.

An orthonormalized set of residual vectors is defined by solution of the residual eigenvalue problem[7],

$$\begin{gathered} [k_\rho] = [\Psi_\rho^T K_O \Psi_\rho] \ , \ [m_\rho] = [\Psi_\rho^T M_O \Psi_\rho] \ , \\ [k_\rho][\varphi_\rho] - [m_\rho][\varphi_\rho][\lambda_\rho] = [0] \ , \ [\Phi_\rho] = [\Psi_\rho][\varphi_\rho] \end{gathered} \tag{13}$$

The augmented trial vector set (replacing the reduction transformation of equation 5) is

$$\left[\overline{\Phi}_{OL}\right] = \left[\Phi_{OL} \quad \Phi_{\rho}\right]. \tag{14}$$

When structural alterations are localized, relatively few residual vectors adequately describe the content of changed system mode shapes, as demonstrated in an offshore oil platform damage sensitivity study[7]. The above described innovation loses its appeal when structural alterations are well-dispersed requiring utilization of many residual vectors.

4. ROBUST STRATEGY (FOR DISPERSED ALTERATIONS)

When structural alterations are well-dispersed, parametric structural changes may affect many physical degrees of freedom and require a description in terms of several independent scaling parameters, "p_i". The expressions for altered stiffness and mass matrices in such a situation are

$$\left[K\right] = \left[K_O\right] + \sum_{i=1}^{N} p_i \left[\Delta K_i\right] \ , \ \left[M\right] = \left[M_O\right] + \sum_{i=1}^{N} p_i \left[\Delta M_i\right], \tag{15}$$

The altered system free vibration matrix equation for this situation is

$$\left[K_O + \sum_{i=1}^{N} p_i \left[\Delta K_i\right]\right]\left[\Phi\right] - \left[M_O + \sum_{i=1}^{N} p_i \left[\Delta M_i\right]\right]\left[\Phi\right]\left[\lambda\right] = \left[0\right], \tag{16}$$

Note that equation 1 describes the baseline system's free vibration behavior.

4.1 RESIDUAL VECTOR FORMULATION

Definition of residual vectors associated with dispersed, independent alterations of a baseline structure, described by equation 1, is accomplished by first computing the lowest frequency mode shapes of the baseline structure (equation 5) as well as the lowest mode shapes associated with each independent alteration of the structure

$$\left[K_O + \overline{p}_i \Delta K_i\right]\left[\Phi_{iL}\right] - \left[M_O + \overline{p}_i \Delta M_i\right]\left[\Phi_{iL}\right]\left[\lambda_{iL}\right] = \left[0\right] \ \text{(for i=1,…,N)}, \tag{17}$$

The selected value of each independent scaling parameter is sufficiently large to produce a substantial change in mode shapes (with respect to the baseline structure). An initial set of trial vectors that adequately (and perhaps redundantly) encompass all potential (low frequency) altered system mode shapes is

$$\left[\Psi\right] = \left[\Phi_{1L} \quad \Phi_{2L} \quad \ldots \quad \Phi_{NL}\right] \tag{18}$$

This set of trial vectors is expressible as the sum of (a) a linear combination of baseline system mode shapes and (b) trial vectors (that are linearly independent of the baseline system mode shapes)

$$\left[\Psi\right] = \left[\Phi_{OL}\right]\left[COR\right] + \left[\Psi'\right] \tag{19}$$

The cross-orthogonality coefficient matrix is determined based on the following least-squares solution

$$\left[\Phi_{OL}^T M_O \Psi\right] = \left[\Phi_{OL}^T M_O \Phi_{OL}\right]\left[COR\right] + \left[\Phi_{OL}^T M_O \Psi'\right] = \left[\mathrm{I}_{OL}\right]\left[COR\right] + \left[0\right], \tag{20}$$

where

$$\left[COR\right] = \left[\Phi_{OL}^T\right]\left[M_0\right]\left[\Psi\right] \tag{21}$$

$$\left[\Psi'\right] = \left[\mathrm{I}_{OL} - \Phi_{OL}\Phi_{OL}^T M_O\right]\left[\Psi\right] \tag{22}$$

The "purified" trial vector set is linearly independent of the baseline system mode shapes in a manner similar to MacNeal's residual vectors, as follows:

$$\begin{aligned}\left[\Psi'^{T} M_O \Phi_{OL}\right] &= \left[\Psi^T\right]\left[\mathrm{I}_{OL} - M_O \Phi_{OL} \Phi_{OL}^T\right]\left[M_O \Phi_{OL}\right] = \left[\Psi^T\right]\left[M_O \Phi_{OL} - M_O \Phi_{OL}\left(\Phi_{OL}^T M_O \Phi_{OL}\right)\right] \equiv [0] \\ \left[\Psi'^{T} K_O \Phi_{OL}\right] &= \left[\Psi^T\right]\left[\mathrm{I}_{OL} - M_O \Phi_{OL} \Phi_{OL}^T\right]\left[K_O \Phi_{OL}\right] = \left[\Psi^T\right]\left[K_O \Phi_{OL} - M_O \Phi_{OL} \lambda_{0L}\right] \equiv [0].\end{aligned} \tag{23}$$

While the "purified" trial vector set has the above property, it includes an unnecessarily large number of vectors. An appropriate, substantially smaller set of residual vectors is identified by singular value decomposition of the matrix

$$[A] = \left[\Psi'^{T} M_O \Psi'\right], \tag{24}$$

The singular value decomposition process involves solution of the eigenvalue problem,

$$[A]\left[\varphi_\rho\right] = \left[\varphi_\rho\right]\left[\lambda_\rho\right], \quad \lambda_{\rho 1} \geq \lambda_{\rho 2} \geq \lambda_{\rho 3} \geq \ldots\ldots \tag{25}$$

A suitable cut-off criterion, noted below, that has been employed over the past ten years with good success in defining the suitable reduced trial vector set, is

$$\frac{\lambda_{\rho N}}{\lambda_{\rho 1}} \leq 10^{-5}. \tag{26}$$

The augmented trial vector set (replacing the reduction transformation of equation 5) is

$$\left[\overline{\Phi}_{OL}\right] = \left[\Phi_{OL} \quad \Psi' \varphi_\rho\right] \tag{27}$$

Experience over the past ten years on a variety of structural systems with distributed alterations indicates that the size of the augmented trial vector set is on the order of the number of independent scaling parameters, p_i.

4.2 MULTI-PARAMETER SENSITIVITY MODELS

The form of the resulting Rayleigh-Ritz, multi-parameter sensitivity model (associated with selected values of the scaling parameters) is

$$\left[k_O + \sum_{i=1}^{N} p_i \left[\Delta k_i\right]\right]\left[\varphi\right] - \left[m_O + \sum_{i=1}^{N} p_i \left[\Delta m_i\right]\right]\left[\varphi\right]\left[\lambda\right] = [0] \quad , \tag{28}$$

where

$$\begin{aligned}&\left[k_O\right] = \left[\overline{\Phi}_{OL}^T K_O \overline{\Phi}_{OL}\right], \quad \left[m_O\right] = \left[\overline{\Phi}_{OL}^T M_O \overline{\Phi}_{OL}\right] \\ &\left[\Delta k_i\right] = \left[\overline{\Phi}_{OL}^T \Delta K_i \overline{\Phi}_{OL}\right], \quad \left[\Delta m_i\right] = \left[\overline{\Phi}_{OL}^T \Delta M_i \overline{\Phi}_{OL}\right].\end{aligned} \tag{29}$$

Recovery of mode shapes in terms of physical degrees-of-freedom is accomplished with

$$\left[\Phi\right] = \left[\overline{\Phi}_{OL}\right]\left[\varphi\right] \tag{30}$$

4.3 COMPONENT MODE SYNTHESIS ENHANCEMENT

It should be noted that the above developed formulation may be adapted for component mode synthesis applications, wherein free vibration of a Craig-Bampton[8] component described by the "boundary" and "interior" displacement partitions is

$$\begin{bmatrix} \overline{M}_{aa} & M_{ao} \\ M_{oa} & M_{oo} \end{bmatrix} \begin{Bmatrix} \ddot{U}_a \\ \ddot{U}_o \end{Bmatrix} + \begin{bmatrix} \overline{K}_{aa} & K_{ao} \\ K_{oa} & K_{oo} \end{bmatrix} \begin{Bmatrix} U_a \\ U_o \end{Bmatrix} = \begin{Bmatrix} 0_a \\ 0_o \end{Bmatrix} \tag{31}$$

And the modal reduction transformation is

$$\begin{Bmatrix} U_a \\ U_o \end{Bmatrix} = \begin{bmatrix} \mathrm{I}_{aa} & 0_{an} \\ -K_{oo}^{-1}K_{oa} & \Phi_{on} \end{bmatrix} \begin{Bmatrix} U_a \\ q_n \end{Bmatrix} \tag{32}$$

The resulting reduced order Craig-Bampton, free-vibration equation set is of the form

$$\begin{bmatrix} M_{aa} & P_{an} \\ P_{na} & \mathrm{I}_{nn} \end{bmatrix} \begin{Bmatrix} \ddot{U}_a \\ \ddot{q}_n \end{Bmatrix} + \begin{bmatrix} K_{aa} & 0_{an} \\ 0_{na} & \lambda_{nn} \end{bmatrix} \begin{Bmatrix} U_a \\ q_n \end{Bmatrix} = \begin{Bmatrix} 0_a \\ 0_n \end{Bmatrix}. \tag{33}$$

By including all physical degrees of freedom associated with structural alteration in the "boundary" set, multi-parameter sensitivity matrices associated with the "boundary" set may be defined following the formulation provided in sections 4.1 and 4.2, where

$$[K_{aa}] = [K_{aa,O}] + \sum_{i=1}^{N} p_i [\Delta K_{aa,i}] \ , \ [M_{aa}] = [M_{aa,O}] + \sum_{i=1}^{N} p_i [\Delta M_{aa,i}] \tag{34}$$

5. ILLUSTRATIVE EXAMPLE AND RECENT APPLICATIONS

A pinned-free Euler-Bernoulli beam finite element model serves as an example to demonstrate the accuracies of the various Rayleigh-Ritz approximations for parametric sensitivity analysis. In addition, two experiences in which the new method was successfully applied are summarized.

5.1 PINNED-FREE BEAM

The pinned-free Euler-Bernoulli beam, illustrated in Figure 1 is characterized by uniform flexural stiffness (EI), uniform mass per unit length (ρA), length (L), and angular stiffness, (K_R) at the pinned end. A finite element model composed of 100 elements is defined, and the baseline structure (with $K_R = 0$) is described by the 10 lowest eigenvalues and mode shapes.

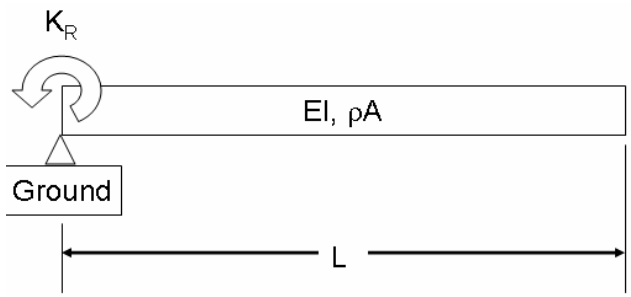

Figure 1: Pinned-Free Euler-Bernoulli Beam

Results of exact and approximate sensitivity analyses, summarized in Table 1 indicate that eigenvalue and mode shape accuracies for both the classical residual and new method (which generated two residual vectors) are superior to results of the truncated (10 mode) Rayleigh-Ritz method.

	Exact Analyses		Approximate Analyses (K_R*L/EI=0.96)								
	K_R*L/EI=0	K_R*L/EI=0.96	No Residual			Classic Residual			New Method		
Mode	f*C_B/L^2	f*C_B/L^2	f*C_B/L^2	err (%)	COR (%)	f*C_B/L^2	err (%)	COR (%)	f*C_B/L^2	err (%)	COR (%)
1	0.00	0.5483	0.5715	4.27	100	0.5483	0.00	100	0.5483	0.00	100
2	2.45	3.438	3.585	4.26	100	3.438	0.00	100	3.439	0.01	100
3	7.95	9.633	10.04	4.27	100	9.633	0.00	100	9.634	0.00	100
4	16.59	18.89	19.70	4.30	99	18.89	0.00	100	18.89	0.00	100
5	28.37	31.24	32.61	4.37	99	31.24	0.00	100	31.24	0.00	100
6	43.30	46.69	48.79	4.48	98	46.70	0.00	100	46.70	0.00	100
7	61.36	65.25	68.31	4.69	97	65.26	0.01	100	65.25	0.00	100
8	82.57	86.91	91.35	5.11	95	86.94	0.03	100	86.91	0.00	100
9	106.91	111.7	118.5	6.08	90	111.8	0.10	100	111.7	0.00	100
10	134.40	139.6	164.0	17.50	88	140.3	0.51	99	139.6	0.00	100

Table 1: Accuracies of Approximate Sensitivity Analysis Methods ($C_B^2 = (EI/\rho A)$)

Additional insight into accuracy of the three approximate analysis methods is provided in Figures 2, which compares envelopes of eigenvalue and mode shape errors as a function of parametric change, respectively. It is clear that both the classical residual and new methods offer reliable accuracies for sensitivity analysis over a wide range of parametric variation.

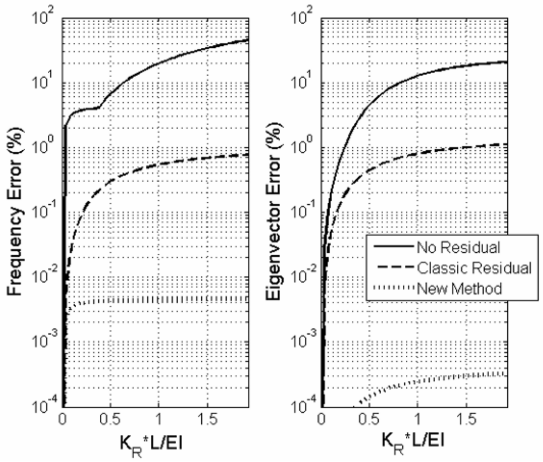

Figure 2: Eigenvalue and Mode shape Error [1-diag(COR)] Envelopes over a Wide Range of Parametric Variation

5.2 APPLICATIONS

The new sensitivity analysis method was first applied as part of the International Space Station P-5 modal test project (see Figure 3) in the spring of 2000 for sensitivity and test-analysis reconciliation[1]. That effort successfully mapped the sensitivity of test article modes primarily associated with spherical joint play and achieved NASA's stated test-analysis reconciliation goals within two weeks of laboratory test completion. This represented the first application of the new method, which appeared to be accurate and effective; however, the developer (R. Coppolino) did not provide rigorous justification of the sensitivity analysis formulation at that time.

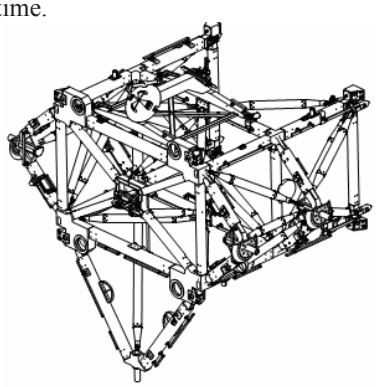

Figure 3: International Space Station P-5 Short Spacer

More recently, as part of a U.S. Army funded SBIR Phase 2 activity, the new method was applied to a study of electronic card cage dynamic characteristics (Figure 4). This study represented the first application of the new sensitivity analysis method employing a component mode synthesis finite element model[9]. Results of the card cage study revealed important sensitivities to "Wedge-lock" card support and screw-down cover plate boundary stiffness uncertainties.

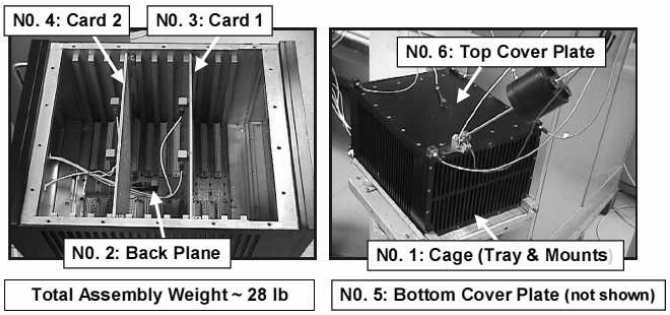

Figure 4: Card Cage Assembly indicating Six Component Substructures

6. CONCLUSIONS AND RECOMMENDATIONS

This paper provides a systematic derivation and assessment of two methods for trial vector definition that enhance the accuracy of Rayleigh-Ritz approximations for eigenvalue and mode shape sensitivity analysis. The first method, utilizing classical quasi-static residual vector augmentation, was first applied in 1980 to the study of offshore oil platform structural damage sensitivity. Classical quasi-static residuals proved to be effective and accurate in that study, since damage scenarios were localized. In subsequent activities, including (1) the P-5 Short Spacer International Space Station component vibration mode survey test (2000) and (2) an investigation of typical card cage dynamic sensitivities, system uncertainties (2007) were quite dispersed (rather than localized). The new approach for trial vector augmentation, described in this paper proved to be quite effective and accurate in these more recent applications. At the heart of the new sensitivity method is reduction of model order by several orders of magnitude, while preserving accuracy of altered system eigenvalues and mode shapes. This efficiency permits calculation of many parametric alterations in a timely manner using modest computer resources.

Due to the presence of uncertainties in as-built systems and systems-in-service (especially as they age), parametric sensitivity analysis should be a standard part of engineering evaluations that determine peak structural loads, stability margins and other safety related metrics. Moreover, efficient parametric sensitivity models should always be available during vibration mode tests to facilitate reliable test-analysis reconciliation activities. The new method featured in this paper appears appropriate for addressing these needs.

REFERENCES

[1] "International Space Station P5 Modal Survey: Test Planning through FEM Reconciliation", R. Coppolino, Proceedings of the 20th International Modal Analysis (IMAC) Conference, Feb 2002
[2] "Rates of Change of Eigenvalues and Eigenvectors", R. I. Fox and M. P. Kapoor, AIAA Journal, Vol. 6, Dec. 1968, pp. 2426-2429
[3] "Simplified Calculation of Eigenvector Derivatives", R. B. Nelson, AIAA Journal, Vol 14, Sept. 1976, pp. 1201-1205
[4] "Über eine neue Methode zur Lösung gewisser Variationsprobleme der mathematischen Physik", W. Ritz, J. reine angew. Math. 135, 1-61, 1908.
[5] "Twenty Years of Structural Dynamic Modification-A Review, Proceedings of the 20th International Modal Analysis (IMAC) Conference, Feb 2002
[6] "A Hybrid Method for Component Mode Synthesis", R. MacNeal, Computers and Structures, Vol. 1, pp 581-601, Dec 1971
[7] "Structural Mode Sensitivity to Local Modification", R. Coppolino, SAE Aerospace Conference and Exposition, Paper 811044, Oct 1981
[8] "Coupling of Substructures for Dynamic Analysis", R. Craig and M. Bampton, AIAA Journal, Vol. 6, July 1968
[9] "Efficient Modal Sensitivity Analysis of Complex Structural Assemblies", R. Coppolino, Spacecraft and Launch Vehicle Dynamic Environments Workshop, June 2008

Uncoupling Techniques for the Dynamic Characterization of Sub-structures

Batista, F. C.[1], Maia, N. M. M.[2]
[1] Polytechnic Institute of Leiria, School of Technology and Management,
Morro do Lena, 2401-951 Leiria, Portugal
[2] IDMEC/IST, Tech. Univ. of Lisbon, Av. Rovisco Pais, 1049-001 Lisboa, Portugal

ABSTRACT
The characterization of the dynamic behavior of sub-structures may be of great importance in certain complex structures. A possible approach is through the use of uncoupling techniques. This is the subject of the present paper, where various issues are raised and different possibilities to circumvent the encountered problems are discussed. These problems are mostly due to numerical instabilities associated to the calculation procedures, namely to the ill-conditioning that often appears and causes complications in the inversion of the involved matrices. The location of the possible points of measurement may also influence the results. Several variations to the main algorithms are tried in order to reduce the numerical problems. This study will be based on numerical simulations to compare the various approaches and to draw some final conclusions.

1 INTRODUCTION

Recently the subject of structural uncoupling (also referred to by some authors as decoupling) has regained interest among the scientific community [1, 2]. Seeking for the dynamic characterization of sub-structures, there are several techniques combining both experimental and analytical/numerical methods. They can be classified in three different groups, according to the working domain, either modal, mechanical impedance or frequency domain.

In the modal domain one has methods that use modal properties, like the classic Craig-Bampton [3], known as Component-Mode Synthesis (CMS). Meanwhile, the Dual Craig–Bampton method has been presented by Rixen [2].

In what mechanical impedance is concerned, one has the system mass, stiffness and damping matrices, as well as external forces and connection forces. Ahmadian *et al.* and Jalali *et al.* [4, 5] developed a method that allows the identification of a bolted joint using the physical matrices of the system.

In the frequency domain there are a vast number of methods based on the classic one developed by Jetmundesn [6], known as "FRF-based sub-structuring method" (FBS) as classified by de Klerk *et al.* [7]. D'Ambrogio [1] developed two methods based on system impedance and mobility using only the connection co-ordinates. As it will be explained in this work, one of the methods presented here will have the same result. In Jetmundesn's method [6] the inherent numerical problems associated to ill-conditioned matrices are well known; moreover, Frequency Response Function (FRF) measurements have inherent associated noise that make the obtaining of acceptable results a difficult job; several strategies have been appointed to overcome the problems, see for instance Ren and Beard [8]; Maia *et al.* [9] proposed a solution avoiding the connection co-ordinates.

In this work several approaches for the classic uncoupling Jetmundesn's method are developed, analyzed and compared, through numerical examples using beams. Adding local inertial elements, a possible way of circumventing the ill-conditioning problems is proposed.

2 THEORETICAL FORMULATION

2.1 *FRF* coupling

Coupling techniques are well known (e.g., see [10]); they can be divided into spatial coupling methods, based upon the system matrices (M, K e C), modal coupling methods, using modal properties (natural frequencies, damping ratios and mode shapes) and frequency response function coupling (*FRF* coupling). Let us concentrate in this latter one.

Let us consider two sub-structures A and B, connected though some co-ordinates as represented in figure 1. Together, they form structure C. Let i represent the co-ordinates exclusively belonging to A, k the ones exclusively belonging to B and j the connection co-ordinates.

T. Proulx (ed.), *Linking Models and Experiments, Volume 2*, Conference Proceedings of the Society for Experimental Mechanics Series 5,
DOI 10.1007/978-1-4419-9305-2_28, © The Society for Experimental Mechanics, Inc. 2011

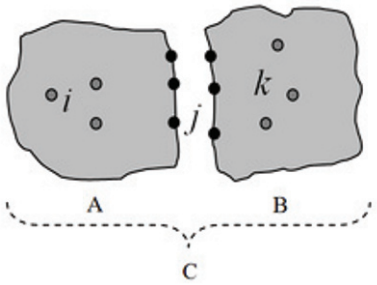

Fig. 1 Coupling of sub-structures A and B, forming structure C

From the equilibrium of forces and the compatibility conditions of displacements one can write:

$$\boldsymbol{f}_i^A + \boldsymbol{f}_i^B = \boldsymbol{f}_i^C \tag{1}$$

$$\boldsymbol{x}_j^A = \boldsymbol{x}_j^B = \boldsymbol{x}_j^C \tag{2}$$

The receptance matrices $\boldsymbol{H}$ relating the amplitudes of the forces to the amplitudes of the displacements are defined as

$$\boldsymbol{X} = \boldsymbol{H}\boldsymbol{F} \tag{3}$$

and therefore, the receptance matrices for sub-structures *A* and *B* and for structure *C* are:

$$\boldsymbol{H}^A = \begin{bmatrix} \boldsymbol{H}_{ii}^A & \boldsymbol{H}_{ij}^A \\ \boldsymbol{H}_{ji}^A & \boldsymbol{H}_{jj}^A \end{bmatrix}; \quad \boldsymbol{H}^B = \begin{bmatrix} \boldsymbol{H}_{jj}^B & \boldsymbol{H}_{jk}^B \\ \boldsymbol{H}_{kj}^B & \boldsymbol{H}_{kk}^B \end{bmatrix}; \quad \boldsymbol{H}^C = \begin{bmatrix} \boldsymbol{H}_{ii}^C & \boldsymbol{H}_{ij}^C & \boldsymbol{H}_{ik}^C \\ \boldsymbol{H}_{ji}^C & \boldsymbol{H}_{jj}^C & \boldsymbol{H}_{jk}^C \\ \boldsymbol{H}_{ki}^C & \boldsymbol{H}_{kj}^C & \boldsymbol{H}_{kk}^C \end{bmatrix} \tag{4}$$

Using equations (1) and (2), one obtains the receptance matrix for *C* [11]:

$$\boldsymbol{H}^C = \left(\begin{bmatrix} \begin{bmatrix} \boldsymbol{H}_{ii}^A & \boldsymbol{H}_{ij}^A \\ \boldsymbol{H}_{ji}^A & \boldsymbol{H}_{jj}^A \end{bmatrix}^{-1} & \boldsymbol{0} \\ \boldsymbol{0} \quad \boldsymbol{0} & \boldsymbol{0} \end{bmatrix} + \begin{bmatrix} \boldsymbol{0} & \boldsymbol{0} \quad \boldsymbol{0} \\ \boldsymbol{0} & \begin{bmatrix} \boldsymbol{H}_{jj}^B & \boldsymbol{H}_{jk}^B \\ \boldsymbol{H}_{kj}^B & \boldsymbol{H}_{kk}^B \end{bmatrix}^{-1} \end{bmatrix} \right)^{-1} \tag{5}$$

The process of inverting three matrices requires – in general – a high computational effort, implying a strong possibility of encountering ill-conditioned matrices. To try and minimize this problem an alternative formulation is often used [12]:

$$\boldsymbol{H}^C = \begin{bmatrix} \boldsymbol{H}_{ii}^A & \boldsymbol{H}_{ij}^A & \boldsymbol{0} \\ \boldsymbol{H}_{ji}^A & \boldsymbol{H}_{jj}^A & \boldsymbol{0} \\ \boldsymbol{0} & \boldsymbol{0} & \boldsymbol{H}_{kk}^B \end{bmatrix} - \begin{bmatrix} \boldsymbol{H}_{ij}^A \boldsymbol{H}_{jj}^{-1} \boldsymbol{H}_{ji}^A & \boldsymbol{H}_{ij}^A \boldsymbol{H}_{jj}^{-1} \boldsymbol{H}_{jj}^A & -\boldsymbol{H}_{ij}^A \boldsymbol{H}_{jj}^{-1} \boldsymbol{H}_{jk}^B \\ \boldsymbol{H}_{jj}^A \boldsymbol{H}_{jj}^{-1} \boldsymbol{H}_{ji}^A & \boldsymbol{H}_{jj}^A \boldsymbol{H}_{jj}^{-1} \boldsymbol{H}_{jj}^A & -\boldsymbol{H}_{jj}^A \boldsymbol{H}_{jj}^{-1} \boldsymbol{H}_{jk}^B \\ -\boldsymbol{H}_{kj}^B \boldsymbol{H}_{jj}^{-1} \boldsymbol{H}_{ji}^A & -\boldsymbol{H}_{kj}^B \boldsymbol{H}_{jj}^{-1} \boldsymbol{H}_{jj}^A & \boldsymbol{H}_{kj}^B \boldsymbol{H}_{jj}^{-1} \boldsymbol{H}_{jk}^B \end{bmatrix} \tag{6}$$

where $\boldsymbol{H}_{jj} = \boldsymbol{H}_{jj}^A + \boldsymbol{H}_{jj}^B$. In a simpler way, one can write:

$$\begin{bmatrix} \boldsymbol{H}_{ii}^C & \boldsymbol{H}_{ij}^C & \boldsymbol{H}_{ik}^C \\ \boldsymbol{H}_{ji}^C & \boldsymbol{H}_{jj}^C & \boldsymbol{H}_{jk}^C \\ \boldsymbol{H}_{ki}^C & \boldsymbol{H}_{kj}^C & \boldsymbol{H}_{kk}^C \end{bmatrix} = \begin{bmatrix} \boldsymbol{H}_{ii}^A & \boldsymbol{H}_{ij}^A & \boldsymbol{0} \\ \boldsymbol{H}_{ji}^A & \boldsymbol{H}_{jj}^A & \boldsymbol{0} \\ \boldsymbol{0} & \boldsymbol{0} & \boldsymbol{H}_{kk}^B \end{bmatrix} - \begin{bmatrix} \boldsymbol{H}_{ij}^A \\ \boldsymbol{H}_{jj}^A \\ -\boldsymbol{H}_{kj}^B \end{bmatrix} \left(\boldsymbol{H}_{jj}^A + \boldsymbol{H}_{jj}^B \right)^{-1} \begin{bmatrix} \boldsymbol{H}_{ji}^A & \boldsymbol{H}_{jj}^A & -\boldsymbol{H}_{jk}^B \end{bmatrix} \tag{7}$$

which replaces the three inversions by only one, restricted to the number of connection co-ordinates j, thereby limiting possible numerical problems.

2.2 *FRF* uncoupling

Let us suppose that our goal is the dynamic characterization of a joint; joints can be considered as complex components, often difficult to analyze and model. A possible solution relies on obtaining their dynamic behavior by an inverse coupling procedure, i.e., an uncoupling procedure, having eq. (7) as a starting point.

If our joint is defined as sub-structure *B*, one has co-ordinates *i* and *j*, whereas co-ordinates *k* (internal to *B*) do not play a role here. Therefore, eq. (7) is re-written as:

$$\begin{bmatrix} \boldsymbol{H}_{ii}^{C} & \boldsymbol{H}_{ij}^{C} \\ \boldsymbol{H}_{ji}^{C} & \boldsymbol{H}_{jj}^{C} \end{bmatrix} = \begin{bmatrix} \boldsymbol{H}_{ii}^{A} & \boldsymbol{H}_{ij}^{A} \\ \boldsymbol{H}_{ji}^{A} & \boldsymbol{H}_{jj}^{A} \end{bmatrix} - \begin{bmatrix} \boldsymbol{H}_{ij}^{A} \\ \boldsymbol{H}_{jj}^{A} \end{bmatrix} \left(\boldsymbol{H}_{jj}^{A} + \boldsymbol{H}_{jj}^{B} \right)^{-1} \begin{bmatrix} \boldsymbol{H}_{ji}^{A} & \boldsymbol{H}_{jj}^{A} \end{bmatrix} \tag{8}$$

From eq. (8) it is clear that there are three possibilities for the evaluation of $\boldsymbol{H}_{jj}^{B}$: using $\boldsymbol{H}_{ii}^{C}$, $\boldsymbol{H}_{ij}^{C}$ or $\boldsymbol{H}_{jj}^{C}$.

2.2.1 Without the use of co-ordinates *j*

Sometimes it may be difficult to undertake measurements on co-ordinates *j*, close to the joint, so ideally one should use measurements on the complete structure *C* involving only co-ordinates *i*. From (8), one has:

$$\boldsymbol{H}_{ii}^{C} = \boldsymbol{H}_{ii}^{A} - \boldsymbol{H}_{ij}^{A} \left(\boldsymbol{H}_{jj}^{A} + \boldsymbol{H}_{jj}^{B} \right)^{-1} \boldsymbol{H}_{ji}^{A} \tag{9}$$

Rearranging (9),

$$\boldsymbol{H}_{ij}^{A} \left(\boldsymbol{H}_{jj}^{A} + \boldsymbol{H}_{jj}^{B} \right)^{-1} \boldsymbol{H}_{ji}^{A} = \boldsymbol{H}_{ii}^{A} - \boldsymbol{H}_{ii}^{C} \tag{10}$$

Pre-multiplying (10) by $\left(\boldsymbol{H}_{ij}^{A} \right)^{-1}$ and post-multiplying by $\left(\boldsymbol{H}_{ji}^{A} \right)^{-1}$ leads to:

$$\left(\boldsymbol{H}_{jj}^{A} + \boldsymbol{H}_{jj}^{B} \right)^{-1} = \left(\boldsymbol{H}_{ij}^{A} \right)^{-1} \left(\boldsymbol{H}_{ii}^{A} - \boldsymbol{H}_{ii}^{C} \right) \left(\boldsymbol{H}_{ji}^{A} \right)^{-1} \tag{11}$$

Note that this operation is mathematically possible only when *i* equals *j*; otherwise, if one of the (pseudo) inversions is possible, the other one is not, and *vice-versa*. Solving for $\boldsymbol{H}_{jj}^{B}$, it follows that

$$\boldsymbol{H}_{jj}^{B} = \boldsymbol{H}_{ji}^{A} \left(\boldsymbol{H}_{ii}^{A} - \boldsymbol{H}_{ii}^{C} \right)^{-1} \boldsymbol{H}_{ij}^{A} - \boldsymbol{H}_{jj}^{A} \tag{12}$$

Generalizing to the case where *i* might be different from *j* (in fact, $i \geq j$), one pre-multiplies equation (10) by an arbitrary matrix $\boldsymbol{W}_{ji}$ and post-multiplies it by $\boldsymbol{W}_{ij}$:

$$\boldsymbol{W}_{ji} \boldsymbol{H}_{ij}^{A} \left(\boldsymbol{H}_{jj}^{A} + \boldsymbol{H}_{jj}^{B} \right)^{-1} \boldsymbol{H}_{ji}^{A} \boldsymbol{W}_{ij} = \boldsymbol{W}_{ji} \left(\boldsymbol{H}_{ii}^{A} - \boldsymbol{H}_{ii}^{C} \right) \boldsymbol{W}_{ij} \tag{13}$$

Rearranging eq. (13), one can write,

$$\left(\boldsymbol{H}_{jj}^{A} + \boldsymbol{H}_{jj}^{B} \right)^{-1} = \left(\boldsymbol{W}_{ji} \boldsymbol{H}_{ij}^{A} \right)^{-1} \boldsymbol{W}_{ji} \left(\boldsymbol{H}_{ii}^{A} - \boldsymbol{H}_{ii}^{C} \right) \boldsymbol{W}_{ij} \left(\boldsymbol{H}_{ji}^{A} \boldsymbol{W}_{ij} \right)^{-1} \tag{14}$$

This is only possible if $i \geq j$, not the other way around (which certainly is not a common case). From (14) one has:

$$\boldsymbol{H}_{jj}^{B} = \boldsymbol{H}_{ji}^{A} \boldsymbol{W}_{ij} \left(\boldsymbol{W}_{ji} \left(\boldsymbol{H}_{ii}^{A} - \boldsymbol{H}_{ii}^{C} \right) \boldsymbol{W}_{ij} \right)^{-1} \boldsymbol{W}_{ji} \boldsymbol{H}_{ij}^{A} - \boldsymbol{H}_{jj}^{A} \tag{15}$$

Now the order of the matrix to invert is equal to the number of co-ordinates *j*. This is advantageous because the size of *j* will be – in general – much smaller than that of *i*. The question is which matrix $\boldsymbol{W}_{ij}$ to use. There is not an easy answer, but probably the most logical one is to use $\boldsymbol{H}_{ij}^{A}$:

$$\boldsymbol{H}_{jj}^{B} = \boldsymbol{H}_{ji}^{A}\boldsymbol{H}_{ij}^{A}\left(\boldsymbol{H}_{ji}^{A}\left(\boldsymbol{H}_{ii}^{A} - \boldsymbol{H}_{ii}^{C}\right)\boldsymbol{H}_{ij}^{A}\right)^{-1}\boldsymbol{H}_{ji}^{A}\boldsymbol{H}_{ij}^{A} - \boldsymbol{H}_{jj}^{A} \tag{16}$$

2.2.2 Using only the coordinates of the joint

Using eq. (7) based on $\boldsymbol{H}_{jj}^{C}$, one has:

$$\boldsymbol{H}_{jj}^{C} = \boldsymbol{H}_{jj}^{A} - \boldsymbol{H}_{jj}^{A}\left(\boldsymbol{H}_{jj}^{A} + \boldsymbol{H}_{jj}^{B}\right)^{-1}\boldsymbol{H}_{jj}^{A} \tag{17}$$

Solving eq. (17) with respect to $\boldsymbol{H}_{jj}^{B}$, it follows that:

$$\boldsymbol{H}_{jj}^{B} = \left(\boldsymbol{H}_{jj}^{A}\left(\boldsymbol{H}_{jj}^{A} - \boldsymbol{H}_{jj}^{C}\right)^{-1} - \boldsymbol{I}_{jj}\right)\boldsymbol{H}_{jj}^{A} \tag{18}$$

Based on the dynamic stiffness matrix of the structure, Ambrogio [1] obtains an alternative formulation (eq. (19) can be derived from eq. (18)):

$$\boldsymbol{H}_{jj}^{B} = \left(\boldsymbol{I}_{jj} - \boldsymbol{H}_{jj}^{C}\left(\boldsymbol{H}_{jj}^{A}\right)^{-1}\right)^{-1}\boldsymbol{H}_{jj}^{C} \tag{19}$$

2.2.3 Using coordinates *i* and *j*

Back again to eq. (8), the third option to evaluate $\boldsymbol{H}_{jj}^{B}$ starts from:

$$\boldsymbol{H}_{ij}^{C} = \boldsymbol{H}_{ij}^{A} - \boldsymbol{H}_{ij}^{A}\left(\boldsymbol{H}_{jj}^{A} + \boldsymbol{H}_{jj}^{B}\right)^{-1}\boldsymbol{H}_{jj}^{A} \tag{20}$$

or

$$\boldsymbol{H}_{ij}^{A}\left(\boldsymbol{H}_{jj}^{A} + \boldsymbol{H}_{jj}^{B}\right)^{-1}\boldsymbol{H}_{jj}^{A} = \boldsymbol{H}_{ij}^{A} - \boldsymbol{H}_{ij}^{C} \tag{21}$$

Using once again arbitrary matrices, now $\boldsymbol{W}_{ji}$ and $\boldsymbol{W}_{jj}$, with *i* greater or equal to *j*, one has

$$\boldsymbol{W}_{ji}\boldsymbol{H}_{ij}^{A}\left(\boldsymbol{H}_{jj}^{A} + \boldsymbol{H}_{jj}^{B}\right)^{-1}\boldsymbol{H}_{jj}^{A}\boldsymbol{W}_{jj} = \boldsymbol{W}_{ji}\left(\boldsymbol{H}_{ij}^{A} - \boldsymbol{H}_{ij}^{C}\right)\boldsymbol{W}_{jj} \tag{22}$$

from which

$$\left(\boldsymbol{H}_{jj}^{A} + \boldsymbol{H}_{jj}^{B}\right)^{-1} = \left(\boldsymbol{W}_{ji}\boldsymbol{H}_{ij}^{A}\right)^{-1}\boldsymbol{W}_{ji}\left(\boldsymbol{H}_{ij}^{A} - \boldsymbol{H}_{ij}^{C}\right)\boldsymbol{W}_{jj}\left(\boldsymbol{H}_{jj}^{A}\boldsymbol{W}_{jj}\right)^{-1} \tag{23}$$

Solving in order to $\boldsymbol{H}_{jj}^{B}$, gives:

$$\boldsymbol{H}_{jj}^{B} = \boldsymbol{H}_{jj}^{A}\boldsymbol{W}_{jj}\left(\boldsymbol{W}_{ji}\left(\boldsymbol{H}_{ij}^{A} - \boldsymbol{H}_{ij}^{C}\right)\boldsymbol{W}_{jj}\right)^{-1}\boldsymbol{W}_{ji}\boldsymbol{H}_{ij}^{A} - \boldsymbol{H}_{jj}^{A} \tag{24}$$

As before, one shall make $\boldsymbol{W}_{ji} = \boldsymbol{H}_{ji}^{A}$ and $\boldsymbol{W}_{jj} = \boldsymbol{H}_{jj}^{A}$:

$$\boldsymbol{H}_{jj}^{B} = \boldsymbol{H}_{jj}^{A}\boldsymbol{H}_{jj}^{A}\left(\boldsymbol{H}_{ji}^{A}\left(\boldsymbol{H}_{ij}^{A} - \boldsymbol{H}_{ij}^{C}\right)\boldsymbol{H}_{jj}^{A}\right)^{-1}\boldsymbol{H}_{ji}^{A}\boldsymbol{H}_{ij}^{A} - \boldsymbol{H}_{jj}^{A} \tag{25}$$

2.2.4 Summary

In summary, one has three formulations that allow us to determine matrix $\boldsymbol{H}_{jj}^{B}$:

First formulation

$$\boldsymbol{H}_{jj}^{B}=\boldsymbol{H}_{ji}^{A}\boldsymbol{H}_{ij}^{A}\left(\boldsymbol{H}_{ji}^{A}\left(\boldsymbol{H}_{ii}^{A}-\boldsymbol{H}_{ii}^{C}\right)\boldsymbol{H}_{ij}^{A}\right)^{-1}\boldsymbol{H}_{ji}^{A}\boldsymbol{H}_{ij}^{A}-\boldsymbol{H}_{jj}^{A} \tag{16}$$

Second formulation

$$\boldsymbol{H}_{jj}^{B}=\left(\boldsymbol{H}_{jj}^{A}\left(\boldsymbol{H}_{jj}^{A}-\boldsymbol{H}_{jj}^{C}\right)^{-1}-\boldsymbol{I}_{jj}\right)\boldsymbol{H}_{jj}^{A} \tag{18}$$

Third formulation

$$\boldsymbol{H}_{jj}^{B}=\boldsymbol{H}_{jj}^{A}\,\boldsymbol{H}_{jj}^{A}\left(\boldsymbol{H}_{ji}^{A}\left(\boldsymbol{H}_{ij}^{A}-\boldsymbol{H}_{ij}^{C}\right)\boldsymbol{H}_{jj}^{A}\right)^{-1}\boldsymbol{H}_{ji}^{A}\boldsymbol{H}_{ij}^{A}-\boldsymbol{H}_{jj}^{A} \tag{25}$$

3 SIMULATION STUDIES

To illustrate the performance of the three formulations one uses the beam of figure 2, constituted by three components, A_1, B and A_2, forming structure C; A_1 and A_2 form sub-structure A.

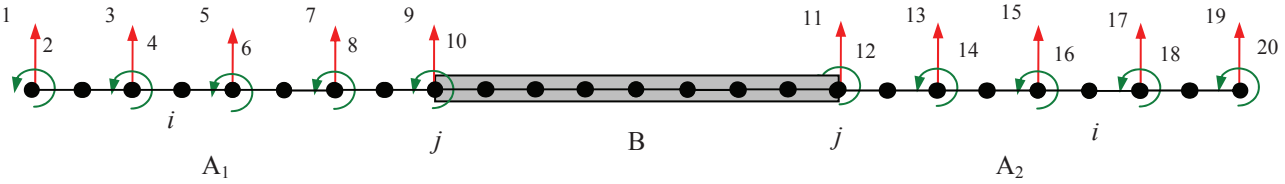

Fig. 2 Test item

The aim is to characterize component B (our "joint"), evaluating $\boldsymbol{H}^{B}$, assuming that $\boldsymbol{H}^{A}$ is calculated analytically and $\boldsymbol{H}^{C}$ is calculated through experiments (simulated, in this case).

Using the finite element method with beam elements with four degrees of freedom, each component is divided into eight elements and considering only the nodes shown in figure 2 as coordinates i and j where it is possible to measure and excite the structure. The characteristics of each component are displayed in table 1.

Table 1 Characteristics of the components of the beam

Beam	Length	Width	Thickness	ν	E	ρ
A_1	300 mm	25 mm	3 mm	0.3	210 GPa	7850 Kg/m^3
B	400 mm	25 mm	6 mm	0.3	210 GPa	7850 Kg/m^3
A_2	300 mm	25 mm	3 mm	0.3	210 GPa	7850 Kg/m^3

3.1 Choice of the formulation

To simulate the experimental errors, one has imposed a 1% perturbation in matrix $\boldsymbol{H}^{C}$ for the three formulations. The elements *11* and *12* (chosen just for comparison) of matrix $\boldsymbol{H}_{jj}^{B}$ obtained with the three formulations are shown in figure 3.

The major disturbances in the responses are due to numerical problems in the matrix inversions in each of the formulations.

The variability of the results in figure 3 is quite high. Figure 4 represents the module of the differences between the numerically exact response and the response obtained by the three formulations. From the three results, the second formulation is the one that produces the smallest error throughout the frequency range.

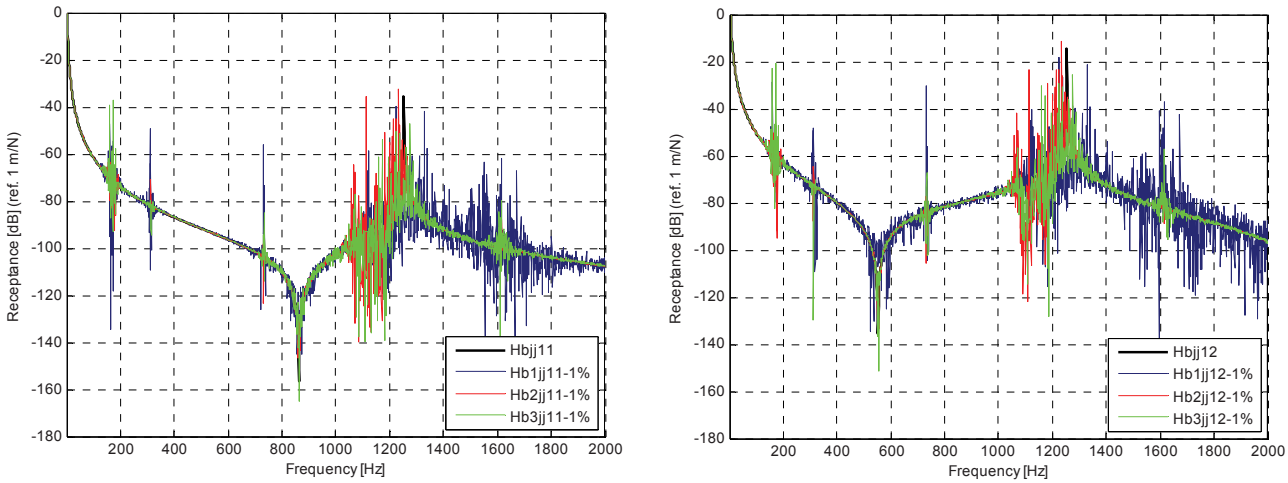

Fig. 3 *FRF*s H_{11}^{B} and H_{12}^{B} for the three formulations

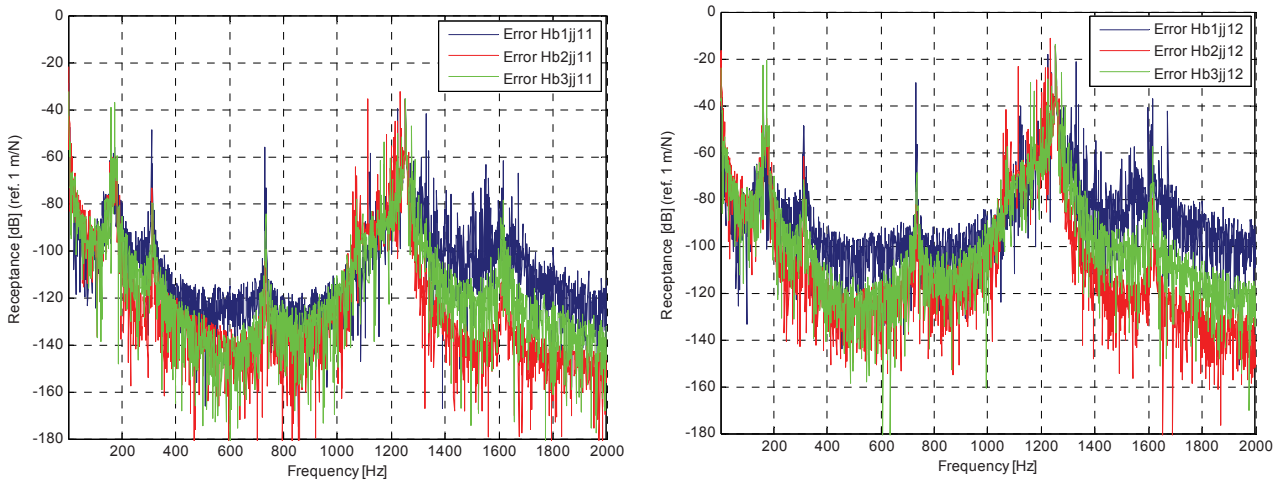

Fig. 4 Errors of *FRF*s H_{11}^{B} and H_{12}^{B} for the three formulations

Let us represent H_{11}^{B} and H_{12}^{B} only for the second formulation, superimposed with the numerically exact response (see figure 5).

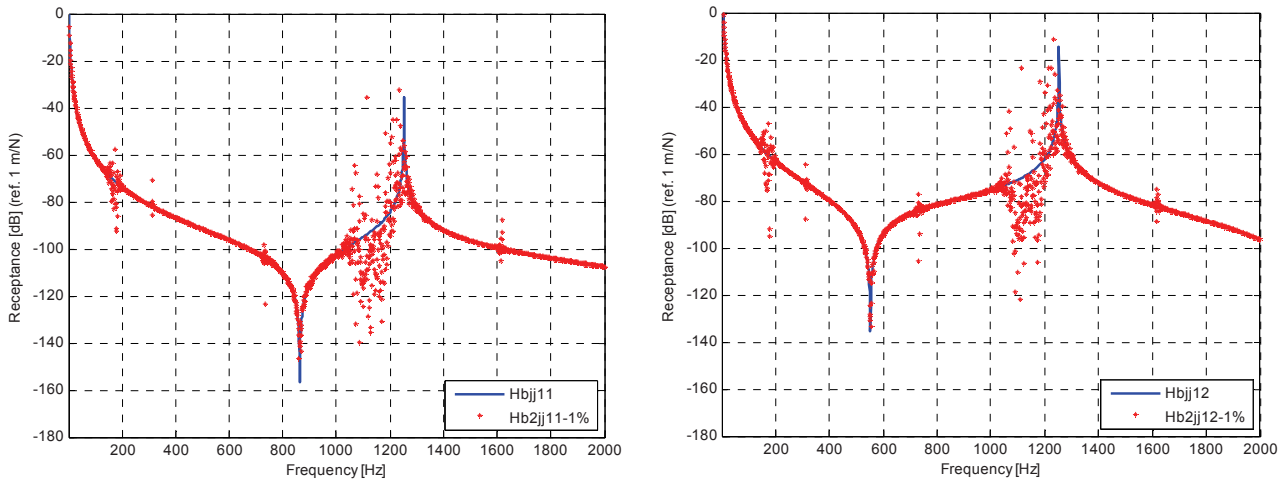

Fig. 5 H_{11}^{B} and H_{12}^{B} for the second formulation

3.2 Strategies to improve the results

It is clear that one cannot be happy with the results of figure 5. Let us try to improve them. From eq. (18) it is apparent that the problems certainly arise in the inversion of $\left(\boldsymbol{H}_{jj}^{A}-\boldsymbol{H}_{jj}^{C}\right)$, namely when this difference is small. To try to increase this difference one will change our structure by adding point masses, so to change the behavior of sub-structure *A* and *C*, while *B* remains unchanged.

3.2.1 Adding mass to sub-structure *A*

A mass of 35 grams has been added to nodes 1, 3, 5 and 15, 17, 19. The new results for H_{11}^{B} and H_{12}^{B} are shown in figure 6.

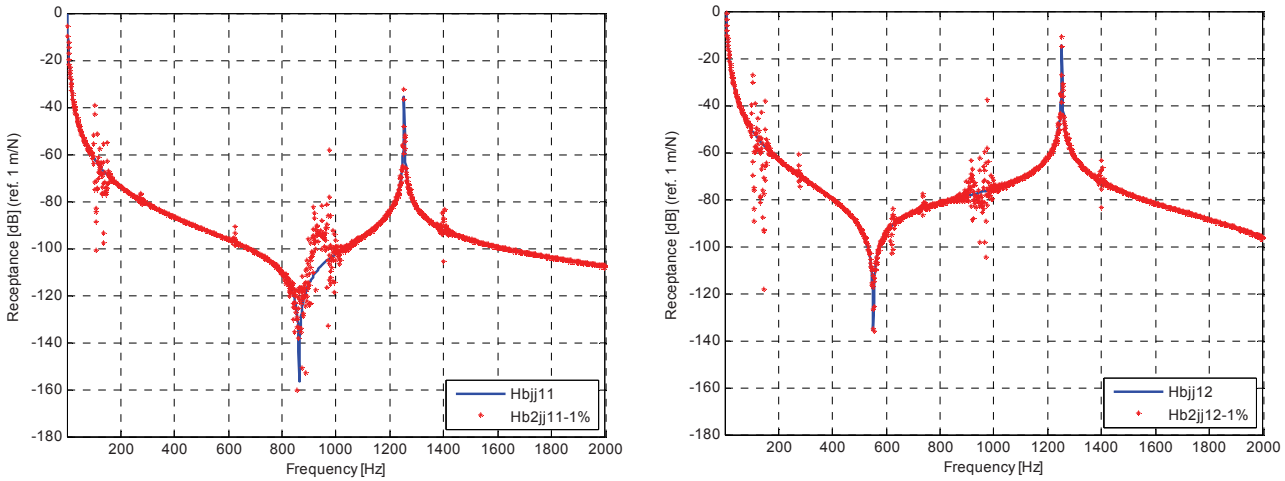

Fig. 6 H_{11}^{B} and H_{12}^{B} with added masses in sub-structure *A*

It can be observed from figure 6 that the disturbance observed between 1000-1200 Hz in figure 5 moves into the range 800-1000 Hz, generally improving the results.

3.2.2 Adding mass to sub-structure *B*

An alternative could be to add mass to the sub-structure *B* itself. Adding 35 grams at co-ordinates *j* = 9 and 11, leads to the results presented in figure 7.

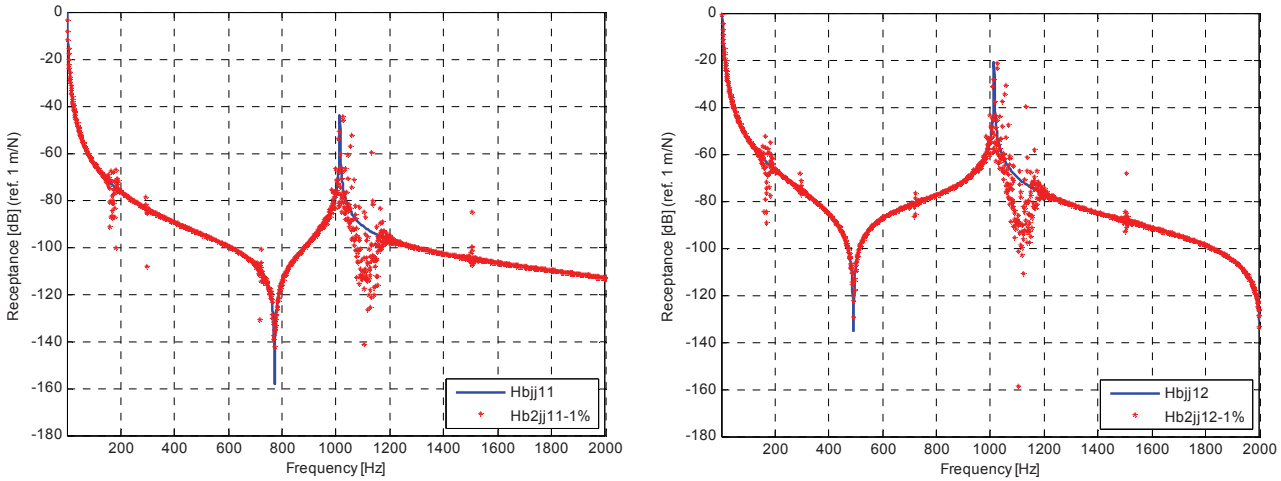

Fig. 7 H_{11}^{B} and H_{12}^{B} with added masses of 35 grams in sub-structure *B*

As sub-structure *B* is altered, its natural frequency (identified in figure 5) changes to the left. However, the disturbances remain in the area of 1000-1200 Hz and one can conclude that they are caused caused by sub-structure *A*. So maybe one can improve the results by adding some more mass to sub-structure *B*, to cause the natural frequency to deviate from the disturbance. Let us now add masses of 70 grams. The results are displayed in figure 8.

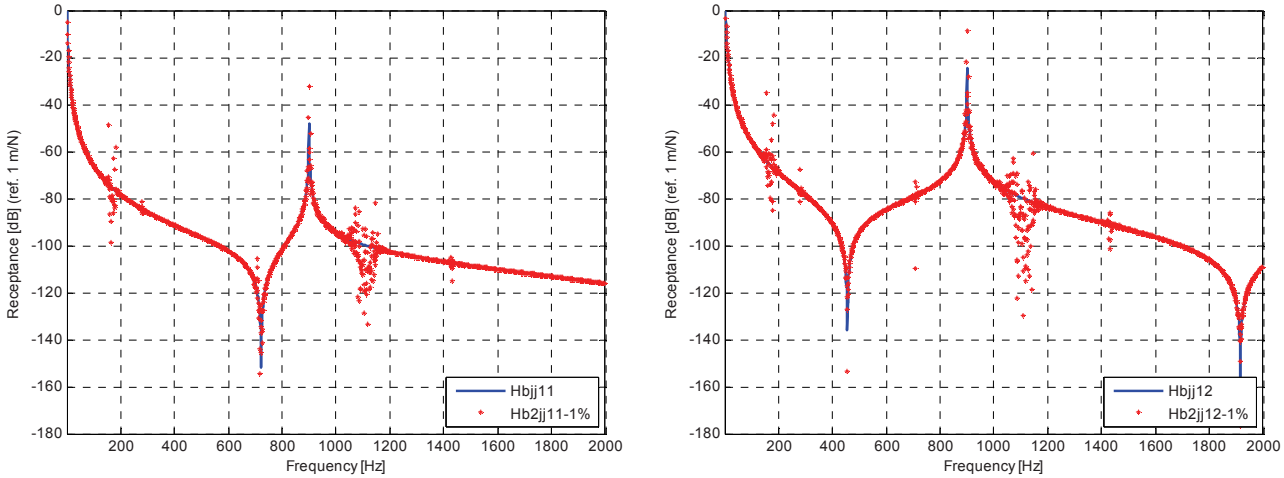

Fig. 8 H_{11}^{B} and H_{12}^{B} with added masses of 70 grams in sub-structure *B*

The results are clearly better. However, to recover the dynamic response of *B*, one has to uncouple the added masses. The results of such an operation are shown in figure 9.

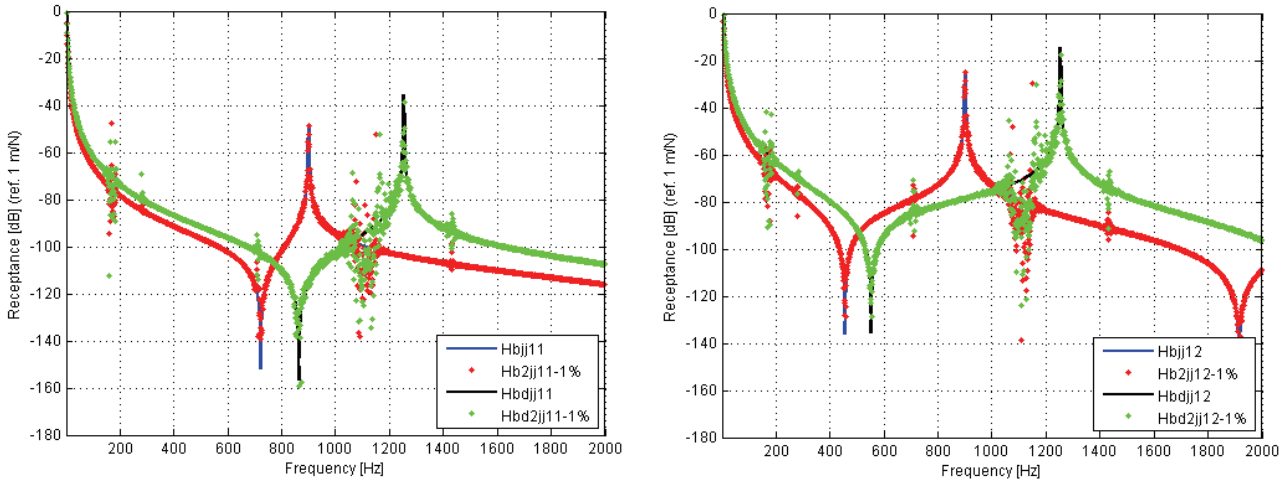

Fig. 9 H_{11}^{B} and H_{12}^{B} with and without the masses of 70 grams in sub-structure *B*

Although the results are better than the initial ones (figure 5), they are worse than those of figure 6, when the masses were added to sub-structure *A*. The disturbances come up again in the same frequency range.

3.3 Coupling

One of the main interests of the dynamic characterization of a sub-structure (like a joint) is to be able to predict the dynamic behavior of another structure (or a modified one), possibly a more complex one, inserting (coupling) the identified results from the uncoupling procedure. Whereas the uncoupling procedure tends to be unstable, as shown in this work, the coupling process is usually quite stable.

Based on the results obtained for sub-structure *B*, a coupling procedure will be undertaken with similar components, two beams *A1* and *A2* but now with a length of 400 mm. Using the results initially obtained from figure 5, one obtains the behavior illustrated in figure 10.

In figure 10 the disturbance in the area of 1000-1200 Hz remains. One can also observe the results of the coupling of B when the masses were added to A, i.e., when using the responses given in figure 6. Figure 11 illustrates this case. The results have improved and the disturbances have moved down, as expected. Most certainly, better solutions would have been obtained if one had performed a modal analysis identification to the results of figure 6, prior to the coupling procedure.

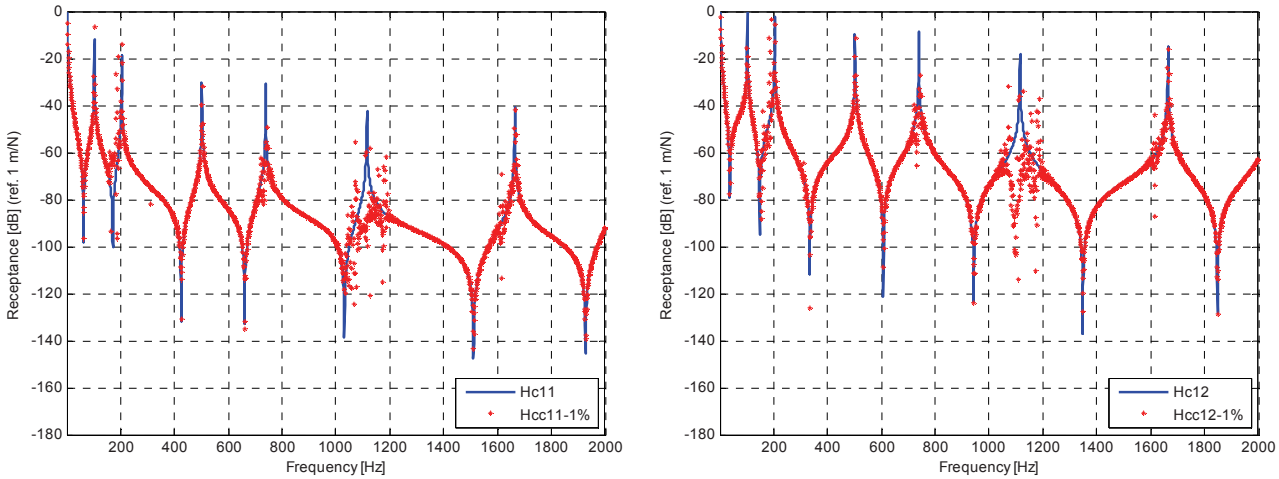

Fig. 10 H_{11}^{C} and H_{12}^{C} resulting from the coupling of *A1* and *A2* with the sub-structure *B*

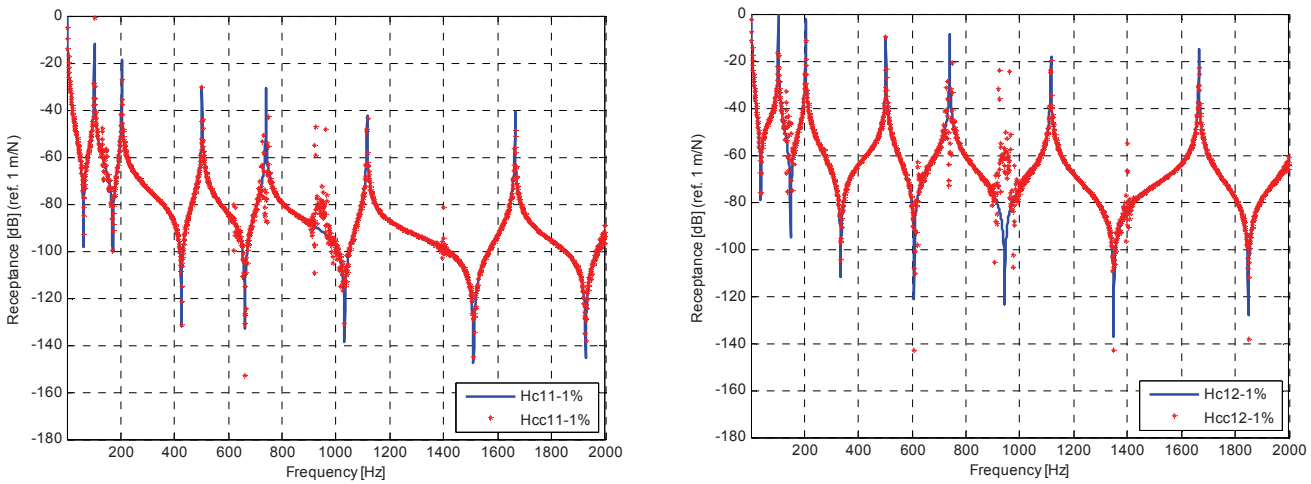

Fig. 11 H_{11}^{C} and H_{12}^{C} resulting from the coupling of *A1* and *A2* with the sub-structure *B*, with the addition of masses in *A*

4 CONCLUSIONS

In this paper the authors have presented three formulations for the uncoupling of sub-structures, something that may be of considerable interest, for instance when trying to model complex joints. The formulation that presented the best results requires measurements at the connection points of the structures; unfortunately, this may not always be possible in practice.
Any of the three formulations revealed to be numerically unstable due to the inversion of difference matrices. This problem has been investigated in this study and improvements have been obtained when adding point masses to the remaining sub-structures other than the one to be characterized. Those added masses move the natural frequencies, allowing to understand the problems that are happening and as already said, improving the results. Together with the use of modal identification methods, the uncoupling techniques may be of interest in various situations. Experimental implementation still has to be further investigated, as the accurate measurement of rotations is quite difficult to obtain.

REFERENCES

[1] D'Ambrogio, W., Fregolent, A.
"Sensitivity of decoupling techniques to uncertainties in the properties"
Proceedings of "Noise and Vibration Engineering" (ISMA 2008), Leuven, Belgium, pp. 3737-3749, 2008.

[2] Rixen, D. J.
"A dual Craig-Bampton method for dynamic substructuring"
Journal of Computational and Applied Mathematics, Vol. 168, pp. 383 – 391, 2004.
[3] Craig, R., Bampton, M.
"Coupling of Substructures for Dynamic Analysis"
AIAA Journal, vol. 6, pp. 1313 – 1319, 1968.
[4] Ahmadian, H., Hadad, H.
"Identification of a Bolted Lap Joint Parameters Using Response Surface Method"
Proceedings of "Noise and Vibration Engineering" (ISMA 2006), Leuven, Belgium, pp. 1259-1272, 2006.
[5] Jalali, H., Ahmadian, H., Mottershead, J.E.
"Identification of nonlinear bolted lap-joint parameters by force-state mapping"
International Journal of Solids and Structures, Vol. 44, Issues 25-26, pp. 8087-8105, 2007.
[6] Jetmundesn, B., Bielawa, R., Flannelly, W.G.
"Generalized Frequency Domain Substruture Synthesis"
Jounal of the American Helicopter Society, Vol. 33, pp. 55–64, 1988.
[7] de Klerk, D., Rixen, D. J., Voormeeren, S. N.
"General Framework for Dynamic Substructuring: History, Review, and Classification of Techniques"
Journal American Institute of Aeronautics and Astronautics, vol. 46 (5), pp.1169-1181, 2008.
[8] Ren, Y., Beards, C. F.
"A new method for the identification of joint proprites using FRF data"
Proceedings of the Florence Modal Analysis Conference, Italy, pp. 663-669, 1991.
[9] Maia, N.M. M., Silva, J. M. M., Ribeiro, A. M. R, Silva, P. L.C. G. C.
"On the dynamic characterization of joints using uncoupling techniques "
Proc. of the 16th International Modal Analysis Conference (IMAC XVI), Sta. Barbara, U.S.A, pp. 1132-1138, 1998.
[10] Urgueira, A.P V.
Dynamic analysis of coupled structures using experimental data
Ph.D. Thesis, Imperial College of Science Technology and Medicine, London, 1989.
[11] Maia, N. M. M., Silva, J. M. M. *et al.*
"Theoretical and Experimental Modal Analysis"
Research Studies Press, Distrib. John Wiley & Sons, pp. 480, 1997.
[12] Skingle, G.W.
Structural Dynamic Modification Using Experimental Data
Ph.D Thesis, Imperial College of Science Technology and Medicine, London, 1989.

Receptance Based Normalization of Operational Mode Shapes

D. Bernal
Northeastern University, Civil and Environmental Engineering Department, Center for Digital Signal Processing, Boston, MA 02192.

ABSTRACT

Normalization of modes obtained from operational modal analysis has received significant attention since the seminal paper on the use of mass perturbations by Parloo et.al., in 2002. The present paper presents a formulation where the square of the scaling constants are obtained from an over-determined linear system of equations. The formulation is exact for arbitrary changes in the modal model when the modal basis is complete, as well as for all conditions where existing uncoupled solutions are exact, independently of truncation. The approach is designated as the Receptance Based Normalization (RBN) scheme because the coefficients in the system of equations are obtained from evaluations of the modal series expression for the Receptance matrix.

INTRODUCTION

The fundamental contribution in resolving the scaling issue for operational modes is credited to Parloo et. al., [1], who showed that the information required is encoded in the derivatives of the eigenvalues with respect to known perturbations. An issue of some concern with the sensitivity-based normalization resides in the fact that the finite difference estimate of the eigenvalue derivatives, which have to be obtained from changes that are sufficiently large to offset variability, may be inaccurate due to nonlinearity in the eigenvalue vs mass perturbation relationships. The potential for significant error from this source has long been recognized and has prompted development of variants of the perturbation approach wherein the scaling constants depend on total eigenvalue changes, instead of the derivatives [2,3.4]. This paper presents a normalization approach that does not call for specific distributions of the perturbation to attain accuracy and applies in the case of complex eigenvectors. The formulation, designated as the Receptance Based Mode Normalization (RBN) method, computes the (square) of the scaling constants from a complex valued over-determined system of equations obtained by evaluating the pole residue form of the Receptance at the eigenvalues of the perturbed condition. A version of RBN restricted to the case of real modes appears in [5].

THE RECEPTANCE APPROACH TO EIGENVECTOR NORMALIZATION

Let ΔM be the mass perturbation and $\overline{\lambda}_j \; and \; \overline{\phi}_j$ be the pole and arbitrarily scaled (complex) eigenvector in the mass perturbed condition for the j^{th} mode. In the derivation that follows it is convenient to treat the eigenvectors as if they are available at all the coordinates, although it will be apparent at the end that only measured coordinates are needed. From the polynomial eigenvalue problem, focusing on the perturbed condition, one has

$$\left[(M + \Delta M)\overline{\lambda}_j^2 + C\overline{\lambda}_j + K \right]\overline{\phi}_j = 0 \tag{1}$$

from where it follows that

$$\left[M\overline{\lambda}_j^2 + C\overline{\lambda}_j + K \right]^{-1} \Delta M \overline{\lambda}_j^2 \overline{\phi}_j = -\overline{\phi}_j \tag{2}$$

T. Proulx (ed.), *Linking Models and Experiments, Volume 2*, Conference Proceedings of the Society for Experimental Mechanics Series 5,
DOI 10.1007/978-1-4419-9305-2_29, © The Society for Experimental Mechanics, Inc. 2011

Inspection of Eq. 2 shows that the inverted matrix is the Receptance of the original system evaluated at $s = \overline{\lambda}_j$, therefore

$$\sum_{\ell=1}^{2N} \left(\frac{\phi_\ell \phi_\ell^T \rho_\ell}{\overline{\lambda}_j - \lambda_\ell}\right) \Delta M \overline{\lambda}_j^2 \overline{\phi}_j = -\overline{\phi}_j \tag{3}$$

which, after some simple rearranging, can be written as

$$\sum_{\ell=1}^{2N} \frac{\phi_\ell (\phi_\ell^T \Delta M \overline{\phi}_j) \overline{\lambda}_j^2}{\lambda_\ell - \overline{\lambda}_j} \rho_\ell = \overline{\phi}_j \tag{4}$$

Eq.4 describes m equations in the 2N modal constants formulated using the j[th] polynomial eigenvalue equation of the perturbed system. By combining the equations for each perturbed mode a linear system of the type $Q\rho = b$ is obtained. In practice there are only 2n identified modes so the summation upper limit in Eq.4 has to be taken as 2n and, after evaluating it at each of the identified modes, the coefficient matrix dimensions is (mx2n)x2n. As is evident from this derivation, except from possible approximation resulting from modal truncation, the RBN formulation is exact.

Obtaining the Coefficient Matrices

The linear system of equations implicit in Eq.4 can be conveniently formulated as follows: let Φ be the set of identified modes in the original state, at whatever coordinates are measured, and $\overline{\Phi}$ the set in the mass modified state (in both cases including the conjugate pairs). The system of equations can be written as

$$Q\ \rho_I = vec(\overline{\Phi}\ ) \tag{5}$$

where $\rho_I = \{\rho_1 \quad \rho_2 \quad . \quad \rho_n\}$, and

$$Q = \begin{bmatrix} \Phi\ \chi_1 \\ \Phi\ \chi_2 \\ . \\ \Phi\ \chi_n \end{bmatrix} \tag{6}$$

with $\chi_j = diag(a_j^1, a_j^2, \ldots a_j^n)$ and

$$a_j^i = \left(\frac{\overline{\lambda}_j^2}{\lambda_i - \overline{\lambda}_j}\right) \phi_i^T \Delta M \overline{\phi}_j \tag{7}$$

As can be seen from Eq.5, the constants ρ_I are coefficients in a projection of the perturbed modes on the basis of the original system. From this perspective one concludes that if the identified eigenvectors (over all coordinates) have the same span in the original and the perturbed conditions the RBN solution is exact, independently of truncation.

The Sensitivity Approach

Since we shall use sensitivity results to contrast the RBN solution we derive the formula for the scaling constant in the sensitivity scheme for the case of complex eigenvectors. Taking the mass change as $\Delta M = \beta M_1$, where β is a scalar with units of mass, and M_1 is a distribution, one has

$$\left[(M + \beta M_1)\lambda^2 + C\lambda + K\right]\psi = 0 \tag{8}$$

Differentiating Eq.8 with respect to β, pre-multiplying by ψ^T and evaluating the result at β=0 one gets, after some simple algebra

$$(2\lambda\phi^T M\phi + \phi^T C\phi)\lambda' + \phi^T M_1\phi\lambda^2 = 0 \tag{9}$$

Taking the eigenvector to be the one for which $\rho = 1$ and, using the fact for $\rho = 1$ one has [6]

$$2\lambda_j\psi_j^T M\psi_j + \psi_j^T C\psi_j = 1 \tag{10}$$

Therefore, substituting Eq.10 into eq.9 one gets

$$\lambda' + \psi^T M_1\psi\lambda^2 = 0 \tag{11}$$

from where it follows, adding the subscript j for specificity, that

$$\rho_j = \frac{-\lambda_j'}{\phi_j^T M_1\phi_j\lambda_j^2} \tag{12}$$

On the premise that only two tests are available the derivative of the eigenvalue has to be estimated with the forward difference and one has

$$\rho_j \cong \frac{\lambda_j - \overline{\lambda}_j}{\phi_j^T \Delta M\phi_j\lambda_j^2} \tag{13}$$

Numerical Examinations

This section presents numerical results illustrating the performance of RBN and contrasts the performance with the sensitivity based solution. The structure selected is a 16-DOF chain system with a mass distribution [1 2 1 2 .. etc] and a uniform stiffness equal to 5000, in some consistent set of units. The mass change distribution consists of three equal masses located at coordinates {4 8 and 13}, with the magnitude varied to achieve different eigenvalue shifts. Sensors are placed at coordinates {4,8,13 and 16}. The damping matrix is defined by prescribing 2% modal damping and subsequently adding external dashpots at DOF #1 and #2, with constants such that the diagonal entries at these two DOF are increased by a factor of 10. Table#1 lists the weighted modal collinearity index (mpcw) for the first 8 modal pairs [7], as well as the poles, the magnitude of the poles, and the damping ratios, defined in standard fashion as the real component of the pole divided by its magnitude. For interest the table also shows the exact undamped natural frequencies, which are not equal to the magnitude of the poles because the system is not classically damped.

Table 1. Some parameters of the 16-DOF structure used in the numerical evaluations

Mode # (pair)	Pole	Absolute Value of Pole (rad/sec)	Exact undamped frequency (rad/sec)	% Damping Ratio	*mpcw*
1	-0.184+ 5.443i	5.446	5.440	3.38	99.94
2	-0.932+16.374i	16.401	16.247	5.68	97.16
3	-1.997+27.227i	27.300	26.847	7.32	84.30
4	-3.236+37.482i	37.622	37.082	8.60	60.53
5	-3.995+46.342i	46.514	46.761	8.59	42.44
6	-3.289+54.558i	54.657	55.613	6.02	48.27
7	-2.346+62.442i	62.486	63.186	3.75	72.44
8	-1.686+68.397i	68.418	68.641	2.46	92.00

The percent error in the square root of the forward difference estimate of the derivative, given by

$$\vartheta = \frac{(\sqrt{\lambda'_{exact}} - \sqrt{\lambda'}) \cdot 100}{\left|\sqrt{\lambda'_{exact}}\right|} \tag{14}$$

is plotted in Fig.1 vs the % change in the magnitude of the pole for the 6th and 8th modes. As can be seen, the error is relatively small in the 6th modes but significant in the 8th. Since error in the sensitivity approach is directly dependent ϑ one anticipates good performance of the sensitivity scheme in the 6th mode but poor results on the 8th.

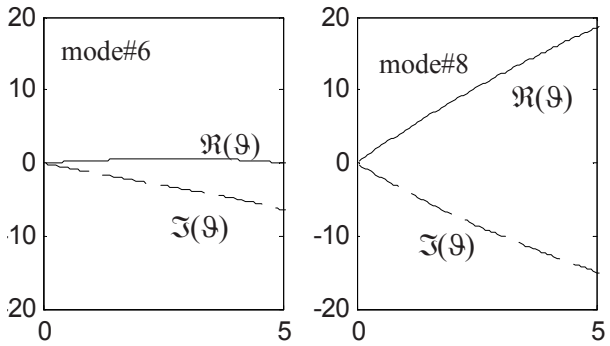

Figure1. Result from Eq.14 vs change in the magnitude of the pole for two modes of the numerical example

Characterizing the Error

The relative error in the scaling constant in simulation k is

$$\eta(k) = \left(\frac{\kappa_{exact} - \kappa(k)}{\left|\kappa_{exact}\right|} \right) \cdot 100 \tag{15}$$

We examine performance in terms of the mean and standard deviation of η obtained from Monte Carlo simulations. In the simulations the real and the imaginary parts of the identified eigenvalues are assigned lognormal distributions with mean values equal to the true values and prescribed standard deviations. In particular, the coefficient of variation of the real part of the eigenvalue is taken as 0.06, and for the imaginary part we take it as 0.003. Eigenvector variability is included by multiplying each entry of the arbitrarily scaled modes by independently selected vectors whose magnitudes and phases are taken from uniform distributions with limits of {0.95 and 1.05} and {-5 and 5} degrees, respectively.

The relative error η is a random variable whose distribution for any mode depends on the magnitude of the mass perturbation. Since the error in the estimate of the derivative does not, however, depend directly on the mass change but on the shift in the pole we use the change in the imaginary part of the pole as the independent variable to display results. Given that η is a random variable either RBN or sensitivity may be most accurate in any given realization. A reasonable approach to contrast performance, however, is to look at what limits of η bound the majority of the realizations. We select the largest of the mean plus or minus two standard deviations which guarantees, accepting the Gaussian premise, that the error is smaller that this limit at least 95% of the time. Fig.2 presents the results for the real and the imaginary parts of the noted limit for the 6^{th} mode and Fig.3 for the 8^{th}. As expected, in the 6^{th} mode the performance of RBN and sensitivity is similar but in the 8^{th}, where the relation between the eigenvalue and the mass perturbation magnitude is highly nonlinear the RBN result is significantly better.

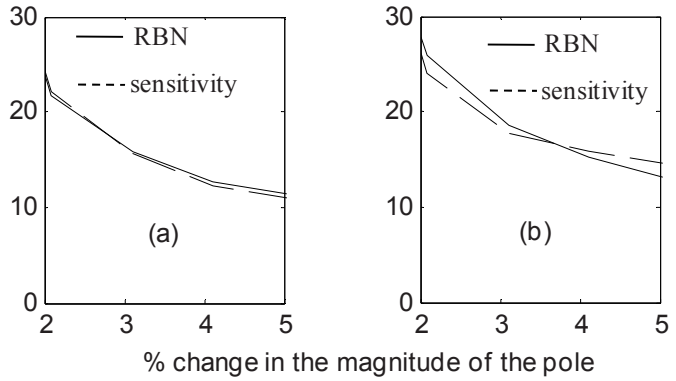

Figure.2 Maximum η computed at the mean of ± 2 standard deviation level for the 6th mode, (a) real part and (b) imaginary part

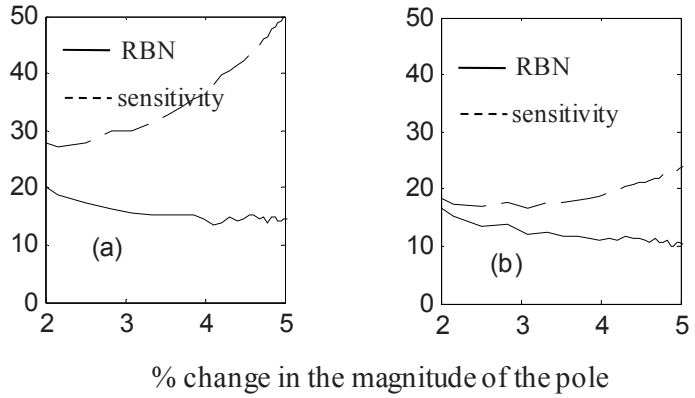

Figure.3 Maximum η computed at the mean of ± 2 standard deviation level for the 8th mode, (a) real part and (b) imaginary part

CONCLUDING REMARKS

The RBN formulation offers gains with respect to sensitivity when the relation between eigenvalue and mass perturbation is strongly nonlinear. A question that arises, independently of how the normalization is realized, is whether it is best to select the complex modal model or to operate with the real mode approximation. The issue, of course, is connected to the question of how variability in the identification affects results. At the level of expectation the more general complex modal model is the best alternative but since one usually works with results from a single realization and the variance of the complex modal model is larger it is not immediately apparent which alternative is preferable. The limiting cases are, of course, clear from a qualitative examination, namely: if the identified modal complexity is small filtering it out by adopting the normal mode model is the preferable approach and if complexity is large (most likely due to small eigenvalue gaps) one expects that adoption of the complex modal model and the complex normalization will lead to improved accuracy; research to identify quantitative guidelines for making this selection seems appropriate.

REFERENCES

1. Parloo, E., Verboven, P., Guillaume, P. and Van Overmeire, M., Sensitivity-based operational mode shape normalization, Mechanical Systems and Signal Processing, 16, (2002) 757-767.
2. Parloo, E., Verboven, P., Cuillame, P., and Overmeire, M. V., Iterative calculation of nonlinear changes by first-order approximations, Proc. of the 20th Int. Modal Anal. Conf., Orlando FL., (2002) 1084-1090.
3. Brinker R., and Andersen P. (2003). "A way of getting scaled mode shapes in output-only modal testing", Proc. of the 21st Int. Modal Anal. Conf., Kissimmee, Fl– on CD.
4. Bernal D.(2004). "Modal scaling from known mass perturbations", J. Eng. Mech. 130 (9)1083-1088.

5. Bernal D. (2010). “A Receptance Based Formulation for Modal Scaling Using Mass Perturbations”, Mechanical Systems and Signal Processing, doi:101016/j.ymssp.2010.08.004.
6. Balmes E. (1997). “New results in the identification of normal modes from experimental complex modes”, Mechanical Systems and Signal Processing, 11 (2), 229-243.
7. Pappa R.S., Elliott K.B., and Schenk A.,(1993). “Consistent-mode indicator for the eigensystem realization algorithm”, J. Guidance, Control, and Dynamics, 16 (5), 852-858.

Fault Simulation in a Gearbox Using Finite Element Model Reduction Techniques

L. Deshpande, N. Sawalhi, R.B. Randall
School of Mechanical and Manufacturing Engineering, University of New South Wales, Sydney 2052

ABSTRACT

A lumped parameter model (LPM) has previously been used to model gear and bearing faults in a gearbox. It was found that simulated signals for localized bearing faults had good correspondence with measured ones in a narrow high frequency band demodulated for envelope analysis. However, for extended faults, there is more interaction with the gearbox structure, as the fault modulates the gear meshing, and the correspondence was poorer. Forces at the bearings from the LPM model were applied to a finite element (FE) model of the casing, and the results improved but were still deficient. This paper has benefited from CMS (component mode synthesis) based FE model reduction techniques to reduce the FE model of a gearbox casing into manageable and well representative degrees of freedom of the casing. The reduced model of the casing was embedded with the LPM of the internals, which was previously obtained with the aid of Simulink® and has the capability of capturing time-varying stiffness nonlinearities arising from gears and bearings and has also the capability of simulating geometrical faults (spalls) for both gears and bearings. In order to extend the validity of the combined /reduced model, the forces are extracted from combined/reduced model and convolved with the impulse responses corresponding to the FRFs of the whole gearbox. The results show the improvements obtained through combining the reduced model of the casing with the LPM model giving a much better correspondence with measured signals. This has been verified for both the fault free and faulty cases.

1. Introduction

The application of Machine Condition Monitoring (MCM) techniques for the detection, diagnosis and prognosis of incipient faults; has traditionally been an integral part of the maintenance strategy which is aimed at improving the productivity. However, with the advances in the computational techniques, it is now possible to simulate the faults and gain an insight into the complex interactions between the various components. Fault simulation allows the analyst to vary the location and dimension of the fault, control the operating conditions and gather data without experiencing the costly failures, thus eliminating the need for large numbers of experiments. The gathered data which is cheaply available can be used to train neural networks in the diagnostic and prognostic process.

This paper describes fault simulation in a geared transmission, one of the critical equipments found virtually in all industries. A typical gearbox is characterised by the complex dynamic interaction among the individual components such as gears, shafts, bearings and the casing.

Lumped parameter models (LPM) are widely utilized to simulate the dynamic behavior of mechanical systems such as gearboxes. LPMs give reasonable representation of the dynamics of the system if masses can be lumped at certain locations, such as gears, shafts, bearings etc. LPMs have the advantage

T. Proulx (ed.), *Linking Models and Experiments, Volume 2*, Conference Proceedings of the Society for Experimental Mechanics Series 5,
DOI 10.1007/978-1-4419-9305-2_30, © The Society for Experimental Mechanics, Inc. 2011

of simulating the structure using a limited number of degrees-of-freedom (DOF), which facilitates studying the behavior of gears and bearings in the presence of nonlinearities and geometrical faults [1, 2]. However, it is difficult to account for the casing flexibility in the LPM models, which is an important consideration in lightweight structures such as in aircraft applications and this results in poor spectral matching over a wide frequency range.

In the case of continuous elastic systems, where masses are distributed over the structure (gearbox casing), other methods, such as finite element analysis (FEA), are often used to study the behavior of the structure. The use of FEA results in a large number of DOF, which in turn complicates simulating the whole system's response to the presence of nonlinearities and to gear and bearing faults. This in turn limits the validity of the simulated results and restricts their later usage in the diagnostics and prognostics of the gears and bearings. Hence there is a growing trend to use FE model reduction methods to create accurate low order dynamic models before calculating eigenfrequencies and eigenmodes [3].

Model reduction is applied to large FE models to give faster computation of the natural frequencies and mode shapes and at the same time compute the static and dynamic responses correctly. Model reduction also plays a role in experimental modal analysis since the mass and stiffness matrices may also be used to compare the analytical and experimental modes by using orthogonality checks [4].

In this paper, a dynamic reduction technique, the so-called Craig–Bampton reduction technique, is used to reduce the finite element model of the UNSW gearbox casing. The reduced model is valid only within a certain frequency range, subject to the number of modes retained in the analysis. The reduced model is then connected to a lumped parameter model of the internals (shafts, gears and bearings) which has the capacity to simulate faults. The combined model is run in Simulink® environment with extended inner race faults.

Thus the total response will not only include the contributions of the dynamics of the internals but also the flexibility and the dynamics of the casing. This makes this approach very attractive as the finite element model has been dramatically reduced from over a hundred thousand degrees of freedom to only 124 DOF. In order to extend the validity of the combined /reduced model, the forces are extracted from combined/reduced model and convolved with the impulse responses corresponding to the FRFs of the whole gearbox (casing and internals). The approach of convolving the forces with the impulse response of the FE model was earlier proposed [5, 6], but only applied to the forces extracted from the LPM model. The current approach has the advantage of maintaining a dynamic interaction in the low/mid frequency regions and improves the validity at higher frequency where it is the modal density rather than the individual modes that are of interest.

2. UNSW Gearbox

The gearbox test rig (Fig.1) under investigation was built by Sweeney [7] to investigate the effect of gear faults on transmission error.

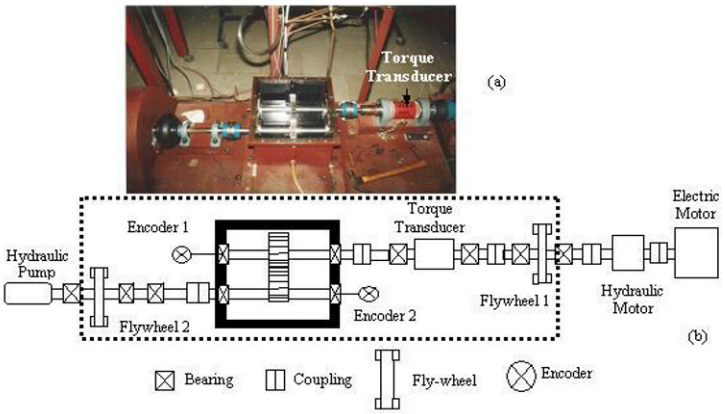

Figure 1: (a) spur gear test rig (b) schematic Diagram of the spur Gearbox Rig (Components of interest contained in dotted box) [7]

In this test rig, the single stage gearbox (in this case a spur gear set with 1:1 ratio and 32 teeth on each gear) is driven primarily by a 3-phase electric motor, but with circulating power via a hydraulic pump/motor set. The input and output shafts of the gearbox are arranged in parallel and each shaft is supported by two double row ball bearings (Koyo 1205). The flywheels are used to reduce the fluctuations of the input and output shaft speeds. The couplings are flexible in torsion and without stiffness in bending, making them very helpful for the attenuation of the shaft torsional vibration.

The bearings under test (Fig 2) were double row self-aligning (Koyo 1205) with a contact angle of 0^o, a ball diameter of 7.12 mm and a pitch diameter of 38.5 mm.

Fig 2: Bearing under test (Koyo 1205) [1]

Fig 3: Extended inner race fault [2]

An extended fault was inserted in the inner race of the bearing by grinding one eighth of the circumference (length 22 mm) as shown in Fig. 3. The elasto-hydrodynamic effect of the oil film was not taken into account. In the simulation model an extended rough profile was programmed into the bearing's S-function to simulate the vibrations generated from the test rig as a result of the extended inner race faults [2]. The tests both in the experiment and in the simulations were carried out at a 10 Hz shaft frequency. The ball pass frequency of the inner race at this speed is roughly 71.1 Hz.

3. Lumped Parameter Model (Internals)

Different mathematical models [7-9] have been developed to study the dynamic effects on the transmission error (TE) of the UNSW gearbox. These were lumped parameter models (LPM), which assume that each shaft mass and inertia is lumped at the bearings or at the gears. In all these models, rolling element bearings (REBs) were modelled as a single degree of freedom (mass-spring) system with

constant stiffness. In [1, 2] Sawalhi and Randall combined the gear model with a bearing model, which has the capacity to model faults. This resulted in a 34 DOF model (Fig.4) .

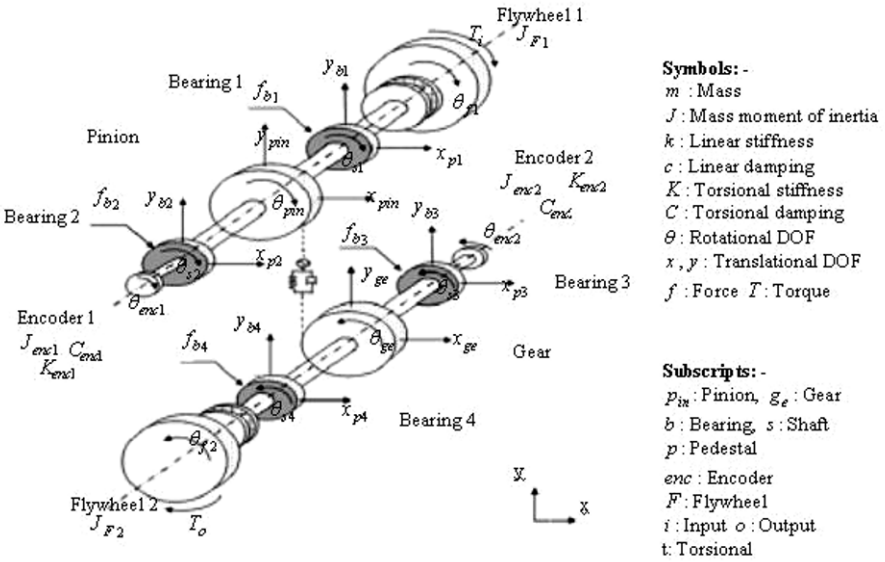

Figure 4: 34 DOF Dynamic Model of the gear test rig. (Vertical direction y aligned with the line of action of the gears) [1]

The 34 DOF in the LPM included a 5 DOF bearing model (Fig. 5). The translational degrees of freedom were considered both along the Line of Action (LoA) and perpendicular to it. The casing model considered was a simple one and contained only two modal frequencies from hundreds available. This still gave a valid simulation of the gearbox for the purpose of studying its behavior for a spalled bearing (envelope signal for demodulation of a high frequency resonance) and also in studying the different interactions that exist in the system by comparing simulations with real measurements, for a variety of localized and extended faults in both gears and bearings [1, 2]. It was noticed however that localized faults gave better results than extended faults when compared to the experimental ones. More details about the LPM model and the bearing model can be found in [1].

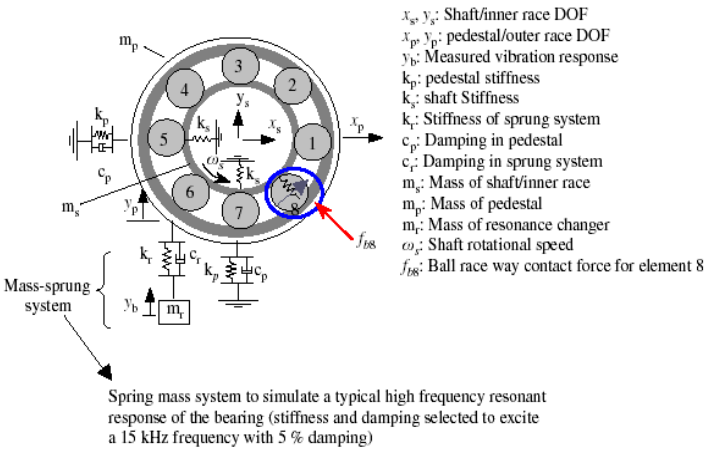

Figure 5: Five degree of freedom bearing-pedestal model [1]

4. The finite element model (Casing)

The finite element model (FEM) of the casing (104 340 degrees of freedom) is shown in figure 6. The casing is supported by rubber pads, which are simulated using spring elements at the corners of the casing. The earlier model used only shell elements [5, 6] and was updated to the new one which has both solid and shell elements. The model has been compared with experimental modal testing and validated for the lower frequency modes [6]. In the current update the nodes on the hub of each bearing are connected to a centre node using rigid body elements. Thus one centre node is formed at the centre of each bearing, which will eventually capture the flexibility of the casing. This also enables the connecting of this model (a reduced version of it) with the LPM model of the internals.

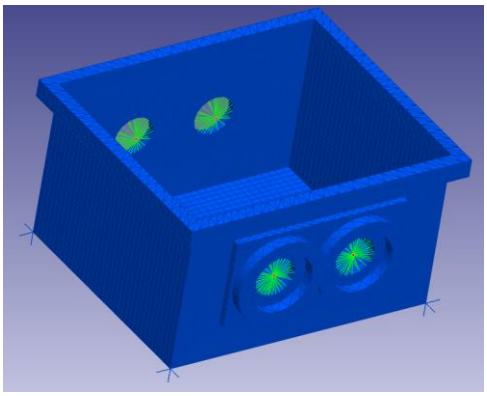

Figure 6: The Finite element model of the UNSW gearbox casing

5. Finite element model reduction techniques

Static analyses require a detailed set of grid points or nodes to map internal stresses and strains and hence the FE models can be very large, perhaps several thousand DOFs which require large computing resources. However, dynamic analyses based upon knowledge of fundamental frequencies and their associated mode shapes need far fewer nodes or DOFs [10]. Various model reduction techniques have been developed in the past decades such as Guyan, Dynamic, CMS, IRS, SEREP etc.

It is impossible to simulate the dynamics of the full system with the reduced model and every reduction transformation is a trade off between the accuracy and computational speed. The comparison of various model reduction techniques shown below is mainly taken from [11, 12].

The static reduction method also known as Irons-Guyan method [13, 14] produces smaller size system matrices by eliminating the coordinates at which no external force is applied. The reduction method is exact for static problems; however, for dynamic problems large errors may be introduced due to the fact that the DOFs eliminated may experience inertia forces, which cause their dynamic displacements to differ from the static, the deviation increasing with frequency [15]. High frequency motion is better approximated using dynamic reduction. However, the transformation matrix T_{dyn} depends on the choice of an appropriate initial frequency ω, which is not a trivial task. Guyan reduction is a special case of dynamic reduction, when $\omega = 0$.

Static reduction methods were further improved by O'Callahan [16], with a technique known as Improved Reduction System (IRS) method. IRS perturbs the static transformation by taking into account the inertia terms as pseudo-static forces. Although the results match the low frequency response

resonances of the full system better than static reduction, the IRS reduced stiffness matrix is stiffer than the Guyan reduced matrix and the mass matrix is less suited for orthogonality checks.

The IRS transformation matrix T_{IRS} depends on the reduced mass and stiffness matrices obtained by static reduction. To minimise the error produced by this scheme, IRS could be extended to the Iterated IRS method [17]. Even though the algorithm converges to yield the eigenvalues of the full system, the method results in a too stiff structure [4].

5.1 Component Mode Synthesis (CMS): Craig-Bampton Method

Dynamic condensation, as an efficient method for model reduction, was proposed in 1965 [3]. One such method known as the Component Mode Synthesis (CMS) technique [18-20] consists of dividing the complex structure into smaller *substructures* (or *superelements*) and recovering afterwards the dynamic behavior of the original structure by assembling the *superelements* and considering the equilibrium of nodes at the interfaces between the various components. The dynamic analyses of large structures are often carried out using *superelements* based on the *substructuring* principle. In such algorithms the reduction takes place by creating master degrees of freedom.

The Craig-Bampton (CB) method [21] is a dynamic reduction method used to reduce the size of the finite element models. In this method, the motion of the whole structure is represented as a combination of boundary points (so called master degrees of freedom) and modes of the structure assuming that the master degrees of freedom are held fixed. Unlike Guyan reduction [13], which only accounts for the stiffness matrix, Craig-Bampton accounts for both the mass and stiffness. Furthermore, it enables defining the frequency range of interest by identifying the modes of interest and including these as a part of the transformation matrix. The decomposition of the model into both physical DOFs (master DOFs) and modal coordinates allows the flexibility of connecting the finite elements to other substructures, while maintaining a reasonably good result within a required frequency range. The algorithmic scheme of CMS is divided into three categories namely, fixed-interface, free-interface, and the residual-flexible free interface. In this paper only the fixed-interface CMS method is considered.

The CMS algorithm does have certain disadvantages and the static term (Guyan) constitutes the source of the largest amount of information loss. The error can be compensated to some extent by increasing the number of CB modes, where coupling of the reduced order model (ROM) into the Multi-Body System (MBS) is not intended [11].

6. Combined (LPM + reduced FEM) model

Fig 7 shows the flowchart to obtain the total response at the measurement point by combining the LPM and reduced FE model of the casing. The reduced mass and stiffness matrices ($[M_{red}]$ $[K_{red}]$) of the casing (obtained using Craig-Bampton based CMS method) were combined with the LPM model in the Simulink® environment. The combination was achieved by re-writing the equations of motion at the connecting nodes. The LPM model of the internals had 22 DOFs. The reduced casing model had 124 DOFS which were made up of 24 master degrees of freedom corresponding to 4 bearing centre nodes (each with 6 DOFs) plus 100 modes with master DOFs fixed. This resulted in a new combined model with a total of 146 DOFs (46 physical DOFs and 100 modal or generalized coordinates). The modal damping $\zeta = 4\%$ was introduced.

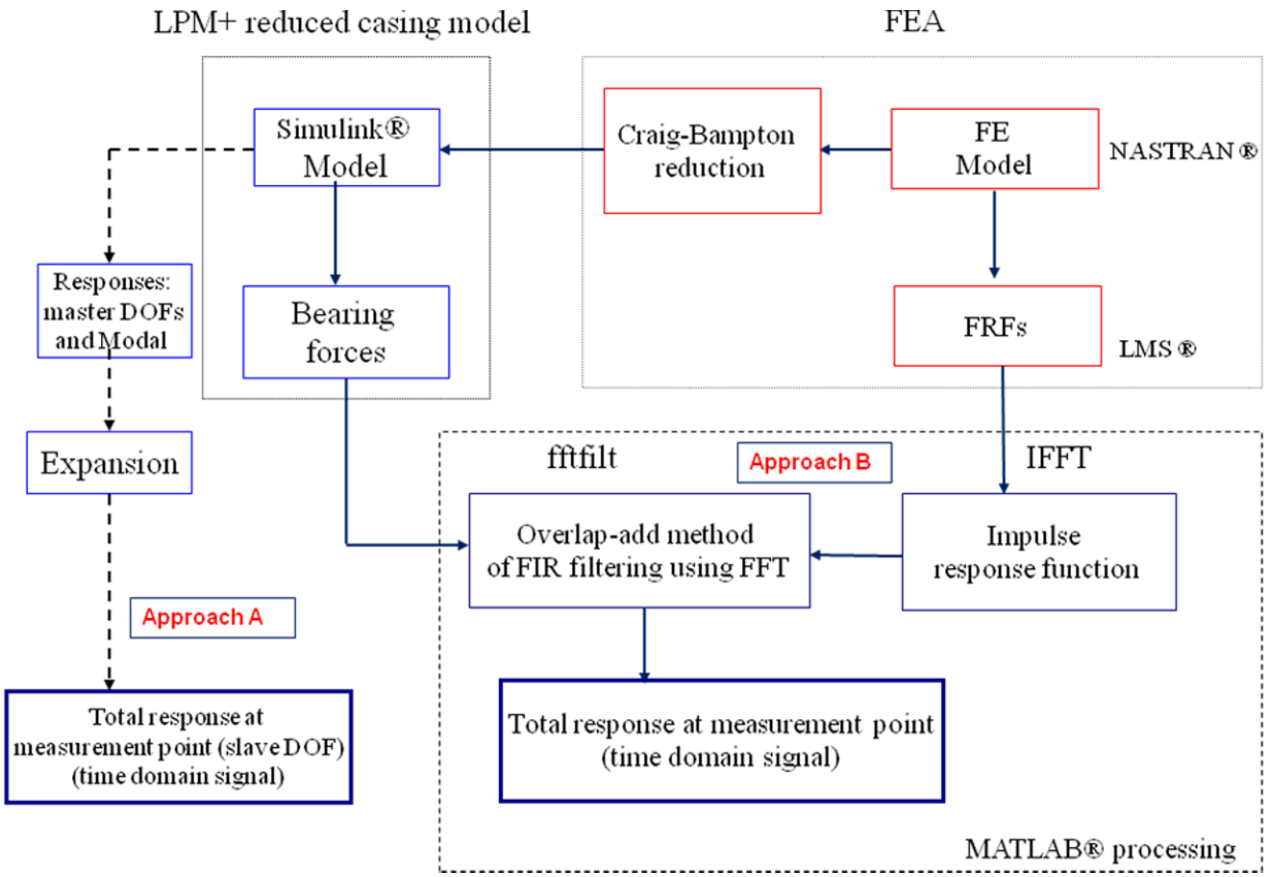

Figure 7: Combining FEM and LPM to evaluate total response

Sawalhi et al. in [22] evaluated the total response by expanding both the physical and modal responses back to the slave DOFs of interest which also represented a virtual sensor corresponding to a physical accelerometer location used in the experimental testing (Approach A, Fig 7). Using this approach, the results were valid only up to 4 kHz (100 modes). In order to improve the accuracy of the combined LPM-reduced model and extend this to a higher frequency range, the forces from the LPM-reduced casing model were extracted and convolved with the impulse response of the gearbox (Approach B, Fig 7). This approach of extracting the forces and convolving them with the impulse response was earlier proposed in [5]. However, when this was done for the LPM model, the dynamic interaction was not fully accounted for in the low frequency region. By reducing the model and then convolving the LPM-reduced forces with the impulse responses, we achieve a more interactive approach which has a higher valid frequency range. This is also viable as at high frequency the main focus is on the modal density rather than the individual modes, and also on the response to local rather than extended faults, already shown to be well modeled by the simpler models.

Hence, in this paper the combination of the LPM and FE reduced model was achieved by extracting the bearing forces from the LPM model and convolving them with the impulse responses corresponding to the frequency response functions (FRFs) of the casing [5] (Fig 7). The FRFs were extracted from the FE model by synthesizing them from the natural frequencies and mode shapes in the LMS Virtual Lab ® environment which compute the FRFs based upon the modal superposition of the selected mode set. The FRFs were calculated between the bearing force location (input points) and accelerometer position (output point) located on the casing directly above the faulty bearing.

7. Results and Discussions

The main important features to show the achieved improvements through the current proposed simulation approach are shown by comparing the power spectrum density for both the faulty and good bearings for simulated and measured signals. A further comparison is made to show the improvement for the good and faulty cases after removing the discrete components. This comparison is done at the cyclic frequency of the shaft speed (10 Hz) and also at zero frequency. Although the graphs shown are to a different scale or dynamic range, the main intention here is to compare the shape of the spectra and the dB difference between the good and the faulty bearing.

7.1 Extended inner race fault – PSD comparison

The experimental results for the smooth extended inner race fault were compared with the results of three different simulations namely; LPM, HUMS [22] and the current simulation model (Fig 8). Note that the comparison of the power spectra at this stage is made without removing the contribution of the gears, so as to show the overall spectrum shape.

It can be said that the overall shape of the spectrum has improved significantly through this current simulation (8.d) as compared to earlier model (8.b and 8.c). This is seen in the low/mid frequency range up to 6 kHz. A number of resonances are also clearly noticed in the high frequency region. The structural damping used to extract the FRF needs to be adjusted (increased) to give a better correspondence. This will be investigated and updated at a later stage.

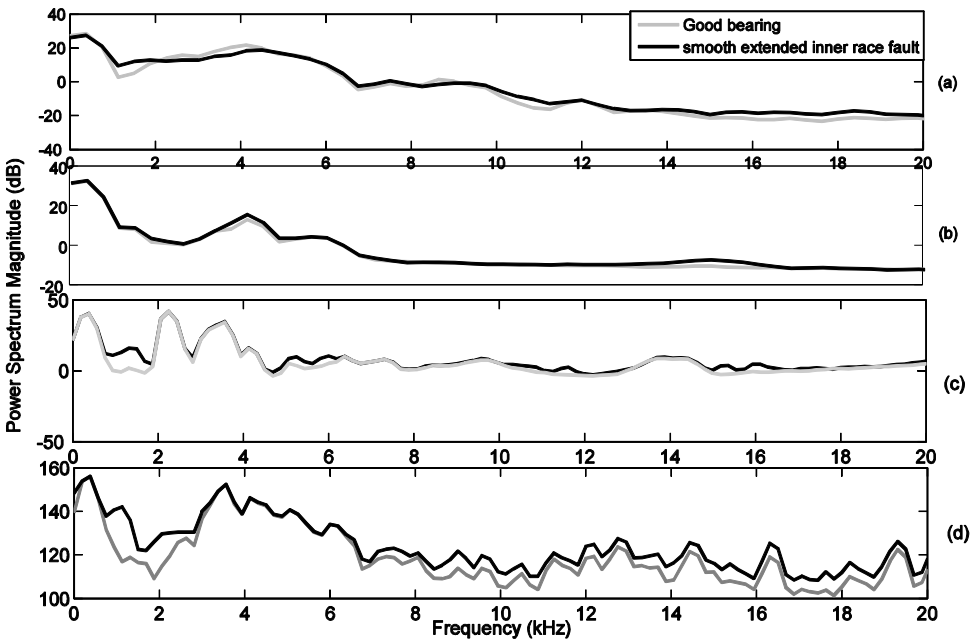

Fig 8: PSD comparison: showing overall response in the useful frequency band (a) Experimental (b) LPM (C) HUMS (no pink noise added) (d) Current model (Forces from the condensed model convolved with the frequency response from the total gearbox)

7.2 Extended inner race fault – Cyclic spectrum comparisons

Fig 9 shows the cyclic spectrum comparisons for the residual signals obtained after removing periodic parts using Discrete Random Separation (DRS) [23, 24] for the experimental (9.I), LPM (9.II) ,HUMS model (9.III) and the current condensed model (9.IV). The comparison is made at a cyclic frequency α = 0 (normal power spectrum comparison) and at α = Ω (shaft speed).

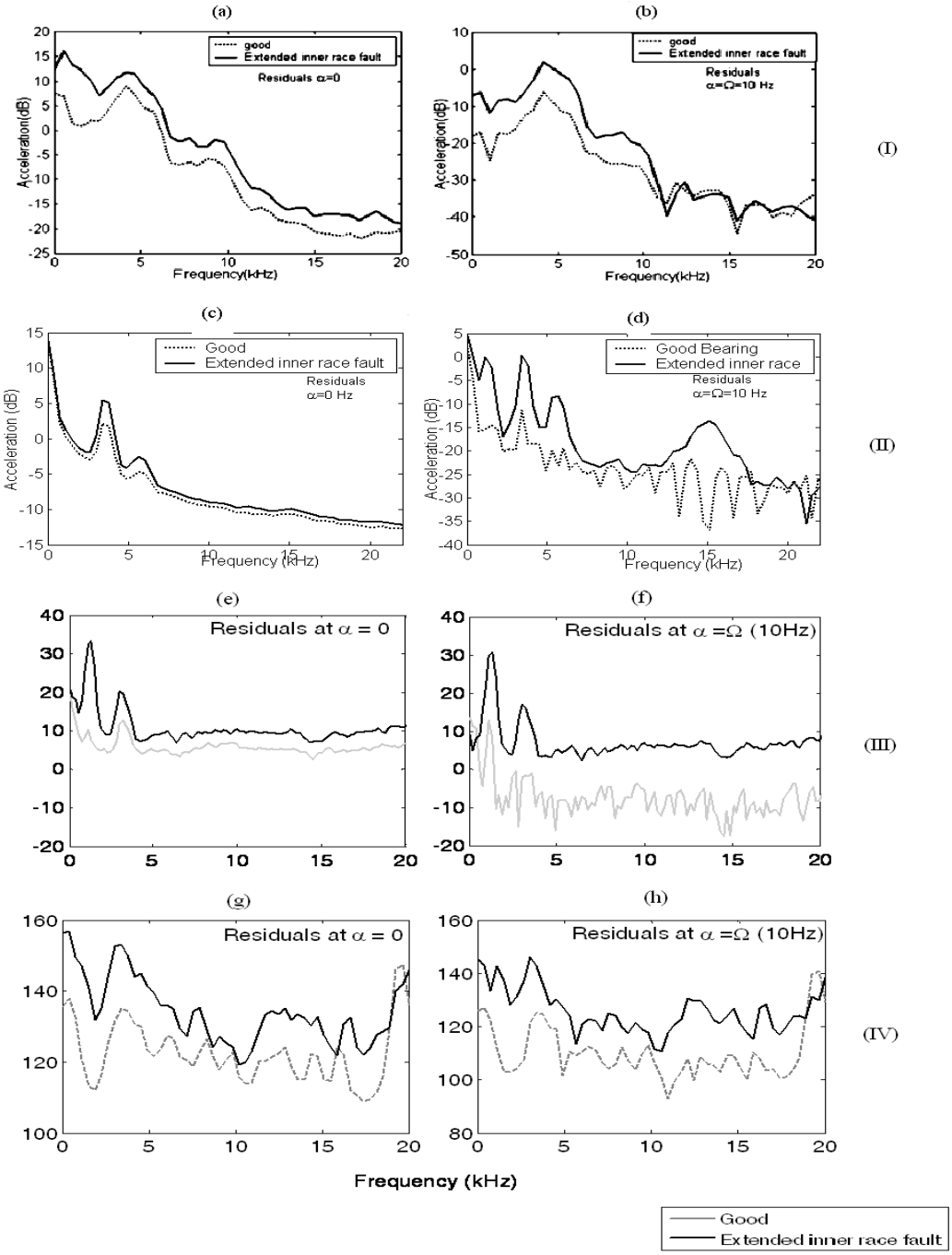

Fig 9: Cyclic Spectrum comparisons after the removal of discrete components
(a) Measured residuals compared at α =0 (b) Measured residuals compared at α = Ω
(b) LPM model residuals compared at α =0 (c) LPM model residuals compared at α = Ω
(d) HUMS model residuals compared at α =0 (e) HUMS model residuals compared at α = Ω
(g) Current model residuals compared at α =0 (h) Current model residuals compared at α = Ω

For $\alpha = 0$, (Figs 9.a, 9.c, 9.e and 9.g), the power spectrum level for the faulty bearing is higher than that of the good bearing for both simulated and measured signals. The increase in the dB difference is observed across the whole frequency range. As the comparison is made at $\alpha = 0$, no conclusion could be drawn as to the source of excitation, as this increase in the dB difference could be the result of an increase in the stationary noise, which is still present at $\alpha = 0$. Note that in the current simulations, the dB difference in the low frequency regions has a better correspondence with the experimental one.

For $\alpha = \Omega$ (Fig 9.b, 9.d, 9.f and 9.h), it is noticed that the highest increase in the dB difference appears mainly in the low frequency region (fault modulates the gearmesh frequencies). The increase in the dB difference at $\alpha = \Omega$ implies the existence of an extended fault in the inner race (as no gear component or stationary noise are present in this comparison). In the measured signal the increase is noticed mainly in the low frequency region, as the fault is quite smooth (the presence of the oil film helps in providing such smoothness) in particular with a smooth exit so that the higher frequency region was not excited. In the simulated signals (both LPM and condensed model) there is an increase in the dB difference in the high frequency region, very likely due to the fact that the exit from the fault is still rather abrupt. The inclusion of the casing model through the Craig-Bampton reduction method, and then through the convolution of the extracted forces by the impulse responses increases the similarities with the experimental results and shows a much better correspondence both in the low and high frequency regions when compared to the initial LPM model and the direct LPM- Craig Brampton reduced model. As this is still an ongoing work, more refinements and adjustments are expected to take place to improve the model. More experimental cases for extended inner and outer race faults are planned and should be compared to simulated results at different speeds and loads.

8. Conclusions

The simulation of the dynamic behavior of a complex structure such as a gearbox is carried out using finite element model reduction technique. The dynamic reduction was based on the Craig-Bampton method and the reduced mass and stiffness matrices of the casing were incorporated into the lumped parameter model of the gearbox. The simulation was carried out for an extended inner race fault. In order to extend the validity of the combined /reduced model, the forces were extracted from combined/reduced model and convolved with the impulse responses corresponding to the FRFs of the whole gearbox (casing and internals). The current approach has the advantage of maintaining a dynamic interaction in the low/mid frequency regions and improves the validity at higher frequency where it is the modal density rather than the individual modes that are of interest.

The inclusion of the casing model through the Craig Bampton reduction method and then through the convolution of the extracted forces with the impulse responses, increases the similarities with the experimental results and shows a much better correspondence both in the low and high frequency regions when compared to the initial LPM model and the direct LPM- reduced Craig-Brampton model. As this is still an ongoing work more refinements and adjustments are expected to take place to improve the model. More experimental cases for extended inner and outer race faults are planned and should be compared to simulated results at different speeds and loads.

Acknowledgements

This research was supported by the Defence Science and Technology Organisation (DSTO) through the Centre of Expertise in Helicopter Structures and Diagnostics at UNSW.

References

[1] N. Sawalhi and R. B. Randall, "Simulating gear and bearing interactions in the presence of faults: Part I. The combined gear bearing dynamic model and the simulation of localised bearing faults," *Mechanical Systems and Signal Processing,* vol. 22, pp. 1924-1951, 2008.

[2] N. Sawalhi and R. B. Randall, "Simulating gear and bearing interactions in the presence of faults: Part II: Simulation of the vibrations produced by extended bearing faults," *Mechanical Systems and Signal Processing,* vol. 22, pp. 1952-1966, 2008.

[3] Z.-Q. Qu, *Model Order Reduction Techniques :with Applications in Finite Element Analysis* Springer, 2004.

[4] L. I. Myklebust and B. Skallerud, "Model Reduction Methods for Flexible Structures," presented at the 15th Nordic Seminar on Computational Mechanics, Aalborg, Denmark, 2002.

[5] N. Sawalhi and R. B. Randall, "A Combined Lumped Parameter and Finite Element Model of a Single Stage Gearbox for Bearing Fault Simulation," presented at the COMADEM 2008 (Condition Monitoring and Diagnostic Engineering Management), Prague, Czech Republic, 2008.

[6] N. Sawalhi and R. B. Randall, "Improved Simulation of Faults in Rolling Element Bearings in Gearboxes," presented at the 9th International Conference on Vibrations in Rotating Machinery, 8-10 September, UK, 2008.

[7] P. Sweeney, "Transmission error measurement and analysis " Ph. D. Dissertation, Mechanical & Manufacturing Engineering, Faculty of Engineering, University of New South Wales, Sydney, Australia, 1994.

[8] S. Du, "Dynamic modelling and simulation of gear transmission error for gearbox vibration analysis," Ph.D. Dissertation, Mechanical & Manufacturing Engineering, Faculty of Engineering, University of New South Wales, Sydney, Australia, 1997.

[9] H. Endo, "Simulation of gear faults and its application to the development of differential diagnostic technique " Ph. D. Dissertation, Mechanical & Manufacturing Engineering, Faculty of Engineering, University of New South Wales, Sydney, Australia, 2005.

[10] J. T. Young. (2000). *Primer on the Craig-Bampton Method, (Based on input from William B. Haile)*.

[11] P. Koutsovasilis and M. Beitelschmidt, "Model order reduction of finite element models: improved component mode synthesis," *Mathematical and Computer Modelling of Dynamical Systems,* vol. 16:1, p. 57 — 73, 2010.

[12] P. Koutsovasilis and M. Beitelschmidt, "Comparison of model reduction techniques for large mechanical systems," *Multibody System Dynamics,* vol. 20, pp. 111-128, 2008.

[13] R. J. Guyan, "Reduction of stiffness and mass matrices," *AIAA Journal,* vol. 30, pp. 772-780, 1965.

[14] B. M. Irons, "Structural eignvalue problems-elimination of unwanted variables," *AIAA journal,* vol. 3, pp. 961-962, 1965.

[15] S. L. Chen and M. Géradin, "An exact model reduction procedure for mechanical systems," *Computer Methods in Applied Mechanics and Engineering,* vol. 143, pp. 69-78, 1997.

[16] J. C. O'Callahan, "A procedure for an improved reduced system (IRS) model," in *Proc. 7. International Modal Analysis Conference*, Las Vegas, 1989.

[17] M. I. Friswell, S. D. Garvey, and J. E. T. Penny, "Model reduction using dynamic and iterated IRS techniques," *Journal of Sound and Vibration,* vol. 186, pp. 311-323, 1995.

[18] C. Carmignani, P. Forte, and G. Melani, "Component modal synthesis modeling of a gearbox for vibration monitoring simulation," presented at the The Sixth International Conference on Condition Monitoring and Machinery Failure Prevention Technologies, Dublin, Ireland, 2009.

[19] S. Ulf, "COMPONENT MODE SYNTHESIS - A method for efficient dynamic simulation of complex technical systems," Technical Report, Department of Machine Design, The Royal Institute of Technology (KTH), S-100 44 Stockholm, Sweden2003.

[20] H. N. Bayoumi, "Interfacing FEA and Multibody Simulation Through Component Mode Synthesis," in *ASME Conference Proceedings*, 2005, pp. 1387-1392.

[21] R. Craig and M. Bampton, "Coupling of substructures for dynamic analysis " *Amer. Inst. Aero. Astro. J.,* vol. 6, pp. 1313–1319, 1968.

[22] N. Sawalhi, L. Deshpande, and R. B. Randall, "Improved simulations of faults in gearboxes for diagnostic and prognostic purposes using a reduced finite element model of the casing," in *7th DSTO International Conference on Health & Usage Monitoring* Melbourne, 2011.

[23] J. Antoni and R. B. Randall, "Unsupervised noise cancellation for vibration signals: part I--evaluation of adaptive algorithms," *Mechanical Systems and Signal Processing,* vol. 18, pp. 89-101, 2004.

[24] J. Antoni and R. B. Randall, "Unsupervised noise cancellation for vibration signals: part II--a novel frequency-domain algorithm," *Mechanical Systems and Signal Processing,* vol. 18, pp. 103-117, 2004.

Response Measurements of DMS Cabinets and Supporting Truss Structures under Environmental and Transient Wind Loads

Robert W. Bolton, Assoc. Prof., Department of Industrial and Civil Engineering,
University of Southern Denmark, Campusvej 55, DK-5230, Odense M, Denmark,
Brent Phares, Assoc. Director and Terry J. Wipf, Director, Bridge Engineering Center
and Pitt-Des Moines Professor of Civil Engineering, Iowa State University,
2711 S. Loop Drive, Suite 4700, Ames, Iowa 50010-8664

ABSTRACT

A detailed understanding of the wind forces on large highway signs is crucial for the safe and economical design of the supporting truss structures. Large dynamic message signs (DMS) are increasingly employed to manage highway traffic flow and to provide accurate, timely information to highway users. Recent field inspection data indicates that truss structures supporting DMS signs may be subject to more complex and extreme wind loads that are not accounted for in current code driven design procedures and are exhibiting increased maintenance and fatigue problems, even in relatively new sign installations. Interim results of a multi-institution 24 month analytical and field monitoring study to better understand the response and critical design characteristics of these new sign structures are present in this paper.

Problem statement

The current design practice for truss structures supporting normal signs and variable or dynamic message signs (VMS) is governed by the AASHTO Standard Specifications for Structural Supports for Highway Signs, Luminaires and Traffic Signals, Fifth Edition released in 2009[1]. These specifications include updated provisions addressing extreme wind loads and new fatigue design provisions. However these provisions utilize a static strength design approach that may not accurately account for the long term effects of low level cyclic stresses resulting from vortex/shedding and buffeting under steady wind conditions, unsteady or gusting wind conditions, and truck induced gusting seen by a specific VMS sup-

(a) (b)

Fig 1 Typical DMS sign installations, (a) 4-chord arched truss design, (b) 4-chord square truss design

T. Proulx (ed.), *Linking Models and Experiments, Volume 2*, Conference Proceedings of the Society for Experimental Mechanics Series 5,
DOI 10.1007/978-1-4419-9305-2_31, © The Society for Experimental Mechanics, Inc. 2011

port structure. Support structures for large DMS cabinets such as the 4-chord trusses depicted in Figure 1 designed per current provisions may have an adequate factor of safety against strength failure but little data is available on the additional aeroelastic and dynamic load effects caused by the added depth, larger projected area, and larger eccentrically positioned mass of DMS cabinets. Figure 2 shows a close-up view a typical DMS cabinet installation that highlights the upstream cabinet offset. This cabinet and the supporting arched truss are the subject of the field data described later in the paper. Fatigue and vibration of non-cantilevered sign support structures were formally addressed by Fouad, et al. in NCHRP Report 494 [2] which included recommendations for new fatigue provisions using equivalent static load design procedure to address individual aeroelastic wind load effects experience by in-service structures.

Fig 2 Typical offset DMS cabinet installation

Selected prior work

Several investigations document fatigue related deterioration of non-cantilevered truss support structures and have developed mitigation strategies to monitor or repair damaged structures. Pantelides,Nadauld and Cercone [3] developed a glass fiber reinforced polymer composites (GFRPs) repair process for cracked aluminum overhead sign structural components. The static load carrying capacity of the undamaged welded connection, and the fatigue damaged (through cracking) connection repaired with GFRP composites are established and resulting in retrofitted connections with GFRP reinforcement achieving between 1.17 to 1.25 times the capacity of the original welded aluminum connection.

Wipf and Phares [4] utilized field load tests to estimate the residual load capacity of a fatigue damaged sign support truss and compared these results to an analysis of an undamaged truss. These data were used to develop a set of management recommendations to monitor, repair, or replace similar structures for the Iowa DOT.

Huckelbridge and Metzger [5] preformed an extensive failure analysis on the near collapse of a 4-chord square sign support truss spanning IR 75 in Ohio caused by the complete fracture of one lower chord member and an adjacent diagonal strut. The assessment utilized data from in-situ traffic-induced vibration measurements near the failure, finite-element simulation estimating the expected dynamic response of the truss, in-service time and inspection history, an estimate of the cumulative vibrational effect of truck traffic, and a metallurgical examination of the failed components. The failure was attributed to extremely high-cycle fatigue of the chord-web diagonal welded connection (possibly exceeding 1 billion cycles over the structure's 40 year in-service life) even though the estimated effective stress range of the Category ET connection was below current AASHTO constant amplitude fatigue limits for the detail.

Park, McLean and Stallings [6, 7] studied the effect of wind induced fatigue on the performance of two VMS truss support structures using simualted dynamic response data and field monitored vibration data. One of these structures exhibited noticable in-service vibration levels and was found to have a finite fatigue life per provisions in the 4th edition of the AASHTO Standard Specifications for Structural Supports for Highway Signs, Luminaires and Traffic Signals that required a long-term monitoring/inspection plan. The researchers reported mixed results in establishing the relative importance of attributing stress levels to natural and truck induced wind gusting.

Other research, both analytical and laboratory based, has been performed to investigate specific aspects of the fatigue problems in standard and DMS sign truss support structures. Foley and Peronto [8, 9] performed an extensive laboratory study to quantify the fatigue-life variability of the AASHTO ET fatigue detail category for welded circular hollow section (CHS) connections commonly used in sign support structures. In the investigation fatigue tests were performed on field harvested and fabricated Y-joint specimens and fatigue lives were predicted via several methodologies. The researchers noted that banding in the microstructure of CHS sections can cause bilinear behavior in the material's stress-strain response in the elastic region resulting in a marked decrease in ductility and fatigue life. These data along with ad-

ditional field monitoring data collected by Foley and Ginal [10]were used to develop a procedure to predict the service lives of full-span overhead sign support trusses.

Rice Lafave and Mehuys [11] investivated end connection effects on the susceptibility of welded aluminum truss tubular web members to vortex shedding induced resonant vibrations. A field test method was developed to reliablely determine the fundamental natural frequency of web components and these data were used to compute vortex-shedding frequencies and estimated the critical wind speeds calibrated to in-situ structural components. These component characterististic were then correlated with wind-related fatigue damaged components identified in field inspections and design recommendations limiting the maximum web member slenderness ratio were developed to minimize vibration problems in new designs.

Constantinescu, Bhatti, and Tokyay [12, 13] performed a detailed CFD study to analytically determine the wind loads and pressure distributions through numerical simulation on large highway sign structures. Parameters studies included; aspect ratio and sign spacing for regular panels, sign depth for the DMS cabinets, presence of back-to-back signs, presence of trucks underneath the signs, and reduction in the mean pressure force on the panels due to presence of small air holes. For complex multi-panel combinations pressure distributions were highly non-symmetrical and not accurately addressed in current design provisions. Authors recommend that CFD simulations be used to improve these wind load estimates and to develop more accurate load and response characteristics of DMS truss structures.

Kacin, Rizzo, and Tajari [14] performed and analitical study to develop an algorithm to determine the fatigue life of an overhead four-chord truss sign structures. The algorithm uses a time varying natural wind loading and a finite element model to extract stress histories of selected critical elements. Complete stress ranges are counted and a linear damage accumulation method is used to find the fatigue life of some critical members.

Current study

A detailed understanding of the wind forces on large highway signs is crucial for the safe and economical design of the supporting truss structures. Large DMS systems are increasingly employed to manage highway traffic flow and to provide accurate, timely information to highway users. Recent field inspection experiences in Iowa indicate that truss structures supporting DMS signs may be subject to more complex and extreme wind loads that are not accounted for in current code driven design procedures and are resulting in increasing maintenance and fatigue problems in relatively new sign installations. The Iowa DOT has commissioned a multi-institution 24 month analytical and field monitoring study to better understand the response and critical design characteristics of these new sign structures. This study will utilize the technical expertise of several universities to execute an extensive analytical and field monitoring test plan using CFD simulations and field observations of several in-service structures to better quantify the environmental wind loads on DMS sign structures and the resulting dynamic response of these structures with particular focus on characterizing cumulative stress cycling envelope of fracture critical components and connections.

Data from prior steady-state CFD simulations at the University of Iowa will be extended to include more detailed unsteady air-flow simulations around DMS sign panels. These simulations will provide quantitative data related to unsteady forces (dynamic loads) on the DMS panels that will be input to structural models of several in-service DSM truss installations to study the vibration characteristics of the supporting truss structures. Project field observations will consist of short-term monitoring of four DMS cabinet/truss installations and long-term monitoring of one DMS cabinet/truss installation. Short-term monitoring objectives are designed primarily to characterize and bound the dynamic response and properties of the individual test structures and critical components subject to transient gusting events from trucks and limited background wind exposure. These structures will be extensively instrumented (approximately 50 data channels) to capture global and component level strain and acceleration response data along with environment wind and temperature measurements.

Data from these short-term monitoring tests will be used to establish a sparser long-term monitoring plan designed to characterize features of extended stress cycling envelope for critical components and to capture a wider range of responses to ambient background and extreme wind loadings. The long-term monitoring will extend over a three to six month period. During this monitoring, strain (a minimum of 8 locations or components), acceleration (approximately 4 locations), temperature (ambient plus 2 structure temperatures), and wind information (speed and direction) information will be collected. Level triggering may be used later in the monitoring period to limit the collection of redundant data. Analysis of these data will focus identifying important dynamic behaviors of the test structure under both ambient and truck induced winds. The numerical simulations developed to characterize structural loads and resulting dynamic re-

sponse will also be compared with selected field observations and these may be used to improve on or calibrate the analytical models of the test structure. This calibrated model can then be used to investigate a broader range of wind and geometric conditions.

Fig 3 Truck in lane 2 passing under Euclid 4-chord arched support structure during short term field test

Preliminary testing

Data from one short-term field monitoring test is presented in this section. In Figure 3 a downstream view of the I235 Euclid test structure is shown as a large truck passes under the instrumented truss and DMS cabinet during testing. The Euclid test structure has a span of 21.0 m between support centerlines. The truss is 1.50 m wide and varies in height from 1.80 m at the supports to 2.40 m at mid span (measured center to center of chords). The truss was fabricated is two symmetric segments. The main top and bottom chords were fabricated from 152 mm diameter by 7.9 mm thick circular hollow welded aluminum tubes. Major web struts were fabricated from 76.0 mm diameter by 7.9 mm thick circular hollow welded aluminum tubes. The total height of the steel support frames are 8.55 m at the shoulder and 7.60 m at the median. The support frames are 2.0 m wide and are fabricated from 254 mm diameter STD. steel pipe. Web struts are fabricated from 76 mm diameter STD steel pipe. The structure has a near east-west orientation. The 8.0 m wide by 1.50 m high by 1.0 m deep DMS cabinet is mounted to the truss structure with a slight offset to the median support. All major structural elements are of welded construction.

Field instrumentation setup

The field monitoring period for the Euclid test was accomplished over a three day period. Installation and tear down of instrumentation was done at night using moving lane closures during the first and third test day. The second test day was used to collect multiple response time windows that were associated with varying combinations of passing vehicle traffic plus quite periods to measure ambient response to background wind conditions. .

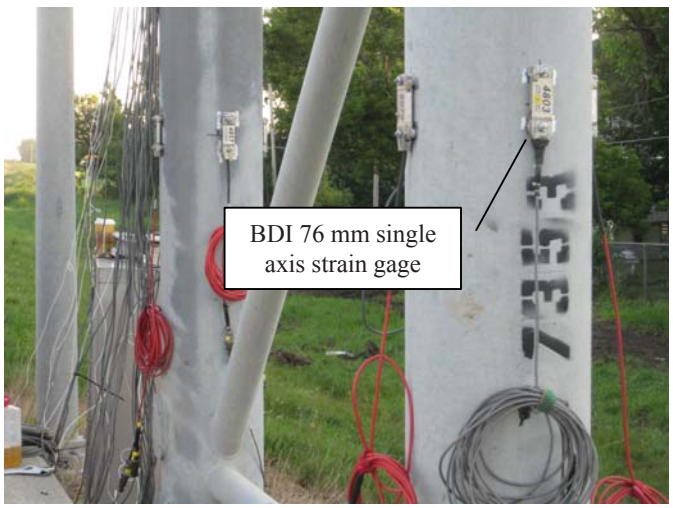

Fig 4 View of strain instrumentation attached near the base of the two steel support columns on the shoulder or east end of the structure. Note the use of 4 gage configuration for bi-axial measurements.

The instrumentation setup for the Euclid test was made up of 47 data channels that included a common time channel, two DMS panel pressure gage channels, wind speed and direction channels, 36 dynamic strain channels that were configured in paired orientations to measure average and bending stains in individual components, and 6 acceleration channels that were configured in pairs to measure horizontal, vertical, and transverse combinations of the global acceleration response of the structure. All channels were synchronously sampled at 250 Hz using triggered time window of approximately eight seconds that included a pre-event buffer period. Dynamic strain measurements were recorded using BDI full-bridge strain transducers. In Figure 4 gage installations on the two east support columns of the Euclid structure are shown. Each BDI gage in the photograph uses an active full-bridge gage configuration to measure average longitudinal dynamic strain over a 76 mm gage length. Paired strain gage installations on the two lower truss chords and on a transverse strut are shown in Figure 5. Also shown in Figure 5 is the bi-axial accelerometer installation on the lower south chord near mid span.

Selected results

The results presented here are preliminary and may be expanded on during presentation of the paper next year. In Figure 5 the typical time response histories are shown for vertical and horizontal accelerometers attached to upper main chord near mid span. The data indicate that the range of vertical accelerations at mid span is lower than the horizontal accelerations. The horizontal accelerations also exhibit a delayed low frequency response. Both traces range between +/-0.010 gs. and exhibit similar frequency content. The horizontal acceleration levels of the upper chord shows a similar response. Horizontal acceleration levels near the base of the DMS cabinet are approximately five times larger than other mid span acceleration levels. The horizontal accelerations of the top of the north east support pole are shown in Figure 7. These accelerations appear to have a range two or three times larger than the mid span accelerations.

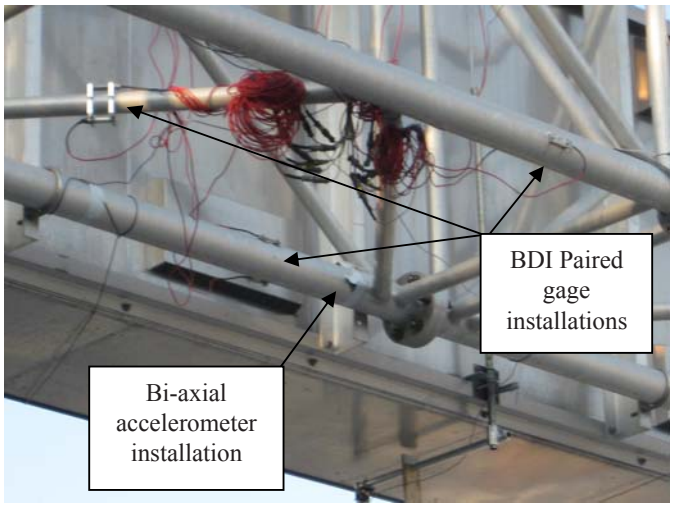

Fig 5 Accelerometer and BDI gage installations near mid span on lower truss chords and connecting struts

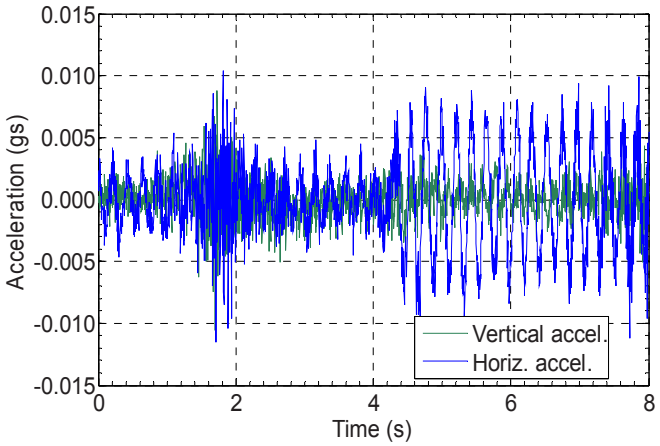

Fig 7 Time history of vertical and horizontal acceleration of top chord at mid span

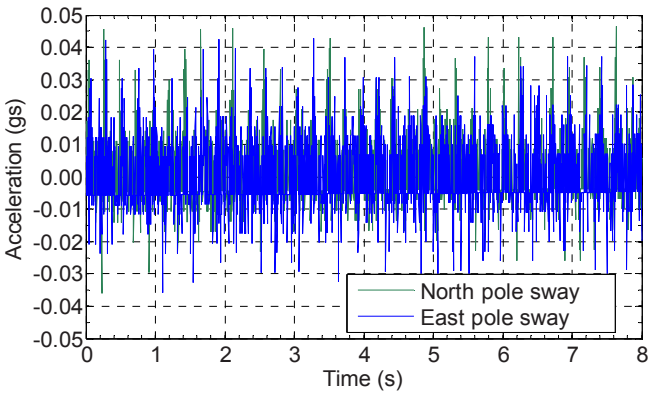

Fig 7 Acceleration of top of north-east support pole

References

1. American Association of State Highway and Transportation Officials. Subcommittee on Bridges and Structures., "Standard specifications for structural supports for highway signs, luminaires, and traffic signals," 5th ed, American Association of State Highway and Transportation Officials, Washington, D.C., p., 2009.
2. Fouad, F.H., "Structural supports for highway signs, luminaires, and traffic signals. NCHRP report,, National Academy Press, Washington, D.C., 2003.
3. Pantelides, C.P., J. Nadauld, and L. Cercone, "Repair of cracked aluminum overhead sign structures with glass fiber reinforced polymer composites," Journal of Composites for Construction, **7**(2), p. 118-126, 2003.
4. Wipf, T.J. and B.M. Phares, "EVALUATION OF INTERSTATE 80 SIGN TRUSS," Iowa State University Iowa Department of Transportation, Ames, IA, p. 14 , 2002.
5. Huckelbridge, A.A. and A.T. Metzger, "Investigation of the dayton, Ohio, IR 75 sign truss failure of september 11, 2006," Journal of Performance of Constructed Facilities, **23**(5), p. 372-378, 2009.
6. Park, J. and J. Stallings, "Fatigue evaluations of variable message sign structures based on AASHTO specifications," KSCE Journal of Civil Engineering, **10**(3), p. 207-217, 2006.
7. Park, J.S., W. McLean, and J.M. Stallings. "Wind-induced fatigue of VMS sign structures," *Proceedings of the 2004 Structures Congress - Building on the Past: Securing the Future* Nashville, TN, p. 407-411, American Society of Civil Engineers, 2004.

8. Peronto, J.L.,"High-Cycle Constant Amplitude Fatigue Life Variability of Welded Round HSS Y-Joints," MS Thesis, Department of Civil and Environmental Engineering, Marquette University, Milwaukee, WI., 2003.
9. Foley, C.M., J.L. Peronto, and R.A. Fournelle, "Fatigue life prediction and variability of new and existing welded CHSY-joints," Engineering Journal-American Institute of Steel Construction Inc, **43**(1), p. 57-79, 2006.
10. Ginal, S.J.,"Fatigue Performance of Full-Span Sign Support Structures Considering Truck-Induced Gust and Natural Wind Pressures,"MS Thesis, Department of Civil and Environmental Engineering, Marquette University, Milwaukee, WI., 2003.
11. Rice, J.A., J.M. Lafave, and C.H. Mehuys, "End connection effects on vortex shedding susceptibility of welded aluminum truss tubular web members," Journal of Performance of Constructed Facilities, **22**(5), p. 297-304, 2008.
12. Constantinescu, G., A. Bhatti, and T. Tokyay. "A numerical study of wind loads on large highway sign structures, Vancouver, BC, Canada, American Society of Civil Engineers, 2008.
13. Constantinescu, G., A. Bhatti, and T. Tokyay,"Improved method for determining wind loads on highway sign and traffic signal structures, Final Report," University of Iowa, Ames, IA, 2007.
14. Kacin, J., P. Rizzo, and M. Tajari, "Fatigue analysis of overhead sign support structures," Engineering Structures, **32**(6), p. 1659-1670, 2010.

Variance Decomposition in the Presence of Epistemic and Aleatory Uncertainty

John McFarland and David Riha

Abstract Variance-based global sensitivity analysis is a powerful approach for understanding the importance of model input variables or groups of variables in driving model output variation. However, input variance is often attributable to both aleatory (irreducible) and epistemic (reducible) uncertainties. This paper presents an approach whereby variance decomposition is used in conjunction with probabilistic analysis. Epistemic uncertainty associated with a model's probabilistic response is decomposed based on probability distribution uncertainty, deterministic model uncertainty, and other epistemic uncertainty sources. The proposed methodology allows for the identification of the epistemic uncertainty sources having the largest contributions to the uncertainty in the model's response. As demonstrated in the numerical example, the proposed methodology may be used to support resource allocation decisions in modeling and simulation activities.

1 Introduction

Probabilistic methods are now commonly used in modeling and simulation activities as a means for taking account of variations and uncertainties associated with model inputs. Many practitioners are aware of the theoretical distinction that is commonly made between two types of uncertainty (aleatory uncertainty and epistemic uncertainty). However, the importance of the distinction, and the implications it has for performing a probabilistic analysis are often unclear.

This paper will present some ideas regarding the roles that aleatory and epistemic uncertainty may play in a probabilistic analysis (in particular, a probabilistic

J.M. McFarland
Research Engineer, Southwest Research Institute, 6220 Culebra Rd., San Antonio, TX 78238

D.S. Riha
Principal Engineer, Southwest Research Institute

T. Proulx (ed.), *Linking Models and Experiments, Volume 2*, Conference Proceedings of the Society for Experimental Mechanics Series 5,
DOI 10.1007/978-1-4419-9305-2_32, © The Society for Experimental Mechanics, Inc. 2011

analysis geared towards computing a probability of failure). The objective will be to demonstrate a methodology that can add significant value to a more traditional probabilistic analysis by highlighting the impact of epistemic uncertainty on confidence and identifying the most effective means of reducing such uncertainty.

Section 2 presents a viewpoint on the role of epistemic uncertainty in probabilistic analysis and some of the factors that help identify whether or not a distinction between reducible and irreducible uncertainty is even important. This section will also review an approach, which has been previously reported in the literature, for computing confidence bounds on reliability predictions.

Section 3 presents a proposed methodology whereby variance decomposition is used to address epistemic uncertainty in a probabilistic analysis in order to identify the most effective avenues for gaining more information and improving confidence in the probabilistic predictions. Some previous work has been done to address sensitivity analysis in the presence of both epistemic and aleatory uncertainties (Guo and Du, 2007; Bae et al, 2003, 2006; Helton et al, 2006), but this work focused on the use of evidence theory with interval analysis. The approach proposed here, on the other hand, is more amenable to characterization of epistemic uncertainties using Bayesian posterior distributions, which plays a significant role when addressing "lack of data" uncertainty associated with input distributions.

Finally, the proposed methodology is illustrated in Section 4 using as a numerical example the deflection of a statically indeterminate beam, and conclusions are given in Section 5.

2 Probabilistic Analysis with Aleatory and Epistemic Uncertainty

In the context of modeling and simulation, a probabilistic analysis addresses variations and/or uncertainties using probability theory, typically by formulating model inputs as random variables. There may be several reasons for performing a probabilistic analysis: to estimate the mean and variance of the model output, to estimate confidence bounds on a model output, to estimate the probability of a response quantity exceeding a given threshold, etc.

Probabilistic analysis allows one to account for the fact that, for whatever reason, the actual values of the model inputs are not known exactly. This is often referred to as *uncertainty*, and two distinct types of uncertainty are commonly recognized. Aleatory uncertainty refers to irreducible uncertainty or "inherent variation." An example is the variation of material properties among individual specimens in a lot. Epistemic uncertainty is reducible uncertainty, which is the result of having imperfect information. An example is the uncertainty about the mean of a random variable when the mean must be estimated based on 10 observed samples: in this case, collecting additional data will reduce this uncertainty.

When conducting a probabilistic analysis, the nature of the uncertainty captured by the probabilistic description of the model inputs will depend on the application.

Oftentimes, no distinction is made between aleatory and epistemic uncertainty, and the inputs are simply defined using probability density functions that capture the overall state of knowledge about possible values for that variable. In other cases, the distinction may be important. For example, a reliability analysis aims to estimate the probability that a device, component, or system will meet some requirement by using probabilistic analysis to compute the probability of a model output exceeding a critical level. This type of analysis lends itself to a Frequentist interpretation of probability, in which case reliability describes the proportion of systems that will meet the requirement over the long run, as many such systems are put into service with random realizations of the loads, geometries, boundary conditions, material properties, etc. As such, it may be important to develop model input distributions that are intended to capture only aleatory uncertainty.

In addition to substantiating a Frequentist interpretation of reliability, maintaining the distinction between the two types of uncertainty enables the analyst to explore the possibility of reducing epistemic uncertainty by obtaining additional information (Der Kiureghian and Ditlevsen, 2009). For example, the view may be taken that the model output statistics, such as the mean, standard deviation, and probability levels, have fixed values. These fixed values depend on the actual probability distributions associated with the model inputs. For model inputs that represent physical quantities, these probability distributions may be estimated by collecting data, but unless it is possible to observe the entire population, perfect information can never be obtained. As a result, there is lack-of-knowledge uncertainty associated with the description of the probabilistic inputs. This is one component of epistemic uncertainty that exists in a probabilistic analysis. Other components may include uncertainty associated with the deterministic model and uncertainty associated with the probabilistic analysis method itself (for example, the finite sample error introduced by Monte Carlo simulation).

To allow some formality, we will introduce the following notation for describing a model output statistic:

$$\gamma = H(\theta), \tag{1}$$

where γ is a model output statistic that is functionally related through $H(\cdot)$ to a set of parameters θ, which may be subject to epistemic uncertainty. For example, γ could be the standard deviation of the deterministic model output, and θ could contain parameters describing the model input distributions, such as the means and standard deviations. The vector θ might also contain error terms associated with the deterministic model and/or probabilistic method. The purpose of $H(\cdot)$ is to emphasize that the model output statistic depends on the parameters θ. The idea is that there is a true value of γ, but that it is subject to epistemic uncertainty because the parameters θ are not known exactly.

A probabilistic analysis that addresses epistemic uncertainty and aleatory uncertainty separately allows the analyst to make statements about the confidence in the model output statistic. If the epistemic uncertainty is also modeled using probability

theory[1], then there is a probability distribution associated with γ, which represents the state of knowledge. One might be interested in computing confidence intervals or conservative bounds on γ, for the purpose of conveying the state of knowledge to the decision maker.

In practice, computing the uncertainty distribution on a model output statistic can be computationally very demanding. In fact, for applications in which the deterministic performance model is expensive to evaluate, computing a single value γ for a particular vector of parameters θ can be challenging (for example, performing a reliability analysis using a finite element model). The use of computationally efficient surrogate models can go a long way towards making such analyses feasible. However, the focus of this paper will not be practical approaches for computing uncertainty distributions on model output statistics due to epistemic uncertainty. This has been previously addressed by the authors (Bichon et al, 2008b; McFarland and Bichon, 2009). Alternatives to constructing the complete uncertainty distribution have also been proposed (for example, Hofer et al, 2002).

Formulation of the epistemic uncertainty distributions is also of interest, and here three cases are considered:

1. Model input distribution parameter uncertainty
2. Deterministic performance model uncertainty
3. Probabilistic method uncertainty

For the first case, distribution parameters defining model input random variables are subject to epistemic uncertainty. A typical example of this is when the probability density function of a model input is estimated based on a finite set of sample data (for example, a collection of material tests to estimate the distribution of yield strength). Since only a limited amount of data can be collected, the true distribution parameters are subject to uncertainty.

A natural framework for quantifying distribution parameter uncertainty is Bayesian statistics, which is particularly powerful because the Bayesian approach models uncertainty using probability distributions. Thus, a Bayesian analysis allows one to compute a so-called *posterior distribution* of the uncertain distribution parameters, conditional on the observed sample data. Bayesian analysis also allows for the incorporation of prior knowledge, through the prior distribution, but in practice it is common to use non-informative prior distributions (also known as vague priors or reference priors) to capture the notion that no information is available before observing the data. Further information on Bayesian inference is available in Lee (2004), and example applications of distribution parameter estimation are given in Bichon et al (2008b); McFarland and Bichon (2009); Marhadi et al (2008).

The second case of epistemic uncertainty listed above refers to uncertainty associated with the deterministic model itself. This may be in the form of model parameter uncertainty, model form uncertainty, convergence error (which may also

[1] Alternatives to probability theory have been documented in the literature and include the Dempster-Shafer theory of evidence (Shafer, 1976), possibility theory (Dubois and Prade, 2001; Zadeh, 1978), and many others (Ferson et al, 2004)

be characterized as an epistemic uncertainty), or others. Model verification and/or validation is often used to address and/or quantify these errors.

The third type of epistemic uncertainty we have listed is related to the probabilistic method itself. One of the simplest cases is when the model output statistic of interest is a reliability and Monte Carlo simulation is used. In this case, random sampling error affects the result, and the behavior of this error is well understood (see Haldar and Mahadevan, 2000). If no other epistemic uncertainties are considered, it is a simple matter to develop confidence intervals on a reliability calculation based on sampling error.

3 Variance Decomposition of Epistemic Variables

Variance decomposition is an approach for global sensitivity analysis, where the objective is to identify important model inputs by assessing how uncertainty associated with each input contributes to uncertainty associated with the model output. The approach is typically used to address questions such as, if the uncertainty associated with one of multiple model inputs could eliminated, what would be the most effective way to reduce the model output uncertainty? Saltelli et al (2000, 2004) give comprehensive overviews of both theory and practice of variance decomposition and other sensitivity analysis methods.

Based on a functional analysis of variance, and under the assumption that the model inputs are independent (Sobol', 1993), the model output variance can be decomposed as

$$V = \sum_{i=1}^{k} V_i + \sum_{i_1=1}^{k} \sum_{i_2=i_1+1}^{k} V_{i_1 i_2} + \cdots + V_{1,\ldots,k}, \tag{2}$$

where V is the total model output variance, k is the number of model inputs, and the subscripted V terms are partial variances corresponding to the various model inputs and combinations thereof. Each global sensitivity index is then defined as the contribution of a partial variance to the total variance:

$$S_{i_1,\ldots,i_s} = V_{i_1,\ldots,i_s}/V. \tag{3}$$

Note that sensitivity indices can be computed for individual variables or groups of variables being treated as a single factor.

A sensitivity index S_i corresponding to a single factor is called the *first-order effect* or *main sensitivity index* for that factor. Sensitivity indices corresponding to two or more factors capture interaction effects and are known as higher-order effects. The total influence of each individual factor is quantified by the *total effects index*, denoted S_{Ti}, which is the sum of all indices involving the factor of interest. In practice, it is common to compute only the first-order and total effects. A significant difference between the total effect and first-order effect for a factor would indicate

that interaction effects play a role for that factor, in which case such effects may be explored further.

A variety of methods have been proposed for the calculation of the sensitivity indices, with emphasis being placed on efficient methods requiring fewer deterministic model evaluations. Saltelli et al (2004) describe a structured Monte Carlo approach, which involves holding constant certain factors while varying others. Another notable approach is the Fourier Amplitude Sensitivity Test (FAST; Cukier et al, 1973, 1978; Koda et al, 1979), which involves a Fourier decomposition and discretization of the inputs over probability space.

The main hypothesis for this work is that variance decomposition can be used to address epistemic uncertainty associated with a *model output statistic*. Note that traditionally, variance decomposition would be applied to the output of the deterministic performance function. However, such an approach may not prove as useful when the inputs to the deterministic performance function are subject to irreducible uncertainty. While the inputs to the deterministic performance function may be subject to aleatory uncertainty, there may still be other sources of epistemic uncertainty that impact the probabilistic solution, as discussed in Section 2. Thus, this work demonstrates an approach for decomposing the variance of the model output statistic with respect to the epistemic variables, such as probability distribution parameters.

The motivation for such an analysis is that it helps identify which factors are contributing the most to uncertainty in the probabilistic solution. For example, once epistemic uncertainty is taken account of, a reliability analysis may demonstrate confidence bounds on the reliability that are too wide to draw a meaningful conclusion. A variance decomposition analysis can help identify where additional resources should be allocated to reduce this uncertainty: this may mean collecting more data to characterize model input distributions or reducing the uncertainty associated with the deterministic performance model.

Variance decomposition of a model output statistic introduces several challenges. Most notably, treatment of uncertain distribution parameters can be difficult. We will assume that the (epistemic) probability distributions for these parameters are obtained as the posterior distributions from a Bayesian analysis. Corresponding to each deterministic model input x_i, we have probability distribution parameters θ_i. Depending on the form of the probability distribution model for x_i, θ_i will be a vector of parameters. For example, if x_i is normally distributed, then θ_i contains the mean and variance parameters. It is important to note that it is not necessary to treat the parameters within θ_i separately: as more data are collected about the variable x_i, the uncertainty about all parameters in θ_i is reduced together. Moreover, the parameters within θ_i are not independent, which would be problematic for the variance decomposition if they were to be treated separately.

As a result, we want to decompose the variance of the model output statistic with respect to each factor group θ_i. This immediately rules out certain variance decomposition methods, such as FAST, which are not amenable to treatment of variables by group. Furthermore, in practice the Bayesian posterior distribution of θ_i will not be constructed analytically but will instead be approximated via random sampling using Markov Chain Monte Carlo (MCMC) methods. Clearly, the avail-

able approaches for variance decomposition with respect to such parameters are limited. Fortunately, the structured Monte Carlo approach outlined by Saltelli et al (2004) can still be used, provided each θ_i is treated as a single factor. The drawback is that this will typically require on the order of thousands of evaluations of the model output statistic, for different combinations of the variables θ. In most cases of practical interest, approximation of the deterministic performance function by an efficient surrogate model will be necessary (some relevant examples are given by Bichon et al, 2008a; Kaymaz, 2005; McFarland et al, 2008; Kennedy et al, 2006; McFarland et al, 2009; McFarland, 2008).

Other types of epistemic variables can also be treated using the structured Monte Carlo approach. For example, deterministic model uncertainty may be characterized using an error term ε having some epistemic uncertainty distribution. The structured Monte Carlo approach would then enumerate various combinations of values of ε (along with the other epistemic parameters). Each evaluation of the model output statistic, γ, would then proceed using a particular fixed realization of deterministic model error, ε.

4 Numerical Example

In order to illustrate these concepts, the reliability analysis of a statically indeterminate beam in considered. The problem is illustrated in Figure 1, and consists of a simple beam with two supports and a distributed load over part of its length. The random variables are the length of the beam, L, the magnitude of the distributed load, w, the range over which the load is applied, b, and the modulus of elasticity of the beam, E.

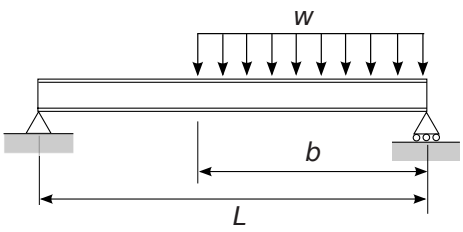

Fig. 1 Schematic of statically indeterminate beam example

The response quantity of interest will be the maximum deflection of the beam. Solution of the maximum displacement can be obtained using the moment-area method (Beer and Johnston, 1992). This requires first finding the location of the maximum displacement along the length of the beam, which involves the solution of a third-order polynomial. For this work, the solution to this polynomial equation is found using the bisection method. Then, magnitude of the maximum displacement is available in closed form, given the location. Further details are given in the Appendix. Calculation of this performance function is fast enough for use directly in

this uncertainty analysis, but as previously mentioned, more complex applications would most likely necessitate the use of surrogate models.

For the purpose of illustration, it is assumed that the model for calculating the maximum displacement is not perfect. We assume a hypothetical validation study has quantified the error associated with prediction of maximum displacement to be ± 0.3 mm. This is an epistemic uncertainty (i.e. the uncertainty could be reduced by making improvements to the model or collecting more experimental data for validation), and it will be quantified here using an additive error term having a normal distribution with zero mean and a standard deviation of 0.10 mm (that is, the ± 0.3 mm error bound is treated as a $\pm 3\sigma$ range).

The objective is to analyze the reliability of the beam, which is defined as the probability that the maximum deflection is less than 0.012 m. The four variables, L, w, b, and E, are all subject to aleatory uncertainty, which could be representative of in-service environmental variations for the load and manufacturing variations for the beam. For the purpose of the analysis, we assume that the probability distributions for the four variables must be inferred based on observed sample data. For this example problem, the sample data are simulated from prescribed distributions, which are presumed unknown during the analysis. The moment of inertia of the beam is assumed to be known and is given by $I = 28.7 \times 10^{-6}$ m^4.

The details of the probability distributions for the variables and the amount of available data are given in Table 1. Note that the probability distribution model forms (e.g. normal or beta) are assumed to be known during the analysis. In actuality, this is an assumption that introduces some additional uncertainty, but for simplicity it is not considered here (see McFarland and Bichon, 2009, for a Bayesian uncertainty analysis that explicitly addresses probability distribution model form uncertainty). Note that the random variables L and b are modeled using beta distributions. This is done because the beta distribution is bounded, and so it prevents extreme values of L and b from causing the solution for maximum displacement to break down. For the purposes of the uncertainty analysis, it is assumed that the bounds for both of these distributions are known, but that the shape and scale parameters (or equivalently, the mean and standard deviation) are uncertain and must be estimated based on the sample data.

Table 1 Description of random variables for beam example

Variable	Units	Distribution[a]	Mean	COV[b]	N[c]
L	m	Beta($l = 3$, $u = 5$)	3.6	0.056	15
w	N/m	Lognormal	25×10^3	0.1	25
b	m	Beta($l = 1.5$, $u = 3$)	2.2	0.091	25
E	Pa	Weibull	200×10^9	0.1	200

[a] For the beta distribution, l and u are the lower and upper bounds
[b] Coefficient of Variation: ratio of standard deviation to mean
[c] Number of observations

The objective is to perform a probabilistic analysis and compute a model output statistic (in this case, a probability of failure), but two sources of epistemic uncer-

tainty have been identified: deterministic model error and probability distribution parameter uncertainty. Thus, an uncertainty analysis will be carried out, as outlined in Section 2, to characterize the uncertainty in the predicted failure probability.

As mentioned above, uncertainty associated with model error has been characterized based on validation studies as $\varepsilon \sim N(\mu = 0,\ \sigma = 0.1)$ mm. A Bayesian analysis using non-informative reference prior distributions is carried out to develop the uncertainty distributions for the probability distribution parameters of the model inputs. That is, the posterior distribution for the uncertain distribution parameters associated with each variable in Table 1 is computed, based on the available sample data. An automatically adapting Markov Chain Monte Carlo approach, based on the work of Haario et al (2001), is used to collect random samples of the distribution parameters from their posterior distributions.

A variance decomposition of the epistemic variables, as discussed in Section 3, is used in order to identify what new information would allow for the greatest reduction in uncertainty. The structured Monte Carlo approach proposed by Saltelli et al (2004) is employed. The output statistic of interest is the failure probability, but here we use $\gamma = \beta$ in Eq. (1), where β is the reliability index, which for FORM is related to the failure probability by

$$\beta = -\Phi^{-1}(p_f), \tag{4}$$

where $\Phi(\cdot)$ is the standard normal inverse cumulative distribution function. The motivation for decomposition of the variance of the reliability index as opposed to the failure probability is that the distribution of the reliability index tends to be more symmetric (see, for example Der Kiureghian and Ditlevsen, 2009, Figure 1). This may improve the conditioning of the variance decomposition analysis, although admittedly further study and comparison is needed to better understand the difference.

Choice of reliability method is an important consideration, both because it needs to be very efficient to be practical within the variance decomposition framework, and because stochastic methods may adversely impact the uncertainty quantification. For this work, the First Order Reliability Method (FORM; see, for example Haldar and Mahadevan, 2000) is utilized for the failure probability calculations.[2] The method is advantageous here both because of its efficiency and because unlike a Monte Carlo approach, it will not introduce additional variance when used inside of variance decomposition. The FORM solution was verified for this problem using Monte Carlo simulation with 100,000 samples.[3]

The variance decomposition is performed using a base sample size of 50,000 ("N" in Saltelli et al, 2004), which necessitates a total of 350,000 evaluations of $H(\theta)$. Total computation time for the entire uncertainty analysis is on the order of six hours using a single-processor Linux machine.

---

[2] Our FORM implementation is based on the nonlinear interior point solver from the Opt++ software package (Meza, 1994)

[3] As mentioned in Section 2, the probabilistic method also introduces epistemic uncertainty to the result. With some ingenuity, it may also be possible to account for this uncertainty in the variance decomposition (similarly to the treatment of deterministic model error) in order to identify whether improvement of the probabilistic solution would be warranted as a means of reducing uncertainty.

The results are given in Table 2, which lists the main and total effects for each epistemic factor. Recall that the main effects indicate, on average, how much the variance could be reduced with perfect information for that factor, and that differences between main and total effects represent the degree to which a factor is involved with interaction effects. A histogram of the reliability index is also given in Figure 2, which can be used to gauge the overall impact of epistemic uncertainty on the reliability assessment.

Table 2 Epistemic factor sensitivities for beam example

	L	w	b	E	ε
Main effect	0.40	0.18	0.15	0.03	0.01
Total effect	0.63	0.40	0.36	0.25	0.23

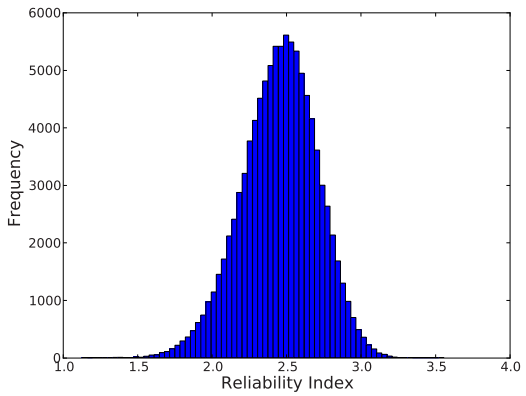

Fig. 2 Histogram of the reliability index for the beam example

The results indicate that on average, 40% of the variance in the reliability index could be reduced by gaining perfect information about the distribution of L. Thus, the best way to reduce uncertainty would be to collect additional samples to characterize the distribution of L. The analysis indicates that uncertainty in the distributions for w and b also contribute significantly to uncertainty in the reliability index. The uncertainty in E, however, is negligible, even though from a deterministic standpoint, the parameter E plays a very important role in the behavior of the beam. The reason that E shows a small main effect is because its distribution is already well-characterized based on 200 samples, so little epistemic uncertainty remains. The results also indicate that the deterministic model error, ε, has a negligible impact on the overall uncertainty: in this case, improving the confidence in the deterministic model would not help reduce the uncertainty in the reliability index.

The total effects, by comparison with the main effects, may be used to gauge the role that interactions play for each factor. In this case, each factor shows a significant difference between main and total effects, which indicates that interactions

among the factors have a significant impact on the uncertainty in the reliability index. If interaction effects were a concern, the variance decomposition analysis could be extended to quantify partial variances between specific factor combinations, as outlined by Saltelli et al (2004).

5 Conclusions

The use of probabilistic approaches is becoming more and more common in engineering analyses. This allows the probabilistic response of a deterministic model to be computed, given probabilistic descriptions of the model inputs. Reliability studies are often performed in this fashion, in which the probability of a response quantity exceeding a specified threshold is of interest.

This work presents several ideas regarding the distinction between aleatory (irreducible) and epistemic (reducible) uncertainty in the context of probabilistic analysis. Previous work has demonstrated approaches for quantifying uncertainty in model output statistics due to epistemic uncertainty in the characterization of the model input distributions. This work proposes a variance decomposition approach for then identifying which uncertainty sources have the largest contribution to the overall epistemic uncertainty. The primary motivation is that the resulting information can be of significant value when making decisions related to resource allocation, such as whether it would be more effective to collect additional data on material properties or load conditions.

The approach is demonstrated via the reliability analysis for the deflection of a statically indeterminate beam. The example problem illustrates the distinction between aleatory and epistemic uncertainty, as the aleatory distributions for the model inputs are estimated based on limited sample data, which introduces epistemic uncertainty about the distribution parameters such as the means and standard deviations. It is shown that the variance decomposition approach can successfully identify a data-rich input as having a negligible contribution to variance, even though the deterministic model is highly sensitive to that input.

Several possible avenues for further work on this topic exist. One area for research is the extent to which stochastic probabilistic methods such as Monte Carlo simulation may be used in conjunction with epistemic variance decomposition: such an approach was avoided here for fear that the stochastic method would add additional variance to the model output statistic, potentially masking the effects of the other epistemic uncertainty sources being considered. Another area for further study is the impact of the parametrization of the model output statistic whose variance is to be analyzed. For the reliability analysis example given here, we chose to analyze the reliability index as opposed to the failure probability: whereas both capture the same information, it was felt that the highly skewed distribution of failure probability might adversely impact the variance decomposition. However, further study would be needed to better understand the role of model output parametrization in variance decomposition.

Acknowledgements The research reported in this paper was funded as part of an Internal Research and Development project at the Southwest Research Institute.

Appendix

Here we give further details regarding the solution for maximum displacement of the beam used as the numerical example in Section 4 (see Figure 1). First, the reactions at the supports can be obtained as follows:

$$\begin{aligned} R_A &= \frac{wb^2}{2L}, \\ R_B &= wb - R_A. \end{aligned} \tag{5}$$

Then the following equation can be constructed using the moment-area method:

$$-\left(\frac{R_A L^2}{6EI} - \frac{wb^4}{24EIL}\right) + \left[\frac{R_A x_m^2}{2EI} - \frac{w}{6EI}(x_m - L + b)^3\right] = 0, \tag{6}$$

where x_m is the location of the maximum displacement, measured from the left support. For well-conditioned values of L and b, the bisection method can be used to solve for x_m. Finally, the magnitude of the maximum displacement, y_m, is calculated as

$$y_m = \frac{R_A x_m^3}{3EI} - \frac{w(L-b)}{6EI}(x_m - L + b)^3 - \frac{w}{8EI}(x_m - L + b)^4. \tag{7}$$

References

Bae HR, Grandhi RV, Canfield RA (2003) Uncertainty quantification of structural response using evidence theory. AIAA Journal 41(10):2062–2068

Bae HR, Grandhi RV, Canfield RA (2006) Sensitivity analysis of structural response uncertainty propagation using evidence theory. Structural and Multidisciplinary Optimization 31(4):270–291

Beer FP, Johnston ER (1992) Mechanics of Materials, 2nd edn. McGraw-Hill, Inc.

Bichon BJ, Eldred MS, Swiler LP, Mahadevan S, McFarland JM (2008a) Efficient global reliability analysis for nonlinear implicit performance functions. AIAA Journal 46(10):2459–2468

Bichon BJ, McFarland JM, Mahadevan S (2008b) Using Bayesian inference and Efficient Global Reliability Analysis to explore distribution uncertainty. In: Proceedings of the 49th AIAA/ASME/ASCE/AHS/ASC Structures, Structural Dynamics, and Materials Conference, Schaumburg, IL

Cukier RI, Fortuin CM, Schuler KE, Petschek AG, Schaibly JH (1973) Study of the sensitivity of coupled reaction systems to uncertainties in rate coefficients.

Journal of Chemical Physics 59(8):3873–3878
Cukier RI, Levine HB, Schuler KE (1978) Nonlinear sensitivity analysis of multiparameter model systems. Journal of Computational Physics 26:1–42
Der Kiureghian A, Ditlevsen O (2009) Aleatory or epistemic? Does it matter? Structural Safety 31(2):105–112
Dubois D, Prade H (2001) Possibility theory, probability theory and multiple-valued logics: A clarification. Annals of Mathematics and Artificial Intelligence 32:55–66
Ferson S, Joslyn CA, Helton JC, Oberkampf WL, Sentz K (2004) Summary from the epistemic uncertainty workshop: consensus amid diversity. Reliability Engineering and System Safety 85(1–3):355–369
Guo J, Du X (2007) Sensitivity analysis with mixture of epistemic and aleatory uncertainties. AIAA Journal 45(9):2337–2349
Haario H, Saksman E, Tamminen J (2001) An adaptive Metropolis algorithm. Bernoulli 7(2):223–242
Haldar A, Mahadevan S (2000) Probability, Reliability, and Statistical Methods in Engineering Design. John Wiley and Sons, Inc., New York
Helton JC, Johnson JD, Oberkampf WL, Sallaberry CJ (2006) Sensitivity analysis in conjunction with evidence theory representations of epistemic uncertainty. Reliability Engineering and System Safety 91(10–11):1414–1434
Hofer E, Kloos M, Krzykacz-Hausmann B, Peschke J, Woltereck M (2002) An approximate epistemic uncertainty analysis approach in the presence of epistemic and aleatory uncertainties. Reliability Engineering and System Safety 77(3):229–238
Kaymaz I (2005) Application of kriging method to structural reliability problems. Structural Safety 27(2):133–151
Kennedy MC, Anderson CW, Conti S, O'Hagan A (2006) Case studies in Gaussian process modelling of computer codes. Reliability Engineering and System Safety 91:1301–1309
Koda M, McRae GJ, Seinfeld JH (1979) Automatic sensitivity analysis of kinetic mechanisms. International Journal of Chemical Kinetics 11:427–444
Lee P (2004) Bayesian Statistics, an Introduction. Oxford University Press, Inc., New York
Marhadi K, Venkataraman S, Pai S (2008) Quantifying uncertainty in statistical distribution of small sample data using Bayesian inference of unbounded Johnson distribution. In: Proceedings of the 49th AIAA/ASME/ASCE/AHS/ASC Structures, Structural Dynamics, and Materials Conference, Schaumburg, IL
McFarland J (2008) Uncertainty analysis for computer simulations through validation and calibration. PhD thesis, Vanderbilt University
McFarland JM, Bichon BJ (2009) Bayesian model averaging for reliability analysis with probability distribution model form uncertainty. In: Proceedings of the 50th AIAA/ASME/ASCE/AHS/ASC Structures, Structural Dynamics, and Materials Conference, Palm Springs, CA

McFarland JM, Mahadevan S, Romero VJ, Swiler LP (2008) Calibration and uncertainty analysis for computer simulations with multivariate output. AIAA Journal 46(5):1253–1265

McFarland JM, Urbina A, Mahadevan S (2009) A top-down approach to the calibration of computer simulations. In: Proceedings of the International Modal Analysis Conference XXVII, Orlando, FL

Meza JC (1994) OPT++: An object-oriented class library for nonlinear optimization. Tech. Rep. SAND94-8225, Sandia National Laboratories

Saltelli A, Chan K, Scott EM (eds) (2000) Sensitivity Analysis. John Wiley & Sons, Ltd

Saltelli A, Tarantola S, Campolongo F, Ratto M (2004) Sensitivity analysis in practice: a guide to assessing scientific models. Wiley

Shafer G (1976) A Mathematical Theory of Evidence. Princeton University Press

Sobol' I (1993) Sensitivity analysis for non-linear mathematical models. Mathematical Modelling & Computational Experiment 1:407–414

Zadeh L (1978) Fuzzy sets as the basis for a theory of possibility. Fuzzy Sets and Systems 1:3–28

A Forecasting Metric for Predictive Modeling

Sezer Atamturktur[1], François Hemez[2], and Cetin Unal[5]

[1]*Department of Civil Engineering, Clemson University, South Carolina, U.S.A., sez@clemson.edu*

[2]*XCP 1-Division, Los Alamos National Laboratory, New Mexico, U.S.A., hemez@lanl.gov*

[3]*CCS DO-Division, Los Alamos National Laboratory, New Mexico, U.S.A., cu@lanl.gov*

1 INTRODUCTION

As the complexity of engineering systems increases, their performance becomes more difficult to predict through modeling and simulation. This paper investigates simulation models used to forecast predictions of the performance of engineering systems in support of high-consequence decision-making. Specifically this paper directs its attention to the validation of the simulation models for certification purposes. Instead of relying on virgin models, i.e. models that are not calibrated or bias-corrected, we envision certification to be applied through a combined experimental and numerical campaign that relies on simulation models calibrated and bias corrected against experimental measurements. We are particularly interested in the quantification and control of errors associated with the forecasting predictions of these calibrated and bias corrected simulation models.

In certification, the purpose of simulation models is to reduce the number of required experiments, and is best illustrated by considering two extreme cases.

(1) Purely empirical certification: the absence of a sound simulation model where certification is only obtained based on experimental measurements.

(2) Purely model-based certification: the availability of a 'perfect' simulation model where certification needs practically no experimental measurements.

In a purely empirical approach, forecasting is commonly achieved by constructing a function that best fits the data produced from an experimental campaign. Then, the best-fitted function is exercised to make forecasting predictions at untested settings. Both the experimental uncertainty and the uncertainty in the curve-fitting process can be considered by making forecasting predictions that are "best estimates" with quantified uncertainties. In purely empirical certifications, the number of experiments necessary to train the best-fitted function can rapidly become prohibitive. Purely empirical certifications are further challenged with the fact that experiments are typically time-consuming and expensive and thus, even in

T. Proulx (ed.), *Linking Models and Experiments, Volume 2*, Conference Proceedings of the Society for Experimental Mechanics Series 5,
DOI 10.1007/978-1-4419-9305-2_33, © The Society for Experimental Mechanics, Inc. 2011

the best cases are only available in limited numbers. Moreover, obtaining the measurements at the desired experimental settings may be prohibitive due to policy regulations or infeasible due to technical limitations. The inevitable experimental scarcity is the primary reason behind the increased reliance on modeling and simulation in various scientific and engineering fields.

The availability of simulation models incorporating sound physics or engineering principles can significantly reduce the number of required experiments for certification. In the most extreme example, if the model can perfectly reproduce reality, the dependency on experimentation can be entirely eliminated. However, simulation models are naturally impaired by imprecise model parameters (known unknowns) and inaccuracies in the interpretation of the underlying physics or engineering principles (unknown unknowns). Therefore, experimental evidence is routinely required to improve the simulation model fidelity. Hence, in model-based certification, experiments are used to calibrate and bias-correct the physics-based simulation models instead of training an arbitrary best-fitted function.

Model calibration is achieved through the comparison of a multitude of model predictions with a family of experimental measurements. This comparison has two main objectives: (1) to reduce the uncertainty in the imprecise input parameters (known unknowns) and (2) to quantitatively estimate the errors due to inadequate or missing physics (unknown unknowns). The manner in which we distinguish between these two interrelated objectives, *parameter calibration versus discrepancy bias*, is explained in Section 2, where we discuss our approach to quantify discrepancy.

The number of experiments needed to successfully achieve these objectives of model calibration is heavily dependent upon the fidelity of the modeled (physics or engineering) principles to reality. If the simulation model lacks **a vital principle, parameter, or interaction between principles or parameters** (i.e., large unknown unknowns), the fundamental ability of this model to capture the phenomena of interest is compromised. If the model is overly crude resulting in too large unknown unknowns, attempts to improve the fidelity through calibration or bias-correction will inevitably be unsatisfactory due to compensating effects. Hence, a crucial first step in certification involves assessing the suitability *of a simulation model* for use in forecasting. In Section 3, we outline three important assertions that we contend play a foundational role in determining the suitability of simulation models for forecasting.

Because the purpose of simulation models is to predict in lieu of experiments, such models calibrated against a reduced number of experimental measurements are routinely applied to ***forecast*** at untested

settings. Forecasting unavoidably brings up *unknown forecasting errors*. However, these unknown forecasting errors can be reduced by improving the fidelity of the simulation model through parameter calibration (known unknowns) and bias-correction (unknown unknowns). Naturally, as the number of experimental measurements available for model calibration is consistently increased, the forecasting errors would be consistently reduced. Once a sufficient number of experiments are obtained, and the forecasting errors are reduced to predetermined acceptable levels, allocating resources to further experimentation would have diminishing returns; and therefore allocation of resources to new experiments would not be justified. In Section 4, we hold out some of the available experiments to estimate the forecasting errors of a given simulation model for a given experimental campaign. Estimating forecasting errors is of particular importance in science and engineering, especially when such forecasts are used to determine the expected performance level of an engineering system under worst-case scenarios. Such applications are common in the context of certification.

In this manuscript, we illustrate estimating forecasting errors for a given set of experimental measurements using a selected set of hold-out experiments. In Sections 5, we illustrate the merit of this procedure using a material model of plasticity representing a data-rich and situation. Compelling as this approach is, a set of premises must be satisfied for the proposed approach to be applicable. In Section 7, we discuss the underlying premises and limitations of our conceptual framework.

2 ESTIMATION OF MODEL DISCREPANCY

The central philosophy of model calibration is to improve the accuracy of model predictions by exploiting a collection of available experimental measurements. Thus, model calibration invariably requires the comparison of large numbers of simulation runs against experimental measurements. Over the past two decades, model calibration has evolved into two strategies, which differ in the methods through which they improve model accuracy. The first type is the parameter calibration approach that captures the inaccuracy of the model parameters. The second type is the bias correction approach that captures the inadequacy of the physics model. These two fundamental concepts are combined together in the landmark study of Kennedy and O'Hagan [1]. Kennedy and O'Hagan's [1] approach simultaneously calibrates model parameters and corrects for discrepancy bias.

The parameter calibration approach has two distinct paradigms used for defining the improved parameter values. In the first approach, calibration is considered as an optimization problem. The

objective function, which constitutes some form of the disagreement between the experimental measurements and model predictions, is minimized over a subset of model parameters appropriately selected based on their uncertainty and sensitivity. The second approach to calibration is Bayesian inference, which explicitly acknowledges the uncertainty in the model parameters. In Bayesian inference, calibration is achieved by reducing the uncertainty in the models parameters and in turn reducing the uncertainty in the model output, and it is therefore considered to be more refined than optimization-based procedures.

The present manuscript implements a Bayesian implementation of Kennedy and O'Hagan's method [1]. This implementation, derived from Higdon et al. [2], is built into a computer code called Gaussian Process Model – Simulation Analysis (GPM-SA) at the Los Alamos National Laboratory. It is deeply rooted in the following relation:

$$\hat{y}_{obs}(x) = y_{sim}(x, \theta) + \delta(x) + \varepsilon(x) \quad (1)$$

In Equation (1), the parameter x denotes the control variables. One must be careful not to mix control parameters, x, with calibration parameters, denoted by θ in Equation (1). Control parameters, which can controlled during experiments, define the domain of applicability. Calibration parameters on the other hand are either introduced by specific choices of assumptions or models, or they represent parameters that cannot be measured or controlled experimentally.

In Equation (1), $y_{sim}(x, \theta)$ corresponds to the model predictions, $\delta(x)$ corresponds to a discrepancy bias that represents the systematic bias, and $\varepsilon(x)$ represents the random experimental error. When these three terms are added together, they yield our best estimate for the "truth", $\hat{y}_{obs}(x)$ over the various settings of x in the domain of applicability. To reiterate Equation (1), if the discrepancy bias associated with a simulation model is known, the truth, $y_{obs}(x)$ can be computed by correcting model predictions, $y_{sim}(x, \theta)$ with the discrepancy bias $\delta(x)$.

One of the primary roles of experimental measurements is to supply information about the discrepancy bias at discrete points within the domain of applicability. We now introduce another term, x^t, which denotes the control parameter settings where the experimental measurements are available.

$$\hat{y}_{obs}(x^t) \sim y_{obs}(x^t) \quad (2)$$

With the formulation of Equation (1), one seeks to obtain the probability distribution of calibration parameters, θ by comparing model predictions $y_{sim}(x^t, \theta)$, to physical observations $y_{obs}(x^t)$ while simultaneously making an independent estimate for the discrepancy bias, $\delta(x^t)$. As seen, the discrepancy bias is fundamentally different than the commonly adapted concept of "goodness-of-fit." Instead, the discrepancy estimated over the domain of applicability provides a notion of predictive maturity of the model or rather, its lack of maturity. The accurate estimation of discrepancy term depends heavily on the quantity of the available experimental measurements for discrepancy bias. Naturally, the discrepancy function would be more reliable if it is trained with a larger amount of discrete data points.

Kennedy and O'Hagan's [1] estimation of the discrepancy term, is closely associated with the calibration of the model parameters. In a later implementation of this approach, Higdon et al. [2] used fast running Gaussian Process Models (GPM) as surrogates to estimate the discrepancy bias. It must be noted that the mathematical definition of the discrepancy term inherently considers the presence of experimental and numerical uncertainty.

3 USEFULNESS OF A SIMULATION MODEL FOR FORECASTING

In a treatment combining parameter calibration and bias correction procedures, experimental measurements improve the numerical model in two distinct ways: (1) by reducing the uncertainty in the model parameters and (2) by quantifying the discrepancy more accurately. As a result, a model calibrated with an increasing amount of experimental information should have increasing fidelity. To formalize this seemingly obvious statement, a series of conceptual assertions must first be made. This section introduces a sequence of three conceptual assertions that ultimately lead to the notion of forecasting metrics.

3.1 Requirements for Forecasting Predictions

We postulate that, a numerical model to be useful for forecasting purposes must satisfy the following two requirements:

(a) *Model predictions must be consistent with the experimental measurements that are relevant to the specific application of the model.*

The estimated functional form for the discrepancy bias introduced in the previous section is a quantitative and rigorous representation of the model's consistency with measurements. This very

effective formulation represents the variations over the entirety of the domain of applicability, not just at a limited number of tested settings.

(b) *Model predictions must be robust to the new evidence. New experimental measurements must further validate the model, not invalidate the model.*

Inspired by the novelty index introduced by Sornette et al. [3], we introduce a unique point of view to robustness. We define robustness in terms of lack of sensitivity of model discrepancy to *new* experimental measurements. It is plausible to assume the predictions of a model would be dominated by different assumptions at different regimes in the domain of applicability. Each new experiment conducted to explore these regimes may validate the underlying assumptions of the model if discrepancy stays stable; or invalidate the underlying assumptions of the model if the discrepancy is increased.

3.2 Possible Trends of Discrepancy Bias

The discrepancy bias, introduced in the previous section, constitutes a key component in defining the predictive maturity of a numerical model. Depending on this predictive maturity, the discrepancy bias, when plotted against the number of available experiments, can take one of three forms:

Case A $\delta(x) \approx$ *zero everywhere in the domain;*

The discrepancy bias is considered insignificant if it is equal to or lower than the experimental uncertainty over the range of controlled parameters $\{x_{min}, x_{max}\}$. The *calibrated* model predictions fit the experimental measurements well throughout the domain of applicability, eliminating the need for bias-correction. Such model can be used for forecasting purposes.

Case B $\delta(x) \approx$ *constant acceptably low value everywhere in the domain;*

There is a systematic, close to constant, acceptably low bias between model predictions and the experiments that cannot be further reduced by calibrating the parameters. The model predictions across the domain of applicability must be corrected by $\delta(x)$ to adjust for this systematic bias before forecasting.

Case C $\delta(x) \approx$ *unacceptably high or non-constant;*

This non-constant or unacceptably high discrepancy bias indicates that the model fails to capture some fundamental engineering or physics phenomena. Different modeling assumptions are validated (or rather invalidated) as the model is compared against experiments conducted at different settings within the domain of applicability. Therefore, the fluctuations in the discrepancy bias are attributable to the invalidation of these underlying modeling assumptions. Thus, predictive forecasting to untested regimes should not be attempted.

3.3 Concept of Stabilization

In this Section, the assertions of Section 3.1 and Section 3.2 are combined in the concept of stabilization. The concept of stabilization states that each new experiment provides fractional new information for model calibration and thus should provide a fractional reduction in discrepancy bias. Therefore, the discrepancy term gradually converges to the 'true discrepancy', henceforth referred to as *model form error*. The point at which a model stabilizes establishes the usefulness of the model. If the model does not stabilize or stabilizes with too high of a model form error, the model will not be useful as a predictive tool.

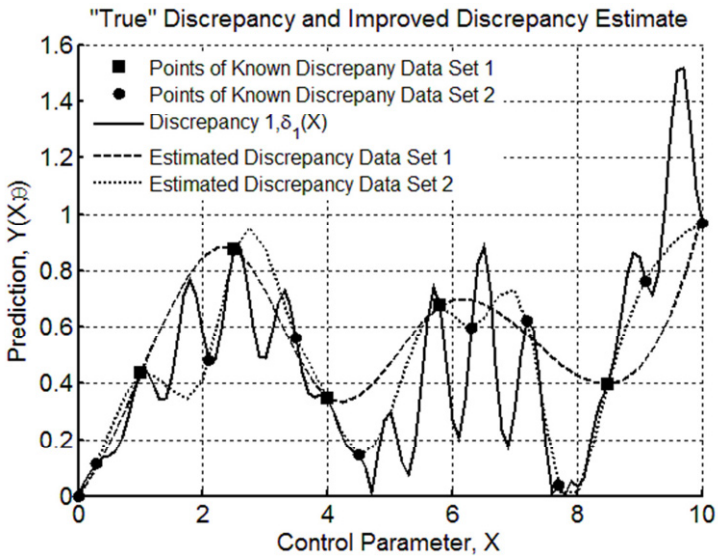

Figure 1: Comparison of discrepancy estimated using five and 15 experimental measurements to the 'true discrepancy.'

In Figure 1, the estimated discrepancy bias is compared against the model form error as the number of experimental data points are increased from five to 15. Figure 1 depicts that with 15 experiments, the

estimated discrepancy more closely predicts the model form error. Naturally, the fidelity of the estimated discrepancy bias to the "true" discrepancy will be increased if it is calibrated with more experimental data.

4 A FORECASTING METRIC FOR PREDICTIVE MODELING

In Section 2, the *discrepancy bias* is defined as the difference between the calibrated model predictions at the settings where experiments are available. At these settings, the discrepancy bias can be obtained with high fidelity. However, simulation models are rarely used to make predictions at settings where experiments are readily available. Therefore, to ensure the success of a certification campaign dominated by forecasts of simulation models, the focus must go beyond the discrepancy bias and consider the errors associated with forecasting that is executing simulation models to predict at settings where experiments are not available. Herein, we introduce a new term, *forecasting error,* known as the difference between the calibrated and bias corrected model solutions at settings where experiments are unavailable.

Knowing the true form of discrepancy function permits the full correction of bias errors. In reality however, the true form of discrepancy function will be unavailable and can only be estimated. Estimated discrepancy bias will inherently have inaccuracies, ultimately contributing to forecasting errors. However, because an increased number of experiments can better define the discrepancy function, the forecasting errors are reduced. Therefore, we use the term "forecasting error" as a forecasting metric to quantify the forecasting ability of a simulation model for a given set of experimental measurements. For this, when the simulation model is used in predictive forecasting, we consider an additional term to be added to Equation 1 to compensate for the inaccuracies in the model simulation caused by (1) the remaining model parameter uncertainties and (2) the remaining inaccuracies in the definition of the discrepancy function.

$$y_{obs}(x^f) = y_{sim}(x^f, \theta) + \delta(x^f) + \varepsilon(x^f) + E(x^f) \tag{3}$$

In Equation 3, x^f represents the settings at which the model is executed to forecast. $Y_{obs}(x^f)$ represents the truth observed at the settings of x^f. The surrogate model $y_{sim}(x^f,\theta)$ is a statistical process that supplies the model prediction, while the discrepancy term $\delta(x^f)$, also a statistical process, supplies the corresponding bias error. This calibrated and bias corrected statistical process model, therefore, yields our best possible estimate. This model is expected to successfully confine the experiments at the tested

settings of (x^t). These experiments are included in the process of tuning the parameters and training the functional form of the discrepancy bias. Therefore, the forecasting metric calculated at tested settings, $E(x^t)$, should be representative of the remaining uncertainty in the parameters and discrepancy bias. However, at settings other than x^t, this calibrated and bias corrected model will not maintain the same level of fidelity, the lack of which would be captured by the proposed forecasting error term.

Because simulation models as well as associated discrepancy bias are statistical processes, the forecasting error will be stochastic in nature. However, the forecasting error can be treated as a *metric* by aggregating uncertainties in various ways such as through the mean and standard deviation statistics, or the RMS norm. In a more conservative approach, the maximum forecasting error a simulation model yields while predicting multiple experiments can be used to determine the upper bound of forecasting metric. The way the forecasting errors are converted into a metric can be determined by the specific application, i.e. if the model is used to forecast a family of predictions with statistical relevance versus the model is exercised to predict at a single critical setting. In any treatment, as more experimental measurements become available to model calibration, the forecasting metric is expected to be reduced. In other words, provided the numerical model exhibits usefulness, either experimental campaigns can be concluded upon the quantification of predetermined acceptable forecasting error, or forecasting error can be quantified at the conclusion of strictly budgeted experimental campaigns. The following section discusses a case study which is a non-trivial, realistic application of the procedure.

5 DATA-RICH CASE STUDY: THE PRESTON-TONKS-WALLACE MODEL FOR TANTULUM

In this section, we illustrate the quantification and control of the forecasting metric for a simulation model that is accompanied with a rich experimental campaign. The Preston-Tonks-Wallace (PTW) model of plastic deformation represents plastic stress in a material as a function of strain, temperature, and strain rate [4]. The PTW model requires seven dimensionless material dependent parameters to be defined, which must be inferred from the experiments for every metal. Even though the PTW model is applicable to make predictions over a wide range of control parameter triplets, no single setting of these seven model parameters can identically reproduce multiple experimental datasets distributed over the domain of applicability. The discrepancy arises perhaps due to some underlying assumptions of the PTW model. The PTW model for instance, assumes plastic stress is independent of the history of material loading. Moreover, the PTW model ignores non-isotropic plasticity as well as the material texture effects.

In PTW model, control parameters that define the three-dimensional validation domain are the strain *(ε)*, temperature *(T)* and strain rate *(dε/dt)*. Symbols σ_S and σ_Y denote the dimensionless work hardening saturation stress and yield stress, respectively. The seven symbols θ, κ, γ, s_0, s_∞, y_0 and y_∞ are dimensionless, calibration variables that depend on the material analyzed.

5.1 PTW Model for Tantalum Metal

The six experimentally obtained strain-stress curves of the Tantalum material, each referred to as a dataset, are depicted in Figure 2. These datasets are conducted at varying control parameter settings indicated in Table 1. Each of these six datasets is subjected to a constant temperature and strain-rate, while strain is varied from zero to their maximum value yielding a stress-strain curve.

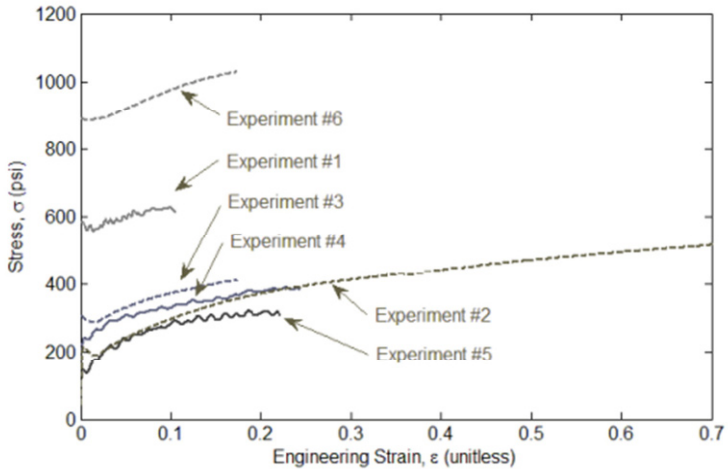

Figure 2: Experiments conducted at varying settings of temperature and strain rate.

Table 1: Settings of temperature and strain rate for the available experiments.

Data Set	n_i	Strain (max)	Temperature (K)	Strain Rate (s^{-1})
1	29	0.2433	298	1300
2	32	0.9757	298	0.001
3	10	0.1057	298	0.1
4	27	0.1737	673	2600
5	31	0.2218	1073	3900
6	31	0.1735	77	0.001

For tantalum metal, the definitions of these seven calibration parameters and the minimum/maximum bounds for each are provided in Table 2. We begin by inferring the parameter values for the seven dimensionless parameters (θ, κ, γ, $y0$, $y\infty$, $s0$, $s\infty$) and estimating the discrepancy bias of the PTW model. The procedure involves 10,000 Markov Chain Monte-Carlo (MCMC) runs exploiting the parameter ranges as defined in Table 2. The Bayesian inference is initiated with 500 runs at seven different levels. The GPM surrogates used to replace the PTW simulations are trained with a 100 run Latin Hypercube maxi-min design-of-computer-experiment.

Table 2: The upper and lower bounds of the seven Parameters of the PTW model.

Symbol	Description	Minimum	Maximum
θ	Initial strain hardening rate	2.78×10^{-5}	0.0336
κ	Material constant in thermal activation energy term (relates to the temperature dependence)	0.438	1.110
γ	Material constant in thermal activation energy term(relates to the strain rate dependence)	6.96×10^{-8}	6.76×10^{-4}
y_0	Minimum yield stress (at T = 0 K)	0.00686	0.0126
y_∞	Maximum yield stress (at T ≈ melting)	7.17×10^{-4}	0.00192
s_0	Minimum saturation stress (at T = 0 K)	0.0126	0.0564
s_∞	Maximum saturation stress (at T ≈ melting)	0.00192	0.00616

5.2 Investigation of Forecasting Error for PTW Model

The investigation of forecasting errors can be facilitated by excluding some of the available measurements, known as hold-out experiments, during calibration. Consider a PTW model which is calibrated and bias corrected with less than the available number of experimental measurements, thereby furnishing us with hold-out experiments. This calibrated and bias corrected PTW model constitutes our best possible estimate for the given amount of experiments. We can now attempt to predict the hold-out experiments by exploiting the availability of this best possible PTW model. The difference between the PTW forecasts and the hold-out experiments yields the forecasting error of this particular PTW model for a given number of calibration experiments.

One of the reasons that PTW models are especially suitable for the illustration of forecasting errors is the availability of a large number of measurements conducted at varying control parameter settings. The measurement points (n_i in Table 1) from all six datasets are combined to obtain a pool of 142 data points, constituting stress measurements and the associated value for strain, strain rate and temperatures. We

randomly select quadruples from this overall pool. The first batch uses only four measurements, that is, four stress values each associated with a triplet of control parameter values. The second batch is generated by randomly selecting eight measurements. The number of measurements that form the next measurement is increased, each time, by four. The 15^{th} and last batch counts a total of 60 data points.

Through a series of comparisons of PTW model predictions against experimental stress measurements conducted at varying settings of control parameters, we obtain the true values for discrepancy term at discrete settings. These discrete discrepancy values at these settings are then used to train the GPM emulator, which represents the discrepancy bias of the PTW simulations within the entire domain of applicability. Next, the calibrated and bias corrected PTW model is executed to forecast at some randomly selected hold-out experiment settings. The number of hold-out experiments is kept four experiments larger than those used in calibration to ensure that, in this random process, at least eight experiments are true forecasting predictions. A PTW model calibrated with four randomly selected measurements is used to forecast eight randomly selected hold-out experiments, while a PTW model calibrated with eight measurements is used to forecast twelve hold-out experiments, and so-on.

Since we are specifically interested in the trends of the forecasting errors as the number of experiments initially selected for the calibration is gradually increased, this procedure is repeated for each one of these 15 batches; for each batch the probability distribution of the forecasting error is determined. The forecasts of hold-out experiments are done with 2000 random draws from the 10,000 accepted random walks of MCMC. For these 2000 draws, the forecasting error is calculated as the difference between each of the stress values predicted by the calibrated and bias corrected PTW model and the measured stress value of that particular hold-out experiment.

If the experimental settings are decided solely based upon expert, yet arbitrary judgments, the obvious question to be determined involves the dependency of the forecasting errors to the sequence of selected experiments (i.e. path-dependency). Independent of the sequence in which the experiments are selected, we expect to see a consistent and monotonic reduction in the forecasting errors. However, it is plausible that the rate of this reduction may exhibit dependency to which experiments are selected from the pool. To reiterate, a lucky experimentalist may conduct the experiments in the optimum sequence and observe a very rapid reduction in forecasting error. An unlucky experimentalist may conduct the experiments in the least optimum sequence and observe a slow reduction in the forecasting error. Our approach at addressing the ‘luck factor’ is to treat the procedure as a random process and repeat both the

random selection of calibration experiments and the hold-out experiments 130 times. Therefore, a total of 1820 random estimates of forecasting errors are obtained. Figure 3 displays the results obtained as a result of this extensive simulation campaign.

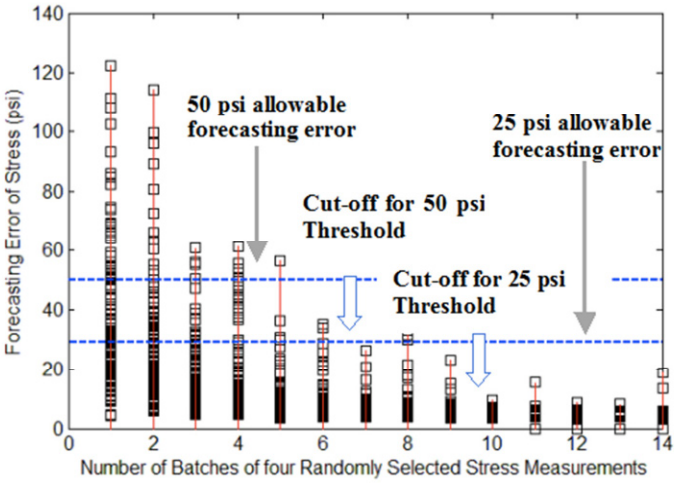

Figure 3: Forecasting errors as a function of number of experiments.

Regarding this example, let's say 50 psi is an acceptable forecasting error for a given application. Figure 3 illustrates that the sixth batch yields a forecasting error less than this allowable limit. To verify consistency, one or two more batches may be desirable. According to Figure 3, we can decide that a total of 6 batches, 24 experiments would be sufficient. At this stage, if a more stringent requirement must be imposed, say for instance a 25 psi threshold for the forecasting error, then additional experiments can be conducted until the forecasting errors are observed to be consistently lower than the allowable errors, which in our example corresponds to the 9^{th} batch. For these allowable forecasting errors, certification of an engineering system can be successfully accomplished by conducting a significantly fewer number of experiments.

6 CONCLUSION

Model-based certification heavily relies on simulation model solutions while determining the capacity of engineering systems. Several approaches to certification are proposed that depend on knowing the mean performance of the system. These methods lack a consideration of additional bias and uncertainty as a result of forecasting. However, certification would not be possible unless the forecasting

errors associated with capacity predictions are determined to be sufficiently low. This study suggests using a recursive strategy that builds upon the strengths of Bayesian statistical inference to assess the upper bounds of forecasting errors. In our approach, measurements are used to (1) improve the models through calibration, (2) assess the usefulness of the simulation model and (3) determine the forecasting errors. These three merits of the approach described in this paper are noteworthy.

Improve the models through calibratio

The strength of the adapted Bayesian calibration tool, GPM/SA comes from the inherent consideration of the parameter uncertainties (known unknowns) and the model form errors (unknown unknowns). For the case studies discussed herein, the prior probability distributions of the parameters are treated as uniform probability distributions. However, GPM/SA is not limited to uniform prior distributions and has the *a priori* capability to operate on other forms of probability density functions.

Assess the usefulness of the simulation model

If the physics or engineering phenomena modeled in a simulation model is not refined enough for certification purposes, the model fidelity cannot be improved through companion experimental campaigns and calibration efforts. Therefore, we consider assessing the usefulness of a simulation model for forecasting as the first necessary step in certification. For a given a simulation model and a companion set of experimental measurements, we formulated a simple approach to determine the usefulness of a simulation model to deliver solutions with sufficient fidelity.

Determine the forecasting errors

By exploiting the available experiments, we estimate an upper bound for forecasting errors. The forecasting error is considered as a metric providing a notion for the effects of uncertainty within the domain of applicability. Benefits of forecasting metric are two fold, for a given experimental budget the forecasting metric can quantify the errors associated with forecasting, secondly the forecasting metric will provide when the sufficient number of experiments have been performed to achieve desired level of forecasting fidelity (quantified error level).

With these assertions comes a caveat, however. While in this study, a non-zero discrepancy bias is considered as an indicator of missing physics, it may also be an indicator of inadequate numerical implementation. Within the scope of this manuscript, we will assume the *a priori* verification of simulation codes to produce converged solutions throughout the domain of applicability. Moreover, the concepts of zero or constant discrepancy bias would only be valid provided that the experiments are well spread to sufficiently explore the domain of applicability. This statement naturally leads to the following question: how much of the domain of applicability must be explored by the experiments? Reference [7] attempts to answer this question by investigating the influence of "coverage" on the predictive maturity of a simulation model.

It should be noted that the above-mentioned merits rely heavily on the decisions made to facilitate model calibration. Perhaps the first decision that must be made early in the process is defining the domain within which the system is expected to operate reliably and safely. This decision also constitutes the domain within which the simulation model is executed to make forecasts. Subsequent necessary steps include the selection of the appropriate model parameters for calibration. Therefore, completing thorough model-based sensitivity analysis, quantifying uncertainty and developing a Parameter Identification and Ranking Table are necessary requirements that must precede model calibration.

The approach described herein relies on a foundational premise: the physics or engineering principles involved in the application of the code remains unchanged when transitioning from tested to untested settings. This migration is best controlled by understanding the underlying phenomena and by exploring the domain of applicability through coverage (i.e. spreading the experiments to explore the domain of applicability). Therefore, a satisfactory understanding of underlying phenomena and a sufficient coverage of the domain of applicability with experiments are prerequisites for successful forecasting.

In the case study examples, the forecasting errors are calculated as the distance between a probability distribution and a scalar value. This approach can be further refined by taking the experimental variability into account.

BIBLIOGRAPHICAL REFERENCES

[1] M. Kennedy and A. O'Hagan, "Predicting the output from a complex computer code when fast approximations are available," *Biometrika*. 87 (2000) 1–13.

[2] D. Higdon, J. Gattiker, B. Williams and M. Rightley, “Computer model calibration using high-dimensional output,” *Journal of the American Statistical Association*. 103, 482 (2008) 570–583.

[3] D. Sornette, A.B. Davis, K. Ide, K.R. Vixie, V. Pisarenko and J.R. Kamm, “Algorithm for model validation: Theory and applications,” *Proceedings of the National Academy of Sciences*. 104, 16 (2007) 6562–6567.

[4] D.L. Preston, D.L. Tonks and D.C. Wallace, “Model of plastic deformation for extreme loading conditions,” *Journal of Applied Physics*. 220 (2003) 93–211.

[5] R.A. Lebensohn, C.S. Hartley, C.N. Tomé and O. Castelnau: "Modeling the mechanical response of polycrystals deforming by climb and glide". Philosophical Magazine, in press.

[6] M.B. Toloczko, F.A. Garner, and S.A. Maloy, “In-reactor Creep of Two Heats of T91 (Modified 9Cr-1Mo) from ~400°C to 600°C,” Los Alamos National Laboratory Technical Report. (2009)

[7] F., Hemez, S., Atamturktur, C., Unal, “Predictive Maturity of Validated Numerical Models,” *Computers and Structures Journal*. 88 (2010) 497–505.